Small-scale Physical and Chemical Structure of Diffuse and Translucent Molecular Clouds along the Line of Sight to the Galactic Center

Dissertation

zur

Erlangung des Doktorgrades (Dr. rer. nat.)

der

Mathemathisch-Naturwissenschaftlichen Fakultät

der

Rheinischen Friedrich–Wilhelms–Universität, Bonn

vorgelegt von

Vivien THIEL

aus

Bonn, Deutschland

Bonn 2018

Angefertigt mit Genehmigung der Mathematisch-Naturwissenschaftlichen Fakultät der Rheinischen Friedrich–Wilhelms–Universität Bonn
Prepared with the permission from the Faculty of Mathematics and Natural Sciences of the University of Bonn

1. Referent: Prof. Dr. Karl M. Menten
2. Referent: Prof. Dr. Pavel Kroupa
Tag der Promotion: 14. März 2019
Erscheinungsjahr: 2019

Diese Dissertation ist auf dem Hochschulschriftenserver der ULB Bonn unter
http://hss.ulb.uni-bonn.de/diss_online elektronisch publiziert

Abstract

Diffuse and translucent molecular clouds constitute a large part of the molecular interstellar medium (ISM) in our Galaxy as well as in other spiral galaxies. In particular, the envelopes of giant molecular clouds (GMCs), which host star forming regions, consist of lower density diffuse and translucent media. Hence, observational studies of diffuse and translucent molecular clouds help to improve our knowledge about their important role in the formation of dense clouds and their interaction with the rest of the ISM.

For this project, we used absorption data from various molecules obtained by the Exploring Molecular Complexity with ALMA (EMoCA) interferometric spectral line survey performed with the Atacama Large Millimeter/submillimeter Array towards the prominent GMC Sagittarius B2 (Sgr B2). This survey allows us to investigate the variations in abundance and isotopic composition for many molecules as a function of galactocentric radius from the region surrounding the Galactic center out to the Solar circle. It also allows us to probe the kinematical properties of individual clouds. This project improves our understanding of the small-scale physical and chemical structure of a sample of diffuse and translucent molecular clouds.

On the basis of data from HCO^+ , we conclude that most line-of-sight clouds towards Sgr B2 are translucent. We also find that CCH and CH are good probes of H_2 in both diffuse and translucent clouds.

The chemical content of diffuse and translucent molecular clouds is similar. We find that the column densities of CH_3OH, SiO, and SO are well correlated and we propose that these molecules trace shocked gas. A second group of correlated species (CCH, HCN, HNC, CS, and CN) likely traces quiescent components.

The spatial structure of the line-of-sight clouds is found to be relatively homogeneous on scales smaller than the extent of the background continuum source (15 arc seconds, that is 0.08 to 0.6 parsec depending on the distance). Our analysis of the column density maps suggests that the driving of clouds' turbulence is mainly solenoidal, which produces small density contrasts and could explain the spatial homogeneity of these clouds.

For many molecules, we also detect lines from some of their less abundant isotopologues. In particular, we report a direct measurement of the $^{14}N/^{15}N$ isotopic ratio in the envelope of Sgr B2. So far, the Galactic center value of this ratio had been poorly known. The value we determine, 350 ± 50, is consistent with that extrapolated from previous measurements at larger galactocentric radii.

We report the detection of four complex organic molecules (COMs) in clouds of the Galactic Center (GC) region and of two COMs in the translucent clouds associated with the Scutum arm of the Galaxy. The COM composition of one of the translucent GC clouds is found to be similar to that of the extremely well-studied diffuse/translucent ISM of a spiral galaxy at redshift $z = 0.89$ seen in absorption in front of PKS 1830–211. This suggests that the processes leading to chemical ISM complexity have remained similar for more than half the age of the Universe. The presence of COMs in the translucent molecular clouds may result from a cyclical interstellar process of cloud contraction and expansion between diffuse and dense states.

Acknowledgements

Now as the journey of writing my PhD-thesis comes to an end, I want to thank everyone who accompanied me on this way. Without the continuous support of many people during that time this work would not have been possible.

First of all, I would like to thank Prof. Dr. Karl M. Menten for giving me the opportunity to write my PhD-thesis in his working group at the MPIfR. It would have been difficult to complete this thesis without his support, he gave me over the last few years. I have enjoyed to work in his group and I am very grateful for all the opportunities he gave me to travel to conferences, Summer Schools or observatories.

A special thanks goes to my day-to-day advisor Dr. Arnaud Belloche, for his kind supervision, encouragement and the advices he provided me over all the time as his PhD student. I was glad to have a supervisor who always had open ears and time for me. I would like to thank him for the steady support and the continuous and constructive feedback.

I would also like to thank Prof. Dr. Pavel Kroupa, who kindly agreed to be the second referee of my thesis. Furthermore, thanks to Prof. Dr. Ian C. Brock and Prof. Dr. Hubert Schorle for joining the PhD examination committee.

I am also very grateful to Dr. Helmut Wiesemeyer and Dr. Andrea Giannetti for their interest in my thesis, their support, and for proof-reading my thesis and giving me constructive feedback.

I would also like to thank Dr. Benjamin Winkel for his support as part of my Thesis Advisory Committee.

Furthermore, I am grateful to the International Max Planck Research School for Astronomy Astrophysics (IMPRS) for their guidance, supporting seminars, the nice atmosphere and community.

I would like to say thank you to my colleagues in the millimetre/submillimetre group and in the IMPRS for their support, their encouragement and the nice working atmosphere during the last few years. Thanks to my office mates through all the time I have spend here for the very friendly climate in the office. A special thanks goes to Melisse Bonfand for the many motivating tea breaks. Thanks to Melisse Bonfand and Arshia Jacob for the motivation Monday cakes which have made the last weeks of writing my thesis much easier.

I also want to thank my family and all my other friends, who always believed in me and support me all the time during my PhD. I want to thank my parents, who raised me to believe that I can do anything what I want and who always supported me on my way. A special thanks to my friend Hannah Hoffmann for her help and the long phone calls giving me motivation. And thanks to my brother who always made me laugh also in difficult situations.

I want to give a very special thank to my partner, Sebastian Werner. His steady support, belief in me and his encouragements have been given me the motivations and strengths needed to finish my PhD project. He is my anchor.

List of publications related to the PhD thesis "Small-scale Physical and Chemical Structure of Diffuse and Translucent Molecular Clouds along the Line of Sight to the Galactic Center", Vivien Thiel

1. **Complex organic molecules in diffuse clouds along the line of sight to Sgr B2**
   Thiel, V., Belloche, A., Menten, K. M., Garrod, R. T., and Müller, H. S. P. 2017, A&A, 605, L6.
   DOI: 10.1051/0004-6361/201731495 [arXiv:1708.07292]

2. **Small-scale physical and chemical structure of diffuse and translucent molecular clouds along the line of sight to Sgr B2**
   Thiel, V., Belloche, A., Menten,K. M., Giannetti, A., Wiesemeyer, H., Winkel, B., Gratier, P., Müller, H. S. P., Colombo, D., and Garrod, R. T., submitted to A&A

Contents

Chapter 1

Introduction

Contents

1.1 The interstellar medium

About 10 per cent of the mass of our Galaxy consists of interstellar medium (ISM). The ISM is made of a mixture of gas and dust particles filling up the space between the stars. The stellar component dominates the baryonic mass in spiral galaxies like the Milky Way (MW) with about $10^{11}\,M_\odot$. The mass of the gas is one order of magnitude and the mass of the dust is three orders of magnitude smaller than the mass of the stellar component (see e.g. Magnani & Shore 2017). In the ISM different gas phases exist, cold and dense, and diffuse and warm (Draine 2011). The densities range from 10^{-3} to $10^{7}\,\mathrm{cm}^{-3}$. The temperatures are between 10 K and 10^7 K. The differences between the phases are not only caused by these physical properties, but also by the distribution, the volume filling factor, the morphology, the physical processes and the interaction with the stellar component. The ISM can be divided into the hot ionised medium (HIM), the warm ionised medium (WIM), the warm neutral medium (WNM) and the cold neutral medium (CNM, see e.g. Draine 2011; Magnani & Shore 2017). The order corresponds to a decrease in temperature and an increase in density. Molecular clouds which are associated with the CNM have high enough densities and low enough temperatures to form molecules. Giant molecular clouds (GMCs) have masses larger than $10^5\,M_\odot$, median sizes of 40 pc and in the densest parts temperatures of about 10 K (Magnani & Shore 2017, and references therein).

The ISM and especially the molecular clouds play a key role in the life cycle of stars (see Fig. 1.1) and in the evolution of galaxies. Stars are formed in dense cores of GMCs. During their evolution, stellar winds give matter back to the ISM, maybe enhanced with atoms up to iron. At the end of their life, stars evolve differently depending on their mass. High-mass stars explode in supernova explosions resulting in supernova remnants. In contrast, low-mass stars return material to the ISM in the form of planetary nebulae.

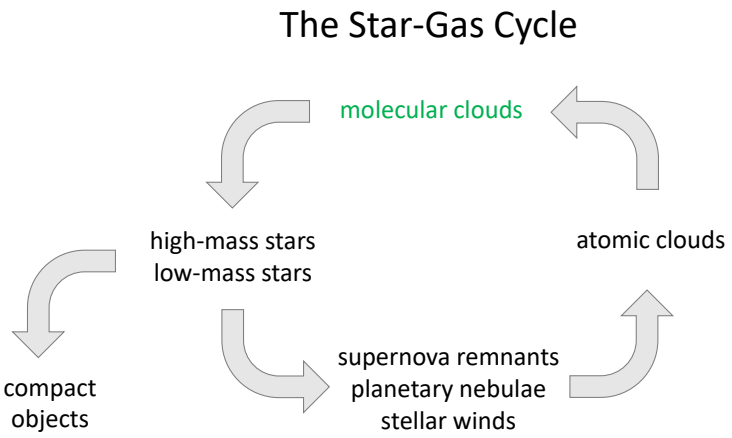

Figure 1.1: The life cycle of stars and gas, based on Figure 1.1 of Magnani & Shore (2017). The stellar winds represent the material ejected during the lifetime of a star. Supernova remnants and planetary nebulae are the leftovers of stars at the end of their life which may contain compact objects.

This hot gas or a fraction of it ejected from stars by stellar winds or ejected at the end of a star's lifetime can cool down to cold neutral medium. A part of the CNM evolves into molecular clouds. Under the correct circumstances involving gravity, turbulence, and magnetic fields, dense molecular clouds can form and collapse; the star formation process starts and the star-gas life cycle repeats.

1.2 Molecular clouds

1.2.1 Physical properties

The physical conditions of molecular clouds divide them into three categories: dense, translucent and diffuse molecular clouds (Snow & McCall 2006, and references therein). The transitions between these different types of clouds are smooth. The density of dense molecular clouds is high enough to protect their inner parts from UV radiation that would otherwise dissociate molecules. On the contrary, the density of diffuse molecular clouds is low enough to result in a stronger exposure to this radiation which often results in lower abundances of molecules. The transition regions between dense and diffuse molecular clouds are filled by translucent molecular clouds. In contrast to dense molecular clouds, these are not completely shielded against UV radiation. Usually, molecular clouds consist of a mixture of all these three types.

Dense molecular clouds have kinetic temperatures[1] between about 10 K and 50 K. In translucent molecular clouds, the kinetic temperature is higher than about 15 K and in diffuse molecular clouds it ranges between about 30 K and 100 K. The total hydrogen densities n_{H}[2] are typically $> 10^4\,\mathrm{cm}^{-3}$, $500 - 5000\,\mathrm{cm}^{-3}$ and $100 - 500\,\mathrm{cm}^{-3}$, respectively. Usually, diffuse molecular clouds have visual extinction A_{V}[3] below 1 mag. A_{V} in translucent molecular clouds is higher than 1 mag and lower than 5 mag, the lower limit for dense molecular clouds (van Dishoeck & Black 1988; Snow & McCall 2006; Magnani & Shore 2017, and references therein). The transition between diffuse atomic and diffuse molecular clouds lies at a total hydrogen

[1] The kinetic temperature is a measure of the energy of the thermal motion in the gas within a cloud.

[2] Hydrogen is by far the most abundant atom in the ISM. Hence, n_{H} represents the total density with $n_{\mathrm{H}} = n(\mathrm{HI}) + 2n(\mathrm{H_2})$. $\mathrm{H_2}$ is the molecular and HI the atomic hydrogen.

[3] The visual extinction describes the absorption and scattering of electromagnetic radiation in the optical wavelength regime in these clouds. A higher value corresponds to a higher column density of the cloud.

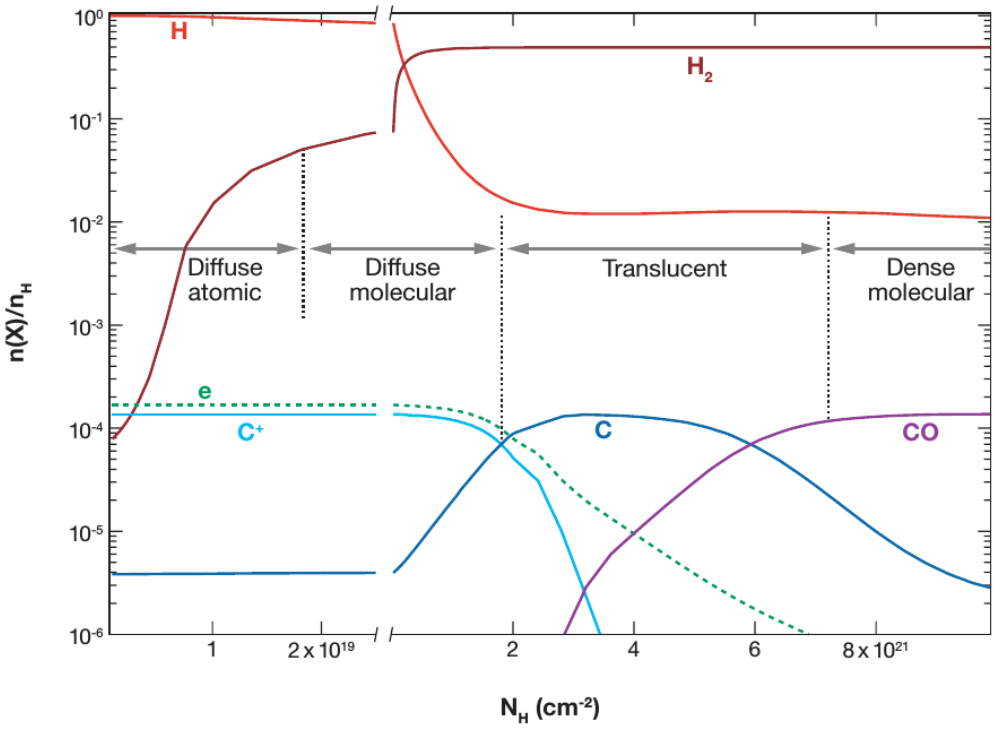

Figure 1.2: Illustration of the definition of molecular cloud types, based on the results from a photodissociation region model from Neufeld et al. (2005). Figure taken from Snow & McCall (2006).

column density[4] of $N_{\mathrm{H}} \approx 10^{19}\,\mathrm{cm}^{-2}$ and the one to translucent molecular clouds at about $2 \times 10^{21}\,\mathrm{cm}^{-2}$ (see Fig. 1.2). These thresholds are only definitions and to separate what in reality is very smooth. Another definition is based on the molecular fraction[5], which is almost 1 in dense and translucent molecular clouds and lower for diffuse molecular clouds. Liszt et al. (2010) determined diffuse molecular clouds to have a molecular fraction of at least 25% up to values close to 1 (see Fig. 1.2). In this thesis, we focus mainly on the diffuse and translucent molecular clouds, the transition between the atomic clouds and the dense molecular clouds.

1.2.2 Diffuse and translucent molecular clouds

The main difference between diffuse and translucent molecular clouds in comparison to dense molecular clouds is the fact that they are not self-gravitating. Their structure and the dynamics of these clouds seem to be dominated by turbulence. The short lifetime (10^6 yr) of the diffuse and translucent molecular clouds makes them transient structures, whose behaviour in the formation and dissipation is comparable to smoke (Magnani & Shore 2017, and references therein).

A large part of the molecular clouds in the ISM in our galaxy as well as in other spiral galaxies consists of diffuse and translucent molecular clouds. The interarm regions in these spiral galaxies are thought to be filled by these clouds as a main component (Sawada et al. 2012). Diffuse molecular clouds are not confined

[4]The column density of a molecule is defined as the number of molecules per unit area summed up along the line of sight.

[5]The molecular fraction describes the fraction of molecular hydrogen with respect to the full hydrogen content in the clouds: $f_{\mathrm{H_2}} = \frac{2n(\mathrm{H_2})}{n_{\mathrm{H}}}$.

to the thin disk of a spiral galaxy which contains the spiral arms, but also in a thick diffuse disk to a much larger height above the galactic disk, as detected in M51 (Pety et al. 2013). This thick disk may also be present in other spiral galaxies. Besides the large volume filling factor, diffuse and translucent molecular clouds form the envelopes of giant molecular clouds (GMCs) which host star forming regions. Hence, the observation and investigation of diffuse and translucent molecular clouds help to improve our knowledge about their important role in the interaction between stars and the surrounding gas (e.g., Arnett 1971).

1.2.3 Absorption lines

The best way to probe such clouds is to observe them in absorption in the direction of continuum sources in the optical/UV, IR, millimetre or submillimetre wavelength regimes (Snow & McCall 2006). In this thesis we focus on the millimetre wavelength regime. The low densities in diffuse and translucent molecular clouds result in low excitation temperatures[6]. For most molecular transitions, the excitation temperature is close to the temperature of the cosmic microwave background (CMB) radiation, which is equal to 2.73 K (Greaves et al. 1992). As a result, the transition lines are subthermally[7] excited and thus very weak in emission. As a result, it is difficult to detect them in emission and much easier to trace them in absorption towards bright background continuum sources.

1.2.4 Rotational transitions

The absorption lines that we see in the millimetre wavelength regime are rotational transitions of molecules. These rotational transitions are caused by a change in angular momentum. A molecule can only have discrete rotational energy states. These discrete quantum mechanical energy states depend on the species of molecule. The frequencies of the resulting spectral lines we observe in the spectra in absorption are unique for each molecule which makes rotational spectroscopy an important tool to investigate the chemical content of the ISM. A molecule has to be polar[8] to interact with microwave radiation, in our case to absorb the radiation. Homo-nuclear diatomic molecules such as O_2 or H_2 do not have a dipole moment and, hence, no pure rotational spectrum.

1.3 Central molecular zone

The central molecular zone (CMZ) describes the inner ~500 pc of our Galaxy. The clouds around the supermassive black hole (SMBH) Sgr A* (see Fig. 1.3) contain about 10% of the ISM gas reservoir of the Milky Way. The molecular gas has a mass of about 2–6×10^7 $M_\odot$ and densities higher than 10^4 cm^{-3} (Morris & Serabyn 1996; Molinari et al. 2014, and references therein). Many remarkable GMCs and star forming regions are located in the CMZ. The GMC population in the CMZ differs from the GMCs in the disk in several points. For example, the mean density is about 1–2 orders of magnitude higher (e.g. Longmore et al. 2013; Kruijssen et al. 2014). Hence, many molecules such as HCN, HCO^+, and HNCO are detected everywhere in the CMZ (e.g. Dahmen et al. 1998; Ferrière et al. 2007; Jones et al. 2012). Furthermore, the linewidth of the CMZ GMCs are larger (e.g. Shetty et al. 2012). Almost all star formation of the CMZ occurs within the central 100 pc. The molecular gas is not symmetrically distributed around the Galactic center. One third of the emission can be found at negative longitudes and two thirds at positive longitudes

[6]The population of an excited state of an atom or a molecule can be described by the excitation temperature (see Eq. 2.22).
[7]The excitation temperature is lower than the kinetic temperature.
[8]A polar molecule has a non-zero electric dipole moment.

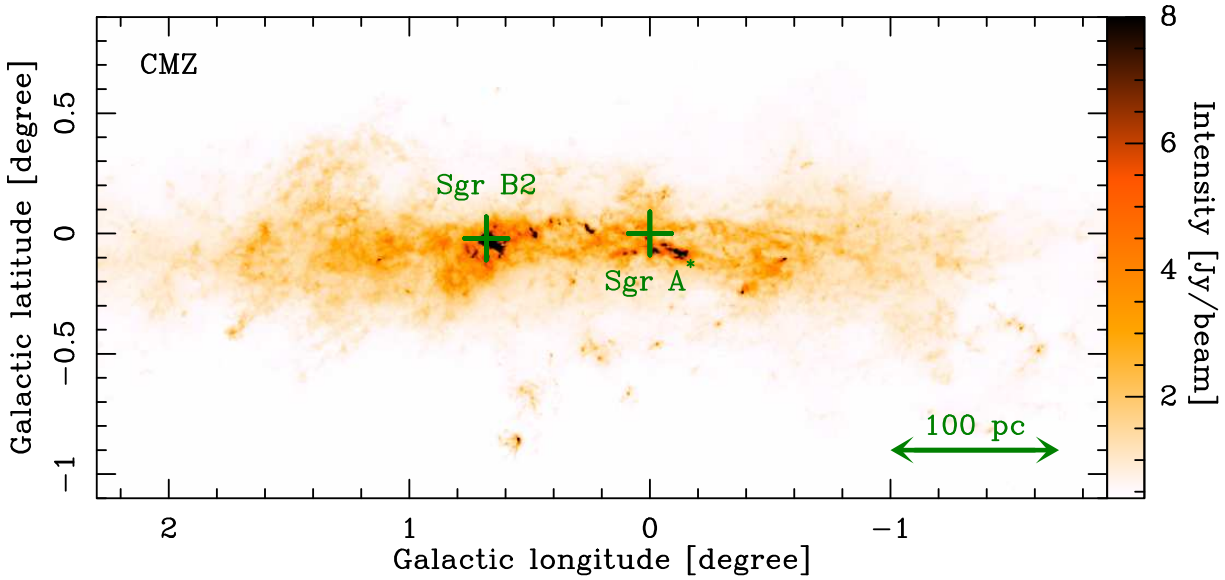

Figure 1.3: Central molecular zone. A combination of ATLASGAL/LABOCA (observed at 870 micron) and Planck dust continuum data (Csengeri et al. 2016).

(e.g. Jones et al. 2012; Henshaw et al. 2016). A very interesting GMC is located at a longitude of about 0.7°, the GMC Sagittarius B2 (see Fig. 1.3).

1.4 GMC Sagittarius B2

For this project, we chose the GMC Sagittarius B2 (Sgr B2) because it is one of the most massive star forming regions in our galaxy and, consequently, emits strong continuum emission throughout the radio and (sub)millimetre wavelength regimes, which makes it an excellent background source for absorption studies. Sgr B2 is located at a projected distance of 100 pc away from the GC, the supermassive blackhole Sgr A*. The GC has a distance of 8.34 ± 0.16 kpc to the sun (Reid et al. 2014). The two main star formation cores are Sgr B2(M) and Sgr B2(N) where M stands for main and N for north (see Fig. 1.4). They are separated by about 45″ (1.9 pc). Next to the main hot cores N1 and N2, Sgr B2 contains several smaller hot cores (Bonfand et al. 2017; Sánchez-Monge et al. 2017) and H II regions (Mehringer et al. 1993; Gaume et al. 1995; De Pree et al. 1998, 2015) that are embedded in a diffuse envelope. The total diameter of Sgr B2 is about 40 pc and its mass is about $10^7 M_\odot$ (Lis & Goldsmith 1990).

The continuum emission of Sgr B2 observed in the millimetre wavelength range consists of free-free radiation and thermal dust emission (e.g., Liu & Snyder 1999). The strong continuum structure of Sgr B2(N) has a size of about 20″. This extended background source gives the great opportunity to study the spatial structure of the diffuse and translucent clouds located along the line of sight on sub-parsec scales. The line of sight to Sgr B2 passes not only the envelope of Sgr B2, but also the Sagittarius, Scutum, 3 kpc, and 4 kpc arms, as well as the Galactic center (GC) clouds up to a distance of about 2 kpc from the GC (e.g., Greaves & Williams 1994; Menten et al. 2011, see Fig. 1.5).

1.5 Molecules in the ISM

Liszt & Wilson (1993) and Liszt (1994) started with a systematic investigation of the molecular content in

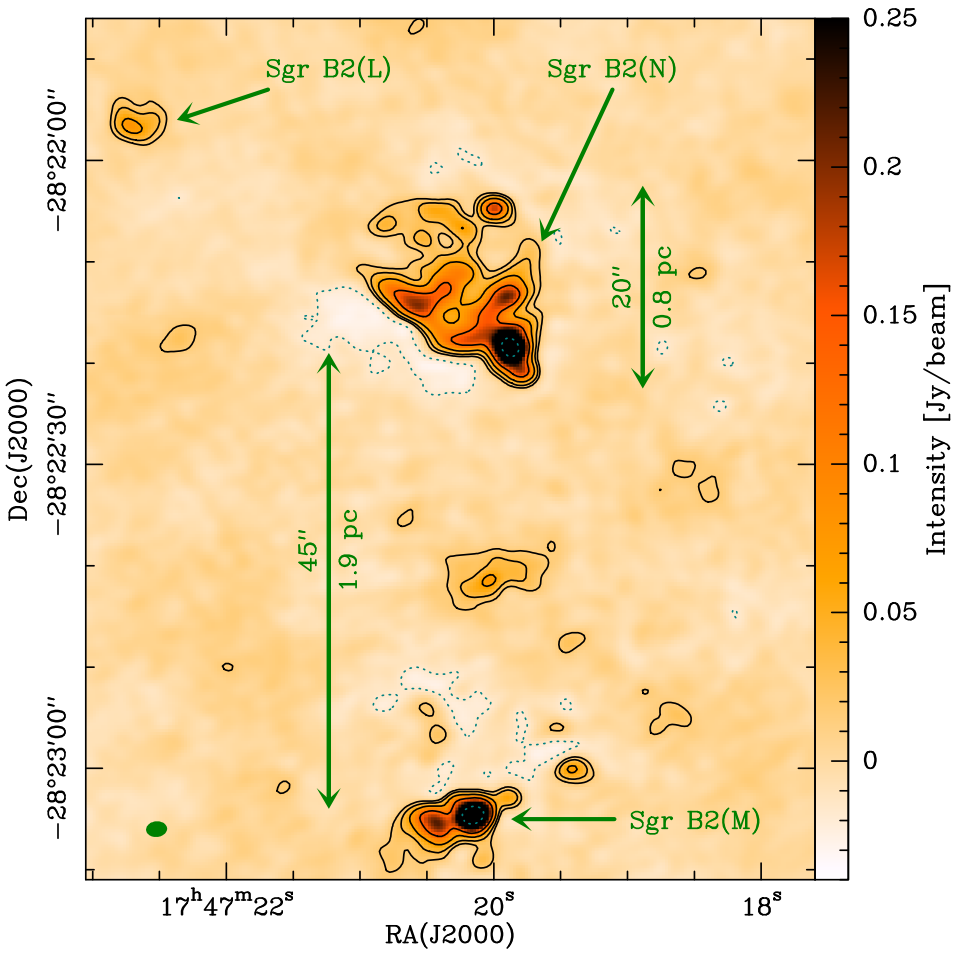

Figure 1.4: Structure of Sagittarius B2: ALMA continuum map at 85 GHz from the EMoCA survey.

diffuse and translucent molecular clouds located in our galaxy. They identified more than 20 lines of sight towards millimetre-wave background sources where carbon monoxide (CO) absorption was detectable. In many following papers, they studied the molecular properties of these clouds in absorption and also emission. They found several other molecules as for example HCN, H_2CO, CH , CCH, and c-C_3H_2 (e.g. Lucas & Liszt 1996, 2000; Liszt & Lucas 2002). As seen in further investigations, the molecules detected in the diffuse clouds in our galaxy are mostly fairly simple molecules like CN, HCN, CCH, HCO^+ or c-C_3H_2 (e.g. Lucas & Liszt 1997; Godard et al. 2010). Hence, the question comes up whether more complex molecules also exist in galactic diffuse and translucent molecular clouds, in which the extinction and the density is relatively low. Up to now, about 200 different molecules have been detected in the ISM[9]. The carbon-bearing molecules which consist of at least six atoms are called complex organic molecules (COMs). Usually, these molecules are detected in dense environments such as for example cold prestellar cores and hot cores or corinos (Herbst & van Dishoeck 2009). The detection is mostly made based on emission lines, but several have also been detected in absorption. The envelope of Sgr B2 contains several COMs seen in absorption (Corby et al. 2015). Not only dense environments are the sources where COMs have been detected. They are also detected in photodissociation regions (PDRs) like the Horsehead nebula (Guzmán et al. 2014) and in absorption in a $z = 0.89$ spiral galaxy (Muller et al. 2011, 2014). The chemical composition concerning

[9]see, e.g. McGuire (2018), https://www.astro.uni-koeln.de/cdms/molecules

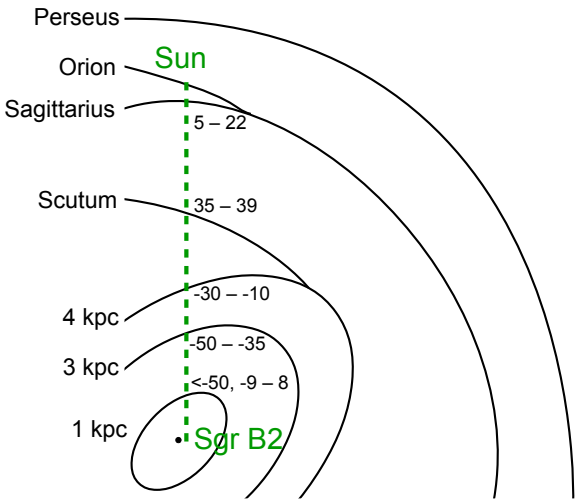

Figure 1.5: Sketch of the Milky Way and the spiral arms along the line of sight to Sgr B2 (based on Greaves & Williams 1994). The velocity ranges of the diffuse and translucent clouds are indicated in km s^{-1}.

simple molecules of the medium in the $z = 0.89$ spiral galaxy traced with the absorption lines suggest that it is consisting of diffuse or translucent molecular clouds. Hence, we may also see COMs in the galactic diffuse and translucent molecular clouds investigated here.

1.6 Motivation

Previous absorption line studies with the aim to investigate diffuse and translucent molecular clouds were performed with single-dish telescopes such as the IRAM 30 m or Herschel telescopes (e.g., Lucas & Liszt 1996; Gerin et al. 2010a; Monje et al. 2011). Many studies focused on the clouds along the line of sight to Sgr B2(N) and Sgr B2(M) (e.g., Greaves & Williams 1994; Neufeld et al. 2000; Polehampton et al. 2005; Lis et al. 2010; Monje et al. 2011; Corby et al. 2015, 2018). But most of these observations do not have the angular resolution to investigate the small-scale physical properties of diffuse and translucent molecular clouds. For instance, Corby et al. (2018) used the Green Bank Telescope to investigate the molecular content of the line of sight to Sgr B2. The angular resolution of their data is between 13′ and 15″. The continuum structure of Sgr B2 is with 20″ (see Fig. 1.4) only slightly larger than their smallest resolution. Using interferometers such as ALMA (Atacama Large Millimeter/submillimeter Array), the investigation of the small-scale structure becomes possible. Corby et al. (2015) observed Sgr B2(N) with the interferometer ATCA (Australia Telescope Compact Array) between 30 and 50 GHz with an angular resolution of 5–10″. They focused their analysis on the envelope of Sgr B2 and its hot cores, and did not have much resolution elements to explore the spatial structure of the line-of-sight clouds. The molecular line survey EMoCA (*Exploring Molecular Complexity with ALMA*) available for this work (Belloche et al. 2016) has an angular resolution and a sensitivity higher by more than one order of magnitude compared to a previous survey carried out with the IRAM 30m telescope (Belloche et al. 2013). The spatial resolution of this ALMA survey is by a factor 3–6 higher than the ATCA survey (Corby et al. 2015). Hence, this interferometric survey performed with ALMA offers the opportunity to study the diffuse and translucent medium at unprecedented angular resolution and sensitivity. The ALMA survey covers the frequency range from 84.1 to 114.4 GHz at an angular resolution of about 1.6″. Many important as well as abundant molecular species have transitions in this frequency regime that are suitable for absorption studies. Therefore, this unbiased line survey

provides an excellent opportunity to study molecular and isotopic abundances not only on sub-parsec scales in Sgr B2 itself, but also along the whole 8 kpc long line of sight to the Galactic center (see Fig. 1.5).

In summary, this survey will allow us to investigate the variations in abundance and isotopic ratios for many molecules as a function of Galactocentric radius from the Galactic center to the Solar circle. It will also probe the kinematics and turbulence of individual clouds using linewidth and velocity centroid information. This project is expected to improve our understanding of the small-scale physical and chemical structure of a significant sample of diffuse and translucent molecular clouds.

1.7 Outline of the Thesis

This thesis is structured as follows. In Chapter 2 we describe the data used in this work and the analysis methods. The chemical diversity and physical properties of molecules detected in the clouds along the line of sight towards six positions in Sgr B2 are discussed in Chapter 3. We describe the selected sample of positions and the detected molecules. Afterwards, we investigate the velocity structure based on column density profiles of the 12 molecules that show the strongest signals: HCO^+, CCH, c-C_3H_2, ^{13}CO, CS, CN, SiO, SO, HCN, HNC, N_2H^+, and CH_3OH. In addition, we discuss isotopic ratios for and the correlations between these twelve molecules. The COMs detected in the spectra towards the ultracompact H II region K4 in Sgr B2(N) are investigated further in Chapter 4. In Chapter 5, we focus on absorption in front of the extended continuum structure of Sgr B2(N) to investigate the spatial structure of the line-of-sight clouds. We investigate the velocity structure across the field of view by automatically fitting synthetic spectra to the detected absorption features to identify individual line-of-sight clouds. Based on opacity maps of several molecules we investigate the spatial and kinematical structure of the identified clouds. We use statistical methods and investigate the correlations between the molecules using a principal component analysis. We finish this chapter with an investigation of the nature of the line-of-sight clouds towards Sgr B2. In the last Chapter (6) we will combine the results from the three previous chapters in an overview.

CHAPTER 2

Observations and Analysis Methods

Contents

Abstract

In this chapter we describe the data we use for our analysis. Before modelling the spectra several steps have to be performed. We describe this procedure and in addition the theory behind the analysis, the radiative transfer equation. Afterwards, we describe the analysis of the parameters we obtain from the fit of the synthetic spectra. Because we used additional data and additional analysis methods only in chapter 5, they are described in Sect. 5.2 and Sect 5.3, respectively.

2.1 Observations

We use data from the Atacama Large Millimeter/submillimeter Array (ALMA) for our analysis. ALMA is an interferometer consisting of several dozens of telescopes. To investigate the molecular content and spatial structure of the line-of-sight clouds in the direction of Sgr B2, we analyse the absorption lines which are detected in the EMoCA (*Exploring Molecular Complexity with ALMA*) survey (Belloche et al. 2016). This spectral line survey aims to explore and expand our knowledge of the chemical complexity of the interstellar medium. It was performed in the direction of Sgr B2(N) with ALMA in Cycles 0 and 1[1]. The phase centre[2] of the survey is located half way between the two main hot cores N1 and N2 in Sgr B2(N) at EQ J2000: $17^{h}47^{m}19.87^{s}$, $-28°22'16''$. The survey covers the frequency range from 84.1 to 114.4 GHz with a spectral resolution of 488 kHz (1.7 to 1.3 km s^{-1}). The five different observed setups are shown in

[1] Cycle 0: 2011–2013, Cycle 1: 2013–2014.
[2] Centre of observation.

Table 2.1: Observational setups of the EMoCA survey.

Setup	Frequency range		Date of	N_a[c]	Baseline	t_{int}[e]
	LSB[b]	USB[b]	observation		range[d]	
	[GHz]	[GHz]	yyyy-mm-dd		[m]	[min]
S1	84.1–87.8	96.2–99.8	2012-08-27	26	17–400	54.7
S2	87.7–91.4	99.7–103.4	2012-09-28	25	20–387	44.1
S3[a]	91.4–95.1	103.4–107.1	2012-06-06	18	15–395	40.2
			2012-06-18	22	15–395	40.4
S4[a]	95.0–98.7	107.0–110.7	2012-07-04	21	17–398	8.1
			2012-08-01	24	19–442	34.9
			2012-08-10	26	21–400	35.0
S5	98.7–102.4	110.7–114.4	2014-04-05	38	15–413	24.4

Notes. Based on Table 1 of Belloche et al. (2016). [(a)] Observations are merged for these setups. [(b)] Lower sideband and upper sideband. [(c)] Number of ALMA 12 m antennas. [(d)] Minimum and maximum projected baseline separations. [(e)] On-source integration time.

Table 2.2: Synthesised beam sizes and noise levels.

Setup	SPW[a]	Frequency range	$HPBW$[b]	$P.A.$[c]	rms[d]	
		[MHz]	[″] × [″]	[°]	[mJy beam^{-1}]	[K]
S1	0	84091 – 85966	2.1 × 1.5	−85	3.0	0.16
	1	85904 – 87779	2.0 × 1.5	−83	2.7	0.14
	2	96154 – 98029	1.8 × 1.4	−85	3.0	0.16
	3	97904 – 99779	1.8 × 1.3	−85	3.1	0.16
S2	0	87729 – 89604	1.9 × 1.7	86	3.1	0.15
	1	89554 – 91429	1.8 × 1.6	52	2.8	0.15
	2	99728 – 101602	1.6 × 1.4	48	2.7	0.14
	3	101552 – 103427	1.6 × 1.4	49	2.7	0.14
S3	0	91368 – 93242	2.9 × 1.5	84	3.4	0.12
	1	93193 – 95067	2.8 × 1.5	83	3.1	0.10
	2	103365 – 105239	2.5 × 1.3	82	3.4	0.11
	3	105189 – 107064	2.5 × 1.3	82	3.6	0.12
S4	0	95021 – 96896	1.9 × 1.4	−82	1.9	0.10
	1	96846 – 98720	1.8 × 1.3	−82	1.9	0.10
	2	107019 – 108893	1.7 × 1.2	−83	2.2	0.11
	3	108843 – 110718	1.6 × 1.2	−82	2.3	0.12
S5	0	98672 – 100546	1.8 × 1.4	−76	2.8	0.14
	1	100496 – 102370	1.7 × 1.4	−76	2.7	0.13
	2	110669 – 112543	1.6 × 1.3	−72	3.5	0.17
	3	112494 – 114368	1.6 × 1.2	−77	4.9	0.24

Notes. Based on Table 2 of Belloche et al. (2016). [(a)] Spectral window. [(b)] Half Power Beam Width. [(c)] Position angle east from north. [(d)] Median rms noise level measured in the channel maps of the continuum-removed data cubes.

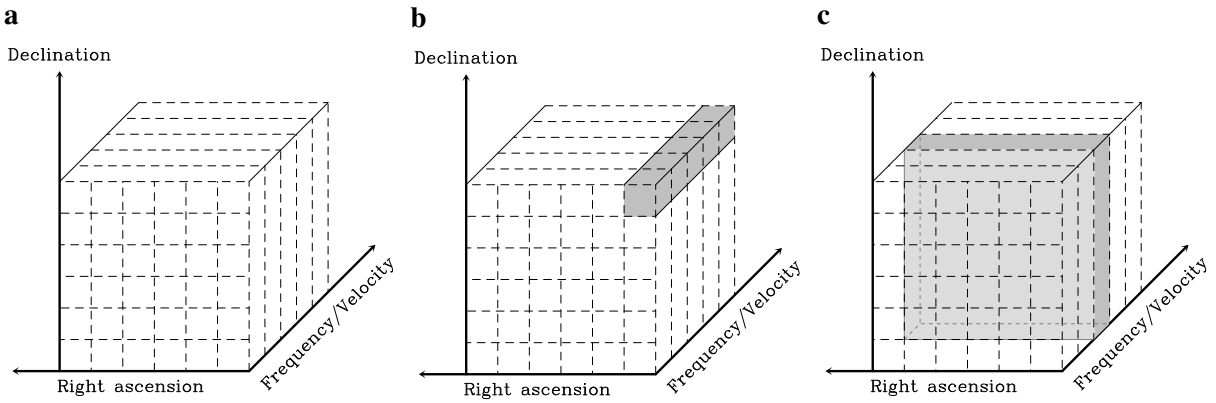

Figure 2.1: **a** Schematic picture of a data cube. **b** Schematic plot of a spectrum. **c** Schematic plot of a channel map.

Table 2.1. Here only information is given for observations during which data was acquired that was used for this work. More details about the observations and the details about the calibration and deconvolution of the data are reported in Belloche et al. (2016). The resulting median angular resolution is about 1.″6. The average noise level per channel is ~ 3 mJy beam^{-1}. The exact values of the spatial resolution and noise level in each spectral window are listed in Table 2.2. The synthesised beam represents the spatial resolution of the data. For an interferometer the angular resolution is given by the wavelength divided by the maximal distance between two telescopes. The complete field of view of the observation is restricted by the size of the primary beam (see Table 2.3), the beam of one single telescope.

2.2 Data cubes

The calibrated and deconvolved ALMA data are available in a data cube. A data cube contains three dimensions: two dimensions give the position in the sky and one dimension the spectral information (see Fig. 2.1a). The x- and y-coordinates describe one pixel. The coordinates are given in Right ascension (x-direction) and Declination (y-direction). The third axis is the frequency axis, containing a certain amount of channels with each a frequency value. Due to the Doppler effect the frequency can be converted into a radial velocity value relative to us. For each combination of these three information the data cube holds an intensity value of the emission or absorption. A spectrum shows the spectral information for one position, one pixel (see Fig. 2.1b). To investigate the spatial structure, we need a channel map, the distribution of intensities as a function of position at a given velocity or frequency and hence for one channel (see Fig. 2.1c).

2.3 Modelling the spectra

2.3.1 Radiative transfer equation

To investigate the spectral features (absorption or emission lines) we have to understand the physical process that generates these features. The underlying process is caused by the radiation of a source with a specific intensity I_ν passing through a medium with length dz on the way to us. It can be described by the radiative

transfer equation (see e.g. Draine 2011), which has to be solved to model the spectral features:

$$\frac{dI_\nu}{dz} = -\kappa_\nu I_\nu + \varepsilon_\nu \tag{2.1}$$

with κ_ν the absorption coefficient of the medium passed by the radiation (unit: length^{-1}) and ε_ν the emission coefficient, the energy emitted by spontaneous emission (unit: power per unit volume), at a given frequency ν. The absorption coefficient describes the attenuation of the specific intensity I_ν, which is defined for a spectral line as:

$$\kappa_\nu = \frac{h\nu}{4\pi}(n_l B_{lu} - n_u B_{ul})\phi_\nu = \frac{c^2}{8\pi\nu^2}\frac{g_u}{g_l} n_l A_{ul}\left(1 - \frac{g_l n_u}{g_u n_l}\right)\phi_\nu \tag{2.2}$$

with n_l the population in the lower level, n_u the population in the upper level, g_u and g_l the upper and lower level degeneracies, h the Planck constant, ν the frequency, $\phi_\nu d\nu$ the probability of the photon in the frequency interval $[\nu, \nu + d\nu]$, B_{lu} the coefficient for absorption, B_{ul} the coefficient of stimulated emission and A_{ul} the spontaneous emission coefficient. The emission coefficient describes the gains in intensity:

$$\varepsilon_\nu = \frac{h\nu}{4\pi} A_{ul} n_u \, \phi_\nu. \tag{2.3}$$

Equation 2.1 ignores scattering processes where for example dust grains or electrons are involved. Usually, we do not know the path length along which the radiation propagates. Instead of the path length, we use the optical depth τ_ν which describes the transparency of the medium along the line of sight to us. If $\tau_\nu << 1$ the matter is almost completely transparent (optically thin) and if $\tau_\nu >> 1$ most of the initial intensity is absorbed in the material along the line of sight, which is called optically thick. Using this definition ($d\tau_\nu = \kappa_\nu dz$), the radiative transfer equation results in:

$$dI_\nu = -I_\nu d\tau_\nu + \frac{\varepsilon_\nu}{\kappa_\nu} d\tau_\nu = -I_\nu d\tau_\nu + S_\nu d\tau_\nu \tag{2.4}$$

with S_ν the source function (Draine 2011). Using this equation and multiplying the radiative transfer equation with e^{τ_ν}, the integrating factor (Draine 2011), the equation can be integrated from a starting point of $\tau_\nu = 0$ with $I_\nu = I_\nu(0)$:

$$\begin{aligned} e^{\tau_\nu}(dI_\nu + I_\nu d\tau_\nu) &= e^{\tau_\nu} S_\nu d\tau_\nu \\ d(e^{\tau_\nu} I_\nu) &= e^{\tau_\nu} S_\nu d\tau_\nu \\ e^{\tau_\nu} I_\nu - I_\nu(0) &= \int_0^{\tau_\nu} e^{\tau'} S_\nu \, d\tau' \end{aligned} \tag{2.5}$$

The multiplication with $e^{-\tau_\nu}$ gives the equation of transfer in the integral form:

$$I_\nu(\tau_\nu) = I_\nu(0) e^{-\tau_\nu} + \int_0^{\tau_\nu} e^{-(\tau_\nu - \tau')} S_\nu \, d\tau'. \tag{2.6}$$

If we make the substitution $\tau'' = \tau_\nu - \tau'$ with $d\tau' = -d\tau''$, we get:

$$I_\nu(\tau_\nu) = I_\nu(0) e^{-\tau_\nu} + \int_0^{\tau_\nu} e^{-\tau''} S_\nu \, d\tau''. \tag{2.7}$$

The explanation of this equation is the following: the intensity I_ν at an optical depth of τ_ν can be described by the initial intensity $I_\nu(0)$ attenuated by the factor $e^{-\tau_\nu}$, plus the integral over the emission of a source $S_\nu \, d\tau'$ which is attenuated by the factor $e^{-\tau''}$.

In the case of a slab of uniform medium with finite extent and with the assumption that one single excitation temperature ($T_{\rm ex}$[3]) describes the population of the energy levels, the radiation field within this medium is the same as the blackbody radiation ($I_\nu = B_\nu(T_{\rm ex})$):

$$I_\nu = B_\nu(T_{\rm ex}) = \frac{2\,h\,\nu^3}{c^2}\left[e^{\frac{h\nu}{k_{\rm B}T_{\rm ex}}} - 1\right]^{-1}, \tag{2.8}$$

with c the speed of light and $k_{\rm B}$ the Boltzmann constant. The radiative transfer equation (see Eq. 2.4) changes to:

$$0 = dI_\nu = -B_\nu d\tau_\nu + S_\nu d\tau_\nu. \tag{2.9}$$

Because $B_\nu(T_{\rm ex}) = S_\nu$, Kirchoff's law is valid, which describes the relation between the blackbody radiation B_ν and the emission and absorption coefficients of the matter:

$$S_\nu = B_\nu(T_{\rm ex}) = \frac{\varepsilon_\nu}{\kappa_\nu}. \tag{2.10}$$

In the case of a uniform slab as discussed before, the integral in the radiative transfer equation can be solved easily if we assume a constant excitation temperature:

$$I_\nu(\tau_\nu) = I_\nu(0)e^{-\tau_\nu} + B_\nu(T_{\rm ex})(1 - e^{-\tau_\nu}). \tag{2.11}$$

In the case of a local thermodynamic equilibrium (LTE) the excitation temperature is equal to the temperature of the medium. Often, instead of the intensity I_ν the equivalent temperature of a blackbody is used ($J_\nu(T) \propto \frac{h\nu}{k}\left(e^{(h\nu/kT)} - 1\right)$):

$$J_\nu(T_{\rm R}) = f\,J_\nu(T_{\rm bg})e^{-\tau_\nu} + f\,J_\nu(T_{\rm ex})[1 - e^{-\tau_\nu}], \tag{2.12}$$

with $T_{\rm R}$ the source radiation temperature, $T_{\rm bg}$ the background radiation temperature and f the beam filling factor, the fraction of the spatial resolution filled by the source.

There are three regimes of the excitation temperature: If $T_{\rm bg} = T_{\rm ex}$ no line is visible, we see only the background continuum radiation. In the case of $T_{\rm bg} > T_{\rm ex}$ the line appears in absorption and in the case of $T_{\rm bg} < T_{\rm ex}$ the line appears in emission.

To model the absorption features in the ALMA spectra with Eq. 2.12, we use the programme Weeds (Maret et al. 2011). This programme solves the radiative transfer equation (see Eq. 2.11) under the assumption of local thermodynamic equilibrium and takes into account the finite angular resolution of the observations. The synthetic spectra are fitted as a collection of Gaussian opacity distributions. More details about the computation of the synthetic spectra and the underlying assumptions are described in Sect. 5.3.3.

2.3.2 Preparing the spectra

The ALMA data used in this Thesis are already calibrated and deconvolved. Before we can model the spectral features by solving the radiative transfer equation, some more prerequisites have to be fulfilled. The unit of the spectra has to be transformed and the data have to be corrected for the primary beam attenuation.

[3]The excitation temperature between two levels of population (lower and upper) is defined in the following way: $\frac{n_u}{n_l} = \frac{g_u}{g_l}e^{-(E_u-E_l)/(kT_{\rm ex})}$ with E_u and E_l the energies of the levels u and l.

2.3.2.1 Transformation of Units

The measured intensity of the ALMA data is the flux density S_ν, given in Jy per beam[4]. For further analysis we need the intensity given as brightness temperature T_B. The effective brightness temperature $T_\mathrm{B}(\nu)$ is defined as:

$$T_\mathrm{B}(\nu) = \frac{c^2}{2k_\mathrm{B}\nu^2} I_\nu \tag{2.13}$$

with c the speed of light, k_B the Boltzmann constant and I_ν the specific Intensity of the source. The flux density is the specific intensity integrated over the beam solid angle:

$$S_\nu = \int_{\Omega_\mathrm{s}} I_\nu d\Omega \approx I_\nu \, \Omega_\mathrm{s} \tag{2.14}$$

The beam solid angle depends on the resolution of the data:

$$\Omega_\mathrm{s} = \frac{\pi \, \theta_0^2}{4 \ln(2)}, \tag{2.15}$$

with θ_0 the full width at half maximum ($FWHM$) of a Gaussian beam. In the case of an elliptical beam the factor θ_0^2 has to be replaced by the product of the major axis θ_maj and the minor axis θ_min. Using this replacement and the combination of Eq. 2.13–2.15 gives the transformation factor between the flux density and the brightness temperature:

$$T_\mathrm{B} = \frac{4 \ln(2) \, c^2}{2\pi \, \nu^2 \, k_\mathrm{B} \, \theta_\mathrm{maj} \, \theta_\mathrm{min}} S_\nu. \tag{2.16}$$

The formula given in the observed units is:

$$T_\mathrm{B}[\mathrm{K}] = \frac{1.2223 \times 10^{12}}{\nu_0^2[\mathrm{MHz}] \, \theta_\mathrm{maj}[''] \, \theta_\mathrm{min}['']} S_\nu[\mathrm{Jy\,beam^{-1}}], \tag{2.17}$$

with ν_0 the rest frequency[5] of the investigated data.

2.3.2.2 Primary beam correction

After transforming the unit, the data have to be corrected for the primary beam attenuation. The primary beam is a Gaussian beam with stronger attenuation at pixels more distant from the phase centre. The correction factor X depends not only on the pixel for which the spectrum is analysed but also on the frequency ν at which the data are observed:

$$X = \exp\left(-\frac{d^2}{2\sigma^2}\right) = \exp\left[-\frac{4 \ln 2 \cdot (x_\mathrm{off}^2 + y_\mathrm{off}^2)}{HPBW_{pb}(\nu)^2}\right]. \tag{2.18}$$

with $HPBW_{pb}(\nu)$ the the Half Power Beam Width ($HPBW$) of the primary beam and x_off and y_off the pixel offsets from the phase centre in Right Ascension and Declination.

In Remijan (2015) the values for $HPBW$ of the ALMA main array antennas are given for two frequencies (see Table 2.3). The $HPBW$ is inversly proportional to the diameter of the telescope D:

$$HPBW = const \frac{\lambda}{D}, \tag{2.19}$$

with λ the wavelength and $const$ a constant factor. Hence, the product of the $HPBW$ and the observed frequency ν ($\lambda = \frac{c}{\nu}$) is a constant C. From the values listed in Table 2.3, we get for the constant factor C:

$$C = HPBW \times \nu = (5805 \pm 9)'' \, GHz. \tag{2.20}$$

Table 2.3: Primary beam correction.

ν^a [GHz]	$HPBW^b$ [″]	C^c [″ GHz]
84	69	5796
114	51	5814

Notes. [(a)] Frequency. [(b)] $HPBW$ of the primary beam (Remijan 2015). [(c)] $C = HPBW \times \nu$.

Table 2.4: Transitions of methanol used to determine the systemic velocity of K4.

${\nu_0}^a$ [MHz]	Transition	${v_{\rm LSR}}^b$ [km s^{-1}]
84521.172 ± 0.012	$5_{1,5,2}$–$4_{0,4,1}$	56.184 ± 0.057
95914.310 ± 0.002	$2_{1,2,0}$–$1_{1,1,0}$	56.186 ± 0.206
97582.798 ± 0.002	$2_{1,1,0}$–$1_{1,0,0}$	56.173 ± 0.171

Notes. [(a)] Rest frequency. [(b)] Velocity.

Our data are divided into 20 spectral windows, each with a spectral width of about 1.8 GHz. Hence, it is interesting to evaluate how large the deviations are, if we use only one single correction factor for a spectral window and not a channel dependent one. The deviations of the primary beam width of using the lowest or the highest frequency in a spectral window instead of the middle frequency is $\frac{\pm 0.9\,GHz}{85\,GHz} = 1.1\,\%$ for the first spectral window with the lowest frequency. Consequently, the resulting deviations are less or equal 1.1 % for all spectral windows and one correction factor or one $HPBW$ can be used for each spectral window.

2.3.3 Systemic velocity of the Sgr B2 envelope

To identify the molecular transitions seen in absorption and to calculate the synthetic spectra, the model of the spectral features, the systemic velocity of the source is needed. The systemic velocity is the characteristic velocity $v_{\rm LSR}$[6] of the source. We determine the systemic velocity of the ultracompact H II region K4 (see Fig. 3.1) using emission lines. Only a few emission lines are detected. To identify them, the systemic velocity is first set to 64 km s^{-1}, the velocity of the main hot core N1 (see Fig. 3.1), because we expect a similar systemic velocity. In a second step we search for well known emission lines. Three methanol lines (CH_3OH) are identified using the Jet Propulsion Laboratory (JPL) molecular spectroscopy catalogue (Pickett et al. 1998). We fitted Gaussian curves to the lines to get the systemic velocity of K4. The centroid velocities are listed in Table 2.4.

The resulting value for the systemic velocity is: (56.181 ± 0.091) km s^{-1}. Because the channel width is between 1.3 and 1.75 km s^{-1} we do not need such a high velocity precision. The frequency axis of the spectra is adjusted to a systemic velocity of 56.2 km s^{-1}.

For the other investigated lines of sight (see Fig. 3.1) almost no emission lines are detected. Hence, we assume the same systemic velocity for all positions.

[4] 1 Jy = $10^{-26}\,\frac{\rm W}{\rm Hz\,m^2}$.
[5] Observed frequency.
[6] Velocity relative to the local standard of rest.

2.3.4 Identification of molecular transition lines

To identify the molecular transitions seen in absorption we use the spectroscopic information provided in the Cologne Database for Molecular Spectroscopy (CDMS, Endres et al. 2016; Müller et al. 2005, 2001) and the Jet Propulsion Laboratory (JPL) molecular spectroscopy catalogue (Pickett et al. 1998). Thereby, we applied the following selection criteria for identifying transitions of a given molecule (Herbst & van Dishoeck 2009):

1. The rest frequencies of the transitions are well known.
2. The synthetic spectrum matches the observed spectrum.
3. The centroid velocities of the Gaussian velocity components can also be found for transitions of other molecules.

Next to these three mandatory selection criteria, usually one or more of the following conditions is valid:

1. The molecule is a simple molecule containing only a few atoms with a low number in the periodic table.
2. The absorption line was found in previous absorption studies.
3. Several lines of the molecule are found.
4. Lines of isotopologues are found.
5. The centroid velocities of the Gaussian velocity components of the molecule and the corresponding isotopologues match.

We compared the possible molecular candidates with the molecular transitions identified previously in the direction of Sgr B2(N) and Sgr B2(M) (see e.g. Hieret 2005; Belloche et al. 2013) to fulfil condition two.

2.4 Column densities

After we had identified the molecular transitions seen in absorption in the spectra, we calculated the synthetic spectra using Weeds. One of the modelled quantities we get is the column density. The column density of a molecule is defined as the number of molecules per unit area summed up along the line of sight. The column density in the upper level u is the integrated number density along a path length dz:

$$N_u = \int n_u dz = \int n_u \frac{d\tau_\nu}{\kappa_\nu} \tag{2.21}$$

If we combine this equation with Eq. 2.2 using the Boltzmann equation for the population of two levels:

$$\frac{n_u}{n_l} = \frac{g_u}{g_l} \mathrm{e}^{-(E_u - E_l)/(kT_{\mathrm{ex}})}, \tag{2.22}$$

the optical depth is directly related to the column density of the level population:

$$\begin{aligned}
\int d\tau_\nu = \tau_\nu &= \int \kappa_\nu dz \\
&= \int \frac{c^2}{8\pi\nu^2}\frac{g_u}{g_l} n_l(z) A_{ul}\left(1 - \frac{g_l n_u(z)}{g_u n_l(z)}\right)\phi_\nu dz \\
&= \int \frac{c^2}{8\pi\nu^2} A_{ul}\left(\frac{g_u}{g_l} n_l(z) - n_u(z)\right)\phi_\nu dz \\
&= \int \frac{c^2}{8\pi\nu^2} A_{ul}\left(n_u(z) \mathrm{e}^{\frac{h\nu}{kT_{\mathrm{ex}}}} - n_u(z)\right)\phi_\nu dz \\
&= \frac{c^2}{8\pi\nu^2} A_{ul} N_u \left[\mathrm{e}^{\frac{h\nu}{kT_{\mathrm{ex}}}} - 1\right]\phi_\nu \\
\int \tau_\nu d\nu &= \int \frac{c^2}{8\pi\nu^2} A_{ul} N_u \left[\mathrm{e}^{\frac{h\nu}{kT_{\mathrm{ex}}}} - 1\right]\phi_\nu d\nu. \\
&= \frac{c^2}{8\pi\nu^2} A_{ul} N_u \left[\mathrm{e}^{\frac{h\nu}{kT_{\mathrm{ex}}}} - 1\right]
\end{aligned} \tag{2.23}$$

In the last step we assumed $\int \phi_\nu d\nu = 1$. Usually we are not using the width of a line in frequency, but in velocity v. With $d\nu = -\frac{\nu dv}{c}$ we get for the column density:

$$N_u = \frac{8\pi\nu^3}{c^3 A_{ul}}\left[\mathrm{e}^{\frac{h\nu}{kT_{\mathrm{ex}}}} - 1\right]^{-1} \int \tau_\nu dv. \tag{2.24}$$

The last factor ($\int \tau_\nu dv$) can be directly calculated from the spectrum in an optically thin case and is a description of the integrated intensity. Because we want to know the total column density N_{tot} of the molecules, we need to relate the column density of the upper level to N_{tot}. If we assume a single excitation temperature T_{rot} for all transitions, the population in the upper level is defined as:

$$\frac{N_{\mathrm{u}}}{N_{\mathrm{tot}}} = \frac{g_{\mathrm{u}}}{Q(T_{\mathrm{rot}})} e^{-E_{\mathrm{u}}/k_{\mathrm{B}}T_{\mathrm{ex}}}, \tag{2.25}$$

with $Q_{\mathrm{rot}} = \sum_i g_i \mathrm{e}^{\frac{-E_i}{kT_{\mathrm{rot}}}}$ the rotational partition function, a measure of the statistical sum over all rotational energy levels. The combination of Eq. 2.24 and 2.4 results in an expression for the total column density:

$$N_{\mathrm{tot}} = \frac{8\pi\nu^3}{c^3 A_{ul}} \frac{Q(T_{\mathrm{rot}})}{g_{\mathrm{u}}} e^{E_{\mathrm{u}}/k_{\mathrm{B}}T_{\mathrm{rot}}}\left[\mathrm{e}^{\frac{h\nu}{kT_{\mathrm{rot}}}} - 1\right]^{-1} \int \tau_\nu \, dv. \tag{2.26}$$

2.5 Population diagrams

The first step to model the absorption features is done under the assumption of a rotation temperature of 2.73 K. If for one molecule several transitions are detected and if the synthetic spectrum does not match the observed spectrum, a population diagram can be created to determine the correct rotational temperature of the molecule (Goldsmith & Langer 1999). To create a population diagram the logarithm of Eq. 2.25 has to be calculated:

$$\ln\left(\frac{N_u}{g_u}\right) = \ln(N_{\mathrm{tot}}) - \ln(Q(T_{\mathrm{rot}})) - \frac{E_{\mathrm{u}}}{k_{\mathrm{B}}T_{\mathrm{rot}}} = const - \frac{1}{T_{\mathrm{rot}}}\frac{E_{\mathrm{u}}}{k_{\mathrm{B}}} \tag{2.27}$$

with $\ln(N_{\mathrm{tot}}) - \ln(Q(T_{\mathrm{rot}}))$ a constant value $const$. The column density or population of a level depends on the upper energy level E_u. The slope of the population diagram is proportional to the inverse of the rotational

temperature. The column density of the upper level N_u is proportional to the optical depth and hence can be described by the line intensity W integrated over a velocity range (Goldsmith & Langer 1999). Because most molecules for which we have to determine a population diagram are only detected in the envelope of Sgr B2, we integrate only over the velocity range of the envelope of Sgr B2. Using the integrated line intensity Eq. 2.27 results in (Goldsmith & Langer 1999):

$$\ln\left(\frac{8\pi k_B \nu^2 W}{hc^3 A_{ul} g_u}\right) = const - \frac{1}{T_{rot}} \cdot \frac{E_u}{k_B}. \tag{2.28}$$

The integrated intensity is determined over the complete envelope of SgrB2, because it is very difficult to differentiate between the different identified velocity components.

If two transitions overlap each other, we apply the following correction which is weighted by the degeneracy factor:

$$\langle E_{up} \rangle = \frac{\sum_{i=1}^{2} g_u^i \cdot E_{up}^i}{\sum_{i=1}^{2} g_u^i}. \tag{2.29}$$

For the population diagram, the mean values of the frequency, the Einstein coefficient, and the degeneracy factor are used.

2.6 Column density profiles

The absorption lines of some of the molecules are partially optically thick. In this case, we cannot differentiate between the velocity components and cannot derive the column density values. Using less abundant isotopologues we can derive the column densities if we assume the isotopic ratios (see Sect. 3.3.3). Hence, we do not compare the spectra to each other but the column density distributions of the molecules, which we derive from the modelling of the spectrum:

$$\frac{N(v)}{\Delta v} = \sum_{i=1}^{n} \frac{N_i}{\sqrt{2\pi\sigma_i^2}} \exp\left[-\frac{(v - v_{off,i} + v_{LSR})^2}{2\sigma_i^2}\right] \Delta v \frac{1}{\Delta v}, \tag{2.30}$$

with $N(v)$ the column density in a given channel with the width Δv, n the number of velocity components detected for one transition, N_i the column density of the velocity component i, σ_i the standard deviation, and $v_{off,i}$ the velocity offset of the i-th component. v_{LSR} is the systemic velocity. σ_i is directly related to the full width at half maximum ($FWHM_i$):

$$FWHM_i = \sigma_i \sqrt{8 \ln(2)}. \tag{2.31}$$

2.7 Uncertainty on the integrated column density

The uncertainty of the integrated column density of a given component depends on the number of channels over which the integrated intensity is calculated. The noise of the integrated intensity ($I = \sum_{i=1}^{N} T_B(v)\Delta v$) is:

$$\sigma_I = \sqrt{N}\, \sigma_{T_B}\, \Delta v, \tag{2.32}$$

with N the number of channels over which it is integrated, σ_{T_B} the noise per velocity channel and Δv the channel width. The signal-to-noise ratio (SNR) can be computed in the following way:

$$\frac{I}{\sigma_I} = \frac{\sum_{i=1}^{N} T_B(v)\Delta v}{\sqrt{N}\, \sigma_{T_B}\, \Delta v}. \tag{2.33}$$

The brightness temperature we determine from the peak temperature $T_{\rm peak}$:

$$T_{\rm B}(v) = T_{\rm peak} \exp\left(-\frac{(v-v_0)^2}{2\sigma^2}\right), \tag{2.34}$$

with v_0 the centroid velocity and σ the standard deviation of the Gaussian. The integrated intensity is the integral over the brightness temperature of the component:

$$I = \int T_{\rm B}(v)\, dv = \int T_{\rm peak} \exp\left(-\frac{(v-v_0)^2}{2\sigma^2}\right) dv = T_{\rm peak}\, \sqrt{2\pi}\sigma = T_{\rm peak} FWHM \frac{\sqrt{\pi}}{2\sqrt{\ln(2)}}. \tag{2.35}$$

We integrate the brightness temperature over a width of 6σ, because this includes 99.73% of the integral of a Gaussian function. The number of velocity channels over this width is:

$$N = \frac{6\sigma}{\Delta v} = \frac{\frac{3FWHM}{\sqrt{2\ln(2)}}}{\Delta v}. \tag{2.36}$$

The resulting equation for the signal-to-noise ratio (SNR) is the following:

$$\frac{I}{\sigma_I} = \frac{T_{\rm peak}\, FWHM\, \frac{\sqrt{\pi}}{2\sqrt{\ln(2)}}}{\sqrt{\frac{3FWHM}{\sqrt{2\ln(2)}\,\Delta v}}\, \sigma_T\, \Delta v} = \frac{1}{\sqrt{6\sqrt{2\ln 2}}}\, T_{\rm peak}\, \sqrt{FWHM}\, \frac{\sqrt{\pi}}{\sigma_T\, \sqrt{\Delta v}}. \tag{2.37}$$

2.8 Pearson's correlation coefficient

To investigate if two datasets X and Y (such as the column densities of two molecules) containing N elements (x_i and y_i) are linearly correlated with each other, we calculate Pearson's correlation coefficient $r_{\rm Pearson}$.

$$r_{\rm Pearson} = \frac{\sum_i (x_i - \bar{x})\,(y_i - \bar{y})}{\sqrt{\sum_i (x_i - \bar{x})^2}\, \sqrt{\sum_i (y_i - \bar{y})^2}}, \tag{2.38}$$

with $\bar{x} = \frac{1}{N} \cdot \sum_i x_i$ and $\bar{y} = \frac{1}{N} \cdot \sum_i y_i$ the mean values of the two datasets. The resulting value of $r_{\rm Pearson}$ can be in the interval [-1,1]. A value of +1 describes a perfect linear correlation and a value of −1 a perfect anti-correlation. A value of 0 means that there is no linear correlation. We use the classification of the strength of the correlation as defined by Evans (1996):

- 0.00–0.19: very weak linear correlation,
- 0.20–0.39: weak linear correlation,
- 0.40–0.59: moderate linear correlation,
- 0.60–0.79: strong linear correlation,
- 0.80–1.00: very strong linear correlation.

CHAPTER 3

Chemical and physical properties of the line-of-sight clouds to Sgr B2

Contents

Abstract

In this chapter, we discuss the chemical diversity and the physical properties of the molecular clouds detected in absorption along the line of sight to Sgr B2 towards several positions associated with Sgr B2(N), Sgr B2(M) and Sgr B2(L). First, we describe the selected sample of positions to investigate the molecular content of the line-of-sight clouds seen in absorption and their spectral properties. We investigate the velocity structure based on column density profiles of the 12 molecules with the strongest absorption signals: HCO^+, CCH, c-C_3H_2, ^{13}CO, CS, CN, SiO, SO, HCN, HNC, N_2H^+, and CH_3OH. Furthermore, we discuss the correlations between the abundances of these molecules and the isotopic ratios determined with different pairs of isotopologues.

The abundances of the molecules change on small scales between the positions associated with Sgr B2(N). The two more distant positions towards Sgr B2(M) and Sgr B2(L) show more pronounced variations in comparison to the other four positions. The mean linewidth of the velocity components representing

the line-of-sight clouds is about 4.5–4.9 km s^{-1}. The clouds associated with the envelope of Sgr B2 have linewidths 2 km s^{-1} broader than the other clouds. CO is not correlated with any of the other molecules. The five molecules CN, HCN, HNC, CS and CCH and the three shock tracers SiO, SO and CH_3OH are all strongly correlated to each other. The isotopic ratios that we determine match the results of previous studies. We measure the isotopic ratio of $^{14}N/^{15}N$ directly in the envelope of Sgr B2 to be about 350. This ratio was previously estimated on the basis of a linear extrapolation of the isotopic ratios determined at larger galactocentric radii.

3.1 Introduction

Previous molecular absorption studies with the aim to investigate the line-of-sight clouds towards Sgr B2(N) and Sgr B2(M) have been mostly performed using single-dish telescopes (e.g., Greaves & Williams 1994; Neufeld et al. 2000; Polehampton et al. 2005; Hieret 2005; Lis et al. 2010; Monje et al. 2011; Corby et al. 2018). To investigate the molecular content of the clouds along the line of sight, models were created which match the detected absorption features. However, these absorption studies do not have the angular resolution needed to resolve the continuum structure of Sgr B2. Using instead an interferometer, this becomes possible. Corby et al. (2015) used data from the interferometer ATCA (Australia Telescope Compact Array) to investigate the clouds detected in absorption towards Sgr B2(N) in the frequency range of 30–50 GHz. But also with their resolution of 5–10″ they cannot resolve all small details of the continuum structure of Sgr B2(N).

We use the EMoCA survey (Belloche et al. 2016) which was performed with the interferometer ALMA. This survey has an angular resolution and a sensitivity higher by more than one order of magnitude compared to a previous survey carried out with the IRAM 30 m telescope (Belloche et al. 2013). Furthermore, the spatial resolution is by a factor 3–6 higher than in the ATCA data used by Corby et al. (2015). The spatial resolution of the EMoCA survey is high enough to resolve the structure of Sgr B2(N), in particularly compact structures such as K4 (see Fig. 3.1). This high angular resolution allows us to investigate absorption lines at several positions across Sgr B2 towards which the continuum is strong enough but which are sufficiently detached from the hot cores that the detected absorption lines are not blended with numerous emission lines. The absorption study towards Sgr B2 gives the opportunity to study for several positions the clouds in the Sagittarius, Scutum, 3 kpc, and 4 kpc spiral arms, and in the Galactic center region up to a distance of about 2 kpc from the GC (e.g., Greaves & Williams 1994; Menten et al. 2011, see Fig. 1.5). The spectral resolution of this ALMA survey (1.5 km s^{-1}) is about 4 times higher than in the ATCA survey mentioned above (Corby et al. 2015) which gives us the possibility to investigate the detailed velocity structure of several positions towards Sgr B2. This ALMA survey covers the frequency range from 84.1 to 114.4 GHz. Many important as well as abundant molecular species have transitions in this frequency regime that are suitable for absorption studies. Therefore, this unbiased line survey provides an excellent opportunity to study molecular and isotopic abundances not only on sub-parsec scales in Sgr B2 itself, but also along the whole 8.3 kpc (Reid et al. 2014) long line of sight to the Galactic center.

In summary, this survey allows to investigate the variations in abundance and isotopic ratios for many molecules as a function of galactocentric distance from the Galactic center to the Solar Circle. It can also probe the correlations in abundance between molecules present along the line of sight, which gives hints on the chemical processes in the line-of-sight clouds.

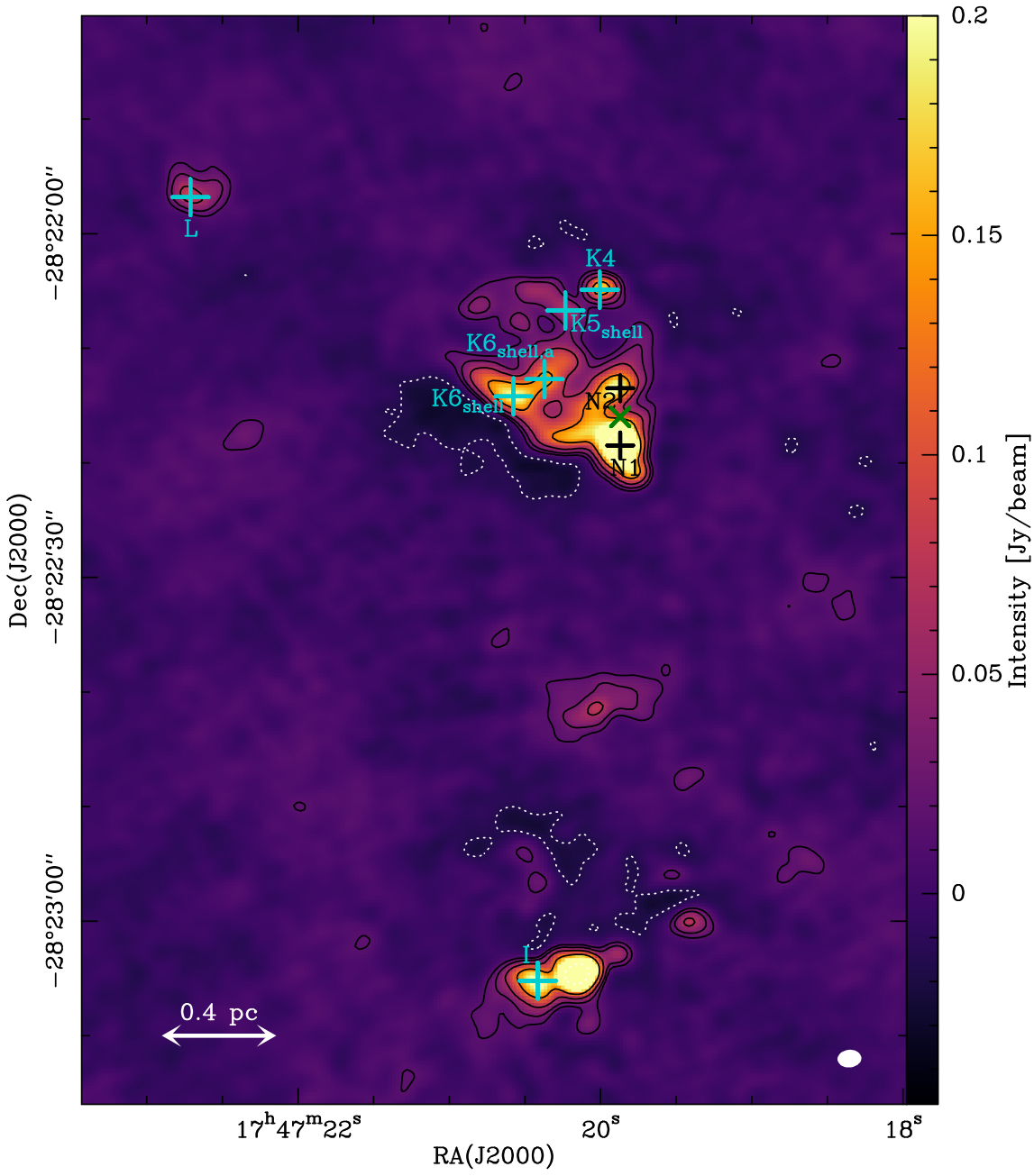

Figure 3.1: ALMA continuum map of Sgr B2 at 85 GHz, not corrected for the primary beam attenuation. The black contour lines show the flux density levels at 3σ, 6σ, 12σ, and 24σ and the dotted one marks -3σ, with σ is the rms noise level of 5.4 mJy beam^{-1}. The black crosses mark the positions of the hot cores Sgr B2(N1) and Sgr B2(N2), the green cross the phase centre ($\alpha, \delta_{\mathrm{J2000}}$: $17^{\mathrm{h}}47^{\mathrm{m}}19.87^{\mathrm{s}}, -28°22'16''$), and the cyan crosses the six positions selected for the analysis. The white ellipse in the lower right corner is the synthesised beam ($2.''1 \times 1.''5$). The pixel size in this image is $0.''3$.

Table 3.1: Absolute coordinates and offsets to the phase centre of the investigated positions.

position	Right ascension[a] α(J2000)	Declination[a] δ(J2000)	$\Delta\alpha^b$ [″]	$\Delta\delta^c$ [″]
K4	$17^h47^m20.^s01$	$-28°22'04.''9$	1.8	11.1
$K6_{shell}$	$17^h47^m20.^s57$	$-28°22'14.''2$	9.3	1.8
$K5_{shell}$	$17^h47^m20.^s37$	$-28°22'12.''7$	6.6	3.3
$K6_{shell,a}$	$17^h47^m20.^s23$	$-28°22'06.''7$	4.8	9.3
I	$17^h47^m20.^s42$	$-28°23'05.''2$	7.2	−49.2
L	$17^h47^m22.^s71$	$-28°21'56.''8$	37.5	19.2

Notes. [(a)] Absolute equatorial coordinates. [(b)] Offset in Right Ascension to the phase centre: $\Delta\alpha = (\alpha_2 - \alpha_1)\cos(\delta_2)$. [(c)] Offset in Declination to the phase centre: $\Delta\delta = \delta_2 - \delta_1$.

3.2 Investigated positions

To investigate the chemical content and the physical properties of the diffuse and translucent molecular clouds along the line of sight to Sgr B2, we selected six positions (see Fig. 3.1 and Table 3.1). These six positions represent peaks in the continuum emission. To measure the positions of these peaks, we determined the peak pixel for each spectral window and calculated the median pixel coordinates and extracted the spectrum from these positions. Four positions are located in Sgr B2(N): the ultracompact H II (UCH II) region K4, two continuum peaks in the shell of the H II region K6 ($K6_{shell}$ and $K6_{shell,a}$), and one continuum peak in the shell of the H II region K5 ($K5_{shell}$). In addition, we selected the H II region Sgr B2(L) and a continuum peak east of Sgr B2(M), which coincides with the H II region I. The labels of the H II regions are taken from Gaume et al. (1995). The positions K4 and $K6_{shell}$ have the highest continuum signal-to-noise ratios (see Tables A.1–A.3). The absolute positions in right ascension and declination and the offsets of these positions from the phase centre are listed in Table 3.1.

3.3 Results

Before we calculate the synthetic spectra towards the six investigated positions using Weeds (Maret et al. 2011) we need to subtract the continuum level for each spectral window. For this purpose, we use the command *base* in CLASS, which fits the continuum baseline with a polynomial function of given order and also gives us the noise level. The values of the mean continuum level, the noise, the signal-to-noise ratio of the continuum and the order of the polynomial function used for the baseline subtraction are listed in Tables A.1–A.3 in Appendix A.

3.3.1 Identification of molecules

The spectrum of $H^{13}CO^+$ 1–0 at 86754.288 MHz towards the UCH II region K4 is shown in Fig. 3.2 as an example for the absorption features we want to investigate. The grey area marks the velocity range of the diffuse and translucent envelope of Sgr B2 itself. A strong and broad absorption feature is located at this velocity range. The absorption features at lower velocities are caused by GC clouds and spiral arm clouds the continuum radiation of Sgr B2 is traversing on the way to us. In the following, we will distinguish between the clouds along the line of sight and those associated with the envelope of Sgr B2.

In total, we identified 28 molecules seen in absorption in the envelope of Sgr B2: CH_3CHO, CH_3CN, CS,

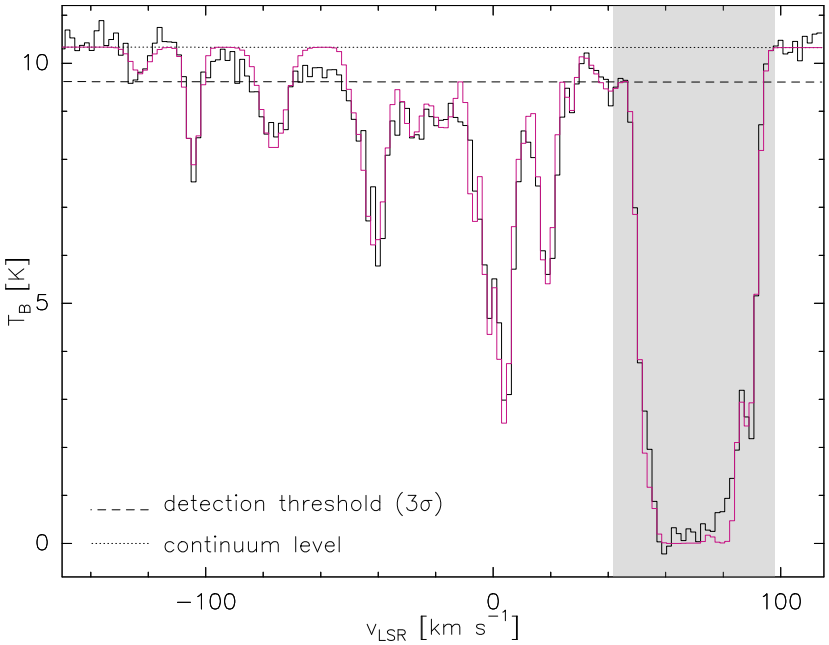

Figure 3.2: ALMA spectrum of $H^{13}CO^+$ 1–0 at 86754.288 MHz towards the UCH II region K4. The spectrum in magenta is the synthetic spectrum modelled using Weeds. The dotted line represents the continuum level and the dashed line the 3σ line detection threshold. The grey area marks the velocity range of the envelope of Sgr B2 (v_{LSR}>42 km s^{-1}).

^{13}CO, OCS, HC_3N, CN, c-C_3H_2, N_2H^+, C_2H_5OH, CCH, NH_2CHO, HCO^+, HCN, HNC, HOC^+, HNCO, CH_3OH, CH_3NH_2, CH_3SH, NS^+, $HOCO^+$, PN, SiO, SO_2, SO, H_2CS, and CCS. In addition, we also detected the following less abundant isotopologues: $C^{34}S$, ^{13}CS, $C^{33}S$, $^{13}C^{34}S$, $C^{18}O$, $C^{17}O$, $H^{13}CCCN$, $HC^{13}CCN$, $HCC^{13}CN$, ^{13}CN, $C^{15}N$, c-$CC^{13}CH_2$, $^{15}NNH^+$, $N^{15}NH^+$, ^{13}CCH, $C^{13}CH$, $H^{13}CO^+$, $HC^{18}O^+$, $HC^{17}O^+$, $H^{13}CN$, $HC^{15}N$, $HN^{13}C$, $H^{15}NC$, $^{13}CH_3OH$, ^{29}SiO, ^{30}SiO, ^{34}SO.

In the diffuse and translucent molecular clouds along the line of sight to Sgr B2, we detected 19 molecules in absorption: CH_3CHO, CH_3CN, CS, ^{13}CO, HC_3N, CN, c-C_3H_2, N_2H^+, CCH, NH_2CHO, HCO^+, HCN, HNC, HOC^+, HNCO, CH_3OH, SiO, SO, and H_2CS. The following less abundant isotopologues are also detected in the line-of-sight clouds: $C^{34}S$, ^{13}CS, $C^{33}S$, $C^{18}O$, $C^{17}O$, ^{13}CN, $H^{13}CO^+$, $HC^{18}O^+$, $H^{13}CN$, $HC^{15}N$, $HN^{13}C$, $H^{15}NC$, $^{13}CH_3OH$, ^{29}SiO, ^{30}SiO.

We detected some complex organic molecules (COMs: carbon-bearing molecules with at least six atoms) in absorption in this survey: CH_3CHO, CH_3CN, C_2H_5OH, NH_2CHO, CH_3OH, CH_3NH_2, and CH_3SH. Some of these molecules are not only detected in the envelope of Sgr B2, but also along the line of sight (CH_3CHO, CH_3CN, NH_2CHO, and CH_3OH). These complex organic molecules are discussed in chapter 4 (Thiel et al. 2017). The molecule c-C_3H_2 is discussed in detail in Chapter 5 where we investigate the spatial structure of the line-of-sight clouds.

In many cases, several transitions of a molecule are detected. Table A.4 gives the detailed list of transitions identified in absorption in this survey. The list is valid for the positions K4 and $K6_{shell}$, which have higher SNR than the other four investigated positions. Hence, we see more transitions from more molecules in the lines of sight to these two positions.

We detected several transitions of the molecule CH_3NH_2 in the spectra towards all positions except towards L, the position with the lowest SNR. Three of these transitions are well detected towards K4 (see

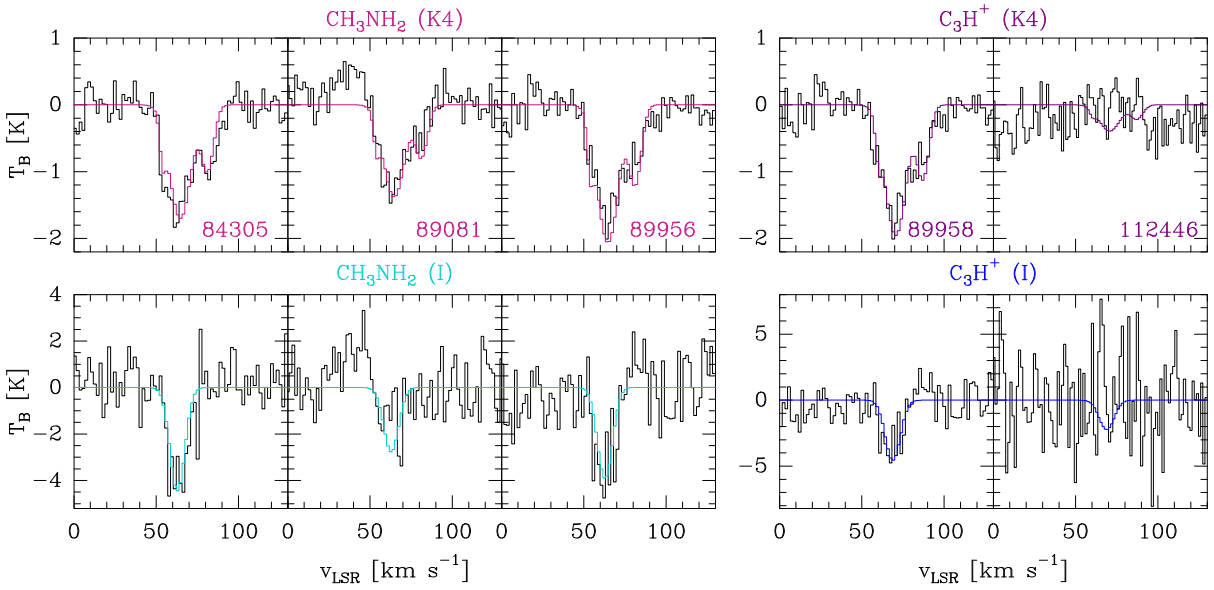

Figure 3.3: ALMA spectrum of three transitions of CH_3NH_2 towards the UCH II region K4 and the H II region I in the left panels. The spectra in magenta and in cyan are the synthetic spectra modelled using Weeds. In the right panels the model for the molecule C_3H^+ are shown. The frequencies of the transitions are indicated in the lower right of the upper panels.

Fig. 3.3). Gerin et al. (2018) investigated ALMA spectra towards Sgr B2(M) and Sgr B2(S) and assigned an absorption feature at the frequency of one of these CH_3NH_2 transitions (at about 89956 MHz) to C_3H^+. We modelled C_3H^+ in the spectra towards K4 and I to compare it to the model of CH_3NH_2 (see Fig. 3.3) and to check which molecule is the correct one causing the absorption feature at about 89956 MHz. The properties of the transitions used to calculated the synthetic spectra are listed in Table 3.2. For the model of CH_3NH_2 we used a rotational temperature of 4.6 K towards K4 and of 5.6 K towards I. To model C_3H^+ we assumed a rotational temperature of 2.73 K equal to the temperature of the CMB. Only two transitions of C_3H^+ are in the frequency range covered by the EMoCA survey. The resulting synthetic spectrum for C_3H^+ fits the observed spectrum. But there are several reasons speaking against C_3H^+ as responsible for the absorption feature at about 89956 MHz towards Sgr B2. The model of CH_3NH_2 simultaneously fits three transitions very well and the centroid velocities of the detected velocity components are all consistent with the velocities found for many other molecules detected in absorption in the envelope of Sgr B2. The molecular lines of CH_3NH_2 at 84.31 GHz and 89.96 GHz have the same upper energy level. As a result the quality of the fit is independent of model parameters such as the excitation temperature of CH_3NH_2. The second argument against the assignment to C_3H^+ is that it would imply a velocity shift of about 6 km s^{-1} in comparison to the centroid velocities fitted for all other molecules detected in absorption in the envelope of Sgr B2. The consistency between the velocities of the absorption features is one of our mandatory selection criteria for the identification of an absorption line (see Sect. 2.3.4). We are therefore confident that the transition at 89956 MHz is due to CH_3NH_2 and not C_3H^+. We determined the column density upper limit for C_3H^+ on the top of CH_3NH_2 assuming the same velocities and found about 5×10^{12} cm^{-2} in the envelope of Sgr B2 towards K4.

Table 3.2: Molecular transitions of CH_3NH_2 and C_3H^+.

Molecule	Transition	$\nu_0{}^a$ [MHz]	E_{up}/k^b [K]	$A_{u,l}{}^c$ [s^{-1}]
CH_3NH_2	$1_{1,5}$–$1_{0,5}$	84305.236	6.6	2.28×10^{-6}
	$2_{1,1}$–$2_{0,0}$	89081.457	10.7	6.55×10^{-6}
	$1_{1,0}$–$1_{0,1}$	89956.068	6.4	6.71×10^{-6}
C_3H^+	4–3	89957.625	10.8	3.39×10^{-5}
	5–4	89081.457	16.2	6.77×10^{-5}

Notes. [(a)] Rest frequency. [(b)] Upper energy level. [(c)] Einstein coefficient.

Table 3.3: Frequencies of unidentified lines towards K4.

Frequency [MHz]	Setup	SPW[c]	possible molecule	also detected towards[e] $K6_{shell}$	$K5_{shell}$	$K6_{shell,a}$	I	L
84946	1	0	C_2H_3CN	-	-	-	-	-
85570	1	0	?	a	a*	a	-	-
88323	2	0	C_2H_5CN	-	-	-	e	-
88593	2	0	?	-	-	-	e	-
89558–89598[b]	2	0	C_2H_5CN	a	a*	a/e	a/e	-
90453	2	1	C_2H_5CN	a	e*	-	e	e*
91336	2	1	?	a	e		e	e
93097	3	0	t-HCOOH	a	-	-	-	-
96921	1	2	C_2H_5CN	-	-	-	-	-
98177[d]	1	3	C_2H_5CN	-	a*	-	-	e
98513–98612[b,d]	1	3	C_2H_5CN	a*	a*	a*	e	e
99681	1	3	C_2H_5CN	a*	a*	-	-	e
100589-100614[b]	2 5	2 1	?	a	a	a	a	-
100614-100641[b]	2 5	2 1	NH_2CN	a	a	a	a	-
101980	2	3	H_2CCO	a	-	-	-	-
102550	2	3	?	-	a	a	a*	-
103051	2	3	?	a*	-	-	-	-
105795[a]	3	3	?	-	-	e		
111285	5	2	?	a	a	a	a*	a
112641	5	3	C_2H_5CN	a	e	a	-	-
113908	5	3	C_2H_5CN	a	e	a	-	-

Notes. The unidentified lines have a peak SNR>5. a and e mean absorption and emission, respectively. [(a)] All but this line are absorption lines towards K4. [(b)] Several absorption features not distinguishable are seen in the frequency range. [(c)] Spectral window. [(d)] These absorption features are not in the spectrum of SPW1 of Setup 3. [(e)] Positions, besides K4, towards which the unidentified lines are also seen. The positions where the feature has a peak SNR smaller than 5, but higher than 4 are marked with a star.

3.3.2 Unidentified lines

We could not assign all absorption and emission features to known molecules. A list with all unidentified lines in the spectrum towards K4 with a peak lower than $-5\sigma_{RMS}$ is reported in Table 3.3. Most unidentified lines are absorption lines. There is only one unidentified emission line at about 105795 MHz which is also detected towards $K6_{shell,a}$. We tried to find candidates for the unidentified lines. A candidate is found when the peak of the absorption or emission feature has the same velocity as the main velocity feature in the envelope of Sgr B2 at about 64 km s^{-1}. A possible molecular candidate for the absorption feature at about 84946 MHz is C_2H_3CN. We see this spectral feature only in the spectrum towards K4. C_2H_5CN, with two more hydrogen atoms, is a possible candidate for several of the unidentified lines. But the absorption features at 98177 MHz and 98513–98612 MHz, for which this molecule is a candidate, are seen in spectral window 3 of setup 1, but not in spectral window 1 of setup 3 where we would also expect to detect it because they cover the same frequency range. Because the spectral windows are deconvolved separately and have different uv coverages, this may be an artefact from the deconvolution process. The absorption that we see in SPW 3 of setup 1 may be a contamination from emission lines of the same molecule, which are seen towards the hot cores (Belloche et al. 2013). This contamination could be caused by the sidelobes of the dirty beam which may be not fully removed during the deconvolution of the data. The dirty beam has next to the main lobe several attenuated negative and positive sidelobes. Depending on the distance to the emission features towards the hot core positions, this artefact is either perceived as an emission or absorption feature. The positions and strengths of the sidelobes of the dirty beam depend on the uv coverage. Hence, different uv coverages result in the feature appearing in the one spectral window but not in the other one although they are covering the same frequency range and the spectra are extracted at the same position. Weak lines that are sometimes seen in absorption and sometimes in emission, or are not detected at all, depending on the investigated position, are most likely artefacts. We tried to model the two molecules C_2H_3CN and C_2H_5CN, but we were not able to find a synthetic spectrum matching the observed one.

The absorption at 93097 MHz may be caused by t-HCOOH. H_2CCO is a likely molecule for the absorption seen at 101980 MHz. These two absorption lines are also seen in the spectrum towards $K6_{shell}$, hence towards the two positions with the highest SNR. Modelling these two molecules we can find a synthetic spectrum that fits these observed absorption features. However, we lack the clear detection of other transitions of these two molecules to confirm these lines' assignment. Other transitions are covered by the EMoCA survey but they are predicted to be weak, with a SNR below 3. A higher sensitivity would help to confirm these candidates. Several unidentified absorption features and emission lines remain unidentified.

The spectra show absorption features next to the two transitions of CH_3CN over a wide range of frequencies: at 91950–91980 MHz and 110315–110378 MHz (see Figs. 3.4 and A.24). We tried to model these absorption lines, but we could not find a synthetic spectrum matching the observed one. These absorption features, not located within the velocity range in which the line-of-sight absorption is expected, may be artefacts of CH_3CN, which has higher energy transitions seen in the hot cores over this frequency range.

3.3.3 Calculating synthetic spectra

We detected several isotopologues for some of the molecules. For the modelling, we assumed the velocity components identified for different isotopologues of a given molecule to have the same centroid velocities, the same $FWHM$, and the same excitation temperature. Hence, to find a proper synthetic spectrum the isotopologues are modelled together starting from the weakest one with the lowest number of velocity components. The main isotopologue is usually optically thick for the velocity components that are also detected in the less abundant isotopologues. In a few cases, particularly for molecules with a hyperfine structure where the individual component lines have enough separation to allow to differentiate between

Table 3.4: Velocity ranges, corresponding locations and assumed isotopic ratios of the line-of-sight clouds towards Sgr B2.

location	$v_{\rm LSR}$ [km s^{-1}]	^{12}C/^{13}C^a	^{16}O/^{18}O^b	^{18}O/^{17}O^c	^{14}N/^{15}C^d
Galactic Center	< -50	20	250	2.88	300
3kpc arm	-50 to -35	40	327	4.16	350
4kpc arm	-30 to -10	40	327	4.16	350
Galactic Center	-9 to 8	20	250	2.88	300
Sgr arm	5 to 22	60	560	4.16	450
Scutum arm	25 to 39	40	327	4.16	350

Notes. References for the velocities: Greaves & Williams (1994); Neufeld et al. (2000); Lis et al. (2010); Menten et al. (2011); Monje et al. (2011); and references therein. We get some overlapping ranges if we combine the velocity ranges mentioned in these papers. We treat the clouds falling in the range between 5 and 8 km s^{-1} as GC clouds. We assume the following isotopic ratios to be the same in all velocity ranges: ^{32}S/^{34}S = 22^b , ^{34}S/^{33}S = 5^e , ^{28}SiO/^{29}SiO = 20^f, ^{29}SiO/^{30}SiO = 1.5^f. References for the isotopic ratios: $^{(a)}$ Milam et al. (2005) $^{(b)}$ Wilson & Rood (1994) $^{(c)}$ Wouterloot et al. (2008) $^{(d)}$ Dahmen et al. (1995) $^{(e)}$ Nummelin et al. (2000) $^{(f)}$ Penzias (1981)

them, such as CN and CCH, it is possible to derive the column densities of the velocity components properly, despite the high optical depth of some of the hyperfine components. Hence, we are able to determine isotopic ratios for CN for example (see Sect. 3.3.8). Some isotopic ratios can be determined using the less abundant isotopologues as for example C^{34}S/C^{33}S and are hence not affected by the optically thick velocity components of the main isotopologue. In the cases in which we cannot determine isotopic ratios we model the less abundant isotopologue and assume the same isotopic ratios as Belloche et al. (2013) to derive the column densities of the main isotopologue or the isotopologues with a higher abundance having optically thick absorption features. Thereby, we use slightly different velocity ranges as Belloche et al. (2013) (see Table 3.4). We assume the same isotopic ratios for the envelope of Sgr B2 as for the GC clouds.

For 12 molecules, at least two transitions with a good SNR are detected: CH_3CHO, CH_3CN, OCS, HC_3N, C_2H_5OH, NH_2CHO, HNCO, CH_3OH, CH_3NH_2, CH_3SH, $HOCO^+$, and ortho H_2CS. It is not possible to see where the absorption caused by CH_3CN in the envelope of Sgr B2 ends and the unidentified absorption features seen at lower frequencies with respect to these transitions start (see Fig. 3.4). Hence, we focus for the modelling of CH_3CN on the line-of-sight clouds and model only a single velocity component in the envelope of Sgr B2. We modelled the rotational temperature $T_{\rm rot}$ of CH_3CN with Weeds. For the other 11 molecules, we created population diagrams for each position where they are detected (see Table 3.5). For this purpose, we selected only the velocity components associated with the envelope of Sgr B2, because they are the strongest ones. Since these features overlap each other, we do not create the population diagram for each component individually. To produce the population diagrams, we first selected the velocity range for each molecule individually. Based on a first guess of $T_{\rm rot}$ we modelled the absorption feature of the envelope of Sgr B2 caused by one transition. Afterwards, we estimated the velocity range ($[v_{\rm low}, v_{\rm up}]$) as follows: $v_{\rm low} = v_1 - 3\sigma_1$ and $v_{\rm up} = v_2 + 3\sigma_2$ with v_1 the lowest and v_2 the highest centroid velocities of the velocity components associated with the envelope of Sgr B2. σ_1 and σ_2 are the corresponding widths of the components. To determine the upper energy level population N_u we have to integrate the spectrum over this range (see Sect. 2.5).

The linear fits to the population diagrams created for CH_3CHO and CH_3SH give rotational temperatures which could be successfully used for the modelling with Weeds (see for example Fig. 3.5). The other population diagrams resulting in $T_{\rm rot}$ values successfully usable with Weeds are shown in Figs. A.1–A.23.

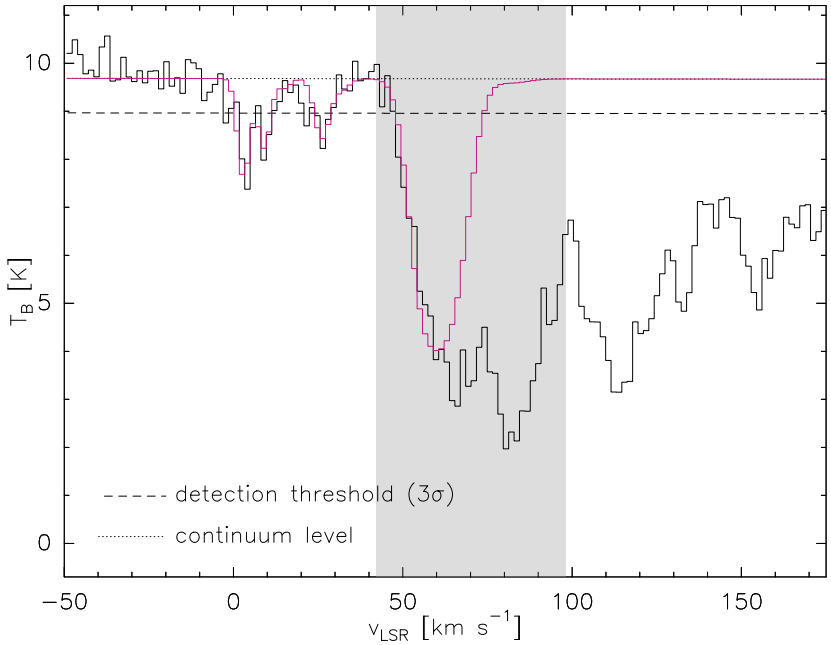

Figure 3.4: ALMA spectrum of CH_3CN $5_{0,0}$–$4_{0,0}$ at 91987.088 MHz towards the UCH II region K4. The spectrum in magenta is the synthetic spectrum modelled using Weeds. The dotted line represents the continuum level and the dashed line the 3σ line detection threshold. The grey area marks the velocity range of the envelope of Sgr B2 (v_{LSR}>42 km s^{-1}). The absorption at the right side of the grey area is not identified.

In all other cases, the synthetic spectrum calculated using T_{rot} fitted with the population diagram does not match the observed spectrum. The measured quantity (the integral of the spectrum over a certain velocity range) has usually very large uncertainties due to a low SNR of the absorption features. Hence, the fitted temperature may not directly result in a synthetic spectrum matching the observed spectrum, but a fit using a rotation temperature value still within the large uncertainty range eventually will. Another reason could be that the assumption of a single excitation temperature as we do by using Weeds for modelling is not valid. The population diagrams that we created for methanol mostly have a positive slope which would give us a negative rotational temperature. Because the absorption in the envelope of Sgr B2 is partially optically thick, we may underestimate the column densities and also the uncertainties. We tried to fit the rotational temperature with Weeds, but we did not find a solution. A reason could be that the assumption of a single excitation temperature is not valid for methanol. Hence, we assumed an excitation temperature of 2.73 K equal to the CMB temperature and fitted a synthetic spectrum matching the transition of methanol at about 96.74 GHz. The rotational temperatures determined with a population diagram for ortho H_2CS are significant below 2.73 K except for the position $K6_{shell,a}$. The upper energy levels are not very different for the two transitions which are detected. Furthermore, the absorption features seem to be contaminated by emission lines. Hence, the integrals to estimate the upper level energy population must have much larger uncertainties and cannot be estimated properly. We also assumed a rotational temperature of 2.73 K for ortho H_2CS .

In this thesis we focus only on the absorption lines. We model one or two emission components in the envelope of Sgr B2 for ^{13}CO to fit the data properly, but we concentrate in the following only on the absorption components.

Table 3.5: Rotational temperatures $T_{\rm rot}$ derived from population diagrams, or assumed.

Molecule	K4	$K6_{shell}$	$K5_{shell}$	$K6_{shell,a}$	I	L
CH_3CHO	4.0 ± 0.3	4.2 ± 0.3	4.2 ± 0.4	4.1 ± 0.3	3.4 ± 0.2	4.9 ± 2.4
CH_3SH	4.1 ± 0.6	3.8 ± 0.4	3.3 ± 0.6	4.4 ± 0.7	3.0 ± 0.7	–
C_2H_5OH	5.1 ± 2.0	3.8[a]	–	–	–	–
CH_3NH_2	4.6[a]	5.6[a]	4.6[a]	5.6[a]	5.6[a]	–
CH_3OH	2.7[b]	2.7[b]	2.7[b]	2.7[b]	2.7[a]	2.7[a]
ortho H_2CS	2.7[c]	2.7[c]	2.7[c]	3.4 ± 7.4	2.7[c]	2.7[c]
HC_3N	6.5 ± 0.2	5.6 ± 0.9	4.4[a]	6.6 ± 2.8	8.0[a]	4.6[a]
NH_2CHO	6.3 ± 1.1	6.0 ± 0.7	4.8[a]	6.0 ± 1.0	6.7 ± 0.8	4.3[a]
HNCO	7.7[a]	5.7[a]	3.2[a]	4.7[a]	6.7[b]	6.3 ± 0.9
$HOCO^+$	8.5[a]	6.3 ± 0.8	5.3[a]	7.0[a]	4.1 ± 0.9	10.0 ± 5.6
OCS	4.3[a]	10.2[a]	5.7[b]	7.2[a]	7.5 ± 2.6	10.2[a]

Notes. The temperatures are given in K. The values with an uncertainty are derived from a fit to the population diagram. The other values are an assumption to produce a synthetic spectrum matching the observed spectrum. [(a)] $T_{\rm rot}$ obtained with the population diagram does not result in a synthetic spectrum matching the observed spectrum. [(b)] Slope of the fit has the wrong sign which would give a negative rotational temperature. [(c)] With $T_{\rm rot}$ derived from the population diagram smaller than $T_{\rm CMB}$. Hence, we assume $T_{\rm rot} = T_{\rm CMB}$.

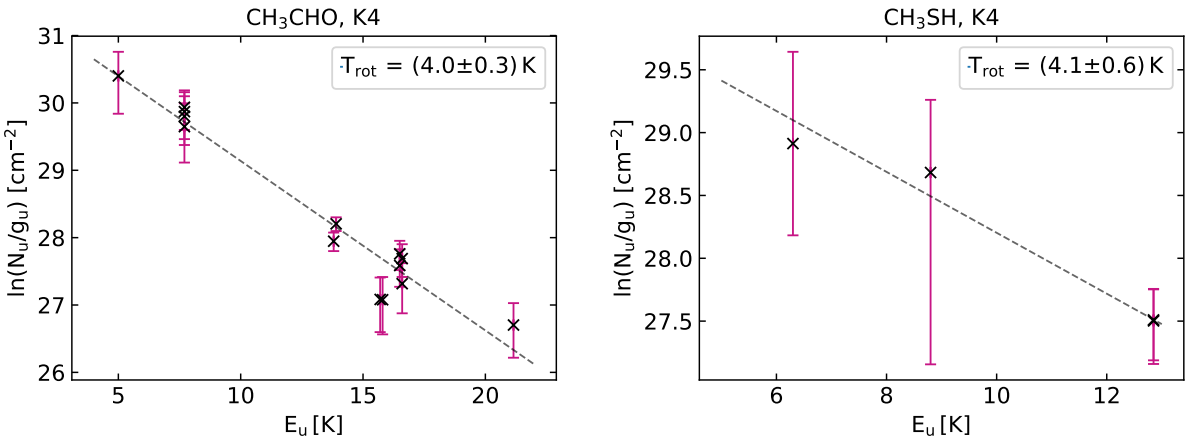

Figure 3.5: Population diagram of CH_3CHO and CH_3SH in the direction of K4. The rotational temperature is the negative inverse slope of the fitted linear relation.

3.3.4 Detected velocity components

We use Weeds (Maret et al. 2011) to model the velocity components detected towards the six positions in absorption. Tables A.5–A.10 list the molecules detected at each position and the centroid velocities of the velocity components. On the basis of the centroid velocity, we can associate the velocity component to a specific location along the line of sight to Sgr B2 (see Table 3.4 and Fig 1.5 for a sketch). The line-of-sight clouds around $v_{\rm LSR}$=0 km s^{-1} can be associated with the GC or the local spiral arm. Gardner & Whiteoak (1982) determined a low isotopic ratio $\frac{^{12}C}{^{13}C}$ of 22 for this velocity range, which strongly suggests a location in the GC region. In Sect. 3.3.8 we investigate isotopic ratios for some of the line of sight clouds and the envelope of Sgr B2. The resulting values for $\frac{^{12}C}{^{13}C}$ of about 20–21 confirm this measurement. Hence, we assume that the strong absorption around 0 km s^{-1} is caused by a cloud located in the GC. Therefore, we

treat the velocity range from −9 to 8 km s^{-1} to be a part of the GC region absorption.

Usually, the envelope of Sgr B2 produces absorption at velocities between 50 and 90 km s^{-1} (Neill et al. 2014), with two main velocity components at about 64 km s^{-1} and 80 km s^{-1} (e.g., Huettemeister et al. 1995; Lang et al. 2010). Because the detailed investigation of c-C_3H_2 reveals a velocity component at about 48 km s^{-1} with properties similar to those of the other line-of-sight clouds (see Section 5.4.2), we also list this component in Tables A.5–A.10 in addition to the envelope of Sgr B2 and the spiral arm clouds mentioned in Table 3.4.

The complete spectrum towards K4 is shown in Fig. A.24 in Appendix A, for which we ignored SPW 2-3 from Setup 1 and SPW 2 and the first half of SPW 3 of Setup 2 for the plot. The frequency range of these SPWs is also covered by other SPWs with a higher SNR for the continuum. The feature at about 91675 MHz is not a real absorption feature, it is a spiky artefact. The synthetic spectrum calculated using Weeds is overlaid on the ALMA spectrum. The molecular transitions detected in absorption are labeled in blue. Most emission lines in the spectra are hydrogen and helium recombination lines (labeled in green). Only the parts of the spectrum showing absorption features are depicted for all six investigated positions in Fig. A.25 in Appendix A. The same numbers of molecules and transitions are detected in the spectra towards K4 and K6$_{\rm shell}$. The SNRs in the spectra towards the other four positions are lower (see Tables A.1–A.3) and hence less molecules are detected. The spectrum towards L has the lowest SNR resulting in the lowest number of detected molecules. The model parameters of all molecules are listed in Tables A.11–A.38 in Appendix A.

3.3.5 Velocity distribution

To investigate the velocity structure of the line-of-sight clouds, in Fig. 3.6 we show the distribution of centroid velocities using all velocity components detected for all molecules. We plotted the histogram for each of the six examined positions individually to compare the different positions to each other. Thereby, we look for common prominent characteristics or prominent differences between the lines of sight. A strong velocity component with higher abundances of the molecules is detected for many molecules and hence is described by a peak in the histogram. A velocity component can be associated with a cloud. Because it is possible that several overlapping velocity components are fitted with one single velocity component, these fitted components represent at least one cloud but may also include multiple clouds.

The envelope of Sgr B2(N) (positions: K4, K6$_{\rm shell}$, K5$_{\rm shell}$, and K6$_{\rm shell,a}$) is described by mainly three velocity components: at ∼64 km s^{-1}, ∼71 km s^{-1}, and ∼81 km s^{-1}. The spectra towards K6$_{\rm shell}$ and K4 have additional main components in the envelope of Sgr B2, one at about 55 km s^{-1} towards both positions and K4 has also one at about 90 km s^{-1}. The spectrum toward I does not show any absorption feature for velocities $v_{\rm LSR}$>70 km s^{-1} for most molecules. The centroid velocities of the velocity components determined for the molecules detected towards L are shifted to lower velocities by about 8 km s^{-1} in comparison to the other five positions. The cloud at about 48 km s^{-1} is mainly detected in the spectra towards K4, K6$_{\rm shell}$, K6$_{\rm shell,a}$, and I. Many velocity components are detected in the Sagittarius, Scutum, and 4 kpc arms. However, no obvious similarities or differences are visible in the histograms for these arms. Two distinct velocity features which are associated with the 3 kpc arm (−48 km s^{-1} and −40 km s^{-1}) are seen towards all six positions. The clouds with velocities around 0 km s^{-1}, associated with the GC, are detected for many molecules, especially in the spectrum towards K4. One velocity component stands out for the GC with $v_{\rm LSR}$<−50 km s^{-1}, the one at −106 km s^{-1}. It is detected for many molecules in the spectra towards Sgr B2(N). This absorption feature is not seen in the spectra towards L and I. They show two velocity components at about −101 km s^{-1} and −109 km s^{-1}.

The distributions of linewidths ($FWHM$) for each of the six positions is shown in Fig. 3.7. Each his-

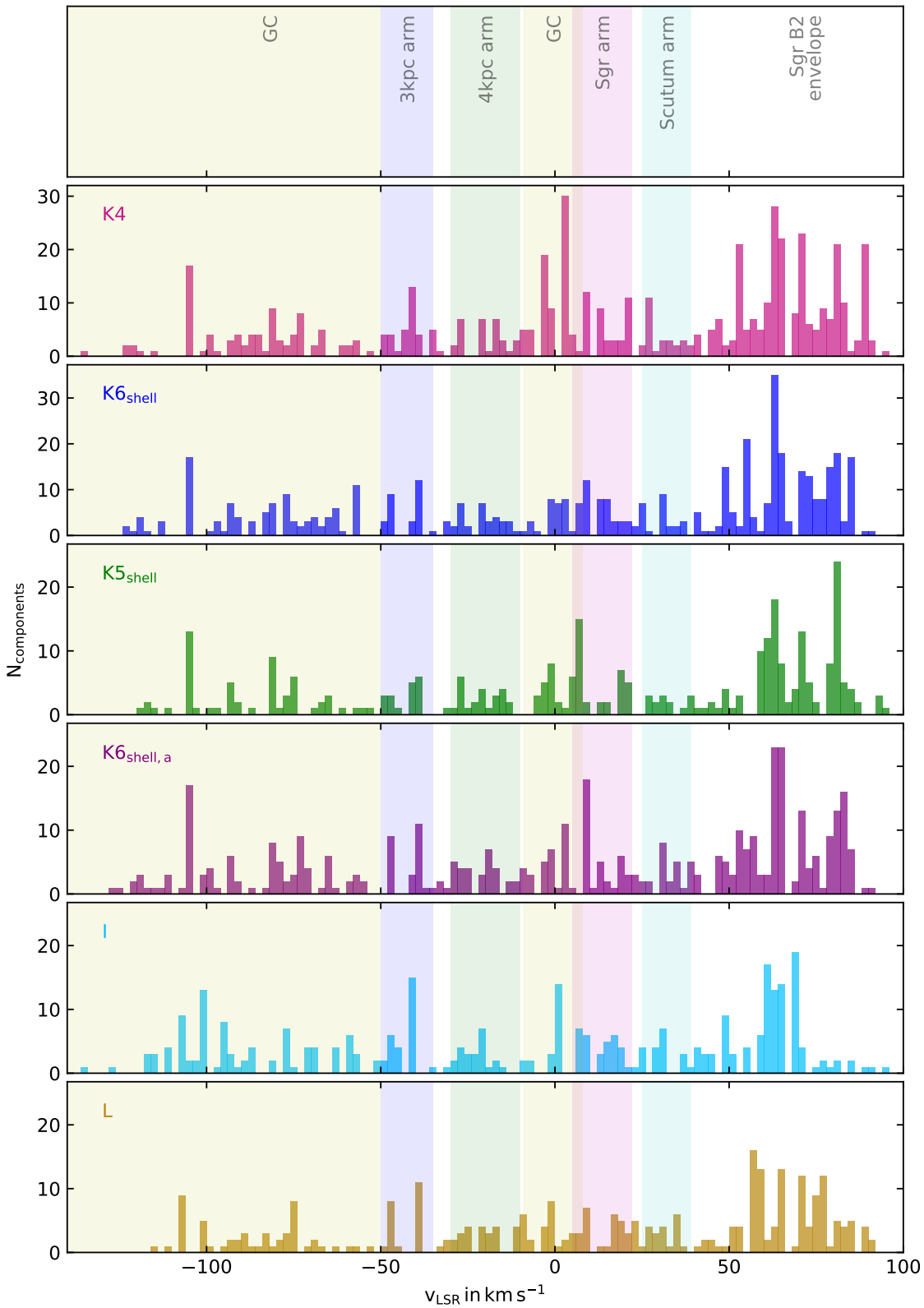

Figure 3.6: Number of velocity components found for all molecules as a function of centroid velocity for each investigated position. The bin width is 2 km s^{-1}. The velocity ranges are colour coded in the background of each panel (see Table 3.4 for references).

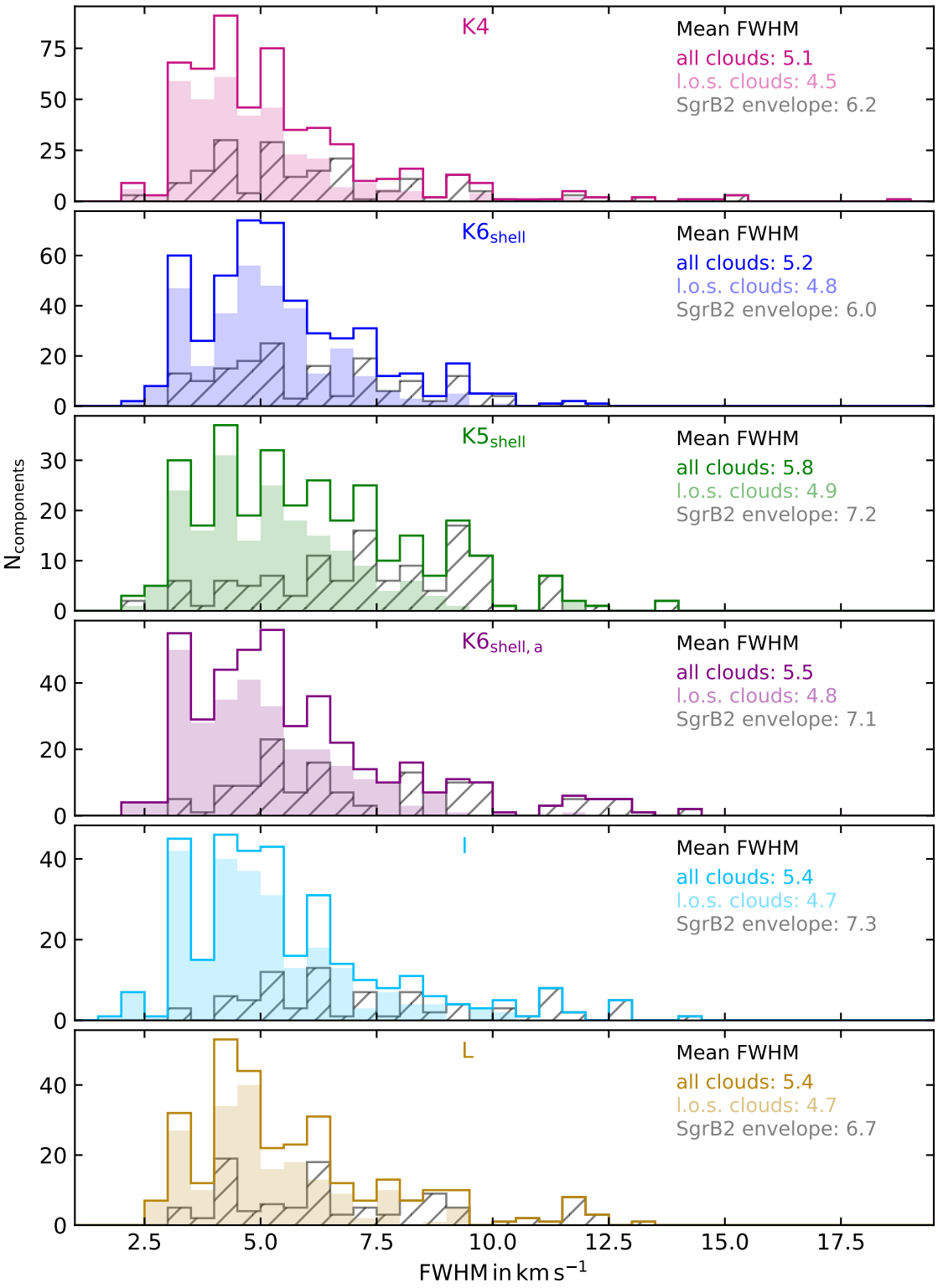

Figure 3.7: Number of velocity components as a function of linewidth for each investigated position. The bin width is 0.5 km s^{-1}. In all panels the line-of-sight clouds are displayed in full colour and the components tracing the diffuse envelope of Sgr B2 ($v_{\rm LSR}$>56 km s^{-1}) in hatched grey. The mean $FWHM$ are given in km s^{-1} for all three categories in each panel.

togram is split into a distribution describing the envelope of Sgr B2 ($v_{\rm LSR}$>56 km s^{-1}) and one describing the line-of-sight clouds. The lower limit of $FWHM$ is 1.5 km s^{-1}, the averaged channel width of the ALMA data. The linewidths cover the range between the lower limit and about 19 km s^{-1}. The majority of the clouds (l.o.s. clouds and Sgr B2 envelope) has a linewidth smaller than 10 km s^{-1}. The tails seen up to 19 km s^{-1} are very weak. The broader velocity components are most likely caused by two or more overlapping components with narrower widths. These broad components are mostly associated with the Sgr B2 envelope showing a broad absorption feature. Maybe these components contain several cloud entities, which we cannot distinguish. In total, the mean $FWHM$ for all clouds is similar for the six positions (5.1–5.8 km s^{-1}). Particularly the l.o.s. clouds have the same properties ($FWHM$=4.5–4.9 km s^{-1}). The mean linewidths of the clouds belonging to the envelope of Sgr B2 are larger (6.2–7.3 km s^{-1}). These larger values may be caused by the optical thickness of the absorption of some molecules in this velocity range. If the absorption is optically thick over a broader velocity range it is difficult or even impossible to fit individual velocity components. On the other hand, optically thin lines can also show broad features. The velocity components in the envelope of Sgr B2 fitted to the spectra towards K4 and K6$_{\rm shell}$ have smaller linewidth (6.0–6.2 km s^{-1}) than those at the other four positions (6.7–7.3 km s^{-1}). The latter four positions have lower SNR. The velocity components are not always well distinguishable and the width of the fitted velocity components can be broader.

3.3.6 Column density profiles

To compare the column density profiles of individual molecules for the six different positions, we created column density distributions using the parameters fitted with Weeds: column densities, $FWHM$, and centroid velocities. For this purpose, we selected the data for the 12 strongest molecules that show many and the most prominent absorption features along the line of sight: HCO^+, CCH, c-C_3H_2, ^{13}CO, CS, CN, SiO, SO, HCN, HNC, N_2H^+, and CH_3OH. It is difficult to use only the spectra to investigate the column density profile across the velocity range, because the absorption of some of these molecules is optically thick over a wide range in velocity (HCO^+ and HCN). Some of the molecules have hyperfine structure or several transitions with similar frequencies resulting in overlapping absorption features caused by the same velocity component (CCH, CN, HCN, N_2H^+, and CH_3OH). But the modelling with Weeds allows us to deconvolve the spectrum from the hyperfine structure of the transitions and thus derive a proper column density profile. For the molecules with optically thick lines, we need less abundant isotopologues to derive the column density profile.

The column density profiles of HNC are shown in Fig. 3.8, those of the other molecules in Figs. A.26–A.36 in Appendix A. In addition, the corresponding spectra are depicted. At first sight, the four positions towards Sgr B2(N) (K4, K6$_{\rm shell}$, K5$_{\rm shell}$, and K6$_{\rm shell,a}$) are more similar to each other than in comparison to the two positions towards Sgr B2(M) and Sgr B2(L). All positions seem to trace roughly the same velocity structure with a few differences. We can identify several strong absorption features in the line-of-sight clouds with one or more peaks for all positions. The GC clouds with velocities smaller than −50 km s^{-1} show four distinct features at about −106 km s^{-1}, −92 km s^{-1}, −85 to −72 km s^{-1}, and a very weak component at about −58 km s^{-1}. The 3 kpc arm is traced by mostly two velocity components at about −48 km s^{-1} and −39 km s^{-1}. The 4 kpc arm can be described by one to three velocity components that are mostly overlapping each other in the velocity range of −35 to −15 km s^{-1}. The GC clouds around 0 km s^{-1} show mostly a strong peak at about 3 km s^{-1} overlaid on a broader structure. A strong absorption peak at about 17 km s^{-1} describes the Sagittarius arm and a weak one at about 30 km s^{-1} the Scutum arm. The envelope of Sgr B2 reveals the same features as those mentioned in the previous section. The spectra as well as the column density profiles of the molecules HNC, CS, and ortho c-C_3H_2 show this structure best (see Figs. 3.8,

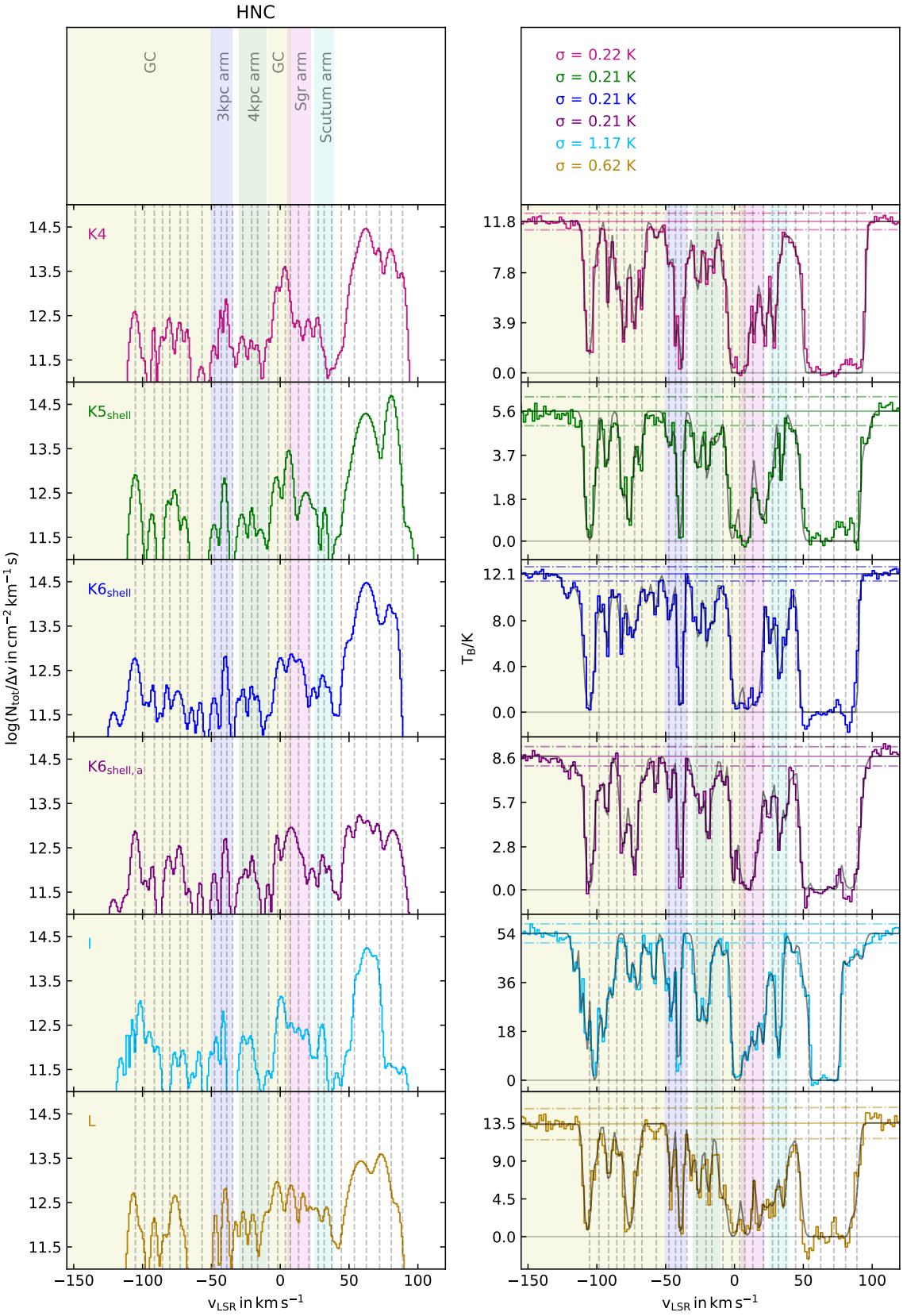

Figure 3.8: Column density profiles of HNC (left panels) calculated from the Weeds model overlaid in grey on the spectra (right panels) at six positions. The dashed lines mark the centroid velocities of the Gaussian components fitted to the spectrum towards K4 with Weeds. The dotted dashed lines mark the $\pm 3\sigma_{\mathrm{RMS}}$ noise level, given in the upper right panel. The solid grey lines mark the zero level, the solid coloured lines the continuum level. The velocity ranges are colour coded in the background of each panel (see Table 3.4 for references).

A.30, and A.28, respectively).

The column density profiles determined towards I do not show any absorption or only weak absorption for velocities higher than $v_{\rm LSR}$ ≈75 km s^{-1}. The only exception is ^{13}CO. To fit the spectra properly for this molecule, we have to add additional emission components in the envelope of Sgr B2. We try to fit as little emission components as possible (one to two). We modelled them simultaneously to the velocity components seen in absorption. From the less abundant isotopologues we get the centroid velocities and $FWHM$ for most of the absorption components of ^{13}CO. For these components, we have only to adjust the column densities.

The column density profiles towards K4 and K5$_{\rm shell}$ are very similar for all investigated molecules as well as the profiles towards K6$_{\rm shell}$ and K6$_{\rm shell,a}$. For example, the first two positions have a stronger absorption caused by GC clouds with velocities around 0 km s^{-1} than at velocities associated with the Sagittarius arm. In contrast, the latter two positions show similarly strong absorptions in these two velocity ranges (for example see Fig. A.32). The absorption caused by the Sagittarius arm is quite strong for HCN, HCO$^+$, and N_2H^+ for K6$_{\rm shell}$ and K6$_{\rm shell,a}$, and for L also for the molecules SO, SiO and CH_3OH. The spectra mostly show weak absorption at velocities tracing the Scutum arm.

The column densities determined between −85 and −65 km s^{-1} towards I are lower than for the other positions compared to the rest of the column density profile (for example see HNC and CS in Figs. 3.8 and A.30, respectively). On the contrary, the spectra towards Sgr B2(L) reveal stronger absorption over this velocity range compared to the absorption feature at about −106 km s^{-1}. For the other five positions, it is the other way round. The spectra towards L do not show absorption as extended in velocity as some molecules do at negative $v_{\rm LSR}$ (see for example Fig. A.26). Usually the SNR in the spectra towards L is lower, which may cause a non-detection of these velocity components. On the other hand, most of the features not detected towards L have relatively high SNR towards other positions and hence the low SNR towards L may be not the only reason for a non-detection of these features (see Fig. A.26).

^{13}CO does not produce an absorption around 0 km s^{-1} as strong as the other molecules do. Furthermore, the spectra of ^{13}CO show stronger absorptions at velocities tracing the 3 kpc and 4 kpc arms.

In summary, the column density profiles of all six positions are relatively similar to each other. The four positions towards Sgr B2(N) are more similar to each other. The two positions more distant to Sgr B2(N) show in comparison larger variations in the column density profiles.

3.3.7 Correlations between molecules

In this section we investigate if there are correlations in abundance between pairs of molecules. For this purpose, we use the parameters fitted using Weeds. We selected only the line-of-sight clouds with $v_{\rm LSR}$<56 km s^{-1}, excluding the envelope of Sgr B2 which has different properties than the line-of-sight clouds (see Sect. 5.4.2). For each pair of molecules, we searched for centroid velocities matching in a range of plus or minus 2 km s^{-1} to find a sample of velocity components detected for both molecules. We want to compare the peak column densities, hence, we take the integrated column density $N_{\rm tot}$ divided by the $FWHM$ of the Gaussian describing a velocity component. We selected the same 12 molecules as used for the column density profile analysis in the previous section. Because the ^{12}C/^{13}C ratio changes depending on the galactocentric distance (see Table 3.4), we determined the CO column densities from the ^{13}CO column densities using the isotopic ratios of Table 3.4. The correlation plots between HNC and CN and HNC and CS are shown in Fig. 3.9. All other correlation plots can be found in Appendix A (see Figs. A.37–A.66). The correlation plot of each pair of molecules shows the column density divided by the $FWHM$ for each pair of velocity components matching within ±2 km s^{-1}. The colours give the positions of the investigated spectra. We fitted two lines to all correlation plots in log-log space: $y = ax+b$ and $y = x+b$. The latter linear

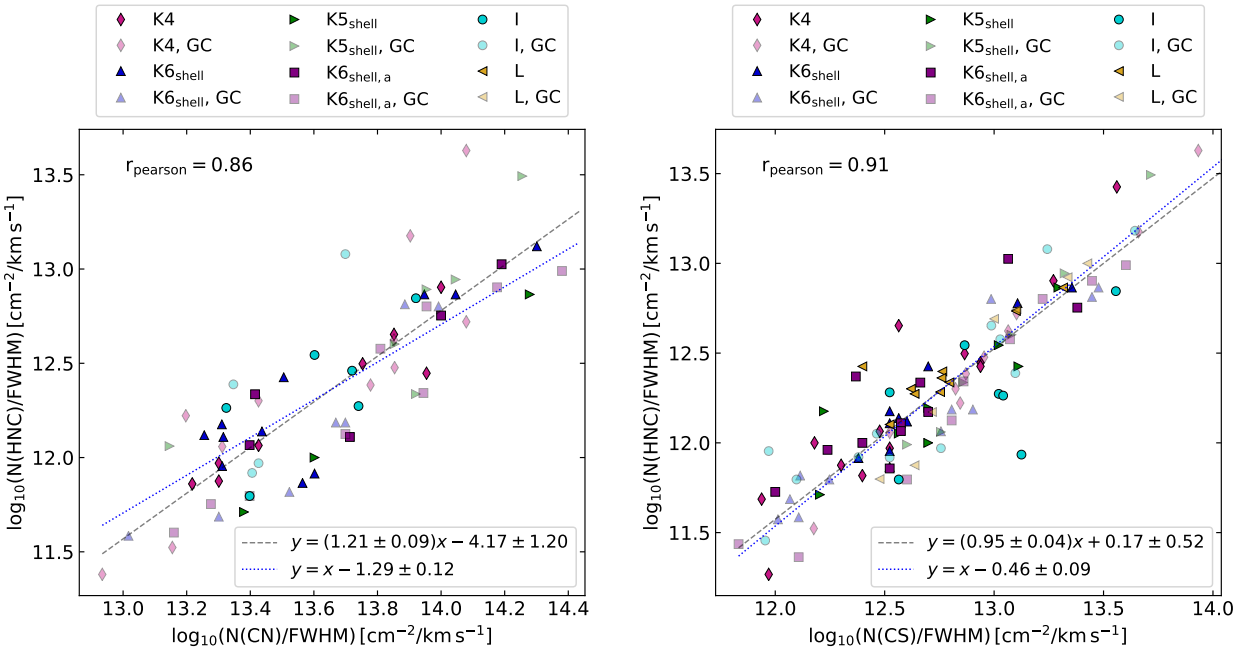

Figure 3.9: Column density divided by $FWHM$ of HNC plotted against the column density divided by the $FWHM$ of CN (left) and CS (right). The blue dotted line represents the fit in log-log space with $y = x + b$, the black dashed line the one with $y = ax + b$. The markers with fainter filling colours represent the velocity components belonging to the GC. The Pearson's correlation coefficient is given in the upper left.

relation describes a direct proportionality between the molecules. In addition, we calculated the Pearson's correlation coefficient r of the correlation plots for an estimation of the strength of the linear correlation. The resulting correlation matrix is given in Table 3.6. The values on the main diagonal are always 1 and the transposed matrix is equal to the original matrix. As described in Sect. 2.8 a Pearson's correlation coefficient with a value between 0.6 and 0.79 describes a strong correlation and with a value larger than 0.8 the correlation between the two datasets is very strong (Evans 1996). Hence, we will only take a closer look at the molecule pairs with $r \geq 0.6$. All Pearson's correlation coefficients with values below 0.6 are coloured in grey in Table 3.6. There are only two pairs of molecules which show a very strong correlation: HNC and CN and HNC and CS with $r = 0.86$ and $r = 0.91$, respectively (see Fig. 3.9). The only molecule which does not show a correlation with any of the other molecules is CO.

Because only two pairs have a very strong correlation ($r > 0.8$), in the following we will refer to all molecule pairs with a Pearson's correlation coefficient larger than 0.6 as strong. The Pearson's correlation matrix indicates the following relationships between several molecules. The molecules CS, CN, HCN, HNC, and CCH are all strongly correlated to each other. Whereas CS does not show any other correlation with r>0.6, the other four molecules show also strong correlation with HCO^+ and N_2H^+. These two molecules are also correlated to each other. The correlation of HCO^+ to CCH is discussed in detail in Sect. 5.5.2. CCH, ortho c-C_3H_2, HCN, HNC, and N_2H^+ make up another group of molecules strongly correlated to each other. HCN is strongly correlated with all other 11 investigated molecules except for CO and SO. SiO, SO, and CH_3OH are strongly correlated to each other, but not to HCO^+.

The inspection of the correlation plots (see Appendix A.8) shows that the number of data points in the correlation plots is relatively low, when the investigated pair of molecules include one of the following molecules: SO, SiO, N_2H^+ and CH_3OH. Hence, we have to treat these correlations carefully. For the

Table 3.6: Pearson's correlation coefficients.

Molecule	HCO^+	CCH	ortho c-C_3H_2	CO	CS	CN	SiO	SO	HCN	HNC	N_2H^+	CH_3OH
HCO^+	1	0.67	0.50	0.27	0.58	0.67	0.52	0.18	0.71	0.69	0.61	0.26
CCH	0.67	1	0.67	-0.02	0.62	0.76	0.73	0.55	0.78	0.75	0.62	0.37
c-C_3H_2-o	0.50	0.67	1	-0.20	0.56	0.49	0.57	0.59	0.61	0.62	0.62	0.58
CO	0.27	-0.02	-0.20	1	0.19	0.24	-0.21	-0.41	-0.02	0.18	-0.01	-0.16
CS	0.58	0.62	0.56	0.19	1	0.76	0.49	0.41	0.62	0.91	0.52	0.41
CN	0.67	0.76	0.49	0.24	0.76	1	0.50	0.46	0.75	0.86	0.69	0.60
SiO	0.52	0.73	0.57	-0.21	0.49	0.50	1	0.71	0.74	0.57	0.65	0.76
SO	0.18	0.55	0.59	-0.41	0.41	0.46	0.71	1	0.56	0.26	0.58	0.74
HCN	0.71	0.78	0.61	-0.02	0.62	0.75	0.74	0.56	1	0.75	0.65	0.72
HNC	0.69	0.75	0.62	0.18	0.91	0.86	0.57	0.26	0.75	1	0.67	0.49
N_2H^+	0.61	0.62	0.62	-0.01	0.52	0.69	0.65	0.58	0.65	0.67	1	0.67
CH_3OH	0.26	0.37	0.58	-0.16	0.41	0.60	0.76	0.74	0.72	0.49	0.67	1

Notes. All correlation coefficients smaller than 0.6 are coloured in grey.

Table 3.7: Average column density ratios of correlated molecules $a = \frac{y}{x}$.

x \ y	HCO^+	CCH	ortho c-C_3H_2	CS	CN	HCN	HNC
HCO^+	1	2.9 ± 0.8	–	–	6.0 ± 1.8	1.6 ± 0.4*	0.28 ± 0.06*
CCH	0.35 ± 0.10*	1	0.037 ± 0.01	0.26 ± 0.07*	1.9 ± 0.6*	0.56 ± 0.16*	0.083 ± 0.021*
c-C_3H_2-o	–	26.9 ± 7.4*	1	–	–	15.5 ± 4.3*	2.3 ± 0.6*
CS	–	3.9 ± 1.0	–	1	7.1 ± 2.0	2.1 ± 0.5*	0.35 ± 0.07
CN	0.17 ± 0.05*	0.52 ± 0.16	–	0.14 ± 0.04*	1	0.28 ± 0.08*	0.051 ± 0.014
HCN	0.65 ± 0.16	1.8 ± 0.5	0.065 ± 0.018	0.48 ± 0.12	3.6 ± 1.1	1	0.17 ± 0.04
HNC	3.6 ± 0.8	12.0 ± 3.0	0.43 ± 0.11	2.9 ± 0.6*	19.5 ± 5.4*	6.0 ± 1.5*	1

Notes. The correlation plots for the molecule pairs of which the ratios are marked with a star are shown in Fig. 3.9 and in Sect. A.8 in Appendix A.

investigation of the molecular ratios we will focus on the other molecules excluding these four molecules as well as CO. We will discuss the strength of the correlation between the molecules HCO^+, CCH, ortho c-C_3H_2, HCN, HNC, CS, and CN. To summarise the relations between these seven molecules: They are strongly correlated with only a few exceptions. First, ortho c-C_3H_2 is only strongly correlated with CCH, HCN, and HNC and secondly, HCO^+ is not strongly correlated with CS and ortho c-C_3H_2.

We calculated the column density ratios between the aforementioned seven molecules for all pairs with a Pearson's correlation coefficient larger than 0.6 (see Table 3.7). For this, we used the resulting parameters of the fit that used the function $y = x + b$.

3.3.8 Isotopic ratios

Because in many cases either lines from the main isotopologue are optically thick or the weaker isotopologue has a too low abundance to be detected, it is difficult to measure the isotopic ratios. For a few molecules, this is possible for some velocity ranges and specific isotopologues. CN has a hyperfine structure. Because the absorption caused by this molecule is optically thin for some of its hyperfine components, we can deduce the column densities of the velocity components of CN directly from the spectrum. We determine the ratios CN/^{13}CN and CN/C^{15}N (see Fig. 3.10). For SiO and HCO^+, we calculated the isotopic ratios between the

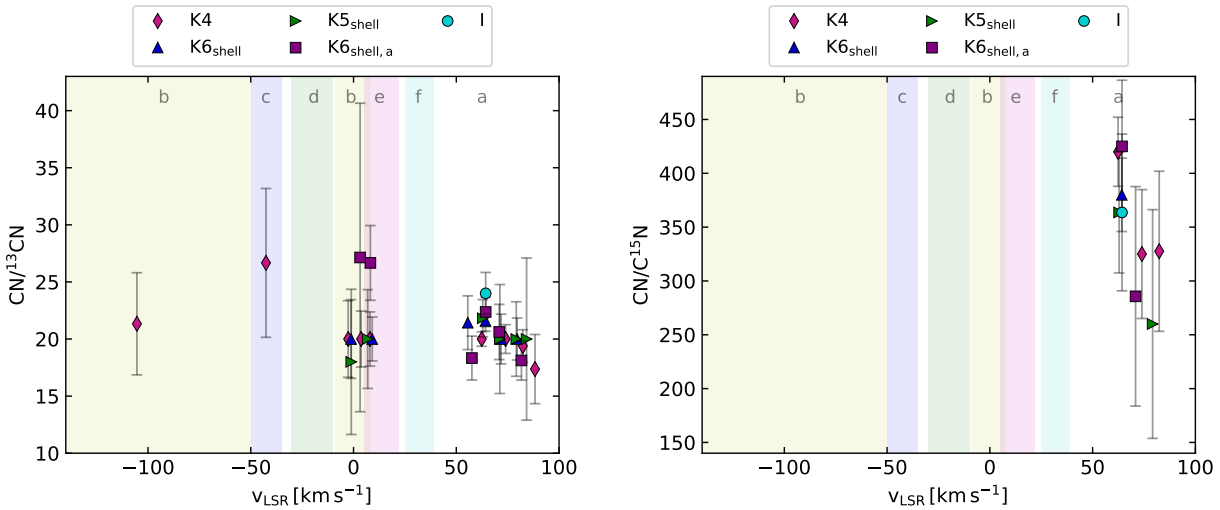

Figure 3.10: Isotopic ratios: CN/^{13}CN and CN/C^{15}N. The velocity ranges are colour coded in the background as in Fig. 3.8 with *a* the envelope of Sgr B2, *b* the GC clouds and *c*, *d*, *e*, and *f* the 3 kpc, 4 kpc, Sagittarius and Scutum arms, respectively (see Table 3.4 for references).

weaker isotopologues: ^{29}SiO/^{30}SiO and HC^{18}O$^+$/HC^{17}O$^+$. Five isotopologues of CS are detected, which gives the possibility to use different combinations of isotopologues to determine an isotopic ratio: CS/^{13}CS and C^{34}S/^{13}C^{34}S for the ratio ^{12}C/^{13}C and CS/C^{34}S and ^{13}CS/^{13}C^{34}S for ^{32}S/^{34}S. The resulting values and the corresponding figures are listed in Table 3.8. Isotopic ratios determined using CS have to be treated carefully, because CS has a relatively high opacity for the used velocity components and hence may be optically thick. Thus, the resulting values are lower limits.

We determined the ratio of ^{12}C/^{13}C using CN in the envelope of Sgr B2 and the GC clouds to be about 20. Using CS, we obtain CS/^{13}CS>17 in the GC clouds and C^{34}S/^{13}C^{34}S=27±6 in the Sgr B2 envelope. The clouds in the 3 kpc arm have a ratio of ^{12}CN/^{13}CN=27±6.

The isotopic ratio of C^{14}N/C^{15}N in the envelope of Sgr B2 is 350±50.

The oxygen isotopic ratio ^{18}O/^{17}O calculated using HCO$^+$ is about 3.3 in the envelope of Sgr B2. The ratio ^{29}SiO/^{30}SiO is equal to 1.5 in the envelope of Sgr B2 and to 1.7 in the GC clouds around 0 km s^{-1}.

We calculated the sulphur isotopic ratios using CS. ^{34}S/^{33}S is 5±2 in the envelope of Sgr B2 and in the GC clouds with velocities around 0 km s^{-1}. The dispersion is relatively large for the velocity components in the envelope of Sgr B2 determined in the spectrum towards K4. All other velocity components determined towards the other positions do not show such a dispersion. We used many components to fit the envelope of Sgr B2 in the spectrum towards K4. Because they overlap each other it is difficult to find the correct number and widths of the components, especially when the number of components has to be the same for all isotopologues. This could explain the dispersion for the individual components and the average value similar to the isotopic ratios determined for the other 5 positions. The ratio of ^{32}S/^{34}S is equal to 18±5 in the envelope of Sgr B2 (using ^{13}CS/^{13}C^{34}S), and larger than about 21 in the GC clouds with velocities below −50 km s^{-1} (using CS/C^{34}S). Using the latter combination of isotopologues, the isotopic ratio CS/C^{34}S for the line-of-sight clouds is >13.

Table 3.8: Mean ($\bar{x}$) and median ($\tilde{x}$) isotopic ratios.

Isotopic ratio	Fig.	Sgr B2 envelope		GC 1[a]		GC 2[b]	
		$\bar{x}$	$\tilde{x}$	$\bar{x}$	$\tilde{x}$	$\bar{x}$	$\tilde{x}$
$CN/^{13}CN$	3.10	20.3 ± 1.6	$20.0^{+1.7}_{-1.1}$	21.3 ± 3.1	$20.0^{+4.9}_{-0.0}$	$21.3 \pm 4.5^{*}$	-
$CN/C^{15}N$	3.10	350 ± 53	364^{+46}_{-67}	-	-	-	-
$^{29}SiO/^{30}SiO$	A.101	1.50 ± 0.12	$1.49^{+0.13}_{-0.10}$	$1.67 \pm 0.29^{*}$	-	-	-
$HC^{18}O^{+}/HC^{17}O^{+}$	A.102	3.33 ± 0.65	$3.45^{+0.38}_{-0.57}$	-	-	-	-
$C^{34}S/C^{33}S$	A.103	5.2 ± 1.9	$5.2^{+1.1}_{-1.7}$	5.2 ± 0.4	$5.2^{+0.3}_{-0.3}$	-	-
$CS/C^{34}S$	A.104	-	-	-	-	$> 20.6 \pm 3.5$	$> 16.1^{+2.8}_{-4.4}$
$^{13}CS/^{13}C^{34}S$	A.105	17.7 ± 4.8	$16.3^{+7.3}_{-2.1}$	-	-	-	-
$CS/^{13}CS$	A.106	-	-	-	-	$> 17.3 \pm 2.2$	$> 17.1^{+2.0}_{-1.6}$
$C^{34}S/^{13}C^{34}S$	A.107	27.3 ± 6.2	$28.3^{+5.8}_{-3.4}$	-	-	-	-

Isotopic ratio	Fig.	3 kpc arm		4 kpc arm		Sgr arm	
		$\bar{x}$	$\tilde{x}$	$\bar{x}$	$\tilde{x}$	$\bar{x}$	$\tilde{x}$
$CN/^{13}CN$	3.10	$26.7 \pm 6.5^{*}$	-	-	-	-	-
$CS/C^{34}S$	A.104	$> 12.8 \pm 5.4$	$> 14.8^{+2.8}_{-8.0}$	$> 15.0 \pm 4.0^{*}$	-	$> 15.6 \pm 0.6$	$> 15.6^{+0.4}_{-0.4}$

Notes. Values marked with a star are derived from a single velocity component detected in this velocity range. Their uncertainties are calculated using the error propagation law. [(a)] -8 km s^{-1}<$v_{\rm LSR}$<9 km s^{-1}. [(b)] $v_{\rm LSR}$<-50 km s^{-1}.

3.4 Discussion

3.4.1 Velocity structure

We identified up to 32 individual velocity components including the envelope of Sgr B2 for HCO^{+} (see Table A.23). The number of detected velocity components depends on the investigated position and the strength of the continuum. A higher SNR and a stronger continuum are needed to also detect weaker velocity components. The molecule N_2H^{+} is a good example (see Fig. A.35). Depending on the position and hence on the strength of the continuum and on the noise level some velocity components are detected or not. The velocity structure of the twelve investigated molecules is similar. The velocity structure of one of these twelve molecules, c-C_3H_2, is investigated in detail in Sect. 5.4.2. The continuum at the position of Sgr B2(N1) is quite strong in comparison to that at the positions investigated here (see Fig. 3.1) and hence weaker velocity components can be detected. However, this hot core produces numerous emission lines which contaminate the absorption features investigated here. This is why we decided not to analyse this position.

3.4.2 Velocity dispersions

The smallest linewidth derived from our fits is 1.5 km s^{-1}, which corresponds to the median channel width of our data. The largest linewidth we fitted to the data is about 19 km s^{-1}. The distributions of the $FWHM$ of the six investigated positions are similar. Corby et al. (2018) investigated also the molecules c-C_3H_2, CS, SO, and SiO, but with GBT data with an angular resolution of 15–41″. The transitions of the four molecules are at 18.3 GHz, 49.0 GHz, 30 GHz and 43.4 GHz, respectively. They found a range of $FWHM$ between ~1 and 20 km s^{-1} with only a few velocity components with a $FWHM$ larger than 10 km s^{-1}. Roughly the same range of $FWHM$ are found for the molecules OH and OH^{+} in the line-of-sight clouds to several continuum sources other than Sgr B2 (Wiesemeyer et al. 2016). The majority (94.7–99.2%) of the linewidths modelled

here is smaller than 10 km s^{-1} for each investigated position, matching roughly the range of $FWHM$ derived for c-C_3H_2 (see Sect. 5.4.2).

The typical $FWHM$ derived in previous investigations of diffuse and translucent molecular clouds is smaller: for example 3–5 km s^{-1} (Belloche et al. 2013), 3–8 km s^{-1} (Menten et al. 2011) in the clouds along the line of sight to Sgr B2 excluding the envelope of Sgr B2. Gerin et al. (2010a) determined a range of 3–6 km s^{-1} for a sample of diffuse molecular clouds along other lines of sight. The mean $FWHM$ of all velocity components of all molecules investigated here are between 5.1 and 5.8 km s^{-1} depending on the position. The mean values for the envelope of Sgr B2 (6.0–7.2 km s^{-1}) are larger than the range derived by Gerin et al. (2010a). The mean values for only the line-of-sight clouds (4.5–4.8 km s^{-1}) fall directly in all the previously determined intervals. If we look at the exact distribution of the $FWHM$ (see Fig. 3.7), we see a cutoff at about 6.5–7.5 km s^{-1}. The majority (84.0–90.1%) of the investigated velocity components has a width smaller than 7.5 km s^{-1}. Towards larger linewidths the number of identified velocity components is decreasing for each investigated position. These tails are possibly caused by overlapping velocity components which could not be identified separately. Most of the velocity components located in these tails are located in the envelope of Sgr B2. The absorption in this velocity range is mostly very broad and sometimes also optically thick which makes it difficult to distinguish between individual velocity components.

3.4.3 Differences between lines of sight

The linewidth distribution of the detected velocity components of all molecules is similar for all six positions, but the centroid velocities and the number of detected velocity components depend on the line of sight. The numbers of velocity components and hence the column density profiles depend on the signal-to-noise ratio of the investigated position. Towards K4, K6$_{\rm shell}$, and I the SNR is higher and more velocity components are detected. The velocity distribution which represents the spiral arm structure is roughly the same for all six positions investigated here. The absorption features of the molecules in the spectra towards the four positions in Sgr B2(N) (K4, K6$_{\rm shell}$, K5$_{\rm shell}$, and K6$_{\rm shell,a}$) show a very similar distribution of the centroid velocities and also similar column density profiles. Especially, the column density profiles determined towards K4 and K5$_{\rm shell}$ are very similar and also those towards K6$_{\rm shell}$ and K6$_{\rm shell,a}$. These two pairs of positions are both located close to each other: 3.″5 and 3.″1, respectively. The corresponding physical distances are 0.12-0.14 pc in the envelope of Sgr B2 and 0.014–0.016 pc in the Sagittarius arm. The velocity structure of the clouds is very similar on scales smaller than about 0.14 pc. The envelope of Sgr B2 is described mainly by three velocity components towards the four positions discussed before: ∼64 km s^{-1}, ∼81 km s^{-1}, and ∼71 km s^{-1}. In the spectrum towards I the latter two velocity components are not visible or only very weak. The angular distance from Sgr B2(N) is about 50″ (2 pc). The centroid velocities in the envelope of Sgr B2 towards L (angular distance towards Sgr B2(N): ≈ 30″, i.e. 1.2 pc) are shifted by about −8 km s^{-1}. The shift of the centroid velocities of the main components in the envelope of Sgr B2 between the positions K4 and L was also noted by Corby et al. (2015) who investigated the molecular content of Sgr B2 using ATCA data in the range of 30–50 GHz. The largest difference seen in the centroid velocities of the line-of-sight clouds concerns the velocity feature at about −106 km s^{-1}. It is detected for many molecules in the spectra towards Sgr B2(N). The spectra towards L and I show two velocity components at about −101 km s^{-1} and −109 km s^{-1}. Because the centroid velocities of these velocity components are similar over a large distance they seem to belong to a large cloud structure, to which the GC clouds in front of Sgr B2(N) do not seem to be associated. But for the other velocities we see strong differences between the positions I and L. For example, the absorption between about −85 and −65 km s^{-1} seen towards I is weaker and towards L stronger than in comparison to the other lines of sight. The four positions towards Sgr B2(N) reveal only slight differences in the column densities of the line-of-sight clouds. In summary, on scales that are smaller than the

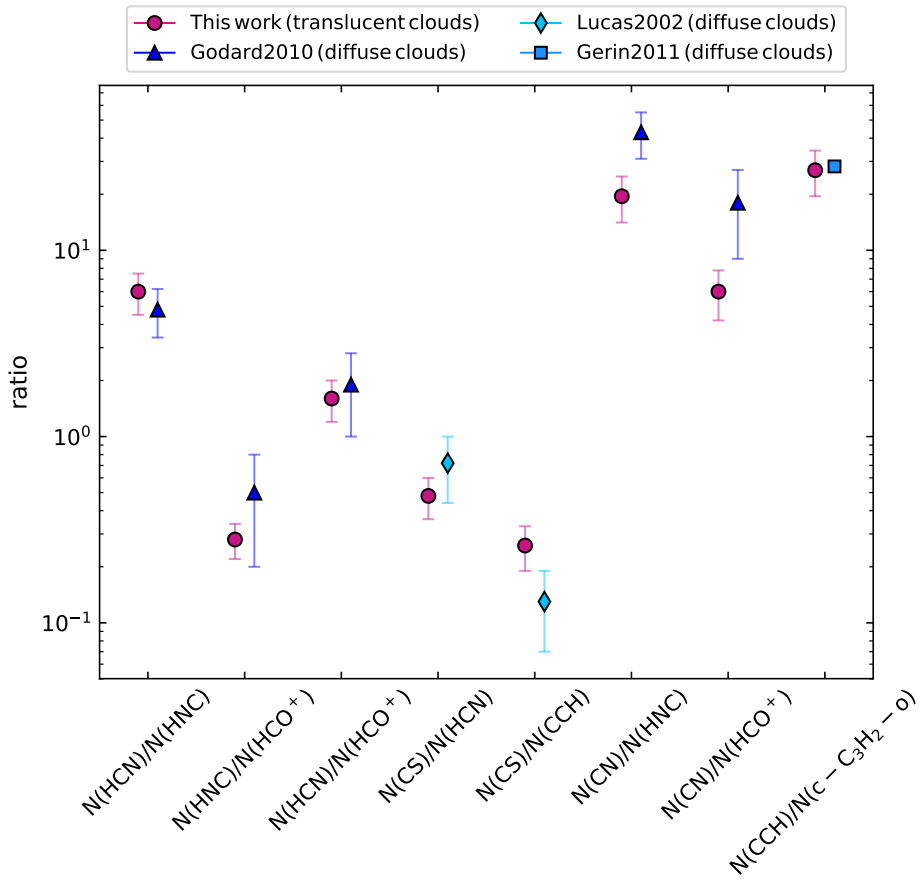

Figure 3.11: Column density ratios of several molecules for translucent and diffuse molecular clouds. The clouds investigated in this Thesis are translucent molecular clouds. The molecular ratios for diffuse molecular clouds are taken from Lucas & Liszt (2002); Godard et al. (2010); Gerin et al. (2011). The uncertainties for the ratio N(CCH)/N(c-C_3H_2-o) of Gerin et al. (2011) are smaller than the marker.

extent of the continuum structure of Sgr B2(N), smaller than about 12″, i.e. 0.5 pc, the angular separation of K4 and $K6_{shell}$, the changes in the velocity structure of the line-of-sight clouds and the envelope of Sgr B2 are only small. The velocity structure of Sgr B2(N) differs more strongly in comparison towards I and L. The differences are seen on scales larger than ≈ 30″ (1.2 pc), the separation between Sgr B2(N) and L. But at about −106 km s^{-1} there seems to be a larger cloud with a similar velocity structure towards I and L, but not towards Sgr B2(N).

3.4.4 Correlations between molecules

We do not see any correlation with CO. The analysis of the column density profiles already revealed differences between ^{13}CO and all the other molecules which makes a correlation unlikely.

CH_3OH, SiO, and SO are all strongly correlated to each other with Pearson's correlation coefficients higher than 0.7. Especially the correlation between CH_3OH and SiO seems to be tight. They are all three shock tracers. Their correlation suggests that they trace a shock component in the investigated line-of-sight clouds. These three molecules have on average larger linewidths than the other group of molecules containing CCH, CN, CS, HNC, and HCN (see Figs. A.108–A.109 in Appendix A).

Because only a few velocity components of the line-of-sight clouds are detected for CH_3OH, N_2H^+, SO, and SiO in comparison to the other molecules, we decided to focus in the following on seven molecules, excluding also CO, to investigate the correlations between them: HCO^+, CCH, ortho c-C_3H_2, HCN, HNC, CS, and CN. We found several pairs of molecules with a strong correlation ($0.6 \leq r_{\mathrm{Pearson}} \leq 0.79$) and two with a very strong correlation ($0.8 \leq r_{\mathrm{Pearson}} \leq 1.00$). The correlation coefficient describes only how strong the linear correlation (polynomial function of order 1) between the logarithmic abundances for a pair of molecules is, but it does not give any information on the coefficients a and b of the linear function ($y = ax + b$) which describes the correlation in log-log space. A proportionality between two molecules (a constant ratio between the column densities of the molecules) is defined by the function $y = x + b$ with a slope of 1 in log-log space. To investigate how good the assumption of a slope of 1 is, we fitted also the function $y = ax + b$ to the correlation plots. The deviation of the slope a is for all pairs with $r_{\mathrm{Pearson}} \geq 0.6$ less than about 30% from 1. This only differs for HCN and CCH, where the slope is 1.64. This means, that a constant ratio between the two molecules is most likely not applicable over the range of column densities covered by our sample of clouds. Hence, with only the exception of the pair HCN and CCH, the assumption of a slope of 1 is mostly suitable. The ratios between the molecules describe the chemical composition of the clouds investigated here. The sample of line-of-sight clouds investigated in this work consists of mostly translucent molecular clouds (see Sect. 5.5.1).

To investigate whether there are differences in the chemistry, we compare the molecular ratios deduced for the translucent molecular clouds (see Table 3.7) to those determined for diffuse molecular clouds (Lucas & Liszt 2002; Godard et al. 2010; Gerin et al. 2011) in Fig. 3.11. The column density ratios of the three molecules HNC, HCN and HCO^+ determined in the translucent molecular clouds match within the uncertainties the values estimated for diffuse molecular clouds by Godard et al. (2010): N(HCN)/N(HNC) = 4.8 ± 1.4, N(HNC)/N(HCO^+)=0.5 ± 0.3, and N(HCN)/N(HCO^+)=1.9 ± 0.9. The column density ratio of CS and HCN is also similar in the translucent molecular clouds compared to the value determined in diffuse molecular clouds (N(CS)/N(HCN) = 0.72 ± 0.28, Lucas & Liszt 2002). Lucas & Liszt (2000) described the correlation between CCH and ortho c-C_3H_2 in diffuse clouds as very tight. The ratio we determined for translucent molecular clouds matches the one for diffuse molecular clouds of N(CCH)/N(ortho c-C_3H_2) = 28.2±1.4 (Gerin et al. 2011). The correlation of the pair CCH and ortho c-C_3H_2 is with a correlation coefficient of 0.67 a strong correlation. But the dispersion of the points in the correlation plot is relatively wide (see Fig. A.42). If we do not assume a slope of 1 for the linear fit in the correlation plot, we get a slope of 0.73 ± 0.09. Hence, there is a strong linear correlation between the logarithmic abundances of these two molecules, but the abundances of these two molecules are not proportional to each other with only a constant factor. We will see in Sect. 5.5.2 that CCH is a good tracer of H_2 in translucent clouds but not c-C_3H_2.

Besides these accordances of molecular ratios, we see also some differences. The ratio of CS and CCH in the translucent molecular clouds of our sample is twice as high (N(CS)/N(CCH)=0.26±0.07) as in diffuse molecular clouds (N(CS)/N(CCH)=0.13±0.07 Lucas & Liszt 2002) indicating either a lower abundance of CCH or a higher one of CS in translucent molecular clouds. The other molecular ratios involving either CS or CCH are similar in diffuse and translucent molecular clouds. Because we know that CCH is a good tracer of H_2 (see Sect. 5.5.2), it is more likely that CS is more abundant in translucent clouds. Because the values for diffuse and translucent molecular clouds match still within the limits of their dispersions which are relatively large, this has to be treated carefully.

Both the ratios between CN and HNC and between CN and HCO^+ are lower in the translucent molecular clouds (N(CN)/N(HNC)=19.5 ± 1.3 and N(CN)/N(HCO^+)=6.0 ± 0.6) than in diffuse molecular clouds (N(CN)/N(HNC) = 34 ± 12 and N(CN)/N(HCO^+)=18 ± 9 Godard et al. 2010). One possibility is that CN is less abundant in translucent molecular clouds in comparison to diffuse molecular clouds. The other possi-

bility would be that HCO^+ and HNC have higher abundances in translucent molecular clouds than in diffuse molecular clouds. We know that HCO^+ has a higher abundance in translucent molecular clouds compared to diffuse molecular clouds (see Sect. 5.5.1). Furthermore, the correlation between CCH and CN is with $r = 0.76$ relatively strong and the dispersion of the data in the correlation plot around the linear fit is low. CCH is a good tracer of H_2 so we conclude that CN is also a good tracer of H_2 from diffuse to translucent clouds, but not HNC and HCO^+.

3.4.5 Isotopic ratios

We determine the mean isotopic ratio $^{12}C/^{13}C$ using CN to be about 20–21 in the envelope of Sgr B2 and the GC clouds. These values match the ratio of about 20 determined by Milam et al. (2005). They measured the molecular abundance of emission lines of CN towards several molecular clouds across our galaxy, including one sight line to Sgr B2. They combined the measured data of the isotopic ratios with previous measurements of H_2CO and CO (Milam et al. 2005, and references therein). Afterwards, they fitted the ratio as a function of the galactocentric radius. Their estimated isotopic ratio of $^{12}C/^{13}C$ in the clouds located near the GC is about 20. If we use the isotopologues of CS instead, we calculate the isotopic ratio $^{12}C/^{13}C$ to be 27.3±6.2 for the envelope of Sgr B2 ($C^{34}S/^{13}C^{34}S$). The uncertainty is quite large due to the low SNR of the $^{13}C^{34}S$ lines, resulting in a slightly higher value for $^{12}C/^{13}C$. Using the more abundant isotopologues, we get a lower limit of $CS/^{13}CS>17$. Only one velocity component of ^{13}CN is detected in the 3 kpc arm. The resulting isotopic ratio is $^{12}C/^{13}C=26.7\pm6.5$ which matches the value of 37 ± 8 determined by Milam et al. (2005) within the uncertainties.

The nitrogen isotopic ratio $^{14}N/^{15}N$ calculated using CN is about 350±53 in the envelope of Sgr B2. Dahmen et al. (1995) determined this ratio using HCN towards several sources detected in emission and fitted it as a function of the galactocentric radius. But they do not have measurements for galactocentric distances smaller than about 3 kpc. They found a linear trend of $^{14}N/^{15}N$ increasing towards larger galactocentric radii. They extrapolated the line fitted to their data to a galactocentric radius of 0 kpc and estimated the ratio $^{14}N/^{15}N$ to be about 300 in the GC clouds. Our result matches with their estimation. Adande & Ziurys (2012) estimated a lower limit of 164 for $^{14}N/^{15}N$ in Sgr B2(NW) from $HN^{13}C$ and $H^{15}NC$ assuming a ratio for $^{12}C/^{13}C$. In contrast, we made a direct measurement of the $^{14}N/^{15}N$ ratio in the GC region.

We estimate the mean ratio of $^{29}SiO/^{30}SiO$ to be 1.5–1.7 for the envelope of Sgr B2 and the GC clouds. Within the uncertainties, it matches the value of about 1.5 previously determined by Penzias (1981) using emission lines of SiO isotopologues in Orion A. Monson et al. (2017) combined data of sources at galactocentric distances between 0 and 9.8 kpc and report a similar abundance as Penzias (1981) which is independent of the galactocentric radius.

Wouterloot et al. (2008) determined the ratio $^{18}O/^{17}O$ ratio to be 2.88±0.11 in the envelope of Sgr B2(M). We determined a value of 3.33±0.65 using HCO^+ isotopologues, which matches this value within the uncertainties.

We determined the sulphur isotopic ratio of $^{34}S/^{33}S$ in the envelope of Sgr B2 and in some GC clouds. The value of 5.2 is similar to the values determined in Sgr B2(N) and Sgr B2(M) by Nummelin et al. (2000) using the molecules SO, CS, and SO_2 detected in emission ($^{34}S/^{33}S\approx 5$). The sulphur isotopic ratio $^{32}S/^{34}S$ is about 22 in Sgr B2 (Frerking et al. 1980; Wilson & Rood 1994). Using the isotopologues of CS, we calculated values of 18–21 for the envelope of Sgr B2 and the GC clouds, matching the $^{32}S/^{34}S$ ratio within the uncertainty. We determined values of >13–16 for the line-of-sight clouds (3 kpc, 4 kpc, and Sagittarius arm).

In summary, the isotopic ratios calculated in this work match those determined or estimated in previous studies. A higher sensitivity could increase the low statistics of some velocity ranges and could also allow

us to detect weaker isotopologues. In previous studies the ratio of $^{14}N/^{15}N$ was only estimated by an extrapolation of a linear fit to low galactocentric radii, whereas we were able to measure the ratio in the envelope of Sgr B2 directly from CN.

3.5 Conclusions

We used the EMoCA survey performed with ALMA to investigate the chemical content of the clouds seen in absorption along the line of sight to Sgr B2(N). The high spatial resolution of this survey allows us to investigate the spectra towards several positions where the continuum emission is strong enough and the absorption features are not blended with many emission lines. We selected six positions: four towards Sgr B2(N), one towards Sgr B2(M) and one towards Sgr B2(L). We investigated the velocity and the column density distributions by fitting the synthetic spectra to the absorption features of all identified molecules. Our main results are summarised as follows:

1. In total, we identified 28 molecules and 27 less abundant isotopologues in absorption in the envelope of Sgr B2. Among them are seven COMs: CH_3CHO, CH_3CN, C_2H_5OH, NH_2CHO, CH_3OH, CH_3NH_2, and CH_3SH. In the diffuse and translucent molecular clouds along the line of sight to Sgr B2, we detected 19 molecules and 15 less abundant isotopologues in absorption. Only four of the COMs identified in the envelope of Sgr B2 are also seen in the line-of-sight clouds: CH_3CHO, CH_3CN, NH_2CHO, and CH_3OH.

2. We found about 20 unidentified lines. We cannot exclude that some of them are artefacts.

3. The velocity distribution is roughly similar for HCO^+, CCH, c-C_3H_2-o, ^{13}CO, CS, CN, SiO, SO, HCN, HNC, N_2H^+, and CH_3OH. The envelope of Sgr B2 can be described by mainly two velocity components at $\sim 64\,km\,s^{-1}$ and $\sim 80\,km\,s^{-1}$. The latter velocity component is not detected towards the position I.

4. The mean $FWHM$ of the line-of-sight clouds is about 4.5–4.9 km s^{-1}. The clouds associated with the envelope of Sgr B2 have larger mean values: 6.2–7.3 km s^{-1}.

5. The column density profiles and the velocity structure of the molecules of the line-of-sight clouds are very similar towards the four positions in Sgr B2(N). There are only weak changes on scales smaller than the extent of Sgr B2(N): 12″ (0.5 pc in the envelope of Sgr B2). The differences in the column density profiles concerning detected velocity components and relative column density ratios between the components between the positions in Sgr B2(N) and the two towards Sgr B2(M) and Sgr B2(L) are sometimes weak, sometimes relatively large. Hence, the structure changes on scales larger than the distance of 30″ to these two positions (1.2 pc in the envelope of Sgr B2).

6. The molecules CN, HCN, HNC, CS and CCH are strongly correlated to each other. The shock tracers SiO, SO and CH_3OH are all strongly correlated to each other. The CO abundances deduced from ^{13}CO are not correlated to the abundances of any of these molecules. CCH and CN are good tracers of H_2 from diffuse to translucent clouds, but not HNC and HCO^+.

7. The molecular ratios of the translucent molecular clouds investigated here are mostly similar to those determined for diffuse molecular clouds (Lucas & Liszt 2002; Godard et al. 2010; Gerin et al. 2011). The abundances of HCO^+ and CS are enhanced in translucent molecular clouds compared to diffuse molecular clouds.

8. We determined the following isotopic ratios in the envelope of Sgr B2: $^{12}C/^{13}C$, $^{14}N/^{15}N$, $^{29}SiO/^{30}SiO$, $^{18}O/^{17}O$, $^{34}S/^{33}S$, and $^{32}S/^{34}S$. For line-of-sight clouds we determined the isotopic ratios of $^{12}C/^{13}C$, $^{29}SiO/^{30}SiO$, $^{34}S/^{33}S$ and lower limits for $^{32}S/^{34}S$. The results are in agreement with the results of previous studies (see Milam et al. 2005; Dahmen et al. 1995; Penzias 1981; Wouterloot et al. 2008; Nummelin et al. 2000; Wilson & Rood 1994, respectively). We measured the isotopic ratio $^{14}N/^{15}N$ directly in the envelope of Sgr B2 to be 350 ± 53. This is in agreement with the value previously estimated from measurements done a larger galactocentric radii.

Our analysis of the velocity structure and the molecular correlations of the line-of-sight clouds detected in absorption towards Sgr B2 can be extended and improved by mainly one factor: A higher sensitivity, which would allow us to detect more velocity components of weak molecules.

Chapter 4

Complex organic molecules in diffuse clouds along the line of sight to Sgr B2

This chapter is adapted from the published letter of Thiel, V., Belloche, A., Menten, K. M., Garrod, R. T., and Müller, H. S. P. 2017, A&A, 605, L6.
DOI: 10.1051/0004-6361/201731495 [arXiv:1708.07292]

Contents

Abstract

Up to now, mostly relatively simple molecules have been detected in interstellar diffuse molecular clouds in our galaxy, but more complex species have been reported in the diffuse/translucent medium of a $z = 0.89$ spiral galaxy.

We aim at searching for complex organic molecules (COMs) in diffuse molecular clouds along the line of sight to Sgr B2(N), taking advantage of the high sensitivity and angular resolution of the Atacama Large Millimeter/submillimeter Array (ALMA).

We use data acquired as part of the EMoCA survey performed with ALMA. To analyse the absorption features of the molecules detected towards the ultracompact H II region K4 in Sgr B2(N), we calculate synthetic spectra for these molecules and fit their column densities, line widths, centroid velocities, and excitation temperatures.

We report the detection of CH_3OH, CH_3CN, CH_3CHO, HC_3N, and NH_2CHO in Galactic center (GC) diffuse clouds and CH_3OH and CH_3CN in a diffuse cloud in the Scutum arm. The chemical composition of one of the diffuse GC clouds is found to be similar to the one of the diffuse/translucent medium of the $z = 0.89$ spiral galaxy.

The chemical processes leading to chemical complexity in the diffuse molecular ISM appear to have remained similar since $z = 0.89$. As proposed in previous studies, the presence of COMs in diffuse molecular clouds may result from a cyclical interstellar process of cloud contraction and expansion between diffuse and dense states.

4.1 Introduction

About 200 different molecules have been detected up to now in the interstellar medium (ISM)[1]. Carbon-bearing molecules with at least six atoms are commonly referred to as complex organic molecules (COMs). They are detected in dense environments such as cold prestellar cores and hot cores or corinos (Herbst & van Dishoeck 2009). They are usually detected in emission, but several have been detected in absorption, for instance in the envelope of Sgr B2 (Corby et al. 2015). COMs have been detected not only in such dense environments, but also in photodissociation regions (PDRs) like the Horsehead (Guzmán et al. 2014). Here, the strong far-ultraviolet (FUV) radiation seems to play an important role: not only can the COMs survive in such environments, but the UV field also seems to enhance their abundance compared to neighbouring dense clouds (Guzmán et al. 2014). In addition, several COMs have been detected in absorption in a $z = 0.89$ spiral galaxy, with a chemical composition of this absorber suggesting that the medium is diffuse/translucent (Muller et al. 2011, 2014). Thus, the question arises as to whether COMs also exist in galactic diffuse clouds, in which dust extinction is modest and densities are low. Up to now, mostly fairly simple molecules, such as CN, HCN, CCH, HCO^+ or c-C_3H_2 , have been detected in diffuse molecular clouds in our galaxy (e.g. Lucas & Liszt 1997; Godard et al. 2010).

The low densities in diffuse molecular clouds result in low excitation temperatures, close to the temperature of the cosmic microwave background (CMB) radiation, that is, 2.73 K (Greaves et al. 1992). Under these conditions, rotational lines are subthermally excited, very weak, and difficult to detect in emission. Absorption studies have a better sensitivity, but a strong continuum background source is needed. The giant molecular cloud Sagittarius B2 (Sgr B2) fulfills this condition. It is located near the Galactic centre (GC) at a projected distance of 100 pc and a distance of 8.34 ± 0.16 kpc to the sun (Reid et al. 2014).

For our analysis, we used the EMoCA survey that aims at exploring the chemical complexity of the interstellar medium (Belloche et al. 2016). This survey was performed towards the star forming region Sgr B2(N) with the Atacama Large Millimeter/submillimeter Array (ALMA) in Cycles 0 and 1. The spatial resolution of this survey is high enough to resolve the structure of Sgr B2(N) (see Fig. B.1a). In this way, we can investigate absorption lines at positions where the continuum is still strong enough but which are sufficiently far away from the hot cores towards which absorption features are blended with numerous emission lines. The ultracompact H II region K4 (Gaume et al. 1995) fulfills these requirements. With the high sensitivity of the EMoCA survey we can search for absorption from COMs along the whole 8 kpc-long line of sight to the Galactic centre.

4.2 Observations and analysis method

We use the EMoCA survey taken with ALMA towards Sgr B2(N). The phase centre (EQ J2000: $17^h47^m19.87^s, -28°22'16''$) is half way between the two main hot cores N1 and N2 (see Fig. B.1a). The survey covers the frequency range from 84.1 to 114.4 GHz with a median angular resolution of $1''.6$. The spectral resolution is 488 kHz or 1.3–1.7 km s^{-1}. The average noise level is ~3 mJy beam^{-1}. The calibration and deconvolution of the data were performed by Belloche et al. (2016). We corrected the spectra for the primary beam attenuation. We use Weeds (Maret et al. 2011) to model the spectra. We assume that all transitions of a molecule have the same excitation temperature and that the beam filling factor is 1. We fit the column density, linewidth, and centroid velocity. We assume the excitation temperature to be equal to the temperature of the CMB (2.73 K) except in the cases where several transitions are detected, for which the temperature is derived from a population diagram.

[1] see, e.g. https://www.astro.uni-koeln.de/cdms/molecules

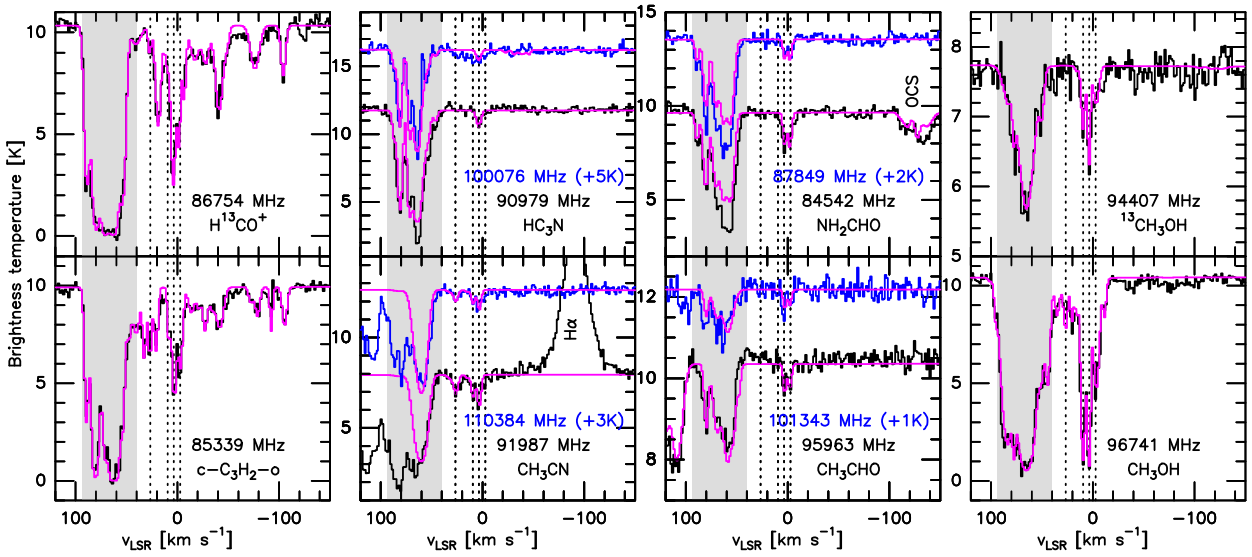

Figure 4.1: Absorption spectra of simple and complex organic molecules towards the UCH II region K4 in Sgr B2(N). The strongest transition is shown in black and the next strongest, if any, in blue. The molecules and rest frequencies of the transitions are given in each panel. The blue spectra are shifted upwards by the value given in parentheses. The synthetic spectra are overlain in magenta. The four dotted lines mark the median centroid velocities of the components detected for the complex species: 26.7, 9.4, 3.4, and −2.8 km s^{-1}. The absorption line at 110 km s^{-1} close to the line of CH_3CHO at 95963 MHz is another transition of the same molecule. The grey area indicates the velocity range of the Sgr B2 envelope.

4.3 Results

To maximise the sensitivity, we searched for absorption lines of COMs towards the ultracompact H II region K4, which is the strongest continuum source in the field of view except for the hot cores (see Fig. B.1a). This source is located at $(\alpha,\delta)_{J2000}$ = ($17^h47^m20.02^s$, −28°22′04.7″), 13.8″ to the north of N1. Many absorption lines are detected towards this position. In total, we identified lines from 19 different molecules in the diffuse molecular clouds along the line of sight to the GC: CN, CCH, c-C_3H_2, HNC, HCN, HCO^+, SiO, SO, CH_3OH, CO, CS, N_2H^+, HOC^+, HNCO, H_2CS, CH_3CN, CH_3CHO, HC_3N, and NH_2CHO. For some of these molecules we detected several isotopologues. For the identification we used the CDMS database (Müller et al. 2005, 2001) and the JPL catalogue (Pickett et al. 1998). In addition, we detected C_2H_5OH, CH_3SH, and CH_3NH_2 in absorption at velocities corresponding to the envelope of Sgr B2.

Here, we focus on the molecules with at least five atoms detected in the diffuse clouds: c-C_3H_2-o (ortho), CH_3OH, CH_3CN, CH_3CHO, HC_3N, and NH_2CHO. For comparison purposes, we also present results for $H^{13}CO^+$. The transitions investigated in this work are listed in Table B.1. Their spectra are shown in Fig. C.8. Apart from c-C_3H_2 and $H^{13}CO^+$ that are detected in more clouds, we detect absorption of these molecules at velocities corresponding to diffuse clouds in the GC and, for CH_3OH and CH_3CN, also in the Scutum arm. These components (at 26.7, 9.4, 3.4, and −2.8 km s^{-1}) are marked with dotted lines in Fig. C.8. The strong absorption components at ~64 km s^{-1} and ~80 km s^{-1} belong to the envelope of Sgr B2 and will not be analysed here. The velocity components at around 9.4, 3.4, and −2.8 km s^{-1} fall roughly in the range of Galactic centre clouds and the component at 26.7 km s^{-1} lies in the range of the Scutum arm (e.g. Indriolo et al. 2015; Menten et al. 2011, and references therein). Figure B.1b shows as an example the intensity map integrated over the velocity range of the GC diffuse clouds in one of the transitions of

Table 4.1: Model parameters for the three diffuse GC clouds.

Molecule	N_{tot} [cm^{-2}]	v_{LSR} [$km\,s^{-1}$]	$FWHM$ [$km\,s^{-1}$]	N_{tot} [cm^{-2}]	v_{LSR} [$km\,s^{-1}$]	$FWHM$ [$km\,s^{-1}$]	N_{tot} [cm^{-2}]	v_{LSR} [$km\,s^{-1}$]	$FWHM$ [$km\,s^{-1}$]	T_{ex} [K]
$H^{13}CO^+$	1.5×10^{12}	9.8	5.5	8.0×10^{12}	3.8	4.5	3.8×10^{12}	−1.7	3.5	2.73 (*)
c-C_3H_2-o	5.0×10^{12}	8.2	3.0	1.9×10^{13}	2.8	4.5	1.2×10^{13}	−3.2	4.5	2.73 (*)
CH_3OH	3.8×10^{14}	9.4	4.0	3.8×10^{14}	3.7	3.0	2.1×10^{14}	−3.6	6.0	2.73 (*)
$^{13}CH_3OH$	2.0×10^{13}	9.4	4.0	2.9×10^{13}	3.7	4.0	2.0×10^{13}	−3.6	6.0	2.73 (*)
CH_3CN	1.0×10^{13}	8.7	4.0	2.0×10^{13}	3.0	4.0	$<6.0\times10^{13}$	−2.8	4.0	4.2 ± 0.7
CH_3CHO	$<1.5\times10^{13}$	9.4	4.0	5.0×10^{13}	2.6	3.5	4.0×10^{13}	−2.4	3.5	3.1 ± 0.1
HC_3N	$<2.5\times10^{13}$	9.4	4.0	6.0×10^{14}	3.7	5.0	$<2.5\times10^{13}$	−2.8	4.0	7.3 ± 0.8
NH_2CHO	$<4.0\times10^{12}$	9.4	4.0	1.7×10^{13}	2.6	3.5	1.8×10^{13}	−2.4	3.5	4.3 ± 0.2

Notes. The excitation temperatures marked with a star are assumed, the other ones were fitted.

Table 4.2: Model parameters for the diffuse cloud in the Scutum arm.

Molecule	N_{tot} [cm^{-2}]	v_{LSR} [$km\,s^{-1}$]	$FWHM$ [$km\,s^{-1}$]	T_{ex} [K]
$H^{13}CO^+$	6.2×10^{11}	27.0	3.5	2.73
c-C_3H_2-o	8.1×10^{12}	26.8	3.5	2.73
CH_3OH	6.2×10^{13}	26.6	5.0	2.73
$^{13}CH_3OH$	$<3.9\times10^{12}$	26.6	5.0	2.73
CH_3CN	1.4×10^{13}	26.2	5.0	4.2
CH_3CHO	$<1.5\times10^{13}$	26.7	4.3	3.1
HC_3N	$<2.5\times10^{13}$	26.7	4.3	7.3
NH_2CHO	$<4.0\times10^{12}$	26.7	4.3	4.3

Notes. We assumed the same excitation temperatures as in Table 4.1.

NH_2CHO. The absorption is detected towards K4 only and the spatial extent of the absorption cannot be measured with our data set due to a lack of sensitivity.

The results of the modelling are given in Table 4.1 for the GC clouds and Table 4.2 for the Scutum arm. To calculate the upper limits for $^{13}CH_3OH$ we assumed the same velocity and linewidth as for CH_3OH. To determine the upper limits for the other non-detected molecules we took the median values of the centroid velocities and linewidths as fixed values. The linewidths range between 3 and 6 $km\,s^{-1}$ for the GC centre clouds and between 3.5 and 5 $km\,s^{-1}$ for the Scutum arm cloud. They fall in the same range as found in other investigations of diffuse molecular clouds along the line of sight to Sgr B2 (e.g. Menten et al. 2011). There are no systematic kinematical differences between the simple molecules $H^{13}CO^+$ and c-C_3H_2 and the more complex molecules, so they probably all trace the same regions.

We plot in Fig. 4.2a the column densities derived for the diffuse clouds and compare them to the column densities in the $z = 0.89$ spiral galaxy in front of the QSO PKS 1830–211 (Muller et al. 2011, 2013, and S. Muller, priv. comm.), the Horsehead PDR (Pety et al. 2005; Goicoechea et al. 2009; Gratier et al. 2013; Guzmán et al. 2013, 2014, and V. Guzmán, priv comm.), the hot core Sgr B2(N2) (Belloche et al. 2017, 2016; Müller et al. 2016), and the envelope of the Class 0 protostar NGC 1333-IRAS 2A (Taquet et al. 2015). The HCO^+ column densities for the diffuse clouds investigated here are derived from the $H^{13}CO^+$ column densities assuming an isotopic ratio $^{12}C/^{13}C$ equal to 20 for the GC and 40 for the Scutum arm (Milam et al. 2005).

The velocity component at around 3.4 km s^{-1} is relatively strong for all molecules. The one at −2.8 km s^{-1} has comparable column densities, except for HC_3N and CH_3CN that are not detected. The component at 9.4 km s^{-1} is in general weaker than the previous ones, except for methanol and methyl cyanide for which it is nearly as strong as the first component. CH_3CN in the Scutum arm cloud (26.7 km s^{-1}) has a similar column density as in the GC clouds, but CH_3OH is weaker.

The H I and H_2 column densities of the GC and Scutum-arm diffuse clouds are also plotted in Fig. 4.2a (see also Table B.2). They were calculated by integrating the column density distributions of Winkel et al. (2017) over velocity ranges equal to the median $FWHM$ of the absorption components in this work. The H I data have an angular resolution of ∼ 37″ (Winkel et al. 2017) and the HF data used to determine the H_2 column densities ∼ 40″ (Bergin et al. 2010). The H I and H_2 column densities in the GC clouds are up to one order of magnitude higher than in the Scutum arm. The molecular fraction is 0.70 for the Scutum-arm cloud and 0.4–0.6 for the GC clouds (Table B.2).

Figure 4.2b shows the abundances relative to methanol. In addition to the sources shown in Fig. 4.2a, the abundances in the translucent cloud CB24 (Turner 1998; Turner et al. 1998, 1999) are also plotted. They correspond to the mean values (and standard deviations as uncertainties) of the different models presented by these authors. Apart from HC_3N, the chemical composition relative to methanol of the 3.4 km s^{-1} GC diffuse cloud is similar to the one of the z = 0.89 spiral galaxy. But no obvious similarity between the COM compositions of these two sources and the other types of sources is apparent in Fig. 4.2. The diffuse GC clouds, the translucent cloud CB24, the hot core Sgr B2(N2), and the z = 0.89 spiral galaxy have similar [CH_3CN]/[CH_3OH] ratios while the Scutum arm cloud and the Horsehead PDR lie one order of magnitude above and the protostellar envelope one order of magnitude below. The diffuse GC clouds, the z = 0.89 absorber, and Sgr B2(N2) have similar [NH_2CHO]/[CH_3OH] ratios while the protostellar envelope is nearly two orders of magnitude below. The [HC_3N]/[CH_3OH] ratio shows a wide spread with the 3.4 km s^{-1} GC component lying four orders of magnitude above the protostellar envelope, and the Horsehead PDR, Sgr B2(N2), CB24, and the z = 0.89 spiral galaxy being at a similar intermediate level. Finally all sources except for Sgr B2(N2) have similar [CH_3CHO]/[CH_3OH] ratios.

4.4 Discussion

All complex molecules reported in Sect. 4.3 are detected in the diffuse GC cloud at ∼3.4 km s^{-1}. These molecules were also reported by Corby et al. (2015) at a velocity around 0 km s^{-1}, but they detected only one velocity component due to their poor spectral resolution (6–10 km s^{-1}). While Corby et al. (2015) did not detect complex molecules outside the GC, we report here the detection of CH_3OH and CH_3CN in a diffuse cloud in the Scutum arm. Figure 4.2 shows that the non-detection of the other complex species in the Scutum arm does not necessarily reflect a different chemical composition compared to the diffuse GC clouds but may simply be due to a lack of sensitivity.

Methanol's high abundance (10^{-9}–10^{-8}) in translucent (and hence perhaps also in diffuse) molecular clouds could be driven by UV photodesorption from dust grains (Turner 1998). This process would not be effective in denser parts of molecular clouds which are mostly shielded against UV radiation. More recently, a process of grain-surface formation and immediate reactive desorption was found to be an important source of gas-phase methanol (Garrod et al. 2007). We find methanol abundances relative to H_2 on the order of 10^{-7} for the diffuse GC and Scutum-arm clouds (Table B.2), which is surprisingly high, one order of magnitude higher than in translucent clouds (Turner 1998) and dense prestellar cores such as L1544 (6×10^{-9} Vastel et al. 2014). Although we cannot rule out that the higher UV radiation field in diffuse clouds may enhance the abundance of methanol, it may be that the abundances we obtain are overestimated due to an underestimate

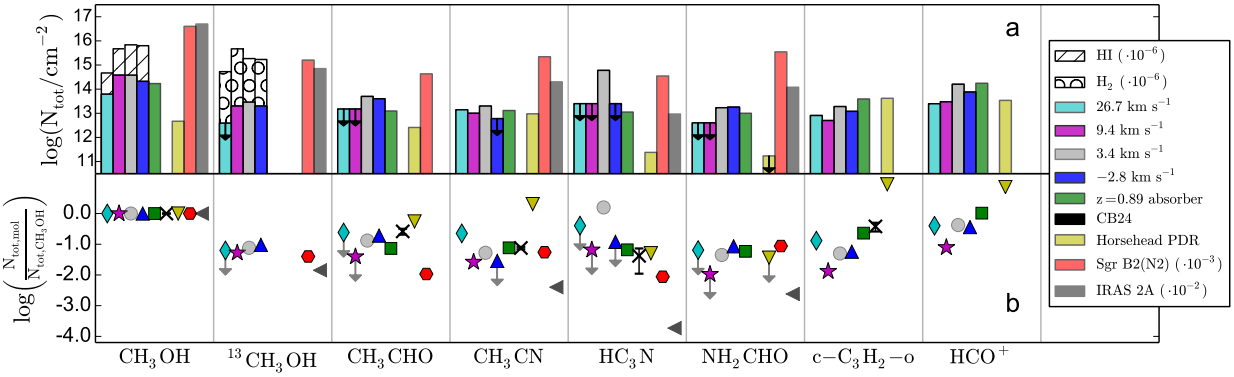

Figure 4.2: **a** Column densities of complex organic molecules and two simpler ones detected in diffuse clouds in the GC and in the Scutum arm compared to the column densities in the $z = 0.89$ spiral galaxy in front of PKS 1830-211, the Horsehead PDR, the hot core Sgr B2(N2), and the protostellar envelope of NGC 1333-IRAS 2A (see references in Sect. 4.3). The column densities of H I and H_2 in the diffuse clouds are shown in the panels of methanol (Winkel et al. 2017). The values for H I, H_2, the hot core, and the protostellar envelope are scaled by the factor given in parentheses. **b** Abundances relative to CH_3OH. The black crosses show the ratios for the translucent cloud CB24 (Turner 1998; Turner et al. 1998, 1999). The arrows indicate upper limits.

of the H_2 column density if the clouds are clumpy on a scale intermediate between the resolution of the Herschel HF data (40″) and our ALMA survey (1.6″). CH_3CN can be formed effectively in the gas phase without requiring grain-surface formation (Turner et al. 1999; Bergner et al. 2017). CH_3CN is enhanced relative to methanol in the Scutum-arm diffuse cloud in comparison to the GC diffuse clouds. This is also the case for the Horsehead PDR. The high abundance of CH_3CHO in translucent clouds cannot be explained by gas-phase chemistry only and represents maybe the border to grain chemistry (Turner et al. 1999). This is most likely also true for the diffuse GC clouds, where we detect CH_3CHO.

The GC and Scutum-arm clouds have a molecular hydrogen fraction between 0.4 and 0.7, implying that they are indeed diffuse molecular clouds (Snow & McCall 2006). However, the H I and H_2 column densities of the diffuse GC clouds are one order of magnitude higher than those of the Scutum-arm cloud while their molecular fraction is lower (Table B.2), which appears to be contradictory. This may be an indication that the molecular parts of these clouds are clumpy, and in turn that the molecular fraction of the regions where H_2 resides is underestimated. This argument supports our previous hypothesis that the methanol abundances derived above are overestimated due to an underestimate of the H_2 column densities.

Price et al. (2003) introduced a theory, further tested by Garrod et al. (2005, 2006), in which interstellar clouds, or clumps within them, cycle between dense and diffuse conditions, with the chemistry of the diffuse stages enriched by the survival of molecules formed under denser conditions. Their models showed abundance enhancements of several orders of magnitude for some of the larger molecules. COMs in diffuse clouds may thus be the remnants of a previous denser phase in this cyclic process.

4.5 Conclusions

We report the detection of the (complex) organic molecules CH_3OH, CH_3CN, CH_3CHO, HC_3N, and NH_2CHO in diffuse GC clouds along the line of sight to Sgr B2(N) and CH_3OH and CH_3CN in a diffuse cloud of the Scutum arm. The chemical composition of one of the diffuse GC clouds is found to be generally similar to the one of the diffuse/translucent medium of the $z = 0.89$ spiral galaxy in front of PKS 1830–211,

suggesting that the chemical processes leading to chemical complexity have remained similar since $z = 0.89$. Some differences are seen, however: HC_3N appears to be much more abundant relative to methanol in this diffuse GC cloud compared to the spiral galaxy, while CH_3CN is enhanced in the Scutum-arm cloud, like in the Horsehead PDR. The presence of COMs in diffuse molecular clouds may result from a cyclical interstellar process of cloud contraction and expansion between diffuse and dense states (Price et al. 2003; Garrod et al. 2005, 2006).

4.6 Acknowledgements

This paper makes use of the following ALMA data: ADS/JAO.ALMA#2011.0.00017.S, ADS/JAO.ALMA#2012.1.00012.S. ALMA is a partnership of ESO (representing its member states), NSF (USA) and NINS (Japan), together with NRC (Canada), NSC and ASIAA (Taiwan), and KASI (Republic of Korea), in cooperation with the Republic of Chile. The Joint ALMA Observatory is operated by ESO, AUI/NRAO and NAOJ. The interferometric data are available in the ALMA archive at https://almascience.eso.org/aq/.

CHAPTER 5

Small-scale physical and chemical structure of diffuse and translucent molecular clouds along the line of sight to Sgr B2

This chapter is adapted from the paper of Thiel, V., Belloche, A., Menten,K. M., Giannetti, A., Wiesemeyer, H., Winkel, B., Gratier, P., Müller, H. S. P., Colombo, D., and Garrod, R. T., submitted to A&A

Contents

Abstract

The diffuse and translucent molecular clouds traced in absorption along the line of sight to strong background sources have been investigated mainly in the spectral domain so far because of limited angular resolution or small sizes of the background sources.

We aim to resolve and investigate the spatial structure of molecular clouds traced by several molecules detected in absorption along the line of sight to Sgr B2(N).

We use spectral line data from the EMoCA survey performed with the Atacama Large Millimeter/submillimeter Array (ALMA), taking advantage of its high sensitivity and angular resolution. The velocity structure across the field of view is investigated by automatically fitting synthetic spectra to the detected absorption features, which allows us to decompose them into individual clouds located in the Galactic Center (GC) region and in spiral arms along the line of sight. We compute opacity maps for all detected molecules. We investigate the spatial and kinematical structure of the individual clouds with statistical methods and perform a principal component analysis to search for correlations between the detected molecules. To investigate the nature of the molecular clouds along the line of sight to Sgr B2, we also use archival Mopra data.

We identify, on the basis of c-C_3H_2, 15 main velocity components along the line of sight to Sgr B2(N) and several components associated with the envelope of Sgr B2 itself. The c-C_3H_2 column densities reveal two categories of clouds. Clouds in Category I (3 kpc arm, 4 kpc arm, and some GC clouds) have smaller c-C_3H_2 column densities, smaller linewidths, and smaller widths of their column density PDFs than clouds in Category II (Scutum arm, Sgr arm, and other GC clouds). We derive opacity maps for the following molecules: c-C_3H_2, $H^{13}CO^+$, ^{13}CO, HNC and its isotopologue $HN^{13}C$, $HC^{15}N$, CS and its isotopologues $C^{34}S$ and ^{13}CS, SiO, SO, and CH_3OH. These maps reveal that most molecules trace relatively homogeneous structures that are more extended than the field of view defined by the background continuum emission (about 15″, that is 0.08 to 0.6 pc depending on the distance). SO and SiO show more complex structures with smaller clumps of size ∼5–8″. Our analysis suggests that the driving of the turbulence is mainly solenoidal in the investigated clouds.

On the basis of HCO^+, we conclude that most line-of-sight clouds towards Sgr B2 are translucent, including all clouds where complex organic molecules were recently detected. We also conclude that CCH and CH are good probes of H_2 in both diffuse and translucent clouds, while HCO^+ and c-C_3H_2 in translucent clouds depart from the correlations with H_2 found in diffuse clouds.

5.1 Introduction

Molecular clouds can be categorised based on their physical conditions into dense, translucent, and diffuse molecular clouds (Snow & McCall 2006, and references therein). The boundaries between the three different phases are loose. Dense molecular clouds are mostly protected from UV radiation which can destroy molecules, while diffuse molecular clouds are more exposed to this radiation which often results in a lower molecular fraction of hydrogen and lower abundances of molecules. Translucent molecular clouds are the transition regions between dense and diffuse molecular clouds, not completely shielded against UV radiation. Usually molecular clouds are a mixture of all these three types. The kinetic temperature is between about 30 and 100 K in diffuse molecular clouds, higher than about 15 K in translucent clouds, and between

about 10 K and 50 K in dense clouds. The typical hydrogen densities are $100 - 500\,\mathrm{cm}^{-3}$, $500 - 5000\,\mathrm{cm}^{-3}$ and $> 10^4\,\mathrm{cm}^{-3}$, respectively (Snow & McCall 2006, and references therein).

Performing absorption studies in the direction of strong background sources offers the opportunity to study the chemical and physical structure of diffuse and translucent molecular clouds along the line of sight. Diffuse molecular clouds make up a large part of the interstellar medium in our galaxy and in other spiral galaxies (e.g., Pety et al. 2013). Their extended structures are thought to be the main component of interarm regions in spiral galaxies (Sawada et al. 2012). A thick diffuse disk may be present in spiral galaxies, as detected in M51 (Pety et al. 2013). In addition, diffuse and translucent molecular clouds form the envelopes of giant molecular clouds (GMCs) in which star formation occurs. Hence, diffuse and translucent molecular clouds play an important role for the interaction between stars and the surrounding gas (e.g., Arnett 1971).

Due to the low densities in diffuse and translucent molecular clouds the excitation temperature of most molecular transitions is close to the temperature of the cosmic microwave background (CMB) radiation, i.e. 2.73 K (Greaves et al. 1992). Rotational lines are thus subthermally excited, very weak, and difficult to detect in emission.

The GMC Sagittarius B2 (Sgr B2) emits strong continuum radiation that can be used as an extended background source to investigate the spatial structure of the diffuse and translucent clouds located along the line of sight. Sgr B2 is located near the Galactic Center (GC) with a projected distance of about 100 pc. The GC has a distance of 8.34 ± 0.16 kpc to the Sun (Reid et al. 2014). The diameter of Sgr B2 is about 40 pc and its mass is about $10^7 M_\odot$ (Lis & Goldsmith 1990). Here, we focus on the dense molecular core Sgr B2(N) that contains several H II regions (Gaume et al. 1995) as well as several hot molecular cores (Bonfand et al. 2017; Sánchez-Monge et al. 2017). The continuum emission of Sgr B2(N) in the millimeter wavelength range consists of free-free radiation and thermal dust emission (e.g., Liu & Snyder 1999).

In the past, several molecular absorption studies along the line of sight to Sgr B2(N) and Sgr B2(M) were made using single-dish telescopes (e.g., Greaves & Williams 1994; Neufeld et al. 2000; Polehampton et al. 2005; Hieret 2005; Lis et al. 2010; Monje et al. 2011; Corby et al. 2018). The profiles of the detected absorption features were modelled to investigate the molecular content of the material along the line of sight. The angular resolution of these previous studies was not high enough to resolve the continuum structure of Sgr B2(N). For instance, Corby et al. (2018) investigated simple molecules along the line of sight to Sgr B2 using the Green Bank Telescope. Their data covered the frequency range between 1 and 50 GHz with a resolution between 13′ and 15″. Corby et al. (2015) performed a spectral survey of Sgr B2 with the Australia Telescope Compact Array (ATCA) between 30 and 50 GHz with an angular resolution of 5–10″ that starts to resolve the continuum emission of Sgr B2(N). They reported variations in the column densities of several molecules seen in absorption across the field of view of their observations but they did not have much resolution elements to perform a detailed study of the spatial structure of the clouds seen in absorption along the line of sight. Mills et al. (2018) also used the ATCA between 23 and 37 GHz to observe Sgr B2(N) with an angular resolution of 3″ in ammonia and methanol, which they detect mainly in emission. They focused their analysis on Sgr B2(N) itself and its hot cores.

We use the EMoCA (*Exploring Molecular Complexity with ALMA*) survey for our analysis. The aim of the survey is to explore and expand our knowledge of the chemical complexity of the interstellar medium (Belloche et al. 2016). This survey was performed towards Sgr B2(N) with the Atacama Large Millimeter/submillimeter Array (ALMA). The angular resolution of this survey is high enough to resolve the continuum emission of Sgr B2(N) (see Fig. 5.1). Hence, we can investigate absorption lines at positions where the continuum is still strong enough but which are sufficiently far away from the hot cores towards which absorption features are blended with numerous emission lines. The survey was carried out in the 3 mm wavelength range (covering frequencies from 84.1 to 114.4 GHz). Many important as well as abundant molecular species have transitions in this frequency regime that are suitable for absorption studies. There-

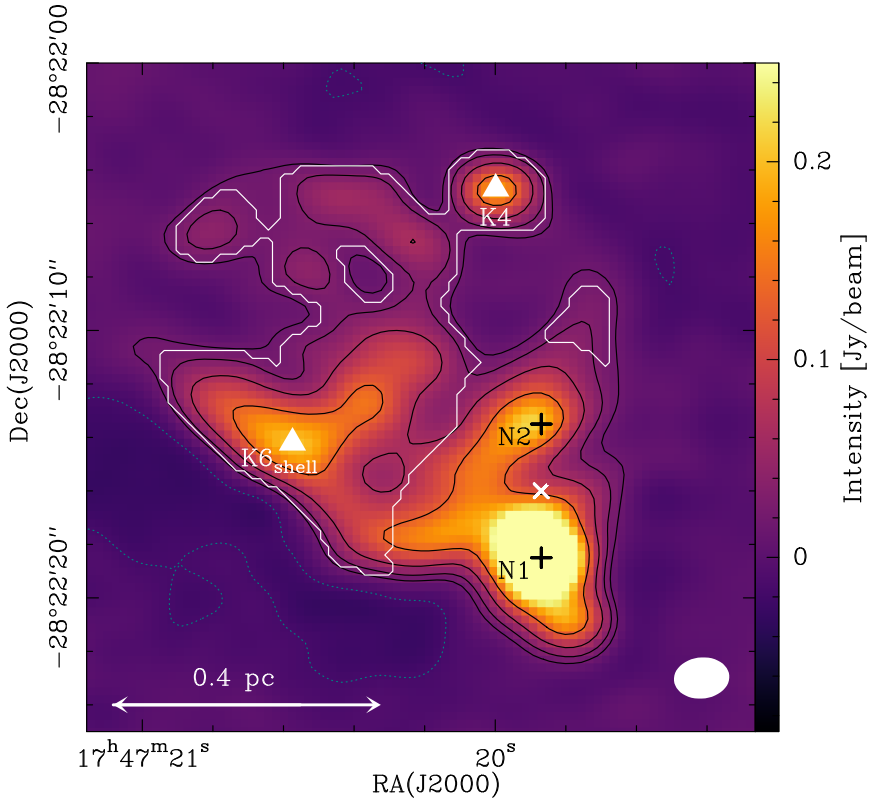

Figure 5.1: ALMA continuum map of Sgr B2(N) at 85 GHz. The black contour lines show the flux density levels at 3σ, 6σ, 12σ, and 24σ and the dotted ones mark -3σ, with σ the rms noise level of 5.4 mJy beam^{-1}. The black crosses mark the positions of the hot cores Sgr B2(N1) and Sgr B2(N2), the white cross the phase centre (EQ J2000: $17^h47^m19.87^s$, $-28°22'16''$), and the white triangles the ultra compact H II region K4 and the peak in the shell of the H II region K6 (Gaume et al. 1995). The white ellipse in the lower right corner is the synthesised beam. The white contour encloses the region selected for the analysis of the absorption features, for the particular case of ortho c-C_3H_2. The pixel size in this image is 0.″3.

fore, this unbiased line survey provides an excellent opportunity to study structures on sub-parsec scales not only in Sgr B2 itself, but also along the whole 8 kpc long line of sight to the Galactic Center. The line of sight to Sgr B2 passes through the Sagittarius, Scutum, 3 kpc, and 4 kpc arms as well as the Galactic Center (GC) clouds up to a distance of about 2 kpc from the GC (e.g., Greaves & Williams 1994; Menten et al. 2011, see Fig. 5.2).

In this paper we investigate the spatial structure of the molecular clouds traced by several molecules detected in absorption along the line of sight to Sgr B2 at much better angular resolution, namely 1.″6. In Sect. 5.2 we briefly describe the dataset we used for this work. The different techniques we adopted to analyse the data are presented in Sect 5.3. We present the results in Sect. 5.4 and discuss them in Sect. 5.5. We give a summary in Sect. 5.6.

5.2 Observations

We analyse the absorption lines detected in the EMoCA survey (Belloche et al. 2016). This spectral line survey was observed with ALMA in Cycles 0 and 1. It was pointed towards Sgr B2(N) with the phase centre

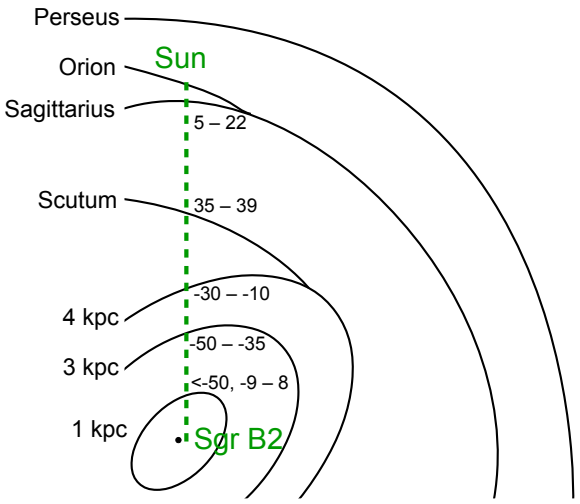

Figure 5.2: Sketch of the Milky Way and the spiral arms along the line of sight to Sgr B2 (based on Greaves & Williams 1994). The velocity ranges of the diffuse and translucent clouds are indicated in km s^{-1}.

located half way between the two main hot cores N1 and N2 at EQ J2000: $17^{h}47^{m}19.87^{s}$, $-28°22'16''$ (see Fig. 5.1). The survey covers the frequency range from 84.1 to 114.4 GHz with a spectral resolution of 488 kHz (1.7 to 1.3 km s^{-1}) at a median angular resolution of 1.″6. The median largest angular scale is 21.″4. The average noise level is ~3 mJy beam^{-1} per channel. Details about the calibration and deconvolution of the data are reported in Belloche et al. (2016).

We also analyse the emission lines of the molecules HCO^+, HNC, CS, and ^{13}CO detected in the 3 mm imaging spectral survey of Sgr B2 performed by Jones et al. (2008). The observations were carried out with the 22 m Mopra Millimetre Telescope in June 2006 in on-the-fly mode, covering an area of 5′ by 5′ centred on the J2000 equatorial position $17^{h}47^{m}19.8^{s}$, $-28°22'17''$ which is close to Sgr B2(N). The survey covers the full frequency range between 82 and 114 GHz with a spectral resolution of 2.2 MHz (6.4 km s^{-1} at 100 GHz). Additional narrow-band spectra with a high resolution of 33 kHz (0.10 km s^{-1} at 100 GHz) were also taken. The angular resolution of the data is about 36″ and the RMS noise level of the broadband spectra in main-beam temperature scale is 0.12–0.42 K depending on the frequency.

5.3 Methods

5.3.1 Selected data sample

To have enough sensitivity, we analyse the absorption features towards positions where the continuum emission is brighter than four times the RMS noise level. The noise level is derived from a Gaussian fit to the flux density distribution of all pixels in the continuum map not corrected for primary beam attenuation. For this, we use the command *go noise* in the GILDAS package GREG[1]. Positions close to the hot cores Sgr B2(N1) and Sgr B2(N2) have spectra full of emission lines of organic molecules (e.g., Bonfand et al. 2017). Therefore, in order to minimise the contamination of the absorption features by emission lines, we perform the analysis towards the positions that are far enough from these hot cores by excluding pixels inside ellipses drawn around them. Because of the slightly different beams and noise levels in the different spectral windows (see Belloche et al. 2016), the mask resulting from these two criteria may differ from molecule

[1] see https://www.iram.fr/IRAMFR/GILDAS/

to molecule. As an example, we show the area selected for c-C_3H_2 on top of the ALMA continuum map in Fig. 5.1. The selected data sample has no emission lines contaminating the absorption features. With a sampling of 0.6″, the Nyquist-sampling condition is still fulfilled and we do not lose information. This results in 322 pixels for c-C_3H_2, which represents an area of about 32 independent beams.

5.3.2 Opacity cubes

When the excitation temperature of a transition seen in absorption is equal to the temperature of the CMB (see Eq. 5.2 below), the opacity, τ, of the absorption line is directly related to the line intensity, I_l, and the continuum level, I_c, through the following equation:

$$\tau(\nu) = -\ln\left(1 + \frac{I_\mathrm{l}(\nu)}{I_\mathrm{c}}\right), \tag{5.1}$$

where I_c is the level of the baseline (representing the continuum emission) in the original spectrum and $I_\mathrm{l}(\nu)$ is the intensity of the absorption line measured in the baseline-subtracted spectrum at a certain frequency. With this definition, I_l is negative for an absorption line. This formula only yields meaningful values for τ when the absorption is not too optically thick, otherwise the value in the parentheses gets close to zero and the logarithm diverges. We can then compute the column density of the molecule from the derived opacity (see Eq. 5.3 below).

Because the size of our data sample is small, we create many realisations of the opacity cube by injecting noise to I_l and I_c (with $\sigma_{I_l} = \sigma_\mathrm{RMS} \sim 3\,\mathrm{mJy\,beam^{-1}}$ and $\sigma_{I_c} << \sigma_{I_l}$) in order to evaluate the impact of the noise on our subsequent analyses. Thereby, we assume the uncertainties on I_l and I_c to have a Gaussian distribution. I_c contributes only little to the uncertainty of τ. Using this assumption we randomly create 1000 opacity cubes from the original line intensity cube. We set the opacity of all pixels with $-I_\mathrm{l} \geq I_\mathrm{c}$ to infinity. Due to the tolerance limit of `python`[2], the opacity of pixels with $0 < 1 + \frac{I_\mathrm{l}}{I_\mathrm{c}} < 10^{-16}$ is also set to infinity. The upper limit corresponds to an opacity of 37.

We keep all pixels with $I_\mathrm{l} \leq 3.1\sigma_\mathrm{RMS}$. The resulting data still contain noisy pixels. With the assumption of a Gaussian noise distribution, this threshold means that less than 0.1% of pure-noise pixels are excluded (the ones with $I_\mathrm{l} \geq 3.1\sigma_\mathrm{RMS}$). In addition, we use the error propagation law to create a cube containing the uncertainties on the opacity, σ_τ.

5.3.3 Modelling

In order to identify and characterise the velocity components present in the absorption spectra, we fit synthetic spectra consisting of a collection of Gaussian opacity distributions. We model the spectra with Weeds (Maret et al. 2011) which solves the radiative transfer equation under the assumption of local thermodynamic equilibrium and takes into account the finite angular resolution of the observations.

Because our data sample contains several hundreds of spectra per molecule, the spectra are fitted automatically. For this, we use the fitting routine MCWeeds (Giannetti et al. 2017), which combines the python package PyMC2 (Patil et al. 2010) and Weeds (Maret et al. 2011). MCWeeds adjusts the parameters for a given number of velocity components and delivers the best result along with uncertainties. For all fitted parameters a set of initial guesses has to be given, along with their probability distribution and the range over which they should be varied.

The synthetic spectra are computed by Weeds in the following way. For a baseline-subtracted spectrum, the intensity of an absorption line in a medium with constant excitation filling the beam is:

[2] `https://www.python.org`

$$T_{\mathrm{B}}(\nu) = \left[J_\nu(T_{\mathrm{ex}}) - T_{\mathrm{c},\nu} - J_\nu(T_{\mathrm{CMB}})\right] \cdot \left(1 - \mathrm{e}^{-\tau(\nu)}\right), \tag{5.2}$$

with $T_{\mathrm{B}}(\nu)$ the brightness temperature at the frequency ν, T_{CMB} the CMB temperature, T_{ex} the excitation temperature of the line, $T_{\mathrm{c},\nu}$ the baseline level in the spectrum before baseline-subtraction, $\tau(\nu)$ the opacity, and $J_\nu(T) = \frac{h\nu/k}{\mathrm{e}^{h\nu/kT}-1}$, with h the Planck constant and k the Boltzmann constant. The opacity $\tau(\nu)$ is calculated as:

$$\tau(\nu) = \frac{c^2}{8\pi\nu^2} \frac{A g_u}{Q(T_{\mathrm{ex}})} \sum_i N^i_{\mathrm{tot}} \mathrm{e}^{-E_u/kT_{\mathrm{ex}}} \left(\mathrm{e}^{h\nu_0/kT_{\mathrm{ex}}} - 1\right) \phi^i, \tag{5.3}$$

with c the speed of light, N^i_{tot} the column density of the molecule, $Q(T_{\mathrm{ex}})$ the rotational partition function at temperature T_{ex} (in LTE, the rotational temperature is equal to the excitation temperature). A the Einstein coefficient for spontaneous emission of the transition, g_u the degeneracy factor of the upper level, E_u the upper level energy, ν_0 the rest frequency, ϕ^i the line profile function, and $\sum_i$ the summation over the velocity components contributing to the absorption. The line profile function is assumed to be Gaussian:

$$\phi^i = \frac{1}{\sqrt{2\pi}\sigma_i} \mathrm{e}^{-\frac{(\nu + \frac{-\Delta\nu}{\Delta v}\Delta v^i_{\mathrm{off}} - \nu^i_0)^2}{2\sigma_i^2}}, \tag{5.4}$$

with σ_i the standard deviation of the Gaussian, $\Delta v^i_{\mathrm{off}}$ the velocity offset of the velocity component, Δv the channel width in velocity, and $\Delta\nu$ the channel width in frequency. From σ_i the full width at half maximum ($FWHM_i$) in velocity units can be calculated:

$$FWHM_i = \frac{c}{\nu^i_0} \sqrt{8\ln 2} \cdot \sigma_i. \tag{5.5}$$

We assume the excitation temperature to be equal to the temperature of the CMB (2.73 K) because we focus on the diffuse and translucent clouds along the line of sight to Sgr B2 excluding those physically associated with Sgr B2 itself. For comparison, Godard et al. (2010) determined a range of excitation temperatures of 2.7–3 K using transitions of HCO^+ for four different lines of sight. Previous absorption studies also assumed excitation temperatures in this range (e.g., Greaves & Williams 1994; Lucas & Liszt 1999; Liszt et al. 2012; Wiesemeyer et al. 2016; Ando et al. 2016).

The fitted parameters are the column density N_{tot}, the width $FWHM$, and the centroid velocity v_0 of each velocity component. An example of synthetic spectrum of ortho c-C_3H_2 $2_{1,2}$–$1_{0,1}$ fitted with MCWeeds towards the ultracompact (UCH II) region K4 (Gaume et al. 1995) is shown in Fig. 5.3. It contains 13 velocity components.

5.3.4 Minimisation method

The absorption features detected in our data consist of many velocity components (see Fig. 5.3). Therefore, many parameters have to be fitted at the same time. A good method to deal with a large number of free parameters is the Powell minimisation method (Powell 1964, see Appendix C.1 for more details). We use a modified version of this method (*fmin_powell* from `scipy`[3]) with MCWeeds. Because this method finds a local minimum of the problem, good initial guesses have to be given to the fitting routine (see Sect. 5.3.5).

[3] see https://scipy.org

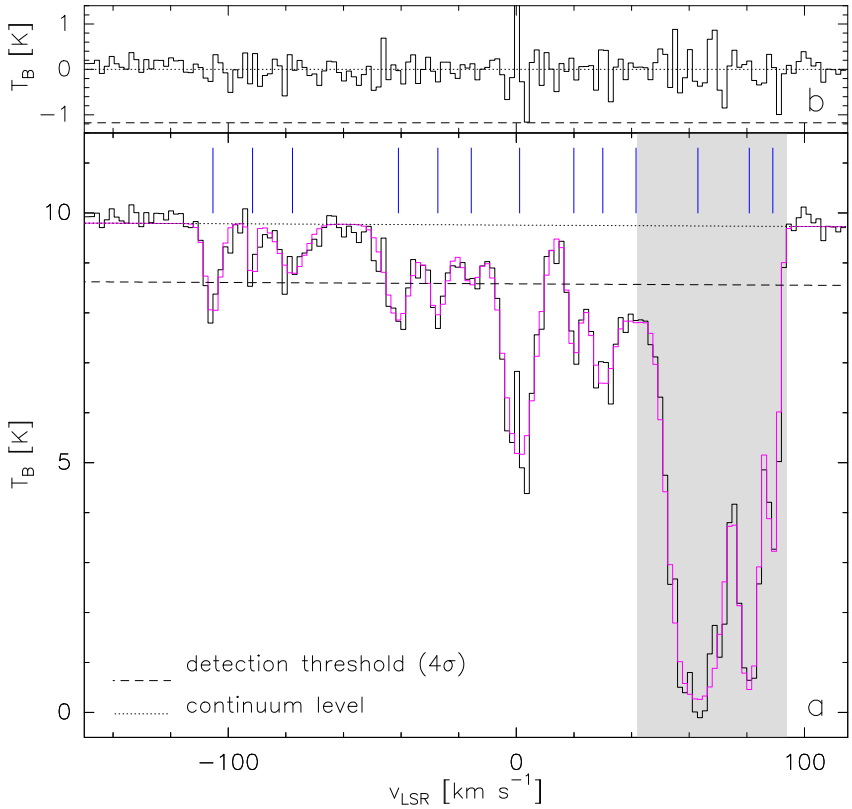

Figure 5.3: **a** ALMA spectrum of ortho c-C_3H_2 $2_{1,2} - 1_{0,1}$ at 85338.896 MHz towards the UCH II region K4 (Gaume et al. 1995). The spectrum in magenta is the synthetic spectrum obtained with MCWeeds. The blue lines show the central velocities of the fitted components. The dotted line represents the continuum level and the dashed line marks the 4σ line detection threshold. The grey area marks the velocity range of the envelope of Sgr B2 ($v_{\mathrm{LSR}} > 42$ km s^{-1}). **b** Residuals, that is the difference between the observed and synthetic spectra. The dashed lines indicate the -4σ level. The spectrum is corrected for the primary beam attenuation.

5.3.5 Automatisation programme

We wrote a `python` programme that searches for appropriate initial guesses and runs the minimisation with MCWeeds in an automatic way for all selected positions. It also automatically determines the number of velocity components that are required to fit the spectrum of each position. The algorithm is described in detail in Appendix C.2. We applied this automatisation programme only to ortho c-C_3H_2.

5.3.6 Two-point auto-correlation of opacity maps

To analyse the structure of the cloud probed in absorption, we calculate the two-point auto-correlation function of the opacity maps. As in Sect. 5.3.1, we use a data sampling of 0.6″. The two-point auto-correlation function $C(r)$ is calculated for a sample of pixel separations r_k with $0 \leq r_k \leq r_{max}$, where r_{max} is the maximal possible separation of two pixels in the opacity maps (about 17″). The value of the two-point auto-correlation function at pixel separation r_k is the average scalar product of the opacities of the pixel pairs

that have a separation r_k:

$$C(r_k) = \frac{1}{N} \sum_{i=1}^{N} \tau(x_{1,i}, y_{1,i}) \tau(x_{2,i}, y_{2,i}), \tag{5.6}$$

with $r_{k-1}^2 < (x_{1,i} - x_{2,i})^2 + (y_{1,i} - y_{2,i})^2 \leq r_k^2$, $x_{1,i}$, $x_{2,i}$ and $y_{1,i}$, $y_{2,i}$ the pixel coordinates, and N the number of pixel pairs fulfilling this condition. To get sufficiently high statistics, $C(r_k)$ is only determined if at least 50 pairs of pixels are available in the range $[r_{k-1}, r_k]$.

We computed the two-point auto-correlation functions of 1000 realisations of the opacity cubes produced in Sect. 5.3.2 to estimate their uncertainties.

We take the average of the 1000 two-point auto-correlation functions as the best estimate and their dispersion as the uncertainty. We also compute $C(r)$ for channels containing only noise (see Appendix C.3.1).

5.3.7 Probability distribution function of the optical depth

To investigate further cloud properties such as turbulence, we calculate the probability distribution function (PDF) of the opacity maps. We use the following normalisation (see, e.g., Schneider et al. 2013):

$$\eta = \ln\left(\frac{\tau}{\bar{\tau}}\right), \tag{5.7}$$

with $\bar{\tau}$ the mean opacity in the map. Here, we ignore all pixels with a negative opacity resulting from the noise because the normalisation η is only defined for positive opacities. We determine the normalised PDF for each of the 1000 realisations of the opacity cubes. For this, we calculate the PDF for bins in η of width 0.1. We calculate the mean value of the PDF and the standard deviation as uncertainty for each bin. The presence of pixels containing only noise results in a broader PDF (Ossenkopf-Okada et al. 2016). To minimise the effect of the noise, we compute the PDF using only the pixels with opacities above the 3σ level implying only positive values for η (see Appendix C.3.2). We fit a normal distribution to the PDF:

$$p(\eta) = \frac{A}{\sqrt{2\pi}\sigma} \cdot \exp\left(-\frac{(\eta - \mu)^2}{2\sigma^2}\right). \tag{5.8}$$

A is the integral below the curve, σ is the dimensionless dispersion, and μ the mean. For a perfect log-normal distribution, μ should be equal to 0 and A to 1.

The fit is only performed if the number of counts per log-bin at the peak of the PDF is higher than 10 and if no more than 10 percent of the available pixels have an opacity value set to infinity.

5.3.8 Principal component analysis

To search for correlations or anti-correlations between the opacity maps of the different molecules, we use the principal component analysis (PCA) (see, e.g., Heyer & Peter Schloerb 1997; Neufeld et al. 2015; Spezzano et al. 2017; Gratier et al. 2017). The PCA applies an orthogonal transformation to a dataset to produce a set of components which are linearly uncorrelated, the so-called principal components (PC). The PCs are orthogonal to each other and make up a new coordinate system to which the data are transformed. The first PC goes in the direction of the largest variance in the data. The number of PCs that are considered has to be smaller than or equal to the number of dimensions of the original data set. In our case the number n of molecules used for the PCA is the dimension of the data set and also the number of calculated PCs. We apply the PCA to opacity maps at a given velocity. In our case, the original data set consists of one-dimensional arrays, one for each molecule, which contain the opacities of the selected pixels. Before starting

the PCA, the array $\vec{a}_i$ of each molecule i is normalised by subtracting the mean $\bar{a}_i$ and by dividing by the standard deviation σ_i (e.g., Neufeld et al. 2015):

$$a_{i,j,\mathrm{normed}} = \frac{a_{i,j} - \bar{a}_i}{\sigma_i}, \tag{5.9}$$

with j the pixel position in the array. After this preparation, the PCA is performed with the `Python` package `scikit-learn` (Pedregosa et al. 2011). The procedure computes the principal components as well as the eigenvalues of the decomposition. The powers (eigenvalue divided by sum of eigenvalues) give the contribution of the different components calculated from the eigenvalues.

To determine the contribution $C_{i,k}$ of each principal component $\vec{PC}_k$ to each molecule array $\vec{a}_{i,\mathrm{normed}}$, the following system of linear equations has to be solved:

$$\vec{a}_{i,\mathrm{normed}} = b_i \sum_k C_{i,k} \cdot \vec{PC}_k, \tag{5.10}$$

with b_i a constant factor, the normalisation condition $\sum_k C_{i,k}^2 = 1$, and with the principal components having a length of 1 and a standard deviation of 1.

To estimate the uncertainties of the contributions $C_{i,k}$, we apply the PCA to the 1000 realisations of the opacity cubes. Two conditions have to be fulfilled to exploit the outcome of these 1000 PCAs. First, the pixel lists must be the same. Therefore we ignore pixels which have an opacity value set to infinity in any of the realisations. The second condition is that the PCs that represent the axes of the new coordinate system have to be aligned to each other. This is not necessarily the case when calculating the PCs for the different realisations of the opacity cubes. To address this, we take the original cubes as reference for the PCA and we align the new coordinate systems (PCs) of the 1000 realisations to this reference by applying with the `Python` package `scipy.linalg`[4] an orthogonal procrustes rotation as described by Babamoradi et al. (2013). After this, we determine the contributions $C_{i,k}$ as explained above and calculate the mean and the standard deviation.

The noise can have a significant influence on the outcome of the PCA. The normalisation can increase the impact of the noise in cases where a molecule has a relatively homogeneous opacity over the field of view or when the absorption is weak and most of the field of view is dominated by noise. To avoid this problem, we select the molecules depending on the dynamic range of their opacity maps. The peak signal-to-noise ratio must be at least 10 and there must be at least 125 pixels (which corresponds to ~ 5 beams of the sample) with a signal-to-noise ratio higher than 5. With these selection criteria we ignore molecules which may have only one compact, strong peak. A meaningful use of the PCA at a given velocity requires at least four molecules.

5.4 Results

5.4.1 Identification of molecules

We performed the identification of the molecules on the basis of the spectroscopic information provided in the Cologne Database for Molecular Spectroscopy (CDMS, Endres et al. 2016; Müller et al. 2005, 2001) and the Jet Propulsion Laboratory (JPL) molecular spectroscopy catalogue (Pickett et al. 1998). In total, we identified 19 molecules seen in absorption in the diffuse and translucent molecular clouds along the line of sight to Sgr B2(N): $C^{13}O$, CS, CN, SiO, SO, HCO^+, HOC^+, HCN, HNC, CCH, N_2H^+, HNCO, H_2CS, c-C_3H_2, HC_3N, CH_3OH, CH_3CN, NH_2CHO, and CH_3CHO. We also detected the following less abundant

[4] see https://scipy.org

Table 5.1: Velocity ranges and associated locations of the clouds along the line of sight to Sgr B2.

location	$v_{\rm LSR}$ [km s^{-1}]
Galactic Center	< -50
3kpc arm	-50 to -35
4kpc arm	-30 to -10
Galactic Center	-9 to 8
Sgr arm	5 to 22
Scutum arm	25 to 39

Notes. References: Greaves & Williams (1994); Neufeld et al. (2000); Lis et al. (2010); Menten et al. (2011); Monje et al. (2011); and references therein. The combination of the velocity ranges mentioned in these papers results in some overlapping ranges. We treat clouds falling in the overlapping velocity range between 5 and 8 km s^{-1} as GC clouds.

isotopologues: $C^{18}O$, $C^{17}O$, $C^{34}S$, ^{13}CS, $C^{33}S$, ^{13}CN, ^{29}SiO, ^{30}SiO, $H^{13}CO^+$, $HC^{18}O^+$, $H^{13}CN$, $HC^{15}N$, $HN^{13}C$, $H^{15}NC$, and $^{13}CH_3OH$. A report on the complex organic molecules detected in absorption in this survey is given in Thiel et al. (2017).

5.4.2 Identification of velocity components based on c-C_3H_2

We selected the molecule c-C_3H_2 to decompose the absorption features into individual velocity components with our automatisation programme and thereby identify the clouds detected in absorption along the line of sight to Sgr B2(N). Absorption from the 85.3 GHz ortho c-C_3H_2 line covers almost the complete velocity range in which the clouds along the line of sight are detected. An advantage compared to other molecules is that the absorption is optically thin, except in parts of the envelope of Sgr B2 (highlighted in grey in Fig. 5.3). We note that absorption from c-C_3H_2 has long been known to trace diffuse interstellar clouds, among others along sight lines to the GC (Cox et al. 1988).

To identify the velocity components, we investigate the distribution of linewidths, $FWHM$, centroid velocities, v, and column densities, $N_{\rm tot}$, obtained for ortho c-C_3H_2 from the fits to all positions where the molecule is detected. In total, 2838 velocity components are detected towards the 322 selected positions. Between 2 and 6 velocity components are detected in the envelope of Sgr B2 at each position and up to 14 velocity components are found by the programme in the clouds along the line of sight.

The number of velocity components detected with c-C_3H_2 in the selected field is shown as a function of centroid velocity in Fig. 5.4a. The distributions of widths and column densities are plotted in panels b and c, respectively. The velocity ranges of the spiral arms, the diffuse Galactic Center clouds and the envelope of Sgr B2 are colour coded in the background of Fig. 5.4 (see Table 5.1 for references and Fig. 5.2 for a sketch). There is an ambiguity between the GC and the local spiral arm for the velocities around 0 km s^{-1}. Due to the compact structure of the absorption component around 0 km s^{-1} along the line of sight to the Galactic Center, Whiteoak & Gardner (1978) suggested this absorption is not caused by local gas. Later, Gardner & Whiteoak (1982) determined a low isotopic ratio $\frac{^{12}C}{^{13}C}$ of 22 for this component, which strongly suggests that it belongs to the Galactic Center region. Hence, we assume that the strong absorption around 0 km s^{-1} belongs to the Galactic Center region and in the following the velocity range from -9 to 8 km s^{-1} will be treated as part of the GC region. c-C_3H_2 is detected in each group of line-of-sight (l.o.s.) molecular clouds which makes it an excellent molecule for a comparative study of these diffuse and translucent molecular clouds.

We identify each elongated structure in Fig. 5.4b and each corresponding peak in Fig. 5.4a as a single

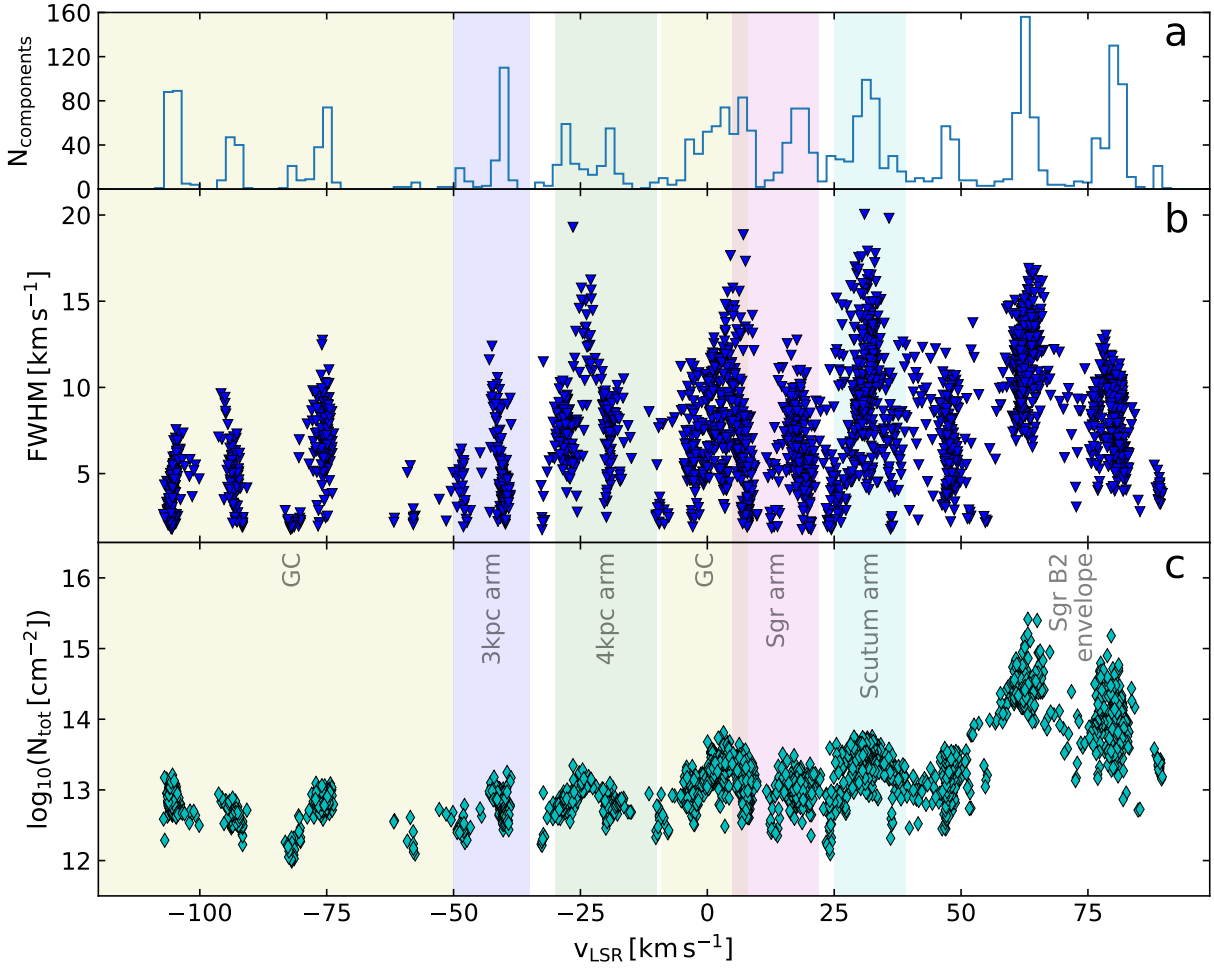

Figure 5.4: **a** Number of velocity components found with ortho c-C_3H_2 in the selected field as a function of centroid velocity. The bin width is one channel, 1.74 km s^{-1}. **b** Distribution of linewidths. **c** Distribution of ortho c-C_3H_2 column densities. The velocity ranges are colour coded in the background of every panel (see Table 5.1 for references).

cloud. In some cases such as the GC clouds in the range −110 to −70 km s^{-1}, it is easy to differentiate the clouds, because the velocity components are well separated. For the GC clouds around 0 km s^{-1} it is more difficult. In the case of the 3 kpc arm we see mainly two clouds, but sometimes only one component with a width larger than the two narrow components detected at other positions. After inspecting the spectra we found out that in these cases the programme could not find two different components because they overlap each other in such a way that they cannot be separated along the velocity axis. The same happens for the Scutum and 4 kpc arms.

The distribution of column densities of ortho c-C_3H_2 as a function of linewidth is plotted in Fig. 5.5a. We also show the column density divided by the linewidth in Fig. 5.5c because, in this representation, the detection limit is roughly horizontal. Another advantage of the latter representation is that it reduces the bias due to the clouds that partially overlap in velocity and could not be fitted separately.

We divide the diffuse and translucent clouds along the line of sight to Sgr B2 with v_{LSR}<42 km s^{-1} into two main categories based on their ortho c-C_3H_2 column densities (see Fig. 5.5b and d). We call Category I the l.o.s. clouds with velocities up to −13 km s^{-1} and Category II the ones with velocities between

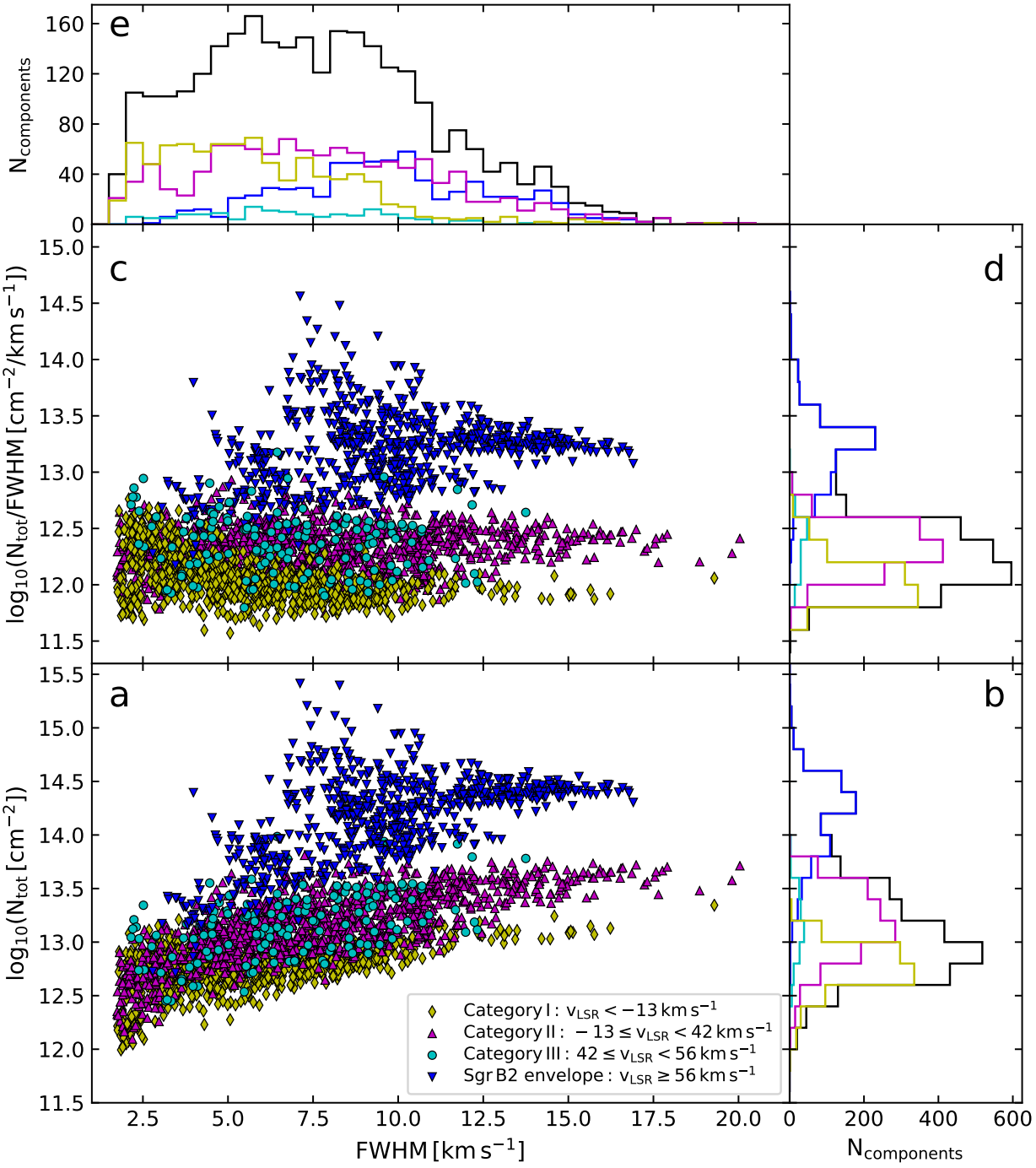

Figure 5.5: **a** Distribution of column densities as a function of linewidth. **b** Number of components as a function of column density. **c** Distribution of column densities divided by linewidth as a function of linewidth. **d** Number of components as a function of column density divided by linewidth. **e** Number of velocity components as a function of linewidth. The bin width is 0.5 km s^{-1}. In all panels the two categories of line-of-sight clouds are coloured in yellow (Category I) and magenta (Category II), the clouds at about 50 km s^{-1} in cyan (Category III), and the components tracing the diffuse envelope of Sgr B2 in blue. In panels b, d, and e, the black histogram represents the full sample of detected components.

Table 5.2: Median linewidths and column densities of the four categories shown in Fig. 5.5.

Category	$v_{\rm LSR}$ [km s^{-1}]	$FWHM$ [km s^{-1}]	$\log_{10} N_{\rm tot}$ [cm^{-2}]	$\log_{10} \frac{N_{\rm tot}}{FWHM}$ [cm^{-2} km^{-1} s]
Category I	$v_{\rm LSR} < -13$	5.4	12.8	12.0
Category II	$-13 \leq v_{\rm LSR} < 42$	7.5	13.2	12.3
Category III	$42 \leq v_{\rm LSR} < 56$	6.7	13.2	12.4
Sgr B2 envelope	$v_{\rm LSR} \geq 56$	9.6	14.2	13.2

-13 km s^{-1} and 42 km s^{-1}. The absorption at velocities between 50 and 90 km s^{-1} is usually considered to be caused by the envelope of Sgr B2 (Neill et al. 2014). The envelope of Sgr B2 ($v_{\rm LSR} \geq 56$ km s^{-1}) contains two main velocity components at about 64 km s^{-1} and 80 km s^{-1} (e.g., Huettemeister et al. 1995; Lang et al. 2010). The velocity component at about 48 km s^{-1} is usually also associated with the envelope of the Sgr B2 complex (e.g., Garwood & Dickey 1989, and references therein). We plot it in cyan in Fig. 5.5 because it stands out with lower column densities compared to the two main components of the Sgr B2 envelope. We call the velocity range between 42 km s^{-1} and 56 km s^{-1} Category III.

The distribution of linewidths is shown in black in Fig. 5.5e. The lower limit is set by the channel width of 1.74 km s^{-1}. The linewidths cover the range between this lower limit and 20 km s^{-1}. The ortho c-C_3H_2 column densities cover a range of three orders of magnitude from 10^{12} cm^{-2} to 10^{15} cm^{-2} (Figs. 5.5a and b). Each histogram of Fig. 5.5 is also split into the four categories of components introduced above. The median linewidths and column densities of these four categories are listed in Table 5.2.

The majority of l.o.s. clouds have a linewidth smaller than 10 km s^{-1}, but there is a tail up to 20 km s^{-1}. We believe that most of these broader components represent two or more overlapping components with narrower widths that could not be fitted individually. Hence, these components could contain several cloud entities. The l.o.s. clouds can be divided into two categories (yellow and magenta in Fig. 5.5). Category I has a median linewidth of 5.4 km s^{-1}. It contains the GC clouds with a velocity lower than -50 km s^{-1} and the clouds of the 3 kpc and 4 kpc arms. The GC clouds around 0 km s^{-1} and the clouds in the Scutum and the Sagittarius arms (Category II) have a somewhat larger median linewidth of 7.5 km s^{-1}. The components in the envelope of Sgr B2 have an even larger median linewidth of 9.6 km s^{-1}. This larger value may partly be due to the optical thickness. The high opacities affecting these components make it indeed sometimes difficult to fit individual velocity components. The components in Category III have a median linewidth of 6.7 km s^{-1}, in between the ones of Categories I and II.

The median column densities of ortho c-C_3H_2, both before and after normalisation by the linewidth, of Categories I, II, and III are similar, on the order of 10^{13} cm^{-2} and 10^{12} cm^{-2} km^{-1} s, respectively, with Category I lying slightly below Categories II and III. While Categories II and III are more affected than Category I by overlapping components that cannot be fitted separately, their higher median column densities do not result from this because they still lie above Category I by a factor of $\sim$2 after normalisation by the linewidth. The components in the Sgr B2 envelope are characterised by much higher column densities, about one order of magnitude compared to Categories II and III, both before and after normalisation by the linewidth.

Overall, the components around 50 km s^{-1} (Category III) have similar properties (linewidths and ortho c-C_3H_2 column densities) as the ones in the Scutum and Sagittarius arms (Category II).

In the following, we ignore the components belonging to the envelope of Sgr B2 because of their high optical depths. In addition, because the velocity component of Category III is blended with the one of the envelope of Sgr B2 at 64 km s^{-1} (see grey shaded area in Fig. 5.3), we focus our subsequent analyses on

Table 5.3: Velocities and localisation of the diffuse and translucent molecular clouds detected with c-C_3H_2 along the line of sight to Sgr B2, excluding Category III and the envelope of Sgr B2.

v_{LSR} [km s^{-1}]	Location[a]	Category[b]	d[c] [kpc]
−105.9	Galactic Center	I	7.0
−93.7	Galactic Center	I	7.0
−81.5	Galactic Center	I	7.0
−74.6	Galactic Center	I	7.0
−48.4	3 kpc arm	I	5.5
−39.7	3 kpc arm	I	5.5
−27.6	4 kpc arm	I	4.3
−18.9	4 kpc arm	I	4.3
−3.2	Galactic Center	II	7.0
2.0	Galactic Center	II	7.0
7.3	Galactic Center	II	7.0
17.7	Sagittarius arm	II	1.0
24.7	Scutum arm	II	2.8
31.6	Scutum arm	II	2.8
36.9	Scutum arm	II	2.8

Notes. [(a)] Location of the clouds. [(b)] See Table 5.2. [(c)] Approximate distance to the Sun.

the clouds belonging to Categories I and II. They can be described with 15 components whose centroid velocities are derived from the peaks in Fig. 5.4a. These 15 components are listed in Table 5.3.

5.4.3 Opacity maps

To investigate the spatial structure of the clouds we look for molecules that reveal absorption over an extended area of the field of view. We do not consider molecules with a resolved hyperfine structure that makes velocity assignments more complicated without fitting. Out of all molecules detected along the line of sight to Sgr B2, eight molecules fulfil these criteria: $H^{13}CO^+$, ^{13}CO, HNC and its isotopologue $HN^{13}C$, $HC^{15}N$, CS and its isotopologues $C^{34}S$ and ^{13}CS, SiO, SO, and CH_3OH. For some components the less abundant isotopologues are useful when the main isotopologue is optically thick. The spectroscopic parameters of the transitions of these selected molecules are listed in Table B.1 and the example spectra towards the two positions K4 and $K6_{shell}$ (see Fig. 5.1) are shown in Fig. C.8 in the Appendix.

We show in Fig. 5.6 the opacity maps of c-C_3H_2 at the 15 velocities listed in Table 5.3, and in Fig. 5.7 the maps of signal-to-noise ratio (SNR). It is important to consider the SNR maps when interpreting the opacity maps because the noise level is not uniform due to the variations of the background continuum emission. The SNR maps are strongly correlated to the continuum map (see Fig. 5.1): the stronger the continuum the lower the opacity noise level.

At first sight, large-scale structures are detected in the opacity maps of nearly all velocity components (Fig. 5.6). The components at −48.4 km s^{-1} and −3.2 km s^{-1} do not show such extended structures but this may simply result from a lack of sensitivity: their SNR maps indicate that the peak SNR is low (less than about 5 if we exclude K4) and only few positions have a SNR above 3.

The component at v_{LSR} = 36.9 km s^{-1} looks more clumpy in Fig. 5.6, with three seemingly prominent,

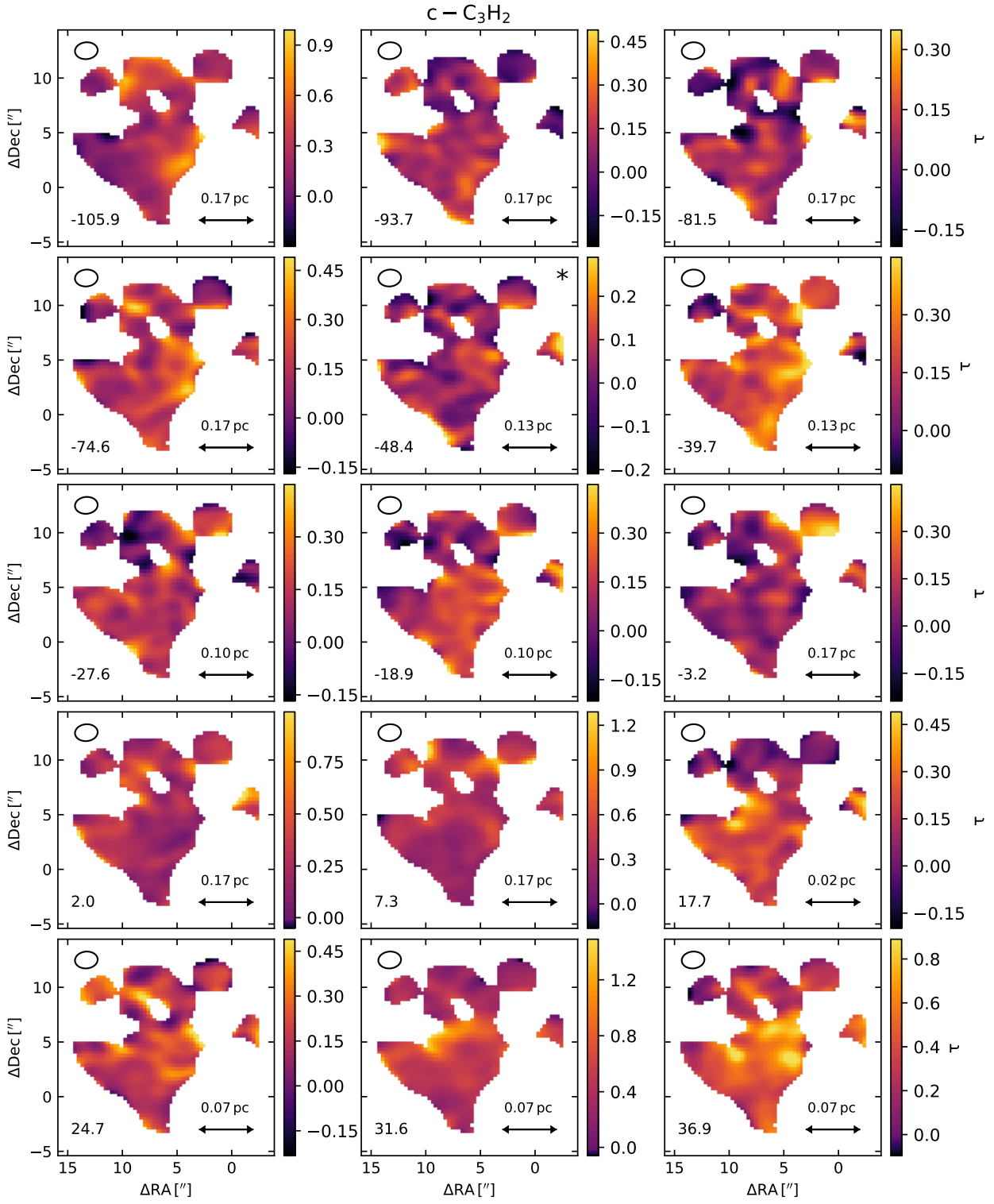

Figure 5.6: Opacity maps of c-C_3H_2 $2_{1,2}$–$1_{0,1}$ for all 15 investigated velocity components. In each panel, the velocity of the channel is given in km s^{-1} in the bottom left corner, the beam (*HPBW*) is shown as an ellipse in the upper left corner, and an approximate physical scale for the assumed distance of the cloud (see Table 5.3) is indicated in the bottom right corner. A star in the upper right corner marks the components with a maximum signal-to-noise ratio τ/σ_τ smaller than 5 (see Fig. 5.7). The equatorial offsets are relative to the phase centre.

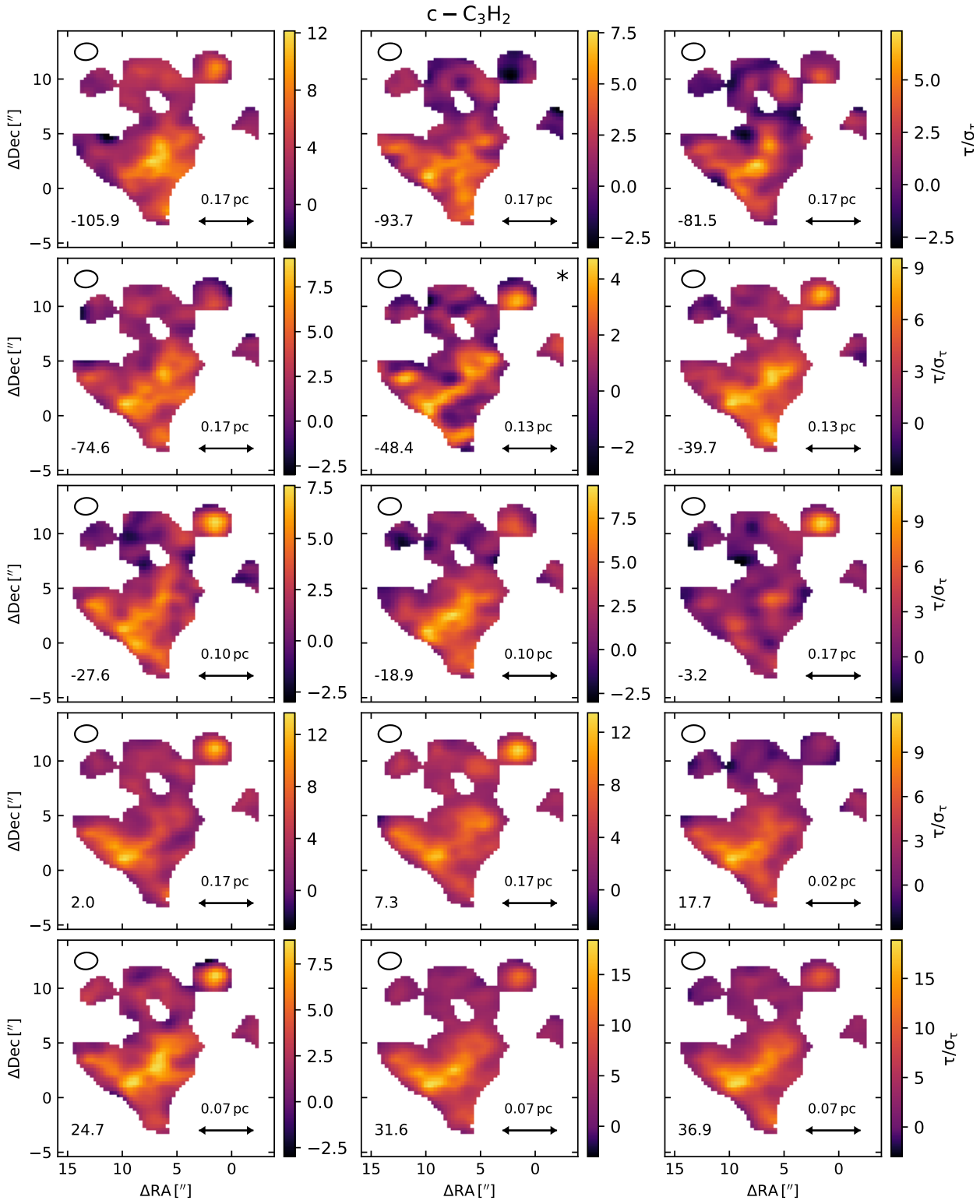

Figure 5.7: Same as Fig. 5.6 but for the signal-to-noise ratio τ/σ_τ of c-C_3H_2 $2_{1,2}$–$1_{0,1}$.

Table 5.4: Rotational transitions used in this work.

Molecule	Transition	$\nu_0{}^a$ [MHz]	E_{up}/k^b [K]	$A_{u,l}{}^c$ [s^{-1}]	References
ortho c-C_3H_2	$2_{1,2}$–$1_{0,1}$	85338.894	4.1	2.32×10^{-5}	1
$HC^{15}N$	1–0	86054.966	4.1	2.20×10^{-5}	10
$H^{13}CO^+$	1–0	86754.288	4.2	3.85×10^{-5}	2
SiO	2–1	86846.985	6.3	2.93×10^{-5}	7
$HN^{13}C$	1–0	87090.825	4.2	2.38×10^{-5}	9
HNC	1–0	90663.568	4.4	2.69×10^{-5}	8
^{13}CS	2–1	92494.308	6.7	1.41×10^{-5}	5
$C^{34}S$	2–1	96412.950	6.9	1.60×10^{-5}	4,5
CH_3OH A*	2_0–1_0	96741.371	7.0	3.41×10^{-6}	11
CS	2–1	97980.953	7.1	1.68×10^{-5}	4,5
SO	2_3–1_2	99299.870	9.2	1.13×10^{-5}	6
^{13}CO	1–0	110201.354	5.3	6.33×10^{-8}	2,3

Notes. The spectroscopic information for the molecule marked with a star is taken from JPL, otherwise from CDMS. [(a)] Rest frequency. [(b)] Upper level energy. [(c)] Einstein coefficient for spontaneous emission from upper level u to lower level l.

References. (1) Spezzano et al. (2012); (2) Schmid-Burgk et al. (2004): (3) Cazzoli et al. (2004); (4) Gottlieb et al. (2003); (5) Bogey et al. (1982); (6) Tiemann (1974); (7) Müller et al. (2013); (8) Saykally et al. (1976); (9) van der Tak et al. (2009); (10) Cazzoli et al. (2005); (11) Müller et al. (2004).

unresolved structures. However, all three opacity peaks have low SNR (~ 5) in Fig. 5.7. They may be noise artefacts and may not trace real compact structures.

The opacity and SNR maps of the other molecules are shown in Figs. C.9–C.30. The velocities of the channels differ slightly from the ones of c-C_3H_2 because of the discrete sampling of the frequency axis. The channels selected for these figures are the ones nearest to the velocities listed in Table 5.3. The pixels that have an opacity set to infinity (see Sect. 5.3.2) are masked (in cyan).

The type of structures seen in the opacity maps is similar for all molecules. In many cases, extended structures are present. Compact clumps that are present in some maps often have a low SNR and may simply be noise artefacts. The SNR of low-abundance molecules such as ^{13}CS is too low to characterise the structural properties of the clouds. A better sensitivity would be needed for these tracers.

Because of the high number of opacity maps, we use in the following sections statistical tools to analyse and quantify the structure of the clouds traced in absorption towards Sgr B2(N).

5.4.4 Cloud substructure

The two-point auto-correlation functions of c-C_3H_2 and $H^{13}CO^+$ are shown in Figs. 5.8 and 5.9, respectively. The two-point auto-correlation functions of the other molecules are displayed in Figs. C.31–C.40. Panels a–d of each of these figures show the two-point auto-correlation functions $C(r)$ of the velocity components and panel (e) their SNR (C/σ_C). The analysis of the two-point auto-correlation function of noise channels performed in Appendix C.3.1 indicates that only SNR values higher than 5 and 4 for pixel separations below and above 6″, respectively, are significant. In addition, the true two-point auto-correlation function cannot be evaluated below a separation corresponding to the size of the beam ($HPBW$). As a result, the values of the two-point auto-correlation functions are significant only in the upper-right part of their SNR curves,

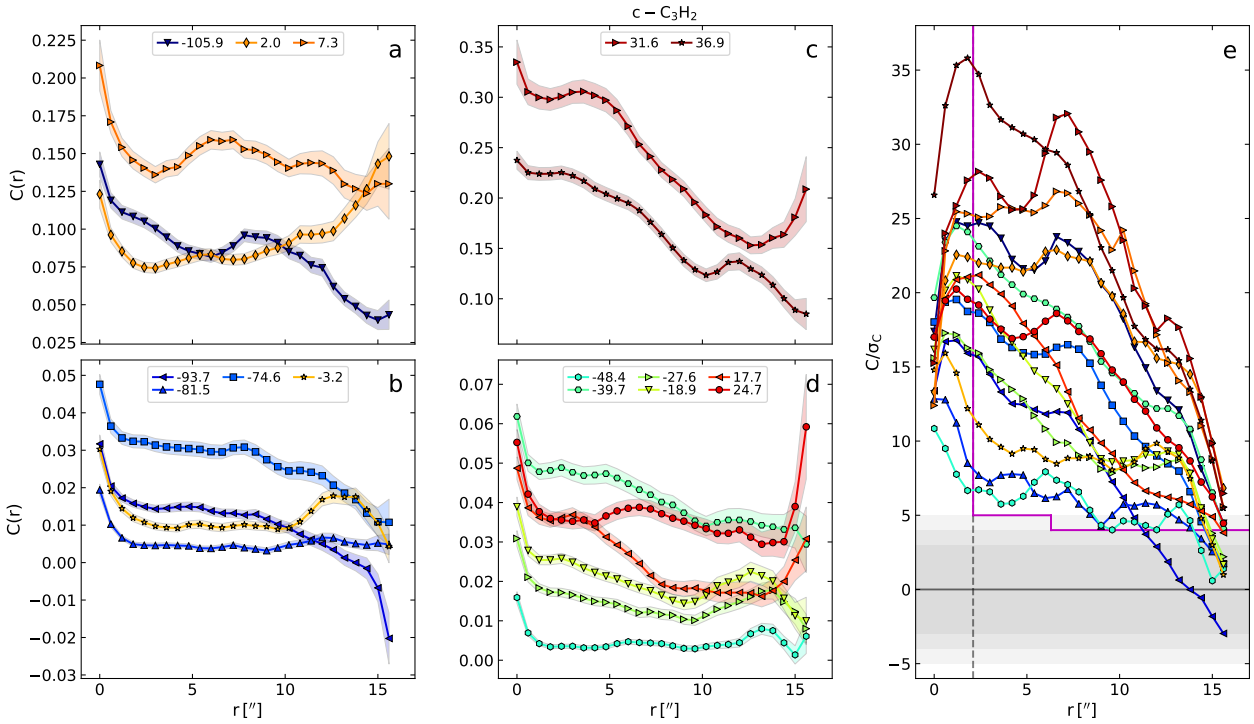

Figure 5.8: **a–d** Two-point auto-correlation functions $C(r)$ as a function of pixel separation r for the velocity components traced with c-C_3H_2. The points give the mean values of the 1000 realisations and the colour-shaded regions represent the standard deviations (1σ). The centroid LSR velocities of the clouds are indicated in km s^{-1} at the top of each panel. **e** Signal-to-noise ratio (SNR) of the two-point auto-correlation functions shown in panels a–d. The SNR levels of ±3, ±4 and ±5 are highlighted in shades of grey. The colours and symbols are the same as in panels a–d. The vertical dashed line shows the size of the beam (HPBW). The area below and left of the magenta line represents the area where the two-point auto-correlation functions are not significant.

above and right of the magenta demarcation in panels (e).

The two-point auto-correlation functions show various shapes: flat, decreasing towards larger pixel separations, or stronger correlation at small and large separations with a dip in between. Flat curves indicate structures that are more extended than the region sampled with our data. Decreasing curves characterise clouds with structures that are somewhat more compact than the extent of the sampled region. The third type of shapes could result from the presence of several compact structures.

The maximum angular separation, $\Delta r_{\rm max}$, at which $C(r)$ drops below the significance threshold (magenta line in panels e) is given for each velocity component and each molecule in Table 5.5. When the SNR is too low, the opacity map is dominated by noise and no statement can be made about the sizes of the detected structures. The components with a peak SNR τ/σ_τ smaller than five are therefore marked with a star in Table 5.5. Most components with a $\Delta r_{\rm max}$ smaller than the beam ($< 2''$) are in this situation. When $\Delta r_{\rm max}$ is equal to the largest available pixel separation, only a lower limit for the size of the structures can be determined. We convert these angular sizes to physical sizes in Table 5.6, using the approximate distances listed in Table 5.3.

The two-point auto-correlation functions of the molecules c-C_3H_2, $H^{13}CO^+$, ^{13}CO, HNC and its isotopologue $HN^{13}C$, $HC^{15}N$, CS and its isotopologues $C^{34}S$ and ^{13}CS, and CH_3OH are discussed in detail in

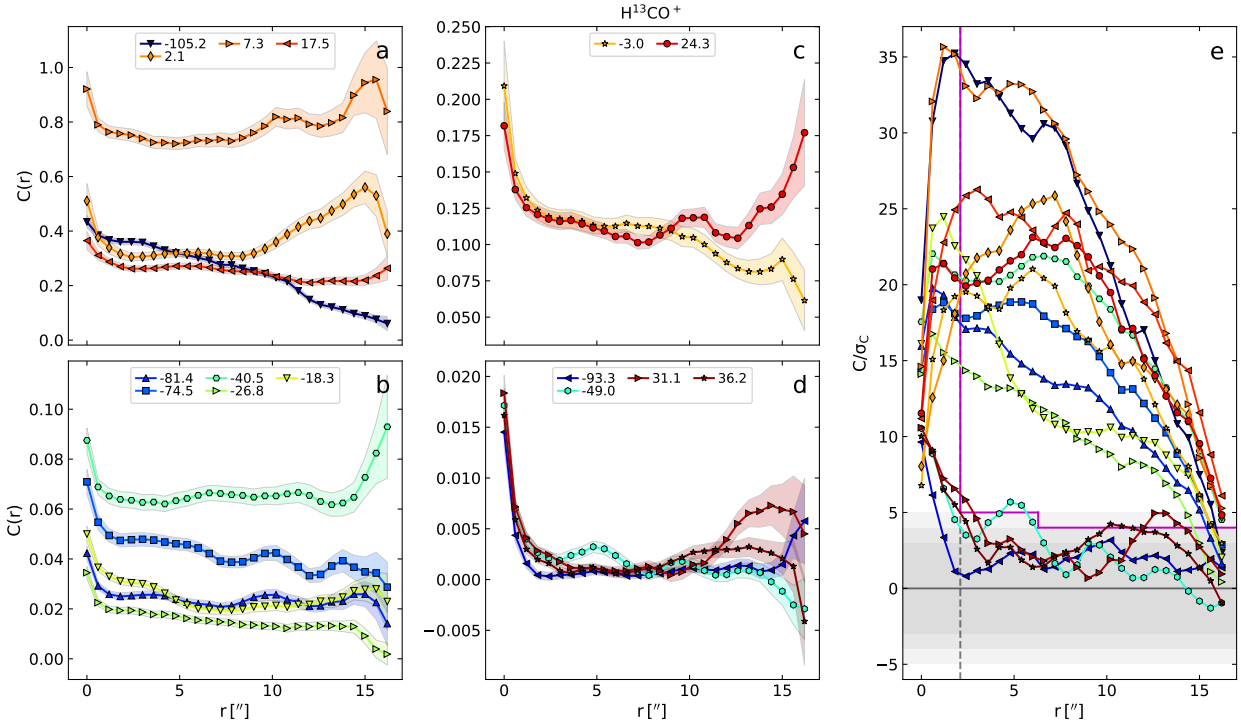

Figure 5.9: Same as Fig. 5.8, but for $H^{13}CO^+$.

Appendix C.8. The opacity maps suggest that most detected structures are extended on the scale of our field of view, ∼15″, or beyond. In a few cases, the two-point auto-correlation functions indicate the presence of smaller structures of sizes ∼4–6″. These structures are mostly seen for less abundant species for which most of the opacity map is dominated by noise. For example, the two GC clouds at 2.0 km s^{-1} and 7.3 km s^{-1} are detected with high sensitivity for all investigated molecules and display structures that are more extended than 15″ (∼0.5 pc). The only exception is $HN^{13}C$, but the shorter correlation length revealed by this tracer results from its lower abundance, hence a lower sensitivity, compared to the main isotopologue, HNC.

The other two molecules, SO and SiO, present a more complex picture (Figs. C.19 and C.21). Among the components with peak SNR higher than 5 in their opacity map (Figs. C.20 and C.22), the following ones reveal large-scale structures of the size of the field of view or larger: 2.4, 6.9, and -39.1 km s^{-1} in SO, and −3.2, 1.9, 7.0, 24.0, and 17.2 km s^{-1} in SiO. The structures traced with SO for three velocity components with a peak SNR of 6–8 in their opacity maps, at −3.5, 32.1, and 36.6 km s^{-1}, are more compact, with correlation lengths of ∼8″, 5″, and unresolved, respectively. A similar type of compact structures with correlation lengths of ∼8″, unresolved, and 5″ is revealed in SiO for the velocity components at −105.5, −27.1, and 37.7 km s^{-1} with peak SNR in their opacity maps of ∼11, 6, and 6, respectively.

The two-point auto-correlation functions of SO and SiO at 7.3 km s^{-1} decrease first and increase again at pixel separations larger than about 10″ (see Figs. C.35-C.36). In the opacity maps two smaller structures of sizes of 5″ appear at offsets of about (1.″5, 11.″0) and (12.″0, 10.″0), with an angular separation of about 10.″5 (see Figs. C.19 and C.21). Because they are at the edges of the available field of view, these structures may be more extended.

The two-point auto-correlation functions plotted depending on the physical distance are shown for the eight strongest molecules (c-C_3H_2, $H^{13}CO^+$, ^{13}CO, CS, SO, SiO, HNC, and CH_3OH) in Fig. C.41–C.48. For the seven molecules c-C_3H_2, ^{13}CO, CS, SO, SiO, HNC, and CH_3OH the auto-correlation functions

Table 5.5: Angular sizes of cloud structures derived from two-point auto-correlation functions.

velocity[a] [km s^{-1}]	c-C_3H_2	$H^{13}CO^+$	^{13}CO	CS	$C^{34}S$	^{13}CS	SO	SiO	HNC	$HN^{13}C$	$HC^{15}N$	CH_3OH
Galactic Center												
−105.9	> 16.2	16.2	> 15.6	> 16.2	13.2	4.8	n^*	8.4	> 15.6	13.8	n^*	12.6
−93.7	11.4	n^*	15.0*	15.6	n^*	n^*	n^*	n^*	14.4	n^*	n^*	n^*
−81.5	14.4	15.6	15.0	> 16.2	13.8	n^*	n^*	3.6*	> 15.6	n^*	> 16.8	n^*
−74.6	15.0	16.2	> 15.6	> 16.2	9.0*	2.4*	n^*	2.4	> 15.6	n^*	15.0	n^*
−3.2	15.0	16.2	6.0	> 16.2	n^*	n^*	7.8	15.6	> 15.6	n	10.8	15.0
2.0	> 16.2	> 16.8	12.6	15.0	15.0	16.2	> 16.2	> 16.2	> 15.6	6.6	15.6	15.6
7.3	> 16.2	> 16.8	15.0	> 16.2	15.0	16.2	> 16.2	> 16.2	> 15.6	16.2	15.0	15.6
3 kpc arm												
−48.4	14.4*	n^*	> 15.6	4.8	n^*	n^*	n^*	n^*	> 15.6	n^*	n^*	n^*
−39.7	> 16.2	> 16.8	> 15.6	> 16.2	15.0	n^*	> 16.2	n^*	> 15.6	n^*	15.6*	n^*
4 kpc arm												
−27.6	15.0	15.0	> 15.6	> 16.2	n^*	n^*	n^*	n	> 15.6	n^*	n^*	n^*
−18.9	15.0	16.2	> 15.6	> 16.2	4.8*	n^*	4.8	n^*	> 15.6	n^*	n^*	n^*
Scutum arm												
24.7	> 16.2	> 16.8	13.2	> 16.2	n^*	n^*	4.2	15.6	> 15.6	n^*	n^*	15.6
31.6	> 16.2	3.0	14.4	15.6	n^*	n^*	4.8	2.4	> 15.6	n^*	n^*	> 16.2
36.9	> 16.2	2.4	12.6	15.6	4.8*	n^*	n	5.4	> 15.6	n^*	n^*	15.0
Sagittarius arm												
17.7	15.6	> 16.8	14.4	> 16.2	9.0	n^*	12.0	> 16.2	> 15.6	7.8	10.8*	13.8

Notes. The sizes are given in arcseconds. Channels with unresolved structures are marked with n and channels with a SNR τ/σ_τ smaller than 5 are marked with a star.
[a] Cloud centroid velocities derived from c-C_3H_2.

decrease strongly for the cloud at a velocity of about 18 km s^{-1}. The physical sizes derived for this cloud which is located in the Sagittarius arm are between 0.04 and 0.08 pc. The auto-correlation functions for this cloud have sometimes the same shape as the first part of the two-point auto-correlation functions seen for other clouds, for example for CS for the velocities of -2.7 and 18.4 km s^{-1} (see Fig. C.44). Hence, we may only see a smaller part of the cloud located closer to us, but with the same properties as of those clouds more distant from us. On the other hand, structures with sizes smaller than 0.04–0.08 pc (structure size in the Sagittarius arm) cannot be resolved in the more distant GC clouds. A better resolution is needed to investigate if there are smaller structures present.

5.4.5 Turbulence in diffuse and translucent clouds

In order to investigate the turbulence properties of the clouds detected in absorption towards Sgr B2, we analyse the PDFs of their opacity maps. To reduce the influence of the noise on the Gaussian fitted to the PDFs (see Section C.3.2), we use a threshold of $3\sigma_{\rm noise}$ to analyse the profile of the PDFs. The PDFs $P(\eta)$ of all 15 velocity components probed with c-C_3H_2 are shown in Fig. 5.10. The PDFs of the other molecules are plotted in Figs. C.49–C.59 in the Appendix. The number of Gaussians fitted to each PDF is indicated in Table C.1. The results of the Gaussian fits to the PDFs are displayed in Figs. C.60 and C.61, and the mean and median widths for each velocity component and for each molecule are listed in Tables C.2 and C.3, respectively. The velocity components that are optically thick and the ones dominated by the noise are marked in Table C.1. The number of fitted Gaussians seems to depend neither on the molecule nor on the velocity component. However, the molecules for which the PDFs are most often well fitted with a single

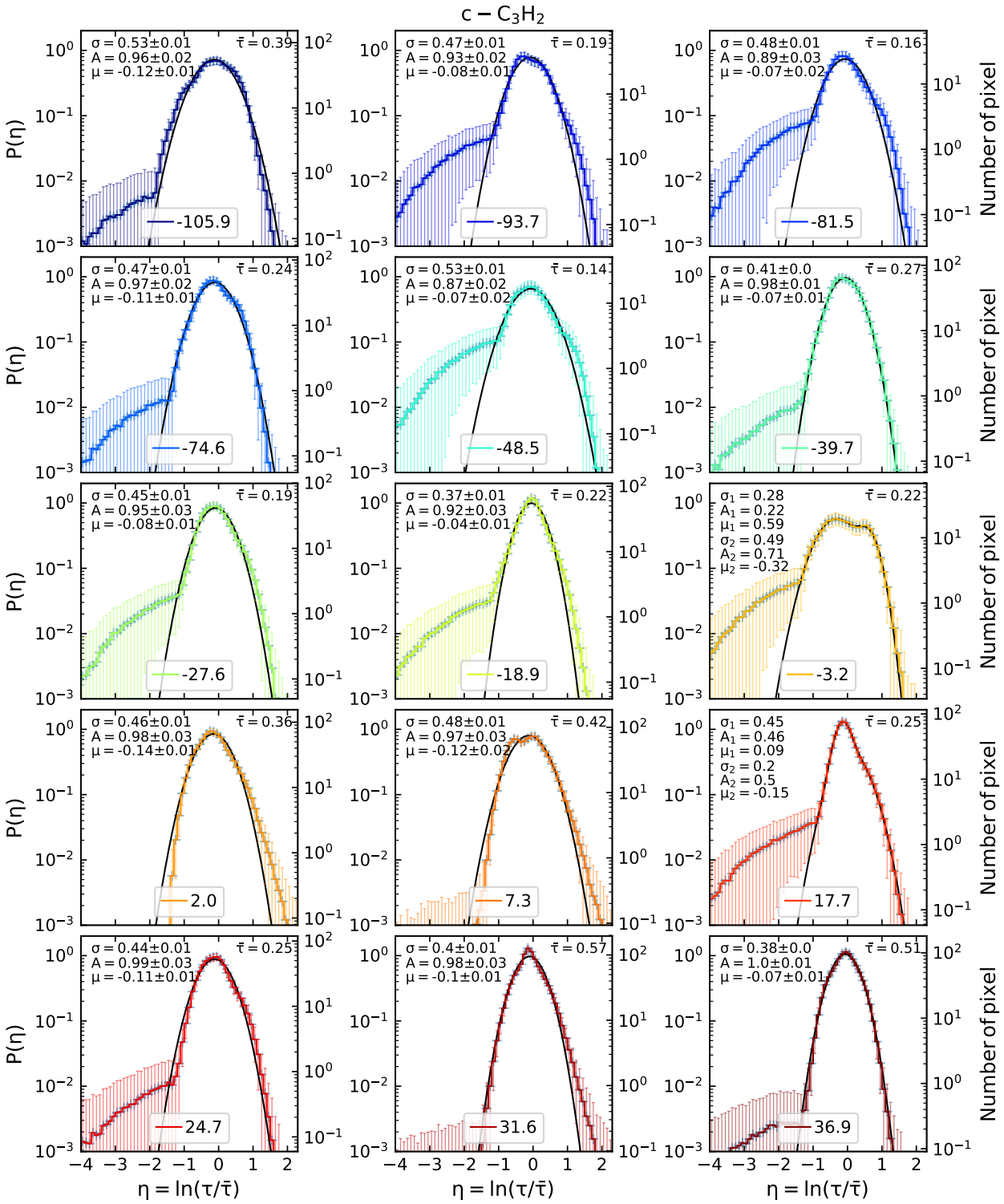

Figure 5.10: Probability distribution functions $P(\eta)$ of the velocity components probed with c-C_3H_2. The velocity of the component is indicated at the bottom of each panel in km s^{-1}. The right y-axis indicates the number of pixels counted in each bin. The mean opacity $\bar{\tau}$ is given in the upper right corner and the parameters of the fitted Gaussian(s) in the upper left corner: dispersion σ, integral A, and centre μ.

Table 5.6: Physical sizes of cloud structures derived from two-point auto-correlation functions.

velocity[a] [km s^{-1}]	c-C_3H_2	$H^{13}CO^+$	^{13}CO	CS	$C^{34}S$	^{13}CS	SO	SiO	HNC	$HN^{13}C$	$HC^{15}N$	CH_3OH
						Galactic Center						
−105.9	> 0.55	0.55	> 0.53	> 0.55	0.45	0.16	n^*	0.29	> 0.53	0.47	n^*	0.43
−93.7	0.39	n^*	0.51*	0.53	n^*	n^*	n^*	n^*	0.49	n^*	n^*	n^*
−81.5	0.49	0.53	0.51	> 0.55	0.47	n^*	n^*	0.12*	> 0.53	n^*	> 0.57	n^*
−74.6	0.51	0.55	> 0.53	> 0.55	0.31*	0.08*	n^*	0.08	> 0.53	n^*	0.51	n^*
−3.2	0.51	0.55	0.2	> 0.55	n^*	n^*	0.26	0.53	> 0.53	n	0.37	0.51
2.0	> 0.55	> 0.57	0.43	0.51	0.51	0.55	> 0.55	> 0.55	> 0.53	0.22	0.53	0.53
7.3	> 0.55	> 0.57	0.51	> 0.55	0.51	0.55	> 0.55	> 0.55	> 0.53	0.55	0.51	0.53
						3 kpc arm						
−48.4	0.38*	n^*	> 0.42	0.13	n^*	n^*	n^*	n^*	> 0.42	n^*	n^*	n^*
−39.7	> 0.43	> 0.45	> 0.42	> 0.43	0.4	n^*	> 0.43	n^*	> 0.42	n^*	0.42*	n^*
						4 kpc arm						
−27.6	0.31	0.31	> 0.33	> 0.34	n^*	n^*	n^*	n	> 0.33	n^*	n^*	n^*
−18.9	0.31	0.34	> 0.33	> 0.34	0.1*	n^*	0.1	n^*	> 0.33	n^*	n^*	n^*
						Scutum arm						
24.7	> 0.22	> 0.23	0.18	> 0.22	n^*	n^*	0.06	0.21	> 0.21	n^*	n^*	0.21
31.6	> 0.22	0.04	0.2	0.21	n^*	n^*	0.07	0.03	> 0.21	n^*	n^*	> 0.22
36.9	> 0.22	0.03	0.17	0.21	0.07	n^*	n^*	0.07	> 0.21	n^*	n^*	0.2
						Sagittarius arm						
17.7	0.08	> 0.08	0.07	> 0.08	0.04	n^*	0.06	> 0.08	> 0.08	0.04	0.05*	0.07

Notes. The sizes are given in pc. Channels with unresolved structures are marked with *n* and channels with a SNR of smaller than 5 in the opacity maps are marked with a star. [(a)] Cloud centroid velocities derived from c-C_3H_2.

Gaussian are HNC and c-C_3H_2, with only one and two velocity component(s) fitted with two Gaussians, respectively.

Tremblin et al. (2014) investigated the structure of the dense gas in several molecular clouds and explained the presence of two log-normal profiles or an enlarged shape of the PDF of a cloud as two different zones existing in the cloud. In the case they studied the turbulent molecular gas creates the low density part in the PDF and the second peak describes a compression zone created by the expansion of ionised gas into the molecular cloud. Another possibility is that the PDFs containing two log-normal profiles result from two different clouds overlapping along the line of sight at different distances from the observer but with the same velocity. We used opacity maps of only one channel and no integrated maps for the calculation of the PDFs to reduce the possibility of two clouds contributing to the same opacity map but such an overlap may still occur. Furthermore, our limited field of view that is set by the strength of the background continuum emission may have an effect on the shape of the PDFs. Because no velocity component shows a PDF with a two-Gaussian shape for all molecules, we believe that this particular shape does probably not characterise the true physical structure of the component. Therefore, to avoid being biased by the decomposition of the PDFs into two Gaussians, in the following we measure the width of each PDF by directly calculating its standard deviation, excluding the noise tail towards lower values of η. This cut may result in a slightly underestimated width of the PDF.

The distribution of PDF widths derived from the direct calculation is plotted in black in Fig. 5.11. The median and mean values are similar, with values of 0.52 and 0.53 for the total distribution, respectively. The distributions corresponding to Categories I and II defined in Sect. 5.4.2 are plotted in blue and magenta. Category I has a mean width of 0.48, somewhat smaller than Category II (0.56).

To investigate whether the shift between the two groups results from the different samples of molecules

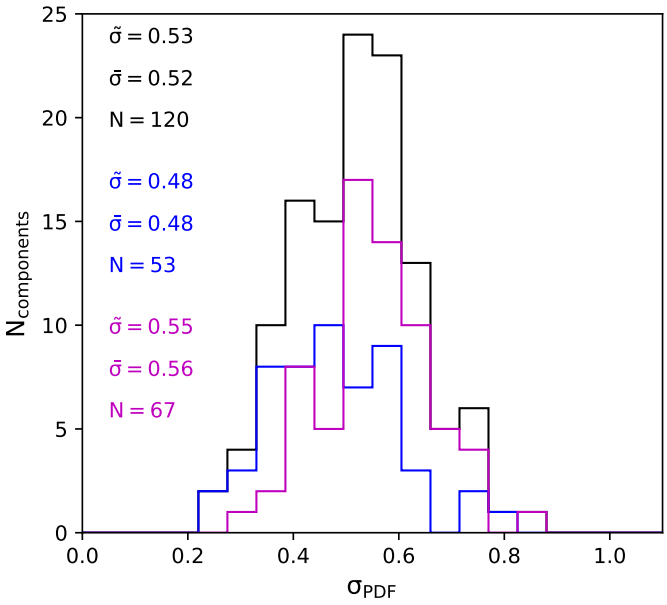

Figure 5.11: Distribution of standard deviations (width) of the PDFs of all molecules for all 15 velocity components. N gives the total number of PDFs used for each histogram, $\bar{\sigma}$ the mean value, and $\tilde{\sigma}$ the median value. The distribution of Categories I and II are shown in blue and magenta, respectively.

used for the different velocity components, we determine the distribution of PDF widths for the following five molecules only: c-C_3H_2, $H^{13}CO^+$, ^{13}CO, CS, and HNC (see Fig. 5.12). These molecules are well detected over the field of view for almost all velocity components. The other molecules are not detected for some of the components. With this reduced sample of molecules, the two categories of velocity components still have mean PDF widths that differ, with values of 0.43 (Category I) and 0.50 (Category II). The widths are smaller than for the sample including all molecules. This is most likely due to the noise affecting the molecules that show weak absorption because the noise tends to broaden the PDF (Ossenkopf-Okada et al. 2016).

The widths of the PDFs of all molecules are plotted in Fig. 5.13 for all velocity components, sorted by their rough distance to the GC, and are listed in Table 5.7. To investigate whether there are systematic differences between the velocity components, we plot the mean and median values of each velocity component in panel b. We also show the mean and median values of each spiral arm and the GC in panel c. These values are also listed in Table 5.7. The median and mean values match each other within the uncertainties.

As seen in Fig. 5.11 there is a difference between Categories I and II. Category I contains the clouds in the 3 kpc and 4 kpc arms and the GC in the velocity range between −106 and −75 km s^{-1}. They have narrower PDF widths than the clouds in Category II. The GC clouds belonging to Category I have widths between 0.47 and 0.52, the GC clouds of Category II have widths between 0.54 and 0.61. Especially the clouds in the 4 kpc arm have a narrower mean width, 0.41±0.08, which is somewhat smaller than the overall mean value (0.52).

We also investigate whether the width of the PDFs depends on the molecule. Figure 5.14a shows the distribution of PDF widths as a function of molecule. The mean and median values are plotted in panel b and listed in Table 5.8. The molecules c-C_3H_2, $H^{13}CO^+$, and HNC have the narrowest widths. The less abundant isotopologues $C^{34}S$, ^{13}CS, $HN^{13}C$, and $HC^{15}N$ and the less abundant molecules SO, SiO, and

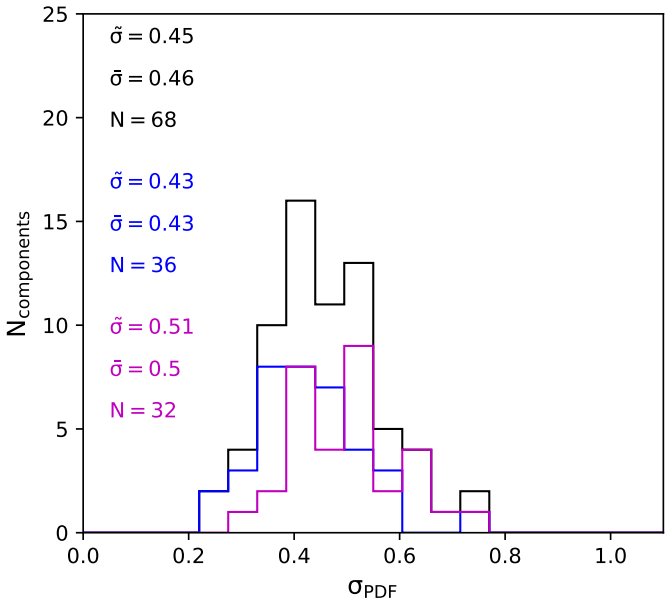

Figure 5.12: Same as Fig. 5.11 but for the sub-sample containing only c-C_3H_2, $H^{13}CO^+$, ^{13}CO, CS, and HNC.

CH_3OH have systematically broader PDF widths than the previous, more abundant molecules. This explains the difference seen between Figs. 5.11 and 5.12.

We use the widths of the PDFs to investigate the turbulent properties of the clouds probed in absorption by calculating the forcing parameter b (e.g., Federrath et al. 2010). For this calculation, we need the Mach number M which is defined as:

$$M = (\sqrt{3} FWHM)/(c_s \sqrt{8\ \ln(2)}) \tag{5.11}$$

with $FWHM$ the linewidth of the molecule[5] and c_s the sound speed

$$c_s = \sqrt{\frac{k_B T_{kin}}{\bar{\mu} m_H}} \tag{5.12}$$

with T_{kin} the kinetic temperature, k_B the Boltzmann constant, m_H the mass of the hydrogen atom, and $\bar{\mu}$ the mean molecular weight (2.37, see, e.g., Kauffmann et al. 2008). Snow & McCall (2006) quote kinetic temperatures between 30 and 100 K for diffuse molecular clouds and between 15 and 50 K for translucent molecular clouds. Here, we assume temperatures of 20, 40, and 80 K. We determine the median $FWHM$ for each velocity component and calculate the Mach number for the assumed temperatures (Table 5.9). We obtain Mach number values between 5.8 and 28.3 for T_{kin} = 20 K and between 2.9 and 14.2 for 80 K.

The forcing parameter b relates the velocity and density fields in a cloud (Padoan et al. 1997; Federrath et al. 2008):

$$\sigma_s^2 = f^2 \sigma_\eta^2 = \ln(1 + b^2 M^2) \tag{5.13}$$

with σ_s the standard deviation of the volume density fluctuations and σ_η the dispersion of the two-dimensional column density or opacity fluctuations. The relation is derived from numerical simulations

[5]We neglect the thermal contribution to the linewidth of the molecules, which is justified given the large measured linewidths, even for a kinetic temperature of 100 K.

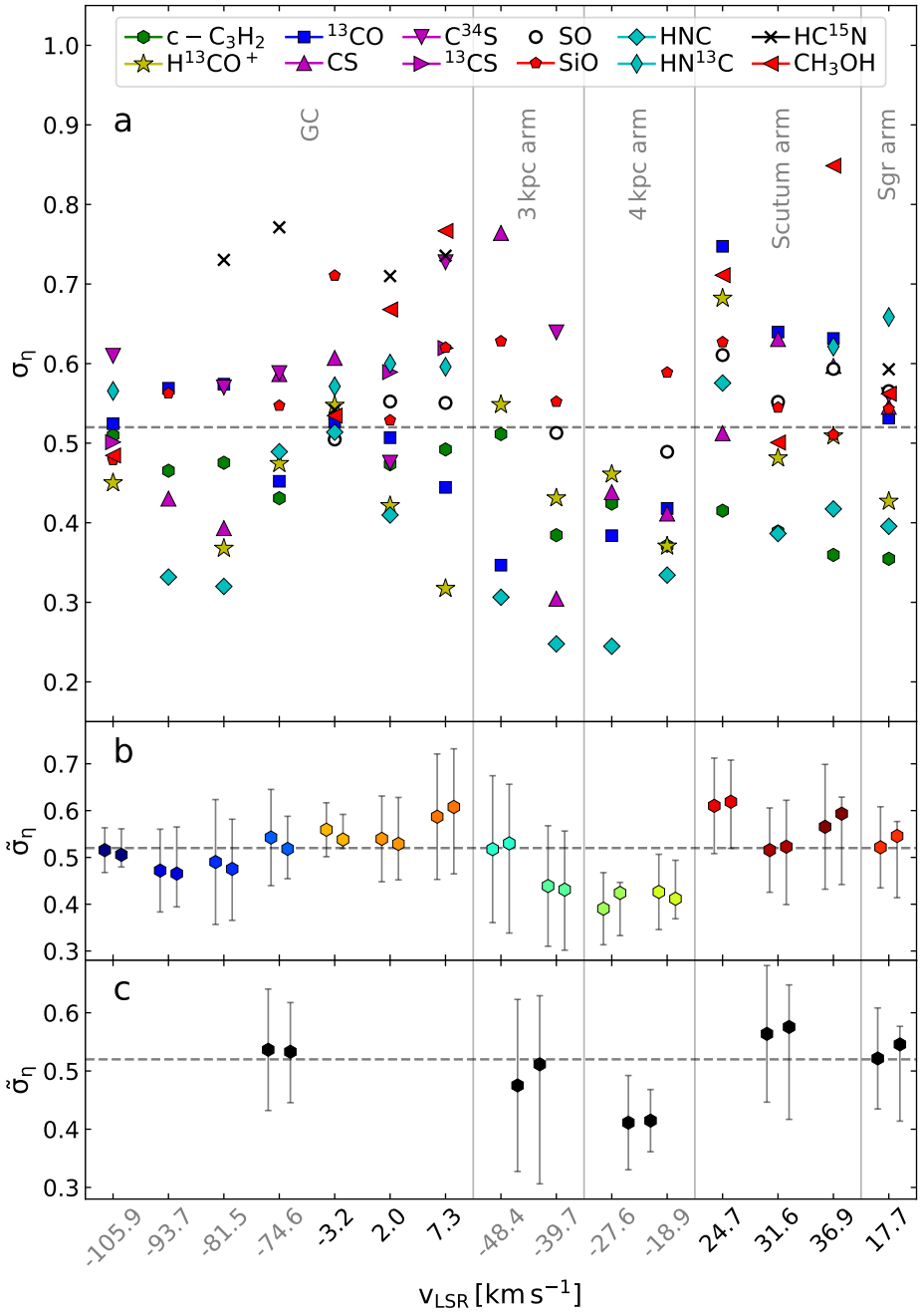

Figure 5.13: **a** Widths of the PDFs of all molecules for the 15 velocity components, roughly sorted by their distance to the Galactic Center. **b** Mean (left) and median (right) values for each velocity component. **c** Mean (left) and median (right) values for each subsample of clouds, from left to right: Galactic Center, 3 kpc arm, 4 kpc arm, Scutum arm, Sagittarius arm. The uncertainties represent the standard deviation for the mean and the corresponding percentiles for the median. The dashed line in each panel marks the mean value of all data points shown in panel a. Velocity components belonging to Category I and II are coloured in grey and black, respectively.

Table 5.7: Mean ($\bar{\sigma}$) and median ($\tilde{\sigma}$) widths directly computed from the PDFs for each velocity component.

$v_{\rm LSR}{}^a$ [km s^{-1}]	$\bar{\sigma}$	$\tilde{\sigma}$	$\bar{\sigma}^b$	$\tilde{\sigma}^b$
		Galactic Center		
−105.9	0.52 ± 0.05	$0.48^{+0.06}_{-0.03}$		
−93.7	0.47 ± 0.09	$0.47^{+0.10}_{-0.07}$		
−81.5	0.49 ± 0.13	$0.48^{+0.11}_{-0.11}$		
−74.6	0.54 ± 0.10	$0.52^{+0.07}_{-0.06}$	0.54 ± 0.10	$0.53^{+0.08}_{-0.09}$
−3.2	0.56 ± 0.06	$0.54^{+0.05}_{-0.02}$		
2.0	0.54 ± 0.09	$0.53^{+0.10}_{-0.08}$		
7.3	0.59 ± 0.13	$0.61^{+0.12}_{-0.14}$		
		3 kpc arm		
−48.4	0.52 ± 0.16	$0.53^{+0.13}_{-0.19}$	0.48 ± 0.15	$0.51^{+0.12}_{-0.21}$
−39.7	0.44 ± 0.13	$0.43^{+0.13}_{-0.13}$		
		4 kpc arm		
−27.6	0.39 ± 0.08	$0.42^{+0.02}_{-0.09}$	0.41 ± 0.08	$0.41^{+0.05}_{-0.05}$
−18.9	0.43 ± 0.08	$0.41^{+0.08}_{-0.04}$		
		Scutum arm		
24.7	0.61 ± 0.10	$0.62^{+0.09}_{-0.10}$		
31.6	0.52 ± 0.09	$0.52^{+0.10}_{-0.12}$	0.56 ± 0.12	$0.58^{+0.07}_{-0.16}$
36.9	0.57 ± 0.13	$0.59^{+0.04}_{-0.15}$		
		Sagittarius arm		
17.7	0.52 ± 0.09	$0.55^{+0.03}_{-0.13}$	0.52 ± 0.09	$0.55^{+0.03}_{-0.13}$

Notes. [a] Channel velocities of c-C_3H_2. [b] Mean and median values for each subsample of clouds for all molecules.

of magnetohydrodynamics (MHD) and hydrodynamics (Padoan et al. 1997; Passot & Vázquez-Semadeni 1998). In Federrath et al. (2010), the value of f is investigated in the extreme cases of purely solenoidal forcing (divergence free) and purely compressive forcing (curl-free): they obtain 2.9 for solenoidal forcing ($f = \sigma_s/\sigma_\eta = 1.32/0.46$) and 2.0 for compressive forcing (3.04/1.51). They also define a parameter ζ that sets the power of compressive forcing with respect to the total power of the turbulence forcing. ζ takes values between 0 (purely compressive) and 1 (purely solenoidal). They show that b is a function of ζ (see their Fig. 8).

To calculate b from Eq. 5.13, we need to know f. Given that f does not vary much between the two extreme forcing cases investigated by Federrath et al. (2010), we assume that it is a simple linear function of ζ and parametrise it as $f = 2.9 \times \zeta + (1 - \zeta) \times 2.0$ (linear interpolation between the values of f obtained for the extreme cases ζ=1 and ζ=0). Equation 5.13 then gives us b as a function of ζ. The intersection of this function with the relation found by Federrath et al. (2010) gives the solution (b,ζ), when it exists. As an example, these functions are plotted for the different velocity components for a kinetic temperature of 40 K in Fig. 5.15. In many cases the two curves do not intersect for ζ between 0 and 1, but they come the closest to each other for $\zeta = 1$. In these cases, we assume a value of 2.9 for f to derive b. In the other cases, the intersection gives us b and ζ.

We consider only the eight molecules with highest SNR to derive b for each velocity component: c-C_3H_2, $H^{13}CO^+$, ^{13}CO, CS, SO, SiO, HNC, and CH_3OH. The median values are listed in Table 5.9. We also compute for each molecule the median value of b over all velocity components (see Table 5.8).

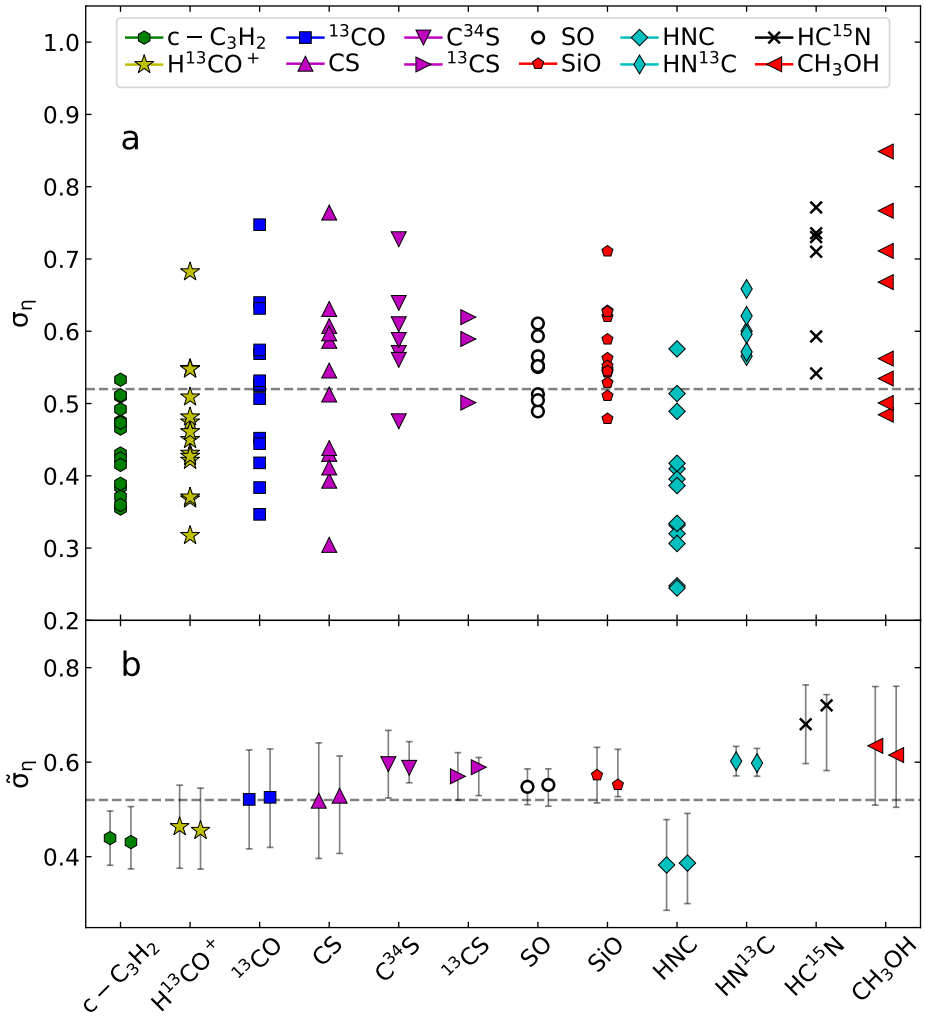

Figure 5.14: **a** Widths of the PDFs of 15 different velocity components along the line of sight sorted by molecule. **b** Mean (left) and median (right) values for each molecule. The uncertainties represent the standard deviation for the mean and the corresponding percentiles for the median. The dashed line in both panels marks the mean and the median value for all components (see Fig. 5.11).

The distribution of forcing parameter b is shown as a function of velocity component in Fig. 5.16 as an example for $T_{\rm kin}$ = 40 K. The median value of the forcing parameter b is 0.26, indicated by the dashed line. b is higher for the velocity components that have low SNR for most molecules, which may be a bias due to the lack of sensitivity ($v_{\rm LSR}$ = −81.5 km s $^{-1}$, −48.4 km s $^{-1}$, and 24.7 km s $^{-1}$). The values for the 4 kpc arm are significantly lower than the averaged value. The uncertainties for these values are relatively low. For a kinetic temperature of 40 K most values of b fall in the range 0.11 to 0.37. The forcing parameters b are smaller if we assume $T_{\rm kin}$ = 20 K (0.08–0.33) and larger for 80 K (0.16–0.47).

The distribution of forcing parameter b as a function of molecule is displayed in Fig. 5.17. Most molecules show similar values of b. Exceptions are $C^{34}S$ and $HC^{15}N$, which lie above the other ones, probably due to their low SNR, and HNC, which lies below the average.

Table 5.8: PDF widths and parameters describing the turbulence for all investigated molecules.

molecule	$\bar{\sigma}^a$	$\tilde{\sigma}^b$	ζ^c			b^d		
			20 K	40 K	80 K	20 K	40 K	80 K
c-C_3H_2	0.44 ± 0.06	$0.43^{+0.08}_{-0.06}$	x	x	x	$0.14^{+0.09}_{-0.07}$	$0.20^{+0.12}_{-0.10}$	$0.28^{+0.07}_{-0.14}$
$H^{13}CO^+$	0.46 ± 0.09	$0.46^{+0.09}_{-0.08}$	x	x	x	$0.13^{+0.12}_{-0.06}$	$0.18^{+0.14}_{-0.08}$	$0.26^{+0.12}_{-0.11}$
^{13}CO	0.52 ± 0.10	$0.53^{+0.10}_{-0.11}$	x	x	0.93	$0.17^{+0.12}_{-0.07}$	$0.25^{+0.08}_{-0.09}$	$0.33^{+0.05}_{-0.11}$
CS	0.52 ± 0.12	$0.53^{+0.08}_{-0.12}$	x	x	0.78	$0.20^{+0.07}_{-0.10}$	$0.28^{+0.05}_{-0.15}$	$0.33^{+0.04}_{-0.14}$
$C^{34}S$	0.60 ± 0.07	$0.59^{+0.6}_{-0.03}$	0.79	0.52	0.38	$0.33^{+0.01}_{-0.13}$	$0.36^{+0.04}_{-0.08}$	$0.45^{+0.06}_{-0.13}$
^{13}CS	0.57 ± 0.05	$0.59^{+0.02}_{-0.06}$	x	0.99	0.58	$0.23^{+0.04}_{-0.05}$	$0.33^{+0.01}_{-0.07}$	$0.34^{+0.01}_{-0.01}$
SO	0.55 ± 0.04	$0.55^{+0.03}_{-0.05}$	x	x	0.74	$0.21^{+0.04}_{-0.08}$	$0.29^{+0.03}_{-0.11}$	$0.33^{+0.02}_{-0.08}$
SiO	0.57 ± 0.06	$0.55^{+0.08}_{-0.03}$	x	x	0.66	$0.21^{+0.12}_{-0.07}$	$0.30^{+0.07}_{-0.10}$	$0.33^{+0.12}_{-0.06}$
HNC	0.38 ± 0.10	$0.39^{+0.11}_{-0.09}$	x	x	x	$0.09^{+0.07}_{-0.04}$	$0.13^{+0.11}_{-0.05}$	$0.19^{+0.14}_{-0.07}$
$HN^{13}C$	0.60 ± 0.03	$0.60^{+0.03}_{-0.03}$	x	0.92	0.60	$0.25^{+0.07}_{-0.04}$	$0.33^{+0.01}_{-0.04}$	$0.34^{+0.04}_{-0.01}$
$HC^{15}N$	0.68 ± 0.08	$0.72^{+0.02}_{-0.14}$	0.80	0.60	0.44	$0.33^{+0.07}_{-0.10}$	$0.36^{+0.12}_{-0.04}$	$0.43^{+0.17}_{-0.09}$
CH_3OH	0.63 ± 0.13	$0.62^{+0.15}_{-0.11}$	x	0.97	0.64	$0.23^{+0.14}_{-0.05}$	$0.32^{+0.16}_{-0.06}$	$0.33^{+0.27}_{-0.01}$

Notes. [a] Mean width of the PDF. [b] Median width of the PDF. [c] Forcing parameter ζ. x means that there is no intersection of the two functions $b(\zeta)$. In these cases, we assume $f = 2.9$ to derive b. [d] Forcing parameter b.

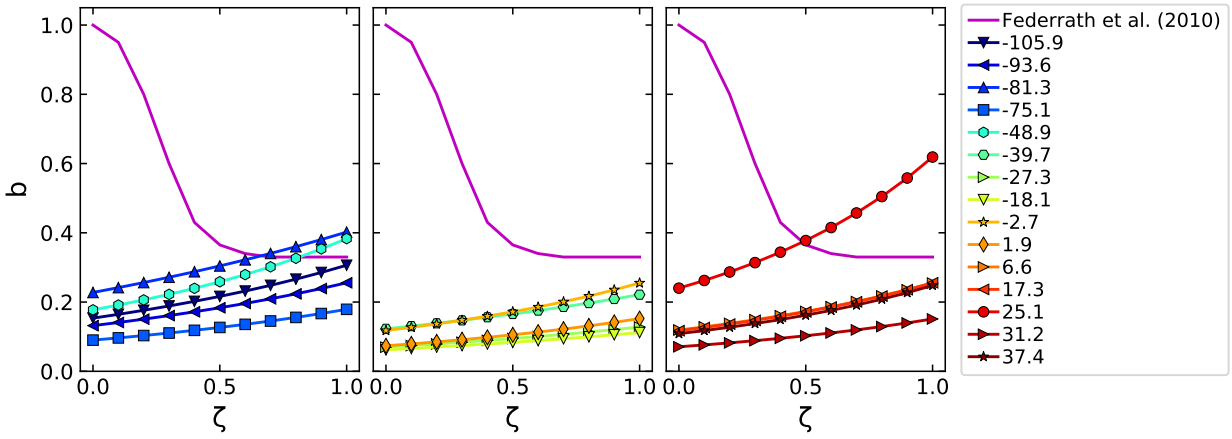

Figure 5.15: Forcing parameter b plotted against ζ for $T_{\rm kin} = 40$ K for all 15 velocity components. The different velocities are colour coded and given in km s $^{-1}$. The magenta line represents the function derived from hydrodynamic simulations by Federrath et al. (2010).

5.4.6 Principal component analysis

Six of the 15 velocity components fulfil the selection criteria defined in Sect. 5.3.8 to perform a principal component analysis. The velocities of these components are: $-105.9\,\mathrm{km\,s^{-1}}$, $2.0\,\mathrm{km\,s^{-1}}$, and $7.3\,\mathrm{km\,s^{-1}}$ in the GC, $24.7\,\mathrm{km\,s^{-1}}$ and $31.6\,\mathrm{km\,s^{-1}}$ in the Scutum arm, and $17.7\,\mathrm{km\,s^{-1}}$ in the Sagittarius arm. The molecules used for each component are listed in Table 5.10. The PCA is performed on the opacity maps after removing the average signal and scaling the standard deviation to 1. Hence, the PCA is sensitive only to the variance on scales smaller than the field of view.

To investigate the influence of the noise on the results of the PCA we performed a PCA on channels that contain only noise (see Appendix C.3.3). We used six molecules. The powers, that is the contributions of

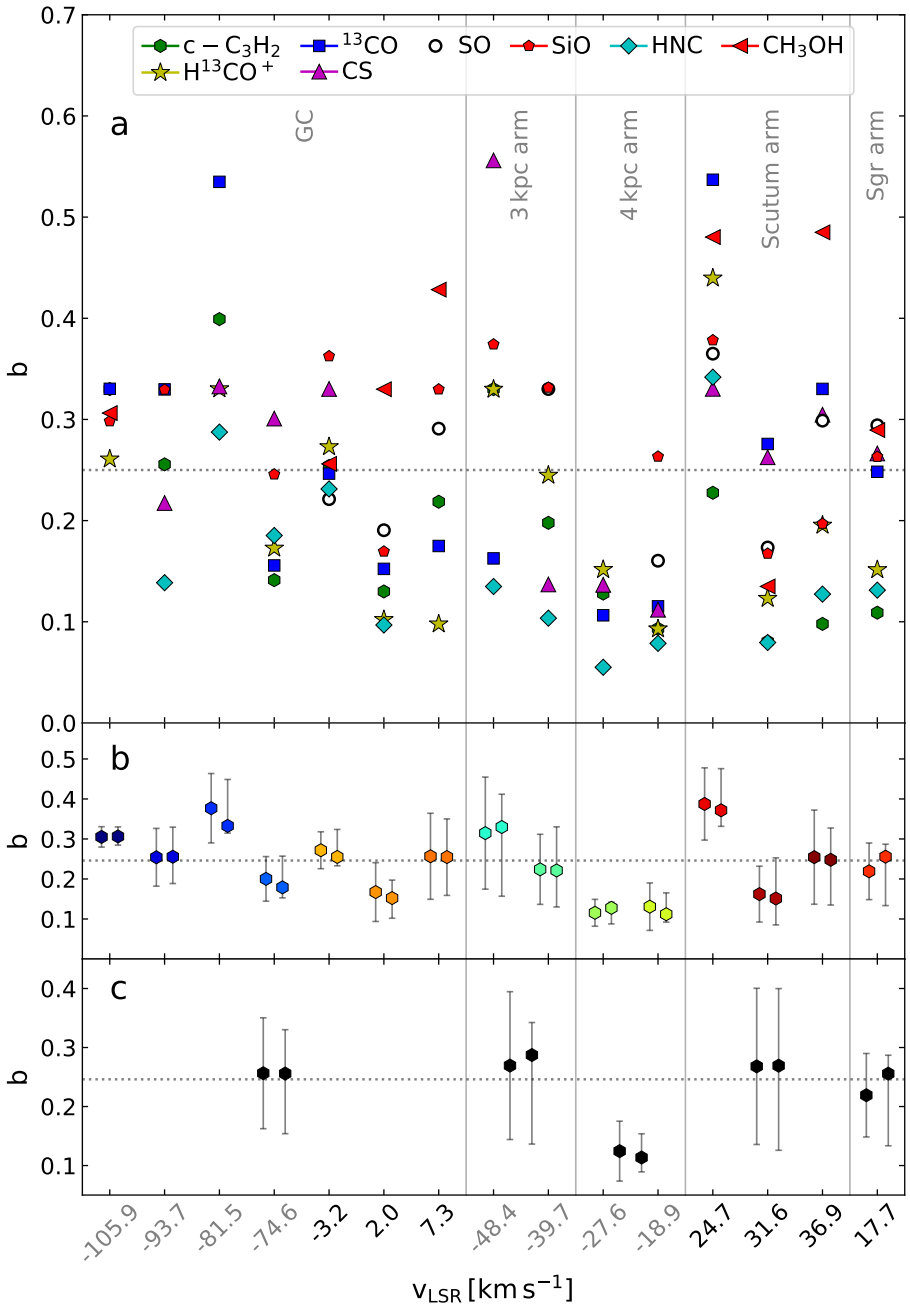

Figure 5.16: **a** Forcing parameter b of eight molecules, assuming $T_{\rm kin}$ = 40 K for the 15 velocity components roughly sorted by their distance to the Galactic Center. **b** Mean (left) and median (right) values for each velocity component. **c** Mean (left) and median (right) values for each subsample of clouds, from left to right: Galactic Center, 3 kpc arm, 4 kpc arm, Scutum arm, Sagittarius arm. The uncertainties represent the standard deviation for the mean and the corresponding percentiles for the median. The dashed line in each panel marks the median value of all data points shown in panel a. The velocities of the components belonging to Categories I and II are coloured in grey and black, respectively.

Table 5.9: PDF widths, linewidths, Mach numbers, and parameters describing the turbulence of the velocity components.

$v_{\rm LSR}$[a]	$\bar{\sigma}$[b]	$\tilde{\sigma}$[c]	$FWHM$[e]	M[f]			ζ[g]			b[h]		
[km s^{-1}]			[km s^{-1}]	20 K	40 K	80 K	20 K	40 K	80 K	20 K	40 K	80 K
Galactic Center												
−105.9	0.49 ± 0.03	$0.48^{+0.03}_{-0.02}$	4.2	11.7	8.1	5.8	x	x	0.63	$0.22^{+0.03}_{-0.02}$	$0.31^{+0.02}_{-0.02}$	$0.34^{+0.02}_{-0.01}$
−93.7	0.47 ± 0.09	$0.47^{+0.10}_{-0.07}$	4.6	12.8	8.9	6.4	x	x	0.85	$0.18^{+0.11}_{-0.05}$	$0.26^{+0.07}_{-0.07}$	$0.33^{+0.04}_{-0.06}$
−81.5	0.43 ± 0.09	$0.39^{+0.12}_{-0.04}$	2.1	5.8	4.1	2.9	x	0.66	0.43	$0.28^{+0.07}_{-0.05}$	$0.33^{+0.12}_{-0.02}$	$0.41^{+0.18}_{-0.05}$
−74.6	0.50 ± 0.05	$0.48^{+0.07}_{-0.03}$	7.1	19.7	13.7	9.9	x	x	x	$0.13^{+0.06}_{-0.02}$	$0.18^{+0.08}_{-0.03}$	$0.25^{+0.08}_{-0.04}$
−3.2	0.56 ± 0.06	$0.53^{+0.07}_{-0.02}$	6.4	17.8	12.4	8.9	x	x	0.89	$0.18^{+0.07}_{-0.02}$	$0.26^{+0.07}_{-0.02}$	$0.33^{+0.01}_{-0.01}$
2.0	0.51 ± 0.08	$0.51^{+0.05}_{-0.09}$	9.4	26.1	18.2	13.1	x	x	x	$0.11^{+0.03}_{-0.04}$	$0.15^{+0.04}_{-0.05}$	$0.22^{+0.06}_{-0.07}$
7.3	0.53 ± 0.14	$0.52^{+0.13}_{-0.10}$	6.1	16.9	11.8	8.5	x	x	0.89	$0.18^{+0.13}_{-0.07}$	$0.25^{+0.10}_{-0.10}$	$0.32^{+0.08}_{-0.09}$
all[d]	0.54 ± 0.10	$0.53^{+0.08}_{-0.09}$										
3 kpc arm												
−48.4	0.52 ± 0.16	$0.53^{+0.13}_{-0.19}$	4.2	11.7	8.1	5.8	x	0.82	0.50	$0.27^{+0.08}_{-0.16}$	$0.33^{+0.08}_{-0.17}$	$0.37^{+0.16}_{-0.14}$
−39.7	0.41 ± 0.11	$0.41^{+0.11}_{-0.11}$	4.1	11.4	7.9	5.7	x	x	x	$0.16^{+0.11}_{-0.06}$	$0.22^{+0.11}_{-0.09}$	$0.30^{+0.06}_{-0.12}$
all[d]	0.48 ± 0.15	$0.51^{+0.12}_{-0.21}$										
4 kpc arm												
−27.6	0.39 ± 0.08	$0.42^{+0.02}_{-0.09}$	7.6	21.1	14.7	10.6	x	x	x	$0.09^{+0.01}_{-0.03}$	$0.13^{+0.01}_{-0.04}$	$0.18^{+0.02}_{-0.06}$
−18.9	0.43 ± 0.08	$0.41^{+0.08}_{-0.04}$	8.2	22.8	15.9	11.4	x	x	x	$0.08^{+0.04}_{-0.01}$	$0.11^{+0.05}_{-0.02}$	$0.16^{+0.07}_{-0.03}$
all[d]	0.41 ± 0.08	$0.41^{+0.05}_{-0.05}$										
Scutum arm												
24.7	0.61 ± 0.10	$0.62^{+0.09}_{-0.10}$	4.1	11.4	7.9	5.7	0.72	0.48	0.38	$0.33^{+0.05}_{-0.07}$	$0.37^{+0.10}_{-0.04}$	$0.47^{+0.14}_{-0.11}$
31.6	0.52 ± 0.09	$0.52^{+0.10}_{-0.12}$	10.2	28.3	19.7	14.2	x	x	x	$0.11^{+0.07}_{-0.05}$	$0.15^{+0.10}_{-0.07}$	$0.21^{+0.11}_{-0.09}$
36.9	0.56 ± 0.14	$0.55^{+0.08}_{-0.12}$	7.4	20.5	14.3	10.3	x	x	0.94	$0.18^{+0.08}_{-0.08}$	$0.25^{+0.08}_{-0.11}$	$0.30^{+0.04}_{-0.11}$
all[d]	0.56 ± 0.12	$0.58^{+0.07}_{-0.16}$										
Sagittarius arm												
17.7	0.49 ± 0.08	$0.54^{+0.02}_{-0.14}$	6.5	18.0	12.6	9.0	x	x	0.89	$0.18^{+0.02}_{-0.09}$	$0.26^{+0.03}_{-0.12}$	$0.33^{+0.01}_{-0.14}$

Notes. The molecules used for this analysis are c-C_3H_2, $H^{13}CO^+$, ^{13}CO, CS, SO, SiO, HNC, and CH_3OH. [(a)] Channel velocities of c-C_3H_2. [(b)] Mean width of the PDF. [(b)] Median width of the PDF. [(d)] Mean and median values of the PDF width for each subsample of clouds. [(e)] Median $FWHM$ for each velocity component determined with c-C_3H_2. [(f)] Mach number for three assumed temperatures. [(g)] Forcing parameter ζ. x means that there is no intersection of the two functions $b(\zeta)$. In these cases, we assume $f = 2.9$ to derive b. [(h)] Forcing parameter b.

the principal components (PCs) to the total variance, are similar for the first three components and on the level of 20–30%. We conclude from this test that powers of the first PCs much higher than 20–30% are required to be considered as significant.

Because our field of view is limited by the extent of the background continuum emission, we performed several tests to examine the robustness of the PCA applied to our data (see Appendix C.4). For these tests we changed the grid size, the number of selected pixels, and the number of selected molecules. The PCA seems to be robust to these changes. However, when no clear structure is dominant for all molecules, decreasing the number of pixels results in more changes in the values of the PC coefficients.

The PCs calculated for $v_{\rm LSR} = 24.7\,{\rm km\,s^{-1}}$ are shown in Fig. 5.18. The fourth component has a very small power of 1×10^{-29}. Hence, it can be neglected and is not displayed. The contribution factors of each PC to the selected molecules are shown in Fig. 5.19. The error bars represent the standard deviation calculated from the 1000 realisations of the opacity cubes. They are relatively small and barely visible. For this velocity component, 73% of the total variance in the data is described by the first principal component. This means a prominent structure is present for most molecules. The second and third PCs describe only small parts of the total variance 18% and 9%, respectively. The first two correlation wheels are plotted in

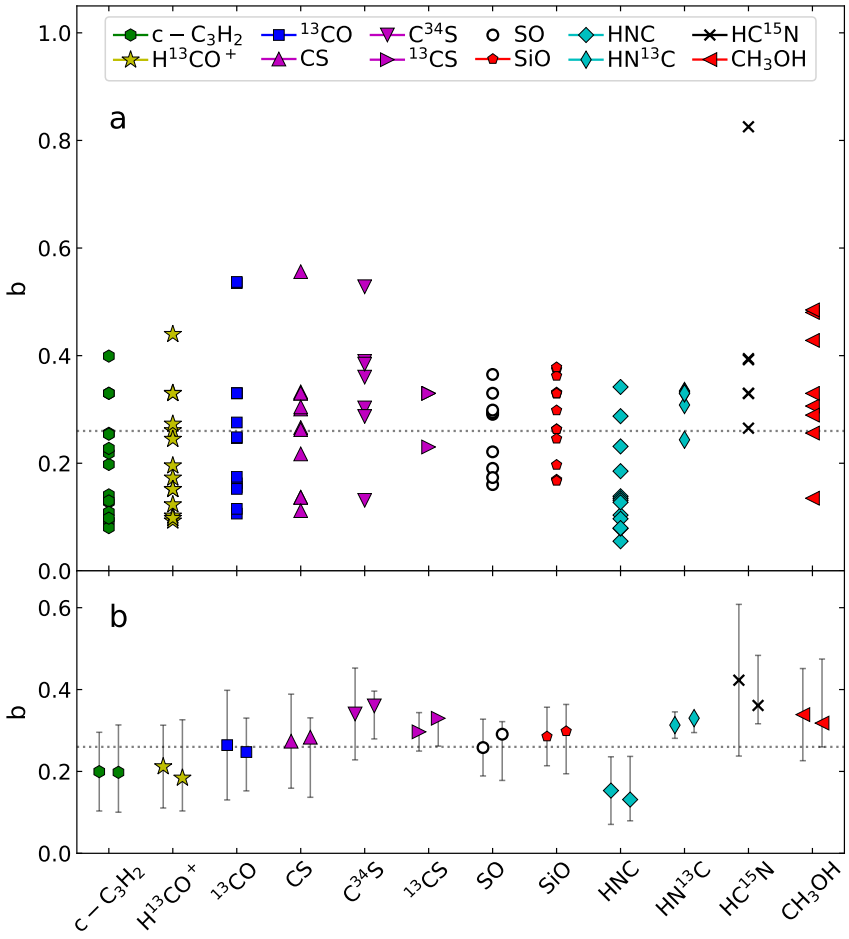

Figure 5.17: **a** Forcing parameter b of up to 15 velocity components sorted by molecule and assuming $T_{\mathrm{kin}} = 40$ K. **b** Mean (left) and median (right) values for each molecule. The uncertainties represent the standard deviation for the mean and the corresponding percentiles for the median. The dashed line in both panels marks the median value of the subsample of molecules used in Fig. 5.16.

Fig. 5.20a. $H^{13}CO^+$, HNC, and CS are anti-correlated to CH_3OH for PC1. $H^{13}CO^+$ and CS are correlated for PC1 and PC3, but anti-correlated for PC2.

The correlation wheels for the other velocity components are displayed in Figs. 5.20b–f, the corresponding PCs and coefficients in Figs. C.62–C.71. The power of the fourth PC is always very low, on the order of 10^{-29}. Hence, the fourth PC is not displayed in these figures. At $v_{\mathrm{LSR}} = 31.6\,\mathrm{km\,s^{-1}}$ (Fig. 5.20e), HNC is anti-correlated to CH_3OH, c-C_3H_2, and CS for PC1. The first component has only a contribution of 49% to the total variance. In PC2 (36%) c-C_3H_2 is strongly anti-correlated to CH_3OH. CS is mostly described by PC3. At $v_{\mathrm{LSR}} = -105.9\,\mathrm{km\,s^{-1}}$ (Fig. 5.20b), c-C_3H_2 and $H^{13}CO^+$ are anti-correlated with CH_3OH and SiO with respect to the first PC. $H^{13}CO^+$ is mostly described by the third PC and CH_3OH mostly by the second one. Here, the first PC has a high contribution of 65%.

The other velocity components have powers of their PCs on the order of 20–30%, similar to those obtained for pure noise channels. The correlation wheels of these components are therefore most likely not significant.

Table 5.10: Molecules used for the PCA for six velocity components.

	Velocity component (km s^{-1})					
molecule	−105.9	2.0	7.3	24.7	31.6	17.7
	[km s^{-1}]					
c-C_3H_2	x	x	x	-	x	x
$H^{13}CO^+$	x	x	x	x	-	x
CS	-	-	-	x	x	x
$C^{34}S$	-	x	-	-	-	-
SiO	x	x	x	-	-	x
HNC	-	-	-	x	x	x
$HN^{13}C$	-	x	x	-	-	-
CH_3OH	x	x	x	x	x	x

Notes. The molecules used for the PCA are marked with x.

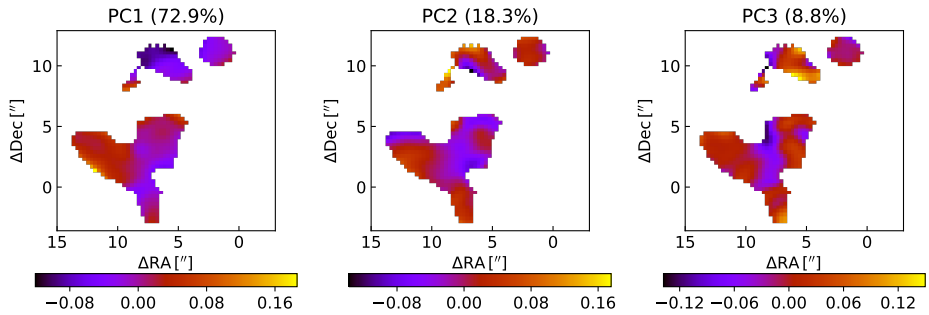

Figure 5.18: Principal components determined at v_{LSR} = 24.7 km s^{-1}. The colours give the intensity. The absolute value of each PC is normalised to 1 as explained in Sect. 5.3.8. The percentages in parentheses give the contributions of the PCs to the total variance.

5.4.7 Nature of the detected line-of-sight clouds

In order to understand the nature of the line-of-sight clouds detected towards Sgr B2(N), that is whether they are diffuse or translucent, we want to estimate their H_2 column densities and visual extinctions, A_v. HCO^+ has been shown to be a good tracer of H_2 in diffuse clouds, with $N(HCO^+)/N(H_2) = 3 \times 10^{-9}$ (Liszt et al. 2010). Here we use the EMoCA spectrum towards K4 to derive the HCO^+ column densities of the clouds detected in absorption. For the velocity components for which HCO^+ 1–0 is optically thick, we model $H^{13}CO^+$ 1–0 and assume the same $^{12}C/^{13}C$ ratios as Belloche et al. (2013) to derive the HCO^+ column densities (see their Table 2). We use Weeds (Maret et al. 2011) to model the velocity components detected towards K4 in absorption. The resulting parameters are listed in Table 5.11 and the synthetic spectra are shown in Fig. 5.21. We obtain H_2 column densities ranging from 3.3×10^{20} to 9.0×10^{22} cm^{-2}, which corresponds to A_v between 0.4 and 96 mag (columns 4 and 5 in Table 5.11).

With the HCO^+ abundance relative to H_2 assumed above, all but three components (at v_{LSR} = −83.9 km s^{-1}, −114.1 km s^{-1}, and −134.6 km s^{-1}) would have visual extinctions higher than 5 mag, which would imply that they are dense molecular clouds. If this were indeed the case, then we would expect to see these clouds in emission towards positions without strong continuum background. To test this, we cannot use the EMoCA survey because of the spatial filtering of the interferometer. Instead, we check the imaging survey of Sgr B2 performed by Jones et al. (2008) with Mopra at 3 mm. We select the following transitions:

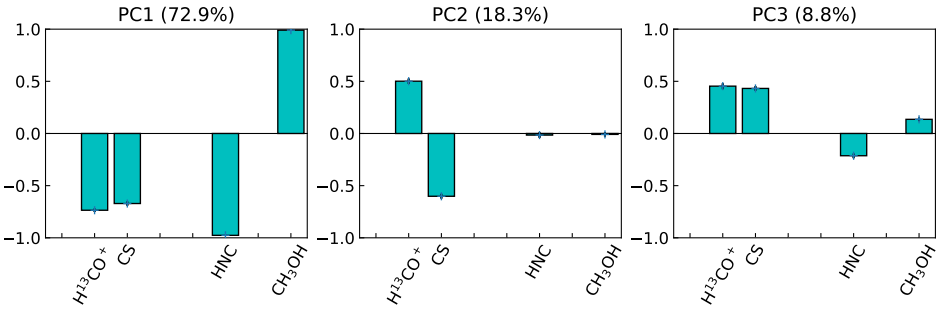

Figure 5.19: Principal component coefficients determined at $v_{\rm LSR}$ = 24.7 km s^{-1}. The contribution factors of each molecule are normalised such that the sum of the squares is equal to 1. The percentages in parentheses give the contributions of the PCs to the total variance.

HCO^+ 1–0, HNC 1–0, CS 2–1, and ^{13}CO 1–0. The HCO^+, HNC, and CS lines are partly seen in absorption in the Mopra data. We mask the pixels where absorption is detected in the velocity range from −100 km s^{-1} to 0 km s^{-1}. For each of these three species, we compute the average Mopra spectrum within a square box of size 156″ centred on the J2000 equatorial position $17^{\rm h}47^{\rm m}19.8^{\rm s}$, −28°22′17″, excluding the masked pixels (see Fig. 5.22). ^{13}CO 1–0 does not show any absorption in the Mopra spectra and we take the average spectrum over a square box of size 84″ centred on the same position (see Fig. C.72). The resulting Mopra spectra are compared to the EMoCA spectra in Figs. 5.23, 5.24, C.73, and C.74.

The ^{13}CO Mopra average spectrum shows two strong velocity components in emission that match well the position of components seen in absorption in the EMoCA spectrum (at −42 km s^{-1} and 5 km s^{-1}, see Fig. 5.24). Two weaker emission peaks at −83 km s^{-1} and −107 km s^{-1} also match absorption components seen with ALMA. None of the components at velocities below −30 km s^{-1} are detected in emission in the HCO^+, HNC, and CS Mopra spectra, but these species show emission at velocities above ∼ −30 km s^{-1}, which may be at least in part associated with the absorption components seen in the ALMA spectra.

We perform non-LTE radiative transfer calculations with RADEX (van der Tak et al. 2007) to estimate the densities and kinetic temperatures that are consistent with the emission seen with Mopra, or its upper limits. We take the spectroscopic parameters and collisional rates with H_2 from the Leiden Atomic and Molecular Database (LAMDA, Schöier et al. 2005) for HCO^+ (Botschwina et al. 1993; Flower 1999; Schöier et al. 2005), CS (CDMS, and Lique et al. 2006), HNC (CDMS, and Dumouchel et al. 2010), and ^{13}CO (CDMS, JPL, and Goorvitch 1994; Cazzoli et al. 2004; Yang et al. 2010). We perform the calculations for a wide range of parameters: 10–130 K for the kinetic temperature and 10–10^7 cm^{-3} for the H_2 density. These ranges cover the values expected for diffuse, translucent, and dense molecular clouds. We explore the following ranges of column densities: $10^{12.5–14.5}$ cm^{-2} for HCO^+, $10^{12.0–14.5}$ cm^{-2} for HNC, $10^{12.5–14.5}$ cm^{-2} for CS, and $10^{15.0–16.5}$ cm^{-2} for ^{13}CO. They correspond to the ranges derived from the absorption features detected with ALMA towards six strong continuum positions covered by EMoCA. The brightness temperatures computed with RADEX for the selected transitions are displayed in Figs. 5.25, C.75, C.76, and C.77, respectively. The solid lines plotted in these figures indicate the level of emission detected with Mopra for the component around 14 km s^{-1}. For ^{13}CO, the dashed lines correspond to the emission component detected around 83 km s^{-1}, while for the other species, they correspond to the emission upper limits (three times the RMS noise level) derived from the Mopra spectra between −110 km s^{-1} and −10 km s^{-1}. We converted the Mopra antenna temperatures into brightness temperatures by multiplying them with a factor 1.7, which roughly corresponds to the extended beam efficiency of ∼ 0.6 measured by Ladd et al. (2005) for sources larger than ∼ 80″, consistent with the extended emission seen in the Mopra channel maps shown in

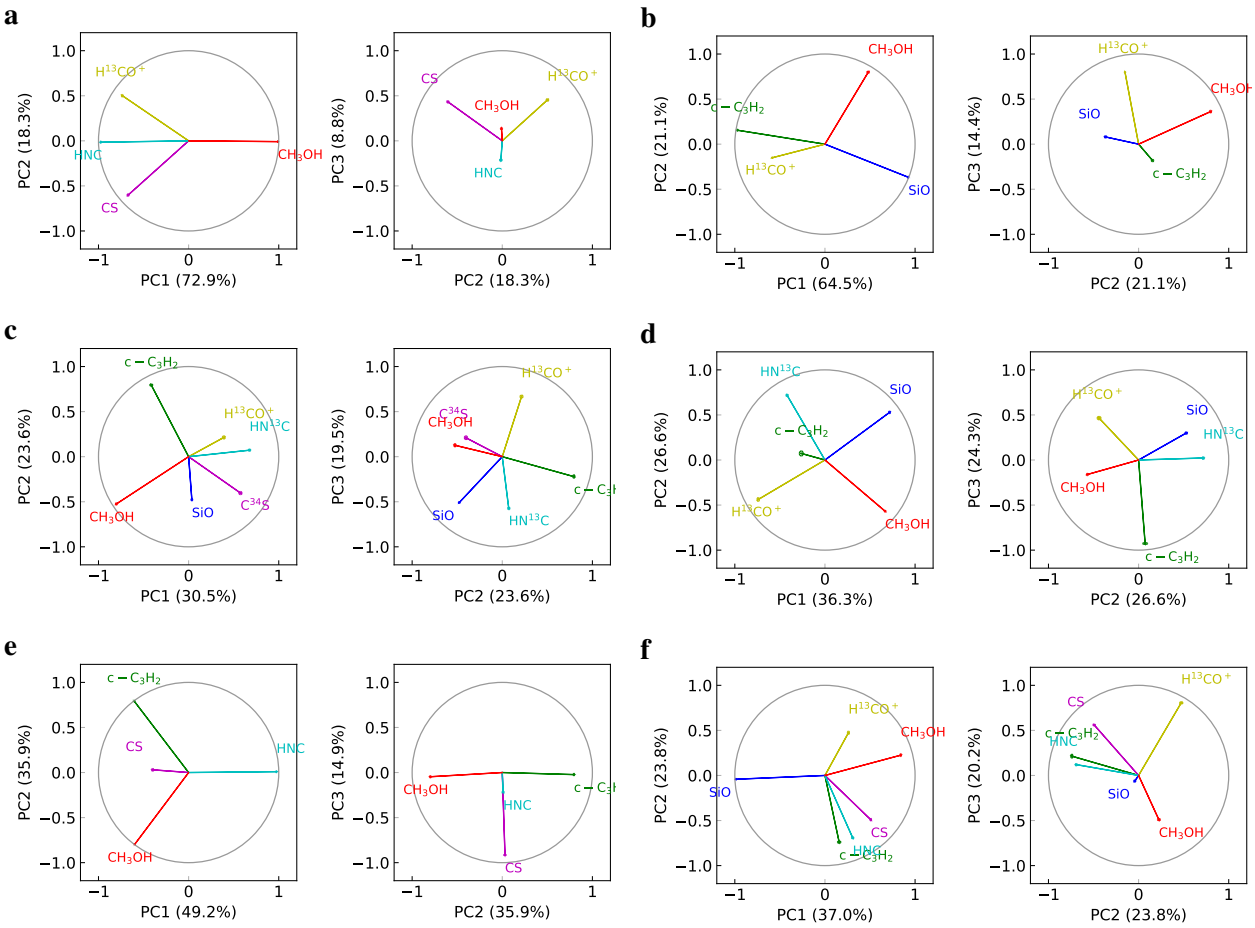

Figure 5.20: Correlation wheels for PCs at $v_{\rm LSR}$ = 24.7 km s^{-1} (panel **a**), −105.9 km s^{-1} (**b**), 2.0 km s^{-1} (**c**), 7.3 km s^{-1} (**d**), 31.6 km s^{-1} (**e**), and 17.7 km s^{-1} (**f**). The percentages in parentheses give the contributions of the PCs to the total variance. The ellipses around the arrow heads show the uncertainties estimated from 1000 realisations of the opacity cubes.

Figs. 5.22 and C.72.

Given the limits assumed for the kinetic temperature, our RADEX analysis provides constraints on the molecular hydrogen densities (see Table 5.12). For the component around 6 km s^{-1}, the ranges of densities derived from HCO$^+$ and ^{13}CO are similar, on the order of 30–5000 cm^{-3}, while the ranges derived for HNC and CS are shifted by nearly one order of magnitude towards higher densities. For the component at −83 km s^{-1}detected in emission in ^{13}CO 1–0, the upper end of the density range is 500 cm^{-2}. The upper limits derived for HCO$^+$, HNC, and CS over the range −110 to −10 km s^{-1} imply densities below 5×10^3 cm^{-3}, 5×10^5 cm^{-3}, and 3×10^4 cm^{-3}, respectively. Some of the RADEX plots also show higher density solutions for CS and ^{13}CO but these solutions would not be consistent with the constraints set by HCO$^+$. Our RADEX analysis does not bring any constraint on the kinetic temperature.

Our calculations with RADEX do not take the collisional excitation by electrons into account. Electrons can have a significant impact on the excitation of molecules at low densities when the electron fraction is high and the CO fraction is small (Liszt & Pety 2016). Taking the collisional excitation by electrons into account in our radiative transfer calculations would lower the densities or upper limits derived in this section.

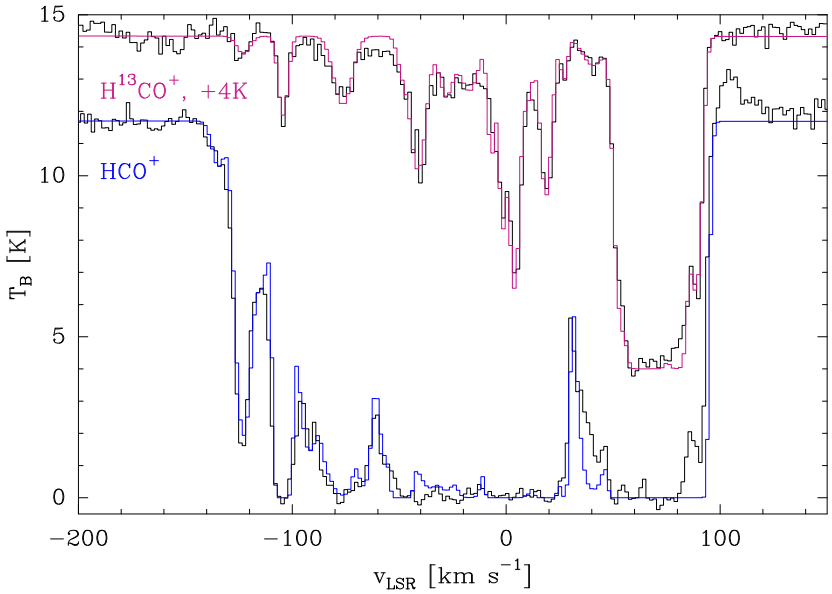

Figure 5.21: ALMA spectra of HCO^+ 1–0 and $H^{13}CO^+$ 1–0 (shifted by +4 K) in the direction of K4 in black. The synthetic spectra of HCO^+ and $H^{13}CO^+$ computed with Weeds are overplotted in blue and magenta, respectively.

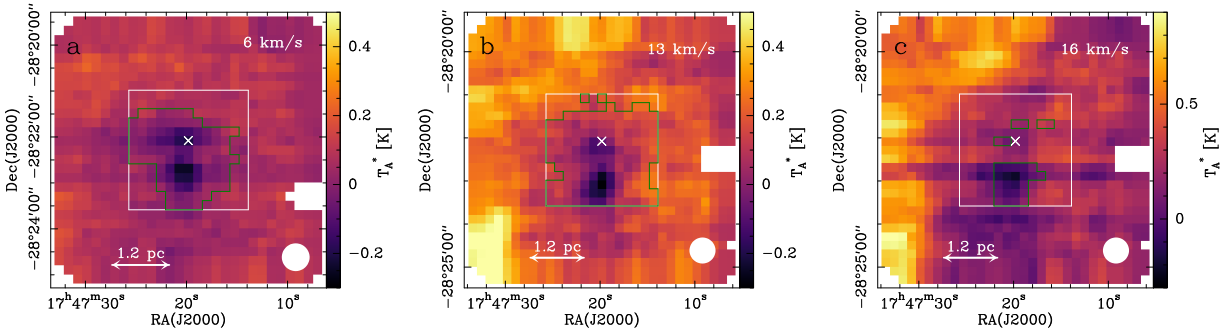

Figure 5.22: Mopra channel maps in the direction of Sgr B2 at about 14 km s^{-1} for HCO^+ 1–0 (panel **a**), HNC 1–0 (**b**), and CS 2–1 (**c**) as observed by Jones et al. (2008). In each panel, the white box shows the region selected to calculate the averaged spectrum and the green contour encloses the pixels that were masked to avoid absorption. The white circle in the lower right corner of each panel represents the beam and the cross indicates the position of K4. The pixel size is 12.″.

5.5 Discussion

5.5.1 Types of line-of-sight clouds

Assuming that HCO^+ has the same abundance relative to H_2 as the one established for diffuse clouds (3×10^{-9}) leads to the conclusion that most clouds seen in absorption in the EMoCA survey would be dense clouds, with visual extinctions higher than 5 mag (Table 5.11). However, the maps obtained towards Sgr B2 with Mopra by Jones et al. (2008) reveal only few velocity components in emission in the tracers HCO^+ 1–0, HNC 1–0, CS 2–1, and ^{13}CO 2–1. Our radiative-transfer analysis indicates that the emission component at $\sim$ 6 km s^{-1} detected in ^{13}CO 2–1 and HCO^+ 1–0 must have an H_2 density lower than a few times 10^3 cm^{-3}.

Table 5.11: H_2 column densities densities and visual extinctions derived from the HCO^+ column densities determined in the ALMA spectrum in the direction of K4.

v_{LSR}[a] [km s^{-1}]	N($H^{13}CO^+$)[b] [cm^{-2}]	N(HCO^+)[c] [cm^{-2}]	N(H_2)[d] [cm^{-2}]	A_v[e] [mag]	N(H_2)[f] [cm^{-2}]	A_v[e] [mag]
40.8	1.3(12)	5.2(13)*	1.7(22)	18.4	3.6(21)	3.8
27.0	6.2(11)	2.4(13)*	8.0(21)	8.5	2.5(21)	2.7
18.6	4.5(12)	2.7(14)*	9.0(22)	95.7	1.4(22)	14.4
9.8	1.5(12)	3.0(13)*	1.0(22)	10.6	2.8(21)	3.0
3.8	8.0(12)	1.6(14)*	5.3(22)	56.7	8.0(21)	8.5
-1.7	3.8(12)	7.6(13)*	2.5(22)	27.0	4.3(21)	4.5
-6.9	2.0(12)	8.0(13)*	2.7(22)	28.4	4.4(21)	4.6
-17.2	2.1(12)	8.4(13)*	2.8(22)	29.8	4.5(21)	4.7
-28.1	1.8(12)	3.2(13)*	1.1(22)	11.3	2.9(21)	3.0
-35.2	–	2.4(13)	8.0(21)	8.5	2.5(21)	2.7
-41.2	5.1(12)	2.1(14)*	7.0(22)	74.5	1.1(22)	11.1
-48.8	5.7(11)	2.3(13)*	7.7(21)	8.2	2.5(21)	2.6
-56.3	–	2.1(13)	7.0(21)	7.4	2.4(21)	2.5
-66.3	–	2.3(13)	7.7(21)	8.2	2.5(21)	2.6
-76.4	2.7(12)	5.6(13)*	1.9(22)	19.9	3.7(21)	3.9
-83.9	–	8.6(12)	2.9(21)	3.0	1.6(21)	1.7
-91.9	–	2.6(13)	8.7(21)	9.2	2.8(21)	2.8
-104.3	1.7(12)	9.2(13)	3.1(22)	32.6	4.7(21)	5.0
-114.1	–	5.0(12)	1.7(21)	1.8	1.2(21)	1.3
-122.8	4.8(11)	1.5(13)	5.0(21)	5.3	2.0(21)	2.1
-134.6	–	1.0(12)	3.3(20)	0.4	3.3(20)	0.4

Notes. $X(Y)$ corresponds to $X \times 10^Y$. The excitation temperature is assumed to be 2.73 K. [(a)] Centroid velocity of the Gaussian component. [(b)] $H^{13}CO^+$ column density. A dash indicates the cases where $H^{13}CO^+$ is too weak. [(c)] HCO^+ column density. A star indicates the cases when it is derived from $H^{13}CO^+$. [(d)] H_2 column density derived from HCO^+ assuming an HCO^+ abundance of 3×10^{-9} relative to H_2 typical for diffuse clouds (Liszt et al. 2010). [(e)] Visual extinction computed from the previous column with the formula $A_v(\text{mag}) = N(H_2)/(9.4 \times 10^{20}\,\text{cm}^{-2})$. [(f)] H_2 column density derived from HCO^+ assuming a HCO^+ abundance of 3×10^{-9} for $N(HCO^+) < 2.8 \times 10^{12}$ cm^{-2}, 2×10^{-8} for $N(HCO^+) > 9.4 \times 10^{13}$ cm^{-2}, and an interpolated value (in log-log space) in between.

In addition, our analysis of the ALMA HCO^+ 1–0 absorption spectrum towards K4 indicates that, except for the component at −83.9 km s^{-1}, the velocity components between −110 and −10 km s^{-1}, which are not detected in emission in the HCO^+ 1–0 Mopra data, have HCO^+ column densities higher than 10^{13} cm^{-2} (Table 5.11). The radiative-transfer calculations then imply that these components have H_2 volume densities below 10^3 cm^{-3} (Fig. 5.25). Finally, the component at ∼ −83 km s^{-1} detected in ^{13}CO 2–1 emission with Mopra also has a low density, less than 500 cm^{-3}, according to our radiative-transfer analysis (Sect. 5.4.7). Taking the collisional excitation of molecules by electrons into account would imply even lower densities. All components between −110 and −10 km s^{-1} and the one at 6 km s^{-1} thus have densities that are too low for them to be dense clouds, which are characterised by densities higher than 10^4 cm^{-3} (Snow & McCall 2006). We note that Greaves (1995) derived densities on the order of 10^4 cm$^{-}3$ for the clouds at velocities −102, −41, −27, and 3 km s^{-1} on the basis of HCN 3–2 probed in absorption with the JCMT, while their CS 2–1 and 3–2 observations of the same clouds in absorption indicate densities lower than 600 cm^{-3}, in rough

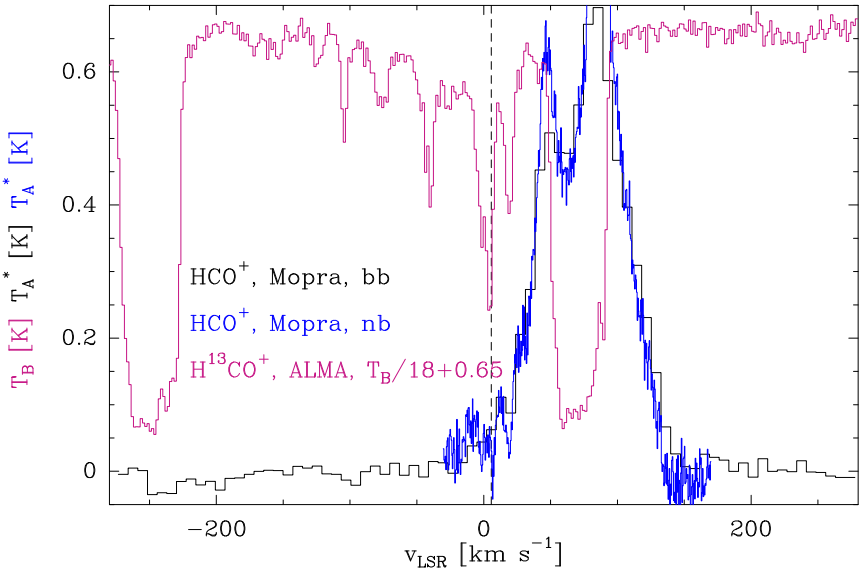

Figure 5.23: Mopra average spectrum of HCO^+ 1–0 towards Sgr B2(N), extracted from the imaging survey of Jones et al. (2008) after excluding pixels with absorption (see Fig. 5.22). The black and blue spectra were obtained with the broadband and narrowband backends, respectively. They are displayed in T_A^* scale. The purple spectrum is the EMoCA spectrum of $H^{13}CO^+$ 1–0 towards K4 in brightness temperature scale. The feature between -280 and -210 km s^{-1} is caused by SiO in the envelope of Sgr B2. The dashed line marks the channel that corresponds to a ^{13}CO emission peak in Fig. 5.24.

agreement with our conclusion above. These authors concluded that a range of densities from $\sim$ 200 cm^{-3} up to 10^4 cm^{-3} must be present in these clouds.

The components discussed in the previous paragraph are not dense clouds, and they cannot represent diffuse clouds either, otherwise we would obtain visual extinctions lower than 1 mag when computing their H_2 column densities with the standard diffuse-cloud abundance of HCO^+. We conclude that the clouds with velocities between -110 and -10 km s^{-1} and at 6 km s^{-1} are translucent clouds, and that the HCO^+ abundance relative to H_2 must be higher than 3×10^{-9} in these clouds, by at least a factor of 2, and maybe even a factor 6 in order to reconcile the visual extinction of the component at -104 km s^{-1} with its translucent nature (A_v should be between 1 and 5 mag). All these conclusions hold only if our assumption that the HCO^+ column densities derived from our ALMA absorption spectra are representative of the HCO^+ column densities at the scales probed with Mopra.

Our conclusion that HCO^+ likely has a higher abundance in translucent clouds compared to diffuse clouds is consistent with the results of the GEMS survey performed by Fuente et al. (2018) with the IRAM 30 m telescope towards the dark cloud TMC1. They report that HCO^+ reaches its maximum abundance relative to H_2 at a visual extinction of 5 mag, with a value of $\sim 2\times10^{-8}$. A visual extinction of 5 mag corresponds to a H_2 column density of 4.7×10^{21} cm^{-2}, which implies a HCO^+ column density of 9.4×10^{13} cm^{-2} assuming the HCO^+ abundance above. The transition between diffuse and translucent clouds at a visual extinction of 1 mag corresponds to an H_2 column density of 9.4×10^{20} cm^{-2}, that is a HCO^+ column density of 2.8×10^{12} cm^{-2} assuming the $\approx$ 7 times lower standard HCO^+ abundance for diffuse clouds (3×10^{-9}). Most components in Table 5.11 have HCO^+ column densities between these two values, implying that they are translucent clouds. The exceptions are the component at -134.6 km s^{-1}, which corresponds to a diffuse cloud, and the components at -41.2 km s^{-1}, 18.6 km s^{-1}, and 3.8 km s^{-1}, which must be dense clouds. To have a better estimate of the H_2 column density and visual extinction of each component, we

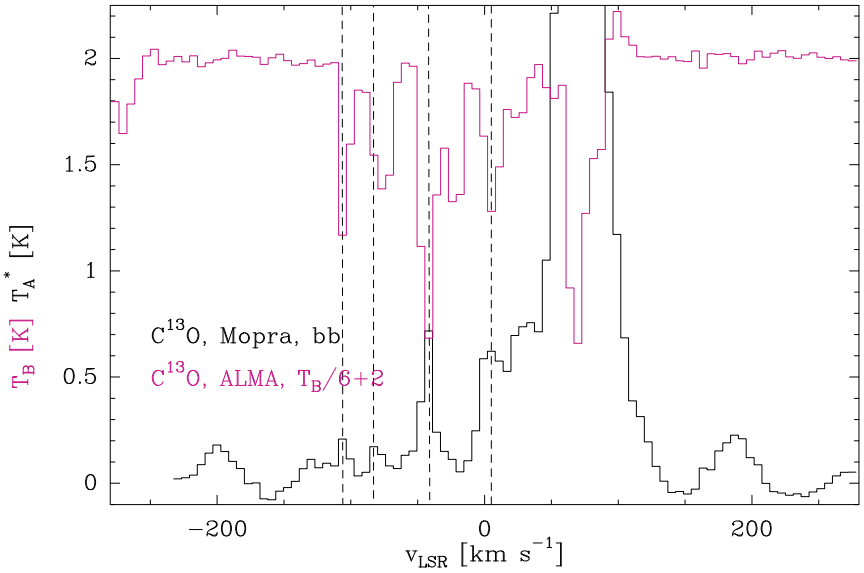

Figure 5.24: Same as Fig. 5.23, but for ^{13}CO 1–0. The ALMA spectrum is resampled to the spectral resolution of the Mopra spectrum. The dashed lines mark emission peaks that match well absorption features of the EMoCA spectrum outside the velocity range of the Sgr B2 envelope.

Table 5.12: H_2 densities derived from the Mopra data.

molecule	v_{LSR} [a] [km s^{-1}]	T_b [b] [K]	n_{H_2} [c] [cm^{-3}]	
HCO^+	6	0.11	4(1)–1(3)	
	x	<0.06	<2(1)–5(3)	
HNC	6	0.37	7(2)–4(4)	
	x	<0.15	<3(2)–5(5)	[>5(5)]
CS	10	0.43	4(2)–2(4)	[>1(5)]
	x	<0.06	<5(1)–3(4)	[>1(5)]
^{13}CO	5	1.06	3(1)–5(3)	[>1(3)]
	−83	0.35	<5(2)	[>5(3)]

Notes. $X(Y)$ corresponds to $X \times 10^Y$. [(a)] x corresponds to the velocity range from −110 to −10 km s^{-1}. [(b)] Measured brightness temperature in the Mopra spectrum, or upper limit of 3σ. [(c)] Range of densities consistent with the detected Mopra emission, or upper limit to the densities. The values in brackets give the high-density solution, when it exists.

recompute these quantities assuming a HCO^+ abundance of 3×10^{-9} for $N(HCO^+) < 2.8 \times 10^{12}$ cm^{-2}, 2×10^{-8} for $N(HCO^+) > 9.4 \times 10^{13}$ cm^{-2}, and an interpolated value (in log-log space) in between (see Table 5.11).

In Thiel et al. (2017), some of us reported on the basis of the EMoCA survey the detection of complex organic molecules in four velocity components (one in the Scutum arm and three in the GC region) that we ascribed to what we termed diffuse clouds. Liszt et al. (2018) questioned the diffuse nature of these clouds on the basis of their high HCO^+ column densities. The detailed analysis performed here confirms that these components with COM detections are not diffuse. Instead, we find that the component in the Scutum arm (at 27 km s^{-1}) and two of the GC components (at 9.8 km s^{-1} and −1.7 km s^{-1}) are translucent clouds. The third GC component has a visual extinction of 8.5 mag suggesting it is somewhat dense, but still close to the

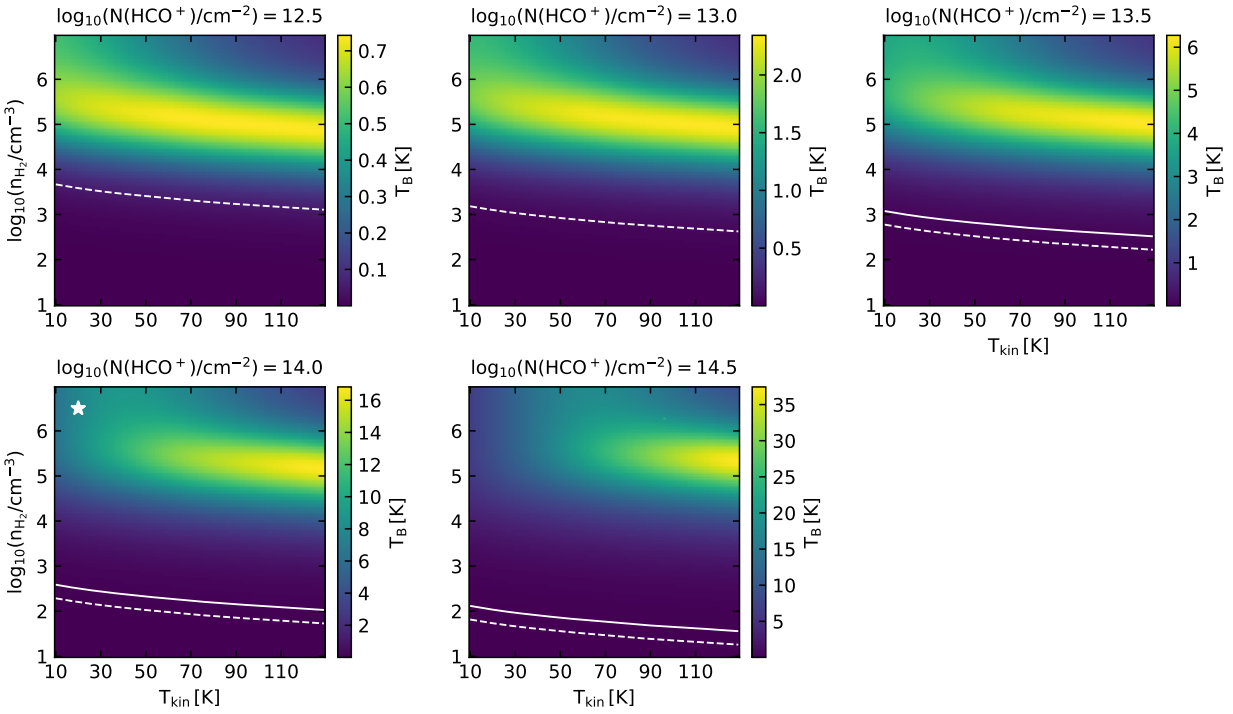

Figure 5.25: HCO^+ 1–0 brightness temperature computed with RADEX as a function of kinetic temperature (x-axis) and H_2 density (y-axis), assuming different column densities. In each panel, the solid line corresponds to the level of emission measured in the Mopra spectrum around 14 km s^{-1} and the dashed line to the upper limit (3σ) over the velocity range from -110 km s^{-1} to -10 km s^{-1}. The solid line is displayed only for the column densities that fall in the range determined from the ALMA absorption map at this velocity and the white star marks the median column density obtained from the ALMA absorption map at this velocity.

border between translucent and dense clouds. Therefore, we conclude that complex organic molecules are present in some translucent clouds along the line of sight to Sgr B2.

5.5.2 Suitable tracers of H_2 in translucent clouds

The fact that HCO^+ has a higher abundance in translucent clouds compared to diffuse clouds has an impact on the analysis of the CH abundance performed by Qin et al. (2010) for the clouds probed in absorption with *Herschel* towards Sgr B2(M). They took HCO^+ as a proxy for H_2 and assumed a uniform abundance of 5×10^{-9}. With this assumption, the distribution of CH and H_2 column densities does not follow the correlation found by previous studies for diffuse clouds. However, if we take into account the variation of the HCO^+ abundance as described above, we find a correlation between CH and H_2 much closer to the diffuse-cloud correlation. The kink at an H_2 column density of 10^{21} cm^{-2} reported by Qin et al. (2010) vanishes (see Fig. C.78). The correlation of CH to H_2 determined by Sheffer et al. (2008) for diffuse molecular clouds is now valid for H_2 column densities up to $10^{21.7}$ cm^{-2}, which means that CH is a good tracer of H_2 up to $A_v \sim 5.3$ mag. At $N_{H_2} \approx 10^{23}$ cm^{-2}, we see a deviation from the correlation. Hence, the CH abundance relative to H_2 must decrease somewhere between $10^{21.7}$ cm^{-2} and 10^{23} cm^{-2}. This is consistent with the drop of CH abundance above a H_2 column density of 5×10^{21} cm^{-2} reported for TMC-1 by Suutarinen et al. (2011).

CCH is strongly correlated with CH in diffuse molecular clouds (Gerin et al. 2010b). There is also a tight correlation between CCH and c-C_3H_2 in translucent clouds (for N(c-C_3H_2) $< 10^{12.5}$ cm^{-2}, Lucas & Liszt 2000; Gerin et al. 2011). Here, we want to investigate whether both CCH and c-C_3H_2 are good tracers of H_2 in translucent clouds. Figure 5.26 shows the distribution of CCH column densities as a function of H_2 column densities for the velocity components detected towards six positions with strong continuum background in our survey, along with measurements reported in the literature for other diffuse and translucent clouds. In this plot, the H_2 column densities are derived from the HCO^+ column densities assuming the same non-uniform HCO^+ abundance profile as in Sect. 5.5.1. Overall, we see that CCH is well correlated with H_2 for both diffuse and translucent clouds. The slope of unity indicates that it can be used as a good tracer of H_2 up to $A_v = 5$ mag at least. The correlation is a bit tighter for the GC translucent clouds than for the ones located in the disk of our Galaxy, with a slope slightly higher and lower than unity for the former and latter, respectively.

Figure C.79 shows the same plot for c-C_3H_2. If we take all data together, there is an overall correlation between c-C_3H_2 and H_2 with a slope close to unity, but a fit limited to the ALMA data only yields a much flatter correlation, with a large dispersion. c-C_3H_2 does not seem to correlate as tightly with H_2 as CCH in the translucent regime. This larger dispersion is dominated by the clouds located in the galactic disk for which there is no correlation between c-C_3H_2 and H_2. The correlation is tighter for the GC clouds with, however, a slope higher than unity. In both cases, c-C_3H_2 thus does not appear as a good tracer of H_2.

The column densities of CCH and c-C_3H_2 are plotted against each other in Fig. C.80. Here also, while there is an overall correlation with a slope close to unity for the full sample of diffuse and translucent clouds, the fit limited to the ALMA data departs significantly from a slope of unity. Therefore, our data do not reveal a tight correlation between CCH and c-C_3H_2 beyond the range of C_3H_2 column densities explored by Lucas & Liszt (2000) and Gerin et al. (2011). This conclusion holds also for the GC or galactic disk clouds taken separately (see magenta and green fits in Fig. C.80).

5.5.3 Velocity components and velocity dispersions

Previous absorption studies revealed velocity components similar to those we found in our data. Corby et al. (2018) used GBT data to investigate ortho c-C_3H_2 ($1_{1,0} - 1_{0,1}$) at 18.343 GHz. They detected many narrow features with $FWHM \lesssim 3$ km s^{-1} which are superimposed on components with widths between 3 and 16 km s^{-1}. They suggested at least ten distinguishable line-of-sight absorption components. Garwood & Dickey (1989) used VLA data with a spectral resolution of 2.6 km s^{-1} to investigate HI in absorption along the line of sight to Sgr B2(M). Because the velocities in the direction of Sgr B2(N) are similar to those in the direction of Sgr B2(M) (Greaves & Williams 1994) we chose these velocities for comparison. The components detected by Corby et al. (2018) and Garwood & Dickey (1989) are compared to ours in Table 5.13.

All velocity components found by Garwood & Dickey (1989) are detected in this work and in the data examined by Corby et al. (2018). Corby et al. (2018) modelled the spectrum using several broad Gaussian components overlaid with narrower Gaussian features resulting in a higher number of velocity components than we investigate here. Corby et al. (2018) detected two velocity components, at −120 km s^{-1} and −58 km s^{-1}, for which we see no clear counterparts in our c-C_3H_2 spectra. The component at −58 km s^{-1} is detected towards a few positions but because of the poor statistics, we decided not to investigate this component. The component at −120 km s^{-1} is detected in other molecules such as HCN or HCO^+ (see Table 5.11), so our non-detection of this component in c-C_3H_2 is due to a lack of sensitivity. Belloche et al. (2013) investigated the velocity components of c-C_3H_2 along the line of sight to Sgr B2 using the IRAM 30 m telescope. They were also able to find a few additional velocity components compared to the

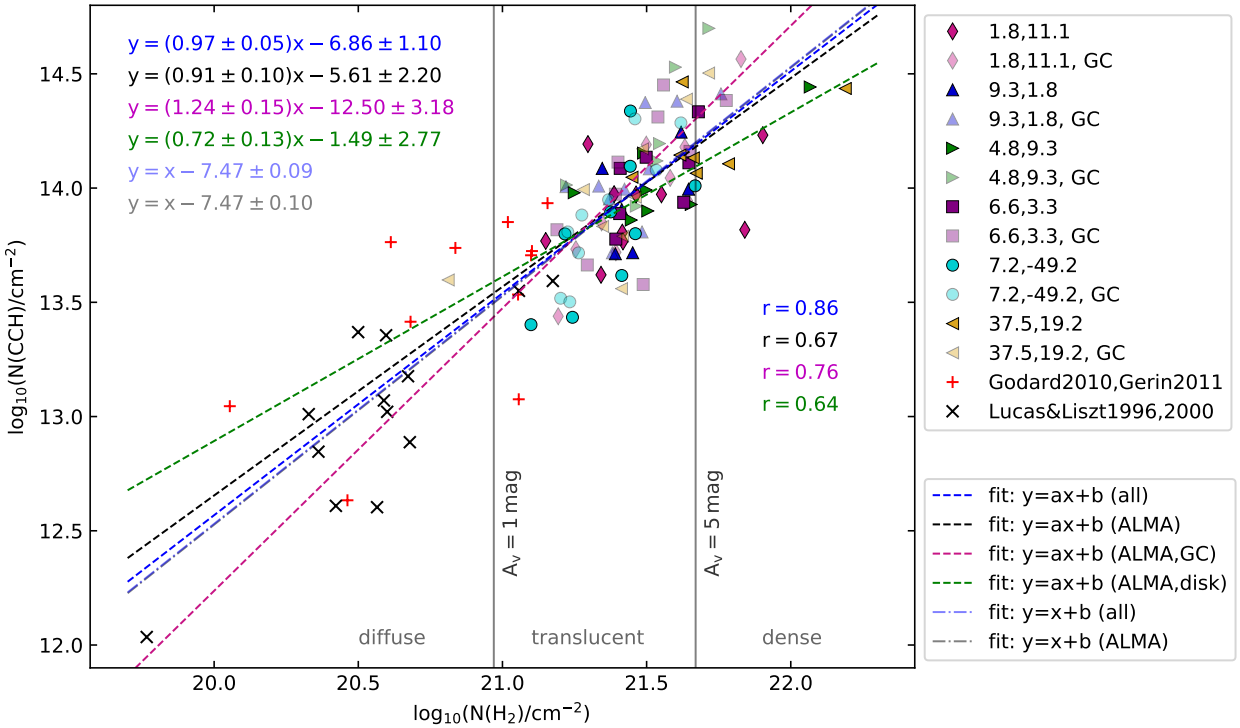

Figure 5.26: Distribution of CCH column densities versus H_2 column densities, calculated from HCO^+ as described in Sect. 5.5.1. The filled symbols represent the values obtained for the velocity components detected toward six positions with strong continuum background in the ALMA data. Their equatorial offsets are indicated to the right. The fainter filling colours are used for the GC components. The red crosses are measurements from Godard et al. (2010) and Gerin et al. (2011) and the black ones from Lucas & Liszt (1996, 2000). The dashed lines are linear fits to the following samples: all data (blue), ALMA data only (black), ALMA GC components only (magenta), and ALMA disk components only (green). The dotted-dashed lines are fits with a slope of unity. The fits results are given in the upper left corner with their uncertainties. The Pearson correlation coefficients *r* are given on the right side. The vertical lines highlight the limits between diffuse, translucent, and dense clouds.

components reported here. In our analysis, we only consider the velocity components associated with the strongest peaks (minima) of the absorption of c-C_3H_2. The programme we wrote to fit synthetic spectra to the 322 investigated positions may underestimate the number of velocity components in some cases because we do not allow peak velocities to be closer to each other than two channels (see Sect. 5.3.5). This approach still yields good fits to the observed spectra (see Fig. 5.3). In addition, the number of identified velocity components depends on the investigated position. Because our main goal is to investigate the spatial structure of the diffuse and translucent clouds seen in absorption, we selected the velocity components for which a cloud is detected towards a sufficient number of positions. The detection of components depends also on the strength of the continuum. The IRAM 30 m and GBT single-dish data have angular resolutions of ~30″ and ~40″, respectively, which means that they are much more sensitive to the extended continuum emission and they include the two main hot cores Sgr B2(N1) and Sgr B2(N2). The stronger continuum of Sgr B2(N1) (see Fig. 5.1) reveals more velocity components in our data but they are too weak to be detected at lower continuum values. These hot-core positions are however affected by contamination from numerous emission lines in the 3 mm atmospheric window, which is the reason why we excluded them from

Table 5.13: Velocities of diffuse and translucent clouds along the line of sight to Sgr B2.

$v_{\mathrm{thiswork}}{}^{a}$ [km s^{-1}]	$v_{\mathrm{Corby}}{}^{b}$ [km s^{-1}]	$v_{\mathrm{Garwood}}{}^{c}$ [km s^{-1}]
–	−120	–
−105.9	−106	−107.6
−93.7	−92	–
−81.5	−80	−81.7
−74.6	−73	–
–	−58	–
−48.4	−47	−51.9/−44.0
−39.7	−40	–
−27.6	−23	−24.4
−18.9		
−3.2		
2.0	0	1.1
7.3		
17.7	20	15.7
24.7		
31.6		31.4
36.9		

Notes. [(a)] LSR cloud velocities of ortho c-C_3H_2 determined in this work. [(b)] LSR cloud velocities determined by Corby et al. (2018) from c-C_3H_2 at 18.343 GHz in absorption. [(c)] LSR cloud velocities determined by Garwood & Dickey (1989) from HI in absorption.

our analysis.

The smallest linewidth we derive for a velocity components traced by c-C_3H_2 is 1.74 km s^{-1}, which is equal to the channel width. The largest width is about 20 km s^{-1} (see Fig. 5.4). Corby et al. (2018) found a range of $FWHM$ between ∼1 and 10 km s^{-1}, plus two broad components with $FWHM \sim 16$ km s^{-1} that probably result from the overlap of several narrower components. The majority (84%) of the widths derived here is smaller than 11 km s^{-1} (see Fig. 5.4), thus falling in the same interval. Belloche et al. (2013) found typical widths of the line-of-sight clouds of 3–5 km s^{-1}, and Menten et al. (2011) values between 3 and 8 km s^{-1}. Gerin et al. (2010a) studied the diffuse and translucent clouds along the line of sight to G10.6-0.4 and found values between 3 and 6 km s^{-1} for the $FWHM$. The median value of Category I, 5.4 km s^{-1} (Table 5.2), lies at the upper edge of these ranges for the $FWHM$. If we look at the width distribution of Category I (see Fig. 5.4a) the majority (75%) of the velocity components have $FWHM$ smaller than about 7.5 km s^{-1}. For larger widths the number of velocity components is decreasing. This tail could be caused by overlapping velocity components that could not be fitted separately.

The largest $FWHM$ derived from our fits is 20 km s^{-1}. Wiesemeyer et al. (2016) investigated OH and OH^+ along the lines of sight to other continuum sources than Sgr B2 and found velocity components with widths up to 18 km s^{-1} for OH and up to 23 km s^{-1} for OH^+ covering the same velocity interval. The distribution of their $FWHM$ shows that most velocity components have smaller widths and only a few have $FWHM$ larger than 10 km s^{-1}. Their explanation for the wide variance of determined $FWHM$ is that the absorption of single clouds may cause the narrow features, whereas the larger widths of the velocity components may be caused by the blending of the contribution from several clouds along the lines of sight.

Furthermore, the large beams of single dish telescopes may cause spatial blending effectively resulting in larger line widths. As explained in Section 5.4.2 the programme we used for the modelling of c-C_3H_2 is not able to distinguish between a single broad Gaussian and multiple overlapping components producing the same shape. In those cases a single Gaussian is assumed, which likely explains the tail we obtain to higher $FWHM$ and a smaller number of velocity components. Corby et al. (2018) investigated the OH absorption spectrum towards Sgr B2 at 1612 MHz and 1667 MHz. The former line shows linewidths larger than 10 km s^{-1} (up to 50 km s^{-1}) for most velocity components while for the latter half of the components have widths smaller than 10 km s^{-1}, but still larger than c-C_3H_2. Here again, the velocity overlap between clouds probably leads to an overestimate of the OH linewidths in some cases. Summarising, it seems that c-C_3H_2 traces less diffuse regions with smaller velocity dispersions than OH.

5.5.4 Cloud sizes

The two-point auto-correlation functions of the opacity maps suggest that most detected structures are extended on the scale of our field of view, ∼15″, or beyond (Sect. 5.4.4). This means that our assumption of a beam filling factor of 1 to fit the spectra is reasonable. In a few cases, the two-point auto-correlation functions indicate the presence of smaller structures of sizes ∼4″–6″. These structures are mostly seen for less abundant species for which most of the opacity map is dominated by noise. For example HN^{13}C shows small structures for the GC cloud at 2.0 km s^{-1}, but the main isotopologue HNC shows an extended structure at this velocity. Therefore, we believe that most of the compact structures suggested by the two-point auto-correlation functions simply result from a lack of sensitivity. More sensitive observations would likely detect the same underlying extended structures traced by the more abundant molecules.

The auto-correlation functions of SO and SiO suggest a clumpy structure for some of the velocity components, which cannot be explained by a lack of sensitivity for these molecules. The signal-to-noise ratio is relatively good for SiO at velocities between −5 km s^{-1} and 25 km s^{-1} and for SO between 0 km s^{-1} and 10 km s^{-1}. Hence, the clumps seen at these velocities are significant. Especially at the velocity of 7.0 km s^{-1}, which corresponds to a translucent cloud, these two molecules have a high SNR and reveal a smaller structure in the opacity maps of size of 5″ at an offset of (1.″5, 11.″0) (see Figs. C.19 and C.21). The physical size of these clumps is on the order of 0.2 pc. SiO also shows a more complex structure at 17.2 km s^{-1} in the Sagittarius arm. A denser clump peaked at (6.″5,5.″0) with a size of about 8″ (0.04 pc) is overlying a more extended structure. Except the clump at (6.″5,5.″0), the clumps detected in SiO and SO are located close to the boundaries of the available field of view. Hence, we may not see the complete structure of the clump and the determined size is only a lower limit.

The structures of sizes 0.04–0.08 pc seen in some molecules at the velocity of the Sagittarius arm can not be spatially resolved for the GC clouds. Observations with higher spatial resolution are needed to investigate if such smaller physical structures are present in the GC clouds.

The absorption components detected towards Sgr B2(N) and Sgr B2(M), which are separated by ∼50″, have similar velocities (Greaves & Williams 1994). This suggests that the structures of the foreground clouds detected in absorption are more extended than 50″, which can be seen in ^{13}CO large-scale emission maps.

5.5.5 Turbulence

The PDFs analysed in Sect. 5.4.5 can be described by one or two log-normal distributions. A log-normal profile characterises the low density part of the PDFs of star-forming regions (e.g Schneider et al. 2013). Isothermal hydrodynamic simulations including turbulence and gravity have shown that a power tail at

higher densities arises due to gravitational collapse/contraction (e.g. Klessen 2000). When gravity is not included in the simulations, only the log-normal part remains in the PDF (Padoan et al. 1997; Kritsuk et al. 2007; Federrath et al. 2008).

The log-normal part of the PDF is not influenced by resolution effects and should be unchanged by using larger beam sizes (Schneider et al. 2015b; Federrath & Klessen 2013). But in cases where the pixel distribution used for determining the PDF is not covering the complete structure, a fall off at lower densities can appear (Schneider et al. 2015a). If the structure is not completely covered by the field of view of the observations, the width can be underestimated and the peak position overestimated (Ossenkopf-Okada et al. 2016). Due to the limitations set by the background continuum emission on our actual field of view, we most likely do not trace the complete structure of the line-of-sight clouds. Hence, the width of their PDFs is likely underestimated.

The volume-weighted density PDF in numerical simulations has a wider dispersion than the column density PDF, but shows similar properties (Federrath et al. 2010). Both PDFs are nearly perfect log-normal distributions in simulations without gravity, only small effects seen as non-Gaussian features are present (see Federrath et al. 2010). The effects can be high- and low-density wings (e.g. Passot & Vázquez-Semadeni 1998; Kritsuk et al. 2007; Federrath et al. 2010). We sometimes see such weak wings in our data (see, e.g., Fig. C.52 at $v_{\rm LSR} = -81.3$ km s^{-1}), but they do not influence the parameters of the fitted log-normal profiles and also have only weak influence on the calculated dispersion of the profiles.

Federrath et al. (2008) investigated the gas density in turbulent supersonic flows by performing numerical simulations. They examined the differences in the column density fields for solenoidal forcing (divergence free) and compressive forcing (curl-free). They fixed the Mach number to 5.5. A result of the analysis is that the compressive forcing leads to a much higher density contrast than the solenoidal forcing despite the same Mach number. Solenoidal forcing is mostly present in more quiescent regions with low star formation rates, which is also seen in observations (Federrath et al. 2010). For both the volume-weighted density PDF and the column density PDF, the width of the lognormal part of the PDF is three times larger for compressive forcing than for solenoidal forcing. The compressive forcing of the turbulence as well as a higher Mach number broaden the PDFs (Federrath & Klessen 2013).

The width of the column density PDF for purely solenoidal forcing is determined in simulations to be $\sigma_\eta = 0.46 \pm 0.06$ (Federrath et al. 2010), which is similar to the average value of our sample of 15 diffuse and translucent clouds (0.52). The larger widths we obtained for low-abundance species ($C^{34}S$, ^{13}CS, $HN^{13}C$, and $HC^{15}N$) is likely due to the lack of sensitivity and the stronger influence of the noise (Ossenkopf-Okada et al. 2016). The width of column density PDFs for purely compressive forcing would be $\sigma_\eta = 1.51 \pm 0.28$ (Federrath et al. 2010). We therefore conclude that on average, the turbulence of the diffuse and translucent clouds traced in absorption in our data is mainly solenoidally driven, provided the bias resulting from our limited field of view is not too strong.

We derived in Sect. 5.4.5 the turbulence parameters ζ and b from the width of the PDFs of all 15 velocity components using c-C_3H_2, $H^{13}CO^+$, ^{13}CO, CS, SO, SiO, HNC, and CH_3OH. Because these parameters depend on the Mach number, the kinetic temperature is needed and we assumed a range of 20 K to 80 K to cover roughly the range of temperature possible in diffuse and translucent molecular clouds. With this range of temperature, the range of Mach number of the velocity components we detected is 2.9–28.3.

The question is which kinetic temperature is more likely: 20 K, 40 K, or 80 K. The investigation of H_2 using far-UV observations shows a temperature for diffuse clouds of 50–150 K depending on the investigated line of sight (Snow & McCall 2006, and references therein). The mean value is about 80 K. The temperatures in the direction of ζ Persei derived using C_2 is 80 ± 15 K, and using H_2 58 ± 8 K (Snow & McCall 2006, and references therein). The temperature in the direction of o Persei is a bit lower, 60 ± 20 K using C_2 and 48 ± 5 K using H_2 (Snow & McCall 2006, and references therein). The temperature seems

to show a high variance. However, as we concluded in Sect. 5.5.1, most clouds along the line of sight to Sgr B2 are translucent. Hence, the kinetic temperature is likely lower than the temperature of diffuse clouds mentioned above. (Fuente et al. 2018) derived a temperature of 13–14 K for visual extinctions below 7.5 mag in TMC-1. Therefore, we believe that the temperature of the translucent clouds investigated here is between ~15 K and ~50 K. Our radiative-transfer calculations (Sect. 5.4.7) do unfortunately not deliver any constraint on the kinetic temperature. In summary, for most of the line-of-sight clouds of our sample we favour temperatures of 20 K or 40 K, but we cannot exclude a higher temperature for the diffuse cloud in our sample.

For any of the three temperatures assumed above, the forcing parameter b is always smaller than 0.5 for all components. This confirms the conclusion drawn above that the turbulence is dominated by solenoidal forcing in the translucent clouds investigated here.

Many values of the forcing parameter b are either smaller than the value expected for purely solenoidal forcing or a bit larger, but still relatively close to 1/3. Values of b <1/3 are in principle not possible in the framework of the turbulence investigated in the simulations (Federrath et al. 2010). The underestimation of b could result from an underestimation of the width of the PDF because of the limited field of view, as mentioned above. A second reason for a low value of b could be an overestimation of the linewidth, for instance due to the overlap of several components along the line of sight. For example, b is relatively small for the following velocity components: −74.6, 2.0, −27.6, −18.9, and 31.6 km s^{-1}. The median $FWHM$ for those components is on average larger in comparison with the other velocity components (7.1–10.2 km s^{-1}).

In summary, our investigation of the PDFs of the clouds along the line of sight to Sgr B2 shows that the driving of the turbulence is purely solenoidal, or at least dominated by solenoidal forcing. Solenoidal forcing causes smaller density contrasts (Federrath et al. 2008), which results in more homogeneous cloud structures. This is consistent with the lack of substructures that we noticed on the basis of our analysis of the two-point autocorrelation functions of the opacity maps.

Studies of three translucent high-latitude clouds, MBM 16, MBM 40, and MBM 3, show that the motions inside the clouds are highly correlated in clumps which have sizes of about 0.5 pc (Magnani et al. 1993; Shore et al. 2003, 2006, 2007). This scale corresponds to the extent of the field of view we have in our ALMA data for the most distant clouds. The clumps in the translucent high-latitude clouds are located in a more diffuse structure. They are not self-gravitating and do not show star-forming activity. Some significant changes in emission at the scale of 0.03 pc are visible resulting in strong density gradients of a factor up to 10. In our data towards Sgr B2, we see, for a few molecules, structures at scales of about 0.04–0.08 pc only for the line-of-sight clouds located closer to us where such scales are resolved. The dynamics in the translucent high-latitude clouds was shown to result from the combination of shear flows and thermal instabilities, with the large-scale shear flow powering the turbulence and the density field maybe caused by thermal instability. Because we see also homogeneous structures on scales up to 0.55 pc roughly the size of the clumps detected in the high-latitude clouds, maybe the same processes are at work in the line-of-sight clouds investigated here.

5.5.6 Meaning of the cloud Categories

We have divided the clouds detected in absorption along the line of sight to Sgr B2 into two categories on the basis of their c-C_3H_2 column densities. Category I, with lower c-C_3H_2 column densities ($10^{12.8}$ cm^{-2} on average), contains the GC clouds with LSR velocities below −50 km s^{-1} and the clouds belonging to the 3 kpc and 4 kpc arms. The GC clouds with velocities around 0 km s^{-1}, the clouds in the Scutum arm and the ones in the Sagittarius arm belong to Category II, with higher c-C_3H_2 column densities ($10^{13.2}$ cm^{-2} on average). Clouds belonging to Category I have on average smaller velocity dispersions ($FWHM$ =

5.4 km s^{-1}) and a smaller PDF width (σ_η = 0.48) than clouds in Category II ($FWHM$=7.5 km s^{-1} and σ_η = 0.56). The statistically higher column densities of Category II do not result from a lack of sensitivity, which could occur if the linewidths are broader, because the column densities per velocity unit show the same trend.

The spiral arms closer to the GC (3 kpc and 4 kpc arms) belong to Category I whereas the more distant Scutum and Sagittarius arms belong to Category II. It is thus a priori surprising that the GC clouds with velocities around 0 km s^{-1} have similar properties as the clouds in the Scutum and Sagittarius arms. Given that absorption at velocities close to 0 km s^{-1} could arise from local clouds, we could be tempted to argue that these clouds were misassigned and are in fact local clouds. The assignment was in part based on the $\frac{^{12}C}{^{13}C}$ isotopic ratio of 22 determined by Gardner & Whiteoak (1982) which is consistent with the Galactic Center value and not with the higher ratio that characterises local clouds. Indeed, the $\frac{^{12}C}{^{13}C}$ isotopic ratio shows a gradient with galactocentric distance, increasing from about 20 in the GC to about 60–70 for local gas (Milam et al. 2005; Halfen et al. 2017). As a further verification, we used the EMoCA data to measure the $\frac{^{12}C}{^{13}C}$ isotopic ratio of the velocity components at −2.6, 3.7, and 8 km s^{-1} (covering the velocity range from −5 to 10 km s^{-1}). We used the absorption spectra of CN and ^{13}CN and derived isotopic ratios of $\frac{^{12}C}{^{13}C}$ = 20 ± 3 for these clouds, confirming once more their location in the GC. This value is robust against optical depth effects because we used the hyperfine components of CN to derive the ratio. Liszt & Gerin (2018) determined a higher isotopic ratio ($\frac{^{12}C}{^{13}C}$ = 64 ± 4) towards J1774 using HCO$^+$ isotopologues in the velocity range of −33 to 13 km s^{-1}, which is dominated by an absorption feature between -10 km s^{-1} and 10 km s^{-1}. The continuum source J1774 is located at small longitudes near the Galactic Center, with a separation of about 3° from Sgr B2. This high isotopic ratio would indicate the clouds producing these absorption features to originate from the disk. The velocity range covered by the velocity components of CN used to dermine the ratio $\frac{^{12}C}{^{13}C}$ in this work is smaller than their velocity range. Hence, we cannot exclude that maybe some gas seen in absorption at velocities between -9 and -5 km s^{-1} is located in the disk and not in the GC (see also the discussions in Sect. 3 of Wirström et al. (2010) and Sect. 5.2 of Corby et al. (2015)). But the components traced with CN seem to be located in the GC. Finally, the clouds in Category III have similar c-C_3H_2 column densities as those in Category II, and a median linewidth (6.7 km s^{-1}) that is closer to the one of Category II than to the one of Category I.

In summary, the GC region seems to contain two distinct populations of line-of-sight clouds (Category I and Categories II+III), but all with turbulence being driven (mainly) solenoidally. In the Galactic disk, the dichotomy correlates with the galactocentric distance: the clouds in Category II are located further away from the GC than the clouds in Category I. It is unclear to us whether this correlation with galactocentric distance is fortuitous or not.

In the Mopra data, HCO$^+$ 1–0, HNC 1–0, and CS 2–1 are detected in emission over a wide range of velocities, from about $v_{\rm LSR}$ = −15 km s^{-1} up to ≈ 130 km s^{-1}. The lower limit corresponds roughly to the border between Categories I and II (see Figs. 5.23, C.73, C.74, respectively). These tracers have higher critical densities than ^{13}CO 2–1, which is detected in emission in both Categories of clouds (Fig. 5.24). This suggests that the clouds in Category I have lower volume densities than the clouds in Category II.

5.5.7 Principal component analysis

We performed the PCA for six velocity components. The first principal component contributes strongly to the total variance of the opacity maps for only two of them: −105.9 km s^{-1} and 24.7 km s^{-1}. This means that a large part of the structures seen in the opacity maps of the different molecules are strongly correlated or anti-correlated for all molecules. Hence, there are spatial structures in these two clouds with smaller extent than the field of view.

The normalisation (mean=0 and standard deviation=1) used for the PCA implies that maps with a relatively uniform emission cannot be distinguished by the PCA from the maps of pure noise channels. Hence, if the maps of several molecules are relatively uniform but with a good signal-to-noise ratio, the PCA is not able to give any indications about the large-scale correlation. At 2.0 km s^{-1} most molecules show indeed extended structures in the opacity maps, especially H^{13}CO$^+$ which has a relatively homogeneous opacity over the field of view (see Fig. C.9). On the contrary, SiO shows a stronger variation of the opacity over the field of view at this velocity (see Fig. C.21). This molecule dominates the structure in the first PC (see Figs. C.64 and C.65).

Overall, the PCA indicates that most clouds probed in absorption towards Sgr B2(N) have relatively homogeneous structures over the field of view, which is consistent with the conclusions we draw from the analysis of the PDFs and auto-correlation functions of their opacity maps.

5.6 Conclusions

We used the EMoCA survey performed with ALMA to resolve and investigate the spatial structure of diffuse and translucent clouds traced by several molecules detected in absorption along the line of sight to Sgr B2(N), taking advantage of the high sensitivity and angular resolution of this survey. We investigated the velocity structure over the field of view by fitting the synthetic spectra to the absorption features of ortho c-C_3H_2. In addition, we investigated the spatial and kinematic structure of the individual clouds using the molecules c-C_3H_2, H^{13}CO$^+$, ^{13}CO, HNC and its isotopologue HN^{13}C, HC^{15}N, CS and its isotopologues C^{34}S and ^{13}CS, SiO, SO, and CH_3OH. Our main results are summarised as follows:

1. We found 15 main velocity components along the line of sight to Sgr B2 on the basis of c-C_3H_2. The strong velocity components match the ones found by previous studies (e.g., Garwood & Dickey 1989; Corby et al. 2018). The envelope of Sgr B2 shows two main components at $\sim$ 63 km s^{-1} and $\sim$ 80 km s^{-1}. In addition, we report the detection of a cloud at 48 km s^{-1}.

2. The absorption features along the line of sight can be divided into two categories on the basis of their c-C_3H_2 column densities: Category I ($v_{\rm LSR} < -13$ km s^{-1}) contains some GC clouds and clouds belonging to the 3 kpc and 4 kpc arms. Category II (-13 km s$^{-1} \leq v_{\rm LSR} < 42$ km s^{-1}) contains other GC clouds and clouds belonging to the Scutum and Sagittarius arms. The clouds of Category II have larger $FWHM$ and broader PDFs and they seem to have higher volume densities.

3. Most clouds detected along the line of sight to Sgr B2 are translucent on the basis of their HCO$^+$ column densities, including most clouds where we previously reported the detection of complex organic molecules. This is in agreement with the densities derived in previous single-dish studies of these clouds.

4. Our analysis of the HCO$^+$ abundance in translucent clouds indicates that HCO$^+$ is not a good tracer of H_2 in translucent clouds. We further find that CCH and CH are good probes of H_2 in translucent clouds, but that c-C_3H_2 is not.

5. The two-point auto-correlation functions reveal that the molecules investigated here trace relatively homogeneous structures as extended as 15″ at least. Smaller structures suggested by the two-point auto-correlation functions are in many cases dubious due to sensitivity limitations.

6. The average width of the column density PDFs is $\sigma_\eta = 0.52$, which is close to the value of 0.46 expected for purely solenoidal forcing. The turbulence in these clouds is thus dominated by solenoidal

forcing, which may explain the relatively homogeneous structures traced by the molecules investigated here.

7. A principal component analysis indicates in most cases a homogeneous distribution of the molecules. Only two of the six investigated velocity components show a structure smaller than the field of view.

Our analysis of the structure of the translucent clouds detected in absorption towards Sgr B2 is limited by two factors: the limited size of the continuum background emission, which results from the spatial filtering of the interferometer, and the finite angular resolution. Combining these ALMA main array data with measurements performed with the ACA would allow us to extend the analysis to scales larger than 15″.

5.7 Acknowledgements

We thank Volker Ossenkopf-Okada and Nicola Schneider for fruitful discussions about PDFs. We thank the referee, Harvey Liszt, for his insightful comments. This paper makes use of the following ALMA data: ADS/JAO.ALMA#2011.0.00017.S, ADS/JAO.ALMA#2012.1.00012.S. ALMA is a partnership of ESO (representing its member states), NSF (USA) and NINS (Japan), together with NRC (Canada), NSC and ASIAA (Taiwan), and KASI (Republic of Korea), in cooperation with the Republic of Chile. The Joint ALMA Observatory is operated by ESO, AUI/NRAO and NAOJ. The interferometric data are available in the ALMA archive at https://almascience.eso.org/aq/. DC acknowledges support by the Deutsche Forschungsgemeinschaft, DFG, through project number SFB956C.

Chapter 6

Conclusions

We used the EMoCA survey performed with the interferometer ALMA towards Sgr B2 to investigate the line-of-sight clouds traced by several molecules in absorption, taking advantage of the high sensitivity and angular resolution of this survey. We investigated the chemical and physical properties on sub-parsec scales in the envelope of Sgr B2 and in the clouds along the line of sight from the Galactic center region to the Solar circle.

Based on the detailed investigation of HCO^+ column densities derived for the molecular clouds along the line of sight to Sgr B2, we deduced that most of clouds are translucent molecular clouds.

The investigation of the column density profiles and the velocity distributions of the line-of-sight clouds revealed that the centroid velocities are similar in the translucent molecular clouds on scales smaller than about 12″ (0.5 pc), the extent of the continuum structure of Sgr B2(N). On scales larger than about 30″ (1.2 pc) the variations in the column density profiles and the velocity structure are strongly visible. Detailed investigation of the resolved spatial structure in the clouds towards Sgr B2(N) over the available field of view indicates that the structures of translucent molecular line-of-sight clouds are mostly homogeneous on scales smaller than about 15″ (0.6 pc), the available field of view. We investigated the turbulence properties of the absorbing clouds by analysing the probability distribution functions of their opacity maps and comparing the results to simulations. The homogeneous structures on these scales are produced by a solenoidal forcing of the turbulence (divergence free), which causes only small density contrasts on these scales in the clouds. Only in a few cases structures smaller than this field of view are seen.

We detected many molecules and for many of them also their less abundant isotopologues in absorption along the line of sight to Sgr B2, which allowed us to determine several isotopic ratios matching previously determined results. We measured the isotopic ratio $^{14}N/^{15}N$ directly in the envelope of Sgr B2 to be 350 ± 53 and found to be consistent with the value extrapolated from previous measurements at larger galactocentric radii. The ratios between the abundances of molecules we found indicate that the chemical contents of diffuse molecular clouds and translucent molecular clouds are similar. However, the abundances of HCO^+ and CS are enhanced in translucent molecular clouds compared to diffuse molecular clouds. The molecules CH_3OH, SiO, and SO trace a shock component in line-of-sight clouds. In contrast, CCH, HCN, HNC, CS, and CN trace a quiescent component. The molecules CCH and CN are good tracers of H_2 column density over a range of cloud types, from diffuse to translucent.

In the envelope of Sgr B2 we detected seven complex organic molecules, of which four are also detected in GC clouds and two of them in the translucent clouds associated with the Scutum arm. The COM composition of one of the translucent GC clouds is found to be generally similar to that of the diffuse/translucent medium of the $z = 0.89$ spiral galaxy in front of the distant quasar PKS 1830–211, suggesting that the chemical processes leading to chemical complexity have remained similar since $z = 0.89$, i.e., a lookback time of more than half the age of the Universe. The presence of COMs in the translucent molecular clouds may result from a cyclical interstellar process of cloud contraction and expansion between diffuse and dense states.

Our analysis of the structure of the translucent clouds detected in absorption towards Sgr B2 is limited by two factors: the limited size of the continuum background emission, which results from the spatial

filtering of the interferometer, and the finite angular resolution. Combining the ALMA main array data with measurements performed with the Atacama Compact Array, which is sensitive to larger angular scales, would allow us to extend the analysis to scales exceeding 15″. The investigation of the velocity structure and the molecular correlations of the line-of-sight clouds detected in absorption towards Sgr B2 can be extended and improved by mainly one factor: The detection of more velocity components of less abundant molecules using measurements with higher sensitivity.

Bibliography

Adande, G. R. & Ziurys, L. M. 2012, ApJ, 744, 194 (Cited on page 45.)

Ando, R., Kohno, K., Tamura, Y., et al. 2016, PASJ, 68, 6 (Cited on page 63.)

Arnett, W. D. 1971, ApJ, 166, 153 (Cited on pages 4 and 59.)

Babamoradi, H., van den Berg, F., & Rinnan, A. 2013, Chemometrics and Intelligent Laboratory Systems, 120, 97 (Cited on pages 66 and 289.)

Belloche, A., Meshcheryakov, A. A., Garrod, R. T., et al. 2017, A&A, 601, A49 (Cited on page 52.)

Belloche, A., Müller, H. S. P., Garrod, R. T., & Menten, K. M. 2016, A&A, 587, A91 (Cited on pages 7, 9, 10, 11, 22, 50, 52, 59, 60 and 61.)

Belloche, A., Müller, H. S. P., Menten, K. M., Schilke, P., & Comito, C. 2013, A&A, 559, A47 (Cited on pages 7, 16, 22, 28, 29, 42, 89, 97 and 99.)

Bergin, E. A., Phillips, T. G., Comito, C., et al. 2010, A&A, 521, L20 (Cited on page 53.)

Bergner, J. B., Öberg, K. I., Garrod, R. T., & Graninger, D. M. 2017, ApJ, 841, 120 (Cited on page 54.)

Bogey, M., Demuynck, C., & Destombes, J. L. 1982, Journal of Molecular Spectroscopy, 95, 35 (Cited on page 74.)

Bonfand, M., Belloche, A., Menten, K. M., Garrod, R. T., & Müller, H. S. P. 2017, A&A, 604, A60 (Cited on pages 5, 59 and 61.)

Botschwina, P., Horn, M., Flügge, J., & Seeger, S. 1993, J. Chem. Soc., Faraday Trans., 89, 2219 (Cited on page 90.)

Cazzoli, G., Puzzarini, C., & Gauss, J. 2005, ApJS, 159, 181 (Cited on page 74.)

Cazzoli, G., Puzzarini, C., & Lapinov, A. V. 2004, ApJ, 611, 615 (Cited on pages 74 and 90.)

Corby, J. F., Jones, P. A., Cunningham, M. R., et al. 2015, MNRAS, 452, 3969 (Cited on pages 6, 7, 22, 42, 50, 53, 59 and 103.)

Corby, J. F., McGuire, B. A., Herbst, E., & Remijan, A. J. 2018, A&A, 610, A10 (Cited on pages 7, 22, 41, 59, 97, 99, 100 and 104.)

Cox, P., Guesten, R., & Henkel, C. 1988, A&A, 206, 108 (Cited on page 67.)

Csengeri, T., Weiss, A., Wyrowski, F., et al. 2016, A&A, 585, A104 (Cited on page 5.)

Dahmen, G., Huttemeister, S., Wilson, T. L., & Mauersberger, R. 1998, A&A, 331, 959 (Cited on page 4.)

Dahmen, G., Wilson, T. L., & Matteucci, F. 1995, A&A, 295, 194 (Cited on pages 29, 45 and 47.)

De Pree, C. G., Goss, W. M., & Gaume, R. A. 1998, ApJ, 500, 847 (Cited on page 5.)

De Pree, C. G., Peters, T., Mac Low, M. M., et al. 2015, ApJ, 815, 123 (Cited on page 5.)

Draine, B. T. 2011, Physics of the Interstellar and Intergalactic Medium (Cited on pages 1 and 12.)

Dumouchel, F., Faure, A., & Lique, F. 2010, MNRAS, 406, 2488 (Cited on page 90.)

Endres, C. P., Schlemmer, S., Schilke, P., Stutzki, J., & Müller, H. S. P. 2016, Journal of Molecular Spectroscopy, 327, 95 (Cited on pages 16 and 66.)

Evans, J. D. 1996, Straightforward statistics for the behavioral sciences (Cited on pages 19 and 38.)

Federrath, C. & Klessen, R. S. 2013, ApJ, 763, 51 (Cited on page 101.)

Federrath, C., Klessen, R. S., & Schmidt, W. 2008, ApJ, 688, L79 (Cited on pages 81, 101 and 102.)

Federrath, C., Roman-Duval, J., Klessen, R. S., Schmidt, W., & Mac Low, M.-M. 2010, A&A, 512, A81 (Cited on pages 81, 83, 85, 101 and 102.)

Ferrière, K., Gillard, W., & Jean, P. 2007, A&A, 467, 611 (Cited on page 4.)

Flower, D. R. 1999, MNRAS, 305, 651 (Cited on page 90.)

Frerking, M. A., Wilson, R. W., Linke, R. A., & Wannier, P. G. 1980, ApJ, 240, 65 (Cited on page 45.)

Fuente, A., Navarro, D., Caselli, P., et al. 2018, submitted to A&A, arXiv:1809.04978 (Cited on pages 94 and 102.)

Gardner, F. F. & Whiteoak, J. B. 1982, MNRAS, 199, 23P (Cited on pages 31, 67 and 103.)

Garrod, R. T., Wakelam, V., & Herbst, E. 2007, A&A, 467, 1103 (Cited on page 53.)

Garrod, R. T., Williams, D. A., Hartquist, T. W., Rawlings, J. M. C., & Viti, S. 2005, MNRAS, 356, 654 (Cited on pages 54 and 55.)

Garrod, R. T., Williams, D. A., & Rawlings, J. M. C. 2006, MNRAS, 373, 577 (Cited on pages 54 and 55.)

Garwood, R. W. & Dickey, J. M. 1989, ApJ, 338, 841 (Cited on pages 70, 97, 99 and 104.)

Gaume, R. A., Claussen, M. J., de Pree, C. G., Goss, W. M., & Mehringer, D. M. 1995, ApJ, 449, 663 (Cited on pages 5, 24, 50, 59, 60, 63 and 64.)

Gerin, M., de Luca, M., Black, J., et al. 2010a, A&A, 518, L110 (Cited on pages 7, 42 and 99.)

Gerin, M., de Luca, M., Goicoechea, J. R., et al. 2010b, A&A, 521, L16 (Cited on page 97.)

Gerin, M., Kaźmierczak, M., Jastrzebska, M., et al. 2011, A&A, 525, A116 (Cited on pages 43, 44, 46, 97 and 98.)

Gerin, M., Liszt, H., Neufeld, D., et al. 2018, accepted by A&A, arXiv:1811.02679 (Cited on page 26.)

Giannetti, A., Leurini, S., Wyrowski, F., et al. 2017, A&A, 603, A33 (Cited on page 62.)

Godard, B., Falgarone, E., Gerin, M., Hily-Blant, P., & de Luca, M. 2010, A&A, 520, A20 (Cited on pages 6, 43, 44, 46, 50, 63, 98 and 345.)

Goicoechea, J. R., Pety, J., Gerin, M., Hily-Blant, P., & Le Bourlot, J. 2009, A&A, 498, 771 (Cited on page 52.)

Goldsmith, P. F. & Langer, W. D. 1999, ApJ, 517, 209 (Cited on pages 17 and 18.)

Goorvitch, D. 1994, ApJS, 95, 535 (Cited on page 90.)

Gottlieb, C. A., Myers, P. C., & Thaddeus, P. 2003, ApJ, 588, 655 (Cited on page 74.)

Gratier, P., Bron, E., Gerin, M., et al. 2017, A&A, 599, A100 (Cited on page 65.)

Gratier, P., Pety, J., Guzmán, V., et al. 2013, A&A, 557, A101 (Cited on page 52.)

Greaves, J. S. 1995, MNRAS, 273, 918 (Cited on page 93.)

Greaves, J. S., White, G. J., Ohishi, M., Hasegawa, T., & Sunada, K. 1992, A&A, 260, 381 (Cited on pages 4, 50 and 59.)

Greaves, J. S. & Williams, P. G. 1994, A&A, 290, 259 (Cited on pages 5, 7, 22, 29, 59, 60, 61, 63, 67, 97 and 100.)

Guzmán, V. V., Goicoechea, J. R., Pety, J., et al. 2013, A&A, 560, A73 (Cited on page 52.)

Guzmán, V. V., Pety, J., Gratier, P., et al. 2014, Faraday Discussions, 168, 103 (Cited on pages 6, 50 and 52.)

Halfen, D. T., Woolf, N. J., & Ziurys, L. M. 2017, ApJ, 845, 158 (Cited on page 103.)

Henshaw, J. D., Longmore, S. N., Kruijssen, J. M. D., et al. 2016, MNRAS, 457, 2675 (Cited on page 5.)

Herbst, E. & van Dishoeck, E. F. 2009, ARA&A, 47, 427 (Cited on pages 6, 16 and 50.)

Heyer, M. H. & Peter Schloerb, F. 1997, ApJ, 475, 173 (Cited on page 65.)

Hieret, C. O. 2005, Absorption studies along the line of sight towards Sgr B2(M), diploma thesis (Cited on pages 16, 22 and 59.)

Huettemeister, S., Wilson, T. L., Mauersberger, R., et al. 1995, A&A, 294, 667 (Cited on pages 32 and 70.)

Indriolo, N., Neufeld, D. A., Gerin, M., et al. 2015, ApJ, 800, 40 (Cited on page 51.)

Jones, P. A., Burton, M. G., Cunningham, M. R., et al. 2008, MNRAS, 386, 117 (Cited on pages 61, 89, 92 and 94.)

Jones, P. A., Burton, M. G., Cunningham, M. R., et al. 2012, MNRAS, 419, 2961 (Cited on pages 4 and 5.)

Kauffmann, J., Bertoldi, F., Bourke, T. L., Evans, II, N. J., & Lee, C. W. 2008, A&A, 487, 993 (Cited on page 81.)

Klessen, R. S. 2000, ApJ, 535, 869 (Cited on page 101.)

Kritsuk, A. G., Norman, M. L., Padoan, P., & Wagner, R. 2007, ApJ, 665, 416 (Cited on page 101.)

Kruijssen, J. M. D., Longmore, S. N., Elmegreen, B. G., et al. 2014, MNRAS, 440, 3370 (Cited on page 4.)

Ladd, N., Purcell, C., Wong, T., & Robertson, S. 2005, PASA, 22, 62 (Cited on page 90.)

Lang, C. C., Goss, W. M., Cyganowski, C., & Clubb, K. I. 2010, ApJS, 191, 275 (Cited on pages 32 and 70.)

Lique, F., Spielfiedel, A., & Cernicharo, J. 2006, A&A, 451, 1125 (Cited on page 90.)

Lis, D. C. & Goldsmith, P. F. 1990, ApJ, 356, 195 (Cited on pages 5 and 59.)

Lis, D. C., Phillips, T. G., Goldsmith, P. F., et al. 2010, A&A, 521, L26 (Cited on pages 7, 22, 29, 59 and 67.)

Liszt, H. 1994, ApJ, 429, 638 (Cited on page 5.)

Liszt, H. & Gerin, M. 2018, A&A, 610, A49 (Cited on page 103.)

Liszt, H., Gerin, M., Beasley, A., & Pety, J. 2018, ApJ, 856, 151 (Cited on pages 95 and 345.)

Liszt, H. & Lucas, R. 2002, A&A, 391, 693 (Cited on page 6.)

Liszt, H., Sonnentrucker, P., Cordiner, M., & Gerin, M. 2012, ApJ, 753, L28 (Cited on page 63.)

Liszt, H. S. & Pety, J. 2016, ApJ, 823, 124 (Cited on page 91.)

Liszt, H. S., Pety, J., & Lucas, R. 2010, A&A, 518, A45 (Cited on pages 3, 89 and 93.)

Liszt, H. S. & Wilson, R. W. 1993, ApJ, 403, 663 (Cited on page 5.)

Liu, S.-Y. & Snyder, L. E. 1999, ApJ, 523, 683 (Cited on pages 5 and 59.)

Longmore, S. N., Bally, J., Testi, L., et al. 2013, MNRAS, 429, 987 (Cited on page 4.)

Lucas, R. & Liszt, H. S. 1996, in IAU Symposium, Vol. 178, Molecules in Astrophysics: Probes & Processes, ed. E. F. van Dishoeck, 421 (Cited on pages 6, 7 and 98.)

Lucas, R. & Liszt, H. S. 1997, in IAU Symposium, Vol. 178, IAU Symposium, ed. E. F. van Dishoeck, 421–430 (Cited on pages 6 and 50.)

Lucas, R. & Liszt, H. S. 1999, in The Physics and Chemistry of the Interstellar Medium, ed. V. Ossenkopf, J. Stutzki, & G. Winnewisser (Cited on page 63.)

Lucas, R. & Liszt, H. S. 2000, A&A, 358, 1069 (Cited on pages 6, 44, 97 and 98.)

Lucas, R. & Liszt, H. S. 2002, A&A, 384, 1054 (Cited on pages 43, 44 and 46.)

Magnani, L., Larosa, T. N., & Shore, S. N. 1993, ApJ, 402, 226 (Cited on page 102.)

Magnani, L. & Shore, S. N., eds. 2017, Astrophysics and Space Science Library, Vol. 442, A Dirty Window - Diffuse and Translucent Molecular Gas in the Interstellar Medium (Cited on pages 1, 2 and 3.)

Maret, S., Hily-Blant, P., Pety, J., Bardeau, S., & Reynier, E. 2011, A&A, 526, A47 (Cited on pages 13, 24, 31, 50, 62 and 89.)

McGuire, B. A. 2018, accepted in ApJS, arXiv:1809.09132 (Cited on page 6.)

Mehringer, D. M., Palmer, P., Goss, W. M., & Yusef-Zadeh, F. 1993, ApJ, 412, 684 (Cited on page 5.)

Menten, K. M., Wyrowski, F., Belloche, A., et al. 2011, A&A, 525, A77 (Cited on pages 5, 22, 29, 42, 51, 52, 60, 67 and 99.)

Milam, S. N., Savage, C., Brewster, M. A., Ziurys, L. M., & Wyckoff, S. 2005, ApJ, 634, 1126 (Cited on pages 29, 45, 47, 52 and 103.)

Mills, E. A. C., Corby, J., Clements, A. R., et al. 2018, accepted by ApJ, arXiv:1810.12852 (Cited on page 59.)

Molinari, S., Bally, J., Glover, S., et al. 2014, Protostars and Planets VI, 125 (Cited on page 4.)

Monje, R. R., Emprechtinger, M., Phillips, T. G., et al. 2011, ApJ, 734, L23 (Cited on pages 7, 22, 29, 59 and 67.)

Monson, N. N., Morris, M. R., & Young, E. D. 2017, ApJ, 839, 123 (Cited on page 45.)

Morris, M. & Serabyn, E. 1996, ARA&A, 34, 645 (Cited on page 4.)

Müller, H. S. P., Belloche, A., Xu, L.-H., et al. 2016, A&A, 587, A92 (Cited on page 52.)

Müller, H. S. P., Menten, K. M., & Mäder, H. 2004, A&A, 428, 1019 (Cited on page 74.)

Müller, H. S. P., Schlöder, F., Stutzki, J., & Winnewisser, G. 2005, Journal of Molecular Structure, 742, 215 (Cited on pages 16, 51 and 66.)

Müller, H. S. P., Spezzano, S., Bizzocchi, L., et al. 2013, Journal of Physical Chemistry A, 117 (Cited on page 74.)

Müller, H. S. P., Thorwirth, S., Roth, D. A., & Winnewisser, G. 2001, A&A, 370, L49 (Cited on pages 16, 51 and 66.)

Muller, S., Beelen, A., Black, J. H., et al. 2013, A&A, 551, A109 (Cited on page 52.)

Muller, S., Beelen, A., Guélin, M., et al. 2011, A&A, 535, A103 (Cited on pages 6, 50 and 52.)

Muller, S., Combes, F., Guélin, M., et al. 2014, A&A, 566, A112 (Cited on pages 6 and 50.)

Neill, J. L., Bergin, E. A., Lis, D. C., et al. 2014, ApJ, 789, 8 (Cited on pages 32 and 70.)

Neufeld, D. A., Ashby, M. L. N., Bergin, E. A., et al. 2000, ApJ, 539, L111 (Cited on pages 7, 22, 29, 59 and 67.)

Neufeld, D. A., Godard, B., Gerin, M., et al. 2015, A&A, 577, A49 (Cited on pages 65 and 66.)

Neufeld, D. A., Wolfire, M. G., & Schilke, P. 2005, ApJ, 628, 260 (Cited on page 3.)

Nummelin, A., Bergman, P., Hjalmarson, Å., et al. 2000, ApJS, 128, 213 (Cited on pages 29, 45 and 47.)

Ossenkopf-Okada, V., Csengeri, T., Schneider, N., Federrath, C., & Klessen, R. S. 2016, A&A, 590, A104 (Cited on pages 65, 80 and 101.)

Padoan, P., Nordlund, A., & Jones, B. J. T. 1997, MNRAS, 288, 145 (Cited on pages 81, 83 and 101.)

Passot, T. & Vázquez-Semadeni, E. 1998, Phys. Rev. E, 58, 4501 (Cited on pages 83 and 101.)

Patil, A., Huard, D., & Fonnesbeck, C. 2010, JStatSoft, 35, 1 (Cited on page 62.)

Pedregosa, F., Varoquaux, G., Gramfort, A., et al. 2011, Journal of Machine Learning Research, 12, 2825 (Cited on page 66.)

Penzias, A. A. 1981, ApJ, 249, 513 (Cited on pages 29, 45 and 47.)

Pety, J., Schinnerer, E., Leroy, A. K., et al. 2013, ApJ, 779, 43 (Cited on pages 4 and 59.)

Pety, J., Teyssier, D., Fossé, D., et al. 2005, A&A, 435, 885 (Cited on page 52.)

Pickett, H. M., Poynter, R. L., Cohen, E. A., et al. 1998, J. Quant. Spectr. Rad. Transf., 60, 883 (Cited on pages 15, 16, 51 and 66.)

Polehampton, E. T., Baluteau, J.-P., & Swinyard, B. M. 2005, A&A, 437, 957 (Cited on pages 7, 22 and 59.)

Powell, M. J. D. 1964, The Computer Journal, 7, 155 (Cited on page 63.)

Price, R. J., Viti, S., & Williams, D. A. 2003, MNRAS, 343, 1257 (Cited on pages 54 and 55.)

Qin, S.-L., Schilke, P., Comito, C., et al. 2010, A&A, 521, L14 (Cited on pages 96 and 344.)

Reid, M. J., Menten, K. M., Brunthaler, A., et al. 2014, ApJ, 783, 130 (Cited on pages 5, 22, 50 and 59.)

Remijan, A., e. 2015, ALMA Cycle 3 Technical Handbook Version 1.0, ALMA (Cited on pages 14 and 15.)

Sánchez-Monge, Á., Schilke, P., Schmiedeke, A., et al. 2017, A&A, 604, A6 (Cited on pages 5 and 59.)

Sawada, T., Hasegawa, T., Sugimoto, M., Koda, J., & Handa, T. 2012, ApJ, 752, 118 (Cited on pages 3 and 59.)

Saykally, R. J., Szanto, P. G., Anderson, T. G., & Woods, R. C. 1976, ApJ, 204, L143 (Cited on page 74.)

Schmid-Burgk, J., Muders, D., Müller, H. S. P., & Brupbacher-Gatehouse, B. 2004, A&A, 419, 949 (Cited on page 74.)

Schneider, N., André, P., Könyves, V., et al. 2013, ApJ, 766, L17 (Cited on pages 65 and 100.)

Schneider, N., Csengeri, T., Klessen, R. S., et al. 2015a, A&A, 578, A29 (Cited on page 101.)

Schneider, N., Ossenkopf, V., Csengeri, T., et al. 2015b, A&A, 575, A79 (Cited on page 101.)

Schöier, F. L., van der Tak, F. F. S., van Dishoeck, E. F., & Black, J. H. 2005, A&A, 432, 369 (Cited on page 90.)

Sheffer, Y., Rogers, M., Federman, S. R., et al. 2008, ApJ, 687, 1075 (Cited on pages 96 and 344.)

Shetty, R., Beaumont, C. N., Burton, M. G., Kelly, B. C., & Klessen, R. S. 2012, MNRAS, 425, 720 (Cited on page 4.)

Shore, S. N., Larosa, T. N., Chastain, R. J., & Magnani, L. 2006, A&A, 457, 197 (Cited on page 102.)

Shore, S. N., Larosa, T. N., Magnani, L., Chastain, R. J., & Costagliola, F. 2007, in IAU Symposium, Vol. 237, Triggered Star Formation in a Turbulent ISM, ed. B. G. Elmegreen & J. Palous, 17–23 (Cited on page 102.)

Shore, S. N., Magnani, L., LaRosa, T. N., & McCarthy, M. N. 2003, ApJ, 593, 413 (Cited on page 102.)

Snow, T. P. & McCall, B. J. 2006, ARA&A, 44, 367 (Cited on pages 2, 3, 4, 54, 58, 59, 81, 93 and 101.)

Spezzano, S., Caselli, P., Bizzocchi, L., Giuliano, B. M., & Lattanzi, V. 2017, A&A, 606, A82 (Cited on page 65.)

Spezzano, S., Tamassia, F., Thorwirth, S., et al. 2012, ApJS, 200, 1 (Cited on page 74.)

Suutarinen, A., Geppert, W. D., Harju, J., et al. 2011, A&A, 531, A121 (Cited on page 96.)

Taquet, V., López-Sepulcre, A., Ceccarelli, C., et al. 2015, ApJ, 804, 81 (Cited on page 52.)

Thiel, V., Belloche, A., Menten, K. M., Garrod, R. T., & Müller, H. S. P. 2017, A&A, 605, L6 (Cited on pages 25, 67 and 95.)

Tiemann, E. 1974, Journal of Molecular Spectroscopy, 51, 316 (Cited on page 74.)

Tremblin, P., Schneider, N., Minier, V., et al. 2014, A&A, 564, A106 (Cited on page 79.)

Turner, B. E. 1998, ApJ, 501, 731 (Cited on pages 53 and 54.)

Turner, B. E., Lee, H.-H., & Herbst, E. 1998, ApJS, 115, 91 (Cited on pages 53 and 54.)

Turner, B. E., Terzieva, R., & Herbst, E. 1999, ApJ, 518, 699 (Cited on pages 53 and 54.)

van der Tak, F. F. S., Black, J. H., Schöier, F. L., Jansen, D. J., & van Dishoeck, E. F. 2007, A&A, 468, 627 (Cited on page 90.)

van der Tak, F. F. S., Müller, H. S. P., Harding, M. E., & Gauss, J. 2009, A&A, 507, 347 (Cited on page 74.)

van Dishoeck, E. F. & Black, J. H. 1988, ApJ, 334, 771 (Cited on page 2.)

Vastel, C., Ceccarelli, C., Lefloch, B., & Bachiller, R. 2014, ApJ, 795, L2 (Cited on page 53.)

Whiteoak, J. B. & Gardner, F. F. 1978, Proceedings of the Astronomical Society of Australia, 3, 266 (Cited on page 67.)

Wiesemeyer, H., Güsten, R., Heyminck, S., et al. 2016, A&A, 585, A76 (Cited on pages 41, 63 and 99.)

Wilson, T. L. & Rood, R. 1994, ARA&A, 32, 191 (Cited on pages 29, 45 and 47.)

Winkel, B., Wiesemeyer, H., Menten, K. M., et al. 2017, A&A, 600, A2 (Cited on pages 53, 54 and 283.)

Wirström, E. S., Bergman, P., Black, J. H., et al. 2010, A&A, 522, A19 (Cited on page 103.)

Wouterloot, J. G. A., Henkel, C., Brand, J., & Davis, G. R. 2008, A&A, 487, 237 (Cited on pages 29, 45 and 47.)

Yang, B., Stancil, P. C., Balakrishnan, N., & Forrey, R. C. 2010, ApJ, 718, 1062 (Cited on page 90.)

Appendix A

Chemical and physical properties of the line-of-sight clouds to Sgr B2

A.1 Continuum levels

Table A.1: Continuum and noise levels of the spectra towards K4 and $K6_{shell}$.

Setup	SPW[a]	K4				$K6_{shell}$			
		o[b]	T_c[c] [K]	σ_{RMS}[d] [K]	SNR[e]	o[b]	T_c[c] [K]	σ_{RMS}[d] [K]	SNR[e]
1	0	2	9.8	0.21	46.1	2	11.5	0.22	52.7
1	1	2	10.3	0.24	43.2	2	11.4	0.23	49.5
1	2	2	8.5	0.24	34.7	1	9.3	0.22	41.6
1	3	1	8.3	0.25	33.2	1	9.0	0.23	38.5
2	0	3	11.6	0.23	51.3	2	10.8	0.21	50.7
2	1	1	11.8	0.22	54.9	2	12.0	0.21	57.6
2	2	1	11.2	0.21	54.5	1	9.9	0.22	46.0
2	3	2	10.7	0.24	45.3	2	9.6	0.21	45.3
3	0	2	8.0	0.20	40.2	2	10.5	0.19	54.7
3	1	4	7.8	0.19	40.5	2	10.6	0.17	63.1
3	2	3	7.7	0.22	35.2	2	8.6	0.19	44.4
3	3	4	8.1	0.23	35.9	2	8.4	0.20	41.5
4	0	2	10.4	0.16	63.4	2	9.9	0.16	62.4
4	1	1	10.4	0.16	65.4	2	9.7	0.16	61.7
4	2	4	9.6	0.20	47.7	2	7.3	0.18	39.4
4	3	2	9.7	0.21	46.5	2	7.1	0.21	33.5
5	0	2	10.9	0.23	48.0	1	10.4	0.21	50.6
5	1	1	10.4	0.22	46.2	2	9.8	0.20	50.0
5	2	4	8.4	0.29	28.6	2	6.0	0.27	22.3
5	3	1	8.2	0.33	25.3	1	5.5	0.29	19.1

Notes. [a] Spectral window. [b] Polynomial order of function used to fit the baseline of the spectral window. [c] Mean continuum level of the spectral window. [d] Noise level. [e] Signal-to-noise ratio of the mean continuum level.

Table A.2: Continuum and noise levels of the spectra towards $K5_{shell}$ and $K6_{shell,a}$.

Setup	SPW[a]	$K5_{shell}$				$K6_{shell,a}$			
		o[b]	T_c[c] [K]	σ_{RMS}[d] [K]	SNR[e]	o[b]	T_c[c] [K]	σ_{RMS}[d] [K]	SNR[e]
1	0	2	3.7	0.21	17.7	2	8.2	0.22	37.1
1	1	3	3.8	0.19	19.7	3	8.7	0.22	40.3
1	2	1	2.8	0.21	13.0	1	7.2	0.22	33.2
1	3	2	2.8	0.20	13.6	1	7.0	0.23	30.7
2	0	2	5.3	0.19	28.1	2	7.7	0.21	37.5
2	1	2	5.5	0.21	26.6	1	8.7	0.21	41.4
2	2	3	3.9	0.22	18.0	1	8.0	0.20	40.1
2	3	2	3.7	0.22	17.0	2	7.9	0.20	38.5
3	0	1	4.1	0.20	21.0	2	7.4	0.20	37.6
3	1	4	3.9	0.17	22.6	2	7.6	0.17	45.4
3	2	5	2.9	0.19	15.3	2	6.1	0.20	31.4
3	3	2	3.2	0.20	15.9	2	5.9	0.22	26.7
4	0	2	4.0	0.15	26.0	2	7.5	0.15	49.9
4	1	3	3.8	0.16	24.1	2	7.5	0.16	47.2
4	2	2	3.1	0.17	18.6	4	5.7	0.17	32.7
4	3	2	3.3	0.20	16.5	2	5.6	0.23	24.9
5	0	2	4.1	0.22	18.9	2	7.8	0.21	37.1
5	1	1	4.0	0.21	19.0	1	7.1	0.21	34.5
5	2	2	3.0	0.25	12.1	2	4.8	0.27	17.8
5	3	2	3.0	0.31	9.6	1	4.7	0.32	14.6

Notes. See Notes of Table A.1.

Table A.3: Continuum and noise levels of the spectra towards I and L.

Setup	SPW[a]	I				L			
		o[b]	T_c[c] [K]	σ_{RMS}[d] [K]	SNR[e]	o[b]	T_c[c] [K]	σ_{RMS}[d] [K]	SNR[e]
1	0	2	50.3	0.93	54.4	2	12.7	0.57	22.5
1	1	4	49.7	0.96	51.5	5	12.8	0.55	23.4
1	2	4	39.5	1.37	28.8	1	11.5	0.81	14.1
1	3	2	38.7	1.47	26.3	2	10.3	0.86	12.0
2	0	5	47.7	1.05	45.3	4	10.0	0.54	18.5
2	1	4	52.3	1.17	44.8	4	12.9	0.62	20.8
2	2	1	43.4	1.49	29.1	6	11.9	0.77	15.5
2	3	5	42.0	1.59	26.5	4	9.6	0.81	11.8
3	0	5	42.1	1.00	42.1	3	10.5	0.54	19.5
3	1	5	44.4	0.97	45.9	4	9.7	0.54	18.1
3	2	5	37.4	1.60	23.4	2	7.7	0.78	9.8
3	3	5	37.1	1.84	20.2	4	6.8	0.87	7.8
4	0	5	43.9	0.92	47.5	2	11.4	0.51	22.3
4	1	6	42.3	0.92	45.8	5	10.3	0.54	19.1
4	2	5	28.0	1.64	17.1	4	9.1	0.82	11.2
4	3	4	24.3	1.89	12.8	4	8.0	0.95	8.4
5	0	1	40.1	1.43	28.0	2	7.4	0.74	10.0
5	1	4	38.4	1.51	25.5	4	7.2	0.78	9.2
5	2	2	37.1	2.68	13.9	4	4.7	1.12	4.2
5	3	2	34.3	3.52	9.7	2	0.1	1.29	0.1

Notes. See Notes of Table A.1.

A.2 Transitions

Table A.4: Molecular transitions detected in absorption towards K4 and $K6_{shell}$.

Molecule		Transition	$\nu_0{}^a$ [MHz]	E_{up}/k^b [K]	$A_{u,l}{}^c$ [s^{-1}]
Acetaldehyde	CH_3CHO	$2_{1,2,0}$–$1_{0,1,0}$	84219.749	5.0	2.38×10^{-6}
		$5_{1,5,0}$–$4_{1,4,0}$	93580.909	15.7	2.63×10^{-5}
		$5_{1,5,1}$–$4_{1,4,1}$	93595.235	15.8	2.63×10^{-5}
		$5_{0,5,2}$–$4_{0,4,2}$	95947.437	13.9	2.95×10^{-5}
		$5_{0,5,0}$–$4_{0,4,0}$	95963.459	13.8	2.95×10^{-5}
		$5_{1,4,2}$–$4_{1,3,2}$	98863.314	16.6	3.10×10^{-5}
		$5_{1,4,0}$–$4_{1,3,0}$	98900.944	16.5	3.11×10^{-5}
		$3_{1,3,1}$–$2_{0,2,2}$	101343.441	7.7	3.91×10^{-6}
		$3_{1,3,0}$–$2_{0,2,0}$	101892.414	7.7	4.04×10^{-6}
		$6_{1,6,0}$–$5_{1,5,0}$	112248.716	21.1	4.67×10^{-5}
		$6_{1,6,1}$–$5_{1,5,1}$	112254.508	21.2	4.67×10^{-5}
Acetonitrile	CH_3CN	$5_{0,0}$–$4_{0,0}$	91987.088	13.2	6.33×10^{-5}
		$6_{0,0}$–$5_{0,0}$	110383.500	18.5	1.11×10^{-4}
Carbon monosulfide	CS	2_0–1_0	97980.953	7.1	1.68×10^{-5}
	$C^{34}S$	2_0–1_0	96412.950	6.9	1.60×10^{-5}
	$C^{33}S$	2_0–1_0	92494.308	6.7	1.41×10^{-5}
	^{13}CS	$2_{0,2}$–$1_{0,2}$	97169.513	7.0	8.74×10^{-6}
		$2_{0,1}$–$1_{0,1}$	97171.840	7.0	1.36×10^{-5}
		$2_{0,3}$–$1_{0,2}$	97171.840	7.0	1.15×10^{-5}
		$2_{0,4}$–$1_{0,3}$	97171.840	7.0	1.64×10^{-5}
		$2_{0,3}$–$1_{0,3}$	97174.996	7.0	4.91×10^{-6}
		$2_{0,2}$–$1_{0,1}$	97175.271	7.0	6.82×10^{-6}
	$^{13}C^{34}S$	2–1	90926.026	6.5	1.34×10^{-5}
Carbon monoxide	^{13}CO	1–0	110201.354	5.3	6.33×10^{-8}
	$C^{18}O$	1–0	109782.173	5.3	6.27×10^{-8}
	$C^{17}O$	1_2–0_3	112358.777	5.4	6.70×10^{-8}
		1_4–0_3	112358.982	5.4	6.70×10^{-8}
		1_3–0_3	112360.007	5.4	6.70×10^{-8}
Carbonyl sulfide	OCS	7–6	85139.103	16.3	1.71×10^{-6}
		8–7	97301.208	21.0	2.58×10^{-6}
		9–8	109463.063*	26.3	3.70×10^{-6}
Cyanoacetylene	HC_3N	10–9	90979.023	24.0	5.81×10^{-5}
		11–10	100076.392	28.8	7.77×10^{-5}

Notes. The transitions marked with a star have a peak intensity lower than $3\sigma_{RMS}$. They are seen in the synthetic spectrum. Hence, they are listed here and labelled in the spectrum. [(a)]Rest frequency. [(b)]Upper energy level. [(c)]Einstein coefficient.

Table A.4: Continued.

Molecule		Transition	$\nu_0{}^a$ [MHz]	$E_{\rm up}/k^b$ [K]	$A_{\rm u,l}{}^c$ [s^{-1}]
		12–11	109173.634	34.1	1.01×10^{-4}
	$H^{13}CCCN$	10–9	88166.832	23.3	5.29×10^{-5}
		11–10	96983.001	27.9	7.07×10^{-5}
	$HC^{13}CCN$	10–9	90593.059	23.9	5.74×10^{-5}
		11–10	99651.849*	28.7	7.67×10^{-5}
	$HCC^{13}CN$	10–9	90601.777	23.9	5.74×10^{-5}
		11–10	99661.467*	28.7	7.67×10^{-5}
Cyanide radical	CN	$1_{0,1,1}$–$0_{0,1,1}$	113123.370	5.4	1.29×10^{-6}
		$1_{0,1,1}$–$0_{0,1,2}$	113144.157	5.4	1.05×10^{-5}
		$1_{0,1,2}$–$0_{0,1,1}$	113170.492	5.4	5.14×10^{-6}
		$1_{0,1,2}$–$0_{0,1,2}$	113191.279	5.4	6.68×10^{-6}
		$1_{0,2,2}$–$0_{0,1,1}$	113488.120	5.4	6.74×10^{-6}
		$1_{0,2,3}$–$0_{0,1,2}$	113490.970	5.4	1.19×10^{-5}
		$1_{0,2,1}$–$0_{0,1,1}$	113499.644	5.4	1.06×10^{-5}
		$1_{0,2,2}$–$0_{0,1,2}$	113508.907	5.4	5.19×10^{-6}
		$1_{0,2,1}$–$0_{0,1,2}$	113520.432	5.4	1.30×10^{-6}
	^{13}CN	$1_{1,1,1}$–$0_{1,1,2}$	108076.969	5.2	5.01×10^{-7}
		$1_{1,1,2}$–$0_{1,1,2}$	108091.335	5.2	4.88×10^{-7}
		$1_{1,0,1}$–$0_{1,1,0}$	108406.091	5.2	9.42×10^{-7}
		$1_{1,0,1}$–$0_{1,1,1}$	108412.862	5.2	3.14×10^{-6}
		$1_{1,0,1}$–$0_{1,1,2}$	108426.889	5.2	6.27×10^{-6}
		$1_{1,1,0}$–$0_{1,0,1}$	108631.121	5.2	9.58×10^{-6}
		$1_{1,1,1}$–$0_{1,0,1}$	108636.923	5.2	9.61×10^{-6}
		$1_{2,1,1}$–$0_{1,1,0}$	108638.212	5.2	3.59×10^{-6}
		$1_{2,1,2}$–$0_{1,1,1}$	108643.590	5.2	2.55×10^{-6}
		$1_{2,1,0}$–$0_{1,1,1}$	108644.346	5.2	9.58×10^{-6}
		$1_{2,1,1}$–$0_{1,1,1}$	108645.064	5.2	2.74×10^{-6}
		$1_{1,1,2}$–$0_{1,0,1}$	108651.297	5.2	9.78×10^{-6}
		$1_{2,1,2}$–$0_{1,1,2}$	108657.646	5.2	7.23×10^{-6}
		$1_{2,1,1}$–$0_{1,1,2}$	108658.948	5.2	3.33×10^{-6}
		$1_{2,2,3}$–$0_{1,1,2}$	108780.201	5.2	1.05×10^{-5}
		$1_{2,2,2}$–$0_{1,1,1}$	108782.374	5.2	7.75×10^{-6}
		$1_{2,2,1}$–$0_{1,1,0}$	108786.982	5.2	5.72×10^{-6}
		$1_{2,2,1}$–$0_{1,1,1}$	108793.753	5.2	4.47×10^{-6}
		$1_{2,2,2}$–$0_{1,1,2}$	108796.400	5.2	2.75×10^{-6}
		$1_{2,1,2}$–$0_{1,0,1}$	109217.567	5.2	6.91×10^{-7}
		$1_{2,1,0}$–$0_{1,0,1}$	109218.323	5.2	8.96×10^{-7}
		$1_{2,1,1}$–$0_{1,0,1}$	109218.919	5.2	8.07×10^{-7}
	$C^{15}N$	$1_{1,1}$–$0_{1,1}$	109689.610	5.3	7.10×10^{-6}
		$1_{1,1}$–$0_{1,0}$	109708.986*	5.3	3.67×10^{-6}

Notes. The transitions marked with a star have a peak intensity lower than $3\sigma_{\rm RMS}$. They are seen in the synthetic spectrum. Hence, they are listed here and labelled in the spectrum. [(a)]Rest frequency. [(b)]Upper energy level. [(c)]Einstein coefficient.

Table A.4: Continued.

Molecule		Transition	$\nu_0{}^a$ [MHz]	$E_{\rm up}/k^b$ [K]	$A_{\rm u,l}{}^c$ [s^{-1}]
		$1_{1,0}$–$0_{1,1}$	109733.657*	5.3	1.08×10^{-5}
		$1_{2,1}$–$0_{1,1}$	110004.091*	5.3	3.70×10^{-6}
		$1_{2,1}$–$0_{1,0}$	110023.540	5.3	7.16×10^{-6}
		$1_{2,2}$–$0_{1,1}$	110024.590	5.3	1.09×10^{-5}
Cyclopropenylidene	ortho c-C_3H_2	$2_{1,2}$–$1_{0,1}$	85338.894	4.1	2.32×10^{-5}
	para c-C_3H_2	$3_{2,2}$–$3_{1,3}$	84727.688	16.1	1.04×10^{-5}
	c-$CC^{13}CH_2$	$2_{1,2}$–$1_{0,1}$	84185.635	6.3	2.17×10^{-5}
Diazenylium	N_2H^+	$1_{1,0}$–$0_{1,1}$	93171.616	4.5	3.63×10^{-5}
		$1_{1,2}$–$0_{1,1}$	93171.911	4.5	5.62×10^{-6}
		$1_{1,2}$–$0_{1,2}$	93171.911	4.5	3.07×10^{-5}
		$1_{1,1}$–$0_{1,0}$	93172.048	4.5	1.85×10^{-5}
		$1_{1,1}$–$0_{1,1}$	93172.048	4.5	4.33×10^{-6}
		$1_{1,1}$–$0_{1,2}$	93172.048	4.5	1.35×10^{-5}
		$1_{2,2}$–$0_{1,1}$	93173.473	4.5	3.07×10^{-5}
		$1_{2,2}$–$0_{1,2}$	93173.473	4.5	5.62×10^{-6}
		$1_{2,3}$–$0_{1,2}$	93173.770	4.5	3.63×10^{-5}
		$1_{2,1}$–$0_{1,0}$	93173.964	4.5	1.14×10^{-5}
		$1_{2,1}$–$0_{1,1}$	93173.964	4.5	2.35×10^{-5}
		$1_{2,1}$–$0_{1,2}$	93173.964	4.5	1.43×10^{-6}
		$1_{0,1}$–$0_{1,0}$	93176.260	4.5	6.46×10^{-6}
		$1_{0,1}$–$0_{1,1}$	93176.260	4.5	8.45×10^{-6}
		$1_{0,1}$–$0_{1,2}$	93176.260	4.5	2.14×10^{-5}
	$^{15}NNH^+$	1_1–0_1	90263.487	4.3	3.30×10^{-5}
		1_2–0_1	90263.912	4.3	3.30×10^{-5}
		1_0–0_1	90264.504	4.3	3.30×10^{-5}
	$N^{15}NH^+$	1_1–0_1	91204.261	4.4	3.40×10^{-5}
		1_2–0_1	91205.991	4.4	3.40×10^{-5}
		1_0–0_1	91208.517	4.4	3.40×10^{-5}
Ethanol	C_2H_5OH	$4_{2,3,2}$–$4_{1,4,2}$	84595.868	13.4	3.25×10^{-6}
		$4_{1,4,2}$–$3_{0,3,2}$	90117.610	9.3	5.23×10^{-6}
		$7_{2,6,2}$–$7_{1,7,2}$	95909.250*	28.5	4.60×10^{-6}
		$2_{2,1,2}$–$1_{1,0,2}$	112807.174	7.5	1.07×10^{-5}
		$2_{2,0,2}$–$1_{1,1,2}$	114064.943	7.5	1.08×10^{-5}
		$5_{1,5,2}$–$4_{0,4,2}$	104808.632	13.4	8.34×10^{-6}
Ethynyl	CCH	$1_{2,1}$–$0_{1,1}$	87284.105	4.2	2.60×10^{-7}
		$1_{2,2}$–$0_{1,1}$	87316.898	4.2	1.53×10^{-6}
		$1_{2,1}$–$0_{1,0}$	87328.585	4.2	1.27×10^{-6}

Notes. The transitions marked with a star have a peak intensity lower than $3\sigma_{\rm RMS}$. They are seen in the synthetic spectrum. Hence, they are listed here and labelled in the spectrum. [(a)]Rest frequency. [(b)]Upper energy level. [(c)]Einstein coefficient.

Table A.4: Continued.

Molecule		Transition	$\nu_0{}^a$ [MHz]	$E_{\rm up}/k^b$ [K]	$A_{\rm u,l}{}^c$ [s^{-1}]
		$1_{1,1}$–$0_{1,1}$	87401.989	4.2	1.27×10^{-6}
		$1_{1,0}$–$0_{1,1}$	87407.165	4.2	1.54×10^{-6}
		$1_{1,1}$–$0_{1,0}$	87446.470	4.2	2.61×10^{-7}
	^{13}CCH	$1_{1,0,1}$–$0_{1,1,2}$	84151.054	4.1	4.41×10^{-7}
		$1_{2,1,1}$–$0_{1,0,1}$	84151.352	4.0	1.37×10^{-6}
		$1_{2,1,2}$–$0_{1,0,1}$	84153.305	4.0	1.37×10^{-6}
		$1_{1,0,1}$–$0_{1,1,1}$	84183.977*	4.1	9.31×10^{-7}
		$1_{1,1,1}$–$0_{1,1,2}$	84192.487*	4.1	9.31×10^{-7}
		$1_{1,1,2}$–$0_{1,1,2}$	84206.865	4.1	1.25×10^{-6}
	C^{13}CH	$1_{2,2,3}$–$0_{1,1,2}$	85229.335	4.1	1.42×10^{-6}
		$1_{2,2,2}$–$0_{1,1,1}$	85232.805	4.1	1.34×10^{-6}
		$1_{1,1,2}$–$0_{1,1,2}$	85307.459	4.1	1.29×10^{-6}
Formamide	NH_2CHO	$4_{0,4}$–$3_{0,3}$	84542.330	10.2	4.09×10^{-5}
		$4_{2,3}$–$3_{2,2}$	84807.795	22.1	3.09×10^{-5}
		$4_{2,2}$–$3_{2,1}$	85093.272	22.1	3.13×10^{-5}
		$4_{1,3}$–$3_{1,2}$	87848.874	13.5	4.30×10^{-5}
		$5_{1,5}$–$4_{1,4}$	102064.267	17.7	7.06×10^{-5}
		$2_{1,2}$–$1_{0,1}$	102217.573	5.9	2.71×10^{-6}
		$5_{0,5}$–$4_{0,4}$	105464.219	15.2	8.11×10^{-5}
		$5_{1,4}$–$4_{1,3}$	109753.503	18.8	8.78×10^{-5}
		$5_{2,4}$–$4_{2,3}$	105972.599	27.2	6.92×10^{-5}
		$5_{2,3}$–$4_{2,2}$	106541.680	27.2	7.03×10^{-5}
Formyl cation	HCO^+	1–0	89188.525	4.3	4.19×10^{-5}
	$H^{13}CO^+$	1–0	86754.288	4.2	3.85×10^{-5}
	$HC^{18}O^+$	1–0	85162.223	4.1	3.64×10^{-5}
	$HC^{17}O^+$	1–0	87057.535	4.2	3.89×10^{-5}
Hydrogen Cyanide	HCN	1_1–0_1	88630.416	4.3	2.41×10^{-5}
		1_2–0_1	88631.848	4.3	2.41×10^{-5}
		1_0–0_1	88633.936	4.3	2.41×10^{-5}
	H^{13}CN	1_1–0_1	86338.735	4.1	2.23×10^{-5}
		1_2–0_1	86340.167	4.1	2.23×10^{-5}
		1_0–0_1	86342.254	4.1	2.23×10^{-5}
	HC^{15}N	1–0	86054.966	4.1	2.20×10^{-5}
Hydrogen isocyanide	HNC	$1_{0,0}$–$0_{0,0}$	90663.568	4.4	2.69×10^{-5}
	HN^{13}C	1–0	87090.825	4.2	2.38×10^{-5}
	H^{15}NC	1–0	88865.715	4.3	1.98×10^{-5}

Notes. The transitions marked with a star have a peak intensity lower than $3\sigma_{\rm RMS}$. They are seen in the synthetic spectrum. Hence, they are listed here and labelled in the spectrum. [(a)]Rest frequency. [(b)]Upper energy level. [(c)]Einstein coefficient.

Table A.4: Continued.

Molecule		Transition	$\nu_0{}^a$ [MHz]	$E_{\rm up}/k^b$ [K]	$A_{\rm u,l}{}^c$ [s^{-1}]
Hydroxymethylidynium	HOC^+	$1_{0,0}$–$0_{0,0}$	89487.414	4.3	2.13×10^{-5}
Isocyanic acid	HNCO	$4_{0,4}$–$3_{0,3}$	87925.237	10.5	8.78×10^{-6}
		$5_{0,5}$–$4_{0,4}$	109905.749	15.8	1.75×10^{-5}
Methanol	CH_3OH	$2_{0,1,0}$–$1_{0,1,0}$	96741.371	7.0	3.41×10^{-6}
		$2_{-1,0,0}$–$1_{-1,0,0}$	96739.358	12.5	2.56×10^{-6}
		$0_{0,0,0}$–$1_{-1,1,0}$	108893.945	13.1	1.47×10^{-5}
	$^{13}CH_3OH$	$2_{0,2,0}$–$1_{0,1,0}$	94407.129	6.8	3.17×10^{-6}
		$0_{0,0,0}$–$1_{-1,1,0}$	109164.120	13.1	1.48×10^{-5}
Methylamine	CH_3NH_2	$1_{1,5}$–$1_{0,5}$	84305.236	6.6	2.28×10^{-6}
		$2_{1,5}$–$2_{0,5}$	84598.179	10.9	1.50×10^{-6}
		$3_{1,0}$–$3_{0,1}$	87782.492	17.0	6.31×10^{-6}
		$2_{0,2}$–$1_{0,3}$	88667.913	6.7	3.06×10^{-7}
		$2_{0,7}$–$1_{0,7}$	88668.704	7.0	3.06×10^{-7}
		$2_{0,5}$–$1_{0,5}$	88669.568	6.8	3.06×10^{-7}
		$2_{0,0}$–$1_{0,1}$	88669.679	6.4	3.06×10^{-7}
		$2_{-1,1}$–$2_{0,0}$	89081.457	10.7	6.55×10^{-6}
		$2_{1,0}$–$1_{-1,1}$	89554.651	10.8	2.36×10^{-7}
		$2_{1,2}$–$1_{-1,3}$	89557.402	10.6	2.36×10^{-7}
		$1_{1,0}$–$1_{0,1}$	89956.068	6.4	6.71×10^{-6}
		$4_{0,2}$–$3_{1,3}$	95145.812*	21.6	2.54×10^{-6}
Methyl mercaptan	CH_3SH	$4_{1,4,0}$–$3_{1,3,0}$	100110.189*	17.1	8.39×10^{-6}
		$4_{1,4,2}$–$3_{1,3,2}$	101029.707*	16.7	8.61×10^{-6}
		$4_{0,4,0}$–$3_{0,3,0}$	101139.111	12.1	9.23×10^{-6}
		$4_{1,3,1}$–$3_{1,2,0}$	101284.348*	18.3	8.69×10^{-6}
		$4_{1,3,0}$–$3_{1,2,0}$	102202.437	17.3	8.93×10^{-6}
		$1_{1,0,0}$–$1_{0,1,0}$	105998.314	6.3	3.85×10^{-6}
		$2_{1,1,0}$–$2_{0,2,0}$	106524.071	8.8	3.88×10^{-6}
Nitrogen sulfide cation	NS^+	2_2–1_2	100196.674	7.2	5.51×10^{-6}
		2_1–1_0	100196.982	7.2	1.23×10^{-5}
		2_2–1_1	100198.474	7.2	1.65×10^{-5}
		2_3–1_2	100198.613	7.2	2.21×10^{-5}
		2_1–1_1	100201.410	7.2	9.19×10^{-6}
Protonated carbon dioxide	$HOCO^+$	$4_{0,4}$–$3_{0,3}$	85531.497	10.3	2.36×10^{-5}
		$5_{0,5}$–$4_{0,4}$	106913.545	15.4	4.71×10^{-5}

Notes. The transitions marked with a star have a peak intensity lower than $3\sigma_{\rm RMS}$. They are seen in the synthetic spectrum. Hence, they are listed here and labelled in the spectrum. [(a)]Rest frequency. [(b)]Upper energy level. [(c)]Einstein coefficient.

Table A.4: Continued.

Molecule		Transition	$\nu_0{}^a$ [MHz]	E_{up}/k^b [K]	$A_{u,l}{}^c$ [s^{-1}]
Phosphorus nitride	PN	2–1	93979.769	6.8	2.92×10^{-5}
Silicon monoxide	SiO	2_0–1_0	86846.985	6.3	2.93×10^{-5}
	^{29}SiO	2_0–1_0	85759.194	6.2	2.82×10^{-5}
	^{30}SiO	2_0–1_0	84746.166	6.1	2.72×10^{-5}
Sulfur dioxide	SO_2	$3_{1,3}$–$2_{0,2}$	104029.418	7.7	1.01×10^{-5}
Sulfur monoxide	SO	2_3–1_2	99299.870	9.2	1.13×10^{-5}
	^{34}SO	2_3–1_2	97715.317	9.1	1.07×10^{-5}
Thioformaldehyde	ortho H_2CS	$3_{1,3}$–$2_{1,2}$	101477.810	8.1	1.26×10^{-5}
		$3_{1,2}$–$2_{1,1}$	104617.032	8.4	1.38×10^{-5}
	para H_2CS	$3_{0,3}$–$2_{0,2}$	103040.452	9.9	1.48×10^{-5}
Thioxoethenylidene	CCS	7_8–6_7	93870.107	19.9	3.74×10^{-5}

Notes. The transitions marked with a star have a peak intensity lower than $3\sigma_{RMS}$. They are seen in the synthetic spectrum. Hence, they are listed here and labelled in the spectrum. [(a)]Rest frequency. [(b)]Upper energy level. [(c)]Einstein coefficient.

A.3 Population diagrams

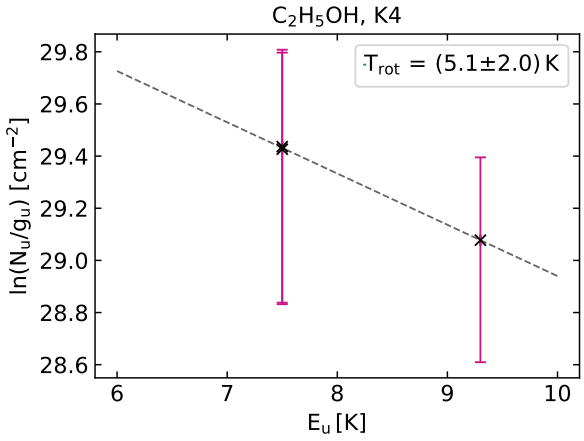

Figure A.1: Same as Fig. 3.5, but for C_2H_5OH towards K4.

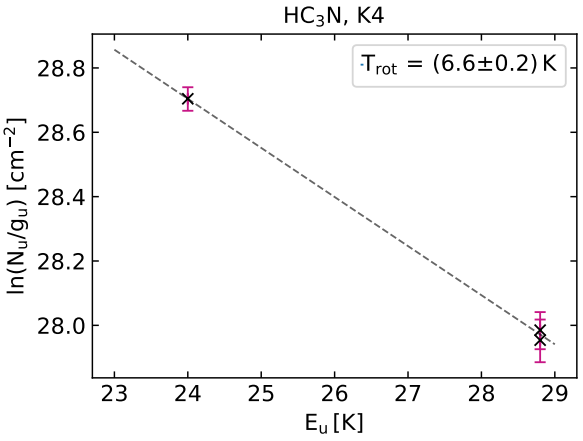

Figure A.2: Same as Fig. 3.5, but for HC_3N towards K4.

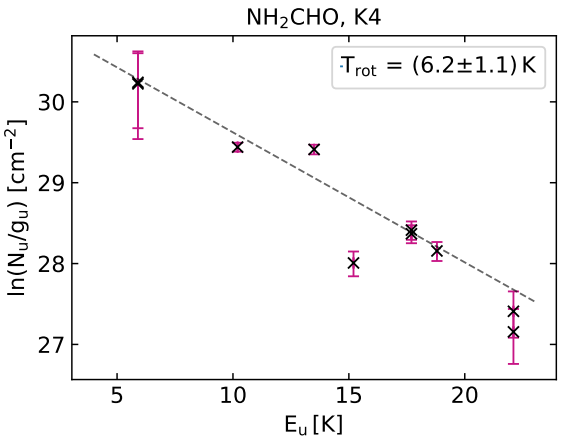

Figure A.3: Same as Fig. 3.5, but for NH_2CHO towards K4.

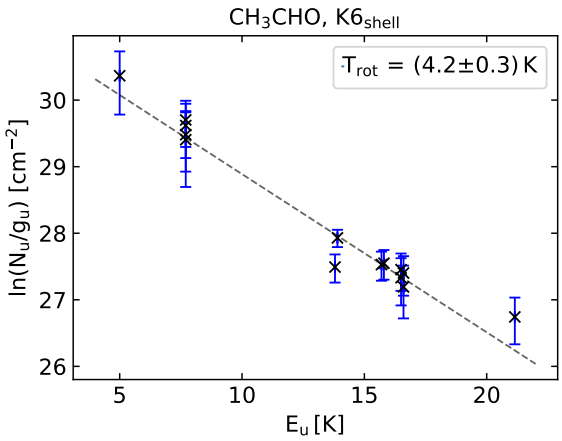

Figure A.4: Same as Fig. 3.5, but for CH_3CHO towards $K6_{shell}$.

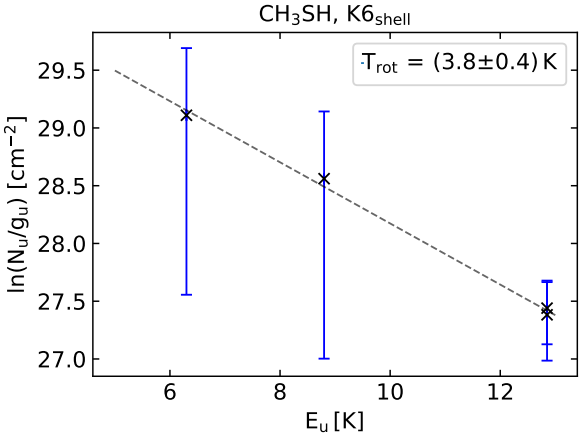

Figure A.5: Same as Fig. 3.5, but for CH_3SH towards $K6_{shell}$.

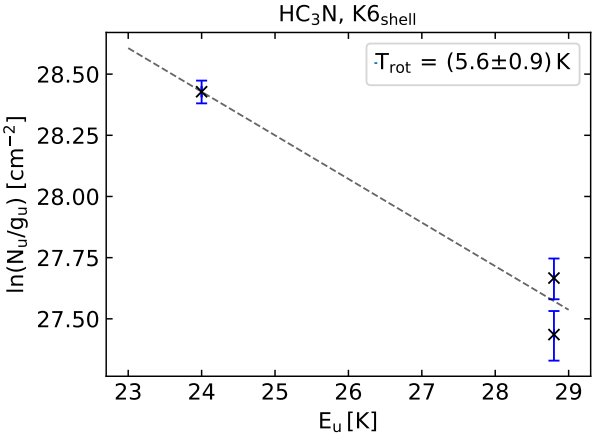

Figure A.6: Same as Fig. 3.5, but for HC_3N towards $K6_{shell}$.

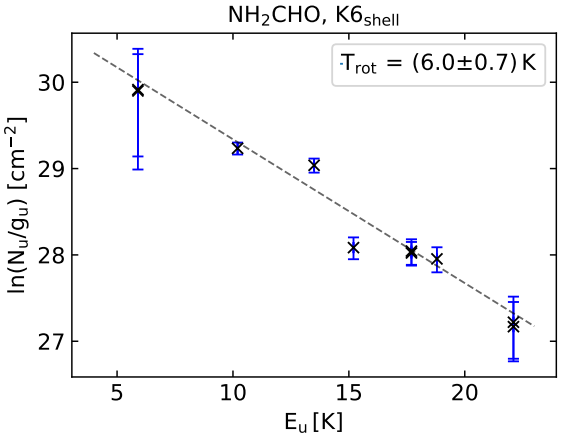

Figure A.7: Same as Fig. 3.5, but for NH_2CHO towards $K6_{shell}$.

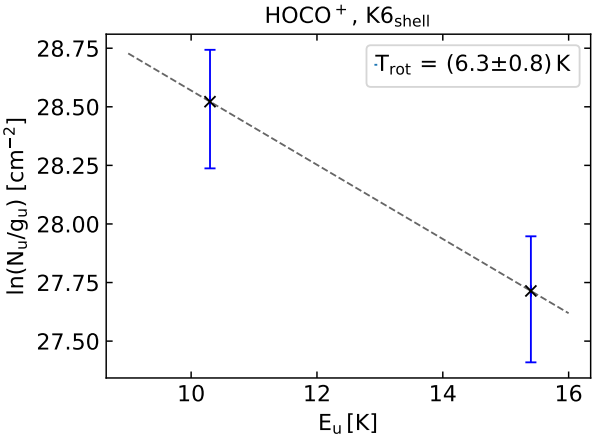

Figure A.8: Same as Fig. 3.5, but for $HOCO^+$ towards $K6_{shell}$.

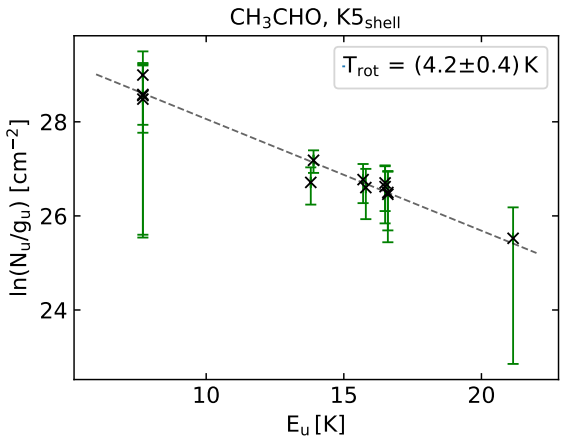

Figure A.9: Same as Fig. 3.5, but for CH_3CHO towards $K5_{shell}$.

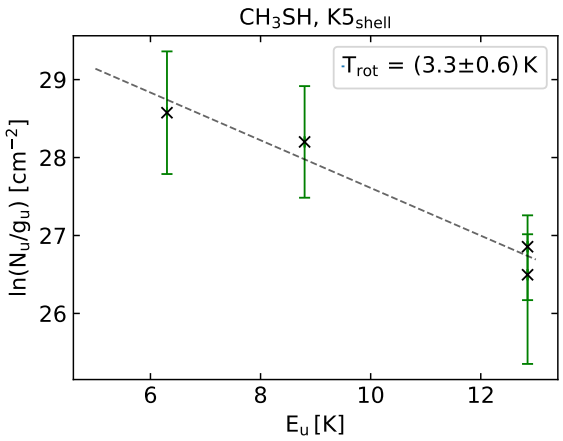

Figure A.10: Same as Fig. 3.5, but for CH_3SH towards $K5_{shell}$.

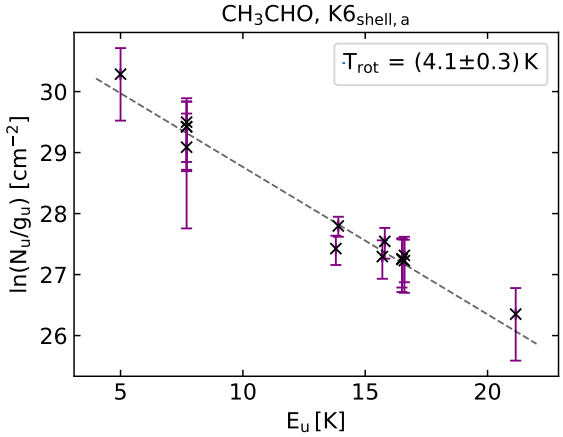

Figure A.11: Same as Fig. 3.5, but for CH_3CHO towards $K6_{shell,a}$.

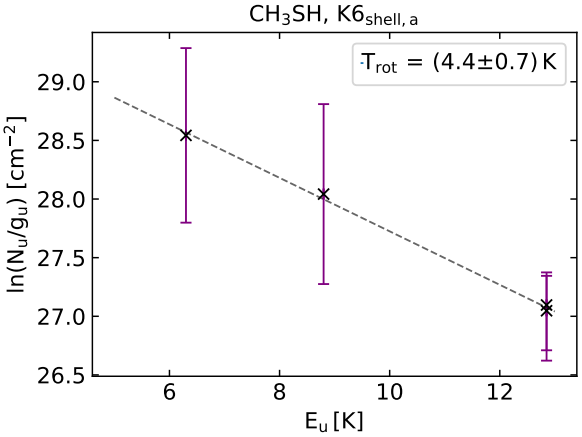

Figure A.12: Same as Fig. 3.5, but for CH_3SH towards $K6_{shell,a}$.

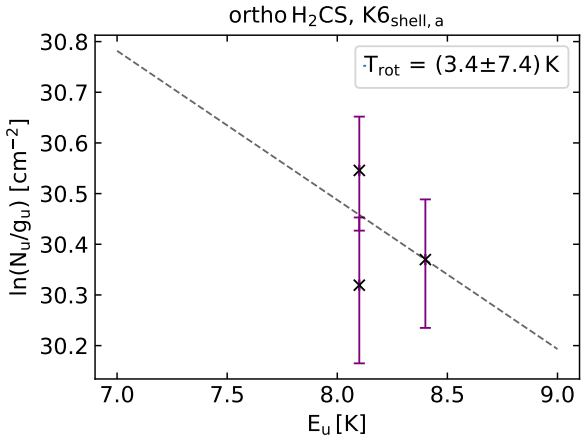

Figure A.13: Same as Fig. 3.5, but for ortho H_2CS towards $K6_{shell,a}$.

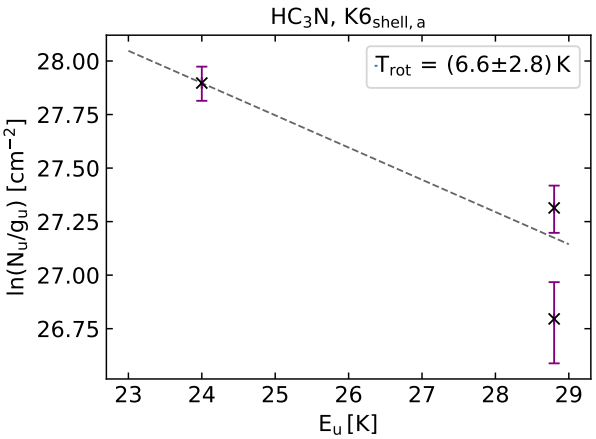

Figure A.14: Same as Fig. 3.5, but for HC_3N towards $K6_{shell,a}$.

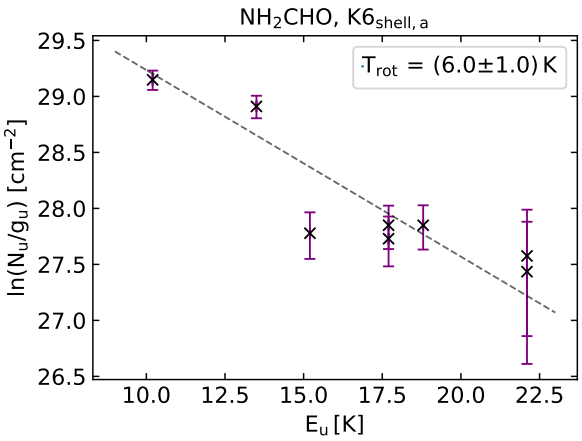

Figure A.15: Same as Fig. 3.5, but for NH_2CHO towards $K6_{shell,a}$.

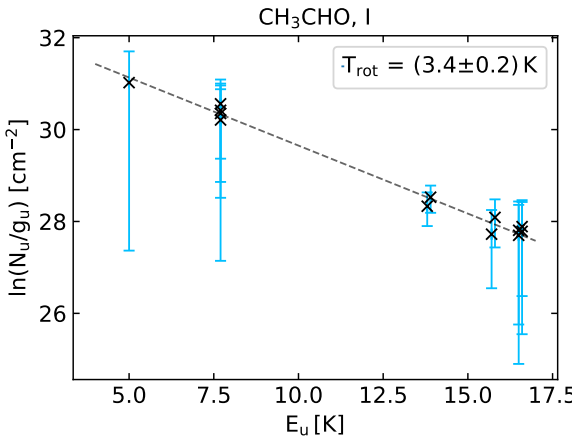

Figure A.16: Same as Fig. 3.5, but for CH_3CHO towards I.

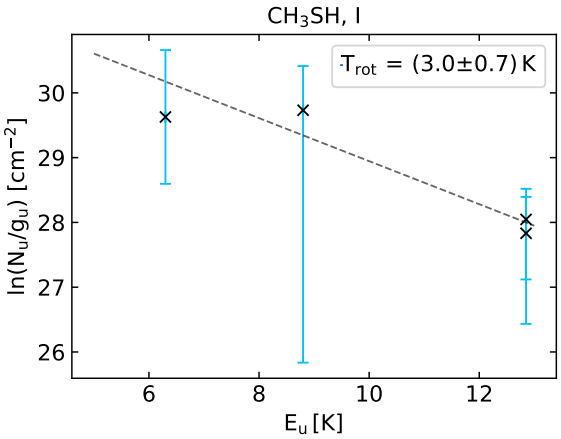

Figure A.17: Same as Fig. 3.5, but for CH_3SH towards I.

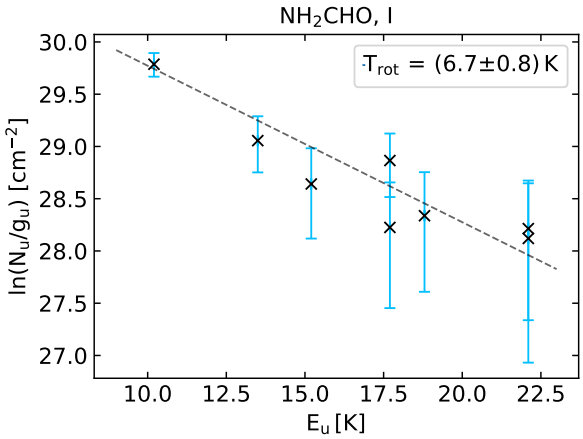

Figure A.18: Same as Fig. 3.5, but for NH_2CHO towards I.

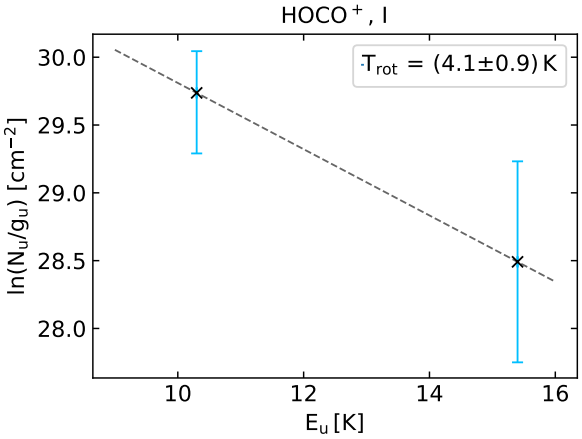

Figure A.19: Same as Fig. 3.5, but for $HOCO^+$ towards I.

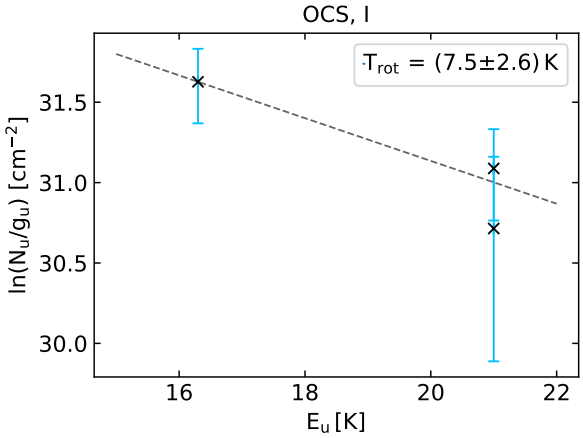

Figure A.20: Same as Fig. 3.5, but for OCS towards I.

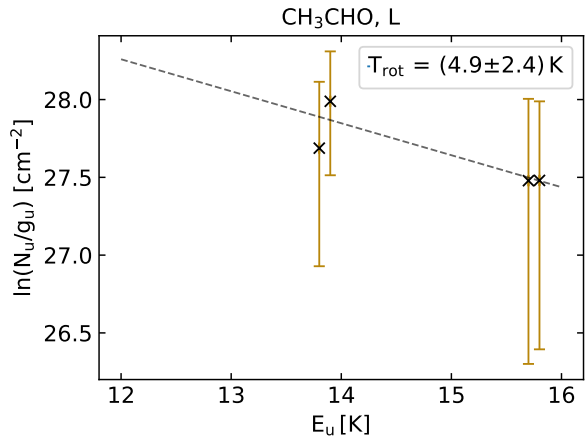

Figure A.21: Same as Fig. 3.5, but for CH_3CHO towards L.

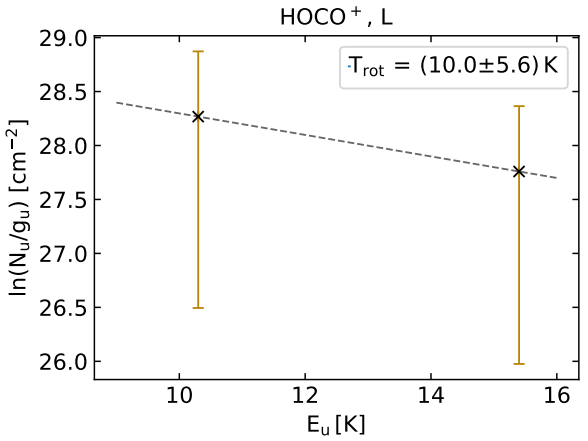

Figure A.22: Same as Fig. 3.5, but for $HOCO^+$ towards L.

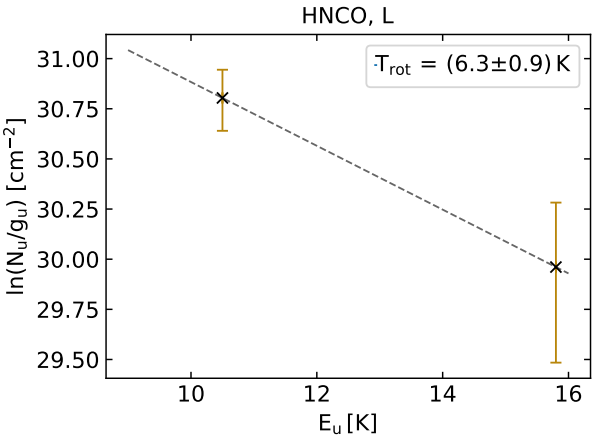

Figure A.23: Same as Fig. 3.5, but for HNCO towards L.

A.4 Detections

Table A.5: Molecular detections towards K4.

Molecule	Sgr B2 envelope[a]	cloud at ~48 km s^{-1}[b]	GC region 1[c]	GC region 2[d]	3 kpc arm[e]	4 kpc arm[f]	Sagittarius arm[g]	Scutum arm[h]
CH_3CHO	x	-	-	x	-	-	-	-
CH_3CN	x	-	-	x	-	-	x	x
CS	x	x	x	x	x	x	x	x
$C^{34}S$	x	x	x	x	x	-	-	x
$C^{33}S$	x	x	-	x	-	-	-	-
^{13}CS	x	x	-	x	-	-	-	-

Notes. [a] $v_{LSR} \geq 56$ km s^{-1}. [b] 42 km s$^{-1} \leq v_{LSR} < 56$ km s^{-1}. [c] $v_{LSR} < -50$ km s^{-1}. [d] -9 km s$^{-1} \leq v_{LSR} < 8$ km s^{-1}. [e] -50 km s$^{-1} \leq v_{LSR} < -35$ km s^{-1}. [f] -30 km s$^{-1} \leq v_{LSR} < -10$ km s^{-1}. [g] 25 km s$^{-1} \leq v_{LSR} < 39$ km s^{-1}. [g] 8 km s$^{-1} \leq v_{LSR} < 22$ km s^{-1}.

Table A.5: Continued.

Molecule	Sgr B2 envelope[a]	cloud at ~48 km s^{-1}[b]	GC region 1[c]	GC region 2[d]	3 kpc arm[e]	4 kpc arm[f]	Sagittarius arm[g]	Scutum arm[h]
$^{13}C^{34}S$	x	-	-	-	-	-	-	-
^{13}CO	x	x	x	x	x	x	x	x
$C^{18}O$	x	-	x	x	x	x	-	-
$C^{17}O$	x	-	-	-	x	-	-	-
OCS	x	-	-	-	-	-	-	-
HC_3N	x	x	-	x	-	-	-	-
$H^{13}CCCN$	x	x	-	-	-	-	-	-
$HC^{13}CCN$	x	x	-	-	-	-	-	-
$HCC^{13}CN$	x	x	-	-	-	-	-	-
CN	x	x	x	x	x	x	x	x
^{13}CN	x	-	x	x	x	-	-	-
$C^{15}N$	x	-	-	-	-	-	-	-
ortho c-C_3H_2	x	x	x	x	x	x	x	x
para c-C_3H_2	x	-	-	-	-	-	-	-
c-$CC^{13}CH_2$	x	-	-	-	-	-	-	-
N_2H^+	x	x	x	x	x	-	-	x
$^{15}NNH^+$	x	-	-	-	-	-	-	-
$N^{15}NH^+$	x	-	-	-	-	-	-	-
C_2H_5OH	x	-	-	-	-	-	-	-
CCH	x	x	x	x	x	x	x	x
^{13}CCH	x	-	-	-	-	-	-	-
$C^{13}CH$	x	-	-	-	-	-	-	-
NH_2CHO	x	-	-	x	-	-	-	-
HCO^+	x	x	x	x	x	x	x	x
$H^{13}CO^+$	x	x	x	x	x	x	x	x
$HC^{18}O^+$	x	x	x	x	-	-	-	-
$HC^{17}O^+$	x	x	-	-	-	-	-	-
HCN	x	x	x	x	x	x	x	x
$H^{13}CN$	x	x	x	x	x	-	x	x
$HC^{15}N$	x	x	x	x	x	-	-	x
HNC	x	x	x	x	x	x	x	x
$HN^{13}C$	x	x	x	x	x	-	x	-
$H^{15}NC$	x	x	-	x	-	-	-	-
HOC^+	x	-	-	x	-	-	-	x
HNCO	x	-	-	x	-	-	-	-
CH_3OH	x	x	-	x	-	x	x	x
$^{13}CH_3OH$	x	x	-	x	-	-	-	x
CH_3NH_2	x	-	-	-	-	-	-	-
CH_3SH	x	-	-	-	-	-	-	-
NS^+	x	-	-	-	-	-	-	-
$HOCO^+$	x	-	-	-	-	-	-	-

Notes. [a]$v_{LSR}\geq 56$ km s^{-1}. [b]42 km s$^{-1}\leq v_{LSR}<56$ km s^{-1}. [c]$v_{LSR}<-50$ km s^{-1}. [d]-9 km s$^{-1}\leq v_{LSR}<8$ km s^{-1}. [e]-50 km s$^{-1}\leq v_{LSR}<-35$ km s^{-1}. [f]-30 km s$^{-1}\leq v_{LSR}<-10$ km s^{-1}. [g] 25 km s$^{-1}\leq v_{LSR}<39$ km s^{-1}. [g] 8 km s$^{-1}\leq v_{LSR}<22$ km s^{-1}.

Table A.5: Continued.

Molecule	Sgr B2 envelope[a]	cloud at ~48 km s^{-1}[b]	GC region 1[c]	GC region 2[d]	3 kpc arm[e]	4 kpc arm[f]	Sagittarius arm[g]	Scutum arm[h]
PN	x	-	-	-	-	-	-	-
SiO	x	x	x	x	x	x	-	x
^{29}SiO	x	x	-	x	-	-	-	-
^{30}SiO	x	x	-	x	-	-	-	-
SO_2	x	-	-	-	-	-	-	-
SO	x	x	-	x	x	x	x	x
^{34}SO	x	-	-	-	-	-	-	-
ortho H_2CS	x	x	-	x	-	-	-	-
para H_2CS	x	x	-	x	-	-	-	-
CCS	x	-	-	-	-	-	-	-

Notes. [a]$v_{\rm LSR}\geq$56 km s^{-1}. [b]42 km s$^{-1}\leq v_{\rm LSR}<$56 km s^{-1}. [c]$v_{\rm LSR}<-$50 km s^{-1}. [d]$-$9 km s$^{-1}\leq v_{\rm LSR}<$8 km s^{-1}. [e]$-$50 km s$^{-1}\leq v_{\rm LSR}<-$35 km s^{-1}. [f]$-$30 km s$^{-1}\leq v_{\rm LSR}<-$10 km s^{-1}. [g] 25 km s$^{-1}\leq v_{\rm LSR}<$39 km s^{-1}. [g] 8 km s$^{-1}\leq v_{\rm LSR}<$22 km s^{-1}.

Table A.6: Molecular detections towards $K6_{\rm shell}$.

Molecule	Sgr B2 envelope[a]	cloud at ~48 km s^{-1}[b]	GC region 1[c]	GC region 2[d]	3 kpc arm[e]	4 kpc arm[f]	Sagittarius arm[g]	Scutum arm[h]
CH_3CHO	x	-	-	-	-	-	-	-
CH_3CN	x	-	-	-	-	-	-	-
CS	x	x	x	x	x	x	x	x
$C^{34}S$	x	x	x	x	x	-	-	x
$C^{33}S$	x	x	-	x	-	-	-	x
^{13}CS	x	x	-	-	-	-	-	-
$^{13}C^{34}S$	x	-	-	-	-	-	-	-
^{13}CO	x	x	x	x	x	x	x	x
$C^{18}O$	x	x	x	x	x	x	-	-
$C^{17}O$	x	-	-	-	-	-	-	-
OCS	x	-	-	-	-	-	-	-
HC_3N	x	-	-	x	-	-	-	-
$H^{13}CCCN$	x	-	-	-	-	-	-	-
$HC^{13}CCN$	x	-	-	-	-	-	-	-
$HCC^{13}CN$	x	-	-	-	-	-	-	-
CN	x	x	x	x	x	x	x	x
^{13}CN	x	x	-	x	-	-	-	x
$C^{15}N$	x	-	-	-	-	-	-	-
ortho c-C_3H_2	x	x	x	x	x	x	x	x
para c-C_3H_2	x	-	-	-	-	-	-	-
c-$CC^{13}CH_2$	x	-	-	-	-	-	-	-
N_2H^+	x	x	x	x	x	x	-	x
$^{15}NNH^+$	x	-	-	-	-	-	-	-
$N^{15}NH^+$	x	-	-	-	-	-	-	-
C_2H_5OH	x	-	-	-	-	-	-	-

Notes. See notes of Table A.5.

Table A.6: Continued.

Molecule	Sgr B2 envelope[a]	cloud at ~48 km s^{-1}[b]	GC region 1[c]	GC region 2[d]	3 kpc arm[e]	4 kpc arm[f]	Sagittarius arm[g]	Scutum arm[h]
CCH	x	x	x	x	x	x	-	x
^{13}CCH	x	-	-	-	-	-	-	-
C^{13}CH	x	-	-	-	-	-	-	-
NH_2CHO	x	-	-	-	-	-	-	-
HCO^+	x	x	x	x	x	x	x	x
H^{13}CO$^+$	x	x	x	x	x	x	x	x
HC^{18}O$^+$	x	x	-	x	x	-	-	x
HC^{17}O$^+$	x	x	-	-	-	-	-	-
HCN	x	x	x	x	x	x	x	x
H^{13}CN	x	x	x	x	x	-	x	x
HC^{15}N	x	x	x	x	-	-	-	x
HNC	x	x	x	x	x	x	x	x
HN^{13}C	x	x	x	x	-	-	-	x
H^{15}NC	x	-	-	-	-	-	-	-
HOC^+	x	-	-	x	-	-	-	x
HNCO	x	x	-	-	-	-	-	-
CH_3OH	x	x	x	x	-	-	x	x
$^{13}CH_3OH$	x	x	-	-	-	-	-	-
CH_3NH_2	x	-	-	-	-	-	-	-
CH_3SH	x	-	-	-	-	-	-	-
NS^+	x	-	-	-	-	-	-	-
$HOCO^+$	x	-	-	-	-	-	-	-
PN	x	-	-	-	-	-	-	-
SiO	x	x	x	x	x	x	-	x
^{29}SiO	x	x	-	-	-	-	-	-
^{30}SiO	x	x	-	-	-	-	-	-
SO_2	x	-	-	-	-	-	-	x
SO	x	x	x	x	x	x	x	x
^{34}SO	x	-	-	-	-	-	-	-
ortho H_2CS	x	x	-	-	-	-	-	-
para H_2CS	x	x	-	-	-	-	-	-
CCS	x	-	-	-	-	-	-	-

Notes. See notes of Table A.5.

Table A.7: Molecular detections towards $K5_{shell}$.

Molecule	Sgr B2 envelope[a]	cloud at ~48 km s^{-1}[b]	GC region 1[c]	GC region 2[d]	3 kpc arm[e]	4 kpc arm[f]	Sagittarius arm[g]	Scutum arm[h]
CH_3CHO	x	-	-	-	-	-	-	-
CH_3CN	x	x	-	-	-	-	-	-
CS	x	x	x	x	x	x	x	x

Notes. See notes of Table A.5.

Table A.7: Continued.

Molecule	Sgr B2 envelope[a]	cloud at ~48 km s^{-1}[b]	GC region 1[c]	GC region 2[d]	3 kpc arm[e]	4 kpc arm[f]	Sagittarius arm[g]	Scutum arm[h]
$C^{34}S$	x	-	x	x	x	-	-	-
$C^{33}S$	x	-	-	x	-	-	-	-
^{13}CS	x	-	-	-	-	-	-	-
$^{13}C^{34}S$	x	-	-	-	-	-	-	-
^{13}CO	x	x	x	x	x	x	-	x
$C^{18}O$	x	-	-	-	x	-	-	-
OCS	x	-	-	-	-	-	-	-
HC_3N	x	-	-	-	-	-	-	-
$H^{13}CCCN$	x	-	-	-	-	-	-	-
CN	x	-	x	x	x	x	x	x
^{13}CN	x	-	-	x	-	-	-	-
$C^{15}N$	x	-	-	-	-	-	-	-
ortho c-C_3H_2	x	x	x	x	x	x	x	x
c-$CC^{13}CH_2$	x	-	-	-	-	-	-	-
N_2H^+	x	-	x	x	x	-	-	x
CCH	x	-	x	x	x	x	x	x
NH_2CHO	x	-	-	-	-	-	-	-
HCO^+	x	x	x	x	x	x	x	x
$H^{13}CO^+$	x	-	x	x	x	x	-	x
$HC^{18}O^+$	x	-	-	-	-	-	-	-
$HC^{17}O^+$	x	-	-	-	-	-	-	-
HCN	x	-	x	x	x	x	x	x
$H^{13}CN$	x	-	x	x	-	-	-	x
$HC^{15}N$	x	-	-	x	-	-	-	-
HNC	x	x	x	x	x	x	x	x
$HN^{13}C$	x	-	x	x	-	-	-	-
$H^{15}NC$	x	-	-	-	-	-	-	-
HOC^+	x	-	-	-	-	-	-	-
HNCO	x	x	-	x	-	-	-	-
CH_3OH	x	x	-	x	-	-	x	x
$^{13}CH_3OH$	x	-	-	-	-	-	-	-
CH_3NH_2	x	-	-	-	-	-	-	-
CH_3SH	x	-	-	-	-	-	-	-
$HOCO^+$	x	-	-	-	-	-	-	-
PN	x	-	-	-	-	-	-	-
SiO	x	-	x	x	-	x	-	x
^{29}SiO	x	-	-	x	-	-	-	-
^{30}SiO	x	-	-	-	-	-	-	-
SO_2	x	-	-	-	-	-	-	-
SO	x	x	-	x	-	x	-	-
^{34}SO	x	-	-	-	-	-	-	-

Notes. See notes of Table A.5.

Table A.7: Continued.

Molecule	Sgr B2 envelope[a]	cloud at ~48 km s^{-1}[b]	GC region 1[c]	GC region 2[d]	3 kpc arm[e]	4 kpc arm[f]	Sagittarius arm[g]	Scutum arm[h]
ortho H_2CS	x	-	-	-	-	-	-	-
para H_2CS	x	-	-	-	-	-	-	-
CCS	x	-	-	-	-	-	-	-

Notes. See notes of Table A.5.

Table A.8: Molecular detections towards $K6_{shell,a}$.

Molecule	Sgr B2 envelope[a]	cloud at ~48 km s^{-1}[b]	GC region 1[c]	GC region 2[d]	3 kpc arm[e]	4 kpc arm[f]	Sagittarius arm[g]	Scutum arm[h]
CH_3CHO	x	-	-	-	-	-	-	-
CH_3CN	x	x	-	-	-	-	-	-
CS	x	x	x	x	x	x	x	x
$C^{34}S$	x	-	x	x	x	-	-	x
$C^{33}S$	x	-	x	x	-	-	-	x
^{13}CS	x	-	-	-	-	-	-	-
$^{13}C^{34}S$	x	-	-	-	-	-	-	-
^{13}CO	x	x	x	x	x	x	x	x
$C^{18}O$	x	x	x	-	x	x	-	-
OCS	x	-	-	-	-	-	-	-
HC_3N	x	-	-	-	-	-	-	-
CN	x	x	x	x	x	x	x	x
^{13}CN	x	-	-	x	-	-	-	x
$C^{15}N$	x	-	-	-	-	-	-	-
ortho c-C_3H_2	x	x	x	x	x	x	x	x
para c-C_3H_2	x	-	-	-	-	-	-	-
c-$CC^{13}CH_2$	x	-	-	-	-	-	-	-
N_2H^+	x	-	x	x	x	x	x	x
CCH	x	x	x	x	x	x	x	x
^{13}CCH	x	-	-	-	-	-	-	-
$C^{13}CH$	x	-	-	-	-	-	-	-
NH_2CHO	x	-	-	-	-	-	-	-
HCO^+	x	x	x	x	x	x	x	x
$H^{13}CO^+$	x	x	x	x	x	x	x	x
$HC^{18}O^+$	x	x	-	-	-	-	-	x
$HC^{17}O^+$	x	x	-	-	-	-	-	-
HCN	x	x	x	x	x	x	x	x
$H^{13}CN$	x	x	x	x	x	x	x	x
$HC^{15}N$	x	x	x	-	-	-	-	x
HNC	x	x	x	x	x	x	x	x
$HN^{13}C$	x	x	x	-	-	-	-	x
$H^{15}NC$	x	-	-	-	-	-	-	-

Notes. See notes of Table A.5.

Table A.8: Continued.

Molecule	Sgr B2 envelope[a]	cloud at ~48 km s^{-1}[b]	GC region 1[c]	GC region 2[d]	3 kpc arm[e]	4 kpc arm[f]	Sagittarius arm[g]	Scutum arm[h]
HOC^+	x	x	-	x	-	-	-	-
HNCO	x	x	-	-	-	-	-	-
CH_3OH	x	x	x	x	-	-	x	x
$^{13}CH_3OH$	x	x	-	-	-	-	-	-
CH_3NH_2	x	-	-	-	-	-	-	-
CH_3SH	x	-	-	-	-	-	-	-
NS^+	x	-	-	-	-	-	-	-
$HOCO^+$	x	-	-	-	-	-	-	-
PN	x	-	-	-	-	-	-	-
SiO	x	x	x	x	x	x	x	x
^{29}SiO	x	x	-	-	-	-	-	-
^{30}SiO	x	x	-	-	-	-	-	-
SO_2	x	-	-	-	-	-	-	-
SO	x	x	x	x	x	x	x	x
^{34}SO	x	-	-	-	-	-	-	-
ortho H_2CS	x	-	-	-	-	-	-	-
para H_2CS	x	-	-	-	-	-	-	-
CCS	x	-	-	-	-	-	-	-

Notes. See notes of Table A.5.

Table A.9: Molecular detections towards I.

Molecule	Sgr B2 envelope[a]	cloud at ~48 km s^{-1}[b]	GC region 1[c]	GC region 2[d]	3 kpc arm[e]	4 kpc arm[f]	Sagittarius arm[g]	Scutum arm[h]
CH_3CHO	x	-	-	-	-	-	-	-
CH_3CN	x	-	-	-	-	-	-	-
CS	x	x	x	x	x	x	x	x
$C^{34}S$	x	x	x	x	x	x	-	-
$C^{33}S$	x	x	x	x	-	-	-	-
^{13}CS	x	x	-	-	-	-	-	-
$^{13}C^{34}S$	x	-	-	-	-	-	-	-
^{13}CO	x	x	x	x	x	x	x	x
$C^{18}O$	x	x	-	-	x	-	-	-
$C^{17}O$	x	-	-	-	x	-	-	-
OCS	x	-	-	-	-	-	-	-
HC_3N	x	-	-	-	-	-	-	-
CN	x	-	x	x	x	x	x	x
^{13}CN	x	-	-	-	-	-	-	-
ortho c-C_3H_2	x	x	x	x	x	x	x	x
para c-C_3H_2	x	-	-	-	-	-	-	-
c-$CC^{13}CH_2$	x	-	-	-	-	-	-	-

Notes. See notes of Table A.5.

Table A.9: Continued.

Molecule	Sgr B2 envelope[a]	cloud at ~48 km s^{-1}[b]	GC region 1[c]	GC region 2[d]	3 kpc arm[e]	4 kpc arm[f]	Sagittarius arm[g]	Scutum arm[h]
N_2H^+	x	-	x	x	x	-	-	x
CCH	x	x	x	x	x	x	x	x
NH_2CHO	x	-	-	-	-	-	-	-
HCO^+	x	x	x	x	x	x	x	x
$H^{13}CO^+$	x	x	x	x	x	x	x	x
$HC^{18}O^+$	x	-	-	x	-	-	-	x
$HC^{17}O^+$	x	-	-	-	-	-	-	-
HCN	x	x	x	x	x	x	x	x
$H^{13}CN$	x	x	x	x	x	x	x	x
$HC^{15}N$	x	-	-	-	-	-	-	-
HNC	x	x	x	x	x	x	x	x
$HN^{13}C$	x	x	x	x	-	-	-	x
$H^{15}NC$	x	-	-	-	-	-	-	-
HOC^+	x	-	-	-	-	-	-	-
HNCO	x	-	-	-	-	-	-	-
CH_3OH	x	x	x	x	-	-	-	x
$^{13}CH_3OH$	x	-	-	-	-	-	-	-
CH_3NH_2	x	-	-	-	-	-	-	-
CH_3SH	x	-	-	-	-	-	-	-
NS^+	x	-	-	-	-	-	-	-
$HOCO^+$	x	-	-	-	-	-	-	-
PN	x	-	-	-	-	-	-	-
SiO	x	x	x	x	x	x	x	x
^{29}SiO	x	x	-	-	-	-	-	-
^{30}SiO	x	-	-	-	-	-	-	-
SO_2	x	-	-	-	-	-	-	-
SO	x	x	-	x	x	-	x	-
^{34}SO	x	-	-	-	-	-	-	-
ortho H_2CS	x	-	-	-	-	-	-	-
para H_2CS	x	-	-	-	-	-	-	-
CCS	x	-	-	-	-	-	-	-

Notes. See notes of Table A.5.

Table A.10: Molecular detections towards L.

Molecule	Sgr B2 envelope[a]	cloud at ~48 km s^{-1}[b]	GC region 1[c]	GC region 2[d]	3 kpc arm[e]	4 kpc arm[f]	Sagittarius arm[g]	Scutum arm[h]
CH_3CHO	x	-	-	-	-	-	-	-
CH_3CN	x	-	-	-	-	-	-	-
CS	x	-	x	x	x	x	x	x
$C^{34}S$	x	-	-	x	x	-	-	x

Notes. See notes of Table A.5.

Table A.10: Continued.

Molecule	Sgr B2 envelope[a]	cloud at ~48 km s^{-1}[b]	GC region 1[c]	GC region 2[d]	3 kpc arm[e]	4 kpc arm[f]	Sagittarius arm[g]	Scutum arm[h]
$C^{33}S$	x	-	-	x	-	-	-	-
^{13}CS	x	-	-	-	-	-	-	-
^{13}CO	x	x	x	-	x	x	x	x
$C^{18}O$	x	-	-	-	x	-	-	-
OCS	x	-	-	-	-	-	-	-
HC_3N	x	-	-	-	-	-	-	-
^{13}CN	x	-	-	-	-	-	-	-
ortho c-C_3H_2	x	x	x	x	x	x	x	x
c-$CC^{13}CH_2$	x	-	-	-	-	-	-	-
N_2H^+	x	x	x	x	x	-	x	x
CCH	x	-	x	x	x	x	x	x
NH_2CHO	x	-	-	-	-	-	-	-
HCO^+	x	x	x	x	x	x	x	x
$H^{13}CO^+$	x	-	x	x	x	x	x	x
$HC^{18}O^+$	x	-	-	-	-	-	-	-
$HC^{17}O^+$	x	-	-	-	-	-	-	-
HCN	x	x	x	x	x	x	x	x
$H^{13}CN$	x	-	x	x	-	x	x	x
$HC^{15}N$	x	-	x	x	-	-	-	x
HNC	x	-	x	x	x	x	x	x
$HN^{13}C$	x	-	-	x	-	-	-	x
$H^{15}NC$	x	-	-	-	-	-	-	-
HNCO	x	x	-	-	-	-	-	-
CH_3OH	x	x	-	-	-	-	x	x
$^{13}CH_3OH$	x	x	-	-	-	-	-	-
$HOCO^+$	x	-	-	-	-	-	-	-
SiO	x	x	x	x	-	x	x	x
^{29}SiO	x	x	-	-	-	-	-	-
^{30}SiO	x	x	-	-	-	-	-	-
SO_2	x	-	-	-	-	-	-	-
SO	x	-	-	-	-	-	-	x
^{34}SO	x	-	-	-	-	-	-	-
ortho H_2CS	x	-	-	-	-	-	-	-
para H_2CS	x	-	-	-	-	-	-	-

Notes. See notes of Table A.5.

A.5 Spectra

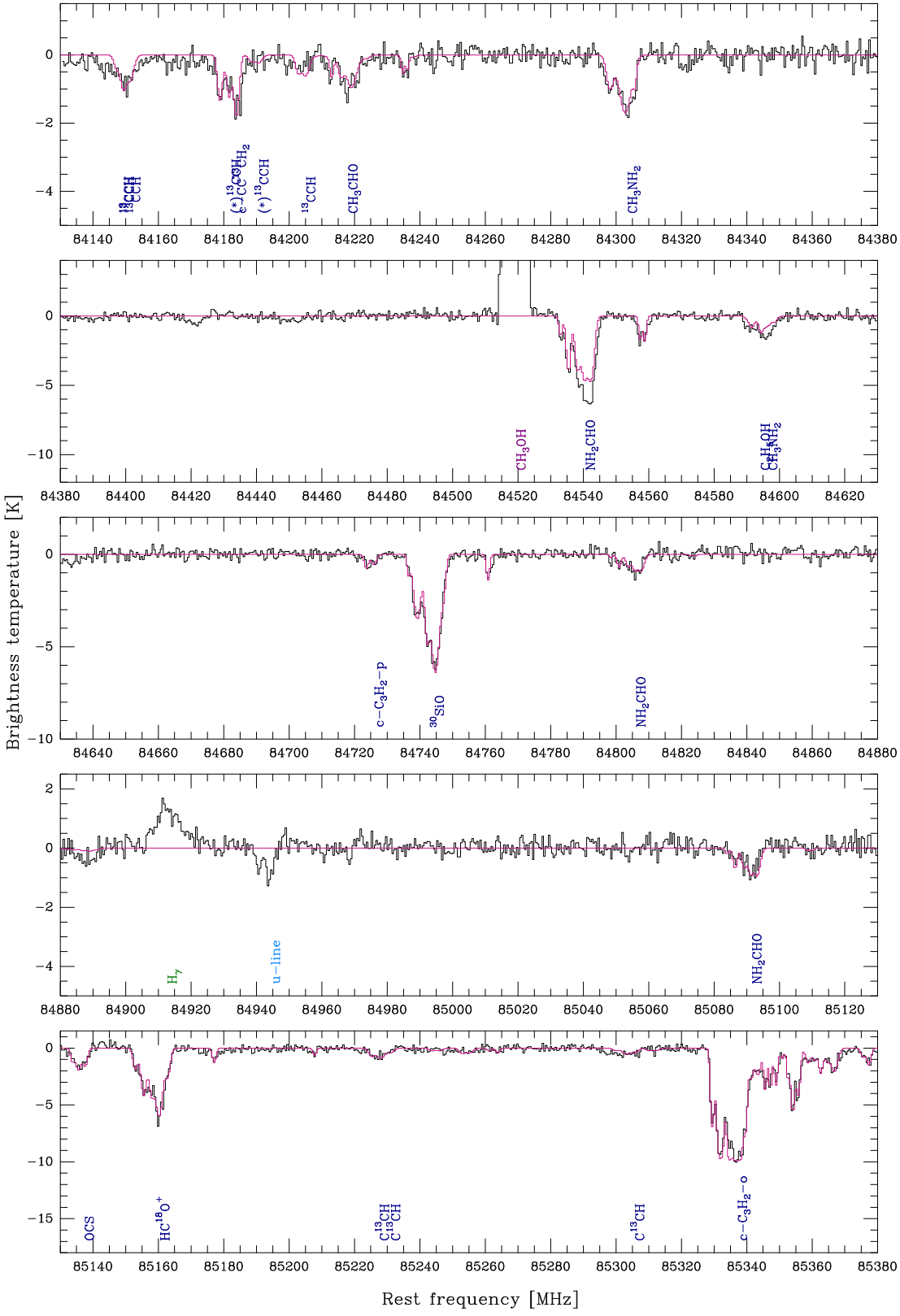

Figure A.24: ALMA spectrum towards K4. The synthetic spectrum is overlaid in magenta. The transitions detected in absorption are labeled in blue, the recombination lines in green, the unidentified lines or artefacts in light blue and the emission lines in purple.

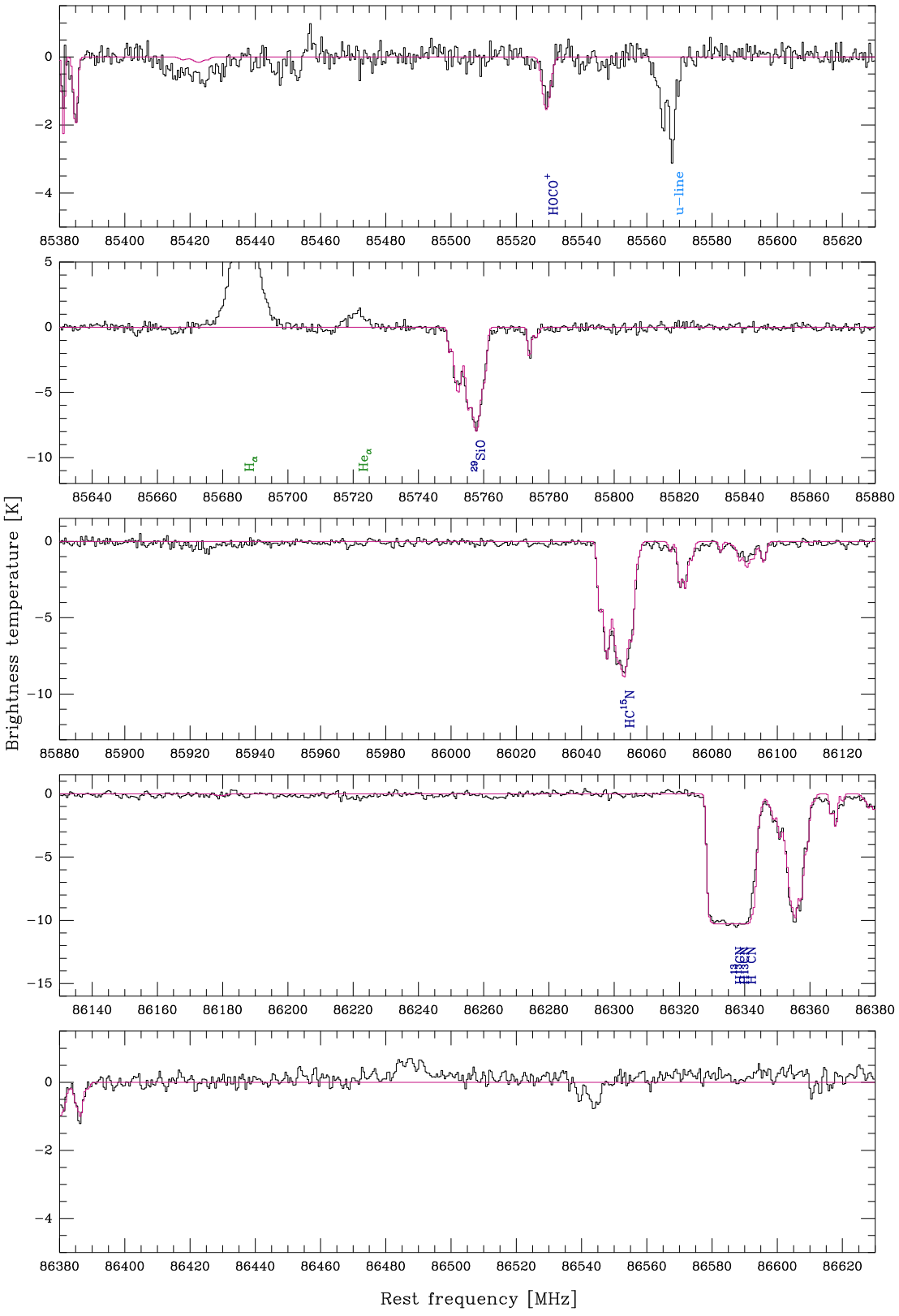

Figure A.24: Continued.

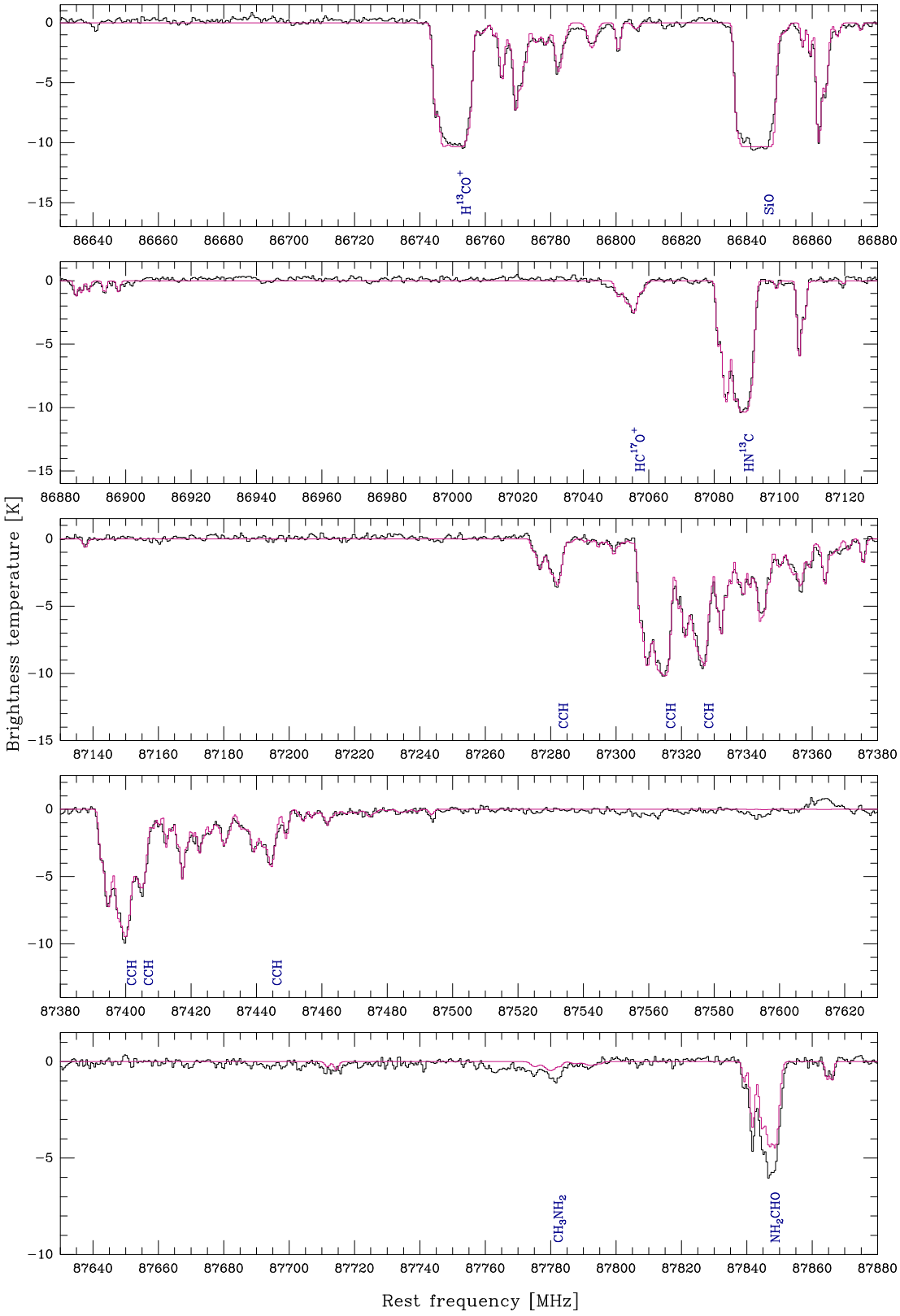

Figure A.24: Continued.

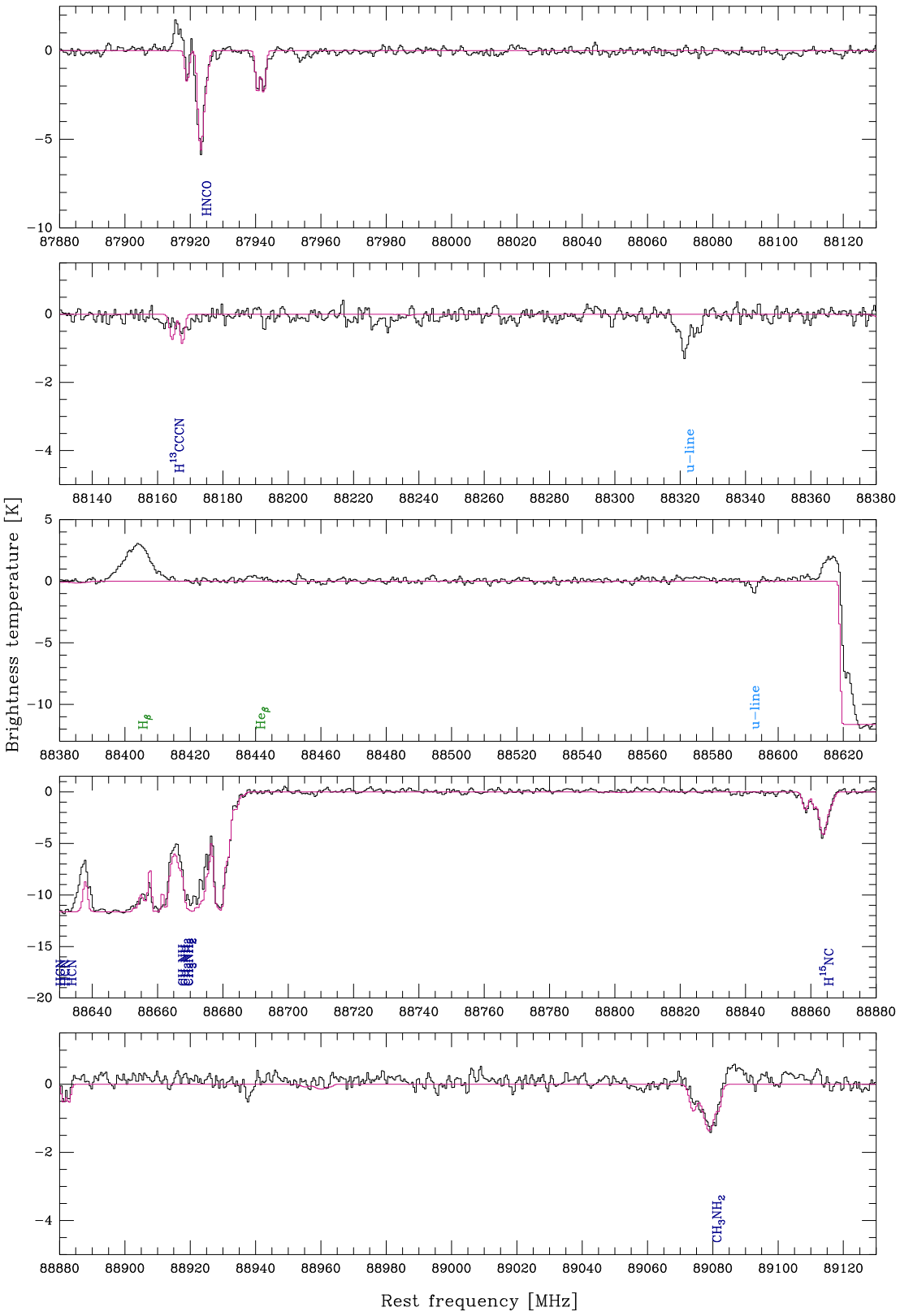

Figure A.24: Continued.

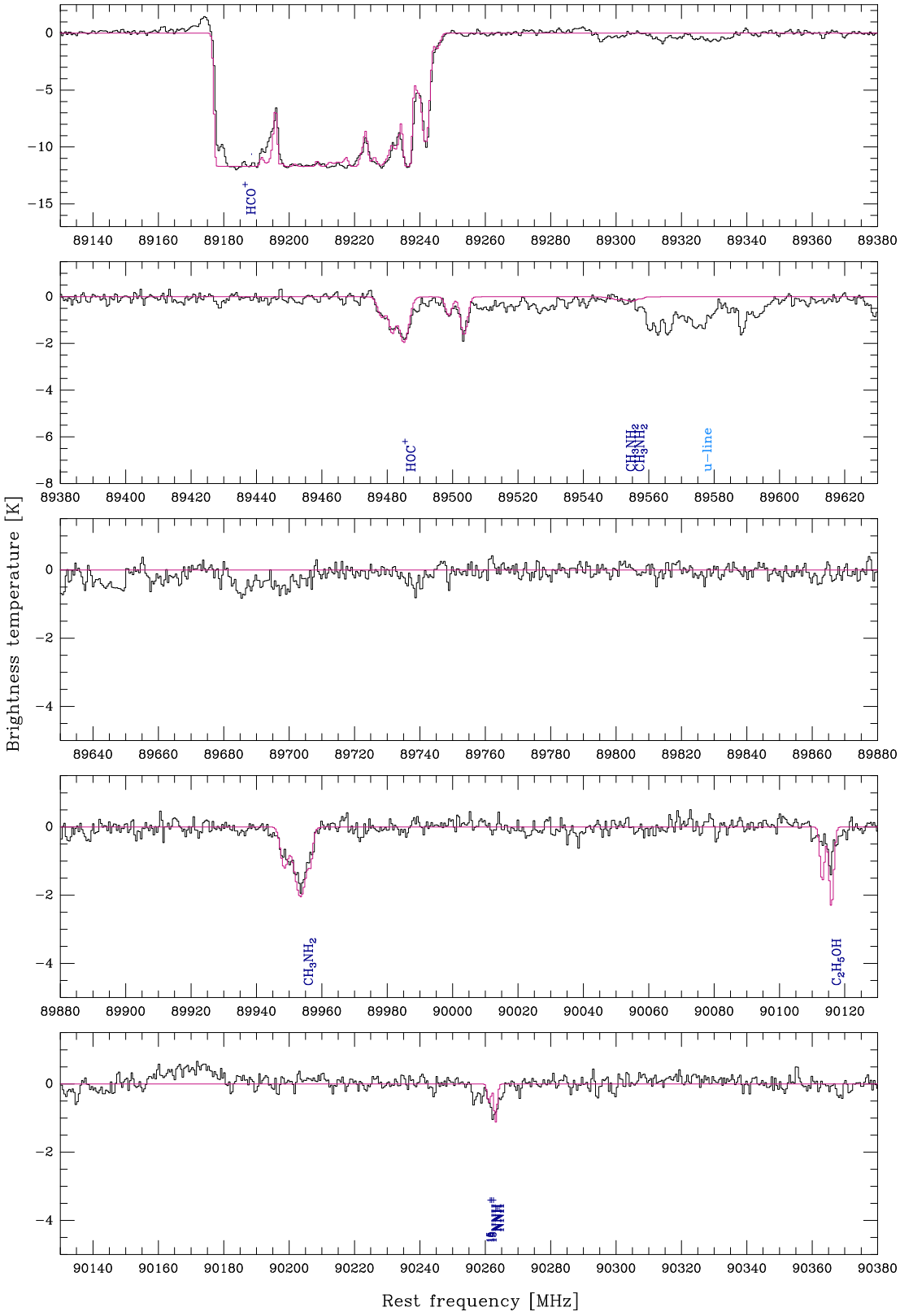

Figure A.24: Continued.

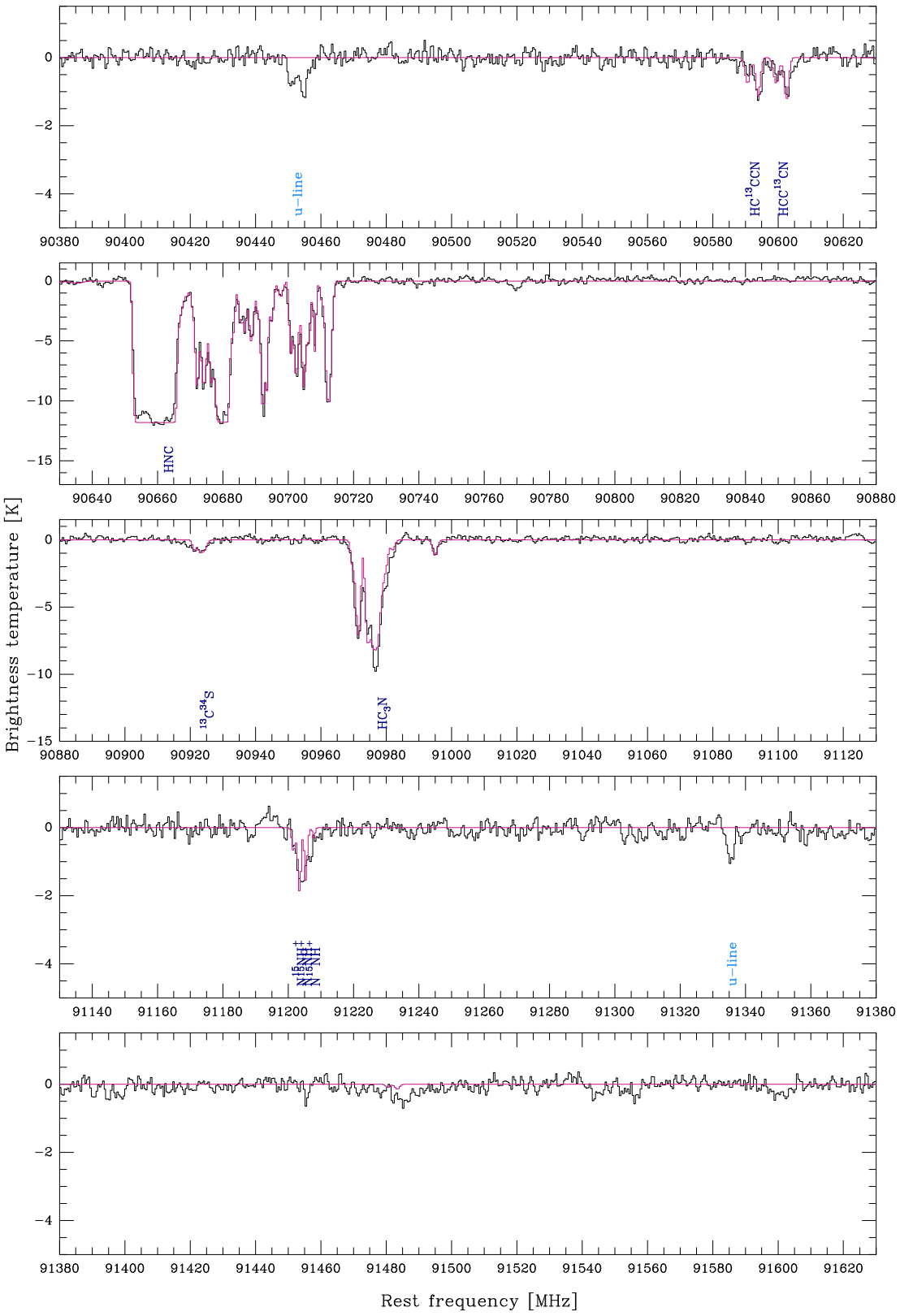

Figure A.24: Continued.

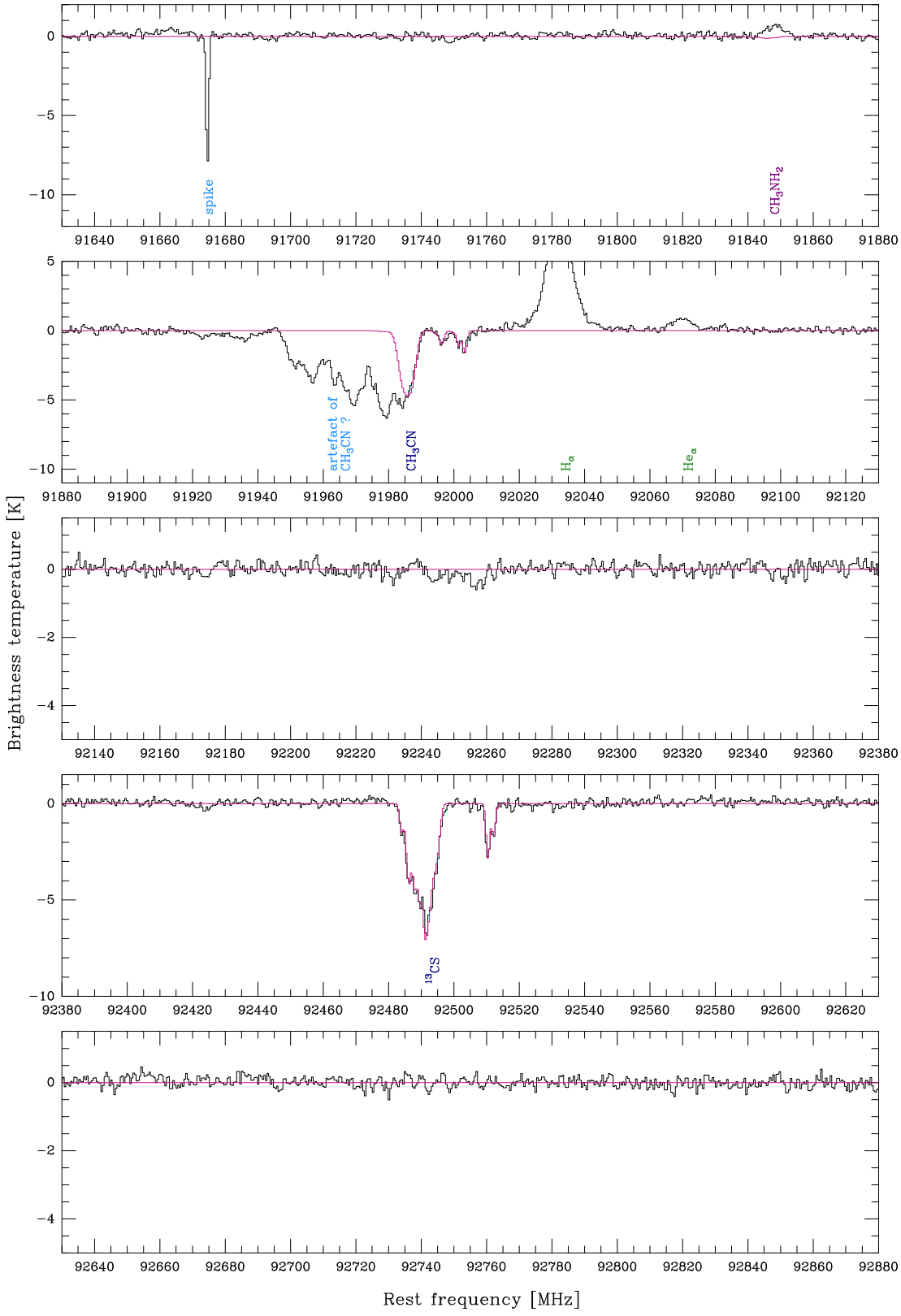

Figure A.24: Continued.

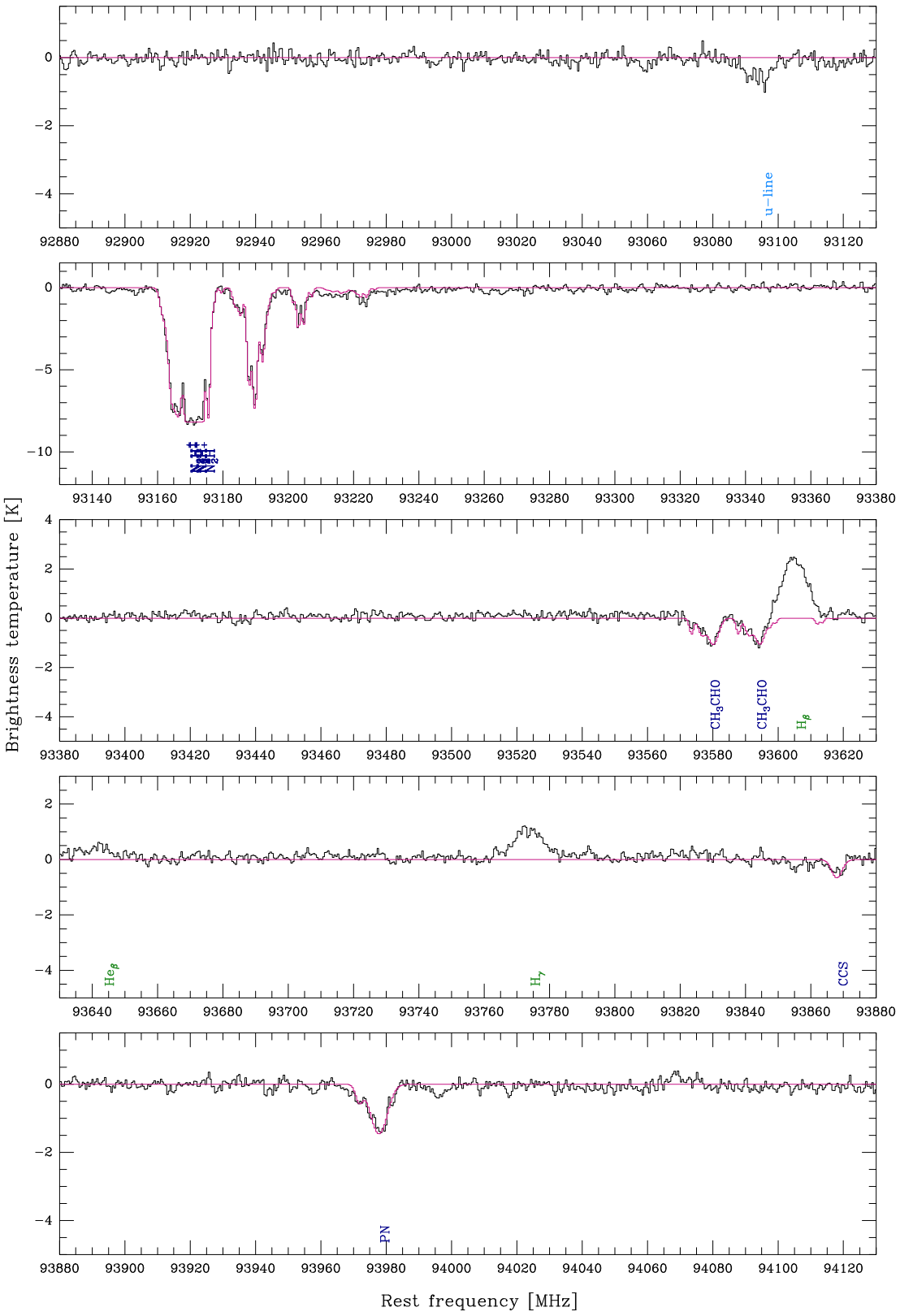

Figure A.24: Continued.

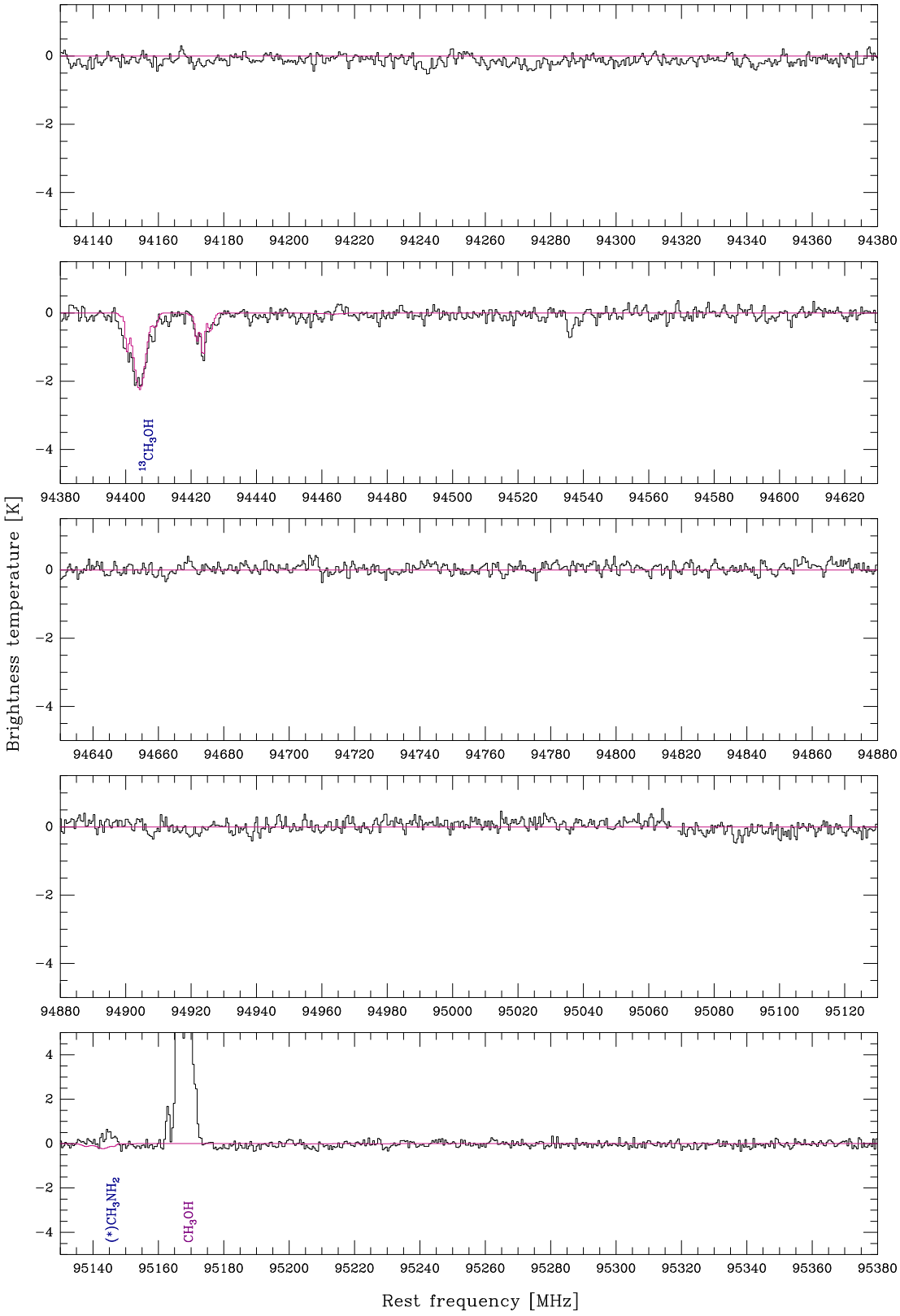

Figure A.24: Continued.

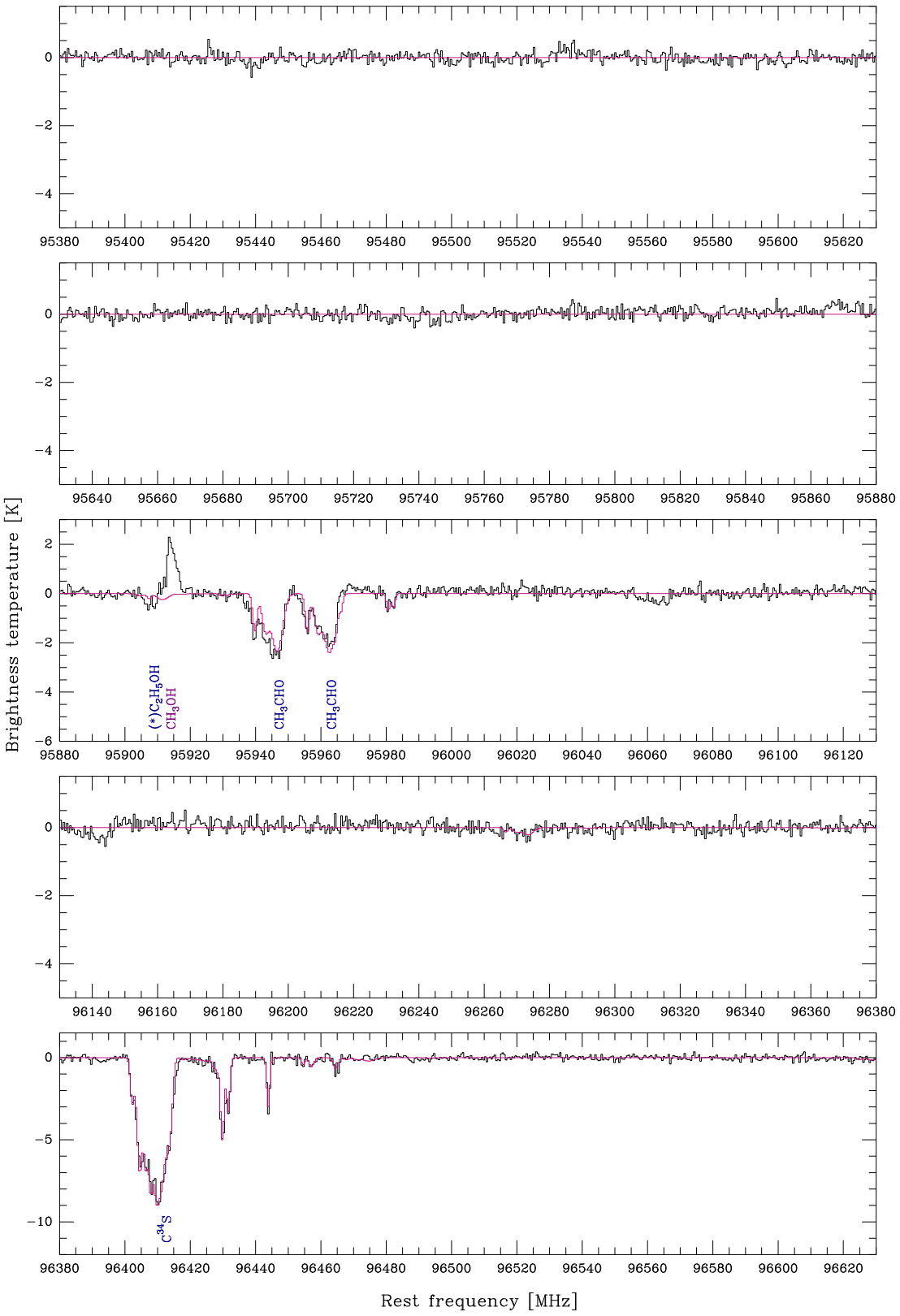

Figure A.24: Continued.

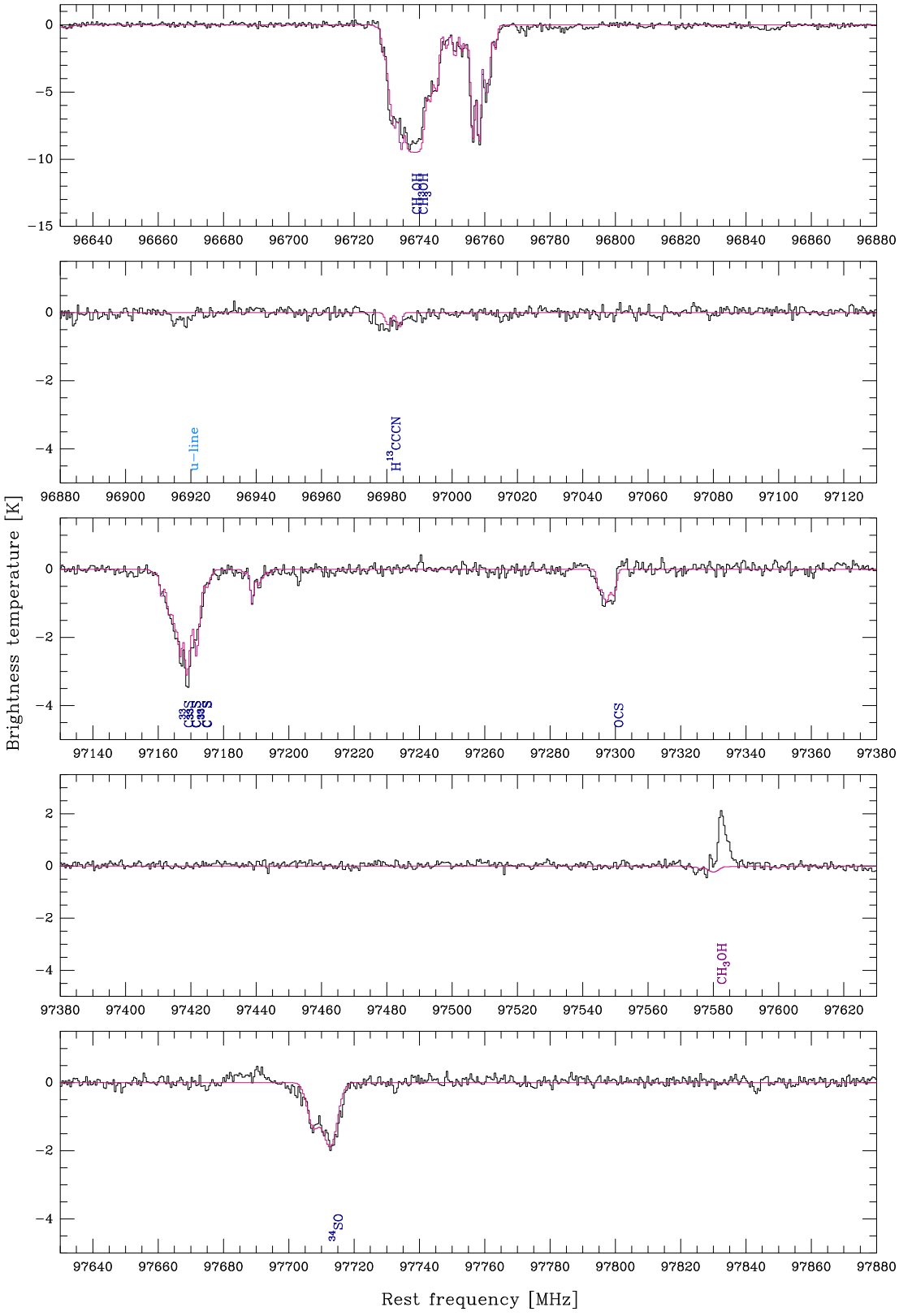

Figure A.24: Continued.

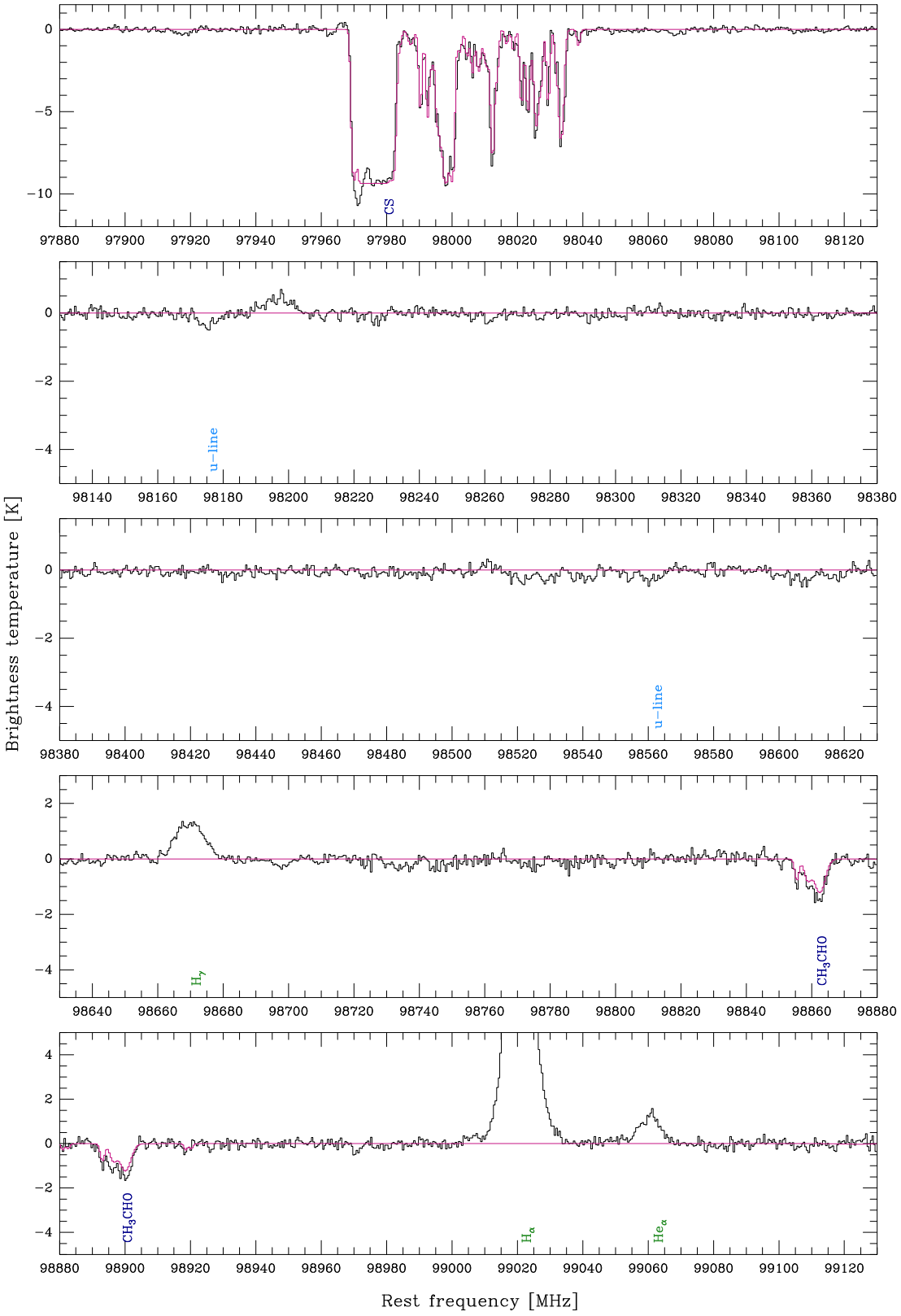

Figure A.24: Continued.

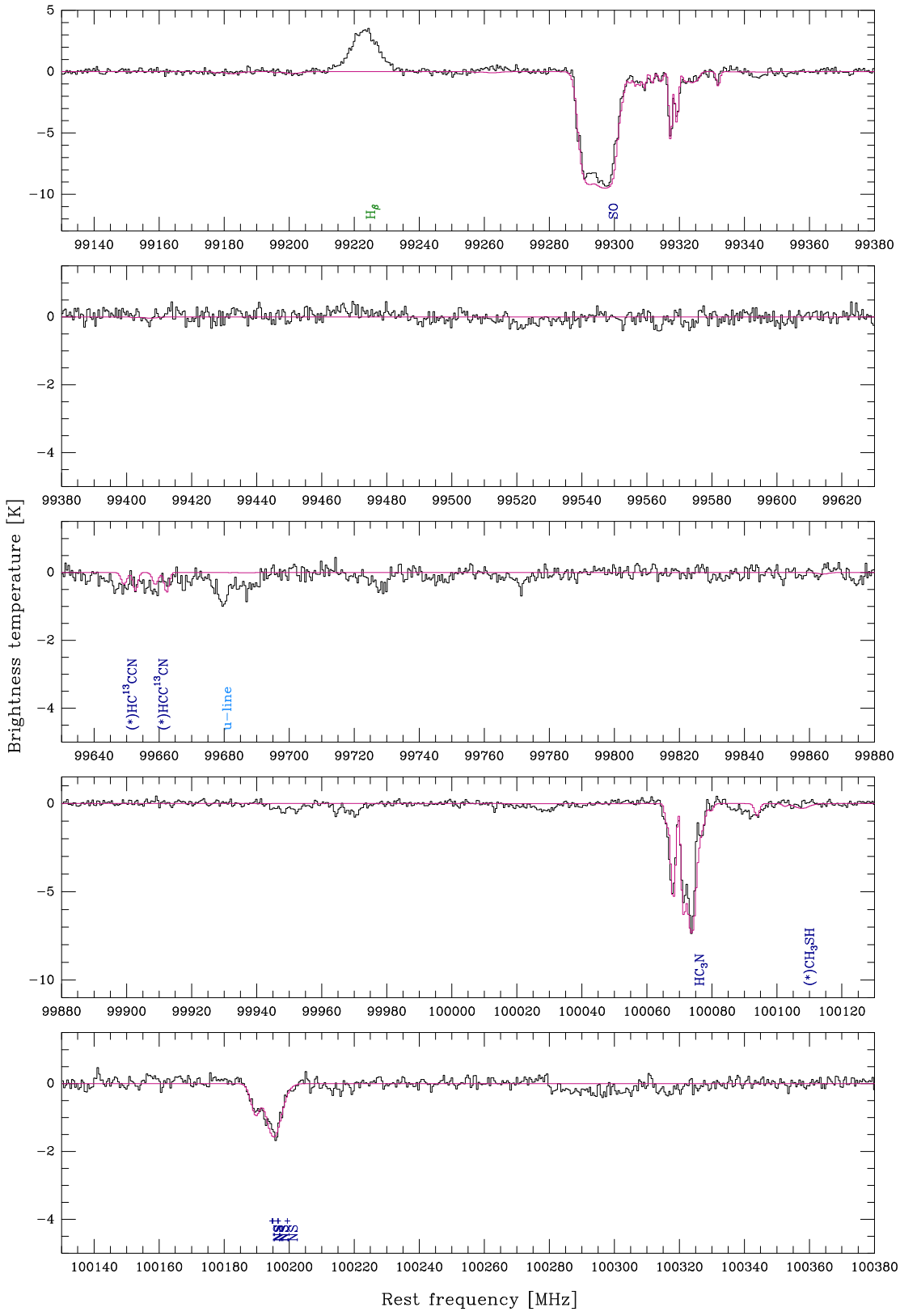

Figure A.24: Continued.

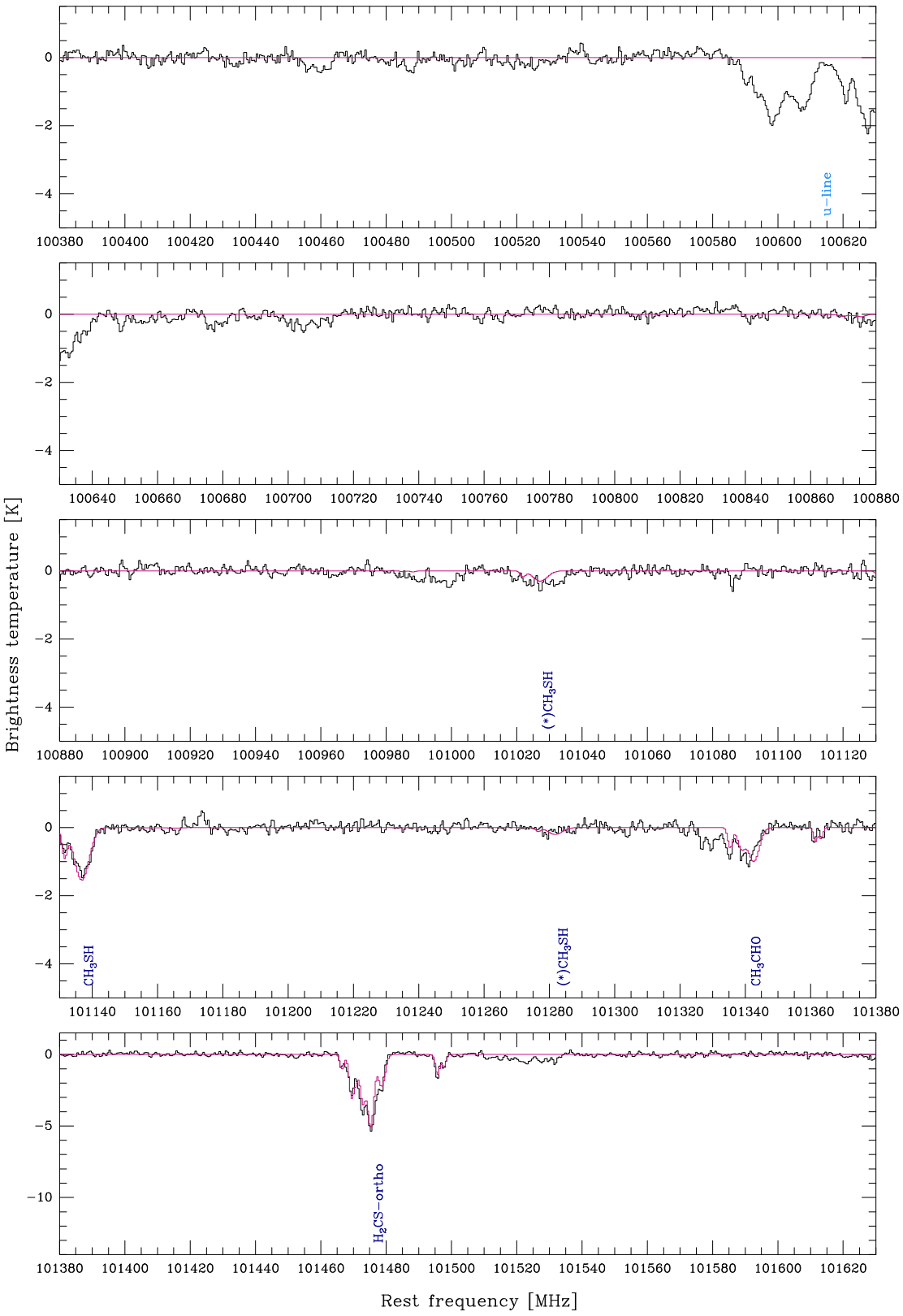

Figure A.24: Continued.

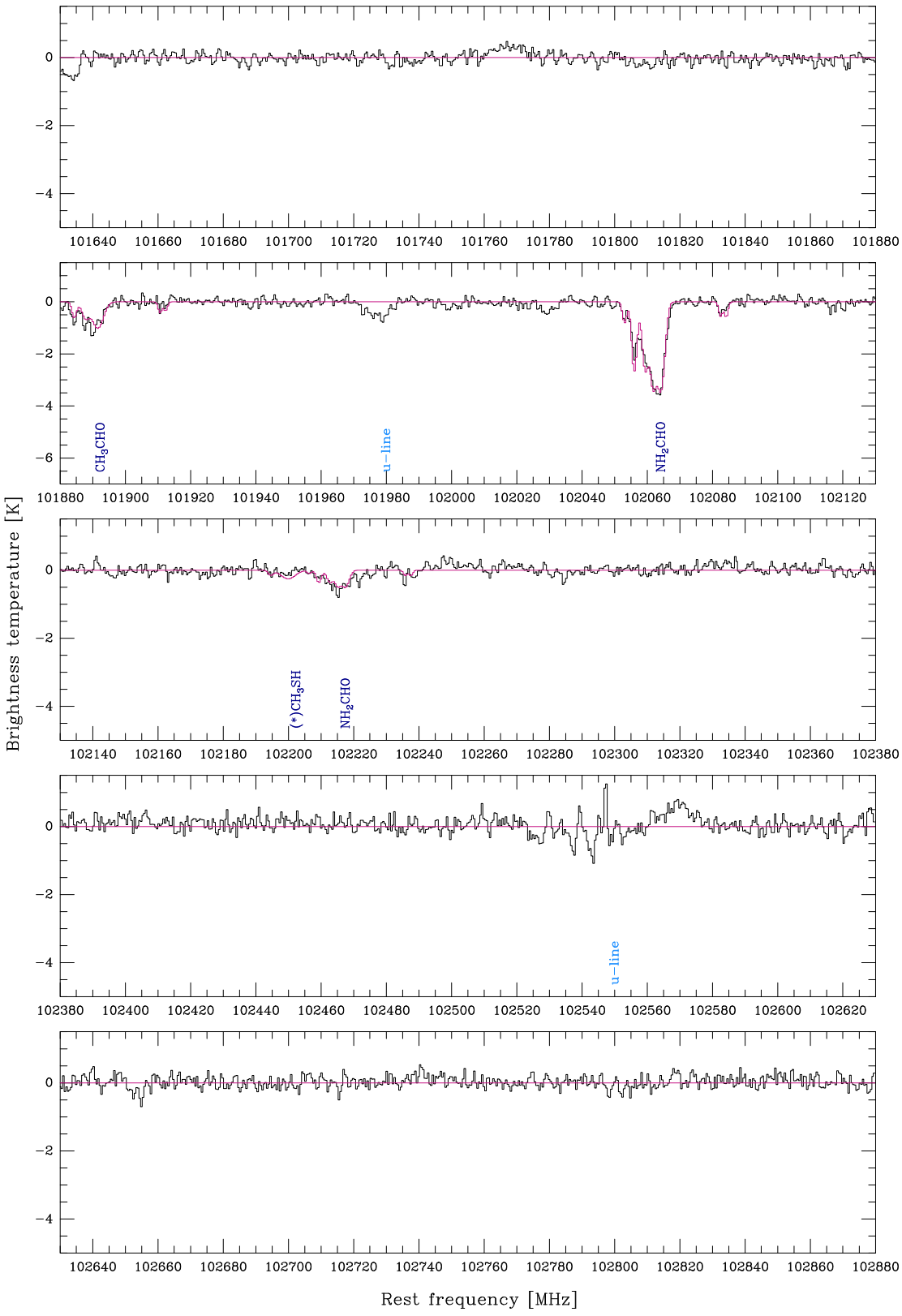

Figure A.24: Continued.

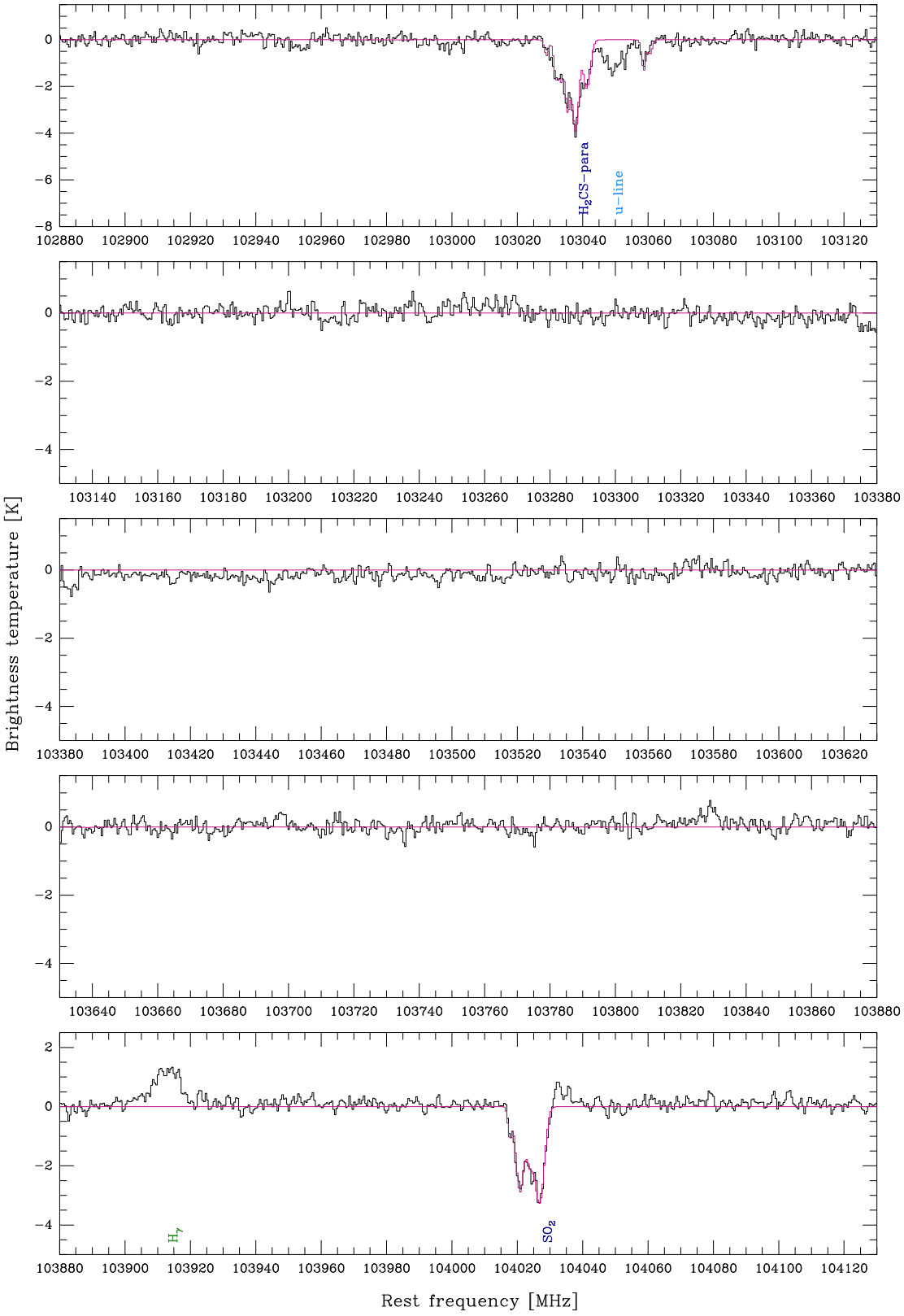

Figure A.24: Continued.

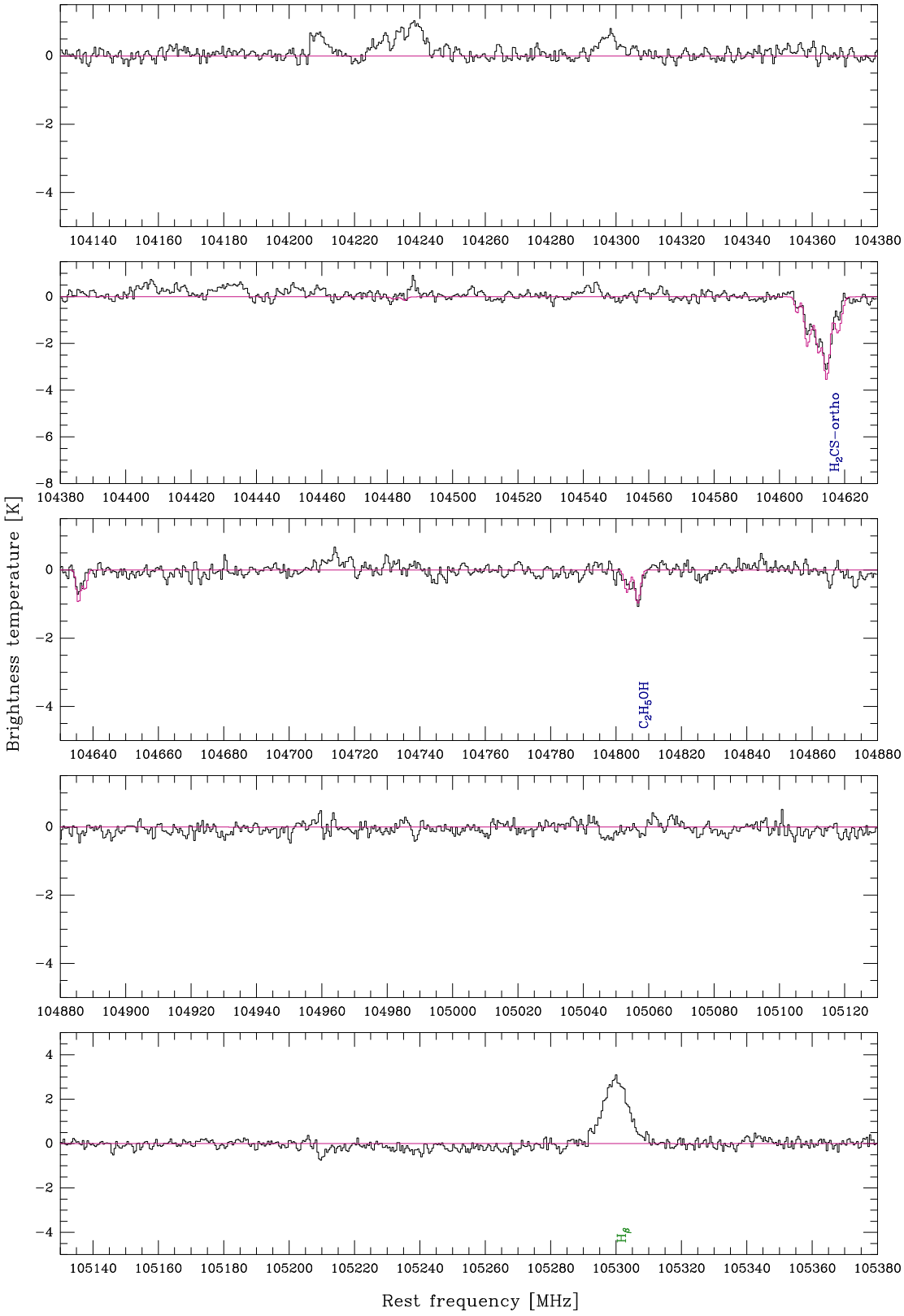

Figure A.24: Continued.

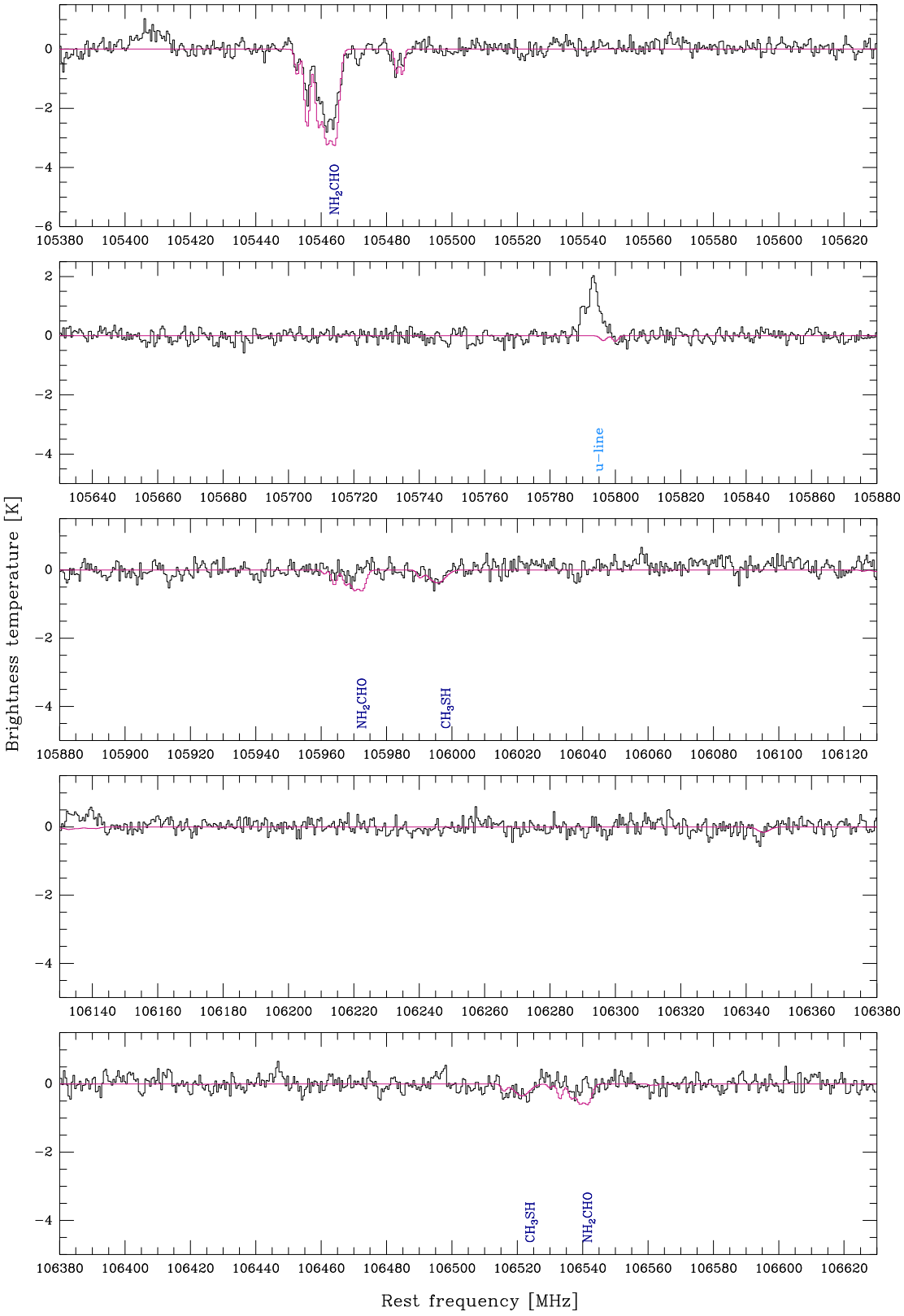

Figure A.24: Continued.

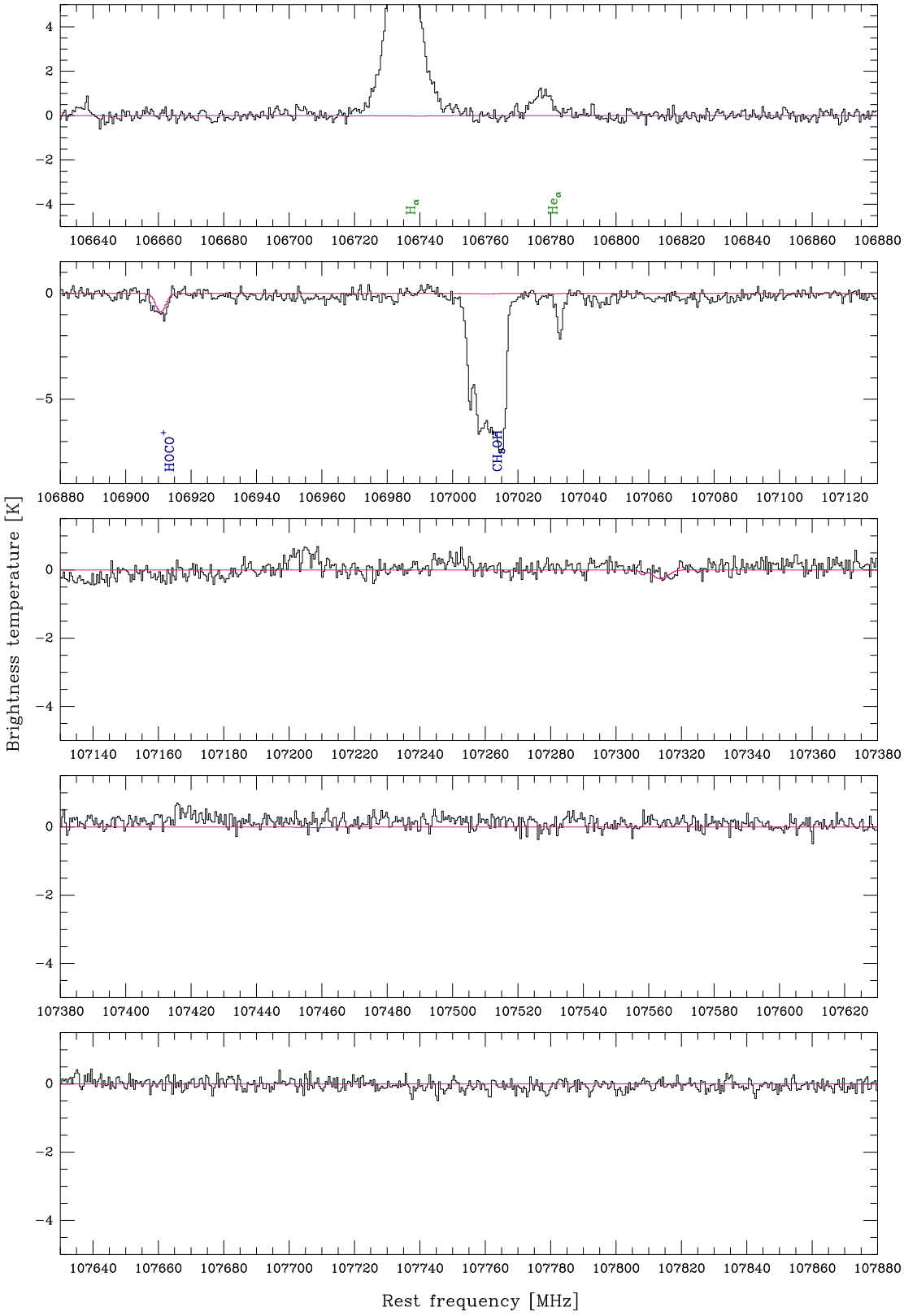

Figure A.24: Continued.

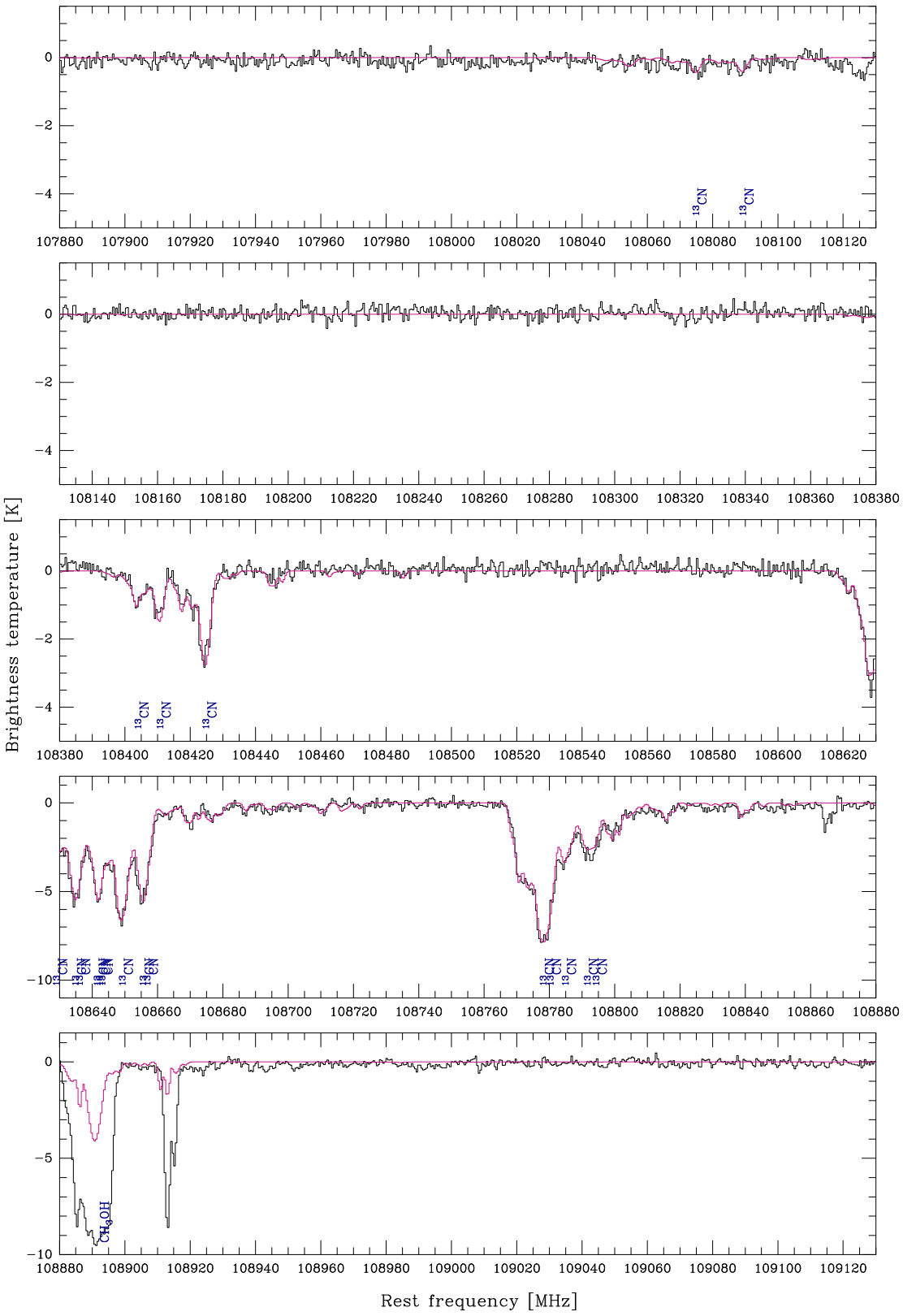

Figure A.24: Continued.

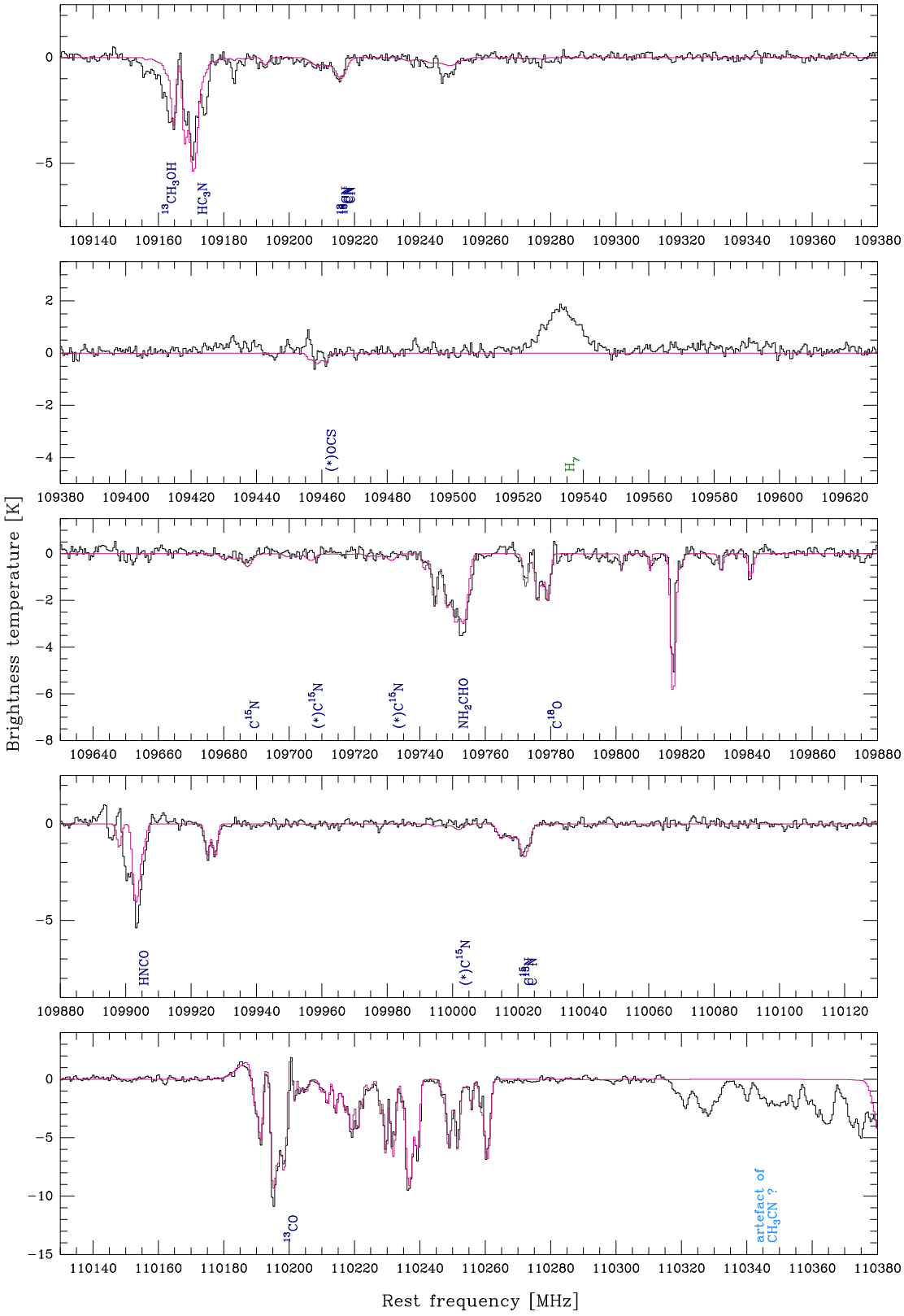

Figure A.24: Continued.

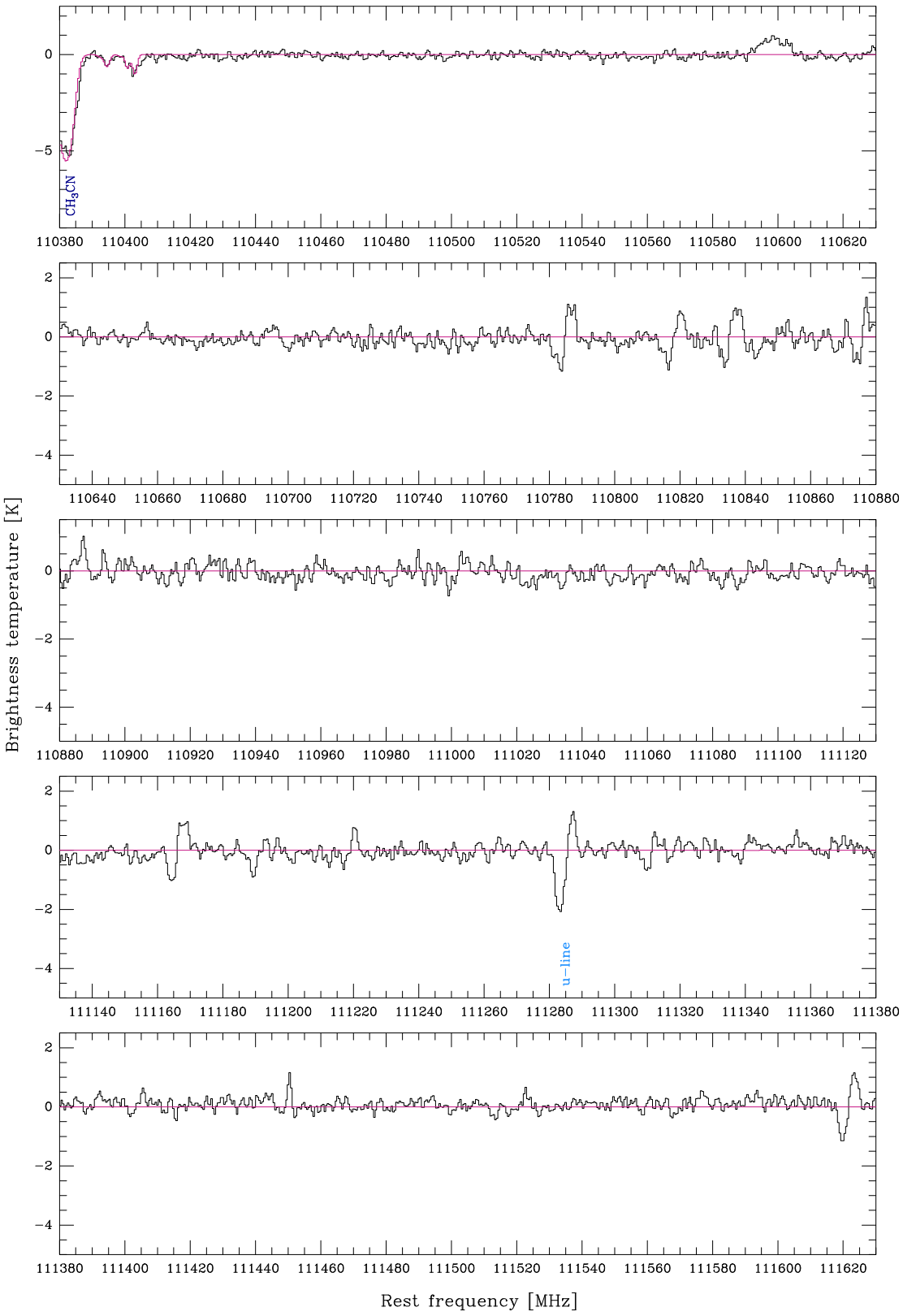

Figure A.24: Continued.

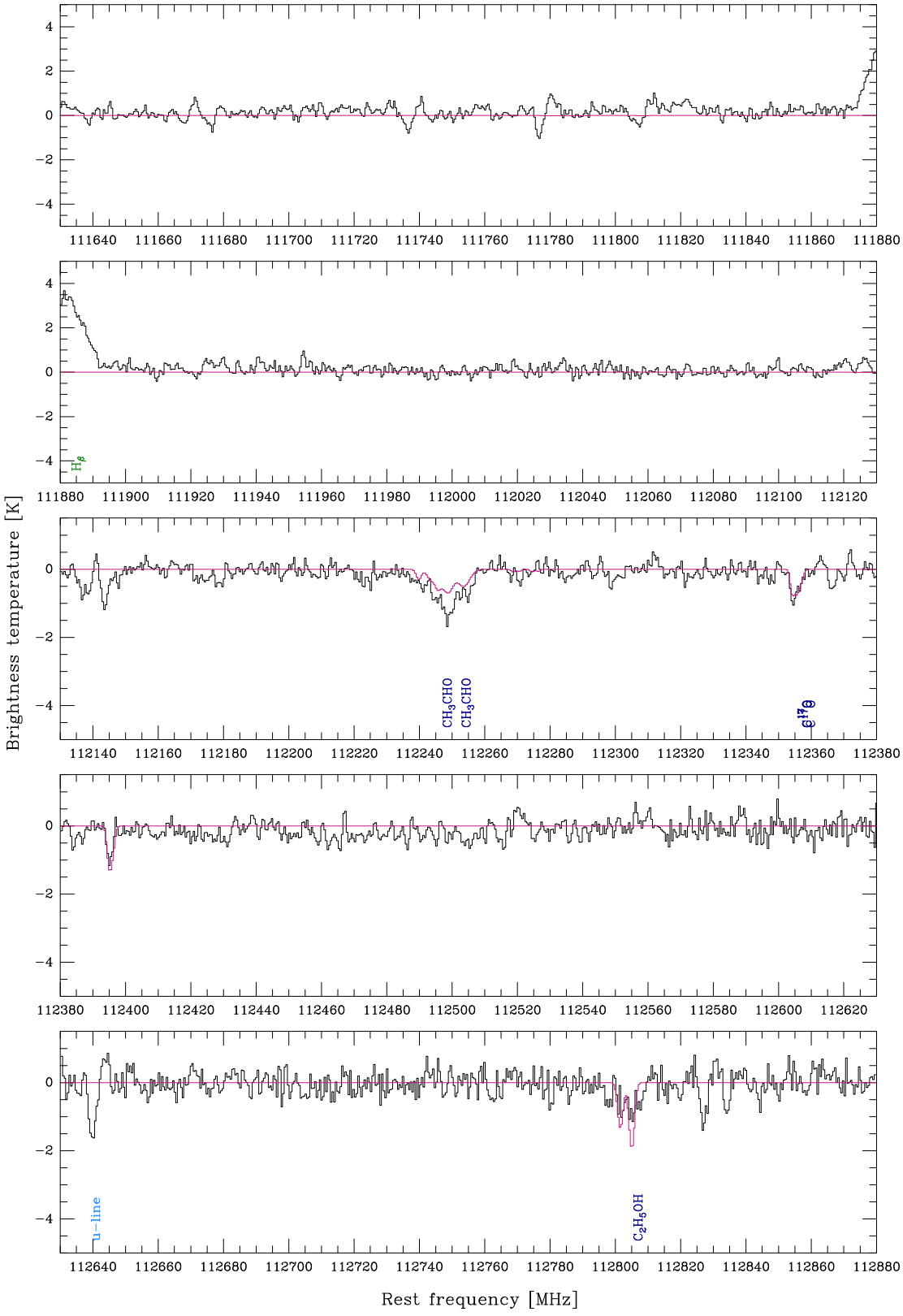

Figure A.24: Continued.

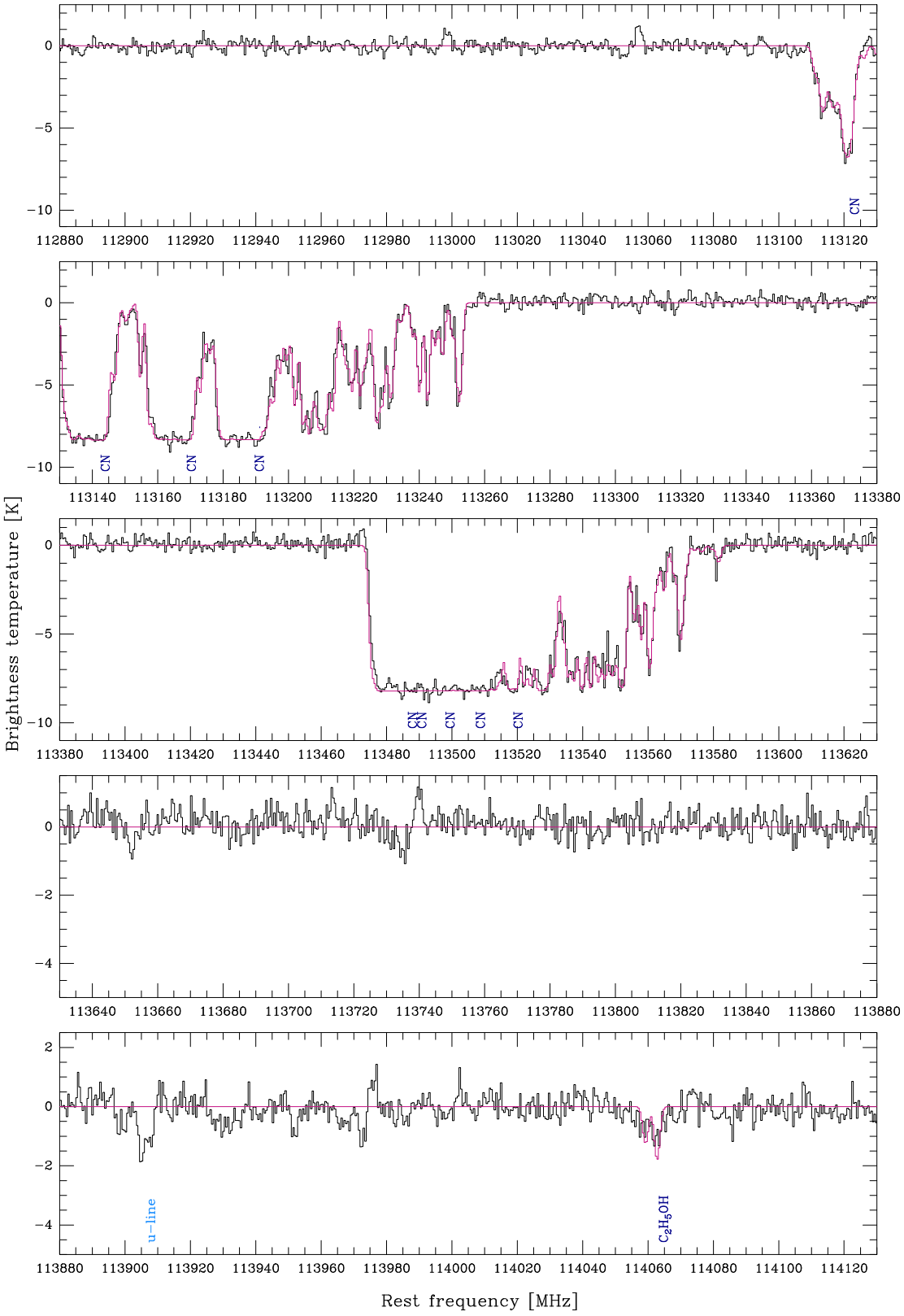

Figure A.24: Continued.

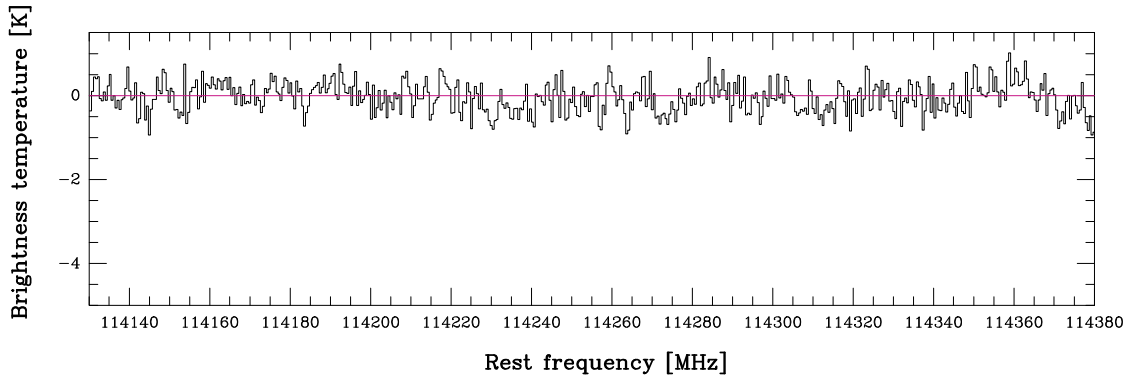

Figure A.24: Continued.

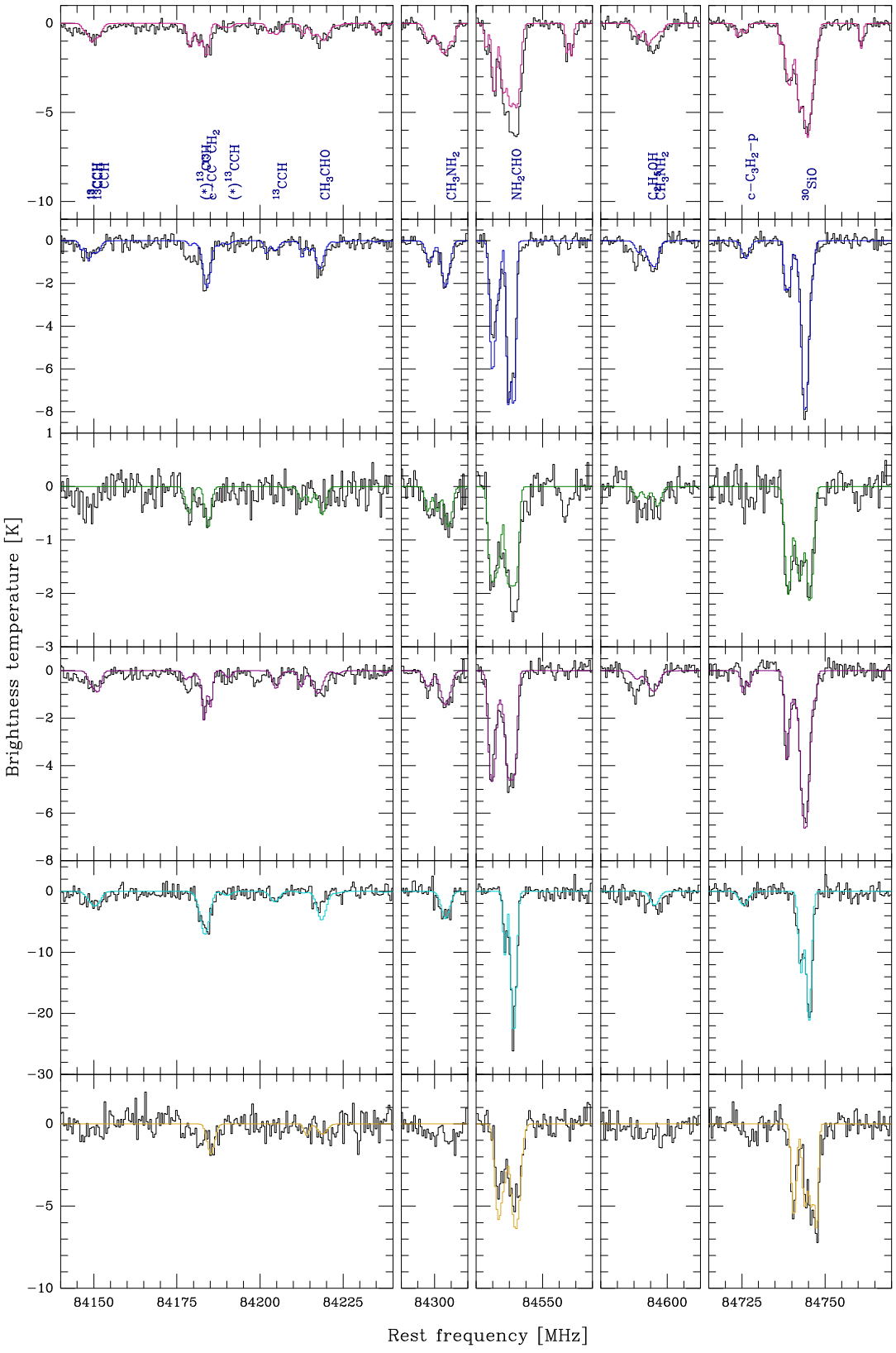

Figure A.25: ALMA spectra in black. The synthetic spectrum towards K4 is overlaid in magenta, towards $K6_{shell}$ in blue, towards $K5_{shell}$ in green, towards $K6_{shell,a}$ in purple, towards I in cyan, and towards L in dark yellow. The detected transitions are labeled in blue in the first panel.

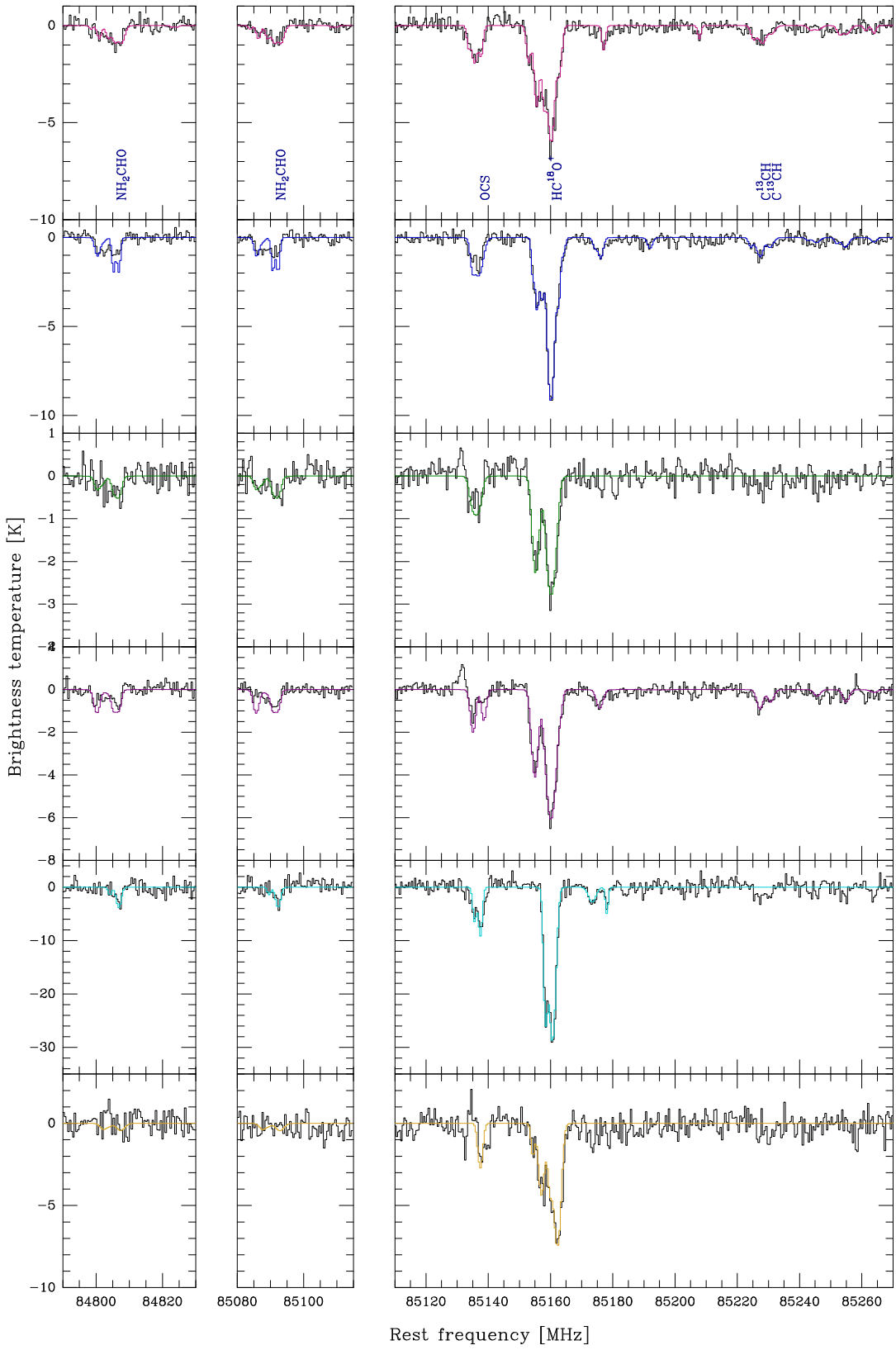

Figure A.25: Continued.

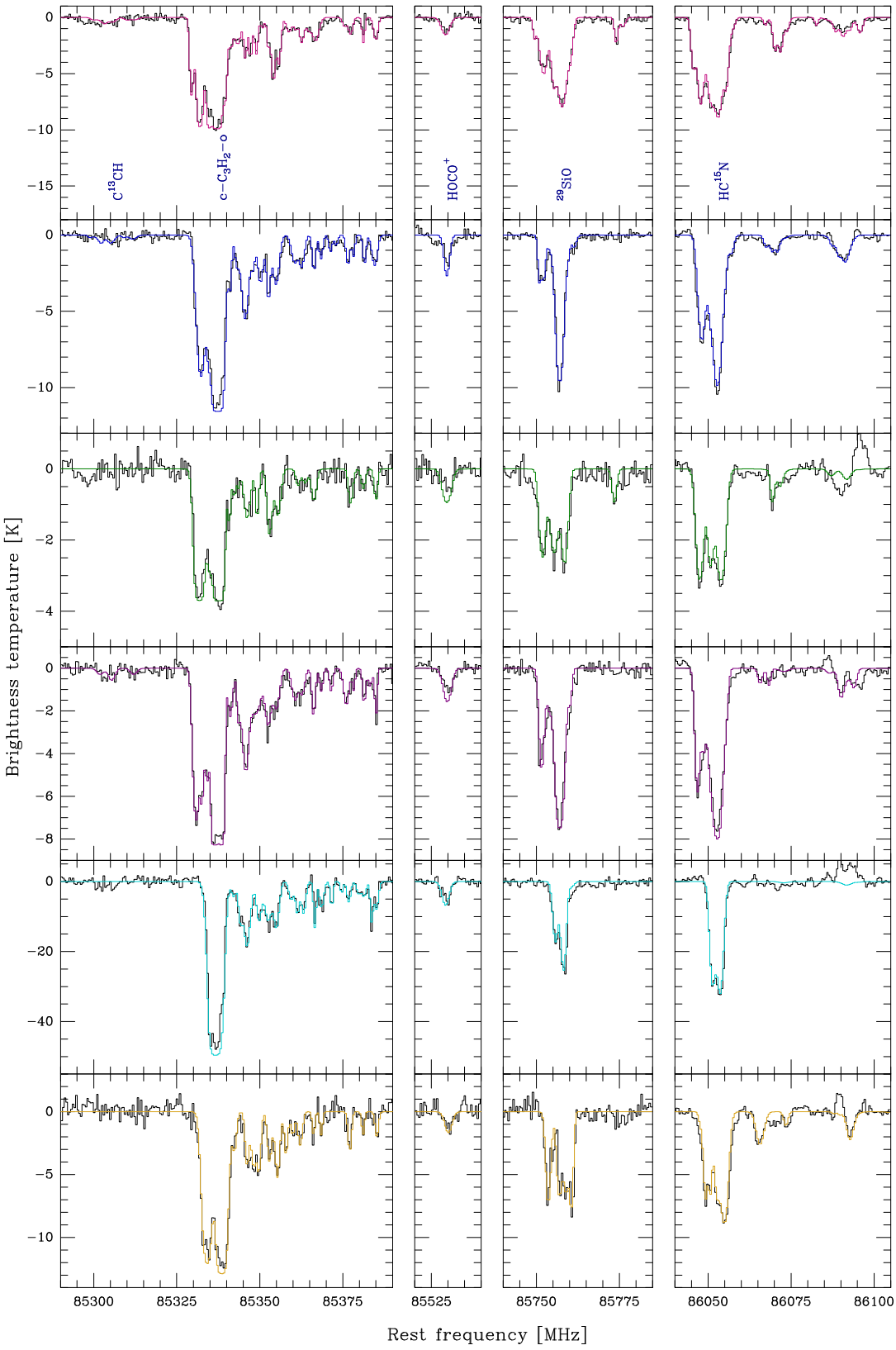

Figure A.25: Continued.

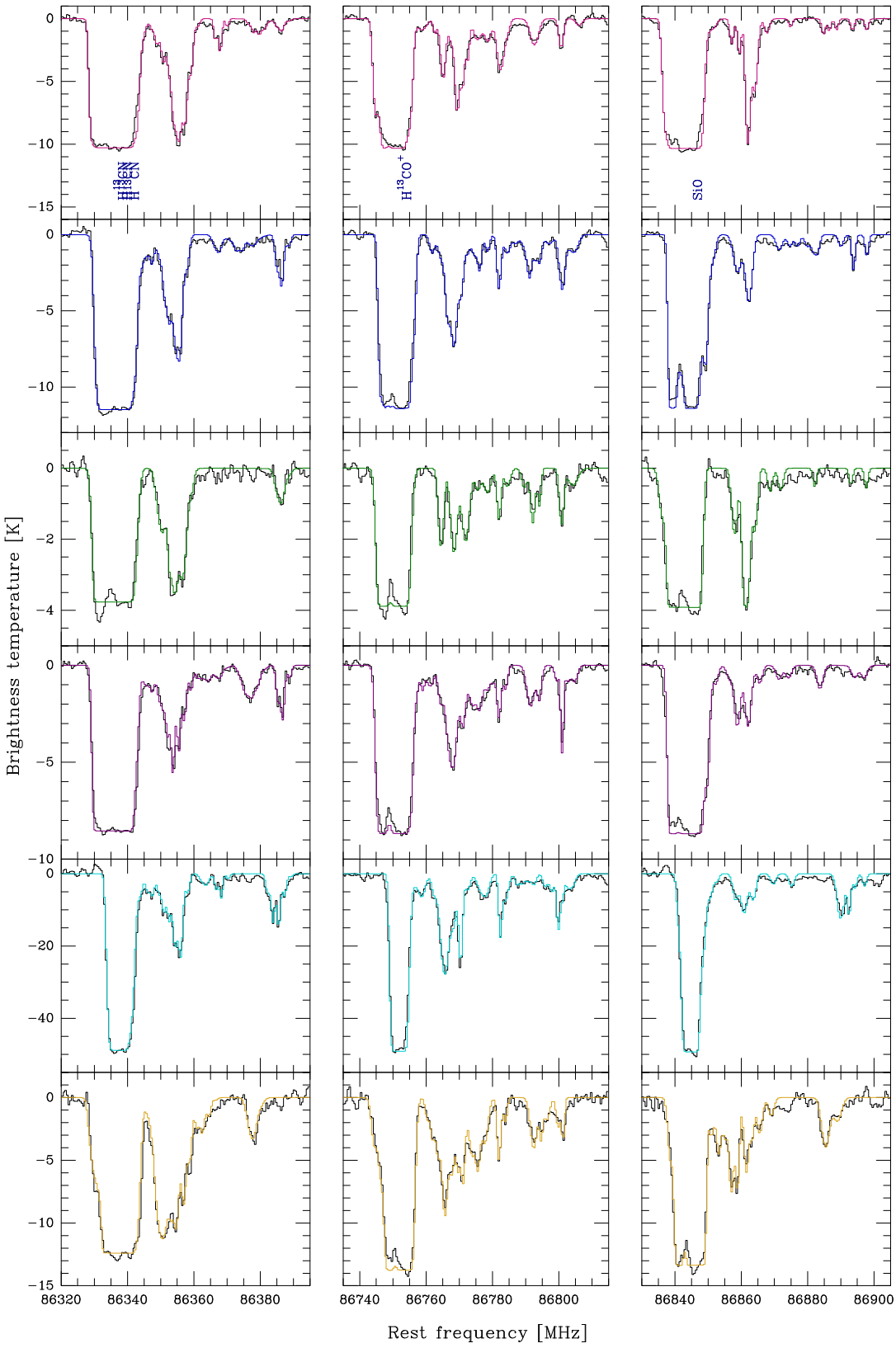

Figure A.25: Continued.

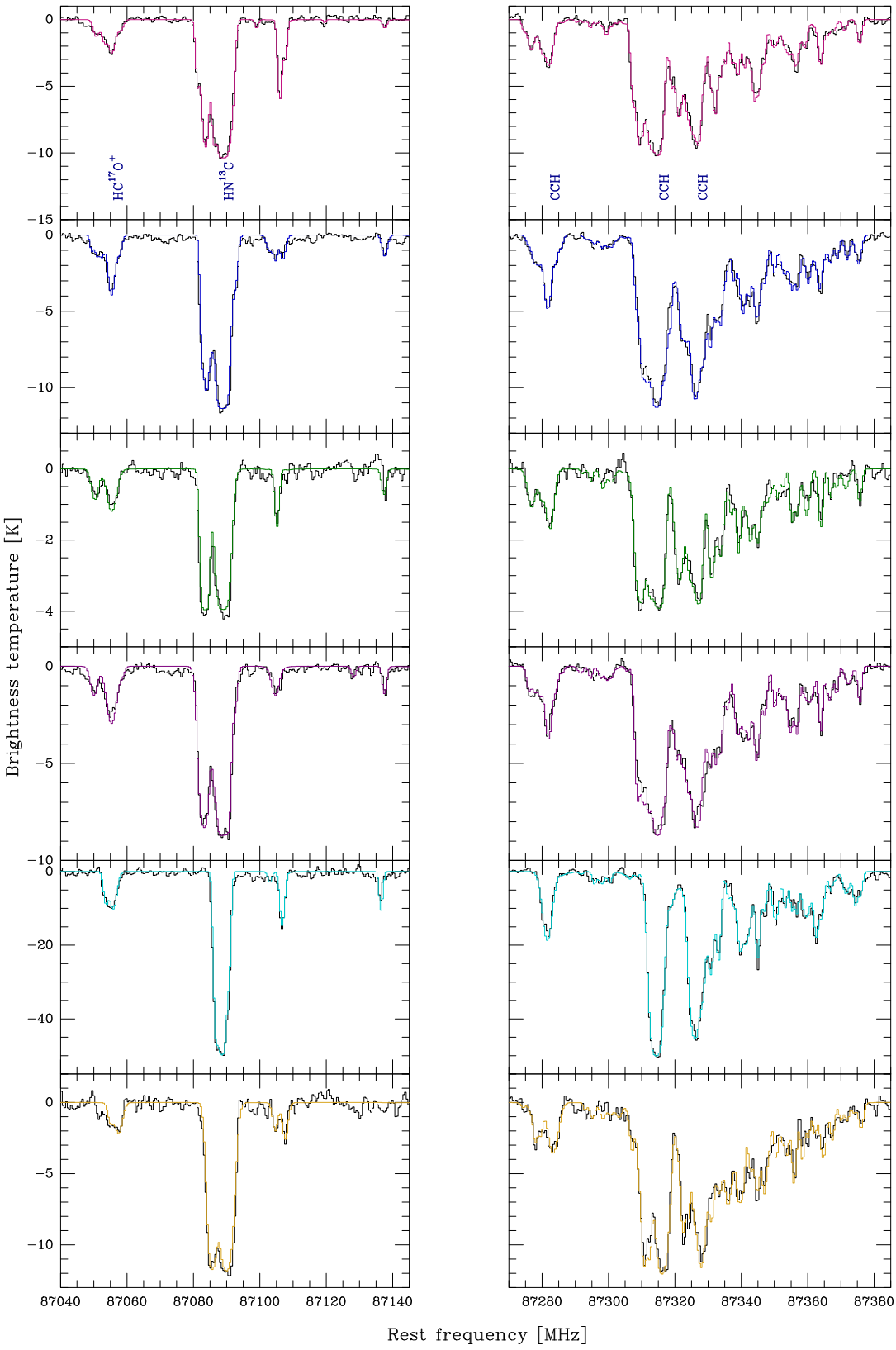

Figure A.25: Continued.

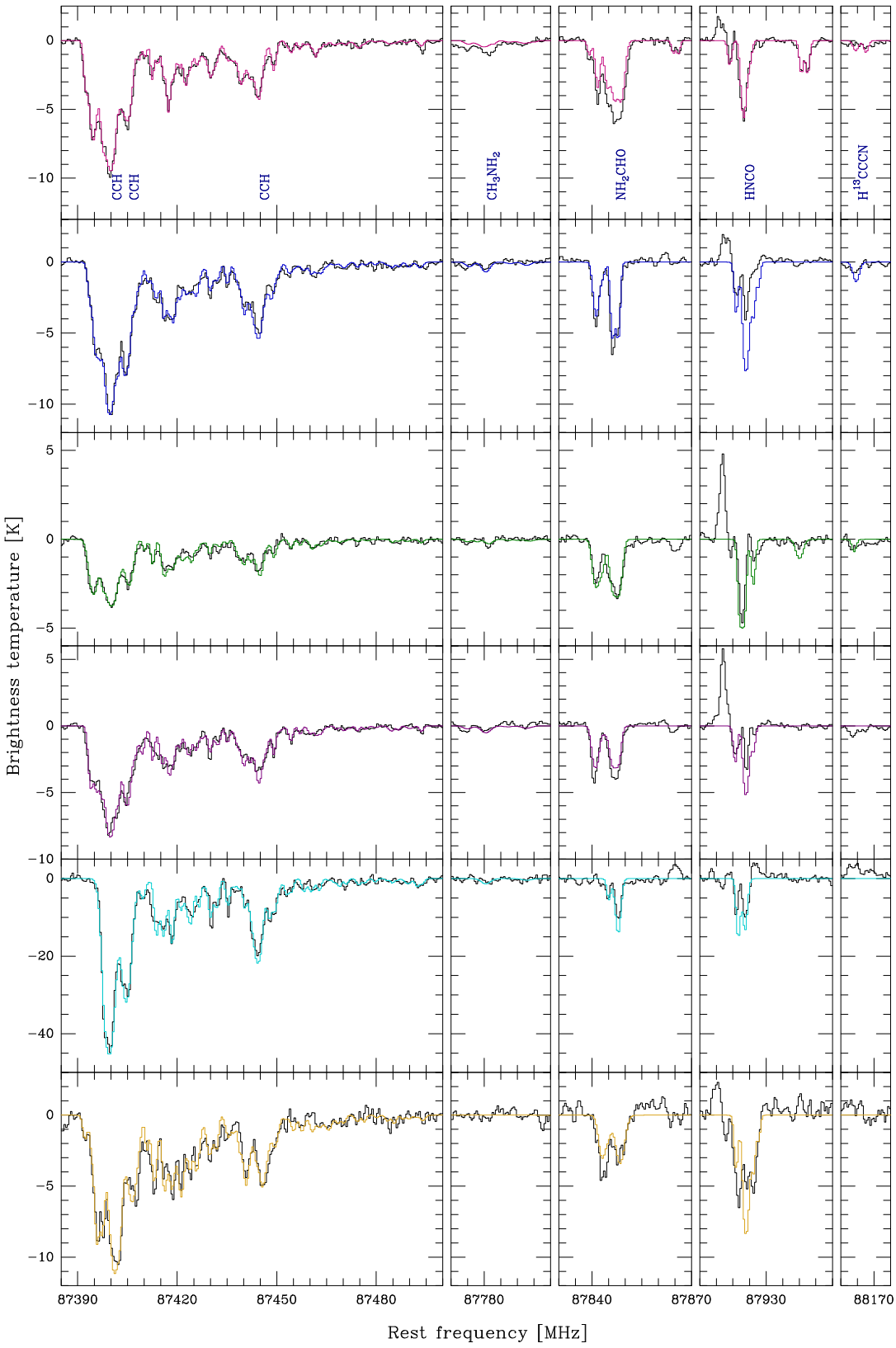

Figure A.25: Continued.

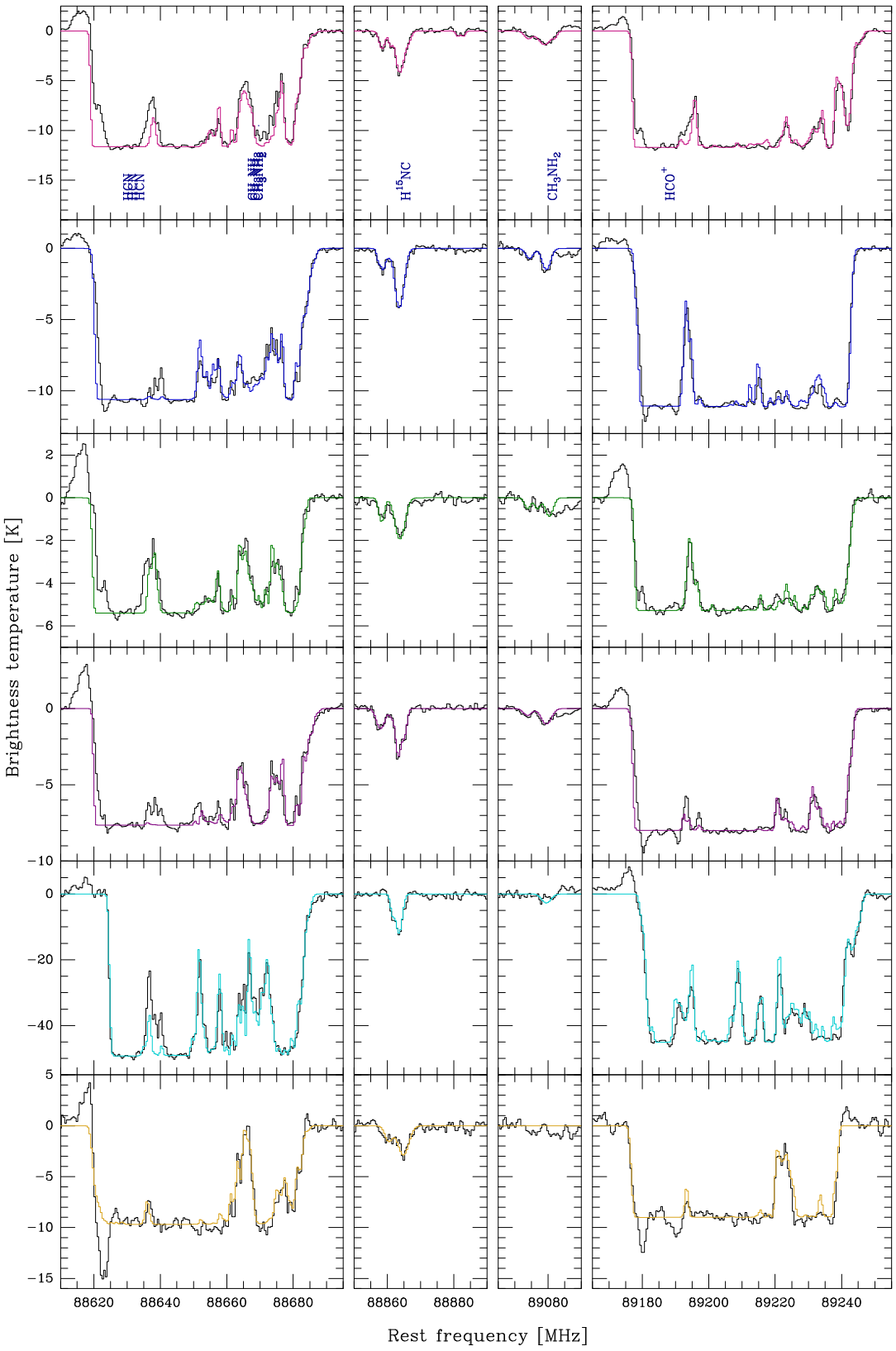

Figure A.25: Continued.

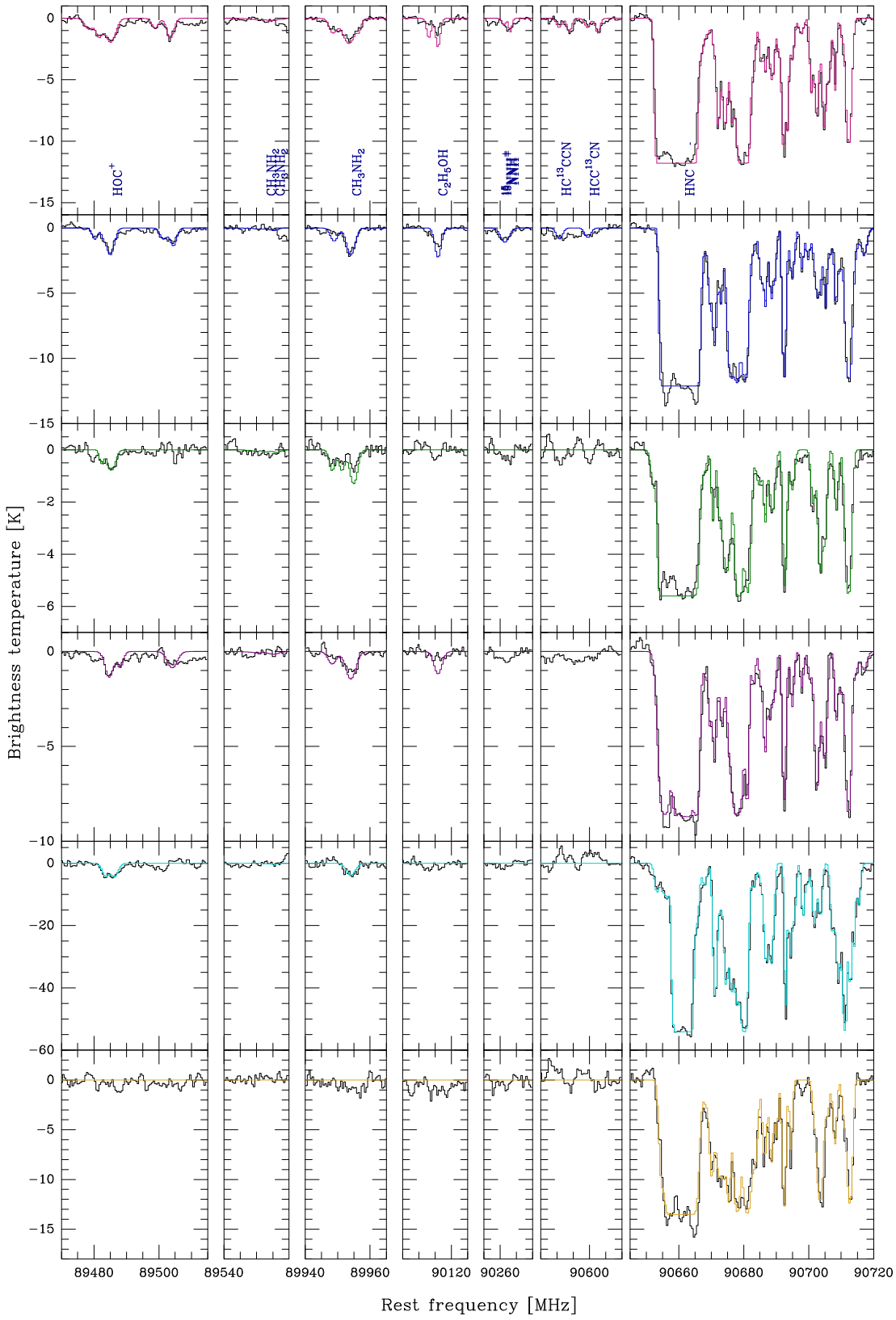

Figure A.25: Continued.

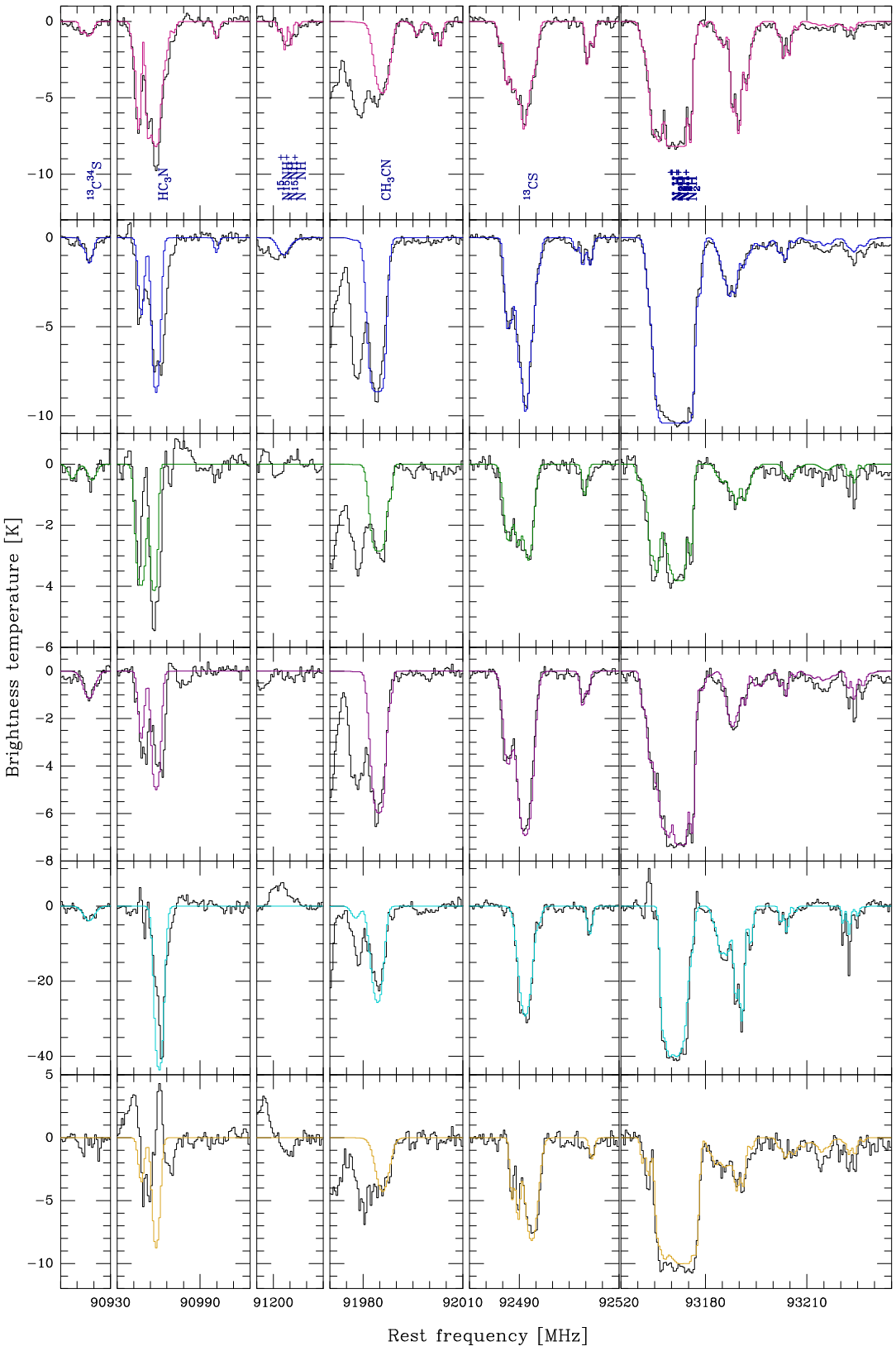

Figure A.25: Continued.

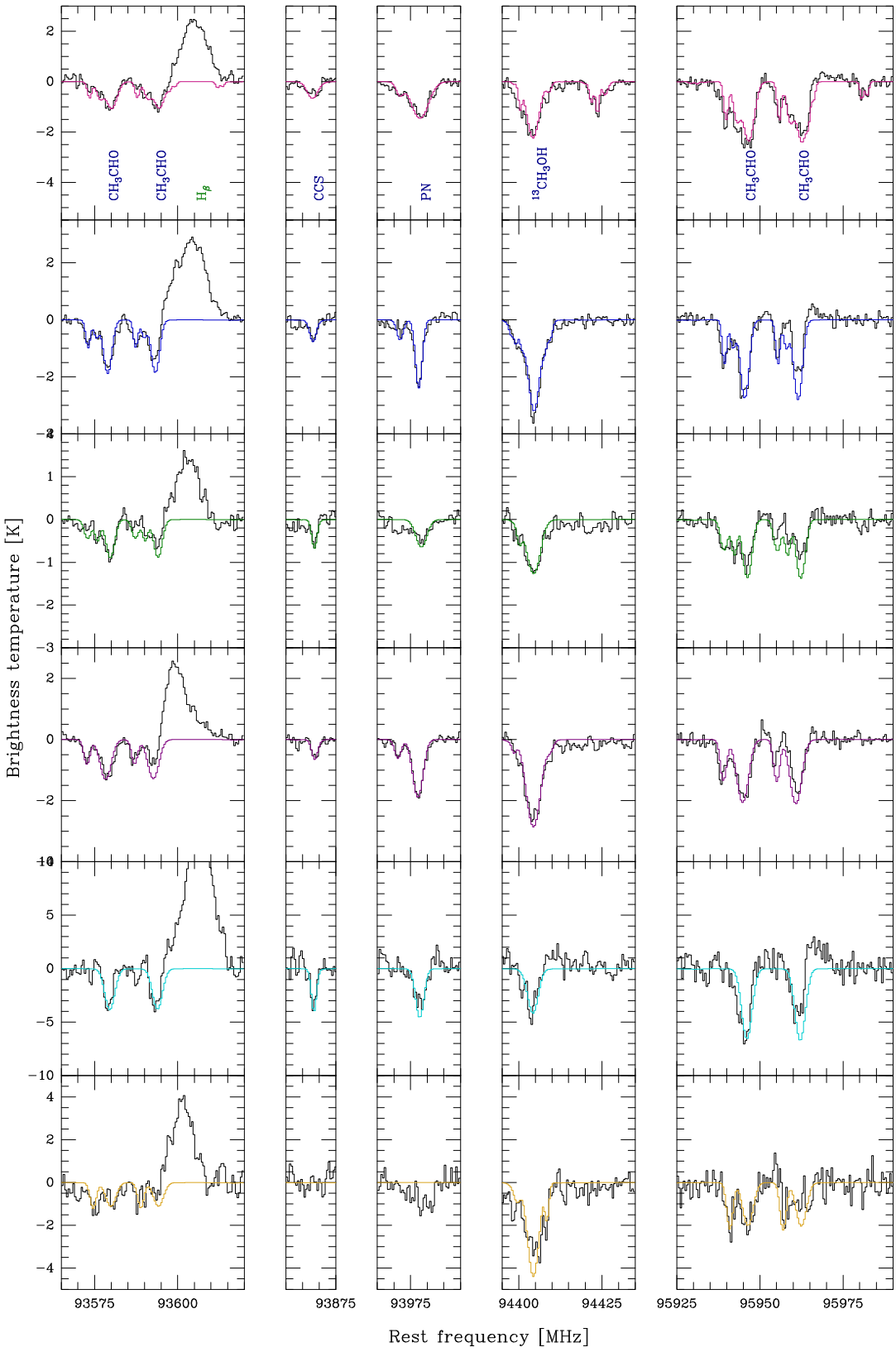

Figure A.25: Continued.

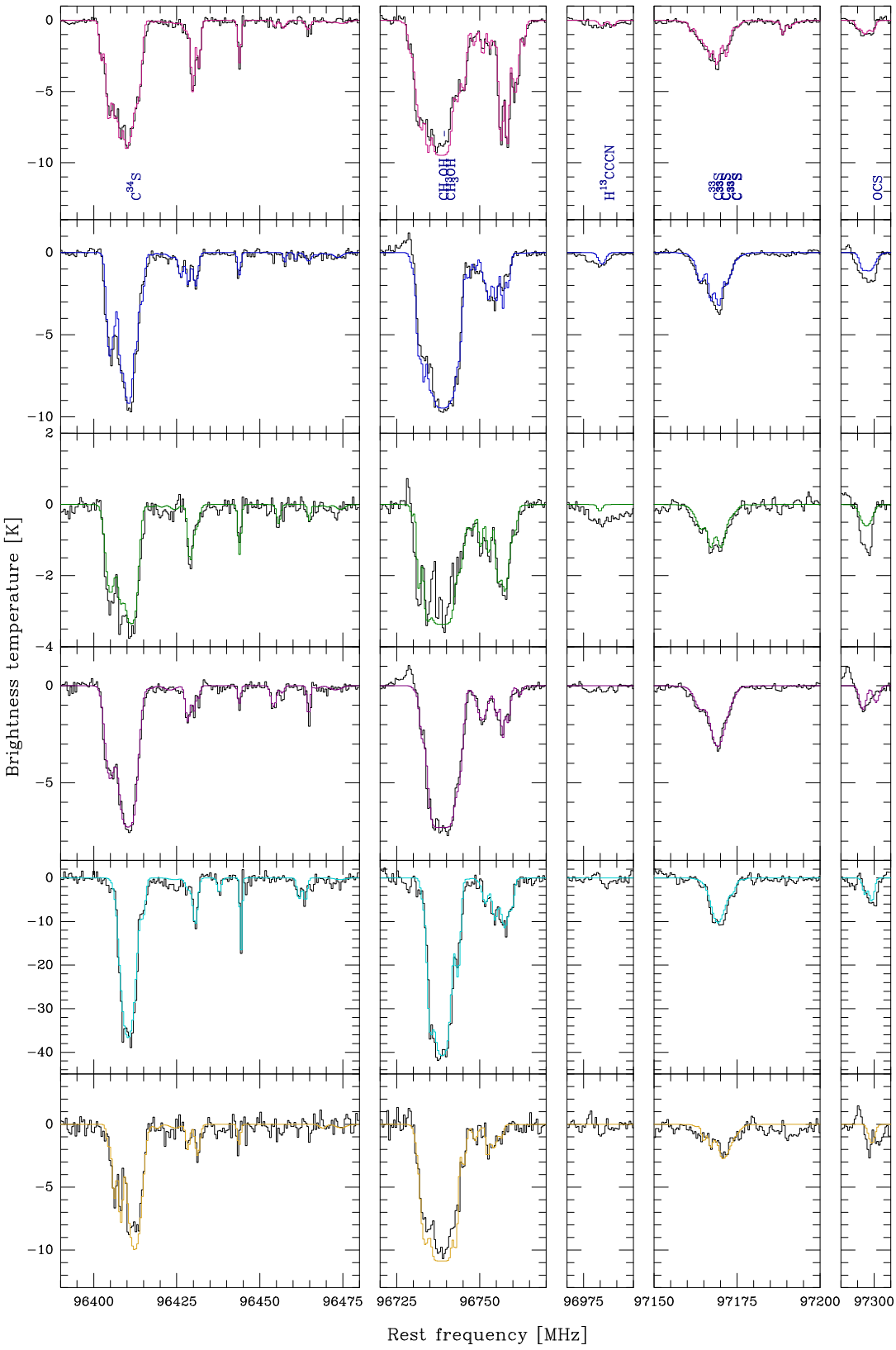

Figure A.25: Continued.

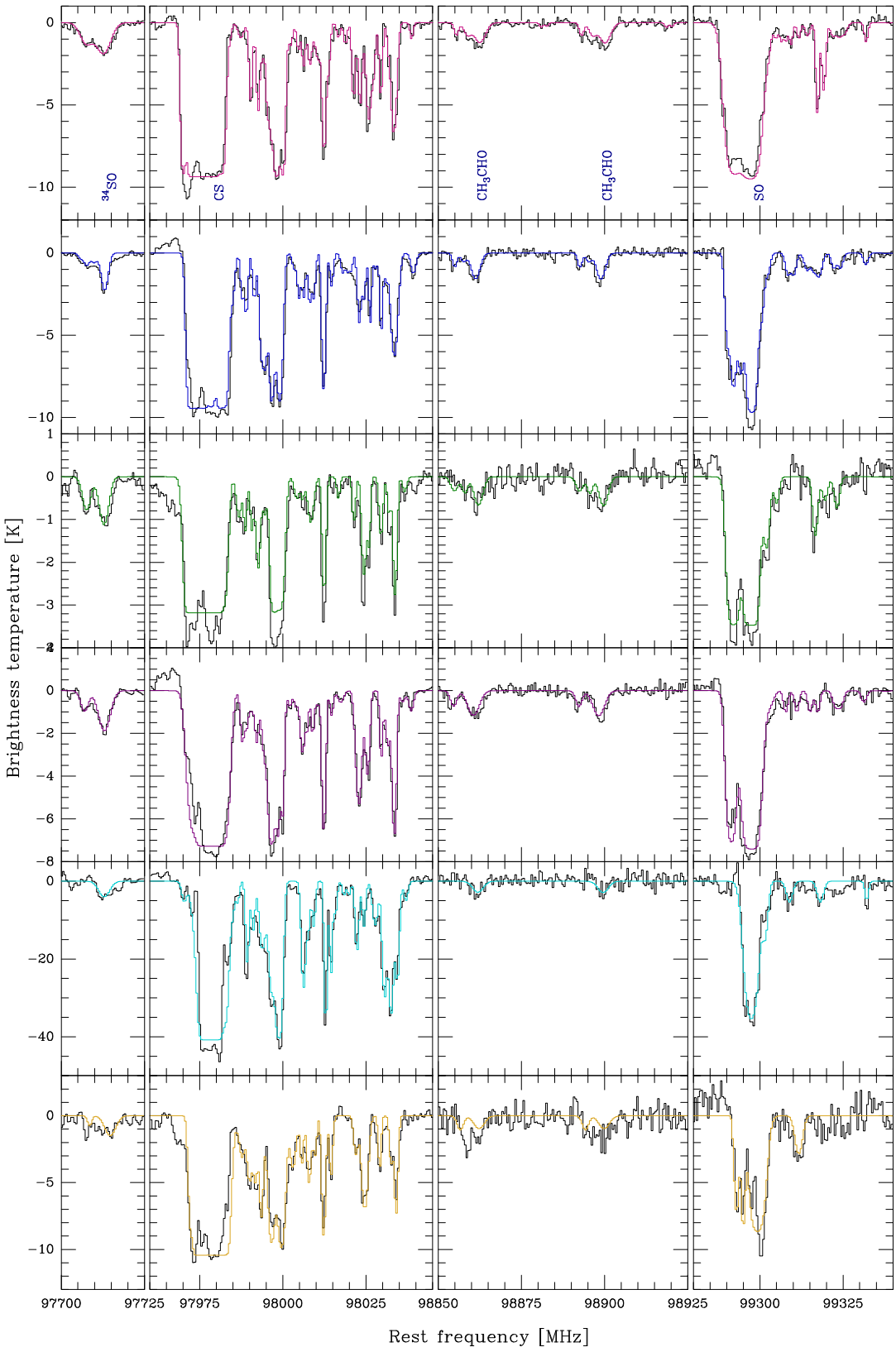

Figure A.25: Continued.

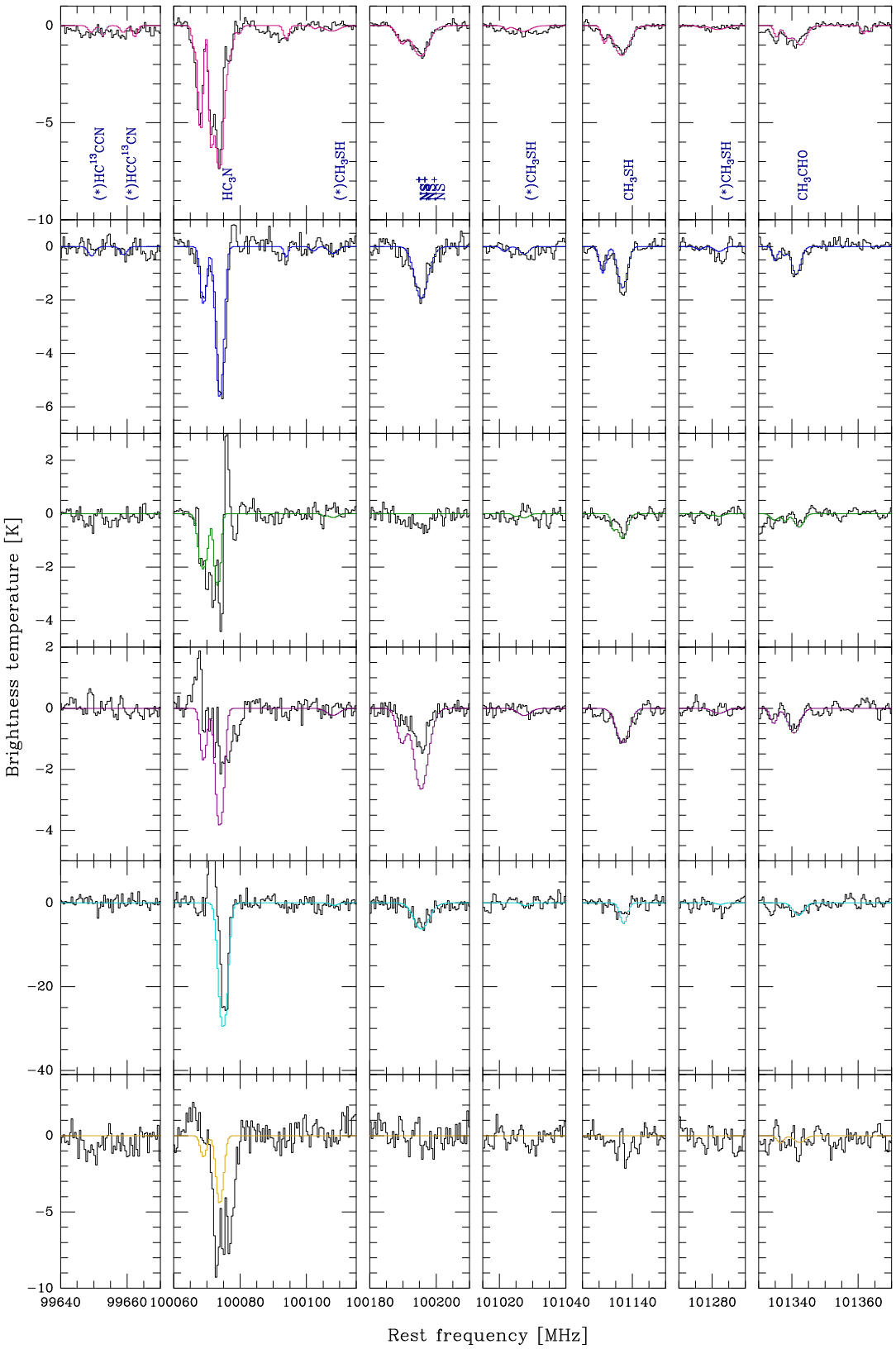

Figure A.25: Continued.

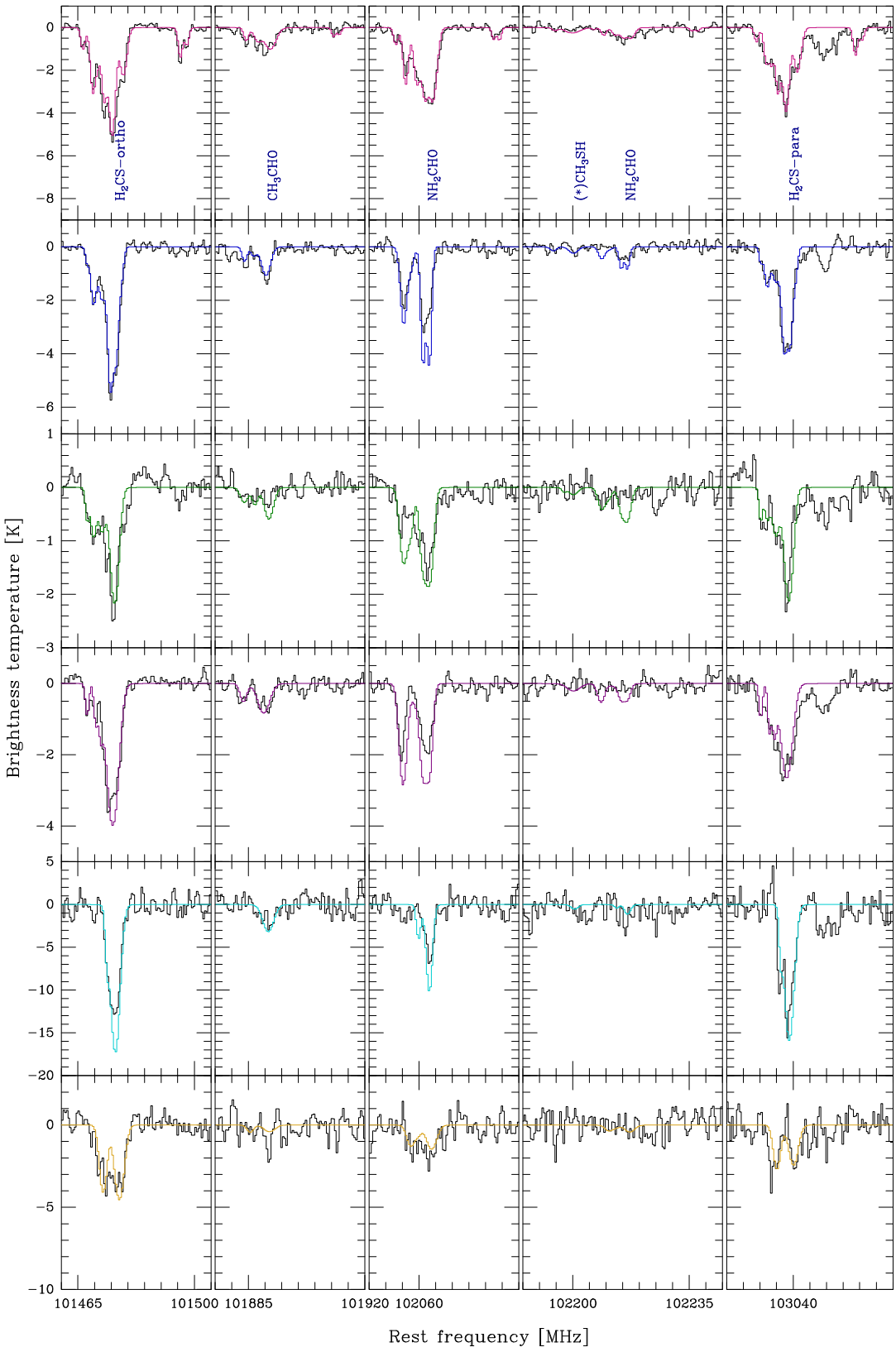

Figure A.25: Continued.

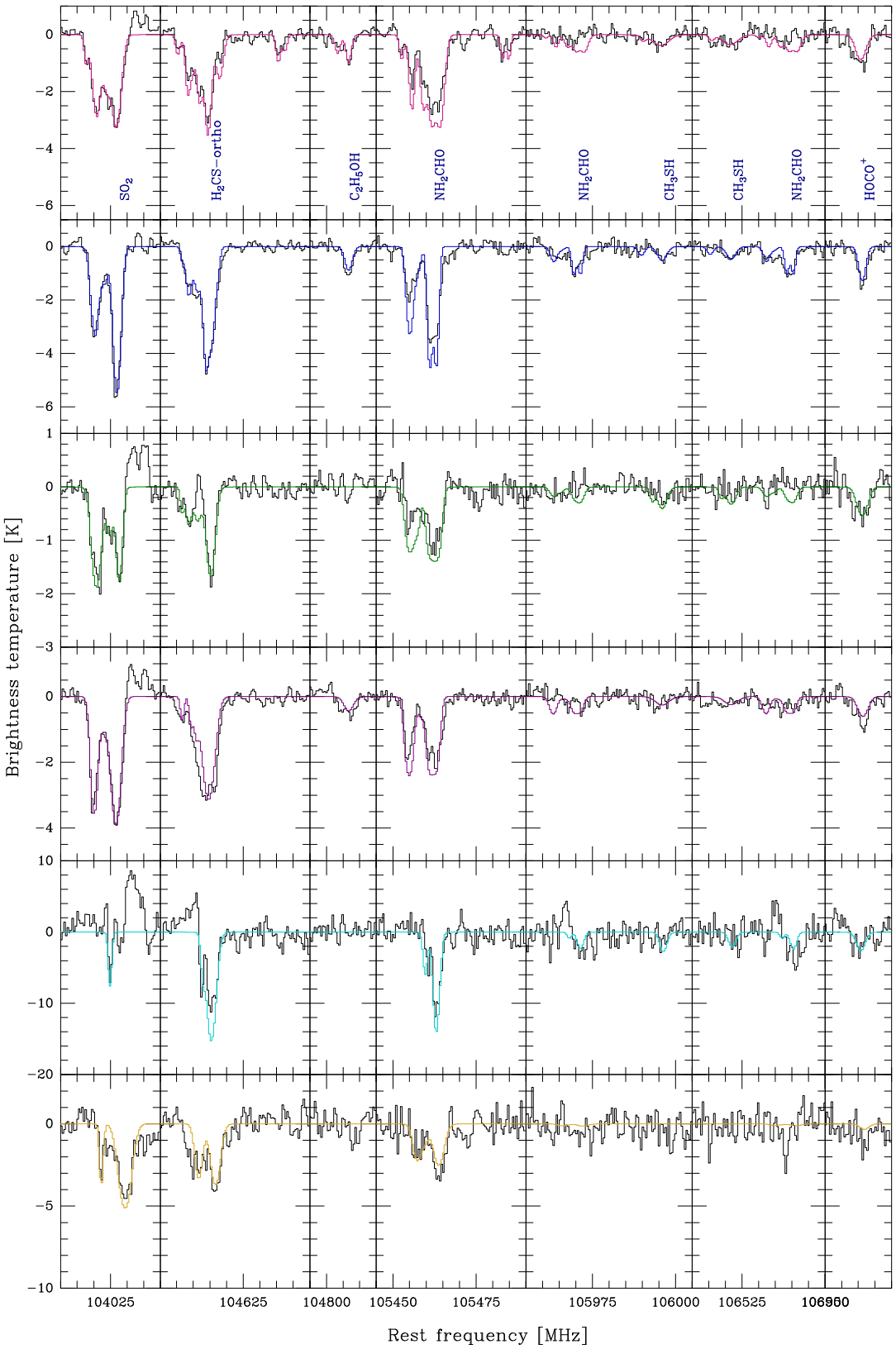

Figure A.25: Continued.

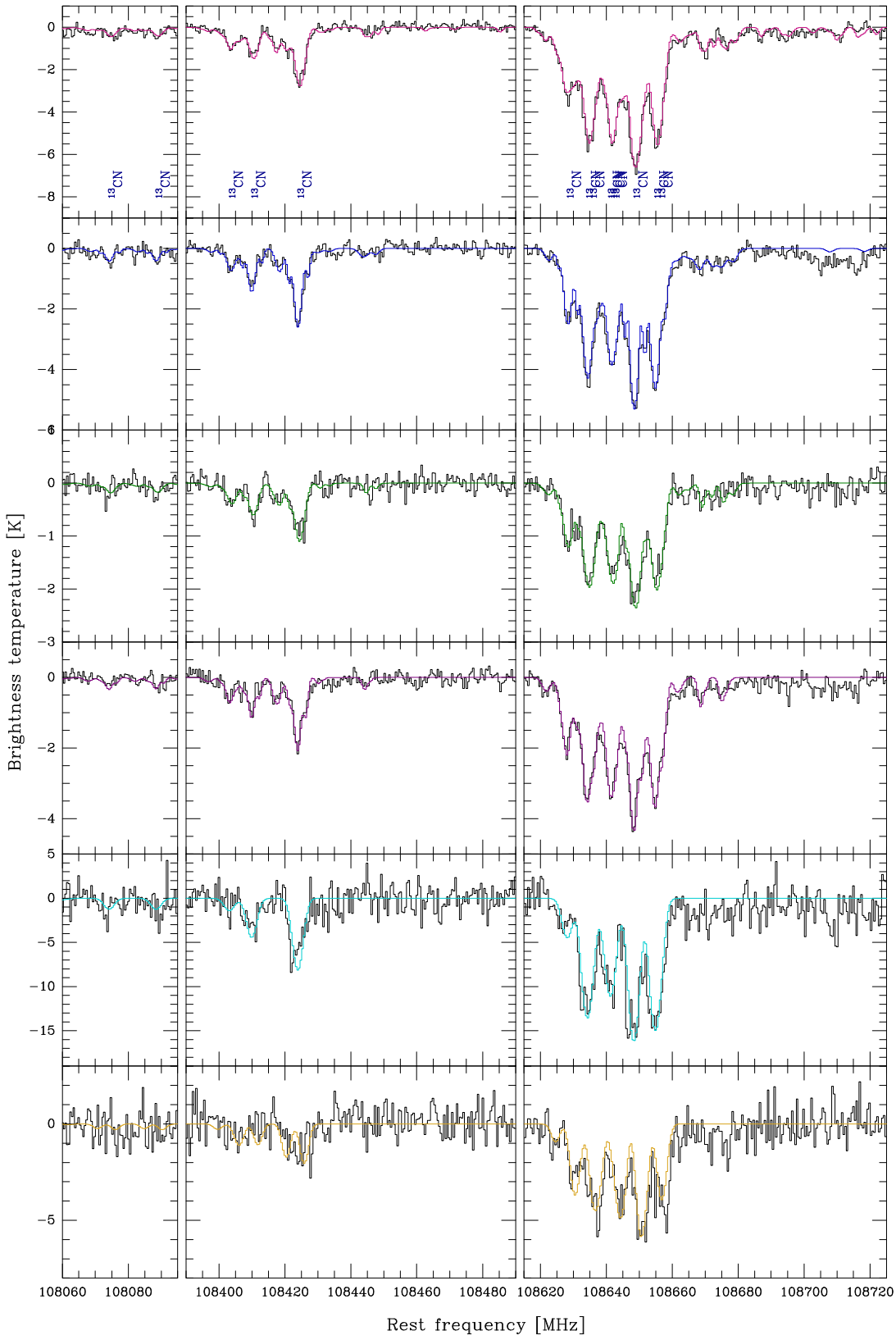

Figure A.25: Continued.

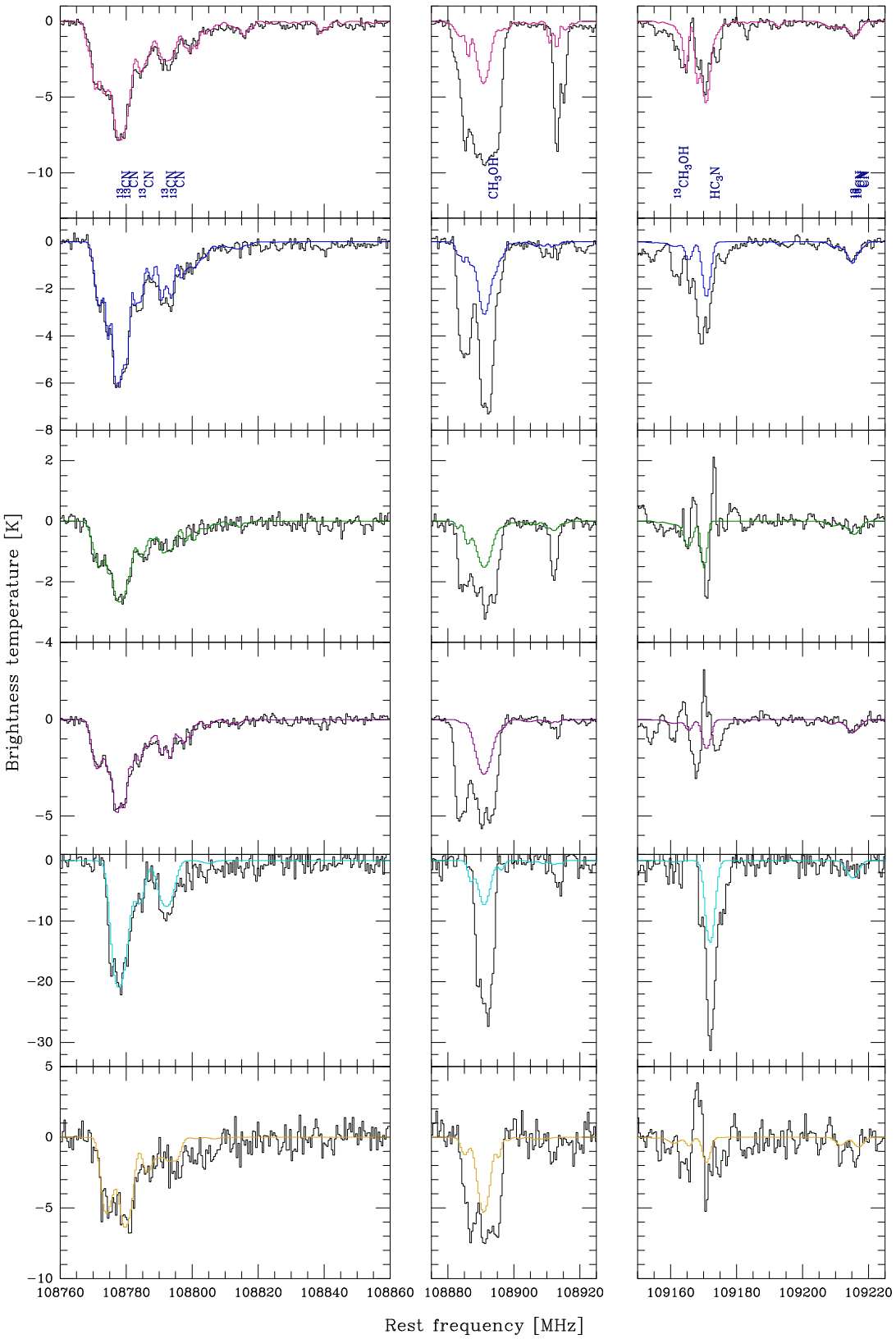

Figure A.25: Continued.

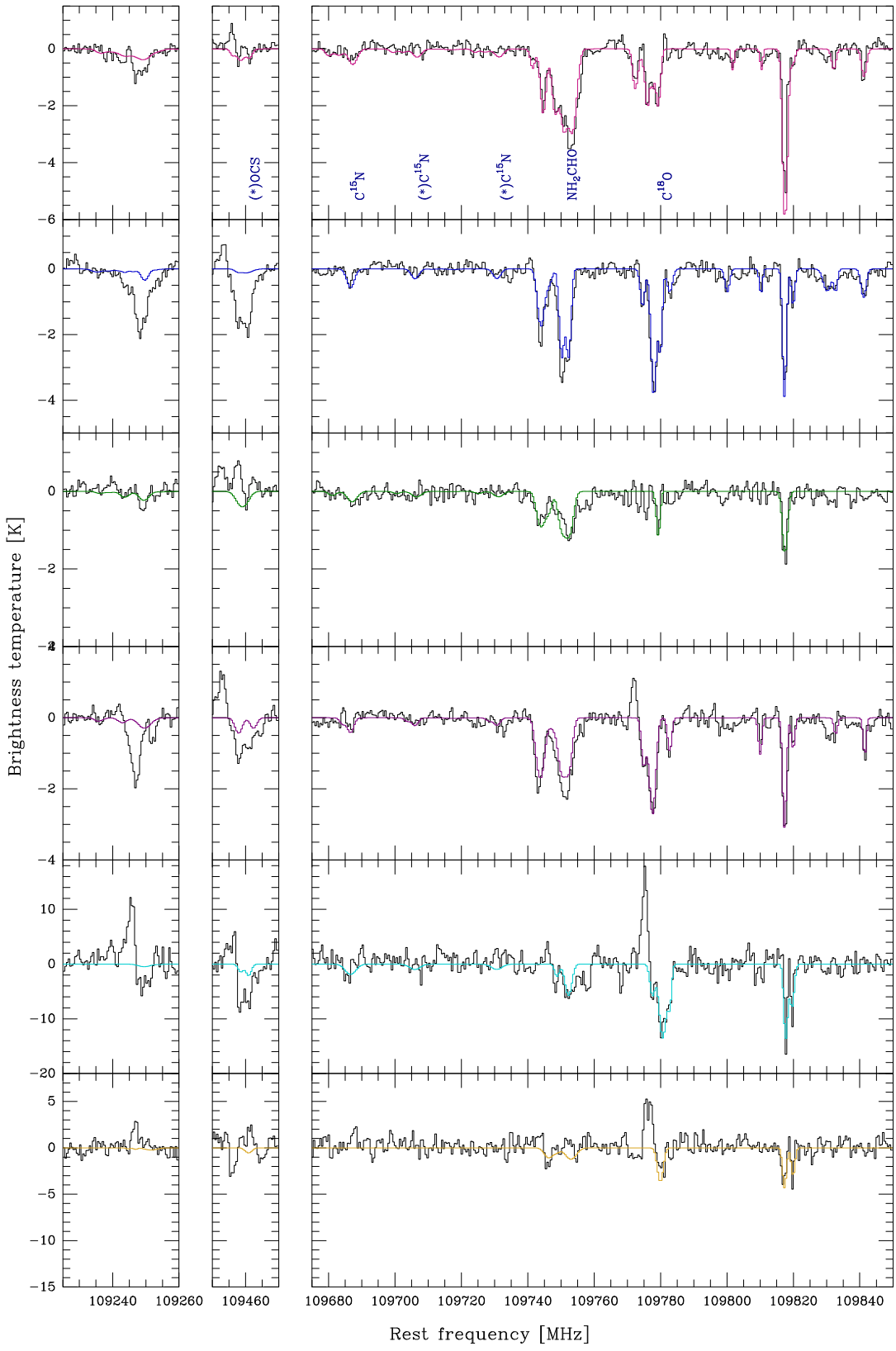

Figure A.25: Continued.

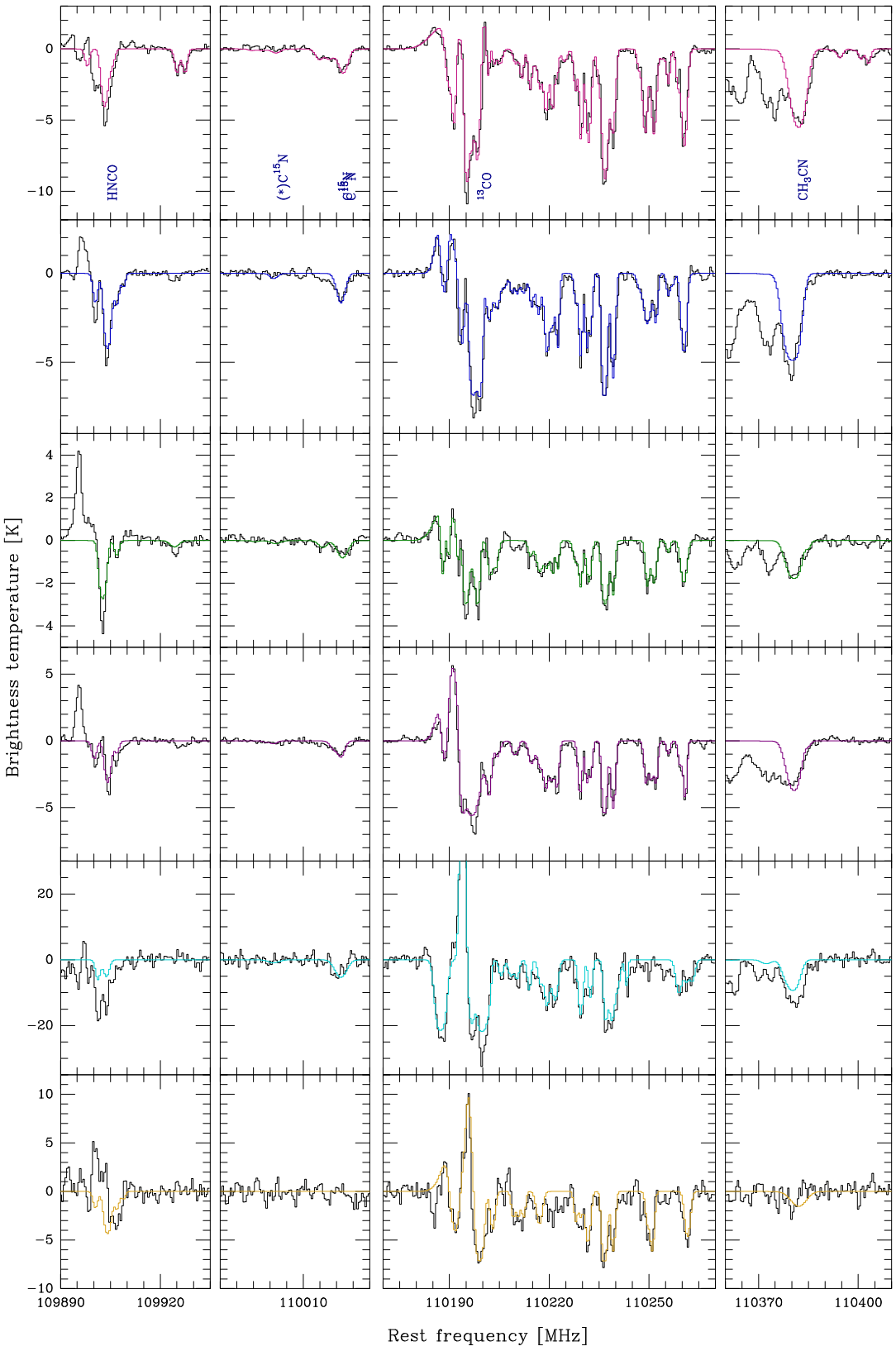

Figure A.25: Continued.

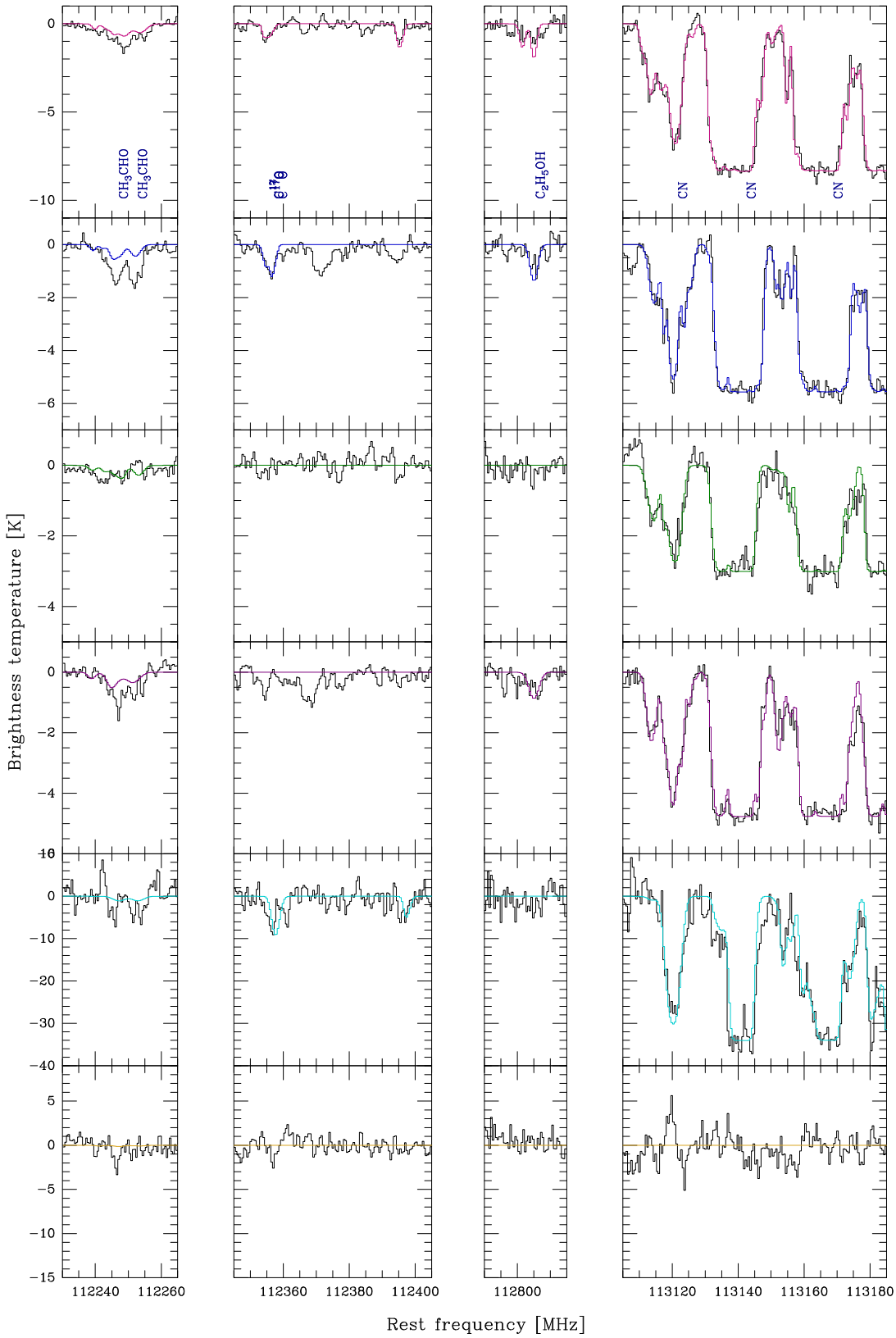

Figure A.25: Continued.

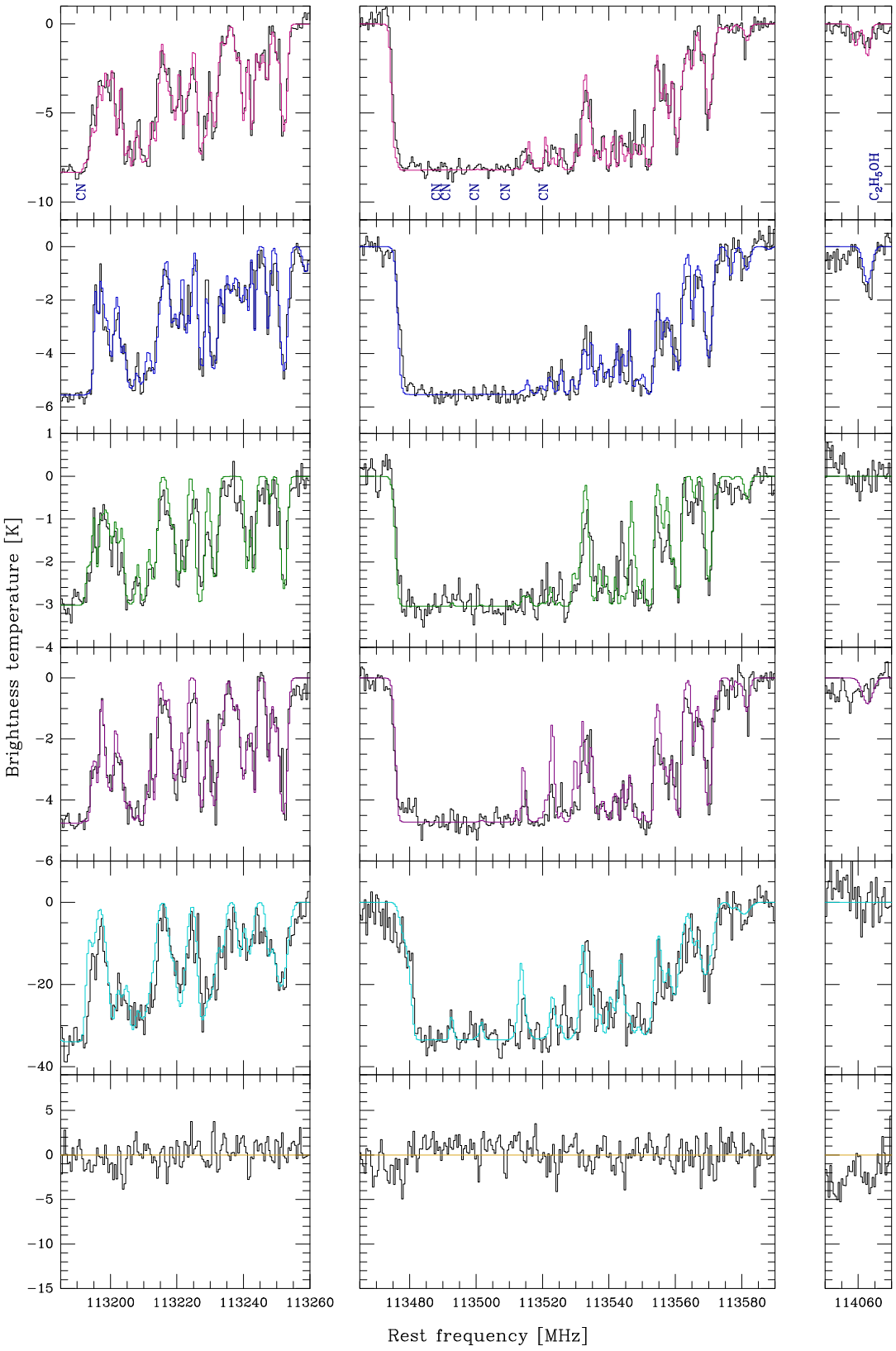

Figure A.25: Continued.

A.6 Model parameters

Table A.11: Parameters of our best-fit model of CH_3CHO.

Molecule	N_{tot}[a] [cm^{-2}]	v_{LSR}[b] [$km\,s^{-1}$]	$FWHM$[c] [$km\,s^{-1}$]	T_{rot}[d] [K]
		K4		
CH_3CHO	1.3×10^{14}	79.9	4.5	4.0
	2.0×10^{14}	69.9	7.5	4.0
	5.3×10^{14}	58.7	11.5	4.0
	5.0×10^{13}	2.6	3.5	3.0
	4.0×10^{13}	–2.4	3.5	3.0
		$K6_{shell}$		
CH_3CHO	1.4×10^{14}	81.4	4.5	4.2
	1.0×10^{14}	73.4	5.5	4.2
	5.3×10^{14}	62.4	9.0	4.2
		$K5_{shell}$		
CH_3CHO	3.5×10^{14}	81.7	7.5	4.2
	3.0×10^{14}	72.2	5.5	4.2
	9.3×10^{14}	59.9	9.0	4.2
		$K6_{shell,a}$		
CH_3CHO	2.4×10^{14}	82.4	6.5	4.1
	7.2×10^{14}	64.4	12.0	4.1
		I		
CH_3CHO	3.0×10^{14}	60.4	11.0	3.4
		L		
CH_3CHO	2.5×10^{14}	76.4	6.5	4.9
	3.8×10^{14}	59.4	11.0	4.9

Notes. [a]Column density. [b]LSR velocity. [c]Linewidth $FWHM$. [d]Rotational temperature.

Table A.12: Parameters of our best-fit model of CH_3CN.

Molecule	N_{tot}[a] [cm^{-2}]	v_{LSR}[b] [$km\,s^{-1}$]	$FWHM$[c] [$km\,s^{-1}$]	T_{rot}[d] [K]
		K4		
CH_3CN	4.0×10^{14}	59.3	11.0	5.8
	1.4×10^{13}	26.2	5.0	4.2
	1.0×10^{13}	9.2	4.0	4.2
	2.0×10^{13}	3.0	4.0	4.2
		$K6_{shell}$		
CH_3CN	1.0×10^{15}	64.4	10.0	4.9
		$K5_{shell}$		
CH_3CN	8.0×10^{14}	63.4	9.0	4.3
	3.0×10^{13}	52.0	4.0	4.3

Notes. See notes of Table A.11.

Table A.12: Continued.

Molecule	$N_{tot}{}^a$ [cm^{-2}]	$v_{LSR}{}^b$ [km s^{-1}]	$FWHM^c$ [km s^{-1}]	$T_{rot}{}^d$ [K]
		$K6_{shell,a}$		
CH_3CN	6.0×10^{14}	63.4	9.0	4.3
	1.3×10^{13}	52.0	4.0	4.3
		I		
CH_3CN	4.0×10^{14}	63.4	9.0	12.3
		L		
CH_3CN	1.2×10^{14}	59.4	13.0	4.3

Notes. See notes of Table A.11.

Table A.13: Parameters of our best-fit model of CS.

Molecule	$N_{tot}{}^a$ [cm^{-2}]	$v_{LSR}{}^b$ [km s^{-1}]	$FWHM^c$ [km s^{-1}]	$T_{rot}{}^d$ [K]
		K4		
CS	1.5×10^{14}	89.3	4.0	2.7
	6.6×10^{14}	82.2	4.0	2.7
	5.8×10^{14}	76.4	4.0	2.7
	7.0×10^{14}	71.6	5.0	2.7
	1.8×10^{15}	65.8	5.0	2.7
	7.6×10^{14}	61.1	5.0	2.7
	1.8×10^{12}	56.9	3.5	2.7
	2.0×10^{14}	53.9	5.5	2.7
	2.6×10^{12}	46.2	3.0	2.7
	5.6×10^{12}	36.4	6.0	2.7
	2.2×10^{13}	27.4	3.0	2.7
	2.6×10^{13}	20.7	3.0	2.7
	8.0×10^{12}	16.6	3.0	2.7
	2.6×10^{13}	12.0	3.0	2.7
	3.8×10^{13}	8.6	3.0	2.7
	3.0×10^{14}	3.7	3.5	2.7
	1.6×10^{14}	−2.1	3.5	2.7
	6.8×10^{12}	−9.1	4.5	2.7
	6.0×10^{12}	−16.4	3.0	2.7
	1.0×10^{13}	−21.2	3.0	2.7
	1.2×10^{13}	−27.0	4.0	2.7
	1.5×10^{13}	−34.7	6.0	2.7
	5.6×10^{13}	−40.1	3.0	2.7
	1.1×10^{13}	−44.3	3.0	2.7
	3.4×10^{12}	−53.3	3.5	2.7
	4.6×10^{12}	−59.6	3.0	2.7
	2.1×10^{13}	−67.1	3.0	2.7

Notes. See notes of Table A.11.

Table A.13: Continued.

Molecule	$N_{\rm tot}{}^a$ [cm^{-2}]	$v_{\rm LSR}{}^b$ [km s^{-1}]	$FWHM^c$ [km s^{-1}]	$T_{\rm rot}{}^d$ [K]
	2.6×10^{13}	−73.3	3.5	2.7
	4.5×10^{13}	−81.2	5.0	2.7
	1.0×10^{13}	−85.8	3.0	2.7
	2.0×10^{13}	−92.3	3.0	2.7
	4.5×10^{12}	−99.3	3.0	2.7
	5.8×10^{13}	−104.2	5.0	2.7
	3.4×10^{12}	−120.5	3.0	2.7
$C^{34}S$	1.2×10^{13}	89.3	4.0	2.7
	5.7×10^{13}	82.2	5.0	2.7
	4.2×10^{13}	76.4	4.0	2.7
	7.0×10^{13}	71.6	4.0	2.7
	1.2×10^{14}	65.8	5.0	2.7
	6.5×10^{13}	61.1	5.0	2.7
	1.3×10^{13}	56.9	3.5	2.7
	3.5×10^{13}	53.9	5.5	2.7
	1.6×10^{12}	12.0	3.0	2.7
	2.4×10^{12}	8.6	3.0	2.7
	2.3×10^{13}	3.7	3.5	2.7
	1.3×10^{13}	−2.1	3.5	2.7
	1.0×10^{13}	−40.1	3.0	2.7
	1.4×10^{12}	−73.3	3.5	2.7
	2.5×10^{12}	−81.2	5.0	2.7
	3.0×10^{12}	−104.2	5.0	2.7
^{13}CS	7.5×10^{12}	89.3	4.0	2.7
	3.3×10^{13}	82.2	5.0	2.7
	2.9×10^{13}	76.4	4.0	2.7
	3.5×10^{13}	71.6	4.0	2.7
	9.0×10^{13}	65.8	5.0	2.7
	3.8×10^{13}	61.1	5.0	2.7
	9.0×10^{12}	56.9	3.5	2.7
	1.8×10^{13}	53.9	5.5	2.7
	1.5×10^{13}	3.7	3.5	2.7
	8.0×10^{12}	−2.0	3.5	2.7
$C^{33}S$	3.4×10^{12}	89.3	4.0	2.7
	7.0×10^{12}	82.2	5.0	2.7
	7.5×10^{12}	76.4	4.0	2.7
	1.1×10^{13}	71.6	4.0	2.7
	1.9×10^{13}	65.8	5.0	2.7

Notes. See notes of Table A.11.

Table A.13: Continued.

Molecule	$N_{tot}{}^a$ [cm^{-2}]	$v_{LSR}{}^b$ [$km\,s^{-1}$]	$FWHM^c$ [$km\,s^{-1}$]	$T_{rot}{}^d$ [K]
	6.0×10^{12}	61.1	5.0	2.7
	8.0×10^{12}	56.9	3.5	2.7
	5.6×10^{12}	53.9	5.5	2.7
	4.8×10^{12}	3.7	3.5	2.7
	2.3×10^{12}	−2.1	3.5	2.7
$^{13}C^{34}S$	2.5×10^{12}	71.6	4.0	2.7
	3.5×10^{12}	65.8	5.0	2.7
	2.6×10^{12}	61.1	5.0	2.7
		$K6_{shell}$		
CS	6.8×10^{14}	81.4	6.0	2.7
	3.0×10^{14}	76.5	4.0	2.7
	6.0×10^{14}	71.1	4.0	2.7
	3.2×10^{14}	63.8	7.5	2.7
	2.8×10^{14}	56.2	3.0	2.7
	2.7×10^{14}	51.8	5.5	2.7
	1.5×10^{13}	44.3	4.5	2.7
	1.0×10^{13}	35.3	3.0	2.7
	1.5×10^{13}	31.5	3.0	2.7
	1.1×10^{13}	24.1	3.0	2.7
	1.9×10^{13}	18.4	3.0	2.7
	6.4×10^{13}	14.7	5.0	2.7
	1.2×10^{14}	8.0	4.0	2.7
	1.4×10^{14}	0.9	5.0	2.7
	4.0×10^{12}	−12.6	4.0	2.7
	1.0×10^{13}	−17.0	3.0	2.7
	1.0×10^{13}	−21.3	3.0	2.7
	1.2×10^{13}	−26.7	3.0	2.7
	1.0×10^{13}	−30.6	3.0	2.7
	6.8×10^{13}	−39.8	3.0	2.7
	7.2×10^{12}	−47.1	3.0	2.7
	5.2×10^{12}	−57.3	4.0	2.7
	3.5×10^{12}	−61.6	3.0	2.7
	3.5×10^{12}	−64.9	3.0	2.7
	2.0×10^{13}	−72.4	3.5	2.7
	1.0×10^{13}	−76.8	3.0	2.7
	1.6×10^{13}	−82.5	2.5	2.7
	3.6×10^{12}	−87.5	3.5	2.7
	2.0×10^{13}	−92.6	2.5	2.7
	5.3×10^{12}	−97.0	3.0	2.7

Notes. See notes of Table A.11.

Table A.13: Continued.

Molecule	$N_{\rm tot}{}^a$ [cm^{-2}]	$v_{\rm LSR}{}^b$ [km s^{-1}]	$FWHM^c$ [km s^{-1}]	$T_{\rm rot}{}^d$ [K]
	6.3×10^{13}	−104.7	6.5	2.7
	6.4×10^{12}	−122.2	5.0	2.7
$C^{34}S$	5.3×10^{13}	81.4	6.0	2.7
	1.4×10^{13}	76.5	4.0	2.7
	3.9×10^{13}	71.1	4.0	2.7
	2.0×10^{14}	63.8	7.5	2.7
	1.8×10^{13}	56.2	3.0	2.7
	1.8×10^{13}	51.8	5.5	2.7
	6.9×10^{12}	14.7	5.0	2.7
	7.9×10^{12}	8.0	4.0	2.7
	1.0×10^{13}	0.9	5.0	2.7
	4.2×10^{12}	−39.8	3.0	2.7
	1.4×10^{12}	−82.5	2.5	2.7
	1.2×10^{12}	−92.6	2.5	2.7
	3.0×10^{12}	−104.7	6.5	2.7
^{13}CS	3.4×10^{13}	81.4	6.0	2.7
	1.5×10^{13}	76.5	4.0	2.7
	3.0×10^{13}	71.1	4.0	2.7
	1.6×10^{14}	63.8	7.5	2.7
	1.4×10^{13}	56.2	3.0	2.7
	1.0×10^{13}	51.8	5.5	2.7
	3.2×10^{12}	14.7	5.0	2.7
	6.0×10^{12}	8.0	4.0	2.7
	7.0×10^{12}	0.9	5.0	2.7
$C^{33}S$	1.3×10^{13}	81.4	6.0	2.7
	3.5×10^{12}	76.5	4.0	2.7
	1.2×10^{13}	71.1	4.0	2.7
	3.2×10^{13}	63.8	7.5	2.7
	5.0×10^{12}	56.2	3.0	2.7
	4.5×10^{12}	52.0	5.5	2.7
$^{13}C^{34}S$	1.2×10^{12}	71.1	4.0	2.7
	8.2×10^{12}	63.8	7.5	2.7
		$K5_{\rm shell}$		
CS	1.5×10^{15}	80.6	9.0	2.7
	1.0×10^{15}	71.1	6.0	2.7
	2.4×10^{15}	61.3	9.5	2.7
	7.1×10^{13}	50.8	5.5	2.7

Notes. See notes of Table A.11.

Table A.13: Continued.

Molecule	$N_{\rm tot}{}^a$ [cm^{-2}]	$v_{\rm LSR}{}^b$ [km s^{-1}]	$FWHM^c$ [km s^{-1}]	$T_{\rm rot}{}^d$ [K]
	1.6×10^{13}	38.3	5.0	2.7
	1.5×10^{13}	32.4	3.0	2.7
	1.5×10^{13}	26.3	3.0	2.7
	4.2×10^{13}	20.5	4.0	2.7
	1.2×10^{13}	14.5	4.0	2.7
	2.6×10^{14}	6.0	5.0	2.7
	2.0×10^{14}	0.1	6.0	2.7
	8.0×10^{12}	−15.0	5.0	2.7
	5.0×10^{12}	−20.3	3.0	2.7
	2.2×10^{13}	−27.7	6.0	2.7
	5.9×10^{13}	−40.1	3.0	2.7
	5.2×10^{12}	−53.1	3.0	2.7
	1.2×10^{13}	−67.4	3.0	2.7
	4.8×10^{13}	−76.8	4.0	2.7
	1.8×10^{13}	−81.5	2.5	2.7
	2.0×10^{13}	−92.4	3.5	2.7
	1.0×10^{13}	−99.8	3.0	2.7
	6.3×10^{13}	−105.3	3.0	2.7
	4.4×10^{12}	−114.2	4.0	2.7
$C^{34}S$	9.4×10^{13}	80.6	9.0	2.7
	6.9×10^{13}	71.1	6.0	2.7
	2.8×10^{14}	61.3	9.5	2.7
	2.5×10^{13}	6.0	5.0	2.7
	1.0×10^{13}	0.1	6.0	2.7
	1.4×10^{13}	−40.1	3.0	2.7
	5.8×10^{12}	−76.8	4.0	2.7
	3.8×10^{12}	−105.3	3.0	2.7
^{13}CS	7.4×10^{13}	80.6	9.0	2.7
	4.9×10^{13}	71.1	6.0	2.7
	1.2×10^{14}	61.3	9.5	2.7
	1.3×10^{13}	6.0	5.0	2.7
$C^{33}S$	1.8×10^{13}	80.6	9.0	2.7
	2.3×10^{13}	71.1	6.0	2.7
	3.7×10^{13}	61.3	9.5	2.7
$^{13}C^{34}S$	7.0×10^{12}	80.6	9.0	2.7
	8.0×10^{12}	61.3	9.5	2.7

Notes. See notes of Table A.11.

Table A.13: Continued.

Molecule	N_{tot}[a] [cm^{-2}]	v_{LSR}[b] [km s^{-1}]	$FWHM$[c] [km s^{-1}]	T_{rot}[d] [K]
		$K6_{shell,a}$		
CS	1.6×10^{14}	81.1	9.5	2.7
	5.6×10^{15}	64.2	12.5	2.7
	3.7×10^{13}	55.0	3.5	2.7
	8.7×10^{13}	49.8	7.5	2.7
	1.5×10^{13}	35.0	4.0	2.7
	7.0×10^{12}	31.0	3.0	2.7
	5.0×10^{12}	27.0	4.0	2.7
	1.5×10^{13}	21.8	4.0	2.7
	2.5×10^{13}	14.7	5.0	2.7
	2.0×10^{14}	8.2	5.0	2.7
	7.9×10^{13}	2.4	3.0	2.7
	5.0×10^{13}	−1.8	3.0	2.7
	4.0×10^{12}	−8.6	4.0	2.7
	3.0×10^{12}	−14.0	3.0	2.7
	2.3×10^{13}	−20.3	5.0	2.7
	5.0×10^{12}	−24.7	2.0	2.7
	1.0×10^{13}	−29.6	3.0	2.7
	3.0×10^{12}	−34.3	3.0	2.7
	7.2×10^{13}	−39.8	3.0	2.7
	5.2×10^{12}	−47.1	3.0	2.7
	4.2×10^{12}	−55.3	6.0	2.7
	6.5×10^{13}	−72.0	5.5	2.7
	2.9×10^{13}	−80.0	4.0	2.7
	1.6×10^{13}	−92.6	2.5	2.7
	2.0×10^{13}	−99.0	5.0	2.7
	8.4×10^{13}	−104.7	3.0	2.7
	3.4×10^{12}	−112.2	5.0	2.7
	6.4×10^{12}	−120.2	5.0	2.7
$C^{34}S$	7.9×10^{13}	81.1	9.5	2.7
	4.2×10^{14}	64.2	12.5	2.7
	1.2×10^{13}	8.2	5.0	2.7
	4.9×10^{12}	2.4	3.0	2.7
	2.5×10^{12}	−1.8	3.0	2.7
	3.6×10^{12}	−39.8	3.0	2.7
	7.2×10^{12}	−72.0	5.5	2.7
	1.8×10^{12}	−80.0	4.0	2.7
	6.2×10^{12}	−104.7	3.0	2.7

Notes. See notes of Table A.11.

Table A.13: Continued.

Molecule	$N_{\rm tot}{}^a$ [cm^{-2}]	$v_{\rm LSR}{}^b$ [km s^{-1}]	$FWHM^c$ [km s^{-1}]	$T_{\rm rot}{}^d$ [K]
^{13}CS	5.9×10^{13}	81.1	9.5	2.7
	2.8×10^{14}	64.2	12.5	2.7
	1.0×10^{13}	8.2	5.0	2.7
	3.9×10^{12}	2.4	3.0	2.7
	3.8×10^{12}	−72.0	5.5	2.7
	4.2×10^{12}	−104.7	3.0	2.7
C^{33}S	1.6×10^{13}	81.1	9.5	2.7
	7.2×10^{13}	64.2	12.5	2.7
^{13}C^{34}S	1.5×10^{13}	64.2	12.5	2.7
		I		
CS	6.3×10^{12}	88.5	5.0	2.7
	5.3×10^{12}	81.5	5.0	2.7
	2.6×10^{15}	64.2	12.5	2.7
	6.0×10^{13}	49.9	4.5	2.7
	1.0×10^{13}	44.3	4.5	2.7
	4.0×10^{12}	39.3	3.0	2.7
	2.2×10^{13}	30.5	3.0	2.7
	1.1×10^{13}	25.1	3.0	2.7
	3.0×10^{13}	16.7	6.0	2.7
	6.4×10^{13}	8.0	6.0	2.7
	2.2×10^{14}	1.3	5.0	2.7
	4.2×10^{13}	−21.2	4.0	2.7
	1.0×10^{13}	−25.7	3.0	2.7
	1.0×10^{13}	−30.6	3.0	2.7
	7.2×10^{13}	−41.6	2.0	2.7
	2.2×10^{13}	−46.5	2.0	2.7
	7.2×10^{12}	−50.5	3.0	2.7
	2.8×10^{12}	−58.3	3.0	2.7
	2.7×10^{12}	−62.9	3.0	2.7
	2.0×10^{13}	−70.3	3.5	2.7
	1.0×10^{13}	−76.8	3.0	2.7
	1.6×10^{13}	−87.1	5.5	2.7
	5.0×10^{13}	−95.8	4.0	2.7
	7.0×10^{13}	−101.7	4.0	2.7
	3.4×10^{13}	−107.4	3.5	2.7
	5.0×10^{12}	−115.2	4.0	2.7
C^{34}S	2.0×10^{14}	64.2	12.5	2.7
	7.0×10^{12}	49.9	4.5	2.7

Notes. See notes of Table A.11.

Table A.13: Continued.

Molecule	$N_{tot}{}^a$ [cm^{-2}]	$v_{LSR}{}^b$ [km s^{-1}]	$FWHM^c$ [km s^{-1}]	$T_{rot}{}^d$ [K]
	3.2×10^{12}	8.0	6.0	2.7
	1.2×10^{13}	1.3	5.0	2.7
	2.8×10^{12}	−21.2	4.0	2.7
	9.6×10^{12}	−41.6	2.0	2.7
	4.2×10^{12}	−95.8	4.0	2.7
	4.5×10^{12}	−101.7	4.0	2.7
^{13}CS	1.3×10^{14}	64.2	12.5	2.7
	3.0×10^{12}	49.9	4.5	2.7
	8.9×10^{12}	1.3	5.0	2.7
	3.4×10^{12}	−95.8	4.0	2.7
C^{33}S	3.7×10^{13}	64.2	12.5	2.7
	1.8×10^{12}	49.9	4.5	2.7
^{13}C^{34}S	8.0×10^{12}	64.2	12.5	2.7
		L		
CS	6.4×10^{13}	82.6	4.0	2.7
	4.8×10^{14}	77.1	4.0	2.7
	7.2×10^{14}	71.1	4.0	2.7
	3.0×10^{15}	58.0	11.5	2.7
	7.5×10^{12}	37.5	4.5	2.7
	1.0×10^{13}	34.6	4.0	2.7
	2.9×10^{13}	28.5	5.0	2.7
	2.3×10^{13}	23.1	4.0	2.7
	4.4×10^{13}	17.6	3.5	2.7
	1.3×10^{14}	8.2	6.0	2.7
	1.6×10^{14}	−0.8	6.0	2.7
	2.5×10^{13}	−11.5	6.0	2.7
	1.3×10^{13}	−19.5	3.0	2.7
	2.5×10^{13}	−26.3	4.0	2.7
	1.0×10^{13}	−31.7	3.0	2.7
	6.2×10^{13}	−39.7	3.0	2.7
	1.7×10^{13}	−46.5	3.0	2.7
	1.2×10^{13}	−69.2	4.0	2.7
	6.0×10^{13}	−77.5	6.0	2.7
	1.3×10^{13}	−91.2	2.5	2.7
	1.3×10^{13}	−101.6	3.0	2.7
	3.8×10^{13}	−106.3	3.0	2.7

Notes. See notes of Table A.11.

Table A.13: Continued.

Molecule	N_{tot}[a] [cm^{-2}]	v_{LSR}[b] [km s^{-1}]	$FWHM$[c] [km s^{-1}]	T_{rot}[d] [K]
$C^{34}S$	5.4×10^{12}	82.6	4.0	2.7
	2.4×10^{13}	77.1	4.0	2.7
	3.6×10^{13}	71.1	4.0	2.7
	1.8×10^{14}	58.0	11.5	2.7
	6.5×10^{12}	8.2	4.0	2.7
	1.0×10^{13}	−0.8	5.0	2.7
	4.2×10^{12}	−39.7	3.0	2.7
^{13}CS	2.4×10^{13}	77.1	4.0	2.7
	3.6×10^{13}	71.1	4.0	2.7
	1.5×10^{14}	58.0	11.5	2.7
	8.0×10^{12}	−0.8	5.0	2.7
$C^{33}S$	5.4×10^{12}	77.1	4.0	2.7
	7.9×10^{12}	71.1	4.0	2.7
	3.4×10^{13}	58.0	11.5	2.7

Notes. See notes of Table A.11.

Table A.14: Parameters of our best-fit model of ^{13}CO.

Molecule	N_{tot}[a] [cm^{-2}]	v_{LSR}[b] [km s^{-1}]	$FWHM$[c] [km s^{-1}]	T_{rot}[d] [K]
		K4		
^{13}CO	1.3×10^{17}	91.4	25.0	30.0
	9.1×10^{16}	56.4	8.0	30.0
	3.3×10^{15}	87.5	6.0	2.7
	3.2×10^{15}	83.3	3.0	2.7
	1.5×10^{16}	72.9	3.0	2.7
	5.2×10^{15}	68.9	3.0	2.7
	9.0×10^{15}	64.1	4.0	2.7
	2.0×10^{15}	55.5	3.0	2.7
	1.0×10^{15}	50.9	4.0	2.7
	6.0×10^{14}	45.5	4.0	2.7
	6.0×10^{14}	32.9	4.0	2.7
	1.0×10^{15}	27.8	3.0	2.7
	1.4×10^{15}	21.1	3.0	2.7
	6.0×10^{14}	16.9	4.0	2.7
	1.3×10^{15}	13.1	3.0	2.7
	3.2×10^{15}	8.1	4.0	2.7
	2.2×10^{15}	2.8	2.5	2.7
	8.5×10^{14}	−0.8	2.5	2.7

Notes. See notes of Table A.11.

Table A.14: Continued.

Molecule	$N_{\rm tot}{}^a$ [cm^{-2}]	$v_{\rm LSR}{}^b$ [km s^{-1}]	$FWHM^c$ [km s^{-1}]	$T_{\rm rot}{}^d$ [K]
	6.0×10^{14}	−7.0	5.0	2.7
	1.5×10^{15}	−16.2	3.0	2.7
	4.0×10^{15}	−20.8	2.0	2.7
	6.0×10^{15}	−26.8	4.0	2.7
	1.0×10^{15}	−35.0	3.0	2.7
	1.5×10^{16}	−40.3	4.0	2.7
	5.0×10^{15}	−46.6	4.0	2.7
	6.0×10^{14}	−68.0	3.0	2.7
	5.0×10^{15}	−73.1	4.0	2.7
	5.0×10^{15}	−80.3	4.0	2.7
	4.0×10^{14}	−87.1	4.0	2.7
	1.2×10^{15}	−92.1	3.0	2.7
	1.2×10^{15}	−99.8	3.0	2.7
	7.0×10^{15}	−105.2	4.5	2.7
$C^{18}O$	7.0×10^{14}	83.3	4.0	2.7
	9.5×10^{14}	72.9	3.0	2.7
	6.0×10^{14}	68.9	3.0	2.7
	1.2×10^{15}	64.1	4.0	2.7
	2.6×10^{14}	2.8	2.0	2.7
	2.5×10^{14}	−20.8	2.0	2.7
	5.0×10^{15}	−40.3	4.0	2.7
	3.0×10^{14}	−46.6	4.0	2.7
	4.0×10^{14}	−80.3	4.0	2.7
	6.0×10^{14}	−105.2	4.5	2.7
$C^{17}O$	4.8×10^{14}	68.9	3.0	2.7
	4.0×10^{14}	64.1	4.0	2.7
	1.0×10^{15}	−40.3	4.0	2.7
		$K6_{\rm shell}$		
^{13}CO	1.9×10^{17}	91.4	11.0	30.0
	5.5×10^{15}	91.4	6.0	2.7
	4.4×10^{15}	76.9	4.0	2.7
	2.5×10^{16}	67.7	4.5	2.7
	2.9×10^{16}	62.3	3.0	2.7
	3.0×10^{15}	54.6	5.0	2.7
	2.1×10^{15}	47.9	5.0	2.7
	6.1×10^{14}	41.8	4.0	2.7
	7.1×10^{14}	35.9	3.0	2.7
	7.1×10^{14}	31.8	3.0	2.7
	1.1×10^{15}	26.4	5.0	2.7

Notes. See notes of Table A.11.

Table A.14: Continued.

Molecule	N_{tot}[a] [cm^{-2}]	v_{LSR}[b] [km s^{-1}]	$FWHM$[c] [km s^{-1}]	T_{rot}[d] [K]
	1.3×10^{15}	19.8	3.0	2.7
	2.1×10^{15}	14.2	4.0	2.7
	5.3×10^{15}	7.2	4.0	2.7
	2.2×10^{15}	2.7	3.0	2.7
	3.5×10^{15}	−1.5	2.5	2.7
	1.0×10^{15}	−16.2	2.5	2.7
	4.1×10^{15}	−20.4	2.5	2.7
	2.8×10^{15}	−25.1	2.0	2.7
	2.8×10^{15}	−28.3	3.0	2.7
	2.8×10^{16}	−39.8	3.0	2.7
	8.0×10^{15}	−46.9	3.0	2.7
	4.5×10^{14}	−67.8	4.0	2.7
	4.5×10^{15}	−74.9	7.0	2.7
	2.0×10^{15}	−81.9	3.0	2.7
	8.0×10^{14}	−92.0	3.0	2.7
	4.0×10^{14}	−95.7	3.0	2.7
	6.0×10^{15}	−104.8	4.5	2.7
$C^{18}O$	9.0×10^{14}	76.9	4.0	2.7
	4.5×10^{15}	67.7	4.5	2.7
	1.8×10^{15}	62.3	3.0	2.7
	6.4×10^{14}	54.6	5.0	2.7
	5.3×10^{14}	7.2	4.0	2.7
	4.1×10^{14}	−20.4	2.5	2.7
	3.3×10^{15}	−39.8	3.0	2.7
	7.0×10^{14}	−46.9	3.0	2.7
	7.5×10^{14}	−104.8	4.5	2.7
	8.5×10^{14}	−74.9	7.0	2.7
	4.0×10^{14}	−81.9	3.0	2.7
$C^{17}O$	9.5×10^{14}	67.7	4.5	2.7
	1.0×10^{15}	62.3	3.0	2.7
		$K5_{shell}$		
^{13}CO	6.8×10^{16}	91.4	18.0	30.0
	4.4×10^{15}	92.4	3.0	2.7
	2.2×10^{15}	87.9	2.0	2.7
	1.7×10^{15}	80.0	2.0	2.7
	1.4×10^{16}	73.4	4.0	2.7
	2.2×10^{15}	67.7	3.0	2.7
	1.2×10^{16}	64.0	3.0	2.7
	3.6×10^{15}	53.6	4.0	2.7

Notes. See notes of Table A.11.

Table A.14: Continued.

Molecule	N_{tot}[a] [cm^{-2}]	v_{LSR}[b] [$km\ s^{-1}$]	$FWHM$[c] [$km\ s^{-1}$]	T_{rot}[d] [K]
	2.5×10^{15}	48.9	4.0	2.7
	1.3×10^{15}	20.8	4.0	2.7
	4.1×10^{15}	13.2	5.5	2.7
	2.8×10^{15}	7.2	4.5	2.7
	2.2×10^{15}	2.7	2.0	2.7
	2.0×10^{15}	−1.5	2.5	2.7
	2.0×10^{15}	−16.2	4.0	2.7
	4.1×10^{15}	−20.4	2.5	2.7
	4.8×10^{15}	−27.1	4.0	2.7
	1.5×10^{16}	−40.3	4.5	2.7
	6.0×10^{15}	−46.9	2.5	2.7
	4.5×10^{15}	−74.9	3.0	2.7
	5.0×10^{15}	−80.3	4.0	2.7
	8.0×10^{14}	−92.0	3.0	2.7
	6.0×10^{15}	−104.8	5.0	2.7
$C^{18}O$	1.8×10^{15}	64.0	3.0	2.7
	3.8×10^{15}	−40.3	4.5	2.7
		$K6_{shell,a}$		
^{13}CO	2.8×10^{17}	87.4	15.0	30.0
	6.5×10^{15}	90.9	5.5	2.7
	1.9×10^{16}	75.9	4.0	2.7
	4.5×10^{16}	68.7	5.5	2.7
	4.5×10^{15}	62.7	3.0	2.7
	2.5×10^{15}	58.7	3.5	2.7
	6.4×10^{15}	54.6	3.5	2.7
	1.5×10^{15}	47.9	5.0	2.7
	7.1×10^{14}	34.9	3.0	2.7
	7.1×10^{14}	31.8	3.0	2.7
	2.3×10^{15}	19.8	5.0	2.7
	2.1×10^{15}	13.2	4.0	2.7
	5.3×10^{15}	8.2	4.0	2.7
	3.8×10^{15}	3.2	4.0	2.7
	4.0×10^{15}	−1.1	3.0	2.7
	5.3×10^{15}	−19.8	3.0	2.7
	2.4×10^{15}	−25.1	2.0	2.7
	2.8×10^{15}	−28.3	3.0	2.7
	1.8×10^{16}	−39.8	3.0	2.7
	1.0×10^{16}	−46.9	3.0	2.7
	3.5×10^{15}	−73.8	3.0	2.7
	3.0×10^{15}	−77.9	3.0	2.7

Notes. See notes of Table A.11.

Table A.14: Continued.

Molecule	$N_{\rm tot}{}^a$ [cm^{-2}]	$v_{\rm LSR}{}^b$ [km s^{-1}]	$FWHM^c$ [km s^{-1}]	$T_{\rm rot}{}^d$ [K]
	3.5×10^{15}	−81.9	3.0	2.7
	8.0×10^{14}	−92.0	3.0	2.7
	1.6×10^{15}	−101.7	3.0	2.7
	5.5×10^{15}	−105.8	2.5	2.7
$C^{18}O$	1.4×10^{15}	75.9	4.0	2.7
	4.5×10^{15}	68.7	5.5	2.7
	8.4×10^{14}	54.6	3.5	2.7
	8.3×10^{14}	−19.8	3.0	2.7
	3.3×10^{15}	−39.8	3.0	2.7
	7.0×10^{14}	−46.9	3.0	2.7
	3.5×10^{14}	−81.9	3.0	2.7
	7.5×10^{14}	−105.8	2.5	2.7
		I		
^{13}CO	3.8×10^{18}	76.4	4.0	120.0
	3.2×10^{16}	94.2	7.0	2.7
	1.2×10^{16}	68.7	4.5	2.7
	3.8×10^{16}	60.3	6.0	2.7
	3.4×10^{15}	54.6	3.0	2.7
	1.3×10^{15}	44.8	4.0	2.7
	1.3×10^{15}	36.9	4.0	2.7
	1.6×10^{15}	31.8	4.0	2.7
	2.3×10^{15}	21.8	3.0	2.7
	2.1×10^{15}	12.6	4.0	2.7
	5.3×10^{15}	7.2	4.0	2.7
	5.2×10^{15}	0.7	5.0	2.7
	6.8×10^{15}	−20.4	3.5	2.7
	3.1×10^{15}	−28.3	3.0	2.7
	8.3×10^{15}	−40.8	3.0	2.7
	1.0×10^{16}	−45.9	4.0	2.7
	2.5×10^{15}	−50.8	4.0	2.7
	1.5×10^{15}	−57.8	2.0	2.7
	4.0×10^{15}	−100.7	5.0	2.7
	2.0×10^{15}	−106.8	4.5	2.7
	2.0×10^{15}	−111.8	4.5	2.7
$C^{18}O$	1.5×10^{15}	68.7	4.5	2.7
	5.8×10^{15}	60.3	6.0	2.7
	1.4×10^{15}	54.6	3.0	2.7
	3.3×10^{15}	−40.8	3.0	2.7
	2.0×10^{15}	−45.9	4.0	2.7

Notes. See notes of Table A.11.

Table A.14: Continued.

Molecule	N_{tot}[a] [cm^{-2}]	v_{LSR}[b] [$km\,s^{-1}$]	$FWHM$[c] [$km\,s^{-1}$]	T_{rot}[d] [K]
$C^{17}O$	2.0×10^{15}	60.3	6.0	2.7
	8.0×10^{14}	−45.9	4.0	2.7
		L		
^{13}CO	4.5×10^{17}	80.4	20.0	30.0
	8.8×10^{16}	71.4	4.0	30.0
	1.4×10^{16}	82.3	8.0	2.7
	2.9×10^{16}	62.3	5.0	2.7
	4.0×10^{15}	51.6	4.0	2.7
	1.9×10^{15}	34.9	3.0	2.7
	1.9×10^{15}	30.8	3.0	2.7
	1.9×10^{15}	26.4	3.0	2.7
	3.9×10^{15}	13.4	5.0	2.7
	2.0×10^{15}	−16.2	2.5	2.7
	2.1×10^{15}	−20.4	3.5	2.7
	6.8×10^{15}	−26.3	4.0	2.7
	2.8×10^{16}	−39.8	3.0	2.7
	8.0×10^{15}	−46.9	3.0	2.7
	2.5×10^{15}	−74.9	3.0	2.7
	8.0×10^{15}	−78.9	3.0	2.7
	6.0×10^{15}	−107.8	4.5	2.7
$C^{18}O$	3.8×10^{15}	62.3	5.0	2.7
	3.3×10^{15}	−39.8	3.0	2.7
	2.0×10^{15}	−46.9	3.0	2.7

Notes. See notes of Table A.11.

Table A.15: Parameters of our best-fit model of OCS.

Molecule	N_{tot}[a] [cm^{-2}]	v_{LSR}[b] [$km\,s^{-1}$]	$FWHM$[c] [$km\,s^{-1}$]	T_{rot}[d] [K]
		K4		
OCS	5.5×10^{14}	75.4	4.0	4.3
	2.0×10^{15}	68.5	7.5	4.3
	1.0×10^{15}	61.0	5.0	4.3
		$K6_{shell}$		
OCS	1.6×10^{15}	70.9	5.0	10.2
	6.2×10^{15}	64.2	11.0	10.2
		$K5_{shell}$		
OCS	1.9×10^{16}	67.0	10.0	5.7
		$K6_{shell,a}$		
OCS	2.7×10^{12}	83.5	7.0	2.7
	1.4×10^{13}	64.4	11.0	2.7

Notes. See notes of Table A.11.

Table A.15: Continued.

Molecule	$N_{tot}{}^a$ [cm^{-2}]	$v_{LSR}{}^b$ [$km\,s^{-1}$]	$FWHM^c$ [$km\,s^{-1}$]	$T_{rot}{}^d$ [K]
		I		
OCS	5.3×10^{14}	68.5	4.5	7.5
	8.6×10^{14}	62.0	5.0	7.5
		L		
OCS	3.2×10^{15}	62.0	6.0	10.2

Notes. See notes of Table A.11.

Table A.16: Parameters of our best-fit model of HC_3N.

Molecule	$N_{tot}{}^a$ [cm^{-2}]	$v_{LSR}{}^b$ [$km\,s^{-1}$]	$FWHM^c$ [$km\,s^{-1}$]	$T_{rot}{}^d$ [K]
		K4		
HC_3N	1.0×10^{14}	86.5	4.0	6.5
	7.0×10^{14}	80.9	4.0	6.5
	9.6×10^{14}	71.2	4.0	6.5
	2.6×10^{15}	64.0	6.0	6.5
	1.5×10^{14}	57.4	4.0	6.5
	1.2×10^{14}	53.5	5.0	6.5
	3.6×10^{13}	46.1	4.5	6.5
	6.0×10^{13}	3.7	5.0	7.3
$H^{13}CCCN$	4.6×10^{13}	64.0	6.0	6.5
	4.6×10^{13}	53.5	5.0	6.5
$HC^{13}CCN$	4.6×10^{13}	64.0	6.0	6.5
	6.0×10^{13}	53.5	5.0	6.5
$HCC^{13}CN$	4.6×10^{13}	64.0	6.0	6.5
	6.5×10^{13}	53.5	5.0	6.5
		$K6_{shell}$		
HC_3N	3.8×10^{14}	78.3	6.0	5.6
	1.8×10^{15}	63.6	7.0	5.6
	3.8×10^{13}	3.8	4.0	6.0
$H^{13}CCCN$	1.3×10^{14}	63.6	7.0	5.6
$HC^{13}CCN$	6.6×10^{13}	63.6	7.0	5.6
$HCC^{13}CN$	5.6×10^{13}	63.6	7.0	5.6
		$K5_{shell}$		
HC_3N	4.8×10^{15}	78.7	8.0	4.4
	7.8×10^{15}	65.7	4.5	4.4

Notes. See notes of Table A.11.

Table A.16: Continued.

Molecule	$N_{tot}{}^a$ [cm^{-2}]	$v_{LSR}{}^b$ [km s^{-1}]	$FWHM^c$ [km s^{-1}]	$T_{rot}{}^d$ [K]
$H^{13}CCCN$	1.6×10^{14}	65.7	4.5	4.4
		$K6_{shell,a}$		
HC_3N	3.8×10^{14}	78.3	6.0	6.6
	1.8×10^{15}	63.6	7.0	6.6
		I		
HC_3N	1.2×10^{15}	60.6	8.0	8.0
		L		
HC_3N	3.8×10^{14}	78.3	6.0	4.6
	1.8×10^{15}	63.6	7.0	4.6

Notes. See notes of Table A.11.

Table A.17: Parameters of our best-fit model of CN.

Molecule	$N_{tot}{}^a$ [cm^{-2}]	$v_{LSR}{}^b$ [km s^{-1}]	$FWHM^c$ [km s^{-1}]	$T_{rot}{}^d$ [K]
		K4		
CN	6.6×10^{14}	88.3	5.5	2.7
	1.9×10^{15}	82.4	5.5	2.7
	2.6×10^{15}	74.0	8.0	2.7
	8.4×10^{15}	62.4	9.0	2.7
	2.4×10^{14}	48.9	4.5	2.7
	3.4×10^{13}	39.5	4.5	2.7
	1.7×10^{14}	28.2	3.0	2.7
	2.7×10^{14}	21.5	3.0	2.7
	2.5×10^{14}	15.9	3.0	2.7
	5.4×10^{14}	8.0	4.5	2.7
	5.4×10^{14}	3.7	4.5	2.7
	3.6×10^{14}	−2.6	4.5	2.7
	8.0×10^{13}	−11.5	6.0	2.7
	6.0×10^{13}	−14.8	3.0	2.7
	6.0×10^{13}	−19.8	3.0	2.7
	1.2×10^{14}	−27.8	4.5	2.7
	3.5×10^{14}	−38.6	3.5	2.7
	3.2×10^{14}	−42.6	4.5	2.7
	6.6×10^{13}	−48.5	4.0	2.7
	4.3×10^{13}	−57.8	5.0	2.7
	6.3×10^{13}	−67.8	4.0	2.7
	2.1×10^{14}	−73.2	3.5	2.7
	2.5×10^{14}	−79.7	3.5	2.7
	8.2×10^{13}	−85.8	4.0	2.7
	1.2×10^{14}	−91.8	4.5	2.7

Notes. See notes of Table A.11.

Table A.17: Continued.

Molecule	$N_{tot}{}^a$ [cm^{-2}]	$v_{LSR}{}^b$ [km s^{-1}]	$FWHM^c$ [km s^{-1}]	$T_{rot}{}^d$ [K]
	5.0×10^{13}	−99.8	3.5	2.7
	3.2×10^{14}	−105.4	4.5	2.7
^{13}CN	3.8×10^{13}	88.3	5.5	2.7
	9.8×10^{13}	82.4	5.5	2.7
	1.3×10^{14}	74.0	8.0	2.7
	4.2×10^{14}	62.4	9.0	2.7
	2.7×10^{13}	8.0	4.5	2.7
	2.7×10^{13}	3.7	4.5	2.7
	1.8×10^{13}	−2.6	4.5	2.7
	1.2×10^{13}	−42.6	4.5	2.7
	1.5×10^{13}	−105.4	4.5	2.7
C^{15}N	5.8×10^{12}	82.4	5.5	2.7
	8.0×10^{12}	74.0	8.0	2.7
	2.0×10^{13}	62.4	8.0	2.7
		K6$_{shell}$		
CN	2.4×10^{15}	79.6	8.5	2.7
	1.4×10^{15}	71.8	3.0	2.7
	9.5×10^{15}	64.2	7.0	2.7
	1.5×10^{15}	55.6	3.5	2.7
	1.2×10^{15}	50.8	6.0	2.7
	6.2×10^{13}	36.8	3.0	2.7
	1.6×10^{14}	31.8	5.0	2.7
	8.2×10^{13}	24.4	3.0	2.7
	3.6×10^{14}	17.2	4.0	2.7
	1.0×10^{15}	9.1	9.0	2.7
	5.0×10^{14}	−1.2	6.5	2.7
	8.2×10^{13}	−15.9	4.0	2.7
	9.2×10^{13}	−20.5	4.5	2.7
	7.2×10^{13}	−27.4	4.0	2.7
	1.1×10^{14}	−30.5	3.0	2.7
	3.1×10^{14}	−40.2	3.5	2.7
	2.0×10^{14}	−47.0	5.0	2.7
	1.0×10^{14}	−57.0	3.0	2.7
	1.0×10^{14}	−62.7	5.0	2.7
	1.2×10^{14}	−71.7	5.0	2.7
	9.0×10^{13}	−76.7	3.0	2.7
	1.0×10^{14}	−82.0	2.0	2.7
	1.4×10^{14}	−92.6	3.0	2.7

Notes. See notes of Table A.11.

Table A.17: Continued.

Molecule	$N_{\rm tot}{}^a$ [cm^{-2}]	$v_{\rm LSR}{}^b$ [km s^{-1}]	$FWHM^c$ [km s^{-1}]	$T_{\rm rot}{}^d$ [K]
	5.4×10^{14}	−105.1	5.5	2.7
	5.2×10^{13}	−122.6	5.0	2.7
^{13}CN	1.2×10^{14}	79.6	7.5	2.7
	7.0×10^{13}	71.8	3.0	2.7
	4.4×10^{14}	64.2	7.0	2.7
	7.0×10^{13}	55.6	3.5	2.7
	5.0×10^{13}	9.1	9.0	2.7
	2.5×10^{13}	−1.2	6.5	2.7
C^{15}N	2.5×10^{13}	64.2	7.0	2.7
		K5$_{\rm shell}$		
CN	1.0×10^{15}	84.2	7.0	2.7
	2.6×10^{15}	79.2	7.0	2.7
	1.4×10^{15}	71.2	4.0	2.7
	1.2×10^{16}	62.9	9.0	2.7
	1.6×10^{14}	26.2	4.0	2.7
	6.1×10^{14}	15.5	7.0	2.7
	9.0×10^{14}	6.9	5.0	2.7
	4.5×10^{14}	−1.1	5.0	2.7
	1.2×10^{14}	−15.8	5.0	2.7
	2.3×10^{14}	−22.5	5.5	2.7
	9.5×10^{14}	−38.4	5.0	2.7
	2.5×10^{14}	−75.8	3.5	2.7
	2.5×10^{14}	−81.2	3.0	2.7
	3.5×10^{13}	−93.7	2.5	2.7
	5.0×10^{14}	−105.2	4.5	2.7
^{13}CN	5.0×10^{13}	84.2	7.0	2.7
	1.3×10^{14}	79.2	7.0	2.7
	7.0×10^{13}	71.2	4.0	2.7
	5.5×10^{14}	62.9	9.0	2.7
	4.5×10^{13}	6.9	5.0	2.7
	2.5×10^{13}	−1.1	5.0	2.7
C^{15}N	1.0×10^{13}	79.2	7.0	2.7
	3.3×10^{13}	62.9	9.0	2.7
		K6$_{\rm shell,a}$		
CN	2.9×10^{15}	81.7	8.0	2.7
	2.0×10^{15}	70.9	5.0	2.7
	8.5×10^{15}	64.3	6.0	2.7

Notes. See notes of Table A.11.

Table A.17: Continued.

Molecule	N_{tot}[a] [cm^{-2}]	v_{LSR}[b] [km s^{-1}]	$FWHM$[c] [km s^{-1}]	T_{rot}[d] [K]
	2.2×10^{15}	57.6	4.0	2.7
	6.2×10^{14}	51.5	4.0	2.7
	9.0×10^{13}	46.2	3.5	2.7
	3.1×10^{14}	34.4	6.0	2.7
	1.5×10^{14}	24.8	6.0	2.7
	6.1×10^{14}	13.5	4.0	2.7
	1.2×10^{15}	8.2	5.0	2.7
	1.9×10^{14}	3.2	3.0	2.7
	2.7×10^{14}	−1.8	3.0	2.7
	1.3×10^{14}	−20.2	5.0	2.7
	4.0×10^{14}	−39.8	4.0	2.7
	8.5×10^{13}	−55.8	4.5	2.7
	6.5×10^{13}	−65.8	4.5	2.7
	2.9×10^{14}	−72.8	4.5	2.7
	1.1×10^{14}	−77.8	4.5	2.7
	2.2×10^{14}	−81.8	2.5	2.7
	1.5×10^{14}	−93.2	3.0	2.7
	7.5×10^{13}	−98.2	3.0	2.7
	7.5×10^{14}	−104.8	5.0	2.7
^{13}CN	1.6×10^{14}	81.7	8.0	2.7
	9.7×10^{13}	70.9	5.0	2.7
	3.8×10^{14}	64.3	6.0	2.7
	1.2×10^{14}	57.6	4.0	2.7
	4.5×10^{13}	8.2	5.0	2.7
	7.0×10^{12}	3.2	3.0	2.7
C^{15}N	7.0×10^{12}	70.9	5.0	2.7
	2.0×10^{13}	64.3	6.0	2.7
		I		
CN	1.2×10^{14}	81.3	8.0	2.7
	1.2×10^{16}	64.3	10.0	2.7
	1.6×10^{14}	30.8	4.0	2.7
	1.5×10^{14}	24.8	6.0	2.7
	2.1×10^{14}	15.5	4.0	2.7
	8.5×10^{14}	6.2	10.0	2.7
	4.4×10^{14}	−22.5	8.0	2.7
	5.0×10^{14}	−40.5	6.0	2.7
	9.5×10^{13}	−46.5	4.5	2.7
	8.5×10^{13}	−56.5	4.5	2.7
	1.2×10^{14}	−70.2	4.5	2.7

Notes. See notes of Table A.11.

Table A.17: Continued.

Molecule	$N_{tot}{}^a$ [cm^{-2}]	$v_{LSR}{}^b$ [$km\,s^{-1}$]	$FWHM^c$ [$km\,s^{-1}$]	$T_{rot}{}^d$ [K]
	1.4×10^{14}	−77.8	5.5	2.7
	1.0×10^{14}	−93.2	4.5	2.7
	5.0×10^{14}	−102.8	10.0	2.7
^{13}CN	5.0×10^{14}	64.3	10.0	2.7
		L		
^{13}CN	2.4×10^{14}	74.1	8.0	2.7
	2.9×10^{14}	59.0	8.0	2.7

Notes. See notes of Table A.11.

Table A.18: Parameters of our best-fit model of ortho c-C_3H_2.

Molecule	$N_{tot}{}^a$ [cm^{-2}]	$v_{LSR}{}^b$ [$km\,s^{-1}$]	$FWHM^c$ [$km\,s^{-1}$]	$T_{rot}{}^d$ [K]
		K4		
ortho c-C_3H_2	2.4×10^{13}	89.2	4.0	2.7
	1.2×10^{14}	80.4	6.0	2.7
	1.2×10^{14}	70.5	5.0	2.7
	3.5×10^{14}	62.2	6.5	2.7
	3.0×10^{13}	53.9	4.5	2.7
	6.6×10^{12}	47.6	4.5	2.7
	1.0×10^{13}	40.4	7.5	2.7
	8.2×10^{12}	32.3	3.5	2.7
	8.1×10^{12}	26.8	3.5	2.7
	8.0×10^{12}	20.8	4.0	2.7
	2.0×10^{12}	14.2	4.0	2.7
	5.0×10^{12}	8.2	3.0	2.7
	1.9×10^{13}	2.8	4.5	2.7
	1.2×10^{13}	−3.2	4.5	2.7
	4.5×10^{12}	−13.9	6.5	2.7
	2.5×10^{12}	−21.0	4.5	2.7
	6.2×10^{12}	−27.3	5.0	2.7
	3.2×10^{12}	−34.2	6.0	2.7
	9.1×10^{12}	−41.9	8.0	2.7
	2.1×10^{12}	−72.6	5.0	2.7
	4.0×10^{12}	−79.0	5.0	2.7
	4.0×10^{12}	−92.5	3.0	2.7
	5.6×10^{12}	−105.5	5.0	2.7
para c-C_3H_2	1.2×10^{14}	70.5	5.0	2.7
	1.1×10^{14}	62.2	6.5	2.7

Notes. See notes of Table A.11.

Table A.18: Continued.

Molecule	$N_{tot}{}^a$ [cm^{-2}]	$v_{LSR}{}^b$ [$km\,s^{-1}$]	$FWHM^c$ [$km\,s^{-1}$]	$T_{rot}{}^d$ [K]
c-$CC^{13}CH_2$	9.0×10^{12}	80.4	6.0	2.7
	6.0×10^{12}	70.5	5.0	2.7
	1.4×10^{13}	62.2	6.5	2.7
		$K6_{shell}$		
ortho c-C_3H_2	7.4×10^{13}	79.2	9.5	2.7
	1.6×10^{13}	71.3	4.0	2.7
	4.0×10^{14}	61.6	9.0	2.7
	6.6×10^{12}	48.7	3.5	2.7
	4.5×10^{12}	41.3	5.0	2.7
	2.5×10^{13}	32.6	8.0	2.7
	4.2×10^{12}	24.3	4.5	2.7
	1.0×10^{13}	16.4	6.5	2.7
	1.0×10^{13}	8.0	4.5	2.7
	1.2×10^{13}	−0.1	7.5	2.7
	6.2×10^{12}	−19.9	7.5	2.7
	5.6×10^{12}	−27.4	6.0	2.7
	4.6×10^{12}	−40.2	4.0	2.7
	2.9×10^{12}	−47.7	4.0	2.7
	2.0×10^{12}	−57.7	4.0	2.7
	1.2×10^{12}	−63.8	4.0	2.7
	4.2×10^{12}	−76.2	4.5	2.7
	2.0×10^{12}	−82.0	3.0	2.7
	3.2×10^{12}	−93.6	3.5	2.7
	6.0×10^{12}	−104.4	6.5	2.7
para c-C_3H_2	1.9×10^{14}	61.6	9.0	2.7
c-$CC^{13}CH_2$	2.0×10^{13}	61.6	9.0	2.7
		$K5_{shell}$		
ortho c-C_3H_2	2.4×10^{14}	81.0	8.0	2.7
	4.0×10^{13}	70.3	6.0	2.7
	4.4×10^{14}	60.6	7.5	2.7
	8.1×10^{12}	49.2	3.0	2.7
	4.7×10^{12}	44.1	4.0	2.7
	2.2×10^{12}	39.6	3.0	2.7
	1.7×10^{13}	30.5	7.5	2.7
	9.2×10^{12}	19.9	4.0	2.7
	2.0×10^{13}	6.7	6.0	2.7
	1.4×10^{13}	−2.2	6.5	2.7
	3.3×10^{12}	−23.3	5.0	2.7
	3.3×10^{12}	−30.8	6.0	2.7

Notes. See notes of Table A.11.

Table A.18: Continued.

Molecule	$N_{tot}{}^{a}$ [cm^{-2}]	$v_{LSR}{}^{b}$ [km s^{-1}]	$FWHM^{c}$ [km s^{-1}]	$T_{rot}{}^{d}$ [K]
	8.1×10^{12}	−40.2	6.0	2.7
	7.5×10^{12}	−79.1	5.0	2.7
	4.0×10^{12}	−92.4	5.0	2.7
	5.4×10^{12}	−105.7	4.0	2.7
c-CC^{13}CH$_2$	1.2×10^{13}	81.0	8.0	2.7
	1.8×10^{13}	60.6	7.5	2.7
	K6$_{shell,a}$			
ortho c-C$_3$H$_2$	6.2×10^{13}	84.4	6.5	2.7
	2.5×10^{13}	78.3	4.0	2.7
	2.5×10^{13}	72.8	5.0	2.7
	3.0×10^{14}	64.6	5.0	2.7
	1.7×10^{14}	57.7	4.5	2.7
	8.6×10^{12}	48.2	5.5	2.7
	6.4×10^{12}	39.6	4.0	2.7
	3.2×10^{13}	32.0	7.5	2.7
	8.0×10^{12}	23.5	7.0	2.7
	7.0×10^{12}	18.0	7.0	2.7
	1.4×10^{13}	8.4	7.5	2.7
	9.3×10^{12}	−0.6	7.5	2.7
	7.2×10^{12}	−20.2	7.5	2.7
	4.4×10^{12}	−27.8	6.0	2.7
	6.3×10^{12}	−39.8	4.0	2.7
	2.8×10^{12}	−47.9	4.0	2.7
	2.8×10^{12}	−58.5	4.0	2.7
	7.4×10^{12}	−74.5	6.5	2.7
	2.0×10^{12}	−82.2	3.0	2.7
	4.0×10^{12}	−93.2	3.5	2.7
	2.4×10^{12}	−99.6	4.5	2.7
	4.7×10^{12}	−105.8	3.0	2.7
para c-C$_3$H$_2$	1.7×10^{14}	64.6	5.0	2.7
	1.1×10^{14}	57.7	4.5	2.7
c-CC^{13}CH$_2$	3.2×10^{12}	84.4	6.5	2.7
	1.3×10^{12}	78.3	4.0	2.7
	1.5×10^{13}	64.6	5.0	2.7
	1.0×10^{13}	57.7	4.5	2.7
	I			
ortho c-C$_3$H$_2$	3.2×10^{14}	63.7	11.0	2.7
	2.2×10^{12}	44.6	5.0	2.7

Notes. See notes of Table A.11.

Table A.18: Continued.

Molecule	$N_{tot}{}^a$ [cm^{-2}]	$v_{LSR}{}^b$ [$km\,s^{-1}$]	$FWHM^c$ [$km\,s^{-1}$]	$T_{rot}{}^d$ [K]
	5.4×10^{12}	37.6	4.5	2.7
	1.7×10^{13}	30.6	7.5	2.7
	7.5×10^{12}	18.0	6.0	2.7
	9.9×10^{12}	8.2	8.0	2.7
	9.6×10^{12}	−0.6	6.5	2.7
	3.0×10^{12}	−16.2	5.5	2.7
	4.6×10^{12}	−22.8	4.5	2.7
	5.0×10^{12}	−29.3	5.0	2.7
	4.8×10^{12}	−41.1	3.0	2.7
	4.0×10^{12}	−48.4	5.0	2.7
	2.5×10^{12}	−59.0	3.0	2.7
	1.1×10^{12}	−69.5	3.0	2.7
	2.8×10^{12}	−77.1	4.5	2.7
	1.8×10^{12}	−87.6	5.0	2.7
	2.2×10^{12}	−93.2	5.0	2.7
	4.0×10^{12}	−101.2	3.0	2.7
	4.3×10^{12}	−106.2	5.0	2.7
para c-C_3H_2	1.4×10^{14}	63.7	11.0	2.7
c-$CC^{13}CH_2$	1.6×10^{13}	63.7	11.0	2.7
		L		
ortho c-C_3H_2	1.2×10^{14}	72.8	9.0	2.7
	2.6×10^{14}	57.4	9.0	2.7
	6.6×10^{12}	43.9	5.0	2.7
	9.0×10^{12}	30.5	4.5	2.7
	1.1×10^{13}	23.5	5.5	2.7
	1.0×10^{13}	18.0	4.5	2.7
	9.0×10^{12}	6.8	5.0	2.7
	1.4×10^{13}	−1.6	5.5	2.7
	6.2×10^{12}	−10.7	4.0	2.7
	3.4×10^{12}	−17.7	4.5	2.7
	5.7×10^{12}	−25.7	5.0	2.7
	2.4×10^{12}	−39.8	3.0	2.7
	2.4×10^{12}	−47.9	3.0	2.7
	5.6×10^{12}	−78.1	4.0	2.7
	2.4×10^{12}	−92.1	3.0	2.7
	3.4×10^{12}	−106.7	4.0	2.7
c-$CC^{13}CH_2$	1.5×10^{13}	57.4	9.0	2.7

Notes. See notes of Table A.11.

Table A.19: Parameters of our best-fit model of N_2H^+.

Molecule	$N_{tot}{}^a$ [cm^{-2}]	$v_{LSR}{}^b$ [$km\,s^{-1}$]	$FWHM^c$ [$km\,s^{-1}$]	$T_{rot}{}^d$ [K]
		K4		
N_2H^+	6.4×10^{12}	89.1	6.5	2.7
	4.9×10^{13}	79.6	5.5	2.7
	8.5×10^{14}	64.7	3.5	2.7
	3.0×10^{14}	58.2	2.0	2.7
	2.0×10^{12}	45.5	3.0	2.7
	3.4×10^{12}	18.2	5.0	2.7
	2.5×10^{13}	4.3	3.5	2.7
	5.0×10^{12}	−2.0	4.5	2.7
	1.7×10^{12}	−7.3	3.0	2.7
	2.0×10^{12}	−39.1	3.0	2.7
	3.4×10^{12}	−43.7	3.0	2.7
	8.0×10^{11}	−72.1	5.0	2.7
	8.0×10^{11}	−82.0	5.0	2.7
	5.0×10^{11}	−86.0	3.0	2.7
	6.0×10^{11}	−96.8	3.0	2.7
	7.0×10^{11}	−100.8	3.0	2.7
	1.5×10^{12}	−105.6	3.0	2.7
$^{15}NNH^+$	3.0×10^{11}	64.7	3.5	2.7
	5.0×10^{11}	58.2	2.0	2.7
$N^{15}NH^+$	1.0×10^{12}	64.7	3.5	2.7
	9.0×10^{11}	58.2	2.0	2.7
		$K6_{shell}$		
N_2H^+	1.2×10^{13}	83.2	7.0	2.7
	5.8×10^{13}	74.5	7.0	2.7
	9.0×10^{14}	64.0	9.5	2.7
	1.7×10^{13}	54.2	5.0	2.7
	2.2×10^{13}	49.1	4.5	2.7
	2.0×10^{12}	18.7	5.5	2.7
	2.4×10^{12}	12.8	4.5	2.7
	3.9×10^{12}	7.9	4.5	2.7
	1.1×10^{12}	0.2	6.0	2.7
	1.2×10^{12}	−5.8	6.0	2.7
	8.8×10^{11}	−22.0	6.5	2.7
	1.8×10^{12}	−40.0	4.5	2.7
	6.0×10^{11}	−67.1	5.0	2.7
	7.0×10^{11}	−76.4	5.0	2.7
	9.0×10^{11}	−82.9	5.0	2.7

Notes. See notes of Table A.11.

Table A.19: Continued.

Molecule	N_{tot}[a] [cm^{-2}]	v_{LSR}[b] [km s^{-1}]	$FWHM$[c] [km s^{-1}]	T_{rot}[d] [K]
	2.5×10^{12}	−105.6	5.5	2.7
	1.1×10^{12}	−116.3	5.5	2.7
$^{15}NNH^+$	1.3×10^{12}	64.0	9.5	2.7
$N^{15}NH^+$	1.5×10^{12}	64.0	9.5	2.7
		$K5_{shell}$		
N_2H^+	3.2×10^{12}	94.0	4.0	2.7
	3.2×10^{13}	82.1	4.5	2.7
	8.8×10^{12}	75.5	5.0	2.7
	4.5×10^{13}	63.7	4.5	2.7
	9.2×10^{13}	58.1	4.0	2.7
	2.6×10^{12}	18.9	5.5	2.7
	5.1×10^{12}	6.9	4.5	2.7
	2.7×10^{12}	−1.8	4.0	2.7
	2.0×10^{12}	−5.9	3.5	2.7
	2.2×10^{12}	−45.8	6.0	2.7
	1.9×10^{12}	−80.8	7.0	2.7
	4.2×10^{12}	−105.8	3.0	2.7
		$K6_{shell,a}$		
N_2H^+	5.1×10^{12}	89.5	4.5	2.7
	9.0×10^{12}	82.4	5.0	2.7
	7.2×10^{12}	78.3	4.5	2.7
	4.6×10^{13}	70.4	5.5	2.7
	1.8×10^{14}	56.9	4.5	2.7
	1.8×10^{12}	38.7	5.5	2.7
	6.9×10^{12}	8.8	7.5	2.7
	1.9×10^{12}	−2.2	3.5	2.7
	1.5×10^{12}	−17.5	6.0	2.7
	1.8×10^{12}	−41.0	3.5	2.7
	1.0×10^{12}	−67.1	5.0	2.7
	9.0×10^{11}	−76.0	5.0	2.7
	9.0×10^{11}	−81.0	5.0	2.7
	5.0×10^{11}	−87.5	5.0	2.7
	4.0×10^{12}	−105.8	3.0	2.7
	1.8×10^{12}	−115.0	6.0	2.7
		I		
N_2H^+	4.1×10^{13}	70.4	4.5	2.7
	4.1×10^{13}	63.7	5.5	2.7
	3.8×10^{13}	58.5	6.5	2.7
	2.6×10^{12}	22.4	5.5	2.7

Notes. See notes of Table A.11.

Table A.19: Continued.

Molecule	N_{tot}[a] [cm^{-2}]	v_{LSR}[b] [$km\,s^{-1}$]	$FWHM$[c] [$km\,s^{-1}$]	T_{rot}[d] [K]
	6.0×10^{12}	15.1	6.5	2.7
	1.8×10^{13}	1.1	4.0	2.7
	2.0×10^{12}	−41.4	3.0	2.7
	3.9×10^{12}	−100.8	2.0	2.7
	7.8×10^{11}	−107.7	6.0	2.7
		L		
N_2H^+	4.2×10^{12}	89.9	3.5	2.7
	4.2×10^{13}	74.9	5.5	2.7
	5.1×10^{13}	64.5	8.5	2.7
	2.1×10^{14}	53.9	5.5	2.7
	2.8×10^{12}	26.7	5.5	2.7
	4.0×10^{12}	16.9	7.5	2.7
	3.8×10^{12}	6.0	5.5	2.7
	5.6×10^{12}	0.1	4.0	2.7
	1.9×10^{12}	−39.9	4.5	2.7
	2.0×10^{12}	−48.8	7.0	2.7
	1.2×10^{12}	−62.6	5.0	2.7
	2.5×10^{12}	−74.6	5.0	2.7
	2.1×10^{12}	−80.4	5.0	2.7
	1.6×10^{12}	−101.3	4.0	2.7
	3.2×10^{12}	−106.3	3.0	2.7

Notes. See notes of Table A.11.

Table A.20: Parameters of our best-fit model of C_2H_5OH.

Molecule	N_{tot}[a] [cm^{-2}]	v_{LSR}[b] [$km\,s^{-1}$]	$FWHM$[c] [$km\,s^{-1}$]	T_{rot}[d] [K]
		K4		
C_2H_5OH	2.6×10^{14}	71.1	5.0	5.1
	4.0×10^{14}	61.8	5.0	5.1
		$K6_{shell}$		
C_2H_5OH	3.3×10^{14}	61.8	7.0	3.8

Notes. See notes of Table A.11.

Table A.21: Parameters of our best-fit model of CCH.

Molecule	N_{tot}[a] [cm^{-2}]	v_{LSR}[b] [$km\,s^{-1}$]	$FWHM$[c] [$km\,s^{-1}$]	T_{rot}[d] [K]
		K4		
CCH	2.3×10^{14}	89.2	4.0	2.7
	1.5×10^{15}	81.2	8.0	2.7

Notes. See notes of Table A.11.

Table A.21: Continued.

Molecule	N_{tot}[a] [cm^{-2}]	v_{LSR}[b] [km s^{-1}]	$FWHM$[c] [km s^{-1}]	T_{rot}[d] [K]
	1.1×10^{15}	70.8	6.5	2.7
	2.7×10^{15}	62.7	9.0	2.7
	1.0×10^{14}	49.0	5.0	2.7
	7.0×10^{13}	34.2	3.5	2.7
	7.0×10^{13}	27.2	3.5	2.7
	2.0×10^{14}	20.2	3.5	2.7
	1.0×10^{14}	14.1	3.5	2.7
	1.3×10^{14}	8.6	3.0	2.7
	4.1×10^{14}	3.7	4.0	2.7
	1.8×10^{14}	−1.8	4.0	2.7
	8.0×10^{13}	−7.3	3.0	2.7
	8.0×10^{13}	−20.8	6.5	2.7
	1.5×10^{14}	−14.8	6.5	2.7
	1.0×10^{14}	−27.0	4.5	2.7
	5.0×10^{13}	−33.0	6.5	2.7
	2.7×10^{14}	−40.3	6.5	2.7
	7.5×10^{13}	−46.8	4.5	2.7
	5.1×10^{13}	−58.8	7.0	2.7
	1.3×10^{14}	−72.4	7.0	2.7
	6.0×10^{13}	−79.3	5.0	2.7
	7.0×10^{13}	−89.8	5.0	2.7
	1.6×10^{14}	−105.3	5.0	2.7
^{13}CCH	7.5×10^{13}	70.8	6.5	2.7
	1.3×10^{14}	62.7	9.0	2.7
C^{13}CH	6.0×10^{13}	70.8	6.5	2.7
	8.3×10^{13}	62.7	9.0	2.7
		K6$_{shell}$		
CCH	2.2×10^{14}	84.5	5.0	2.7
	6.2×10^{14}	78.8	5.0	2.7
	6.0×10^{14}	74.0	5.0	2.7
	3.8×10^{15}	64.3	9.0	2.7
	3.9×10^{14}	55.4	3.5	2.7
	2.9×10^{14}	50.5	4.5	2.7
	1.0×10^{14}	24.7	5.0	2.7
	3.2×10^{14}	16.0	8.0	2.7
	2.5×10^{14}	8.2	4.0	2.7
	2.4×10^{14}	3.0	4.5	2.7
	2.6×10^{14}	−2.0	4.5	2.7
	1.0×10^{14}	−7.3	4.5	2.7

Notes. See notes of Table A.11.

Table A.21: Continued.

Molecule	N_{tot}[a] [cm^{-2}]	v_{LSR}[b] [km s^{-1}]	$FWHM$[c] [km s^{-1}]	T_{rot}[d] [K]
	9.0×10^{13}	−15.4	6.5	2.7
	2.0×10^{14}	−25.5	7.0	2.7
	1.2×10^{14}	−39.4	4.5	2.7
	8.0×10^{13}	−47.6	5.5	2.7
	6.0×10^{13}	−57.7	4.0	2.7
	7.3×10^{13}	−69.9	5.5	2.7
	1.3×10^{14}	−75.4	4.5	2.7
	1.1×10^{14}	−82.2	4.5	2.7
	1.4×10^{14}	−92.6	5.5	2.7
	1.9×10^{14}	−104.1	6.5	2.7
^{13}CCH	6.0×10^{13}	74.0	5.0	2.7
	8.0×10^{13}	64.3	9.0	2.7
C^{13}CH	3.0×10^{13}	74.0	5.0	2.7
	9.0×10^{13}	64.3	9.0	2.7
		K5$_{shell}$		
CCH	2.2×10^{15}	80.8	9.0	2.7
	8.3×10^{14}	71.0	5.0	2.7
	3.8×10^{15}	62.1	9.0	2.7
	1.2×10^{14}	28.2	4.0	2.7
	3.2×10^{14}	19.7	4.0	2.7
	7.1×10^{14}	7.4	6.0	2.7
	5.8×10^{14}	−1.5	7.5	2.7
	1.5×10^{14}	−14.6	6.5	2.7
	1.4×10^{14}	−20.9	3.5	2.7
	1.0×10^{14}	−26.4	4.0	2.7
	1.0×10^{14}	−39.6	3.5	2.7
	1.0×10^{14}	−49.6	5.5	2.7
	1.5×10^{14}	−75.4	3.5	2.7
	1.1×10^{14}	−81.4	4.5	2.7
	1.6×10^{14}	−91.2	6.5	2.7
	2.1×10^{14}	−105.4	4.5	2.7
		K6$_{shell,a}$		
CCH	6.2×10^{14}	83.7	5.0	2.7
	6.2×10^{14}	77.8	5.0	2.7
	6.7×10^{14}	72.4	5.0	2.7
	3.4×10^{15}	63.4	8.0	2.7
	3.9×10^{14}	55.2	4.0	2.7
	1.5×10^{14}	49.3	4.5	2.7
	2.0×10^{14}	30.2	6.0	2.7

Notes. See notes of Table A.11.

Table A.21: Continued.

Molecule	N_{tot}[a] [cm^{-2}]	v_{LSR}[b] [km s^{-1}]	$FWHM$[c] [km s^{-1}]	T_{rot}[d] [K]
	2.5×10^{14}	19.8	4.0	2.7
	3.5×10^{14}	9.0	6.0	2.7
	2.3×10^{14}	3.0	3.5	2.7
	2.7×10^{14}	−1.6	4.5	2.7
	4.0×10^{13}	−7.5	3.5	2.7
	9.0×10^{13}	−17.5	3.5	2.7
	2.0×10^{14}	−25.4	6.0	2.7
	6.0×10^{13}	−31.8	3.5	2.7
	1.4×10^{14}	−39.4	3.5	2.7
	1.2×10^{14}	−47.6	5.5	2.7
	6.0×10^{13}	−58.3	5.0	2.7
	2.3×10^{14}	−74.5	6.5	2.7
	1.0×10^{14}	−81.8	3.0	2.7
	1.3×10^{14}	−93.6	7.5	2.7
	1.7×10^{14}	−105.5	4.0	2.7
^{13}CCH	1.7×10^{14}	63.4	8.0	2.7
C^{13}CH	1.2×10^{14}	63.4	8.0	2.7
		I		
CCH	3.8×10^{15}	64.7	11.0	2.7
	1.0×10^{14}	48.8	7.0	2.7
	4.0×10^{13}	40.8	7.0	2.7
	6.0×10^{13}	29.7	5.0	2.7
	2.5×10^{14}	16.0	4.5	2.7
	3.5×10^{14}	8.3	6.5	2.7
	2.3×10^{14}	0.0	4.5	2.7
	3.0×10^{13}	−9.6	4.5	2.7
	7.0×10^{13}	−15.5	4.5	2.7
	1.5×10^{14}	−20.9	4.5	2.7
	1.0×10^{14}	−27.8	4.0	2.7
	1.2×10^{14}	−40.6	4.5	2.7
	9.0×10^{13}	−46.9	5.0	2.7
	6.0×10^{13}	−57.7	4.0	2.7
	3.3×10^{13}	−69.9	3.5	2.7
	7.3×10^{13}	−75.4	3.5	2.7
	3.1×10^{13}	−80.2	3.5	2.7
	1.5×10^{14}	−91.6	7.5	2.7
	1.5×10^{14}	−101.1	4.5	2.7
	1.0×10^{14}	−106.4	4.5	2.7

Notes. See notes of Table A.11.

Table A.21: Continued.

Molecule	$N_{tot}{}^a$ [cm^{-2}]	$v_{LSR}{}^b$ [$km\,s^{-1}$]	$FWHM^c$ [$km\,s^{-1}$]	$T_{rot}{}^d$ [K]
		L		
CCH	1.2×10^{14}	89.5	5.0	2.7
	1.5×10^{14}	82.7	3.5	2.7
	9.2×10^{14}	77.4	4.5	2.7
	8.0×10^{14}	71.9	5.0	2.7
	2.9×10^{15}	58.7	11.5	2.7
	1.2×10^{14}	25.7	3.0	2.7
	4.5×10^{14}	18.0	6.0	2.7
	4.5×10^{14}	7.3	6.0	2.7
	3.5×10^{14}	−0.6	6.5	2.7
	5.0×10^{14}	−9.5	7.5	2.7
	2.0×10^{14}	−19.4	5.5	2.7
	1.5×10^{14}	−25.5	4.0	2.7
	1.6×10^{14}	−39.4	5.5	2.7
	1.2×10^{14}	−46.6	3.5	2.7
	5.0×10^{13}	−59.3	4.0	2.7
	1.3×10^{14}	−70.4	4.5	2.7
	1.8×10^{14}	−77.4	4.5	2.7
	8.1×10^{13}	−86.2	4.5	2.7
	8.1×10^{13}	−92.6	4.5	2.7
	4.5×10^{13}	−99.5	4.5	2.7
	1.4×10^{14}	−106.9	5.5	2.7

Notes. See notes of Table A.11.

Table A.22: Parameters of our best-fit model of NH_2CHO.

Molecule	$N_{tot}{}^a$ [cm^{-2}]	$v_{LSR}{}^b$ [$km\,s^{-1}$]	$FWHM^c$ [$km\,s^{-1}$]	$T_{rot}{}^d$ [K]
		K4		
NH_2CHO	3.0×10^{13}	89.0	4.0	6.3
	1.4×10^{14}	80.3	5.0	6.3
	1.6×10^{14}	70.4	6.0	6.3
	2.0×10^{14}	63.4	6.0	6.3
	2.8×10^{14}	56.4	7.5	6.3
	1.7×10^{13}	2.6	3.5	4.3
	1.8×10^{13}	−2.4	3.5	4.3
		$K6_{shell}$		
NH_2CHO	2.0×10^{14}	82.2	6.0	6.0
	4.4×10^{13}	75.8	6.0	6.0
	2.7×10^{14}	65.0	4.0	6.0
	2.7×10^{14}	59.5	4.0	6.0

Notes. See notes of Table A.11.

Table A.22: Continued.

Molecule	$N_{tot}{}^a$ [cm^{-2}]	$v_{LSR}{}^b$ [km s^{-1}]	$FWHM^c$ [km s^{-1}]	$T_{rot}{}^d$ [K]
		$K5_{shell}$		
NH_2CHO	4.4×10^{14}	82.2	7.0	4.8
	1.7×10^{14}	75.8	6.0	4.8
	4.0×10^{14}	65.0	6.0	4.8
	7.0×10^{14}	59.5	7.0	4.8
		$K6_{shell,a}$		
NH_2CHO	4.2×10^{14}	82.7	7.0	6.0
	6.0×10^{13}	71.8	8.0	6.0
	3.0×10^{14}	65.0	6.0	6.0
	3.0×10^{14}	59.5	6.0	6.0
		I		
NH_2CHO	3.0×10^{13}	69.0	4.0	6.7
	1.2×10^{14}	59.5	6.0	6.7
		L		
NH_2CHO	1.1×10^{14}	75.8	8.0	4.3
	3.0×10^{13}	69.0	6.0	4.3
	1.6×10^{14}	57.5	10.0	4.3

Notes. See notes of Table A.11.

Table A.23: Parameters of our best-fit model of HCO^+.

Molecule	$N_{tot}{}^a$ [cm^{-2}]	$v_{LSR}{}^b$ [km s^{-1}]	$FWHM^c$ [km s^{-1}]	$T_{rot}{}^d$ [K]
		K4		
HCO^+	1.9×10^{14}	88.7	5.5	2.7
	1.1×10^{15}	79.6	6.5	2.7
	1.0×10^{15}	71.1	6.0	2.7
	2.4×10^{15}	63.1	8.0	2.7
	2.6×10^{14}	53.8	6.0	2.7
	5.2×10^{13}	40.8	11.5	2.7
	2.4×10^{13}	27.0	3.5	2.7
	2.7×10^{14}	18.6	5.5	2.7
	3.0×10^{13}	9.8	5.5	2.7
	1.6×10^{14}	3.8	4.5	2.7
	7.6×10^{13}	−1.7	3.5	2.7
	8.0×10^{13}	−6.9	3.5	2.7
	8.4×10^{13}	−17.2	9.5	2.7
	3.2×10^{13}	−28.1	7.5	2.7
	2.4×10^{13}	−35.2	7.0	2.7
	2.1×10^{13}	−41.2	8.0	2.7
	2.3×10^{14}	−48.8	5.0	2.7

Notes. See notes of Table A.11.

Table A.23: Continued.

Molecule	$N_{\rm tot}{}^a$ [cm^{-2}]	$v_{\rm LSR}{}^b$ [km s^{-1}]	$FWHM^c$ [km s^{-1}]	$T_{\rm rot}{}^d$ [K]
	2.1×10^{13}	−56.3	8.0	2.7
	2.3×10^{13}	−66.3	6.0	2.7
	5.6×10^{13}	−76.4	9.5	2.7
	8.6×10^{12}	−83.9	5.5	2.7
	2.6×10^{13}	−91.9	10.5	2.7
	9.2×10^{13}	−104.3	5.0	2.7
	5.0×10^{12}	−114.1	7.5	2.7
	1.5×10^{13}	−122.8	7.0	2.7
	1.0×10^{12}	−134.6	6.5	2.7
$H^{13}CO^+$	9.7×10^{12}	88.7	5.5	2.7
	5.6×10^{13}	79.6	6.5	2.7
	5.0×10^{13}	71.1	6.0	2.7
	1.2×10^{14}	63.1	8.0	2.7
	1.3×10^{13}	53.8	6.0	2.7
	1.3×10^{12}	40.8	11.5	2.7
	6.2×10^{11}	27.0	3.5	2.7
	4.5×10^{12}	18.6	5.5	2.7
	1.5×10^{12}	9.8	5.5	2.7
	8.0×10^{12}	3.8	4.5	2.7
	3.8×10^{12}	−1.7	3.5	2.7
	2.0×10^{12}	−6.9	3.5	2.7
	2.1×10^{12}	−17.2	9.5	2.7
	1.8×10^{12}	−28.1	7.5	2.7
	5.1×10^{12}	−41.2	8.0	2.7
	5.7×10^{11}	−48.8	5.0	2.7
	2.7×10^{12}	−76.4	9.5	2.7
	1.7×10^{12}	−104.3	5.0	2.7
	4.8×10^{11}	−122.8	7.0	2.7
$HC^{18}O^+$	1.5×10^{12}	88.7	5.5	2.7
	4.5×10^{12}	79.6	6.5	2.7
	4.0×10^{12}	71.1	6.0	2.7
	9.5×10^{12}	63.1	8.0	2.7
	2.2×10^{12}	53.8	6.0	2.7
	8.0×10^{11}	3.8	4.5	2.7
	3.7×10^{11}	−104.3	4.0	2.7
$HC^{17}O^+$	1.1×10^{12}	79.6	6.5	2.7
	1.3×10^{12}	71.1	6.0	2.7

Notes. See notes of Table A.11.

Table A.23: Continued.

Molecule	$N_{tot}{}^a$ [cm^{-2}]	$v_{LSR}{}^b$ [km s^{-1}]	$FWHM^c$ [km s^{-1}]	$T_{rot}{}^d$ [K]
	2.8×10^{12}	63.1	8.0	2.7
	6.0×10^{11}	53.8	6.0	2.7
		$K6_{shell}$		
HCO^+	3.3×10^{12}	89.7	4.5	2.7
	2.4×10^{14}	84.0	3.5	2.7
	6.2×10^{14}	79.2	4.5	2.7
	5.6×10^{14}	73.6	5.0	2.7
	2.0×10^{15}	63.5	8.0	2.7
	5.0×10^{14}	54.7	4.5	2.7
	1.1×10^{14}	49.3	4.5	2.7
	4.2×10^{12}	43.5	3.5	2.7
	4.2×10^{12}	37.5	3.5	2.7
	3.2×10^{13}	30.0	5.5	2.7
	7.2×10^{13}	20.8	6.5	2.7
	8.8×10^{13}	13.9	5.5	2.7
	1.7×10^{14}	7.3	6.5	2.7
	5.6×10^{13}	−0.1	5.0	2.7
	3.1×10^{13}	−6.8	5.0	2.7
	3.4×10^{13}	−13.8	5.5	2.7
	5.6×10^{13}	−19.5	4.5	2.7
	2.5×10^{13}	−27.6	4.5	2.7
	7.3×10^{12}	−34.1	4.5	2.7
	9.2×10^{13}	−39.6	4.5	2.7
	3.8×10^{13}	−48.4	6.5	2.7
	3.0×10^{13}	−56.9	6.0	2.7
	3.2×10^{13}	−65.9	7.0	2.7
	4.0×10^{13}	−71.6	5.5	2.7
	1.1×10^{13}	−77.3	3.0	2.7
	2.4×10^{13}	−81.8	5.0	2.7
	8.0×10^{12}	−86.9	4.0	2.7
	1.8×10^{13}	−91.9	9.0	2.7
	7.2×10^{12}	−97.9	4.0	2.7
	6.2×10^{13}	−105.4	6.5	2.7
	1.4×10^{13}	−113.1	5.5	2.7
	6.8×10^{13}	−118.4	8.5	2.7
$H^{13}CO^+$	1.2×10^{13}	84.0	3.5	2.7
	3.1×10^{13}	79.2	4.5	2.7
	2.8×10^{13}	73.6	5.0	2.7
	2.0×10^{14}	63.5	8.0	2.7
	2.5×10^{13}	54.7	4.5	2.7

Notes. See notes of Table A.11.

Table A.23: Continued.

Molecule	$N_{\rm tot}{}^a$ [cm^{-2}]	$v_{\rm LSR}{}^b$ [km s^{-1}]	$FWHM^c$ [km s^{-1}]	$T_{\rm rot}{}^d$ [K]
	5.6×10^{12}	49.3	4.5	2.7
	8.2×10^{11}	30.0	5.5	2.7
	1.2×10^{12}	20.8	6.5	2.7
	4.4×10^{12}	13.9	5.5	2.7
	8.5×10^{12}	7.3	6.5	2.7
	2.8×10^{12}	−0.1	5.0	2.7
	7.7×10^{11}	−6.8	5.0	2.7
	8.7×10^{11}	−13.8	5.5	2.7
	1.4×10^{12}	−19.5	4.5	2.7
	6.3×10^{11}	−27.6	4.5	2.7
	2.3×10^{12}	−39.6	4.5	2.7
	9.5×10^{11}	−48.4	6.5	2.7
	4.0×10^{11}	−56.9	6.0	2.7
	6.0×10^{11}	−65.9	7.0	2.7
	2.0×10^{12}	−71.6	5.5	2.7
	5.4×10^{11}	−77.3	3.0	2.7
	1.2×10^{12}	−81.8	5.0	2.7
	6.2×10^{11}	−91.9	9.0	2.7
	3.2×10^{12}	−105.4	6.5	2.7
	3.2×10^{11}	−113.1	5.5	2.7
	1.1×10^{12}	−118.4	8.5	2.7
$HC^{18}O^+$	1.0×10^{12}	84.0	3.5	2.7
	2.5×10^{12}	79.2	4.5	2.7
	2.2×10^{12}	73.6	5.0	2.7
	1.6×10^{13}	63.5	8.0	2.7
	2.0×10^{12}	54.7	4.5	2.7
	4.5×10^{11}	49.3	4.5	2.7
	3.4×10^{11}	13.9	5.5	2.7
	8.8×10^{11}	7.3	6.5	2.7
	4.5×10^{11}	−48.4	6.5	2.7
$HC^{17}O^+$	4.9×10^{11}	84.0	3.5	2.7
	7.5×10^{11}	78.7	4.5	2.7
	8.5×10^{11}	73.6	5.0	2.7
	4.3×10^{12}	63.5	8.0	2.7
	6.4×10^{11}	54.7	4.5	2.7
		$K5_{\rm shell}$		
HCO^+	2.8×10^{15}	80.8	8.0	2.7
	5.6×10^{15}	63.3	11.0	2.7
	3.6×10^{13}	45.5	8.5	2.7

Notes. See notes of Table A.11.

Table A.23: Continued.

Molecule	$N_{tot}{}^a$ [cm^{-2}]	$v_{LSR}{}^b$ [$km\,s^{-1}$]	$FWHM^c$ [$km\,s^{-1}$]	$T_{rot}{}^d$ [K]
	1.2×10^{13}	31.0	6.5	2.7
	3.6×10^{14}	20.8	5.5	2.7
	1.7×10^{14}	7.3	7.0	2.7
	1.5×10^{14}	−4.8	8.0	2.7
	7.6×10^{13}	−17.5	6.5	2.7
	8.4×10^{13}	−27.6	8.5	2.7
	1.0×10^{14}	−39.6	4.0	2.7
	4.8×10^{13}	−48.4	6.5	2.7
	2.0×10^{13}	−56.9	6.0	2.7
	2.4×10^{13}	−65.9	6.0	2.7
	6.8×10^{13}	−74.8	5.0	2.7
	3.0×10^{13}	−81.8	3.0	2.7
	2.2×10^{13}	−87.9	9.0	2.7
	1.5×10^{13}	−97.1	6.5	2.7
	6.4×10^{13}	−104.8	4.5	2.7
	3.9×10^{13}	−116.4	11.5	2.7
$H^{13}CO^+$	1.4×10^{14}	80.8	8.0	2.7
	2.8×10^{14}	63.3	11.0	2.7
	6.2×10^{12}	20.8	5.5	2.7
	8.5×10^{12}	7.3	7.0	2.7
	7.7×10^{12}	−4.8	8.0	2.7
	1.4×10^{12}	−17.5	6.5	2.7
	2.1×10^{12}	−27.6	8.5	2.7
	2.6×10^{12}	−39.6	4.0	2.7
	1.2×10^{12}	−48.4	6.5	2.7
	1.2×10^{12}	−65.9	6.0	2.7
	3.4×10^{12}	−74.8	5.0	2.7
	1.5×10^{12}	−81.8	3.0	2.7
	3.2×10^{12}	−104.8	4.5	2.7
	1.9×10^{12}	−116.4	11.5	2.7
$HC^{18}O^+$	9.5×10^{12}	80.8	8.0	2.7
	1.9×10^{13}	63.3	11.0	2.7
$HC^{17}O^+$	2.5×10^{12}	80.8	8.0	2.7
	4.9×10^{12}	63.3	11.0	2.7
		$K6_{shell,a}$		
HCO^+	2.0×10^{15}	81.7	9.0	2.7
	5.6×10^{15}	63.5	11.5	2.7
	1.3×10^{14}	52.2	4.5	2.7

Notes. See notes of Table A.11.

Table A.23: Continued.

Molecule	$N_{\rm tot}{}^a$ [cm^{-2}]	$v_{\rm LSR}{}^b$ [km s^{-1}]	$FWHM^c$ [km s^{-1}]	$T_{\rm rot}{}^d$ [K]
	2.2×10^{13}	46.0	3.5	2.7
	1.6×10^{13}	40.0	4.5	2.7
	2.5×10^{13}	34.0	4.5	2.7
	2.5×10^{13}	30.0	4.5	2.7
	1.3×10^{14}	20.8	6.5	2.7
	1.3×10^{14}	13.8	5.5	2.7
	2.0×10^{14}	8.3	8.5	2.7
	6.8×10^{13}	−2.1	6.0	2.7
	1.1×10^{14}	−11.8	8.0	2.7
	9.6×10^{13}	−19.5	6.5	2.7
	5.2×10^{13}	−27.6	6.5	2.7
	2.0×10^{13}	−33.8	4.5	2.7
	9.2×10^{13}	−39.6	4.5	2.7
	3.8×10^{13}	−46.4	4.5	2.7
	2.7×10^{13}	−56.9	9.0	2.7
	1.2×10^{13}	−63.9	5.0	2.7
	6.0×10^{13}	−72.6	8.5	2.7
	3.0×10^{13}	−81.8	5.0	2.7
	1.7×10^{13}	−91.9	8.0	2.7
	2.4×10^{13}	−100.1	5.5	2.7
	7.4×10^{13}	−105.4	2.0	2.7
	2.4×10^{13}	−111.1	5.5	2.7
	2.4×10^{13}	−118.4	6.5	2.7
	2.8×10^{12}	−126.4	4.5	2.7
$H^{13}CO^+$	1.0×10^{14}	81.7	8.0	2.7
	2.8×10^{14}	63.5	11.5	2.7
	6.7×10^{12}	52.2	4.5	2.7
	8.2×10^{11}	46.0	3.5	2.7
	1.0×10^{12}	40.0	4.5	2.7
	6.2×10^{11}	34.0	4.5	2.7
	6.2×10^{11}	30.0	4.5	2.7
	2.2×10^{12}	20.8	6.5	2.7
	2.2×10^{12}	13.8	5.5	2.7
	9.8×10^{12}	8.3	8.5	2.7
	3.4×10^{12}	−2.1	6.0	2.7
	2.7×10^{12}	−11.8	8.0	2.7
	2.4×10^{12}	−19.5	6.5	2.7
	1.3×10^{12}	−27.6	6.5	2.7
	5.3×10^{11}	−33.8	4.5	2.7
	2.3×10^{12}	−39.6	4.5	2.7

Notes. See notes of Table A.11.

Table A.23: Continued.

Molecule	N_{tot}[a] [cm^{-2}]	v_{LSR}[b] [km s^{-1}]	$FWHM$[c] [km s^{-1}]	T_{rot}[d] [K]
	9.5×10^{11}	−46.4	4.5	2.7
	3.0×10^{12}	−72.6	8.5	2.7
	1.5×10^{12}	−81.8	5.0	2.7
	7.2×10^{11}	−100.1	5.5	2.7
	3.2×10^{12}	−105.4	2.0	2.7
	7.2×10^{11}	−111.1	5.5	2.7
	8.8×10^{11}	−118.4	6.5	2.7
$HC^{18}O^+$	6.9×10^{12}	81.7	8.0	2.7
	1.9×10^{13}	63.5	11.5	2.7
	4.5×10^{11}	52.2	4.5	2.7
	1.2×10^{12}	8.3	8.5	2.7
$HC^{17}O^+$	1.9×10^{12}	81.7	8.0	2.7
	5.9×10^{12}	63.5	11.5	2.7
	2.5×10^{11}	52.2	4.5	2.7
		I		
HCO^+	1.3×10^{12}	84.7	4.5	2.7
	1.8×10^{13}	77.2	5.5	2.7
	5.1×10^{13}	69.6	5.0	2.7
	2.4×10^{14}	61.8	8.0	2.7
	9.0×10^{12}	49.3	6.5	2.7
	2.0×10^{13}	41.0	8.5	2.7
	4.1×10^{13}	28.0	5.5	2.7
	6.0×10^{13}	16.9	9.5	2.7
	5.0×10^{13}	7.3	6.5	2.7
	7.2×10^{13}	0.3	3.5	2.7
	1.5×10^{13}	−6.8	6.0	2.7
	4.0×10^{13}	−20.5	8.5	2.7
	4.0×10^{13}	−26.6	7.5	2.7
	6.3×10^{12}	−35.1	4.5	2.7
	8.0×10^{13}	−40.9	3.0	2.7
	5.6×10^{13}	−46.4	6.5	2.7
	1.6×10^{13}	−58.9	5.0	2.7
	5.4×10^{12}	−63.9	3.0	2.7
	1.4×10^{13}	−69.6	7.5	2.7
	1.2×10^{13}	−76.3	5.0	2.7
	8.9×10^{12}	−81.8	3.5	2.7
	1.9×10^{13}	−87.8	5.0	2.7
	2.5×10^{13}	−94.8	5.0	2.7
	4.6×10^{13}	−101.4	3.0	2.7

Notes. See notes of Table A.11.

Table A.23: Continued.

Molecule	$N_{\rm tot}{}^a$ [cm^{-2}]	$v_{\rm LSR}{}^b$ [km s^{-1}]	$FWHM^c$ [km s^{-1}]	$T_{\rm rot}{}^d$ [K]
	1.9×10^{13}	−105.4	3.0	2.7
	1.4×10^{13}	−111.1	5.5	2.7
	1.6×10^{13}	−116.4	6.5	2.7
	4.4×10^{12}	−127.1	7.5	2.7
	1.3×10^{12}	−134.4	5.5	2.7
$H^{13}CO^+$	6.3×10^{13}	69.6	5.0	2.7
	1.4×10^{14}	61.8	8.0	2.7
	4.5×10^{11}	49.3	6.5	2.7
	1.5×10^{12}	41.0	8.5	2.7
	8.2×10^{11}	28.0	5.5	2.7
	1.0×10^{13}	16.9	9.5	2.7
	2.5×10^{12}	7.3	6.5	2.7
	3.6×10^{12}	0.3	3.5	2.7
	7.7×10^{11}	−6.8	6.0	2.7
	1.0×10^{12}	−20.5	8.5	2.7
	1.0×10^{12}	−26.6	7.5	2.7
	2.0×10^{12}	−40.9	3.0	2.7
	1.4×10^{12}	−46.4	6.5	2.7
	4.6×10^{11}	−58.9	5.0	2.7
	2.2×10^{11}	−63.9	3.0	2.7
	4.4×10^{11}	−69.6	7.5	2.7
	4.0×10^{11}	−76.3	5.0	2.7
	5.2×10^{11}	−87.8	5.0	2.7
	7.2×10^{11}	−94.8	5.0	2.7
	1.8×10^{12}	−101.4	3.0	2.7
	7.2×10^{11}	−105.4	3.0	2.7
	5.2×10^{11}	−111.1	5.5	2.7
	5.8×10^{11}	−116.4	6.5	2.7
$HC^{18}O^+$	4.2×10^{12}	69.6	5.0	2.7
	8.6×10^{12}	61.8	8.0	2.7
	6.9×10^{11}	16.9	9.5	2.7
	4.8×10^{11}	0.3	3.5	2.7
$HC^{17}O^+$	1.2×10^{12}	69.6	5.0	2.7
	2.3×10^{12}	61.8	8.0	2.7
		L		
HCO^+	5.6×10^{13}	90.0	6.5	2.7
	6.0×10^{13}	84.0	4.5	2.7
	1.5×10^{15}	74.2	7.5	2.7

Notes. See notes of Table A.11.

Table A.23: Continued.

Molecule	$N_{\rm tot}{}^a$ [cm^{-2}]	$v_{\rm LSR}{}^b$ [km s^{-1}]	$FWHM^c$ [km s^{-1}]	$T_{\rm rot}{}^d$ [K]
	8.0×10^{14}	64.6	6.0	2.7
	3.0×10^{15}	56.2	8.5	2.7
	2.7×10^{13}	45.0	6.5	2.7
	3.2×10^{13}	35.0	4.5	2.7
	6.8×10^{13}	29.4	4.5	2.7
	1.5×10^{14}	23.8	4.5	2.7
	4.8×10^{14}	16.9	5.5	2.7
	2.0×10^{14}	9.6	6.5	2.7
	5.8×10^{13}	2.9	4.0	2.7
	7.6×10^{13}	−2.1	4.0	2.7
	1.5×10^{13}	−6.8	5.0	2.7
	1.1×10^{14}	−11.8	5.5	2.7
	1.2×10^{14}	−17.5	4.5	2.7
	1.2×10^{14}	−24.6	7.5	2.7
	1.7×10^{13}	−32.6	4.5	2.7
	1.0×10^{14}	−39.6	4.0	2.7
	3.2×10^{13}	−46.4	3.5	2.7
	5.2×10^{12}	−56.4	8.5	2.7
	6.2×10^{12}	−66.4	6.5	2.7
	6.8×10^{13}	−75.8	7.5	2.7
	2.8×10^{13}	−83.5	3.0	2.7
	4.8×10^{13}	−89.4	6.5	2.7
	4.8×10^{13}	−101.4	6.5	2.7
	2.8×10^{13}	−106.4	2.5	2.7
	4.2×10^{12}	−111.1	3.5	2.7
$H^{13}CO^+$	2.8×10^{12}	90.0	6.5	2.7
	3.0×10^{12}	84.0	4.5	2.7
	7.8×10^{13}	74.2	7.5	2.7
	4.0×10^{13}	64.6	6.0	2.7
	1.5×10^{14}	56.2	8.5	2.7
	8.2×10^{11}	35.0	4.5	2.7
	1.7×10^{12}	29.4	4.5	2.7
	2.5×10^{12}	23.8	4.5	2.7
	8.4×10^{12}	16.9	5.5	2.7
	4.9×10^{12}	9.6	6.5	2.7
	2.9×10^{12}	2.9	4.0	2.7
	3.8×10^{12}	−2.1	4.0	2.7
	7.7×10^{11}	−6.8	5.0	2.7
	2.9×10^{12}	−11.8	5.5	2.7
	3.1×10^{12}	−17.5	4.5	2.7

Notes. See notes of Table A.11.

Table A.23: Continued.

Molecule	$N_{tot}{}^a$ [cm^{-2}]	$v_{LSR}{}^b$ [km s^{-1}]	$FWHM^c$ [km s^{-1}]	$T_{rot}{}^d$ [K]
	3.0×10^{12}	−24.6	7.5	2.7
	2.6×10^{12}	−39.6	4.0	2.7
	7.9×10^{11}	−46.4	3.5	2.7
	3.4×10^{12}	−75.8	7.5	2.7
	1.2×10^{12}	−83.5	3.0	2.7
	1.2×10^{12}	−89.4	6.5	2.7
	1.2×10^{12}	−101.4	4.5	2.7
	1.2×10^{12}	−106.4	2.5	2.7
$HC^{18}O^+$	9.5×10^{11}	84.0	4.5	2.7
	3.9×10^{12}	74.2	7.5	2.7
	2.7×10^{12}	64.6	6.0	2.7
	9.2×10^{12}	56.2	8.5	2.7
$HC^{17}O^+$	9.0×10^{11}	64.6	6.0	2.7
	2.1×10^{12}	56.2	8.5	2.7

Notes. See notes of Table A.11.

Table A.24: Parameters of our best-fit model of HCN.

Molecule	$N_{tot}{}^a$ [cm^{-2}]	$v_{LSR}{}^b$ [km s^{-1}]	$FWHM^c$ [km s^{-1}]	$T_{rot}{}^d$ [K]
		K4		
HCN	1.9×10^{15}	88.9	4.5	2.7
	6.0×10^{15}	81.1	6.5	2.7
	7.6×10^{15}	69.7	7.0	2.7
	7.8×10^{15}	62.2	6.5	2.7
	3.0×10^{15}	54.6	4.5	2.7
	3.4×10^{14}	47.9	5.5	2.7
	2.6×10^{13}	30.2	4.0	2.7
	6.4×10^{13}	25.9	4.0	2.7
	2.3×10^{14}	20.5	4.0	2.7
	4.8×10^{14}	13.1	4.0	2.7
	9.2×10^{14}	3.2	4.5	2.7
	4.2×10^{14}	−2.8	4.5	2.7
	1.2×10^{14}	−9.4	4.5	2.7
	4.2×10^{13}	−17.4	5.5	2.7
	4.2×10^{13}	−27.4	5.5	2.7
	1.8×10^{14}	−40.3	3.0	2.7
	3.2×10^{13}	−49.6	7.0	2.7
	7.2×10^{12}	−60.6	5.0	2.7
	2.2×10^{13}	−68.2	6.0	2.7

Notes. See notes of Table A.11.

Table A.24: Continued.

Molecule	$N_{\rm tot}{}^a$ [cm^{-2}]	$v_{\rm LSR}{}^b$ [km s^{-1}]	$FWHM^c$ [km s^{-1}]	$T_{\rm rot}{}^d$ [K]
	9.0×10^{13}	−75.5	5.0	2.7
	2.0×10^{13}	−80.8	3.0	2.7
	3.2×10^{13}	−86.1	6.0	2.7
	1.0×10^{13}	−91.9	3.0	2.7
	8.0×10^{13}	−104.9	5.0	2.7
	3.0×10^{12}	−120.9	5.0	2.7
$H^{13}CN$	9.3×10^{13}	88.9	4.5	2.7
	3.0×10^{14}	81.1	6.5	2.7
	3.8×10^{14}	69.7	9.0	2.7
	3.9×10^{14}	62.2	6.5	2.7
	1.5×10^{14}	54.6	5.5	2.7
	1.7×10^{13}	47.9	5.5	2.7
	6.4×10^{11}	30.2	4.0	2.7
	1.6×10^{12}	25.9	4.0	2.7
	3.7×10^{12}	20.5	4.0	2.7
	8.0×10^{12}	13.1	4.0	2.7
	4.6×10^{13}	3.2	4.5	2.7
	2.2×10^{13}	−2.8	4.5	2.7
	6.0×10^{12}	−9.4	4.5	2.7
	4.5×10^{12}	−40.3	3.0	2.7
	1.4×10^{12}	−75.5	5.0	2.7
	1.0×10^{12}	−80.8	3.0	2.7
	1.6×10^{12}	−86.1	6.0	2.7
	2.0×10^{12}	−104.9	5.0	2.7
$HC^{15}N$	6.2×10^{12}	88.9	4.5	2.7
	2.0×10^{13}	81.1	6.5	2.7
	2.7×10^{13}	69.7	9.0	2.7
	2.6×10^{13}	62.2	6.5	2.7
	1.2×10^{13}	54.6	5.5	2.7
	1.3×10^{12}	47.9	5.5	2.7
	6.3×10^{11}	13.1	4.0	2.7
	3.6×10^{12}	3.2	4.5	2.7
	3.7×10^{12}	−2.8	4.5	2.7
	1.3×10^{12}	−9.4	4.5	2.7
	6.0×10^{11}	−40.3	3.0	2.7
	1.2×10^{12}	−60.6	5.0	2.7
	1.9×10^{12}	−68.2	6.0	2.7
	9.2×10^{11}	−75.5	5.0	2.7
	1.9×10^{12}	−86.1	6.0	2.7

Notes. See notes of Table A.11.

Table A.24: Continued.

Molecule	$N_{\rm tot}{}^a$ [cm^{-2}]	$v_{\rm LSR}{}^b$ [km s^{-1}]	$FWHM^c$ [km s^{-1}]	$T_{\rm rot}{}^d$ [K]
		$K6_{\rm shell}$		
HCN	4.8×10^{15}	80.0	8.0	2.7
	1.5×10^{15}	71.4	6.0	2.7
	1.2×10^{16}	63.6	9.0	2.7
	4.8×10^{14}	55.4	4.5	2.7
	4.2×10^{14}	49.0	5.5	2.7
	1.3×10^{14}	31.5	4.5	2.7
	6.4×10^{13}	23.1	4.0	2.7
	6.8×10^{14}	12.9	5.0	2.7
	5.0×10^{14}	2.2	5.5	2.7
	1.9×10^{13}	−15.4	4.5	2.7
	2.9×10^{13}	−21.4	4.0	2.7
	2.2×10^{13}	−27.4	4.0	2.7
	8.4×10^{13}	−39.4	6.0	2.7
	2.5×10^{13}	−47.8	4.5	2.7
	2.0×10^{13}	−56.8	4.5	2.7
	3.6×10^{13}	−63.3	5.5	2.7
	2.9×10^{13}	−69.3	7.0	2.7
	2.8×10^{13}	−76.3	7.0	2.7
	1.3×10^{13}	−82.3	3.0	2.7
	2.3×10^{13}	−92.3	4.0	2.7
	1.3×10^{14}	−104.8	4.5	2.7
	1.2×10^{13}	−119.8	6.5	2.7
$H^{13}CN$	2.4×10^{14}	80.0	8.0	2.7
	7.5×10^{13}	71.4	6.0	2.7
	6.0×10^{14}	63.6	9.0	2.7
	2.4×10^{13}	55.4	4.5	2.7
	2.1×10^{13}	49.0	5.5	2.7
	3.2×10^{12}	31.5	4.5	2.7
	1.6×10^{12}	23.1	4.0	2.7
	1.3×10^{13}	12.9	5.0	2.7
	2.5×10^{13}	2.2	5.5	2.7
	2.3×10^{12}	−39.4	6.0	2.7
	9.9×10^{11}	−56.8	4.5	2.7
	1.8×10^{12}	−63.3	5.5	2.7
	1.4×10^{12}	−76.3	7.0	2.7
	6.5×10^{12}	−104.8	4.5	2.7
$HC^{15}N$	1.6×10^{13}	80.0	8.0	2.7
	5.0×10^{12}	71.4	6.0	2.7

Notes. See notes of Table A.11.

Table A.24: Continued.

Molecule	$N_{tot}{}^a$ [cm^{-2}]	$v_{LSR}{}^b$ [km s^{-1}]	$FWHM^c$ [km s^{-1}]	$T_{rot}{}^d$ [K]
	3.8×10^{13}	63.6	9.0	2.7
	1.6×10^{12}	55.4	4.5	2.7
	1.4×10^{12}	49.0	5.5	2.7
	7.6×10^{11}	12.3	5.0	2.7
	1.0×10^{12}	5.9	4.5	2.7
	1.0×10^{12}	0.4	4.5	2.7
	5.0×10^{11}	−56.8	4.5	2.7
	1.2×10^{12}	−63.3	5.5	2.7
	1.9×10^{12}	−69.3	7.0	2.7
	6.3×10^{11}	−76.1	7.0	2.7
		$K5_{shell}$		
HCN	9.0×10^{15}	82.1	7.5	2.7
	3.4×10^{15}	70.7	6.5	2.7
	1.0×10^{16}	59.7	9.0	2.7
	1.1×10^{13}	38.4	4.0	2.7
	1.1×10^{13}	31.4	4.0	2.7
	3.8×10^{14}	18.8	8.0	2.7
	5.4×10^{14}	8.2	3.0	2.7
	5.8×10^{14}	5.8	4.0	2.7
	1.4×10^{14}	−2.0	6.5	2.7
	4.9×10^{13}	−16.0	6.0	2.7
	3.9×10^{13}	−26.0	5.0	2.7
	8.9×10^{13}	−40.0	6.0	2.7
	1.9×10^{13}	−48.0	3.0	2.7
	4.0×10^{12}	−55.0	3.5	2.7
	5.0×10^{12}	−61.0	5.5	2.7
	2.6×10^{13}	−67.5	7.0	2.7
	3.3×10^{13}	−74.4	3.5	2.7
	3.3×10^{13}	−81.4	3.5	2.7
	1.3×10^{13}	−92.8	3.5	2.7
	1.4×10^{14}	−104.8	7.0	2.7
	1.2×10^{13}	−111.8	3.5	2.7
$H^{13}CN$	4.5×10^{14}	82.1	7.5	2.7
	2.7×10^{14}	70.7	6.5	2.7
	5.2×10^{14}	59.7	9.0	2.7
	1.6×10^{13}	18.8	8.0	2.7
	1.9×10^{13}	8.2	3.0	2.7
	2.7×10^{13}	5.8	4.0	2.7
	2.9×10^{13}	−2.0	6.5	2.7
	6.9×10^{12}	−104.8	7.0	2.7

Notes. See notes of Table A.11.

Table A.24: Continued.

Molecule	$N_{\rm tot}{}^a$ [cm^{-2}]	$v_{\rm LSR}{}^b$ [km s^{-1}]	$FWHM^c$ [km s^{-1}]	$T_{\rm rot}{}^d$ [K]
$HC^{15}N$	2.9×10^{13}	82.1	7.5	2.7
	1.8×10^{13}	70.7	6.5	2.7
	3.5×10^{13}	59.7	9.0	2.7
	2.7×10^{12}	5.8	4.0	2.7
	2.0×10^{12}	−2.0	6.5	2.7
		$K6_{\rm shell,a}$		
HCN	5.6×10^{15}	84.6	5.0	2.7
	2.2×10^{15}	78.1	5.0	2.7
	2.4×10^{15}	71.4	6.0	2.7
	2.6×10^{16}	63.6	9.0	2.7
	9.0×10^{14}	54.4	4.5	2.7
	7.2×10^{13}	39.2	5.0	2.7
	1.2×10^{14}	30.5	4.5	2.7
	3.6×10^{15}	18.8	5.0	2.7
	2.6×10^{14}	9.3	3.5	2.7
	1.3×10^{14}	3.4	3.5	2.7
	1.0×10^{14}	−2.3	3.5	2.7
	6.4×10^{13}	−9.8	3.5	2.7
	5.2×10^{13}	−19.4	6.0	2.7
	7.6×10^{13}	−28.4	6.0	2.7
	6.4×10^{13}	−40.4	6.0	2.7
	1.8×10^{13}	−47.4	4.0	2.7
	1.0×10^{13}	−57.4	4.0	2.7
	4.2×10^{13}	−66.0	6.5	2.7
	7.8×10^{13}	−72.9	7.5	2.7
	3.8×10^{13}	−79.9	5.5	2.7
	1.7×10^{13}	−92.8	4.0	2.7
	1.9×10^{14}	−105.8	4.0	2.7
	8.0×10^{12}	−119.8	4.0	2.7
	3.0×10^{12}	−124.8	4.0	2.7
$H^{13}CN$	2.8×10^{14}	84.6	5.0	2.7
	1.1×10^{14}	78.1	5.0	2.7
	1.2×10^{14}	71.4	6.0	2.7
	1.3×10^{15}	63.6	9.0	2.7
	4.5×10^{13}	54.4	4.5	2.7
	1.8×10^{12}	39.2	5.0	2.7
	3.0×10^{12}	30.5	4.5	2.7
	6.0×10^{12}	18.8	5.0	2.7
	1.3×10^{13}	9.3	3.5	2.7
	6.7×10^{12}	3.4	3.5	2.7

Notes. See notes of Table A.11.

Table A.24: Continued.

Molecule	$N_{\rm tot}{}^a$ [cm^{-2}]	$v_{\rm LSR}{}^b$ [km s^{-1}]	$FWHM^c$ [km s^{-1}]	$T_{\rm rot}{}^d$ [K]
	5.0×10^{12}	−2.3	3.5	2.7
	1.6×10^{12}	−9.8	3.5	2.7
	1.3×10^{12}	−19.4	6.0	2.7
	1.9×10^{12}	−28.4	6.0	2.7
	1.6×10^{12}	−40.4	6.0	2.7
	2.1×10^{12}	−66.0	6.5	2.7
	3.9×10^{12}	−72.9	7.5	2.7
	1.9×10^{12}	−79.9	5.5	2.7
	6.9×10^{12}	−105.8	4.0	2.7
$HC^{15}N$	1.4×10^{13}	84.6	5.0	2.7
	7.0×10^{12}	78.1	5.0	2.7
	8.0×10^{12}	71.4	6.0	2.7
	6.5×10^{13}	63.6	9.0	2.7
	2.3×10^{12}	54.4	4.5	2.7
	1.0×10^{12}	18.8	5.0	2.7
	8.6×10^{11}	9.3	3.5	2.7
	2.2×10^{12}	−66.0	6.5	2.7
	1.2×10^{12}	−79.9	5.5	2.7
		I		
HCN	7.4×10^{14}	68.7	6.0	2.7
	1.9×10^{15}	60.7	7.0	2.7
	5.0×10^{13}	43.2	5.0	2.7
	1.0×10^{14}	30.5	4.5	2.7
	1.6×10^{14}	18.8	4.0	2.7
	6.4×10^{13}	13.0	5.0	2.7
	6.4×10^{13}	7.9	3.0	2.7
	2.2×10^{14}	1.0	4.5	2.7
	4.4×10^{13}	−19.9	4.5	2.7
	5.6×10^{13}	−25.9	5.5	2.7
	8.8×10^{13}	−41.5	3.0	2.7
	3.4×10^{13}	−47.4	4.5	2.7
	2.9×10^{13}	−58.4	2.5	2.7
	2.6×10^{13}	−71.0	5.0	2.7
	1.1×10^{13}	−77.0	4.0	2.7
	3.1×10^{13}	−89.0	4.0	2.7
	6.2×10^{13}	−95.0	4.0	2.7
	8.2×10^{13}	−101.3	3.0	2.7
	3.2×10^{13}	−107.0	4.0	2.7
	1.6×10^{13}	−115.0	6.0	2.7

Notes. See notes of Table A.11.

Table A.24: Continued.

Molecule	$N_{\rm tot}{}^a$ [cm^{-2}]	$v_{\rm LSR}{}^b$ [km s^{-1}]	$FWHM^c$ [km s^{-1}]	$T_{\rm rot}{}^d$ [K]
$H^{13}CN$	1.8×10^{14}	68.7	6.0	2.7
	2.4×10^{14}	60.7	7.0	2.7
	2.5×10^{12}	43.2	5.0	2.7
	2.5×10^{12}	30.5	4.5	2.7
	2.6×10^{12}	18.8	4.0	2.7
	3.2×10^{12}	13.0	5.0	2.7
	3.2×10^{12}	7.9	3.0	2.7
	1.1×10^{13}	1.0	4.5	2.7
	1.4×10^{12}	−25.9	5.5	2.7
	2.2×10^{12}	−41.5	3.0	2.7
	3.1×10^{12}	−95.0	4.0	2.7
	4.1×10^{12}	−101.3	3.0	2.7
	1.6×10^{12}	−107.0	4.0	2.7
$HC^{15}N$	1.2×10^{13}	68.7	6.0	2.7
	1.6×10^{13}	60.7	7.0	2.7
		L		
HCN	3.2×10^{13}	89.7	6.0	2.7
	6.5×10^{13}	81.0	4.0	2.7
	3.5×10^{13}	76.0	4.0	2.7
	4.9×10^{13}	71.1	3.0	2.7
	5.8×10^{13}	64.2	6.0	2.7
	1.3×10^{14}	56.2	8.0	2.7
	9.0×10^{13}	48.2	6.5	2.7
	1.2×10^{14}	31.5	5.5	2.7
	3.6×10^{15}	18.8	9.0	2.7
	5.8×10^{14}	5.9	4.5	2.7
	2.4×10^{14}	−2.2	4.5	2.7
	1.4×10^{14}	−8.1	4.5	2.7
	1.3×10^{14}	−21.3	4.5	2.7
	6.4×10^{13}	−28.3	4.5	2.7
	5.6×10^{13}	−39.3	4.5	2.7
	1.2×10^{13}	−45.3	2.5	2.7
	8.6×10^{12}	−53.3	2.5	2.7
	1.4×10^{14}	−75.4	7.5	2.7
	3.4×10^{13}	−85.4	4.5	2.7
	1.8×10^{13}	−95.4	4.5	2.7
	3.1×10^{13}	−106.4	4.5	2.7
	5.1×10^{12}	−114.4	4.5	2.7
$H^{13}CN$	1.5×10^{13}	89.7	6.0	2.7

Notes. See notes of Table A.11.

Table A.24: Continued.

Molecule	$N_{\rm tot}{}^a$ [cm^{-2}]	$v_{\rm LSR}{}^b$ [km s^{-1}]	$FWHM^c$ [km s^{-1}]	$T_{\rm rot}{}^d$ [K]
	1.6×10^{13}	81.0	4.0	2.7
	1.6×10^{14}	76.0	4.0	2.7
	1.2×10^{14}	71.1	3.0	2.7
	1.9×10^{14}	64.2	6.0	2.7
	4.4×10^{14}	56.2	8.0	2.7
	3.0×10^{12}	31.5	5.5	2.7
	6.1×10^{13}	18.8	9.0	2.7
	2.9×10^{13}	5.9	4.5	2.7
	1.2×10^{13}	−2.2	4.5	2.7
	7.9×10^{12}	−8.1	4.5	2.7
	4.2×10^{12}	−21.3	4.5	2.7
	1.6×10^{12}	−28.3	4.5	2.7
	7.2×10^{12}	−75.4	7.5	2.7
HC^{15}N	8.4×10^{11}	81.0	4.0	2.7
	8.1×10^{12}	76.0	4.0	2.7
	6.0×10^{12}	71.1	3.0	2.7
	9.8×10^{12}	64.2	6.0	2.7
	2.2×10^{13}	56.2	8.0	2.7
	4.6×10^{12}	18.8	9.0	2.7
	1.0×10^{12}	−8.1	4.5	2.7
	2.8×10^{12}	−75.4	7.5	2.7

Notes. See notes of Table A.11.

Table A.25: Parameters of our best-fit model of HNC.

Molecule	$N_{\rm tot}{}^a$ [cm^{-2}]	$v_{\rm LSR}{}^b$ [km s^{-1}]	$FWHM^c$ [km s^{-1}]	$T_{\rm rot}{}^d$ [K]
		K4		
HNC	1.2×10^{14}	88.9	4.0	2.7
	7.0×10^{14}	80.7	6.5	2.7
	3.4×10^{14}	72.2	3.5	2.7
	2.8×10^{15}	62.6	9.0	2.7
	1.6×10^{14}	53.9	6.0	2.7
	3.4×10^{12}	44.4	7.0	2.7
	7.4×10^{11}	37.4	4.0	2.7
	1.8×10^{12}	31.9	3.5	2.7
	1.1×10^{13}	27.6	3.5	2.7
	1.4×10^{13}	20.9	5.0	2.7
	1.2×10^{13}	13.3	4.5	2.7
	2.1×10^{13}	7.4	4.0	2.7

Notes. See notes of Table A.11.

Table A.25: Continued.

Molecule	$N_{\rm tot}{}^a$ [cm^{-2}]	$v_{\rm LSR}{}^b$ [km s^{-1}]	$FWHM^c$ [km s^{-1}]	$T_{\rm rot}{}^d$ [K]
	1.7×10^{14}	3.8	4.0	2.7
	6.0×10^{13}	−1.8	4.0	2.7
	4.0×10^{12}	−8.4	4.0	2.7
	3.0×10^{12}	−16.4	4.0	2.7
	2.8×10^{12}	−20.7	3.0	2.7
	5.8×10^{12}	−27.2	5.0	2.7
	2.3×10^{12}	−34.6	3.5	2.7
	2.0×10^{13}	−38.8	2.5	2.7
	9.0×10^{12}	−42.8	2.0	2.7
	2.9×10^{12}	−47.7	4.0	2.7
	1.2×10^{12}	−56.8	5.0	2.7
	5.0×10^{12}	−67.2	3.0	2.7
	9.7×10^{12}	−72.6	4.0	2.7
	1.2×10^{13}	−80.2	4.0	2.7
	4.0×10^{12}	−85.5	3.5	2.7
	4.0×10^{12}	−91.4	2.0	2.7
	1.0×10^{12}	−98.5	3.0	2.7
	2.1×10^{13}	−105.2	5.0	2.7
$HN^{13}C$	6.0×10^{12}	88.9	4.0	2.7
	3.5×10^{13}	80.7	6.5	2.7
	1.7×10^{13}	72.2	3.5	2.7
	1.4×10^{14}	62.6	9.0	2.7
	1.4×10^{13}	53.9	6.0	2.7
	5.5×10^{11}	27.6	3.5	2.7
	8.3×10^{12}	3.8	4.0	2.7
	3.0×10^{12}	−1.8	4.0	2.7
	1.5×10^{11}	−42.8	2.0	2.7
	7.0×10^{11}	−105.2	5.0	2.7
$H^{15}NC$	2.5×10^{12}	80.7	6.5	2.7
	1.1×10^{12}	72.2	3.5	2.7
	9.0×10^{12}	62.6	9.0	2.7
	1.2×10^{12}	53.9	6.0	2.7
	4.8×10^{11}	3.8	4.0	2.7
	4.8×10^{11}	−1.8	4.0	2.7
		$K6_{\rm shell}$		
HNC	2.0×10^{14}	84.2	3.5	2.7
	4.6×10^{14}	79.7	4.5	2.7
	1.2×10^{14}	74.9	4.5	2.7
	3.2×10^{15}	63.1	10.0	2.7

Notes. See notes of Table A.11.

Table A.25: Continued.

Molecule	$N_{\rm tot}{}^a$ [cm^{-2}]	$v_{\rm LSR}{}^b$ [km s^{-1}]	$FWHM^c$ [km s^{-1}]	$T_{\rm rot}{}^d$ [K]
	6.6×10^{13}	49.5	5.0	2.7
	1.5×10^{12}	41.0	4.5	2.7
	4.5×10^{12}	36.0	3.5	2.7
	1.2×10^{13}	31.2	4.5	2.7
	5.5×10^{12}	24.7	4.0	2.7
	3.9×10^{13}	14.5	6.5	2.7
	3.3×10^{13}	8.4	4.5	2.7
	3.9×10^{13}	0.7	6.0	2.7
	1.6×10^{12}	−8.4	5.0	2.7
	3.6×10^{12}	−16.2	4.0	2.7
	4.5×10^{12}	−20.5	3.0	2.7
	4.6×10^{12}	−26.4	3.5	2.7
	2.2×10^{12}	−30.3	3.0	2.7
	2.2×10^{13}	−39.4	3.0	2.7
	3.7×10^{12}	−47.5	4.5	2.7
	2.3×10^{12}	−57.6	3.5	2.7
	1.7×10^{12}	−63.8	3.5	2.7
	8.7×10^{12}	−73.9	7.5	2.7
	4.6×10^{12}	−81.8	3.0	2.7
	1.5×10^{12}	−86.6	4.0	2.7
	4.6×10^{12}	−92.0	3.0	2.7
	2.5×10^{12}	−96.5	4.0	2.7
	3.8×10^{13}	−105.1	6.0	2.7
	1.5×10^{12}	−112.5	5.5	2.7
	2.5×10^{12}	−120.6	6.5	2.7
$HN^{13}C$	1.0×10^{13}	84.2	3.5	2.7
	2.3×10^{13}	79.7	4.5	2.7
	8.0×10^{12}	74.9	4.5	2.7
	1.6×10^{14}	63.1	10.0	2.7
	3.3×10^{12}	49.5	5.0	2.7
	1.3×10^{12}	14.5	6.5	2.7
	1.5×10^{12}	8.4	4.5	2.7
	1.9×10^{12}	0.7	6.0	2.7
	1.7×10^{12}	−105.1	6.0	2.7
$H^{15}NC$	8.0×10^{11}	84.2	3.5	2.7
	1.6×10^{12}	79.7	4.5	2.7
	5.1×10^{11}	74.9	4.5	2.7
	1.1×10^{13}	63.1	10.0	2.7

Notes. See notes of Table A.11.

Table A.25: Continued.

Molecule	$N_{\rm tot}{}^a$ [cm^{-2}]	$v_{\rm LSR}{}^b$ [km s^{-1}]	$FWHM^c$ [km s^{-1}]	$T_{\rm rot}{}^d$ [K]
		$K5_{\rm shell}$		
HNC	3.5×10^{12}	93.2	6.0	2.7
	3.2×10^{15}	81.2	6.0	2.7
	2.3×10^{15}	62.6	11.0	2.7
	1.2×10^{13}	49.0	4.5	2.7
	1.8×10^{12}	42.0	5.5	2.7
	4.7×10^{12}	32.9	3.0	2.7
	3.5×10^{12}	26.2	3.5	2.7
	2.8×10^{13}	19.1	8.0	2.7
	1.4×10^{14}	6.7	4.5	2.7
	3.9×10^{13}	−2.3	5.0	2.7
	3.6×10^{12}	−13.9	7.0	2.7
	4.5×10^{12}	−20.2	3.0	2.7
	6.2×10^{12}	−27.4	5.5	2.7
	2.2×10^{13}	−40.0	3.0	2.7
	3.3×10^{12}	−47.5	5.0	2.7
	4.4×10^{12}	−69.1	4.5	2.7
	1.6×10^{13}	−76.2	4.0	2.7
	7.6×10^{12}	−81.1	3.5	2.7
	4.6×10^{12}	−92.7	4.0	2.7
	4.4×10^{13}	−104.7	5.0	2.7
$HN^{13}C$	1.2×10^{14}	81.2	6.0	2.7
	1.3×10^{14}	62.6	11.0	2.7
	5.3×10^{12}	6.7	4.5	2.7
	2.2×10^{12}	−104.2	5.0	2.7
$H^{15}NC$	3.3×10^{12}	81.2	6.0	2.7
	1.1×10^{13}	62.6	11.0	2.7
		$K6_{\rm shell,a}$		
HNC	8.0×10^{13}	82.2	9.5	2.7
	5.1×10^{13}	71.2	4.5	2.7
	8.2×10^{13}	64.1	6.0	2.7
	8.9×10^{13}	57.8	5.0	2.7
	5.3×10^{13}	50.2	5.0	2.7
	1.5×10^{12}	41.0	4.5	2.7
	4.5×10^{12}	36.0	3.5	2.7
	8.2×10^{12}	31.2	3.5	2.7
	6.4×10^{12}	23.7	5.5	2.7
	5.2×10^{12}	16.7	3.5	2.7
	8.3×10^{13}	8.4	8.5	2.7

Notes. See notes of Table A.11.

Table A.25: Continued.

Molecule	$N_{\rm tot}{}^a$ [cm^{-2}]	$v_{\rm LSR}{}^b$ [km s^{-1}]	$FWHM^c$ [km s^{-1}]	$T_{\rm rot}{}^d$ [K]
	1.9×10^{13}	−1.8	3.0	2.7
	1.6×10^{12}	−8.4	3.0	2.7
	2.1×10^{12}	−16.2	4.0	2.7
	6.5×10^{12}	−20.0	3.0	2.7
	3.0×10^{12}	−24.4	3.0	2.7
	3.6×10^{12}	−28.3	5.0	2.7
	1.7×10^{13}	−39.4	3.0	2.7
	3.2×10^{12}	−47.5	3.5	2.7
	1.7×10^{12}	−57.6	3.0	2.7
	1.4×10^{12}	−65.8	3.5	2.7
	1.7×10^{13}	−72.8	4.5	2.7
	1.1×10^{13}	−80.6	5.0	2.7
	4.0×10^{12}	−92.4	3.0	2.7
	2.5×10^{12}	−97.5	4.0	2.7
	3.6×10^{13}	−104.8	4.5	2.7
	1.5×10^{12}	−112.0	5.5	2.7
	1.5×10^{12}	−120.6	6.5	2.7
$HN^{13}C$	6.0×10^{13}	82.2	9.5	2.7
	1.1×10^{13}	71.2	4.5	2.7
	1.1×10^{14}	64.1	6.0	2.7
	4.9×10^{13}	57.8	5.0	2.7
	3.3×10^{12}	50.2	5.0	2.7
	3.3×10^{12}	8.4	8.5	2.7
	7.0×10^{11}	−72.8	4.5	2.7
	1.8×10^{12}	−104.8	4.5	2.7
$H^{15}NC$	4.0×10^{12}	82.2	9.5	2.7
	7.5×10^{11}	71.2	4.5	2.7
	7.2×10^{12}	64.1	6.0	2.7
	2.9×10^{12}	57.8	5.0	2.7
		I		
HNC	1.9×10^{12}	90.2	5.0	2.7
	1.7×10^{12}	84.2	5.0	2.7
	2.2×10^{12}	79.2	5.0	2.7
	3.8×10^{14}	70.2	4.0	2.7
	1.5×10^{15}	63.5	8.0	2.7
	9.4×10^{13}	55.7	3.0	2.7
	4.3×10^{12}	49.5	5.0	2.7
	1.3×10^{12}	41.5	4.5	2.7
	1.4×10^{13}	30.9	4.0	2.7

Notes. See notes of Table A.11.

Table A.25: Continued.

Molecule	$N_{\rm tot}{}^a$ [cm^{-2}]	$v_{\rm LSR}{}^b$ [km s^{-1}]	$FWHM^c$ [km s^{-1}]	$T_{\rm rot}{}^d$ [K]
	2.5×10^{12}	25.2	4.0	2.7
	1.1×10^{13}	19.7	4.0	2.7
	1.3×10^{13}	14.0	4.5	2.7
	1.7×10^{13}	8.4	4.5	2.7
	7.6×10^{13}	1.2	5.0	2.7
	1.6×10^{12}	−8.4	5.0	2.7
	1.0×10^{12}	−16.2	4.0	2.7
	7.5×10^{12}	−21.0	4.0	2.7
	8.6×10^{12}	−26.4	4.5	2.7
	1.4×10^{13}	−40.9	2.0	2.7
	5.5×10^{12}	−46.0	3.0	2.7
	2.5×10^{12}	−50.0	3.0	2.7
	2.7×10^{12}	−58.6	3.0	2.7
	1.0×10^{12}	−63.3	3.5	2.7
	4.2×10^{12}	−70.3	4.5	2.7
	2.9×10^{12}	−76.3	3.5	2.7
	4.5×10^{12}	−88.6	4.0	2.7
	1.1×10^{13}	−94.6	4.5	2.7
	4.2×10^{13}	−101.2	3.5	2.7
	9.0×10^{12}	−106.9	2.0	2.7
	4.0×10^{12}	−110.5	1.5	2.7
	2.5×10^{12}	−115.3	4.0	2.7
HN^{13}C	1.9×10^{13}	70.2	4.0	2.7
	7.7×10^{13}	63.5	7.0	2.7
	4.7×10^{12}	55.7	3.0	2.7
	6.3×10^{11}	14.0	4.5	2.7
	3.8×10^{12}	1.2	5.0	2.7
	2.0×10^{12}	−101.2	3.5	2.7
H^{15}NC	1.3×10^{12}	70.2	4.0	2.7
	4.7×10^{12}	63.5	7.0	2.7
		L		
HNC	1.4×10^{13}	85.2	5.0	2.7
	3.5×10^{14}	73.9	8.5	2.7
	3.5×10^{14}	59.1	12.0	2.7
	1.7×10^{12}	40.0	4.5	2.7
	1.2×10^{13}	34.2	4.5	2.7
	1.5×10^{13}	26.7	6.0	2.7
	9.2×10^{12}	21.7	4.0	2.7
	1.9×10^{13}	17.0	3.5	2.7

Notes. See notes of Table A.11.

Table A.25: Continued.

Molecule	$N_{\rm tot}{}^a$ [cm^{-2}]	$v_{\rm LSR}{}^b$ [km s^{-1}]	$FWHM^c$ [km s^{-1}]	$T_{\rm rot}{}^d$ [K]
	4.6×10^{13}	8.4	5.5	2.7
	6.0×10^{13}	−1.8	6.0	2.7
	1.1×10^{13}	−9.7	5.5	2.7
	7.5×10^{12}	−19.5	4.0	2.7
	7.6×10^{12}	−26.4	3.5	2.7
	3.8×10^{12}	−31.8	3.0	2.7
	2.2×10^{13}	−39.4	3.0	2.7
	4.8×10^{12}	−46.5	2.5	2.7
	2.2×10^{12}	−69.8	3.5	2.7
	2.7×10^{13}	−75.9	5.5	2.7
	2.5×10^{12}	−83.6	4.0	2.7
	5.2×10^{12}	−91.0	3.5	2.7
	3.0×10^{12}	−100.5	4.0	2.7
	2.5×10^{13}	−106.2	4.5	2.7
$HN^{13}C$	5.4×10^{13}	73.9	8.5	2.7
	8.2×10^{13}	59.1	12.0	2.7
	2.1×10^{12}	8.4	5.5	2.7
	3.0×10^{12}	−1.8	6.0	2.7
$H^{15}NC$	3.4×10^{12}	73.9	8.5	2.7
	9.8×10^{12}	59.1	12.0	2.7

Notes. See notes of Table A.11.

Table A.26: Parameters of our best-fit model of HOC^+.

Molecule	$N_{\rm tot}{}^a$ [cm^{-2}]	$v_{\rm LSR}{}^b$ [km s^{-1}]	$FWHM^c$ [km s^{-1}]	$T_{\rm rot}{}^d$ [K]
		K4		
HOC^+	1.8×10^{12}	86.2	9.5	2.7
	2.4×10^{12}	75.8	7.5	2.7
	5.0×10^{12}	63.8	11.5	2.7
	1.3×10^{12}	17.8	7.5	2.7
	2.9×10^{12}	2.2	8.0	2.7
		$K6_{\rm shell}$		
HOC^+	1.2×10^{12}	80.0	6.0	2.7
	5.3×10^{11}	71.3	5.0	2.7
	4.3×10^{12}	64.1	9.0	2.7
	1.5×10^{12}	9.2	8.0	2.7
	2.3×10^{12}	−1.0	7.5	2.7

Notes. See notes of Table A.11.

Table A.26: Continued.

Molecule	$N_{tot}{}^a$ [cm^{-2}]	$v_{LSR}{}^b$ [km s^{-1}]	$FWHM^c$ [km s^{-1}]	$T_{rot}{}^d$ [K]
		$K5_{shell}$		
HOC^+	1.2×10^{12}	73.1	4.5	2.7
	3.6×10^{12}	62.9	9.0	2.7
		$K6_{shell,a}$		
HOC^+	4.1×10^{12}	65.2	9.5	2.7
	1.7×10^{12}	53.8	6.5	2.7
	3.0×10^{12}	0.2	11.5	2.7
		I		
HOC^+	1.8×10^{12}	69.0	7.5	2.7
	2.1×10^{12}	59.8	8.5	2.7

Notes. See notes of Table A.11.

Table A.27: Parameters of our best-fit model of HNCO.

Molecule	$N_{tot}{}^a$ [cm^{-2}]	$v_{LSR}{}^b$ [km s^{-1}]	$FWHM^c$ [km s^{-1}]	$T_{rot}{}^d$ [K]
		K4		
HNCO	9.6×10^{13}	77.2	4.0	7.7
	6.4×10^{14}	63.0	5.0	7.7
	1.2×10^{14}	57.4	5.0	7.7
	1.4×10^{14}	3.6	4.0	7.7
	1.4×10^{14}	−2.9	4.0	7.7
		$K6_{shell}$		
HNCO	1.6×10^{14}	70.5	4.0	5.7
	1.2×10^{15}	60.5	5.0	5.7
	1.8×10^{14}	53.0	4.0	5.7
	5.2×10^{13}	47.5	3.0	5.7
		$K5_{shell}$		
HNCO	2.2×10^{15}	64.5	5.0	3.2
	1.8×10^{14}	53.0	4.0	3.2
	1.5×10^{14}	5.6	8.0	4.7
		$K6_{shell,a}$		
HNCO	1.6×10^{14}	71.5	4.0	4.7
	7.2×10^{14}	60.5	5.0	4.7
	1.0×10^{14}	53.0	4.0	4.7
		I		
HNCO	1.2×10^{14}	68.5	4.0	6.7
	1.2×10^{14}	61.5	5.0	6.7
		L		
HNCO	1.6×10^{14}	70.5	4.0	6.3
	1.2×10^{15}	60.5	5.0	6.3

Notes. See notes of Table A.11.

Table A.27: Continued.

Molecule	$N_{tot}{}^a$ [cm^{-2}]	$v_{LSR}{}^b$ [$km\,s^{-1}$]	$FWHM^c$ [$km\,s^{-1}$]	$T_{rot}{}^d$ [K]
	1.8×10^{14}	53.0	4.0	6.3
	5.2×10^{13}	47.5	3.0	6.3

Notes. See notes of Table A.11.

Table A.28: Parameters of our best-fit model of CH_3OH.

Molecule	$N_{tot}{}^a$ [cm^{-2}]	$v_{LSR}{}^b$ [$km\,s^{-1}$]	$FWHM^c$ [$km\,s^{-1}$]	$T_{rot}{}^d$ [K]
		K4		
CH_3OH	2.2×10^{13}	95.2	3.0	2.7
	6.0×10^{14}	84.0	10.0	2.7
	4.2×10^{14}	77.5	3.0	2.7
	3.6×10^{15}	64.8	12.0	2.7
	1.6×10^{14}	50.0	5.0	2.7
	1.6×10^{14}	44.2	5.0	2.7
	4.2×10^{13}	35.1	5.0	2.7
	6.2×10^{13}	26.6	5.0	2.7
	3.3×10^{13}	20.2	3.0	2.7
	3.8×10^{14}	9.4	4.0	2.7
	3.8×10^{14}	3.7	3.0	2.7
	2.1×10^{14}	−3.6	6.0	2.7
	3.4×10^{13}	−11.7	3.5	2.7
$^{13}CH_3OH$	2.1×10^{13}	77.5	3.0	2.7
	1.8×10^{14}	64.8	12.0	2.7
	1.2×10^{13}	50.0	5.0	2.7
	2.0×10^{13}	9.4	4.0	2.7
	2.9×10^{13}	3.7	3.0	2.7
	2.0×10^{13}	−3.6	6.0	2.7
		$K6_{shell}$		
CH_3OH	2.4×10^{14}	85.6	5.0	2.7
	2.0×10^{14}	81.4	3.0	2.7
	3.6×10^{14}	76.1	5.5	2.7
	3.6×10^{15}	64.0	11.5	2.7
	3.4×10^{14}	54.0	5.0	2.7
	2.4×10^{14}	48.7	5.0	2.7
	4.1×10^{13}	40.4	5.5	2.7
	2.0×10^{13}	33.6	4.0	2.7
	2.6×10^{13}	25.9	4.0	2.7
	7.4×10^{13}	21.0	5.0	2.7
	7.8×10^{13}	14.4	5.0	2.7
	6.0×10^{13}	8.0	3.0	2.7

Notes. See notes of Table A.11.

Table A.28: Continued.

Molecule	$N_{\rm tot}{}^a$ [cm^{-2}]	$v_{\rm LSR}{}^b$ [km s^{-1}]	$FWHM^c$ [km s^{-1}]	$T_{\rm rot}{}^d$ [K]
	5.3×10^{13}	3.1	4.5	2.7
	1.6×10^{13}	−99.7	3.0	2.7
	1.8×10^{13}	−105.1	3.0	2.7
$^{13}CH_3OH$	1.2×10^{13}	85.6	5.0	2.7
	1.0×10^{13}	81.4	3.0	2.7
	1.8×10^{13}	76.1	5.5	2.7
	1.8×10^{14}	64.0	11.5	2.7
	1.7×10^{13}	54.0	5.0	2.7
	1.4×10^{13}	48.7	5.0	2.7
		$K5_{\rm shell}$		
CH_3OH	1.7×10^{14}	86.2	3.5	2.7
	6.8×10^{14}	78.2	5.0	2.7
	4.8×10^{15}	64.2	13.5	2.7
	2.0×10^{14}	47.4	7.0	2.7
	7.5×10^{13}	37.5	7.5	2.7
	7.5×10^{13}	28.5	4.0	2.7
	1.1×10^{14}	21.1	5.0	2.7
	1.6×10^{14}	12.5	4.5	2.7
	4.3×10^{14}	5.8	7.5	2.7
	6.3×10^{13}	−3.2	5.5	2.7
$^{13}CH_3OH$	3.4×10^{13}	78.2	5.0	2.7
	2.4×10^{14}	64.2	13.5	2.7
		$K6_{\rm shell,a}$		
CH_3OH	7.5×10^{13}	83.5	5.0	2.7
	5.6×10^{15}	64.4	14.0	2.7
	2.8×10^{14}	48.7	7.0	2.7
	1.2×10^{14}	26.9	10.0	2.7
	4.6×10^{13}	13.4	5.0	2.7
	6.0×10^{13}	8.0	3.0	2.7
	6.3×10^{13}	3.1	4.5	2.7
	1.4×10^{13}	−7.9	4.5	2.7
	1.3×10^{13}	−65.8	4.0	2.7
	1.3×10^{13}	−72.8	4.0	2.7
	1.5×10^{13}	−99.7	3.0	2.7
	1.8×10^{13}	−105.1	3.0	2.7
$^{13}CH_3OH$	1.3×10^{13}	83.5	5.0	2.7
	2.8×10^{14}	64.4	14.0	2.7
	1.4×10^{13}	48.7	7.0	2.7

Notes. See notes of Table A.11.

Table A.28: Continued.

Molecule	$N_{tot}{}^a$ [cm^{-2}]	$v_{LSR}{}^b$ [$km\,s^{-1}$]	$FWHM^c$ [$km\,s^{-1}$]	$T_{rot}{}^d$ [K]
		I		
CH_3OH	3.6×10^{14}	75.5	5.0	2.7
	2.0×10^{15}	64.2	11.0	2.7
	1.7×10^{14}	49.8	5.0	2.7
	3.8×10^{13}	24.5	6.0	2.7
	6.0×10^{13}	15.4	5.5	2.7
	1.1×10^{14}	6.0	8.0	2.7
	3.0×10^{13}	−0.9	4.5	2.7
	1.6×10^{13}	−96.7	3.0	2.7
	2.4×10^{13}	−102.1	3.0	2.7
$^{13}CH_3OH$	5.0×10^{13}	64.9	11.0	2.7
		L		
CH_3OH	6.2×10^{14}	80.4	7.0	2.7
	5.8×10^{15}	64.6	10.5	2.7
	4.0×10^{14}	52.0	4.0	2.7
	8.0×10^{13}	44.7	5.0	2.7
	2.9×10^{13}	33.7	5.0	2.7
	3.4×10^{13}	22.3	3.0	2.7
	5.8×10^{13}	16.4	7.0	2.7
	1.8×10^{13}	9.0	4.0	2.7
$^{13}CH_3OH$	3.1×10^{13}	80.4	7.0	2.7
	2.9×10^{14}	64.6	10.5	2.7
	4.0×10^{13}	52.0	4.0	2.7

Notes. See notes of Table A.11.

Table A.29: Parameters of our best-fit model of CH_3NH_2.

Molecule	$N_{tot}{}^a$ [cm^{-2}]	$v_{LSR}{}^b$ [$km\,s^{-1}$]	$FWHM^c$ [$km\,s^{-1}$]	$T_{rot}{}^d$ [K]
		K4		
CH_3NH_2	5.7×10^{14}	81.3	8.5	4.6
	1.8×10^{15}	64.7	14.5	4.6
	1.7×10^{14}	54.1	4.0	4.6
		$K6_{shell}$		
CH_3NH_2	7.7×10^{14}	79.9	8.5	5.6
	1.9×10^{15}	62.9	9.5	5.6
		$K5_{shell}$		
CH_3NH_2	8.7×10^{14}	81.9	6.5	4.6
	8.7×10^{14}	71.9	6.5	4.6
	2.0×10^{15}	59.9	8.5	4.6

Notes. See notes of Table A.11.

Table A.29: Continued.

Molecule	N_{tot}[a] [cm^{-2}]	v_{LSR}[b] [$km\,s^{-1}$]	$FWHM$[c] [$km\,s^{-1}$]	T_{rot}[d] [K]
		$K6_{shell,a}$		
CH_3NH_2	8.7×10^{14}	81.9	9.5	5.6
	2.5×10^{15}	62.9	11.5	5.6
		I		
CH_3NH_2	7.0×10^{14}	62.9	10.5	5.6

Notes. See notes of Table A.11.

Table A.30: Parameters of our best-fit model of CH_3SH.

Molecule	N_{tot}[a] [cm^{-2}]	v_{LSR}[b] [$km\,s^{-1}$]	$FWHM$[c] [$km\,s^{-1}$]	T_{rot}[d] [K]
		K4		
CH_3SH	4.2×10^{13}	79.2	5.0	4.1
	2.2×10^{14}	63.6	15.0	4.1
		$K6_{shell}$		
CH_3SH	6.0×10^{13}	80.4	6.0	3.8
	1.4×10^{14}	62.7	9.0	3.8
		$K5_{shell}$		
CH_3SH	6.0×10^{13}	71.1	4.0	3.3
	2.2×10^{14}	62.7	9.0	3.3
		$K6_{shell,a}$		
CH_3SH	2.4×10^{14}	62.7	13.0	4.4
		I		
CH_3SH	7.0×10^{13}	61.7	7.0	3.0

Notes. See notes of Table A.11.

Table A.31: Parameters of our best-fit model of NS^+.

Molecule	N_{tot}[a] [cm^{-2}]	v_{LSR}[b] [$km\,s^{-1}$]	$FWHM$[c] [$km\,s^{-1}$]	T_{rot}[d] [K]
		K4		
NS^+	6.0×10^{12}	82.2	8.0	2.7
	1.7×10^{13}	65.2	14.0	2.7
		$K6_{shell}$		
NS^+	2.1×10^{13}	64.7	12.0	2.7
		$K6_{shell,a}$		
NS^+	5.5×10^{12}	82.2	8.0	2.7
	2.0×10^{13}	64.7	12.0	2.7
	3.3×10^{15}	70.2	6.5	7.2
	2.0×10^{15}	58.0	6.0	7.2

Notes. See notes of Table A.11.

Table A.31: Continued.

Molecule	$N_{tot}{}^a$ [cm^{-2}]	$v_{LSR}{}^b$ [$km\,s^{-1}$]	$FWHM^c$ [$km\,s^{-1}$]	$T_{rot}{}^d$ [K]
		I		
NS^+	1.8×10^{13}	64.7	14.0	2.7

Notes. See notes of Table A.11.

Table A.32: Parameters of our best-fit model of $HOCO^+$.

Molecule	$N_{tot}{}^a$ [cm^{-2}]	$v_{LSR}{}^b$ [$km\,s^{-1}$]	$FWHM^c$ [$km\,s^{-1}$]	$T_{rot}{}^d$ [K]
		K4		
$HOCO^+$	1.1×10^{14}	64.0	9.5	8.5
		$K6_{shell}$		
$HOCO^+$	5.4×10^{13}	62.7	6.5	6.3
		$K5_{shell}$		
$HOCO^+$	2.2×10^{14}	62.7	9.5	5.3
		$K6_{shell,a}$		
$HOCO^+$	1.0×10^{14}	62.2	9.5	7.0
		I		
$HOCO^+$	2.3×10^{13}	64.0	8.5	4.1
		L		
$HOCO^+$	3.2×10^{13}	61.0	8.5	6.0

Notes. See notes of Table A.11.

Table A.33: Parameters of our best-fit model of PN.

Molecule	$N_{tot}{}^a$ [cm^{-2}]	$v_{LSR}{}^b$ [$km\,s^{-1}$]	$FWHM^c$ [$km\,s^{-1}$]	$T_{rot}{}^d$ [K]
		K4		
PN	2.4×10^{12}	81.8	8.0	2.7
	1.7×10^{13}	62.4	18.5	2.7
		$K6_{shell}$		
PN	2.2×10^{12}	81.5	7.0	2.7
	8.2×10^{12}	63.5	7.0	2.7
		$K5_{shell}$		
PN	9.9×10^{12}	61.0	12.0	2.7
		$K6_{shell,a}$		
PN	3.5×10^{13}	81.7	8.0	2.7
	1.1×10^{14}	63.4	12.0	2.7
		I		
PN	4.2×10^{12}	62.6	9.0	2.7

Notes. See notes of Table A.11.

Table A.34: Parameters of our best-fit model of SiO.

Molecule	$N_{\rm tot}{}^a$ [cm^{-2}]	$v_{\rm LSR}{}^b$ [km s^{-1}]	$FWHM^c$ [km s^{-1}]	$T_{\rm rot}{}^d$ [K]
		K4		
SiO	3.2×10^{13}	90.3	5.0	2.7
	5.0×10^{14}	80.6	8.5	2.7
	3.4×10^{14}	70.1	5.5	2.7
	1.1×10^{15}	61.2	9.5	2.7
	1.6×10^{13}	52.2	5.6	2.7
	1.8×10^{12}	45.2	6.5	2.7
	1.8×10^{12}	39.8	7.5	2.7
	3.6×10^{12}	21.0	4.0	2.7
	5.0×10^{12}	13.2	3.5	2.7
	5.6×10^{13}	4.2	4.0	2.7
	1.9×10^{13}	−2.8	6.0	2.7
	2.6×10^{12}	−15.6	5.5	2.7
	1.0×10^{12}	−40.0	3.5	2.7
	2.0×10^{12}	−74.5	3.5	2.7
	1.4×10^{12}	−80.6	3.0	2.7
	1.4×10^{12}	−88.1	3.5	2.7
	1.4×10^{12}	−104.6	3.5	2.7
	1.4×10^{12}	−119.4	3.5	2.7
^{29}SiO	2.5×10^{12}	90.3	3.5	2.7
	2.3×10^{13}	80.6	9.0	2.7
	1.7×10^{13}	70.1	5.5	2.7
	5.5×10^{13}	61.2	9.5	2.7
	8.0×10^{12}	52.2	5.5	2.7
	4.0×10^{12}	4.2	4.0	2.7
	1.9×10^{12}	−2.8	6.0	2.7
^{30}SiO	1.5×10^{12}	90.3	3.5	2.7
	1.5×10^{13}	80.6	9.0	2.7
	1.2×10^{13}	70.1	5.5	2.7
	3.8×10^{13}	61.2	9.5	2.7
	4.6×10^{12}	52.2	5.5	2.7
	2.4×10^{12}	4.2	4.0	2.7
		$K6_{\rm shell}$		
SiO	8.0×10^{13}	85.0	3.5	2.7
	1.0×10^{14}	80.8	4.5	2.7
	3.8×10^{13}	73.9	6.5	2.7
	2.2×10^{15}	63.7	6.0	2.7
	4.2×10^{13}	55.2	4.5	2.7
	3.0×10^{13}	48.6	5.5	2.7

Notes. See notes of Table A.11.

Table A.34: Continued.

Molecule	$N_{tot}{}^a$ [cm^{-2}]	$v_{LSR}{}^b$ [km s^{-1}]	$FWHM^c$ [km s^{-1}]	$T_{rot}{}^d$ [K]
	4.6×10^{12}	41.5	7.0	2.7
	8.2×10^{12}	15.1	9.0	2.7
	1.4×10^{13}	3.3	7.5	2.7
	2.6×10^{12}	−28.4	7.5	2.7
	1.5×10^{12}	−39.4	5.5	2.7
	1.5×10^{12}	−47.4	5.5	2.7
	1.5×10^{12}	−57.4	5.5	2.7
	2.2×10^{12}	−64.2	5.5	2.7
	1.7×10^{12}	−68.6	4.5	2.7
	1.5×10^{12}	−92.4	5.5	2.7
	3.5×10^{12}	−105.6	3.5	2.7
	2.0×10^{12}	−119.5	3.5	2.7
^{29}SiO	4.0×10^{12}	85.0	3.5	2.7
	5.0×10^{12}	80.8	4.5	2.7
	1.9×10^{12}	73.9	6.5	2.7
	5.5×10^{13}	63.7	8.0	2.7
	2.1×10^{12}	55.2	4.5	2.7
	1.5×10^{12}	48.6	5.5	2.7
^{30}SiO	2.8×10^{12}	85.0	3.5	2.7
	3.8×10^{12}	80.8	4.5	2.7
	1.3×10^{12}	73.9	6.5	2.7
	3.5×10^{13}	63.7	8.0	2.7
	1.6×10^{12}	55.2	4.5	2.7
		$K5_{shell}$		
SiO	1.1×10^{13}	93.3	7.0	2.7
	6.0×10^{14}	81.9	7.0	2.7
	7.4×10^{14}	69.5	9.5	2.7
	6.8×10^{14}	58.4	7.0	2.7
	1.5×10^{13}	18.2	6.0	2.7
	1.2×10^{14}	6.2	5.5	2.7
	1.3×10^{13}	−2.9	5.5	2.7
	3.9×10^{12}	−18.9	5.5	2.7
	3.6×10^{12}	−29.9	5.5	2.7
	2.2×10^{12}	−65.2	3.5	2.7
	1.9×10^{12}	−102.9	3.5	2.7
	2.3×10^{12}	−118.9	3.5	2.7
^{29}SiO	3.0×10^{13}	81.9	7.0	2.7
	3.7×10^{13}	69.5	9.5	2.7

Notes. See notes of Table A.11.

Table A.34: Continued.

Molecule	$N_{\rm tot}{}^a$ [cm^{-2}]	$v_{\rm LSR}{}^b$ [km s^{-1}]	$FWHM^c$ [km s^{-1}]	$T_{\rm rot}{}^d$ [K]
	3.4×10^{13}	58.4	7.0	2.7
	6.2×10^{12}	6.2	5.5	2.7
^{30}SiO	2.0×10^{13}	81.9	7.0	2.7
	2.2×10^{13}	69.5	9.5	2.7
	2.2×10^{13}	58.4	7.0	2.7
		K6$_{\rm shell,a}$		
SiO	1.7×10^{15}	63.7	9.0	2.7
	6.0×10^{13}	52.6	4.0	2.7
	2.5×10^{13}	46.6	5.0	2.7
	2.8×10^{12}	38.0	6.0	2.7
	1.8×10^{12}	24.0	6.0	2.7
	1.2×10^{13}	15.3	7.0	2.7
	1.2×10^{13}	4.0	7.0	2.7
	2.6×10^{12}	−8.0	6.0	2.7
	2.3×10^{12}	−28.0	7.0	2.7
	2.1×10^{12}	−38.0	7.0	2.7
	4.0×10^{12}	−70.7	7.0	2.7
	2.0×10^{12}	−106.7	7.0	2.7
	2.0×10^{12}	−116.7	7.0	2.7
	1.6×10^{14}	82.9	6.5	2.7
	3.2×10^{13}	74.2	6.5	2.7
^{29}SiO	8.5×10^{13}	63.7	9.0	2.7
	3.0×10^{12}	52.6	4.0	2.7
	1.3×10^{13}	82.7	5.5	2.7
	3.5×10^{12}	74.9	6.0	2.7
^{30}SiO	5.5×10^{13}	63.7	9.0	2.7
	2.0×10^{12}	52.6	4.0	2.7
	3.6×10^{14}	82.7	5.5	2.7
	1.1×10^{14}	74.9	6.0	2.7
		I		
SiO	5.0×10^{12}	76.3	4.0	2.7
	2.0×10^{14}	68.2	6.0	2.7
	3.4×10^{14}	59.7	6.0	2.7
	1.4×10^{13}	51.1	6.0	2.7
	3.2×10^{12}	43.3	6.0	2.7
	7.2×10^{11}	36.2	4.0	2.7
	3.7×10^{12}	17.1	6.0	2.7
	6.7×10^{12}	8.2	7.0	2.7

Notes. See notes of Table A.11.

Table A.34: Continued.

Molecule	$N_{\rm tot}{}^a$ [cm^{-2}]	$v_{\rm LSR}{}^b$ [km s^{-1}]	$FWHM^c$ [km s^{-1}]	$T_{\rm rot}{}^d$ [K]
	3.7×10^{12}	−1.2	6.0	2.7
	1.4×10^{12}	−22.2	6.0	2.7
	1.7×10^{12}	−41.2	6.0	2.7
	8.7×10^{12}	−92.3	8.0	2.7
	3.7×10^{12}	−101.1	3.0	2.7
	1.4×10^{12}	−107.1	4.0	2.7
	1.2×10^{12}	−117.1	4.0	2.7
^{29}SiO	1.0×10^{13}	68.2	6.0	2.7
	1.7×10^{13}	59.7	6.0	2.7
	7.0×10^{11}	51.1	6.0	2.7
^{30}SiO	6.7×10^{12}	68.2	6.0	2.7
	1.2×10^{13}	59.7	6.0	2.7
		L		
SiO	1.0×10^{13}	84.9	5.5	2.7
	3.6×10^{14}	75.7	5.5	2.7
	3.4×10^{14}	64.1	6.0	2.7
	3.2×10^{14}	56.9	6.0	2.7
	2.8×10^{14}	51.4	4.0	2.7
	6.1×10^{12}	42.3	6.0	2.7
	8.0×10^{12}	34.5	5.0	2.7
	6.6×10^{12}	27.5	6.0	2.7
	1.4×10^{13}	21.4	4.0	2.7
	1.4×10^{13}	15.3	4.0	2.7
	1.2×10^{13}	5.8	5.0	2.7
	4.7×10^{12}	−0.3	4.0	2.7
	5.7×10^{12}	−8.1	6.0	2.7
	2.7×10^{12}	−20.1	6.0	2.7
	1.2×10^{13}	−76.8	9.0	2.7
	5.2×10^{12}	−89.0	9.0	2.7
^{29}SiO	1.8×10^{13}	75.7	5.5	2.7
	1.7×10^{13}	64.1	6.0	2.7
	1.6×10^{13}	56.9	6.0	2.7
	1.4×10^{13}	51.4	4.0	2.7
^{30}SiO	1.2×10^{13}	75.7	5.5	2.7
	1.1×10^{13}	64.1	6.0	2.7
	1.1×10^{13}	56.9	6.0	2.7
	1.0×10^{13}	51.4	4.0	2.7

Notes. See notes of Table A.11.

Table A.35: Parameters of our best-fit model of SO_2.

Molecule	$N_{tot}{}^a$ [cm^{-2}]	$v_{LSR}{}^b$ [$km\,s^{-1}$]	$FWHM^c$ [$km\,s^{-1}$]	$T_{rot}{}^d$ [K]
		K4		
SO_2	1.6×10^{13}	89.8	3.5	2.7
	1.0×10^{14}	80.8	7.5	2.7
	4.7×10^{13}	72.2	6.5	2.7
	1.4×10^{14}	63.7	9.0	2.7
		$K6_{shell}$		
SO_2	1.1×10^{14}	82.0	8.0	2.7
	2.2×10^{13}	73.3	5.0	2.7
	2.0×10^{14}	63.2	7.0	2.7
	3.2×10^{13}	8.2	10.0	2.7
		$K5_{shell}$		
SO_2	2.5×10^{14}	81.0	8.5	2.7
	6.7×10^{13}	69.5	6.5	2.7
	1.5×10^{14}	61.2	5.5	2.7
		$K6_{shell,a}$		
SO_2	2.5×10^{14}	64.1	9.0	2.7
	7.7×10^{14}	81.7	8.0	2.7
	2.4×10^{15}	63.4	12.0	2.7
		I		
SO_2	2.2×10^{13}	69.3	3.0	2.7
		L		
SO_2	6.7×10^{13}	76.8	3.0	2.7
	3.5×10^{14}	56.2	11.5	2.7

Notes. See notes of Table A.11.

Table A.36: Parameters of our best-fit model of SO.

Molecule	$N_{tot}{}^a$ [cm^{-2}]	$v_{LSR}{}^b$ [$km\,s^{-1}$]	$FWHM^c$ [$km\,s^{-1}$]	$T_{rot}{}^d$ [K]
		K4		
SO	1.2×10^{15}	80.1	13.0	2.7
	2.2×10^{15}	64.3	15.0	2.7
	1.6×10^{13}	47.8	4.5	2.7
	1.4×10^{13}	41.2	4.5	2.7
	1.4×10^{13}	36.2	3.5	2.7
	1.4×10^{13}	32.2	3.5	2.7
	1.7×10^{13}	27.5	3.5	2.7
	1.2×10^{13}	20.5	3.5	2.7
	1.4×10^{13}	12.5	5.0	2.7
	8.8×10^{13}	3.5	3.0	2.7
	6.5×10^{13}	−2.3	3.5	2.7
	1.5×10^{13}	−10.5	5.5	2.7

Notes. See notes of Table A.11.

Table A.36: Continued.

Molecule	$N_{tot}{}^a$ [cm^{-2}]	$v_{LSR}{}^b$ [km s^{-1}]	$FWHM^c$ [km s^{-1}]	$T_{rot}{}^d$ [K]
	1.5×10^{13}	−16.1	5.5	2.7
	1.2×10^{13}	−21.1	5.5	2.7
	1.5×10^{13}	−40.7	3.5	2.7
^{34}SO	5.6×10^{13}	80.1	13.0	2.7
	1.0×10^{14}	64.3	15.0	2.7
		$K6_{shell}$		
SO	1.3×10^{14}	85.0	5.0	2.7
	2.8×10^{14}	79.7	5.0	2.7
	2.6×10^{14}	73.0	6.0	2.7
	1.3×10^{15}	63.2	7.0	2.7
	8.1×10^{13}	54.2	5.0	2.7
	2.1×10^{13}	48.5	5.0	2.7
	2.3×10^{13}	30.4	5.0	2.7
	2.3×10^{13}	25.0	5.0	2.7
	2.2×10^{13}	12.8	6.0	2.7
	9.0×10^{12}	7.5	4.0	2.7
	3.6×10^{13}	2.5	7.0	2.7
	1.6×10^{13}	−11.4	5.0	2.7
	1.6×10^{13}	−17.4	5.0	2.7
	1.2×10^{13}	−40.4	5.0	2.7
	1.2×10^{13}	−105.4	5.0	2.7
^{34}SO	6.0×10^{12}	85.0	5.0	2.7
	1.3×10^{13}	79.7	5.0	2.7
	1.2×10^{13}	73.0	6.0	2.7
	6.0×10^{13}	63.2	7.0	2.7
		$K5_{shell}$		
SO	1.5×10^{15}	79.8	8.5	2.7
	2.6×10^{15}	63.8	9.5	2.7
	1.2×10^{14}	49.6	6.0	2.7
	3.1×10^{13}	40.5	5.0	2.7
	8.0×10^{13}	5.5	5.0	2.7
	3.0×10^{13}	−3.3	5.5	2.7
	4.1×10^{13}	−14.0	5.5	2.7
^{34}SO	7.0×10^{13}	79.8	8.5	2.7
	1.2×10^{14}	63.8	9.5	2.7
		$K6_{shell,a}$		
SO	2.1×10^{13}	46.3	7.5	2.7
	2.1×10^{13}	32.3	4.5	2.7

Notes. See notes of Table A.11.

Table A.36: Continued.

Molecule	$N_{tot}{}^a$ [cm^{-2}]	$v_{LSR}{}^b$ [km s^{-1}]	$FWHM^c$ [km s^{-1}]	$T_{rot}{}^d$ [K]
	2.1×10^{13}	22.3	4.5	2.7
	2.1×10^{13}	10.3	4.5	2.7
	2.1×10^{13}	3.3	4.5	2.7
	1.8×10^{13}	−12.7	5.5	2.7
	1.8×10^{13}	−17.7	5.5	2.7
	1.3×10^{13}	−38.7	5.5	2.7
	1.8×10^{13}	−105.7	4.5	2.7
	5.5×10^{12}	82.2	8.0	2.7
	2.0×10^{13}	64.7	12.0	2.7
^{34}SO	1.8×10^{13}	82.7	5.5	2.7
	5.5×10^{12}	74.9	6.0	2.7
		I		
SO	8.1×10^{14}	63.6	11.5	2.7
	7.0×10^{13}	50.9	5.5	2.7
	3.0×10^{13}	28.9	6.5	2.7
	3.0×10^{13}	0.9	6.5	2.7
	1.5×10^{13}	−41.1	3.5	2.7
^{34}SO	3.7×10^{13}	63.6	11.5	2.7
		L		
SO	2.1×10^{14}	77.0	4.0	2.7
	2.5×10^{14}	70.9	3.0	2.7
	1.2×10^{15}	58.0	11.5	2.7
	9.0×10^{13}	20.5	7.5	2.7
^{34}SO	1.0×10^{13}	77.0	4.0	2.7
	5.5×10^{13}	58.0	11.5	2.7

Notes. See notes of Table A.11.

Table A.37: Parameters of our best-fit model of ortho H_2CS.

Molecule	$N_{tot}{}^a$ [cm^{-2}]	$v_{LSR}{}^b$ [km s^{-1}]	$FWHM^c$ [km s^{-1}]	$T_{rot}{}^d$ [K]
		K4		
ortho H_2CS	2.0×10^{13}	89.5	4.0	2.7
	8.0×10^{13}	80.6	5.0	2.7
	2.4×10^{13}	76.2	3.5	2.7
	9.0×10^{13}	70.7	5.0	2.7
	1.8×10^{14}	63.6	6.0	2.7
	7.6×10^{13}	53.7	7.0	2.7

Notes. See notes of Table A.11.

Table A.37: Continued.

Molecule	N_{tot}[a] [cm^{-2}]	v_{LSR}[b] [km s^{-1}]	$FWHM$[c] [km s^{-1}]	T_{rot}[d] [K]
	2.8×10^{13}	3.0	4.0	2.7
	1.6×10^{13}	−2.7	4.0	2.7
para H_2CS	8.0×10^{12}	89.5	4.0	2.7
	2.6×10^{13}	80.6	5.0	2.7
	1.6×10^{13}	76.2	3.5	2.7
	5.0×10^{13}	70.7	5.0	2.7
	8.0×10^{13}	63.6	6.0	2.7
	4.4×10^{13}	53.7	7.0	2.7
	1.6×10^{13}	3.0	4.0	2.7
	7.0×10^{12}	−2.7	4.0	2.7
		$K6_{shell}$		
ortho H_2CS	1.0×10^{13}	85.8	3.0	2.7
	5.8×10^{13}	80.2	5.0	2.7
	7.3×10^{13}	72.6	7.0	2.7
	1.8×10^{14}	65.2	5.0	2.7
	1.3×10^{14}	60.1	5.0	2.7
	2.3×10^{13}	55.2	4.0	2.7
para H_2CS	6.0×10^{12}	85.8	3.0	2.7
	2.5×10^{13}	80.2	5.0	2.7
	3.0×10^{13}	72.6	7.0	2.7
	7.5×10^{13}	65.2	5.0	2.7
	7.0×10^{13}	60.1	5.0	2.7
	1.3×10^{13}	55.2	4.0	2.7
		$K5_{shell}$		
ortho H_2CS	3.0×10^{13}	85.8	3.0	2.7
	6.8×10^{13}	80.2	5.0	2.7
	8.3×10^{13}	72.6	7.0	2.7
	3.3×10^{14}	61.3	8.0	2.7
para H_2CS	2.0×10^{13}	85.8	3.0	2.7
	2.8×10^{13}	80.2	5.0	2.7
	6.3×10^{13}	72.6	7.0	2.7
	2.3×10^{14}	61.3	8.0	2.7
		$K6_{shell,a}$		
ortho H_2CS	2.3×10^{13}	85.8	3.0	3.4
	2.8×10^{13}	78.2	3.0	3.4
	4.3×10^{13}	73.8	4.0	3.4
	4.3×10^{14}	63.1	11.0	3.4

Notes. See notes of Table A.11.

Table A.37: Continued.

Molecule	$N_{tot}{}^a$ [cm^{-2}]	$v_{LSR}{}^b$ [$km\,s^{-1}$]	$FWHM^c$ [$km\,s^{-1}$]	$T_{rot}{}^d$ [K]
para H_2CS	1.3×10^{13}	85.8	3.0	3.4
	1.8×10^{13}	78.2	3.0	3.4
	2.3×10^{13}	73.8	4.0	3.4
	1.3×10^{14}	63.1	11.0	3.4
		I		
ortho H_2CS	2.3×10^{13}	68.2	3.0	2.7
	2.3×10^{14}	60.8	9.0	2.7
para H_2CS	1.3×10^{13}	68.2	3.0	2.7
	1.3×10^{14}	60.8	9.0	2.7
		L		
ortho H_2CS	1.9×10^{14}	71.6	7.0	2.7
	2.8×10^{14}	57.2	9.0	2.7
para H_2CS	6.9×10^{13}	71.6	7.0	2.7
	7.8×10^{13}	57.2	9.0	2.7

Notes. See notes of Table A.11.

Table A.38: Parameters of our best-fit model of CCS.

Molecule	$N_{tot}{}^a$ [cm^{-2}]	$v_{LSR}{}^b$ [$km\,s^{-1}$]	$FWHM^c$ [$km\,s^{-1}$]	$T_{rot}{}^d$ [K]
		K4		
CCS	5.2×10^{14}	62.9	11.5	2.7
		$K6_{shell}$		
CCS	2.7×10^{14}	62.5	7.0	2.7
		$K5_{shell}$		
CCS	5.6×10^{14}	61.1	5.5	2.7
		$K6_{shell,a}$		
CCS	3.0×10^{14}	60.7	6.5	2.7
		I		
CCS	2.6×10^{14}	61.5	5.5	2.7

Notes. See notes of Table A.11.

A.7 Column density profiles

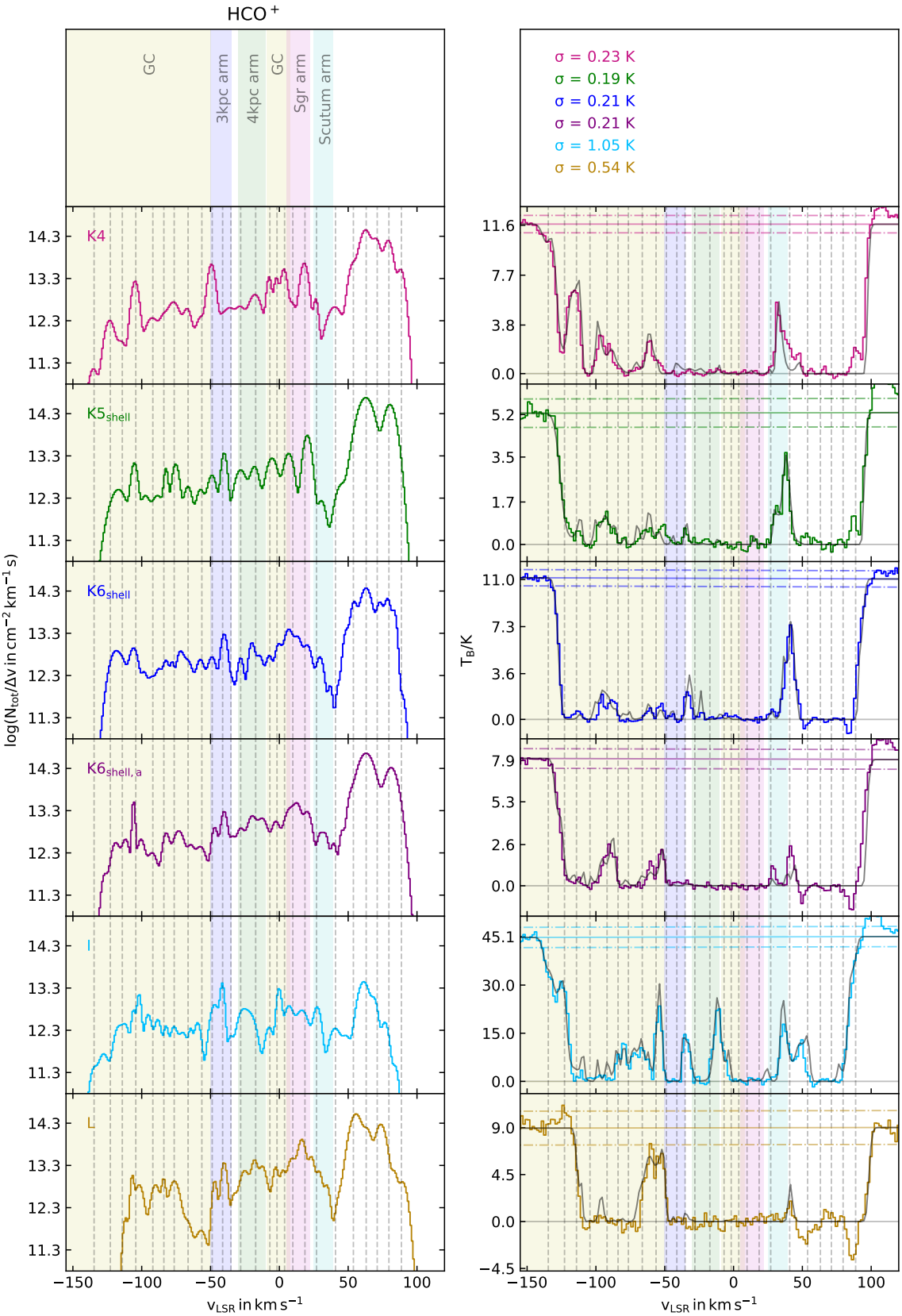

Figure A.26: Same as Fig. 3.8, but for HCO^+.

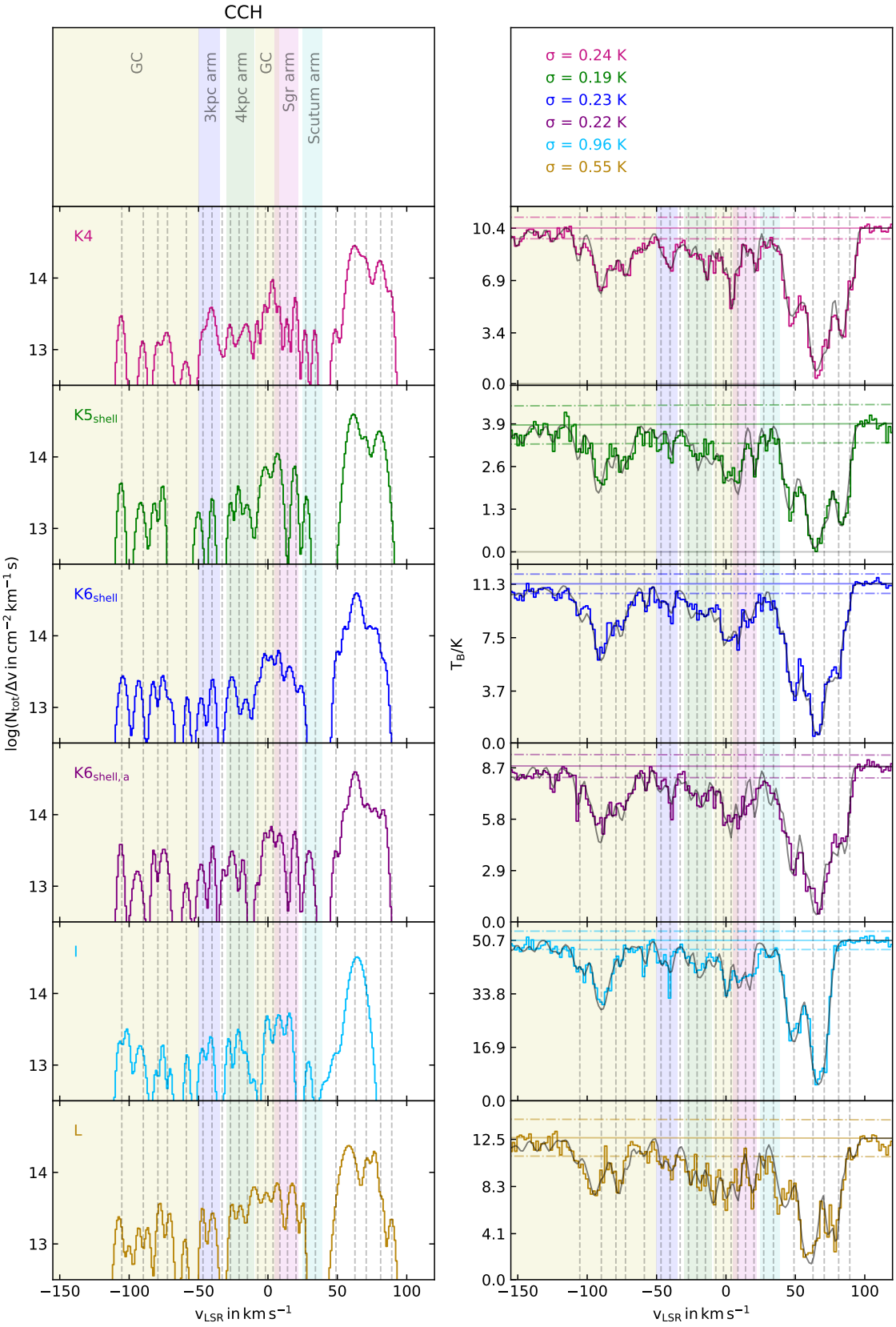

Figure A.27: Same as Fig. 3.8, but for CCH.

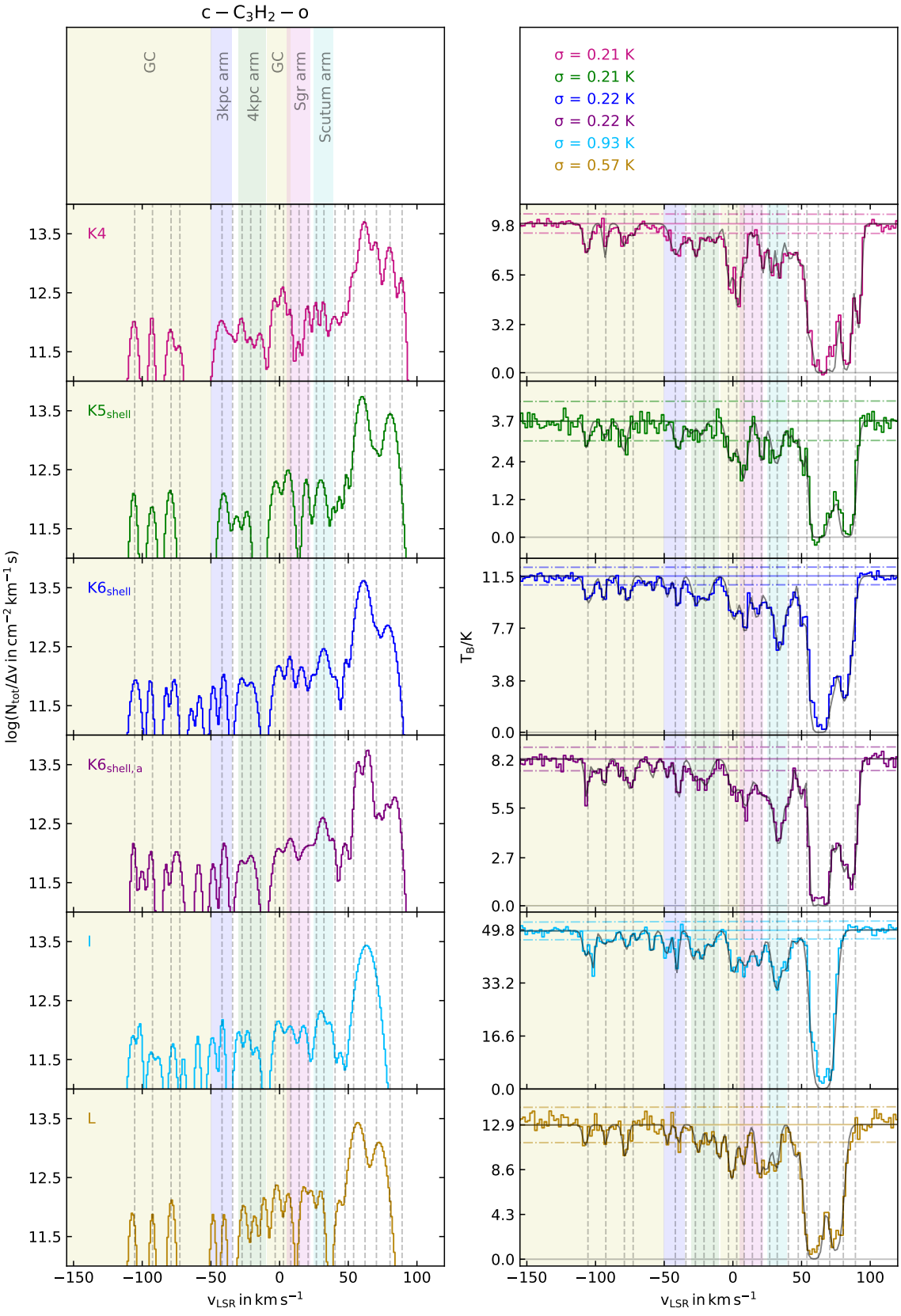

Figure A.28: Same as Fig. 3.8, but for ortho c-C_3H_2.

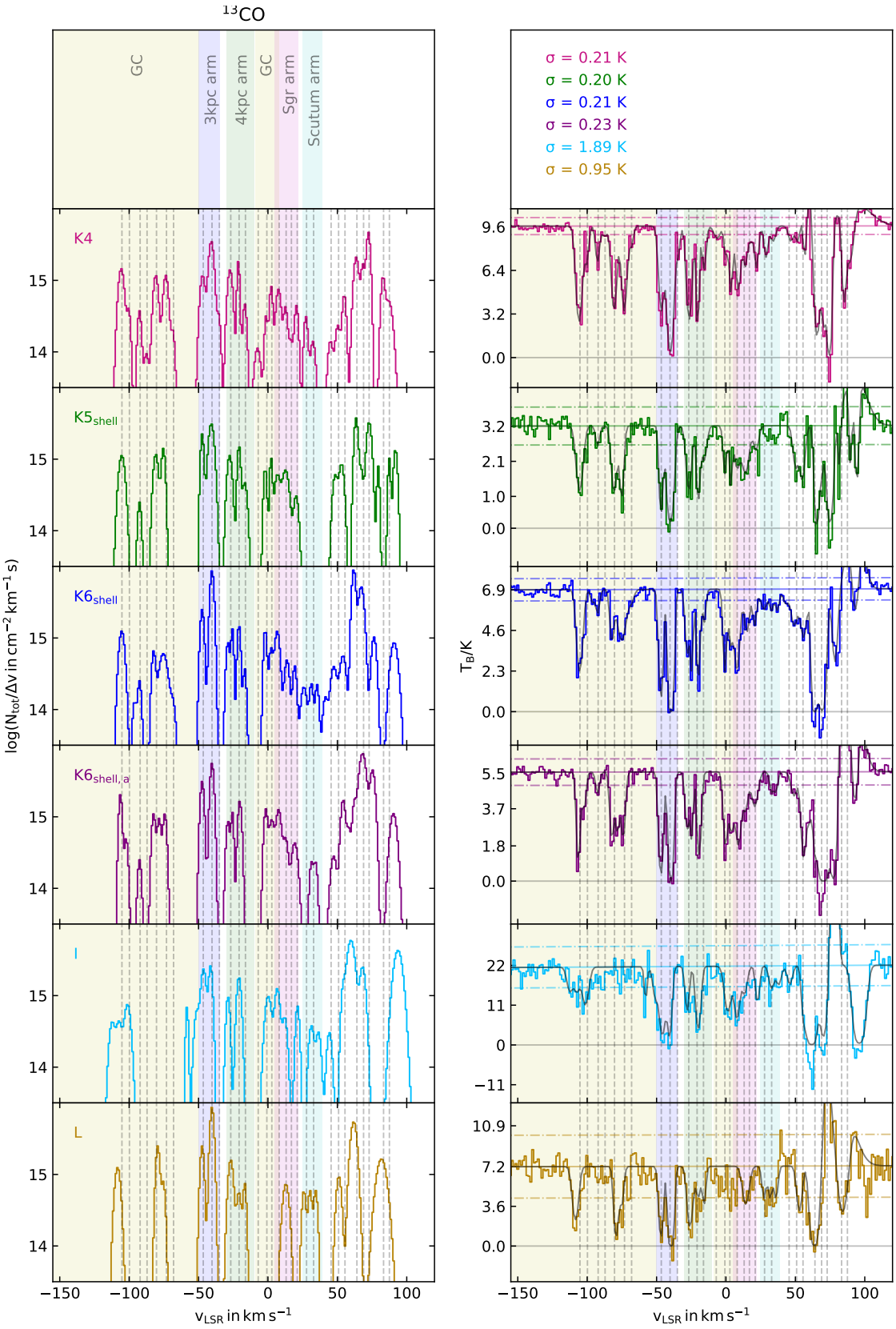

Figure A.29: Same as Fig. 3.8, but for ^{13}CO.

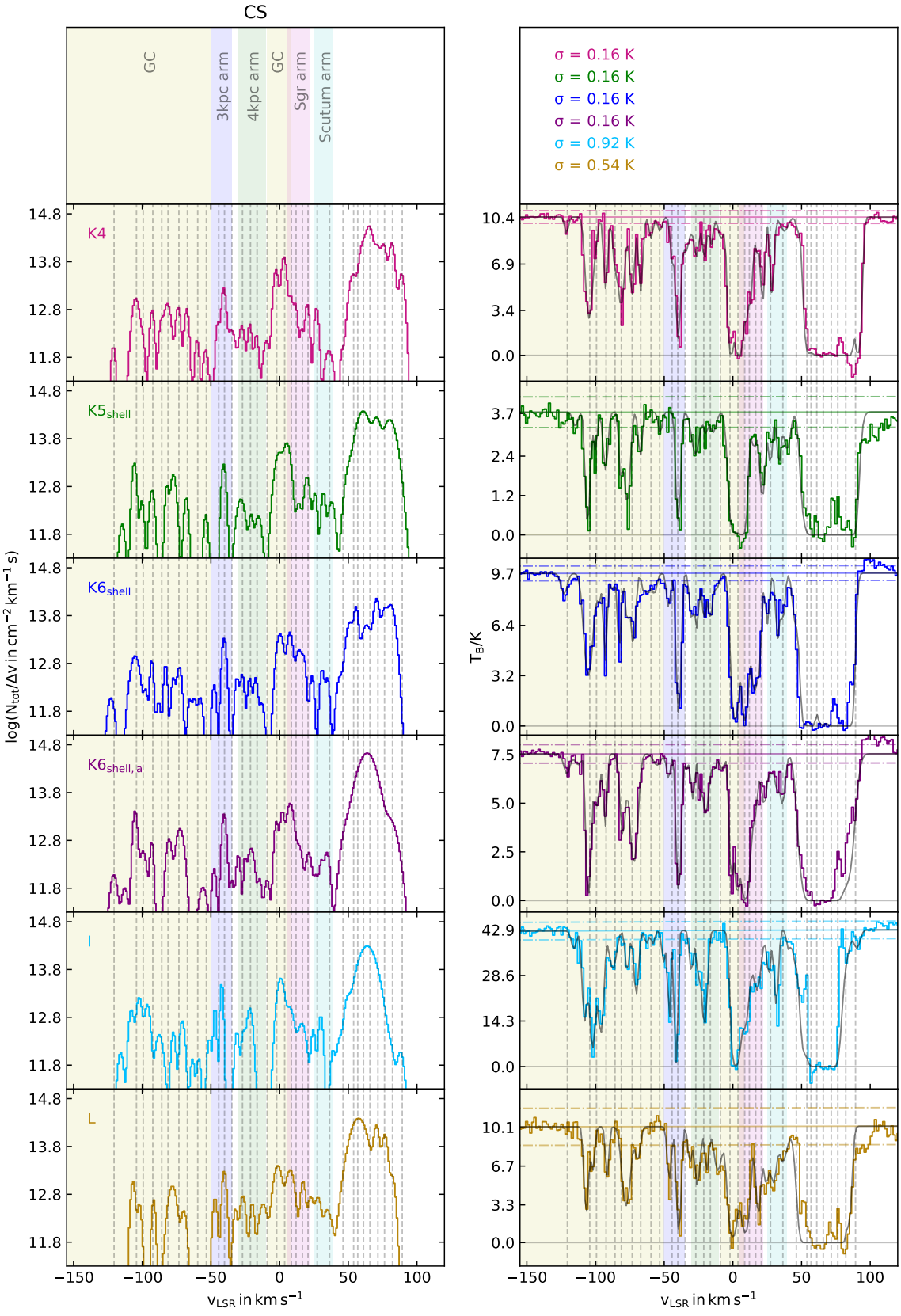

Figure A.30: Same as Fig. 3.8, but for CS.

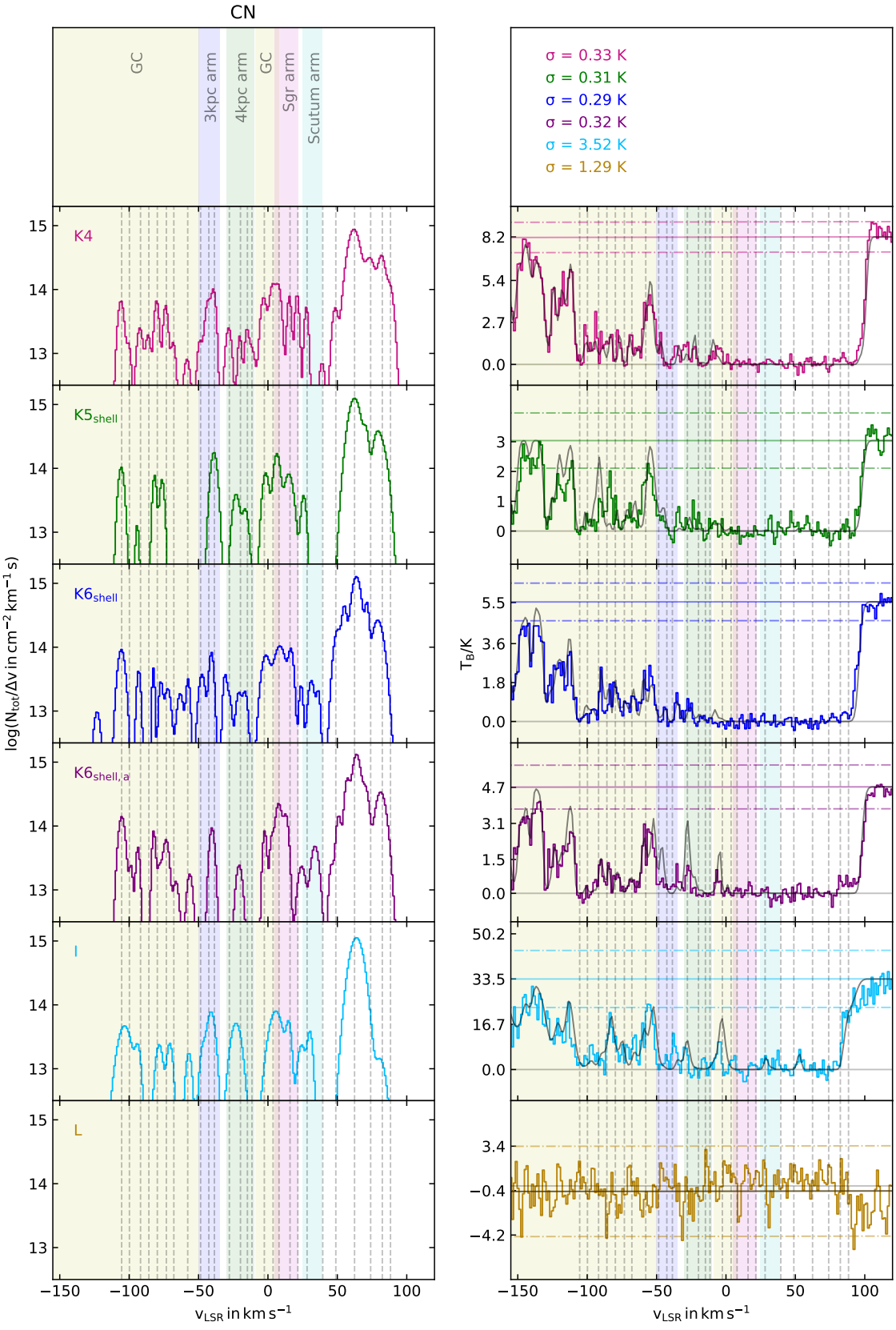

Figure A.31: Same as Fig. 3.8, but for CN.

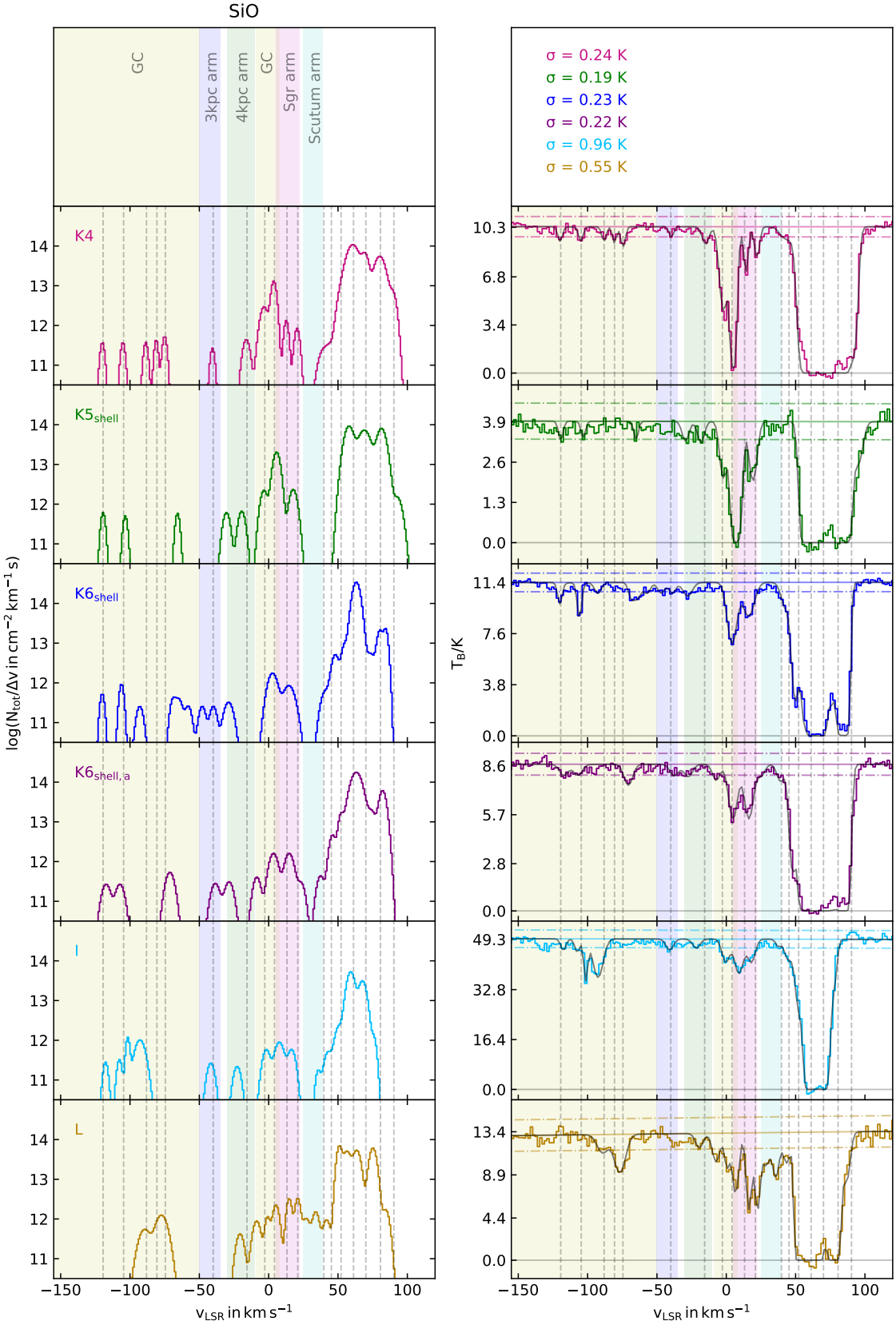

Figure A.32: Same as Fig. 3.8, but for SiO.

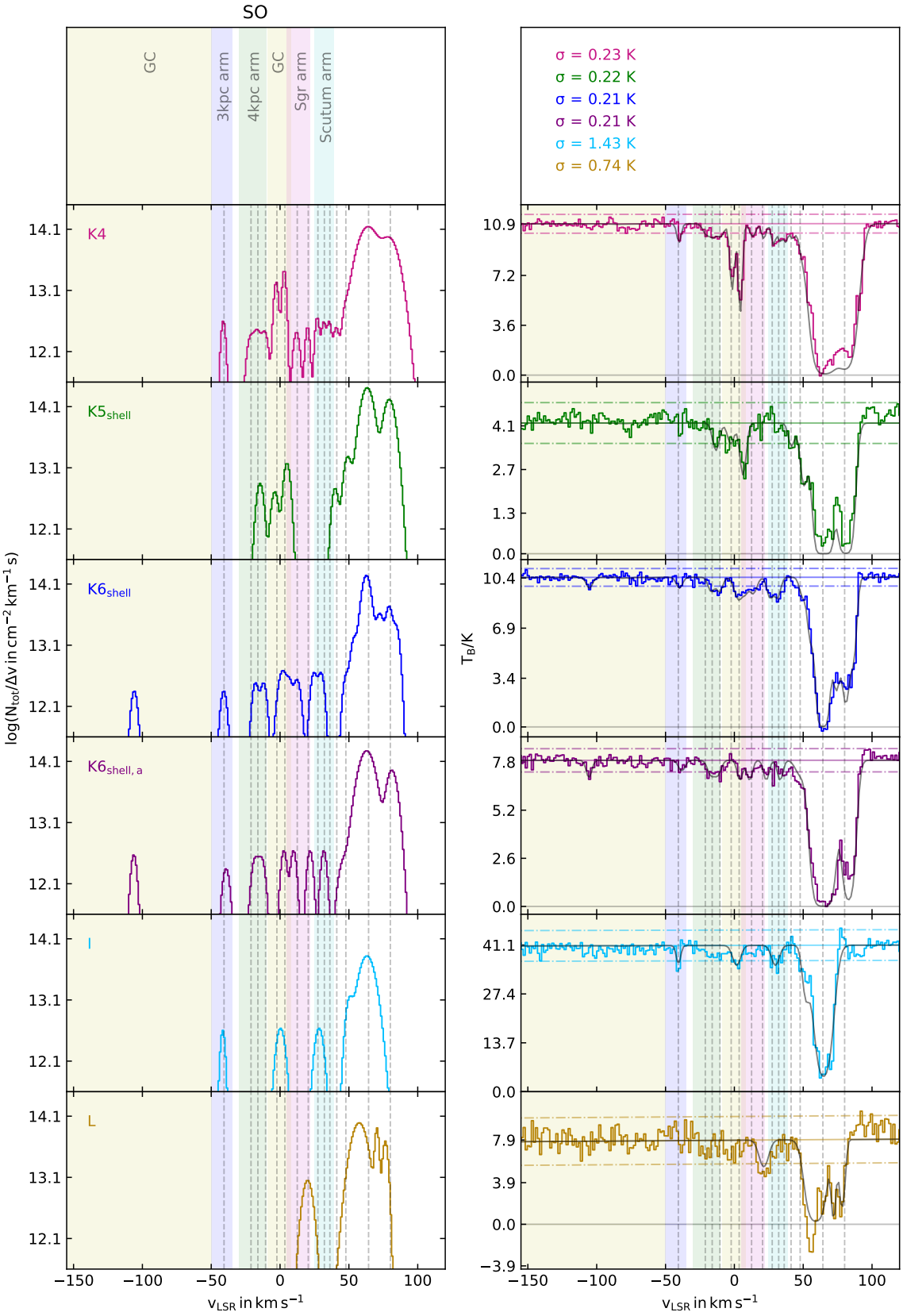

Figure A.33: Same as Fig. 3.8, but for SO.

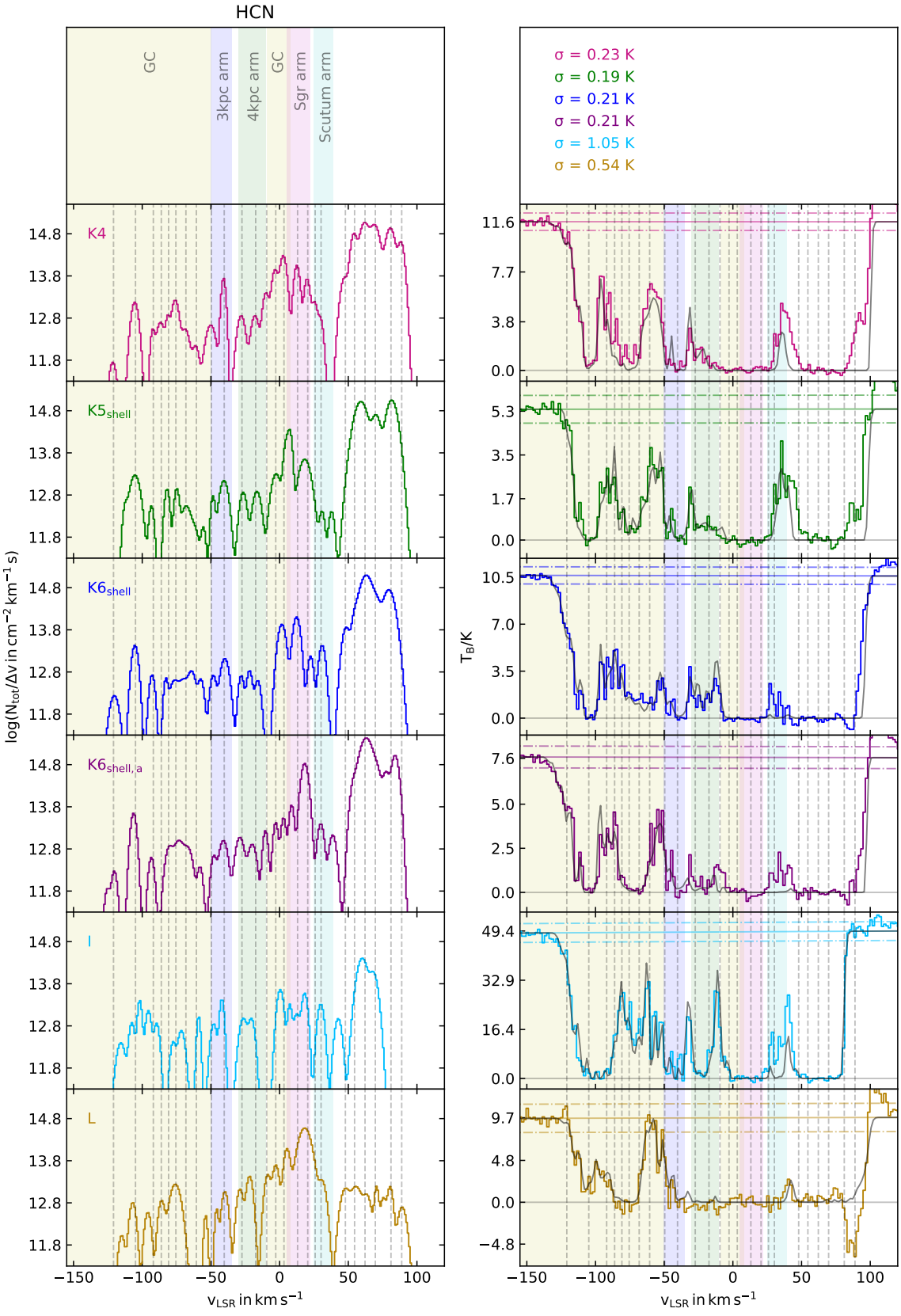

Figure A.34: Same as Fig. 3.8, but for HCN.

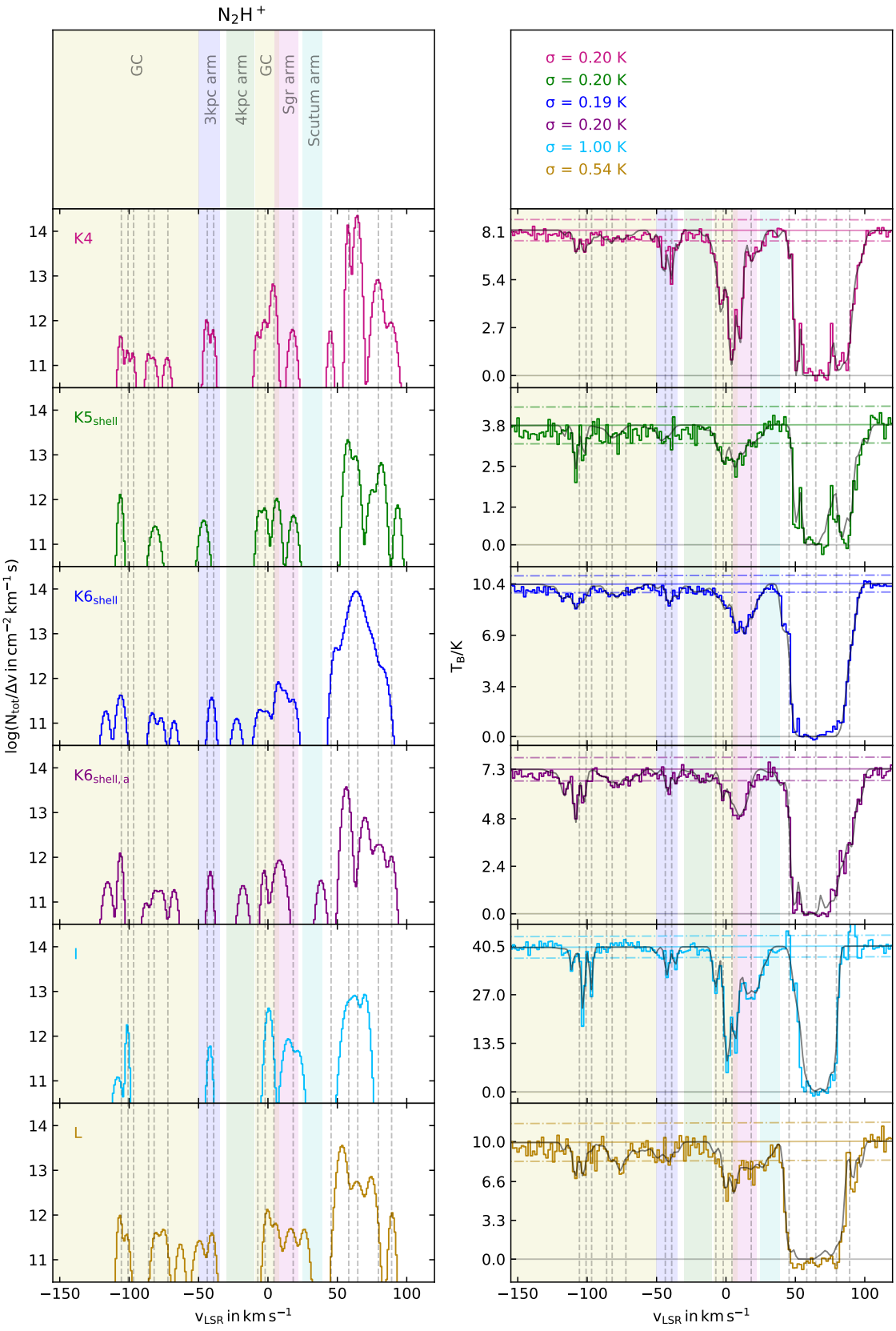

Figure A.35: Same as Fig. 3.8, but for N_2H^+.

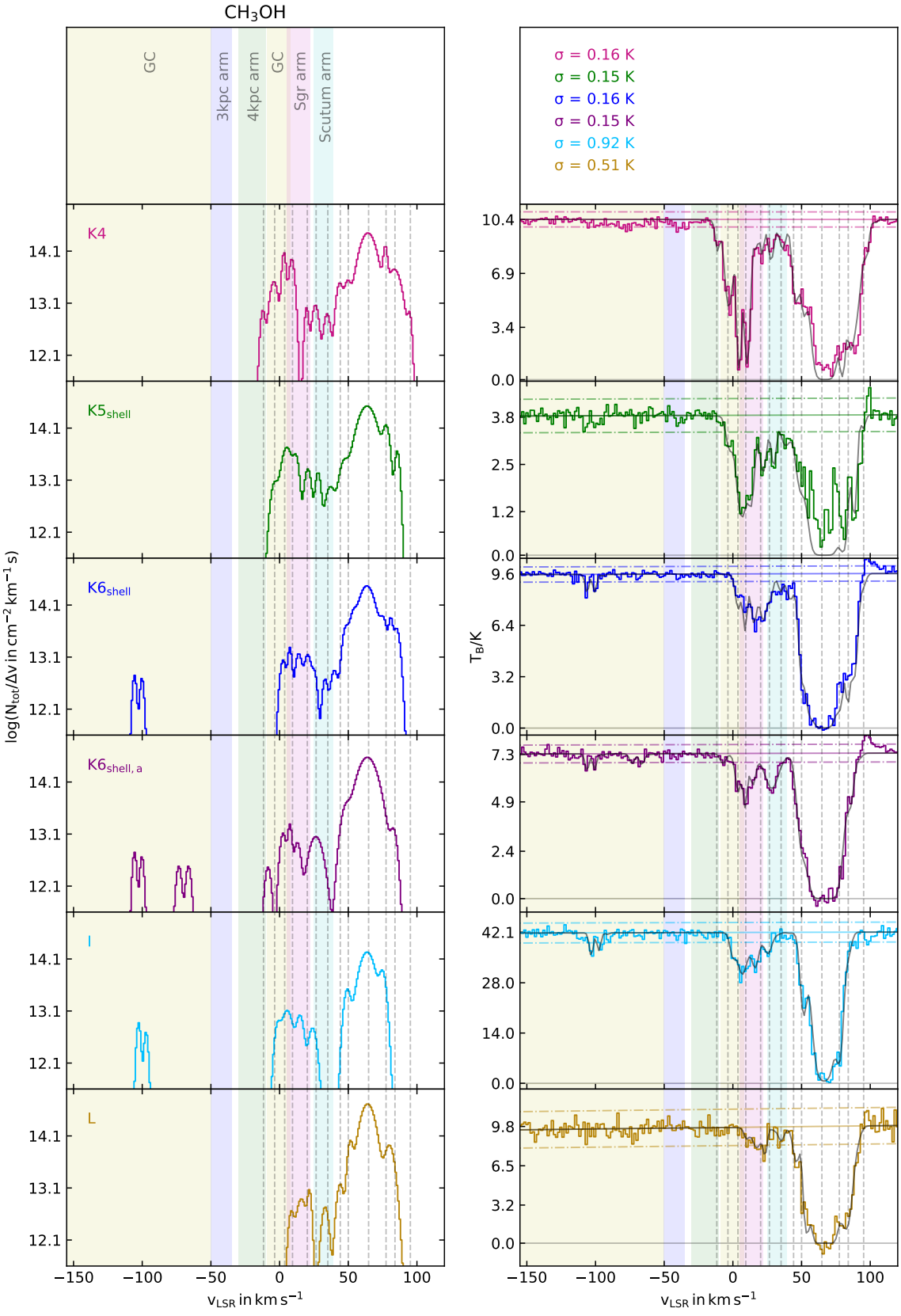

Figure A.36: Same as Fig. 3.8, but for CH_3OH.

A.8 Correlation between molecules

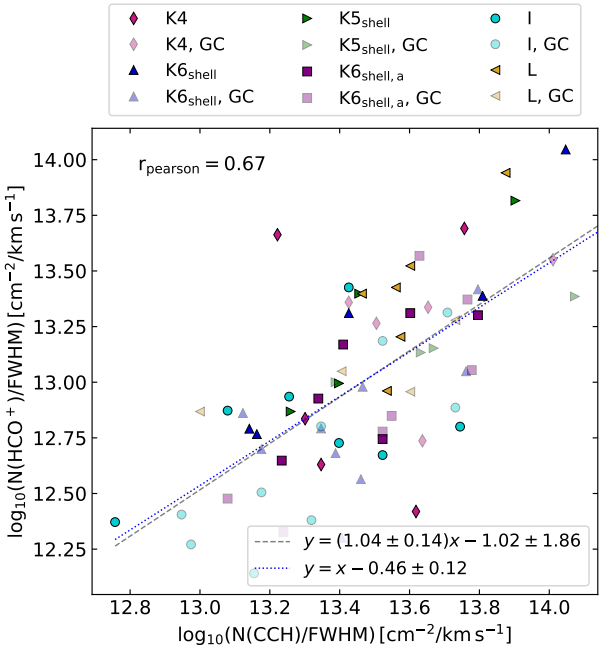

Figure A.37: Same as Fig. 3.9, but for HCO^+ and CCH.

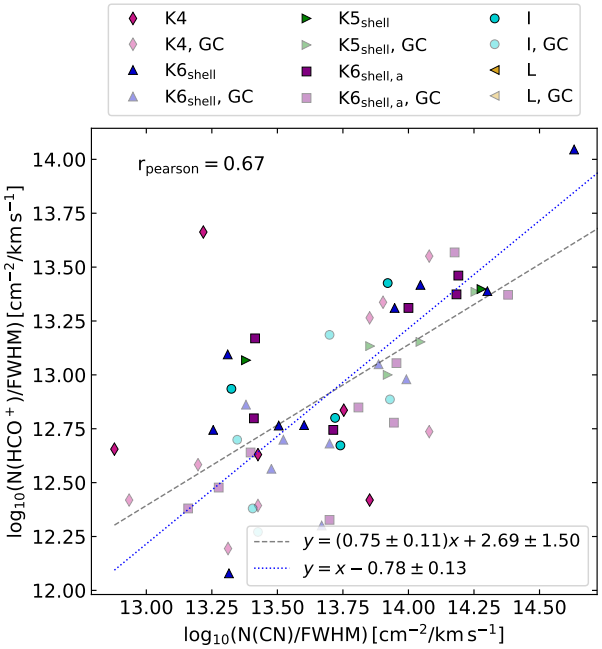

Figure A.38: Same as Fig. 3.9, but for HCO^+ and CN.

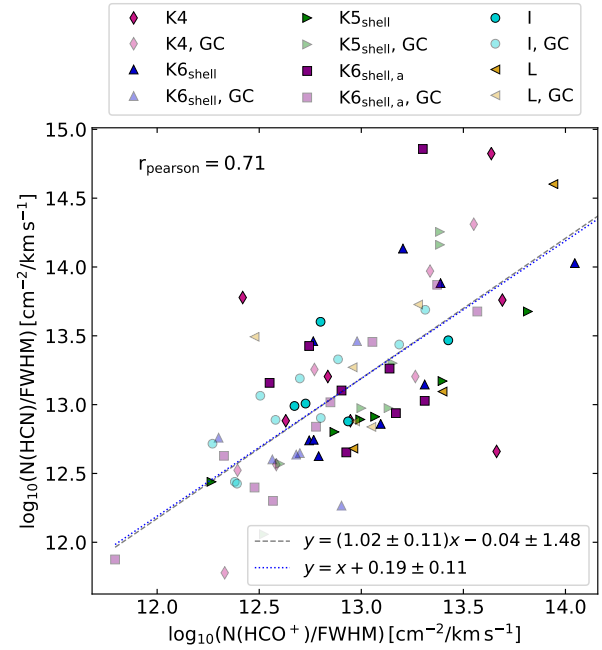

Figure A.39: Same as Fig. 3.9, but for HCN and HCO^+.

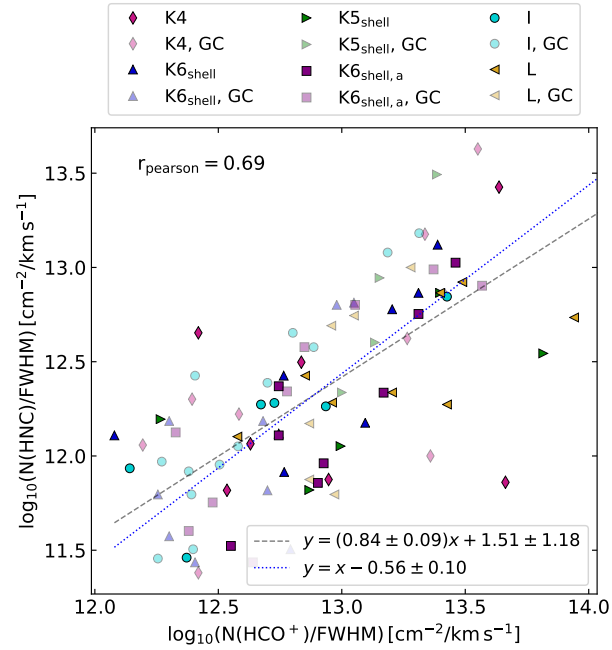

Figure A.40: Same as Fig. 3.9, but for HNC and HCO^+.

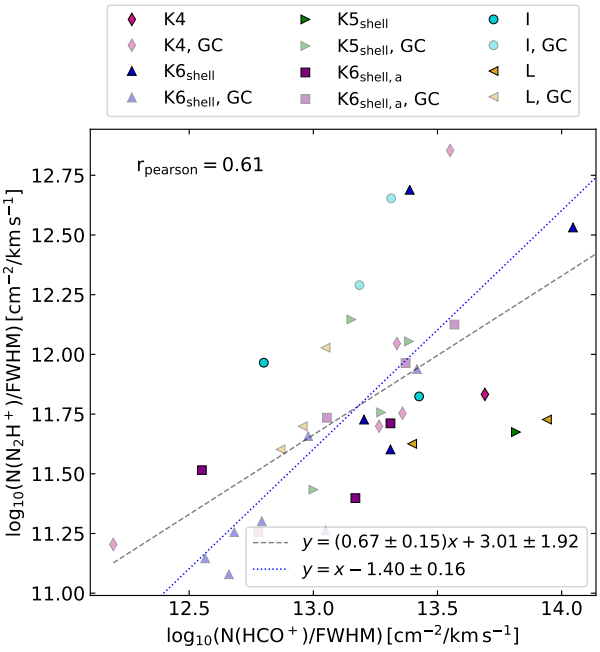

Figure A.41: Same as Fig. 3.9, but for N_2H^+ and HCO^+.

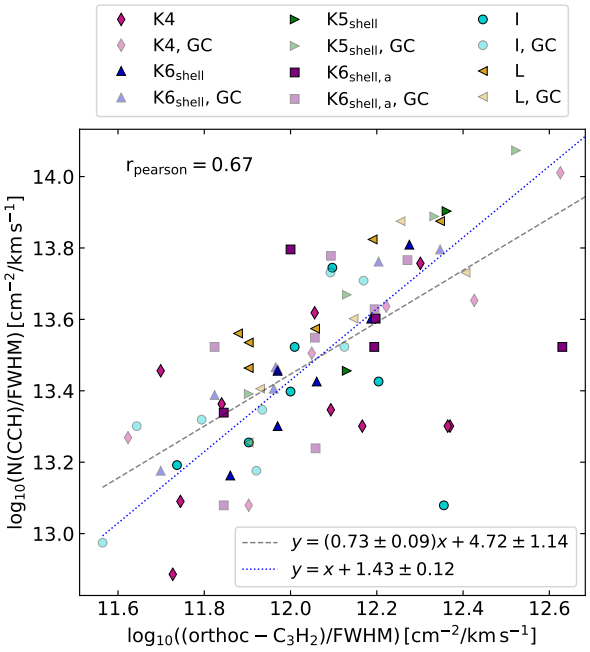

Figure A.42: Same as Fig. 3.9, but for CCH and ortho c-C_3H_2.

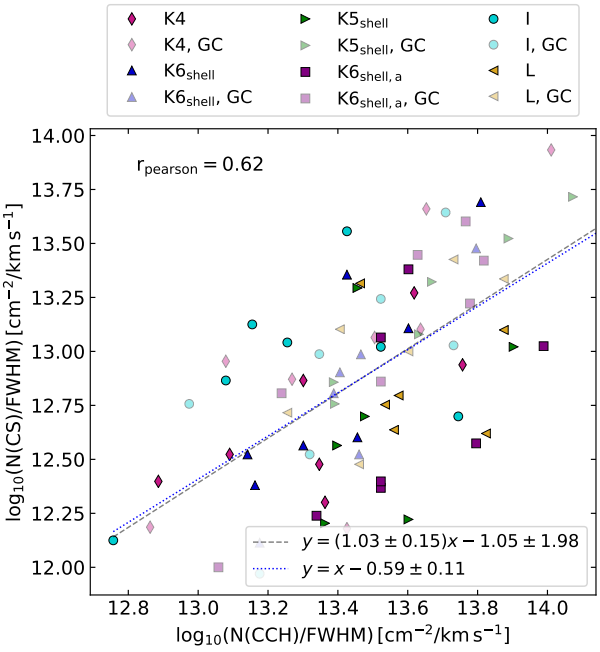

Figure A.43: Same as Fig. 3.9, but for CS and CCH.

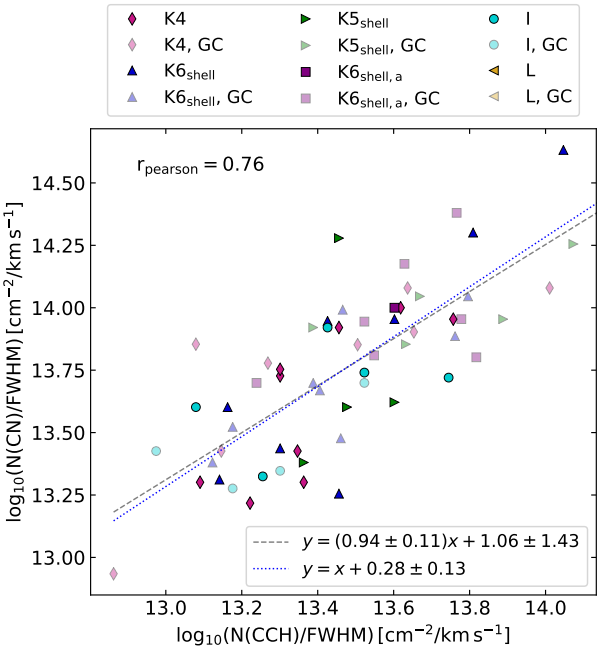

Figure A.44: Same as Fig. 3.9, but for CN and CCH.

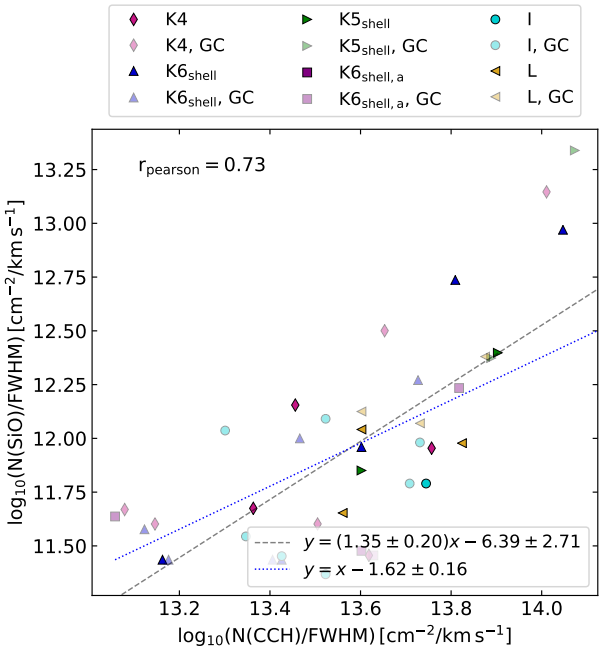

Figure A.45: Same as Fig. 3.9, but for SiO and CCH.

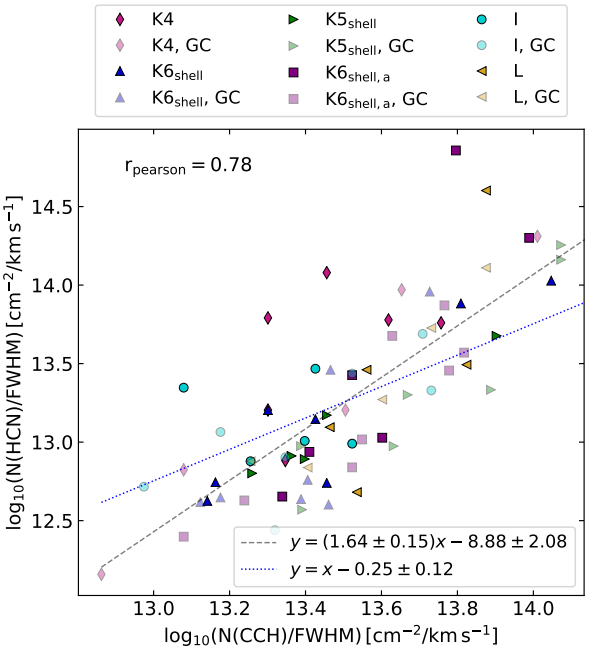

Figure A.46: Same as Fig. 3.9, but for HCN and CCH.

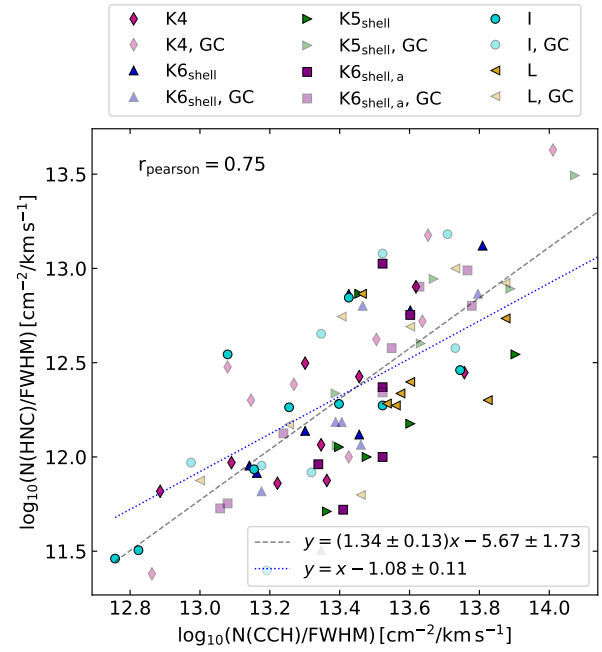

Figure A.47: Same as Fig. 3.9, but for HNC and CCH.

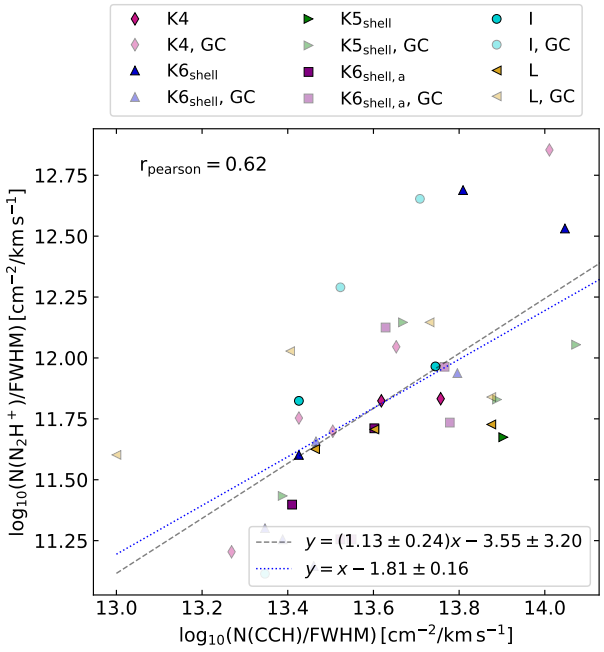

Figure A.48: Same as Fig. 3.9, but for N_2H^+ and CCH.

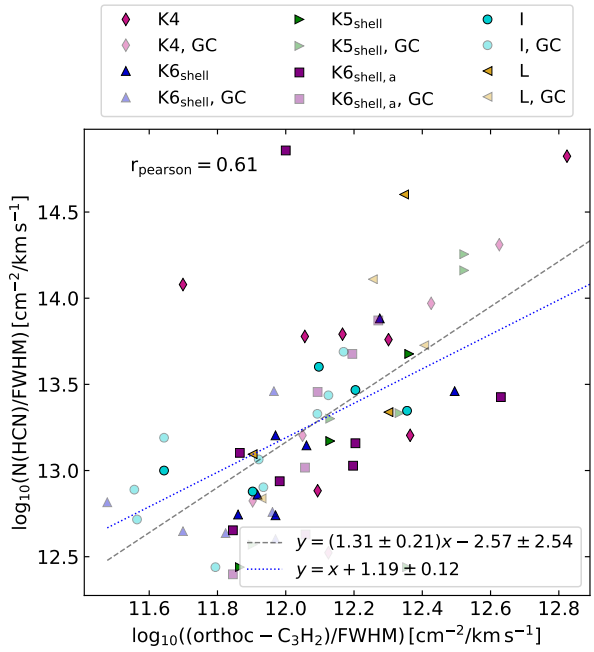

Figure A.49: Same as Fig. 3.9, but for HCN and ortho c-C_3H_2.

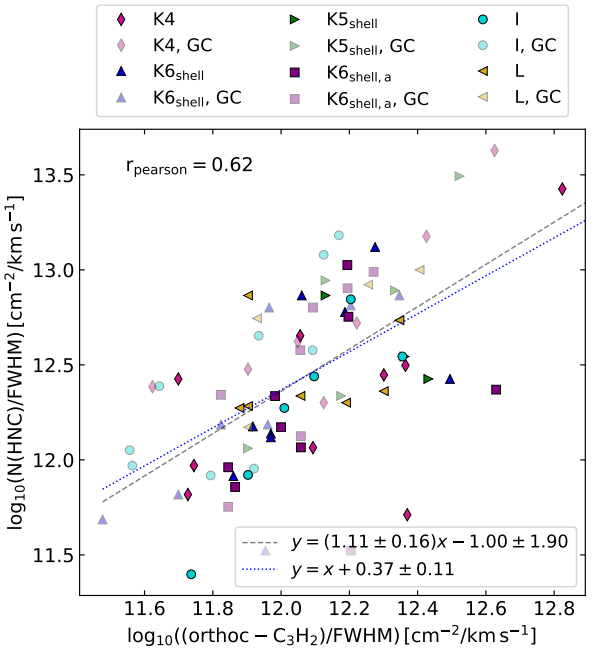

Figure A.50: Same as Fig. 3.9, but for HNC and ortho c-C_3H_2.

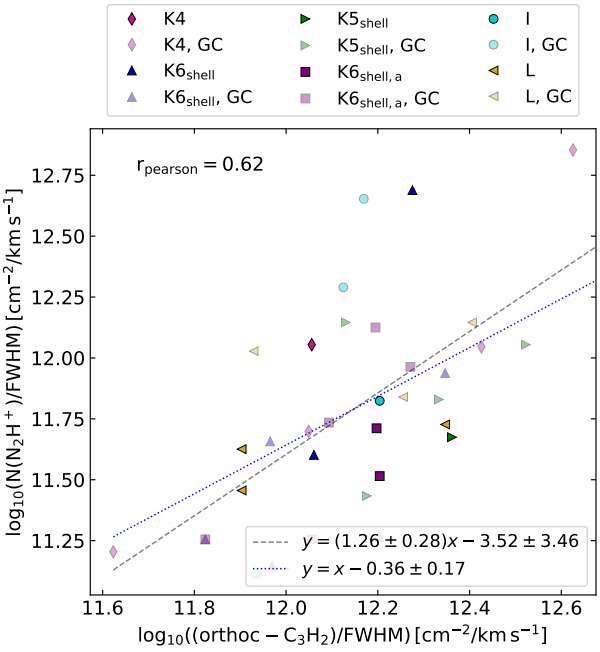

Figure A.51: Same as Fig. 3.9, but for N_2H^+ and ortho c-C_3H_2.

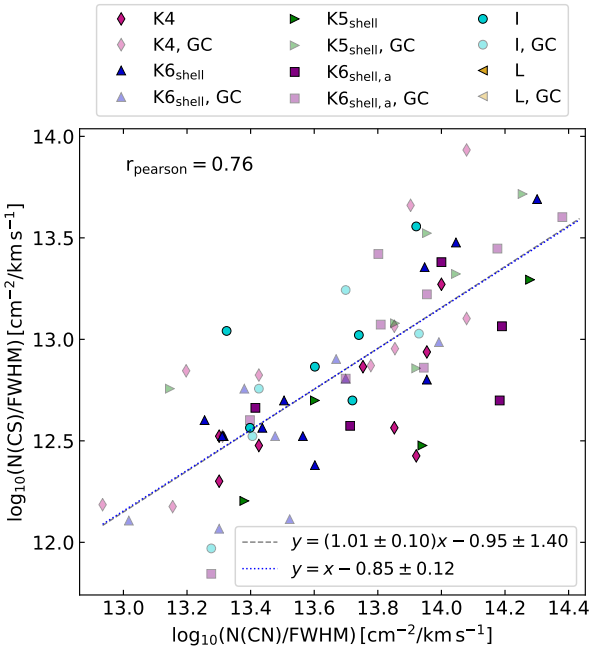

Figure A.52: Same as Fig. 3.9, but for CS and CN.

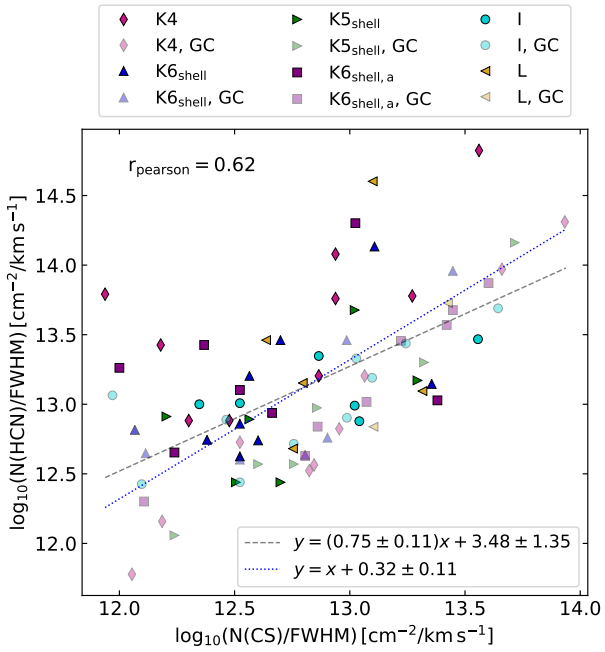

Figure A.53: Same as Fig. 3.9, but for HCN and CS.

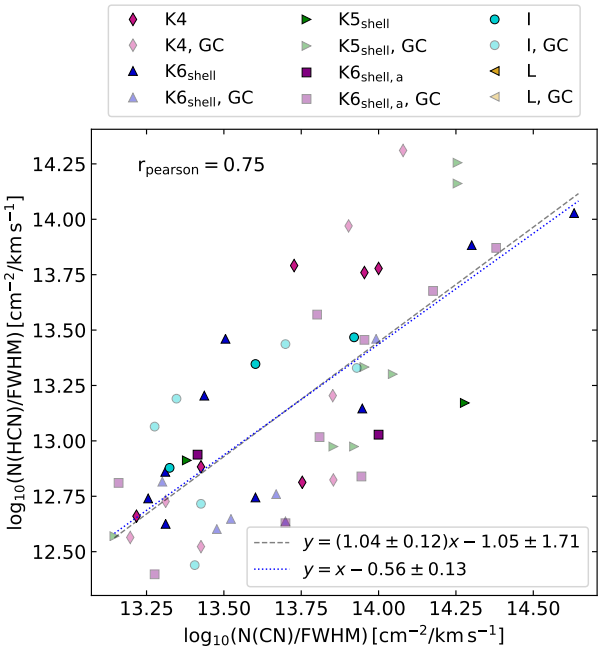

Figure A.54: Same as Fig. 3.9, but for HCN and CN.

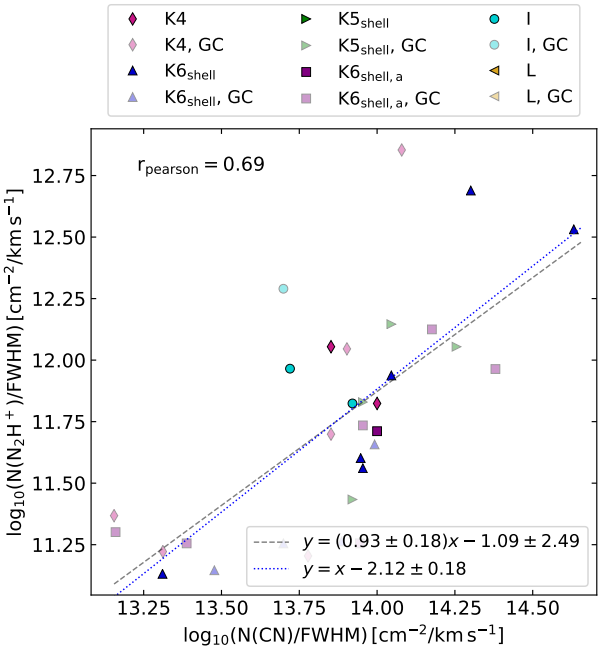

Figure A.55: Same as Fig. 3.9, but for N_2H^+ and CN.

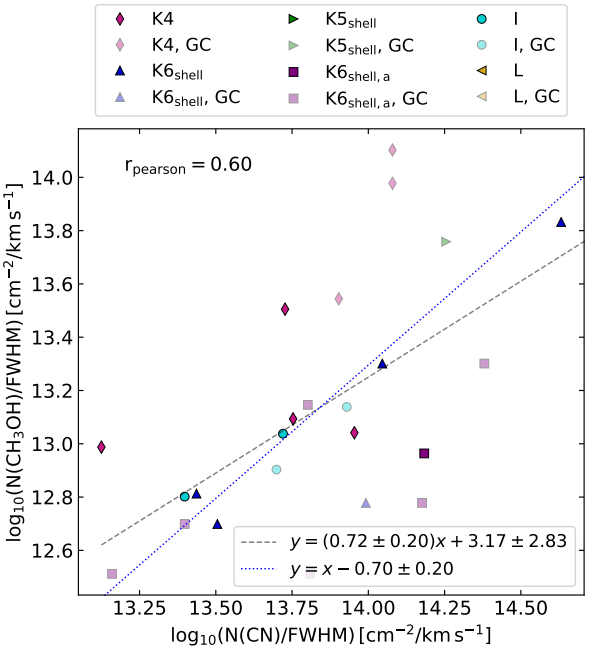

Figure A.56: Same as Fig. 3.9, but for CH_3OH and CN.

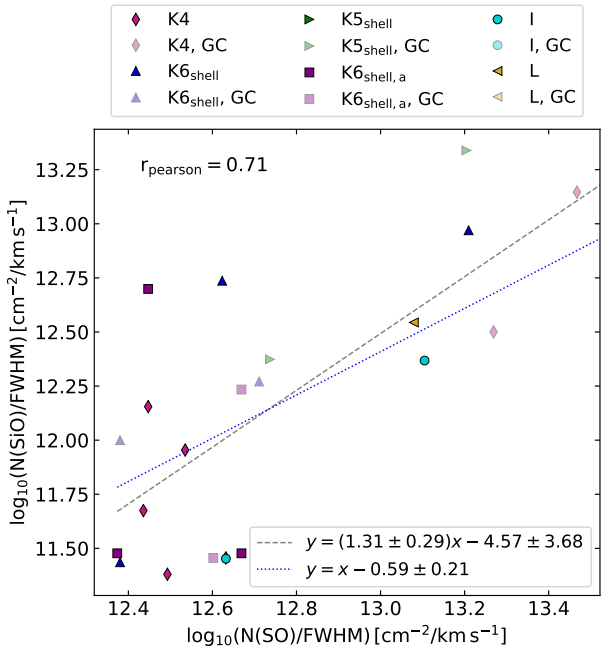

Figure A.57: Same as Fig. 3.9, but for SiO and SO.

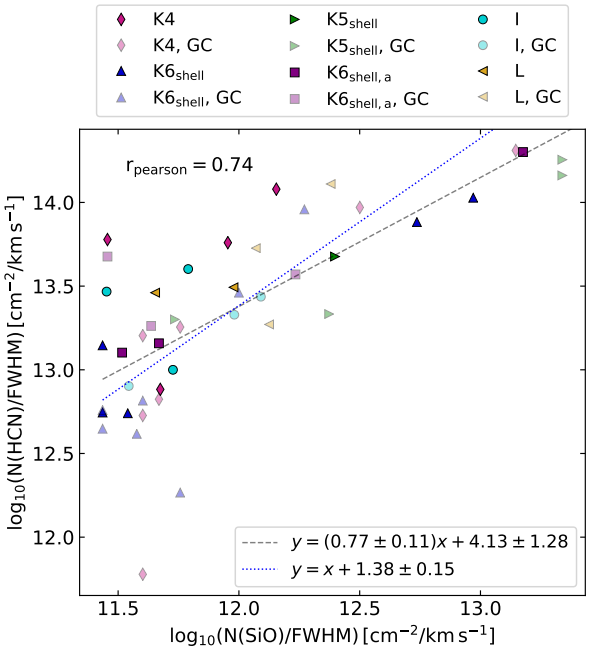

Figure A.58: Same as Fig. 3.9, but for HCN and SiO.

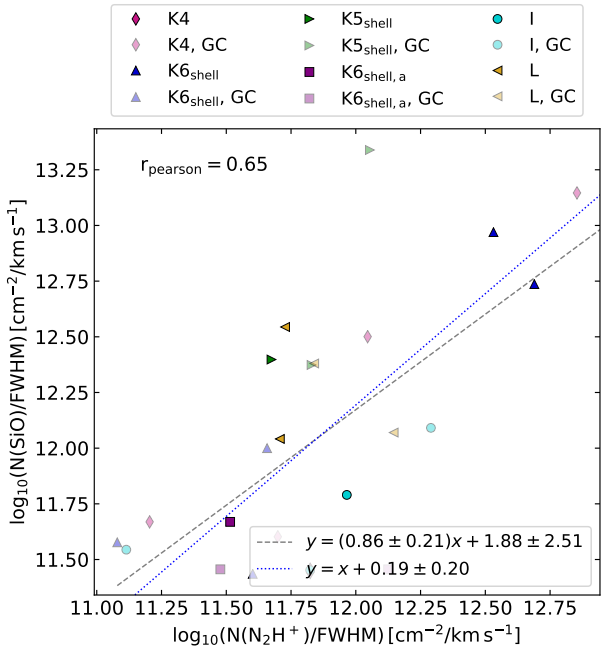

Figure A.59: Same as Fig. 3.9, but for SiO and N_2H^+.

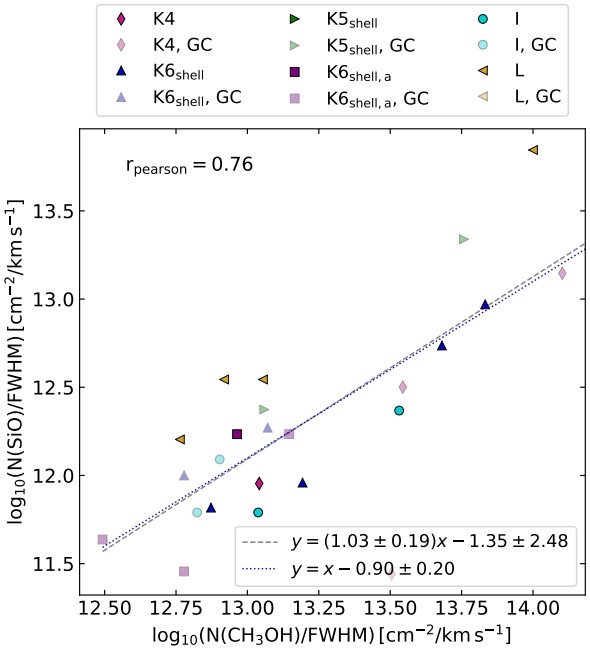

Figure A.60: Same as Fig. 3.9, but for SiO and CH_3OH.

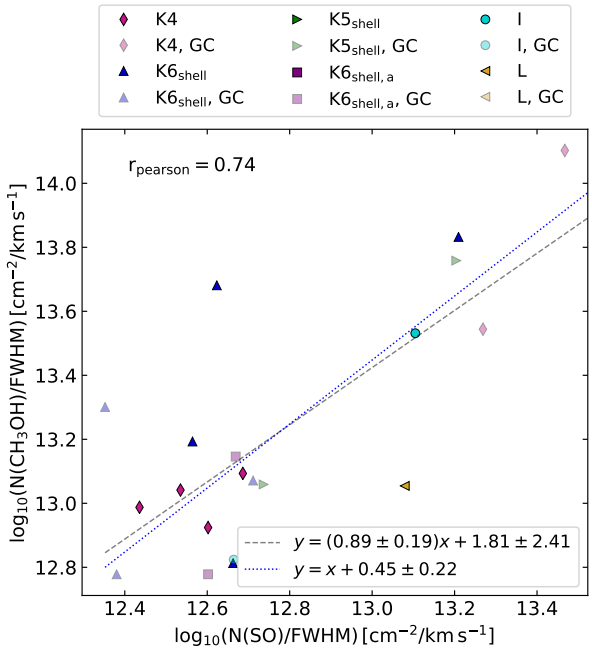

Figure A.61: Same as Fig. 3.9, but for CH_3OH and SO.

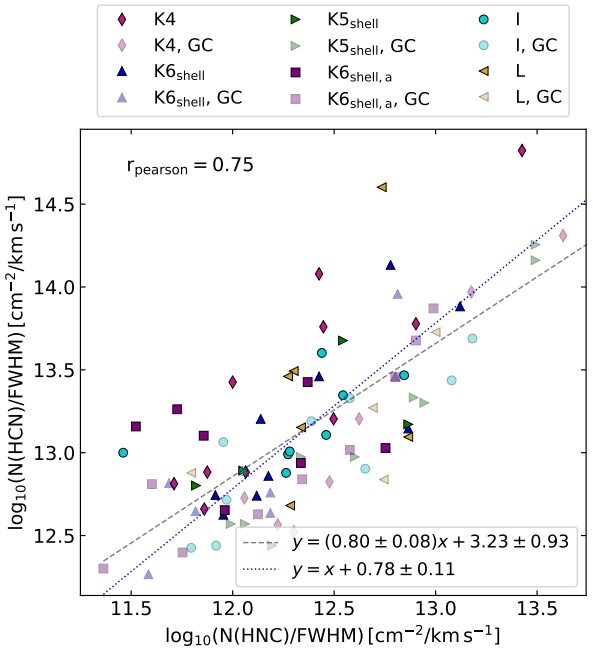

Figure A.62: Same as Fig. 3.9, but for HCN and HNC.

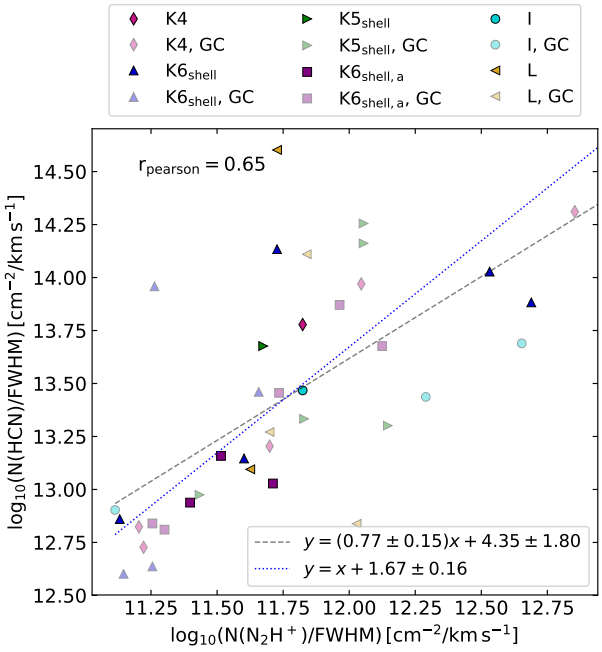

Figure A.63: Same as Fig. 3.9, but for HCN and N_2H^+.

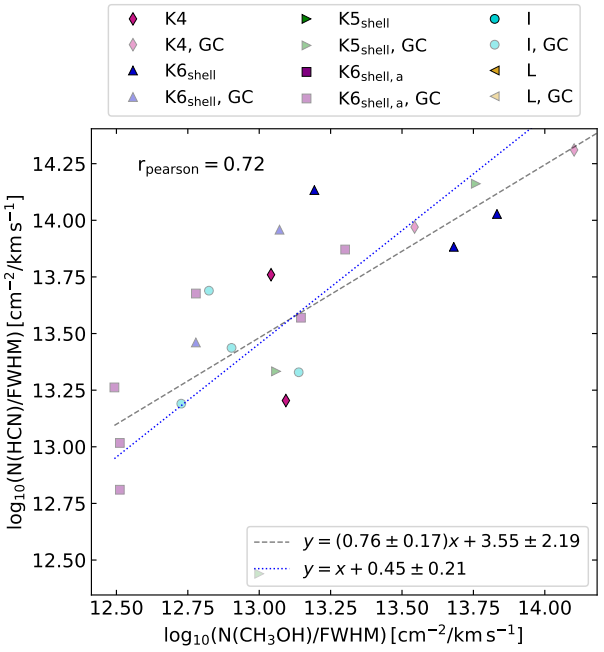

Figure A.64: Same as Fig. 3.9, but for HCN and CH_3OH.

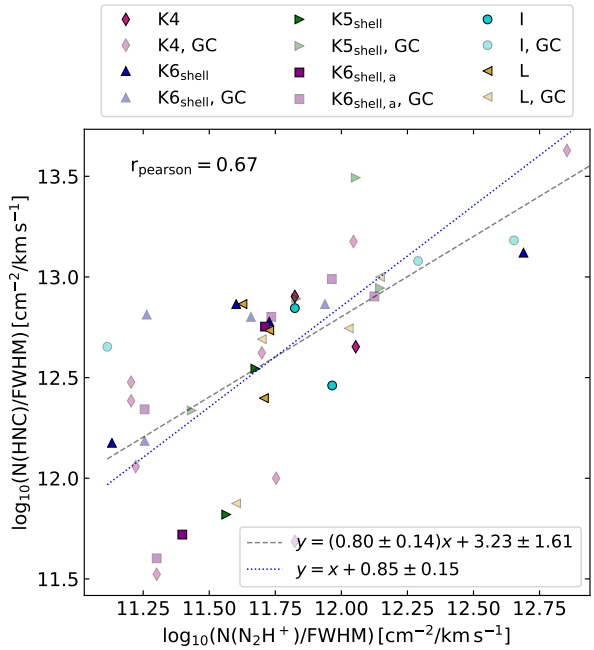

Figure A.65: Same as Fig. 3.9, but for HNC and N_2H^+.

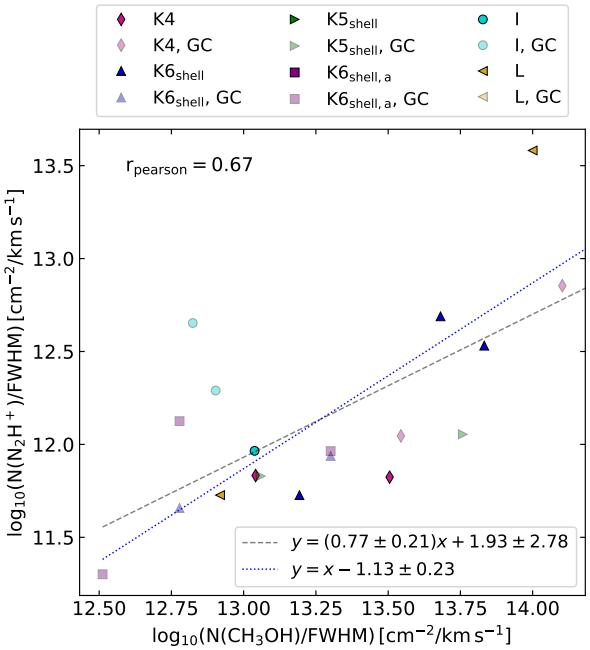

Figure A.66: Same as Fig. 3.9, but for N_2H^+ and CH_3OH.

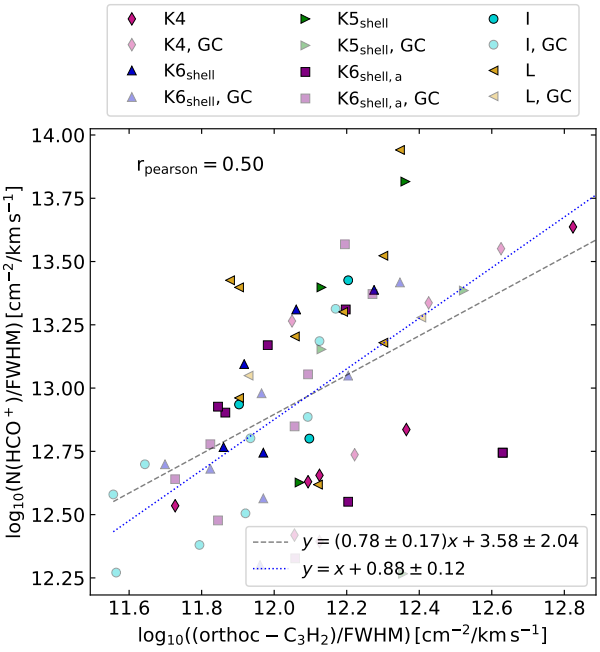

Figure A.67: Same as Fig. 3.9, but for HCO^+ and ortho c-C_3H_2.

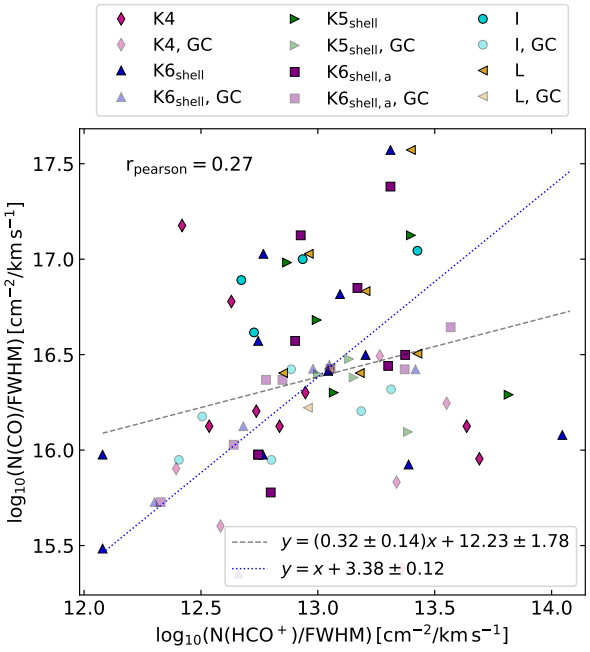

Figure A.68: Same as Fig. 3.9, but for CO and HCO^+.

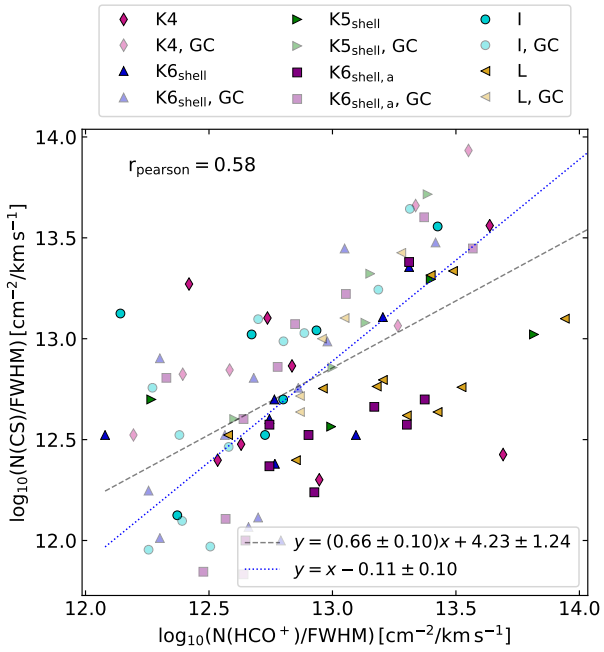

Figure A.69: Same as Fig. 3.9, but for CS and HCO^+.

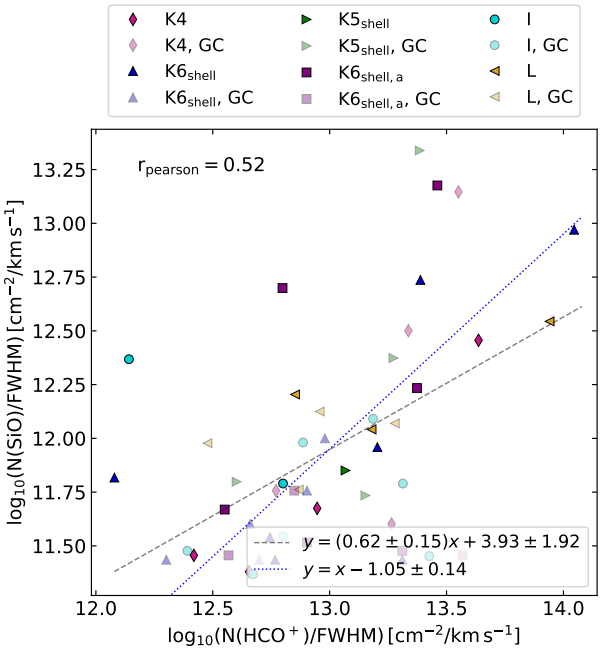

Figure A.70: Same as Fig. 3.9, but for SiO and HCO^+.

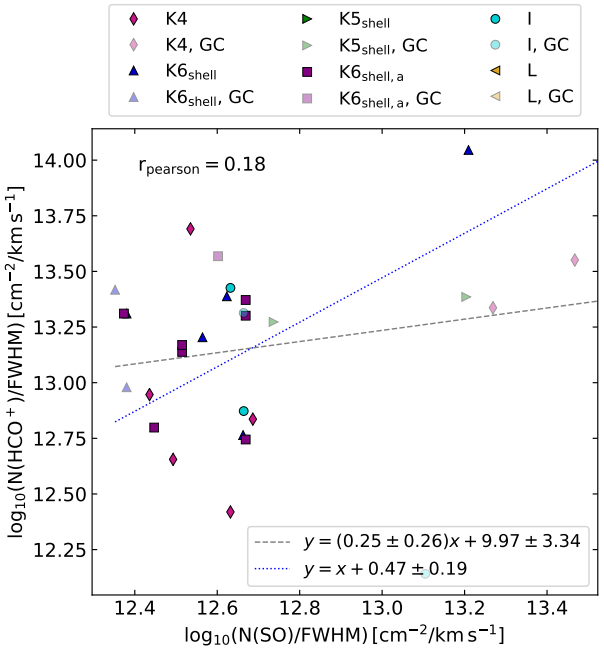

Figure A.71: Same as Fig. 3.9, but for HCO^+ and SO.

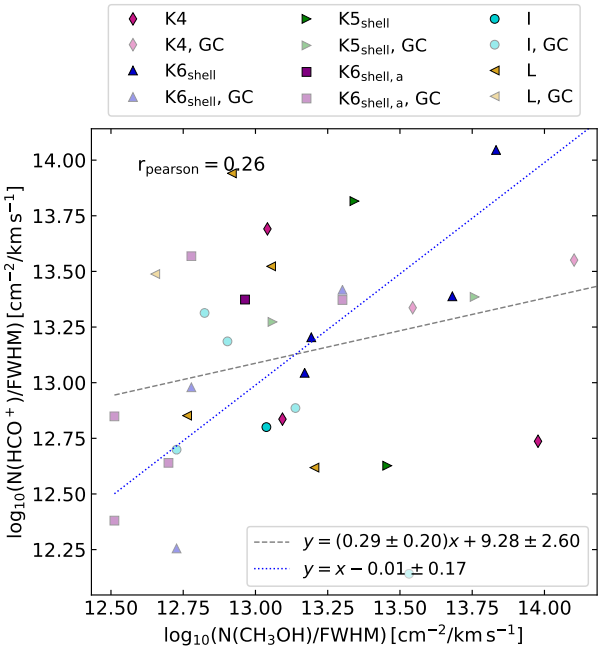

Figure A.72: Same as Fig. 3.9, but for HCO^+ and CH_3OH.

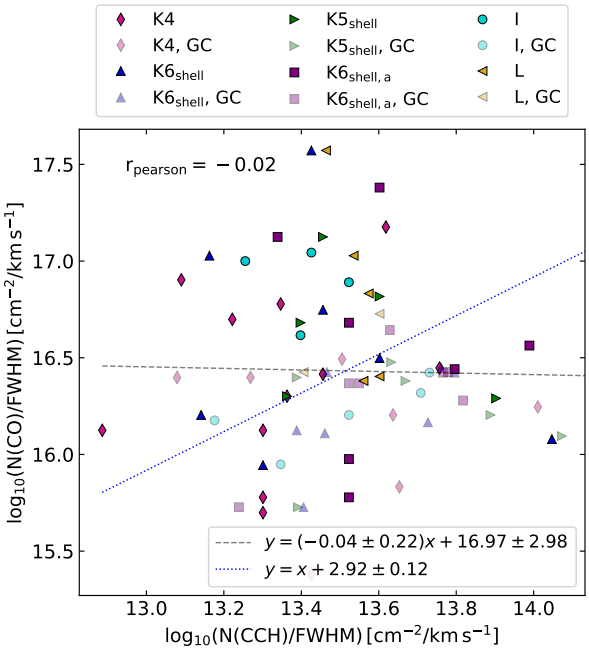

Figure A.73: Same as Fig. 3.9, but for CO and CCH.

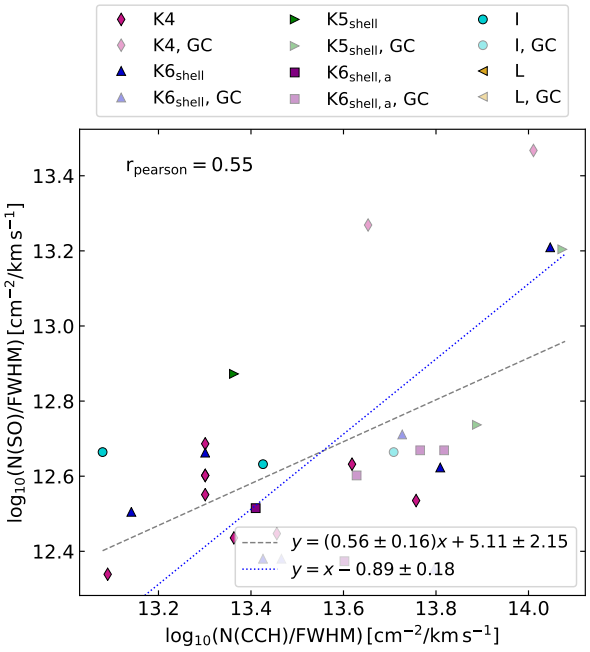

Figure A.74: Same as Fig. 3.9, but for SO and CCH.

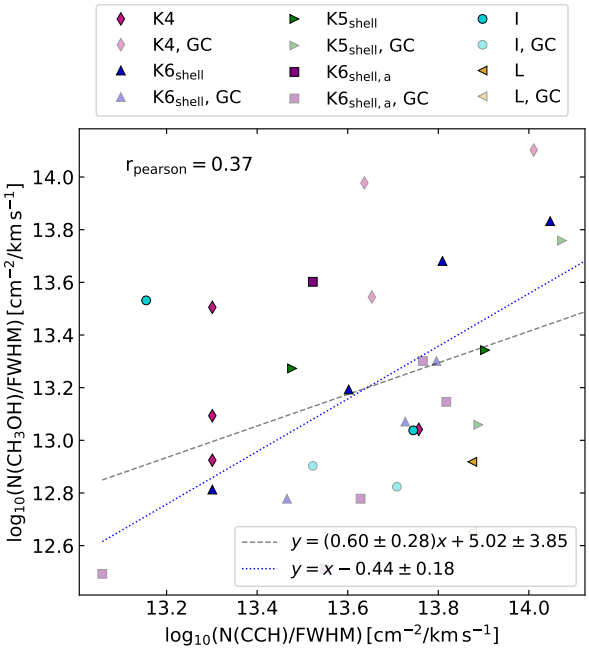

Figure A.75: Same as Fig. 3.9, but for CH_3OH and CCH.

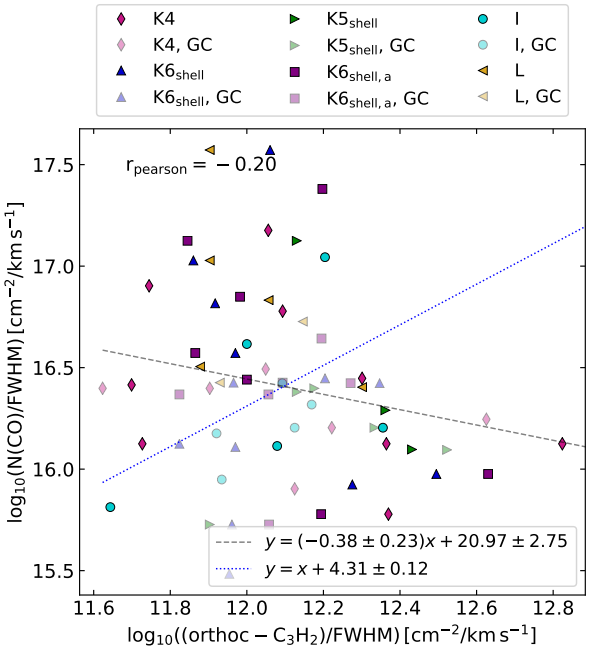

Figure A.76: Same as Fig. 3.9, but for CO and ortho c-C_3H_2.

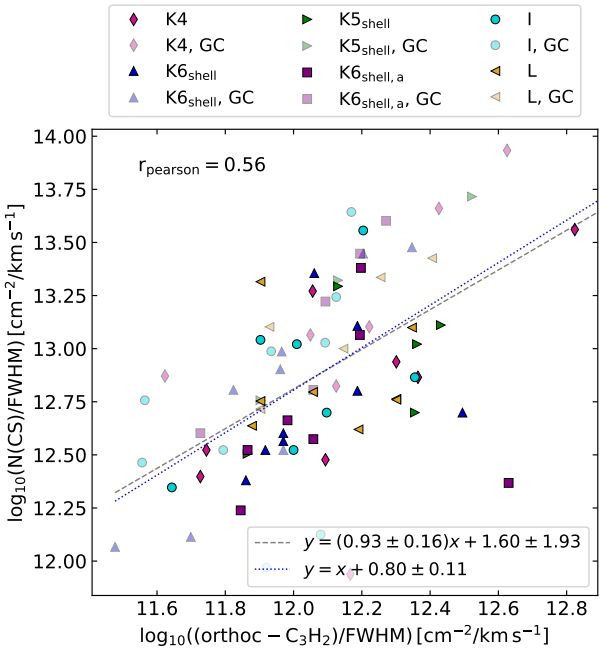

Figure A.77: Same as Fig. 3.9, but for CS and ortho c-C_3H_2.

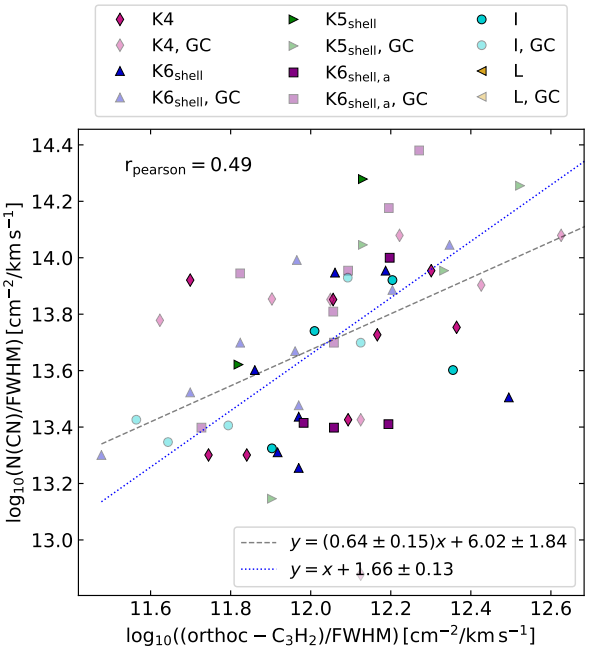

Figure A.78: Same as Fig. 3.9, but for CN and ortho c-C_3H_2.

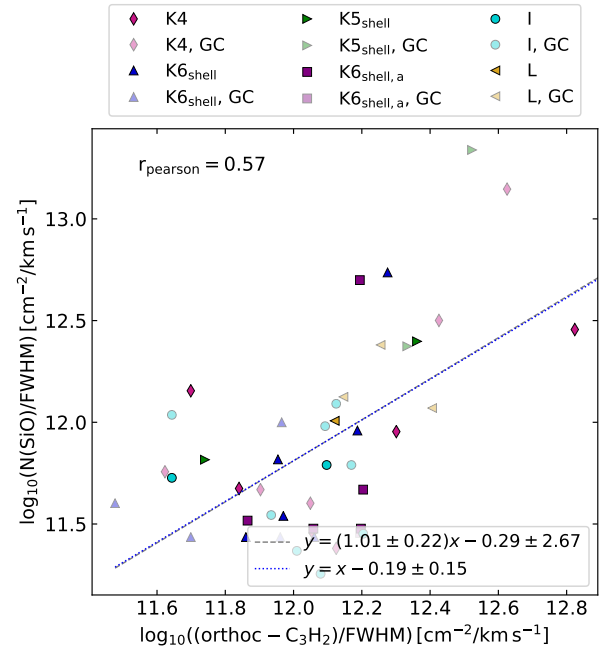

Figure A.79: Same as Fig. 3.9, but for SiO and ortho c-C_3H_2.

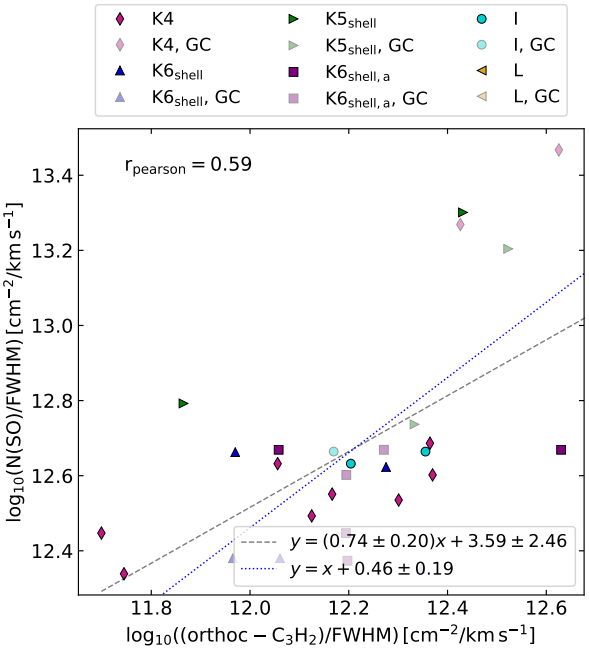

Figure A.80: Same as Fig. 3.9, but for SO and ortho c-C_3H_2.

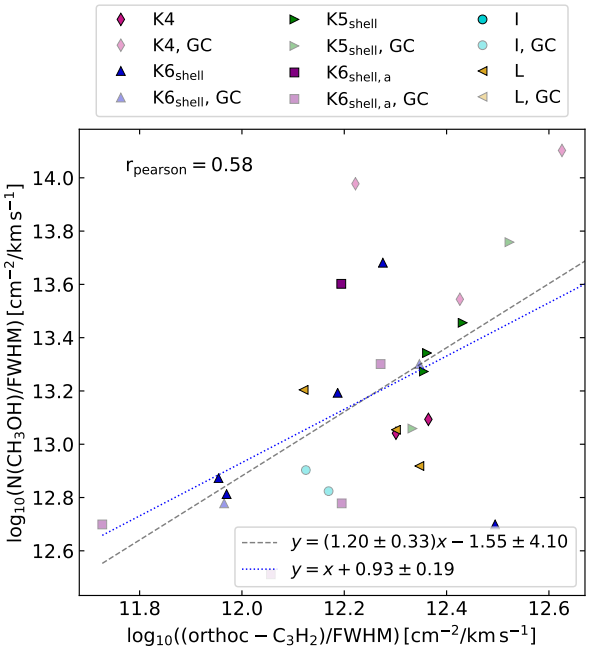

Figure A.81: Same as Fig. 3.9, but for CH_3OH and ortho c-C_3H_2.

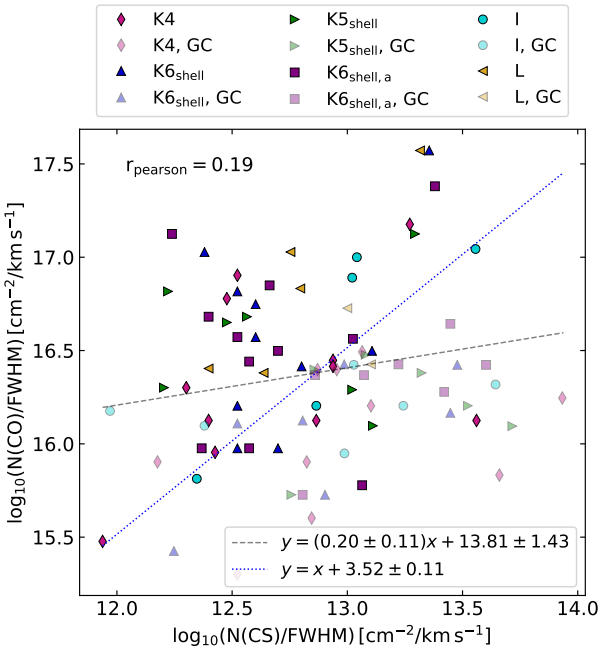

Figure A.82: Same as Fig. 3.9, but for CO and CS.

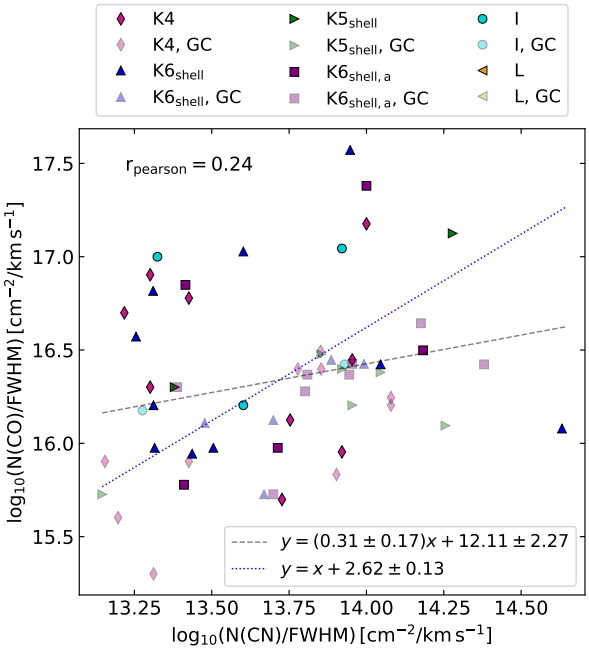

Figure A.83: Same as Fig. 3.9, but for CO and CN.

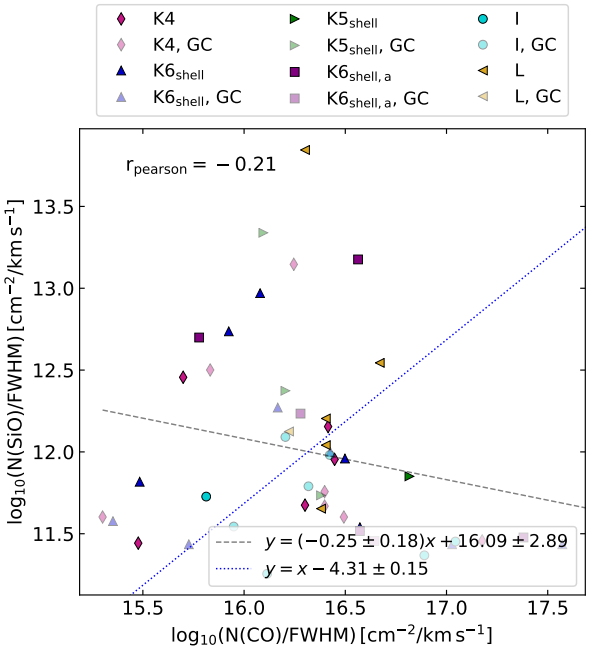

Figure A.84: Same as Fig. 3.9, but for SiO and CO.

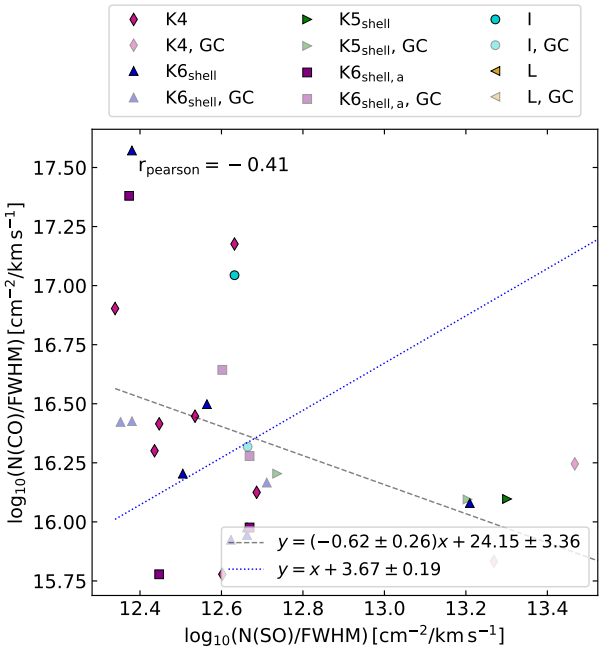

Figure A.85: Same as Fig. 3.9, but for CO and SO.

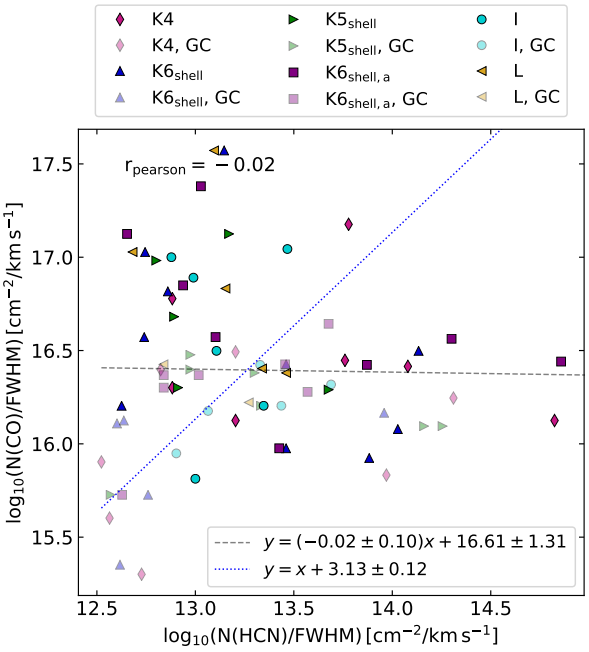

Figure A.86: Same as Fig. 3.9, but for CO and HCN.

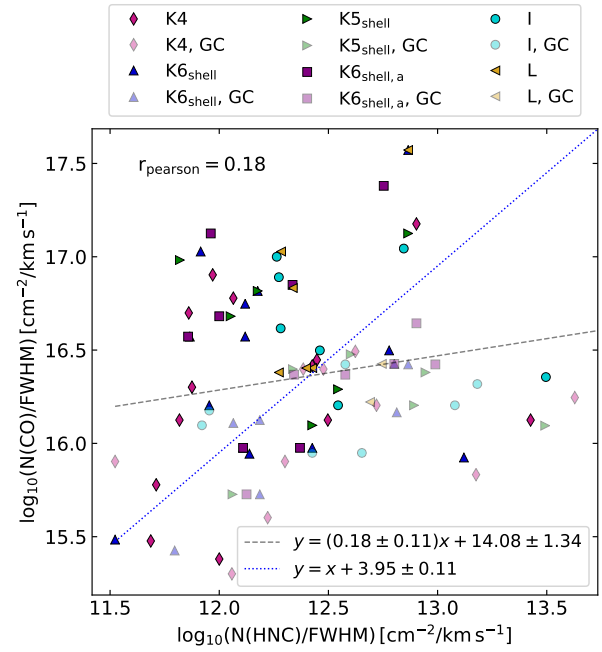

Figure A.87: Same as Fig. 3.9, but for CO and HNC.

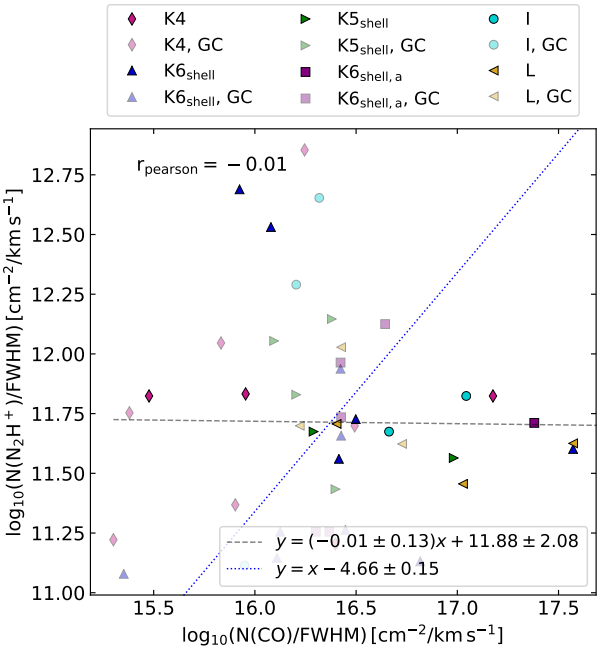

Figure A.88: Same as Fig. 3.9, but for N_2H^+ and CO.

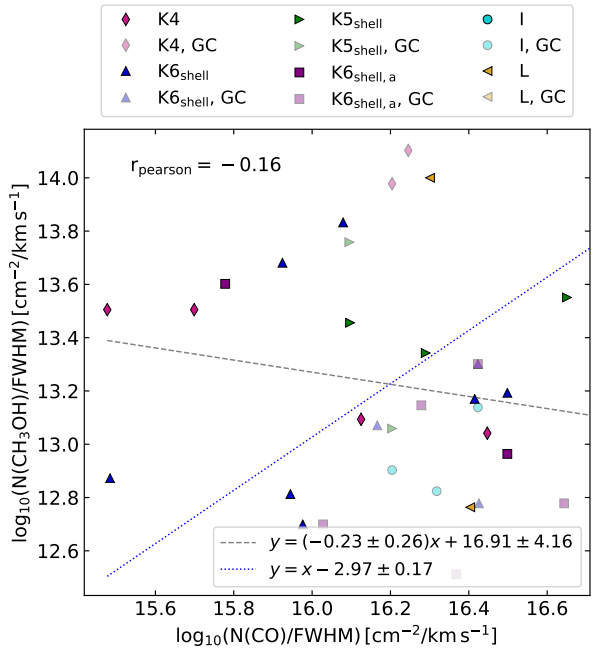

Figure A.89: Same as Fig. 3.9, but for CH_3OH and CO.

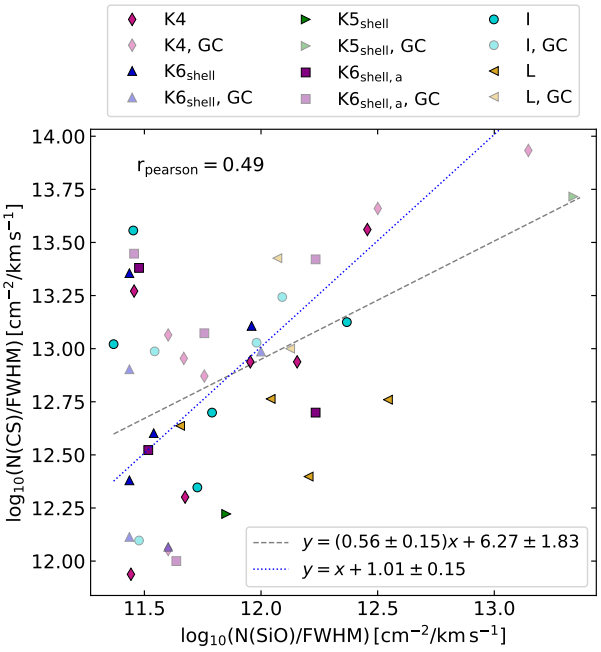

Figure A.90: Same as Fig. 3.9, but for CS and SiO.

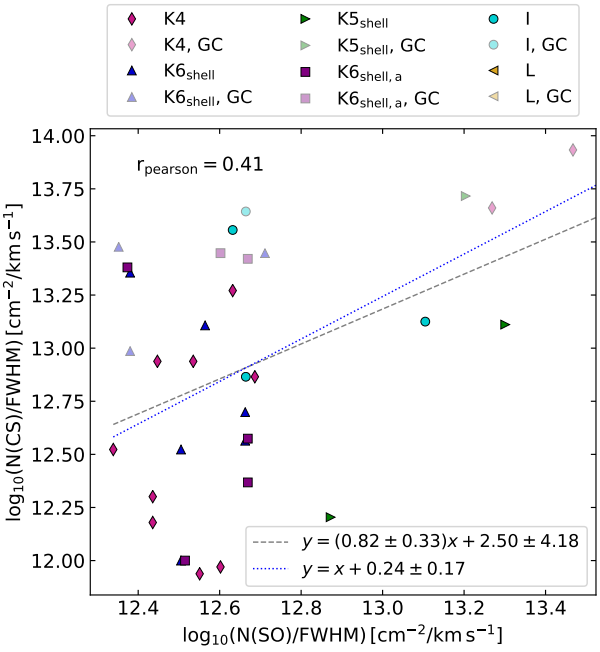

Figure A.91: Same as Fig. 3.9, but for CS and SO.

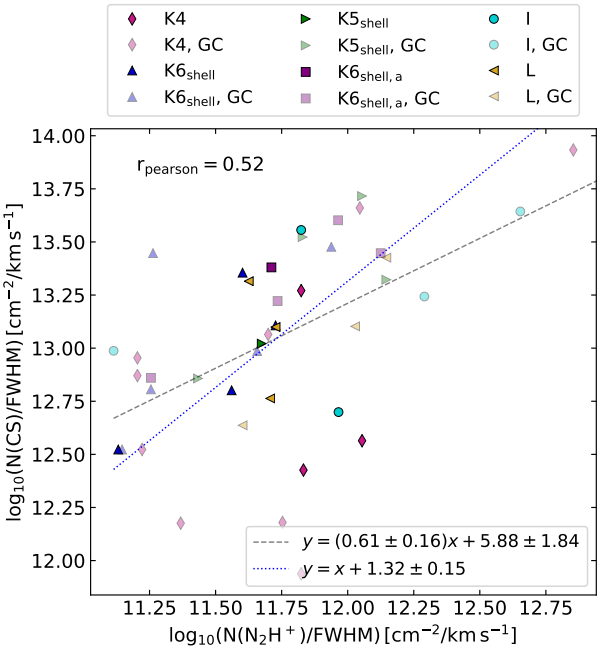

Figure A.92: Same as Fig. 3.9, but for CS and N_2H^+.

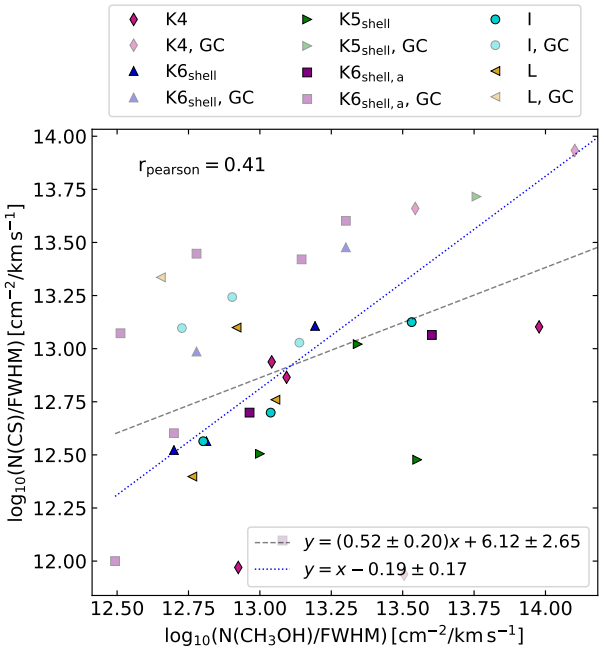

Figure A.93: Same as Fig. 3.9, but for CS and CH_3OH.

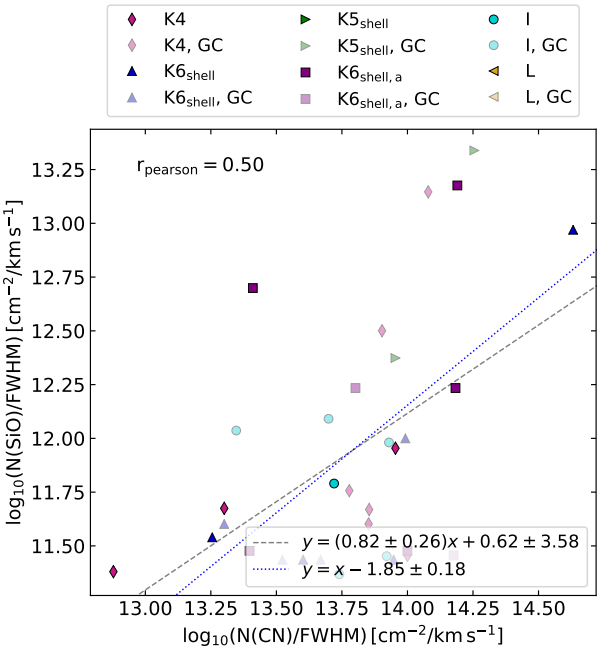

Figure A.94: Same as Fig. 3.9, but for SiO and CN.

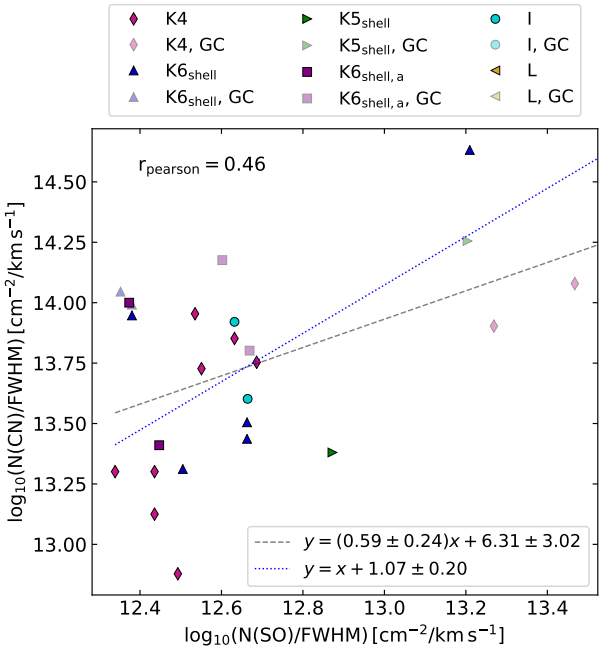

Figure A.95: Same as Fig. 3.9, but for CN and SO.

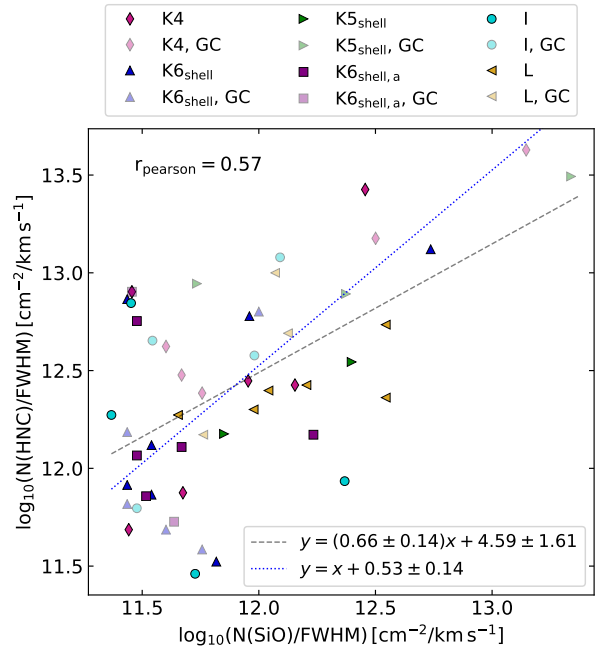

Figure A.96: Same as Fig. 3.9, but for HNC and SiO.

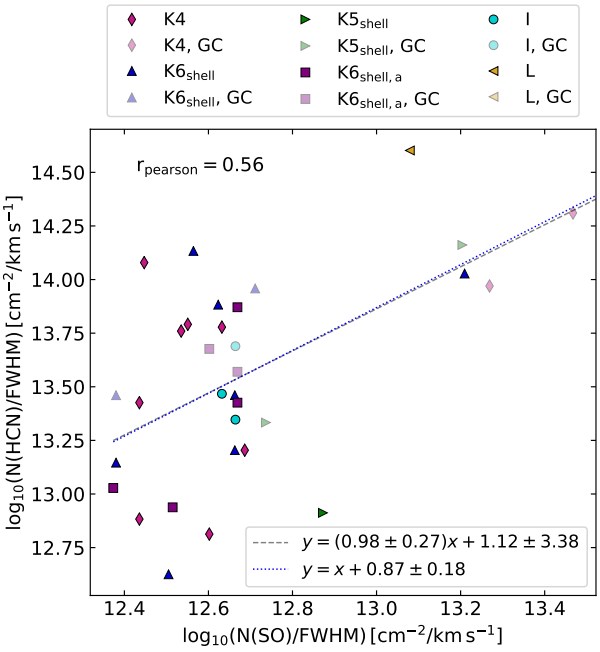

Figure A.97: Same as Fig. 3.9, but for HCN and SO.

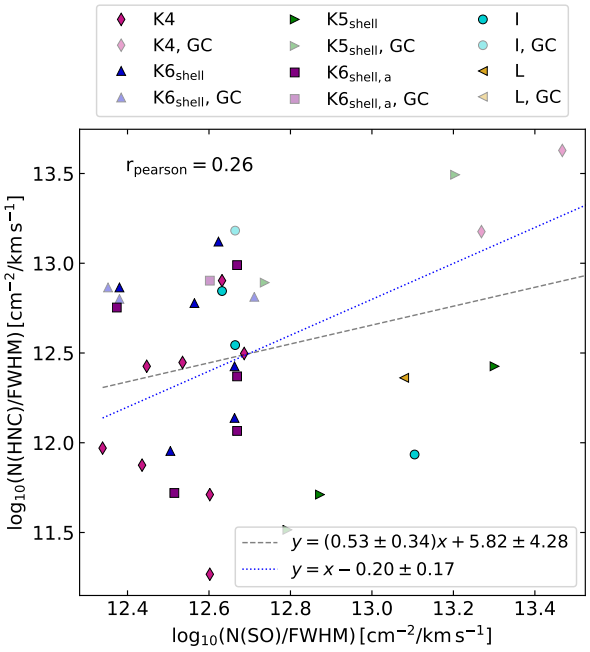

Figure A.98: Same as Fig. 3.9, but for HNC and SO.

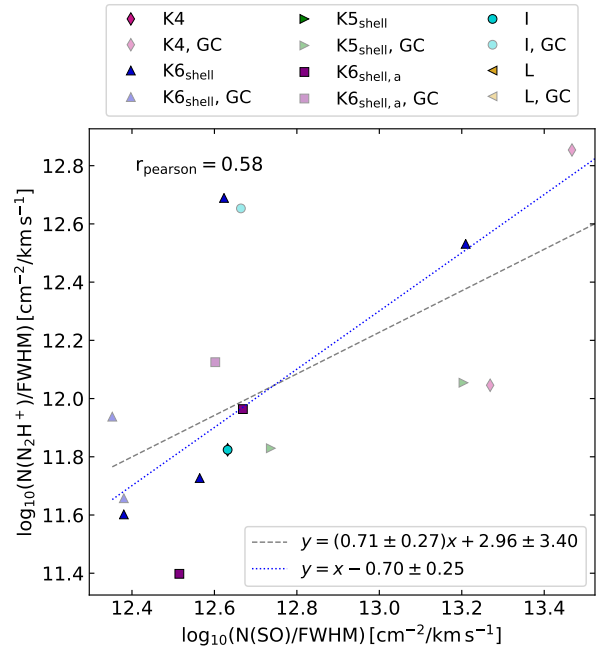

Figure A.99: Same as Fig. 3.9, but for N_2H^+ and SO.

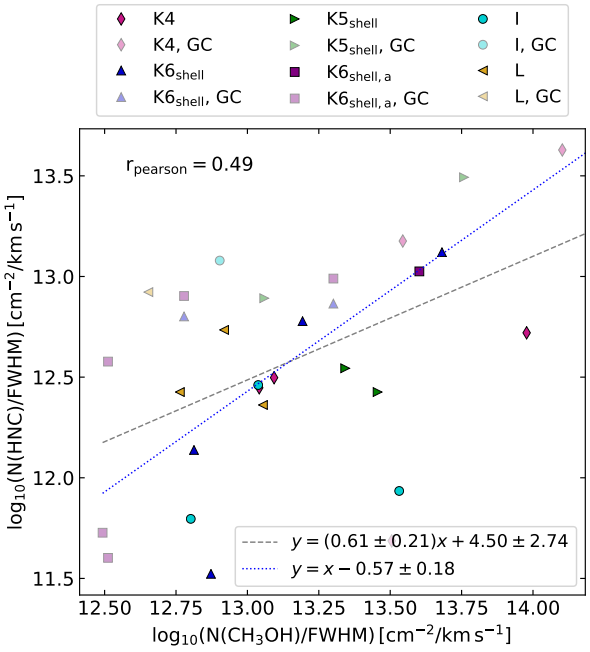

Figure A.100: Same as Fig. 3.9, but for HNC and CH_3OH.

A.9 Isotopic ratios

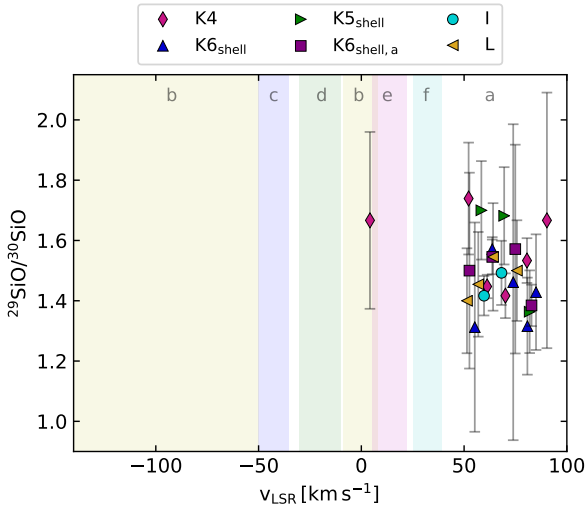

Figure A.101: Same as Fig. 3.10, but for $^{29}SiO/^{30}SiO$.

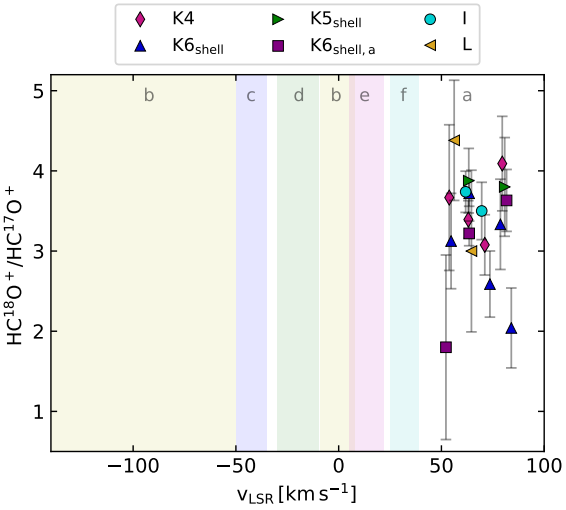

Figure A.102: Same as Fig. 3.10, but for $HC^{18}O^+/HC^{17}O^+$.

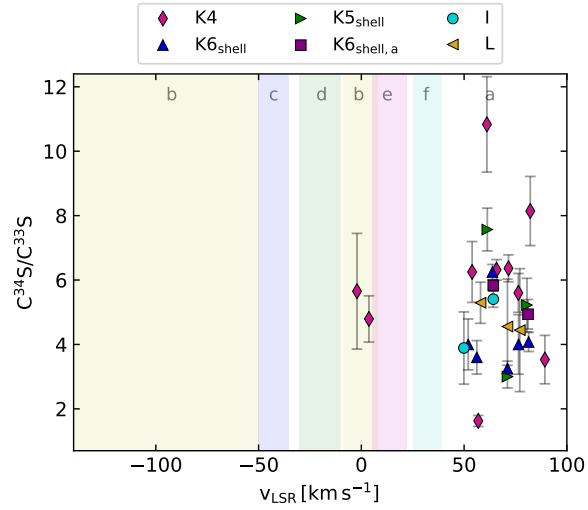

Figure A.103: Same as Fig. 3.10, but for $C^{34}S/C^{33}S$.

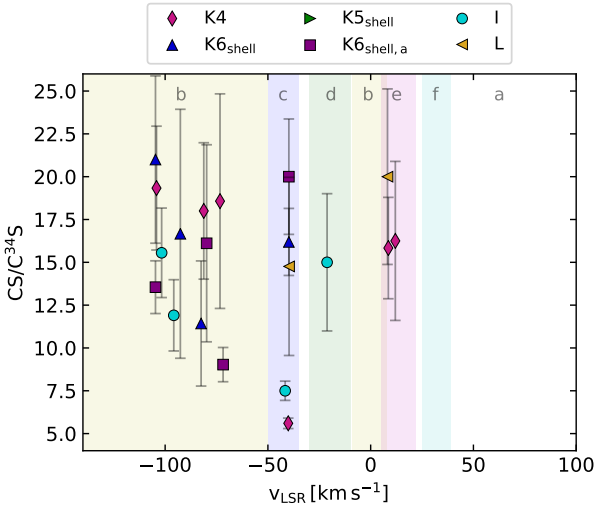

Figure A.104: Same as Fig. 3.10, but for $CS/C^{34}S$.

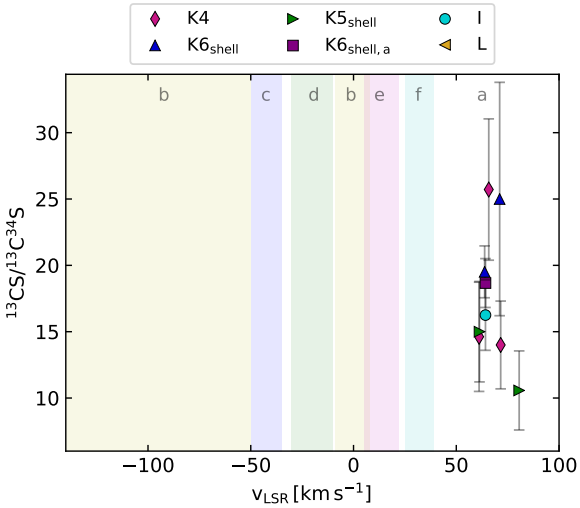

Figure A.105: Same as Fig. 3.10, but for $^{13}CS/^{13}C^{34}S$.

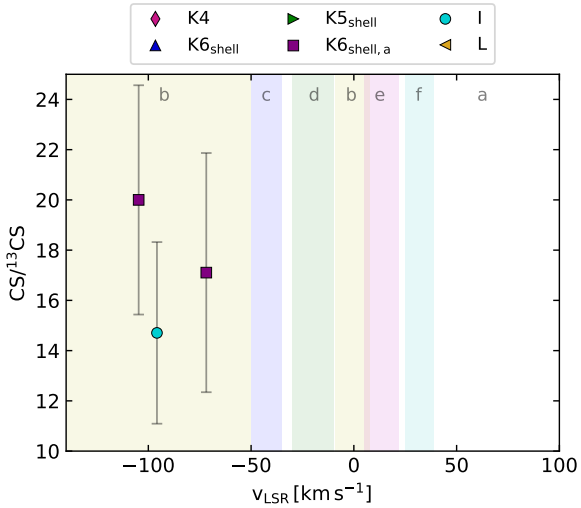

Figure A.106: Same as Fig. 3.10, but for $CS/^{13}CS$.

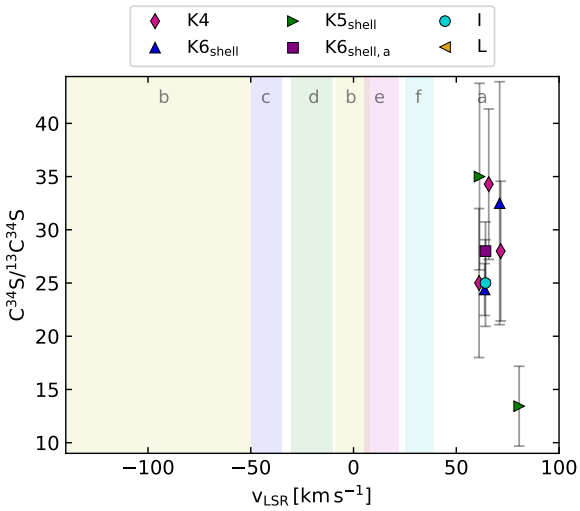

Figure A.107: Same as Fig. 3.10, but for $C^{34}S/^{13}C^{34}S$.

A.10 Statistics of $FWHM$

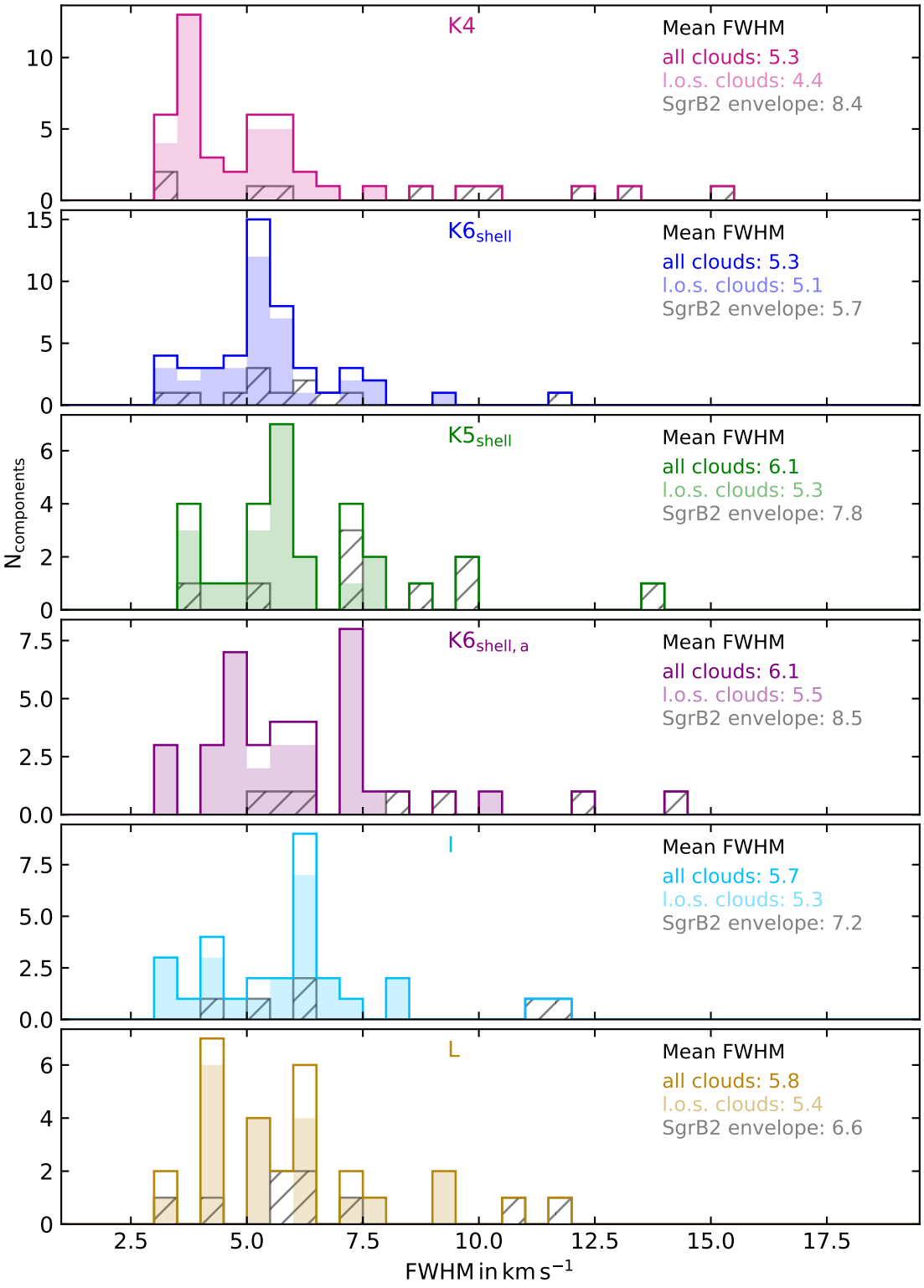

Figure A.108: Same as Fig. 3.7, but only for the molecules CH_3OH, SiO, and SO.

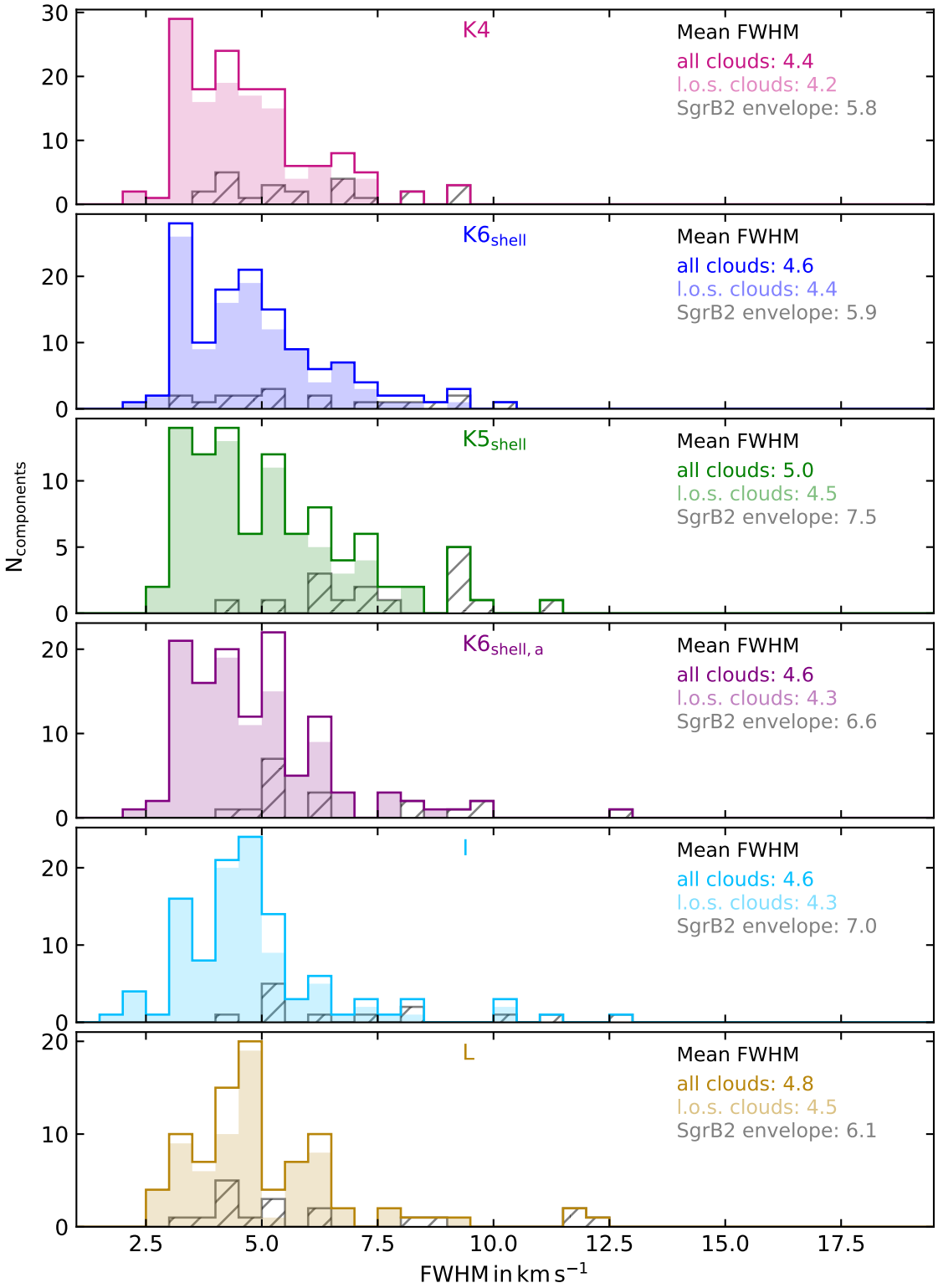

Figure A.109: Same as Fig. 3.7, but only for the molecules CCH, CN, CS, HNC, and HCN.

Appendix B

Complex organic molecules in diffuse clouds along the line of sight to Sgr B2

B.1 Additional figures

B.2 Additional tables

Table B.1: Rest frequencies (ν_0), upper energy levels ($E_{\rm up}$) and Einstein coefficients for spontaneous emission ($A_{\rm u,l}$) from upper level u to lower level l of the molecular transitions investigated in this work.

Molecule	Transition	ν_0 [MHz]	$E_{\rm up}$ [K]	$A_{\rm u,l}$ [$\rm s^{-1}$]
$H^{13}CO^+$	$1-0$	86754.288	4.2	3.85×10^{-5}
c-C_3H_2-o	$2_{1,2}-1_{0,1}$	85338.894	4.1	2.32×10^{-5}
CH_3OH	$2_{0,1,0}-1_{0,1,0}$	96741.371	7.0	3.41×10^{-6}
$^{13}CH_3OH$	$2_{0,2,0}-1_{0,1,0}$	94407.129	6.8	3.17×10^{-6}
CH_3CN	$5_{0,0}-4_{0,0}$	91987.088	13.2	6.33×10^{-5}
	$6_{0,0}-5_{0,0}$	110383.500	18.5	1.11×10^{-4}
CH_3CHO	$2_{1,2,0}-1_{0,1,0}$	84219.749	5.0	3.38×10^{-6}
	$5_{0,5,0}-4_{0,4,0}$	95963.459	13.8	2.95×10^{-5}
	$3_{1,3,1}-2_{0,2,2}$	101343.441	7.7	3.91×10^{-6}
HC_3N	$10-9$	90979.023	24.0	5.81×10^{-5}
	$11-10$	100076.392	28.8	7.77×10^{-5}
NH_2CHO	$4_{0,4}-3_{0,3}$	84542.330	10.2	4.09×10^{-5}
	$4_{1,3}-3_{1,2}$	87848.874	13.5	4.30×10^{-5}
	$5_{1,5}-4_{1,4}$	102064.267	17.7	7.06×10^{-5}
	$5_{0,5}-4_{0,4}$	105464.219	15.2	8.11×10^{-5}

Table B.2: H I and H_2 column densities and molecular hydrogen fraction f_{H_2} determined by Winkel et al. (2017), and abundance of methanol relative to H_2.

$v_{\rm LSR}$ [$\rm km\,s^{-1}$]	$N_{\rm H\,I}$ [$\rm cm^{-2}$]	N_{H_2} [$\rm cm^{-2}$]	f_{H_2}	$\frac{N_{CH_3OH}}{N_{H_2}}$
26.7	4.7×10^{20}	5.3×10^{20}	0.70	1.2×10^{-7}
9.4	4.7×10^{21}	4.7×10^{21}	0.55	8.1×10^{-8}
3.4	6.9×10^{21}	1.9×10^{21}	0.36	2.0×10^{-7}
−2.8	6.3×10^{21}	1.7×10^{21}	0.40	1.2×10^{-7}

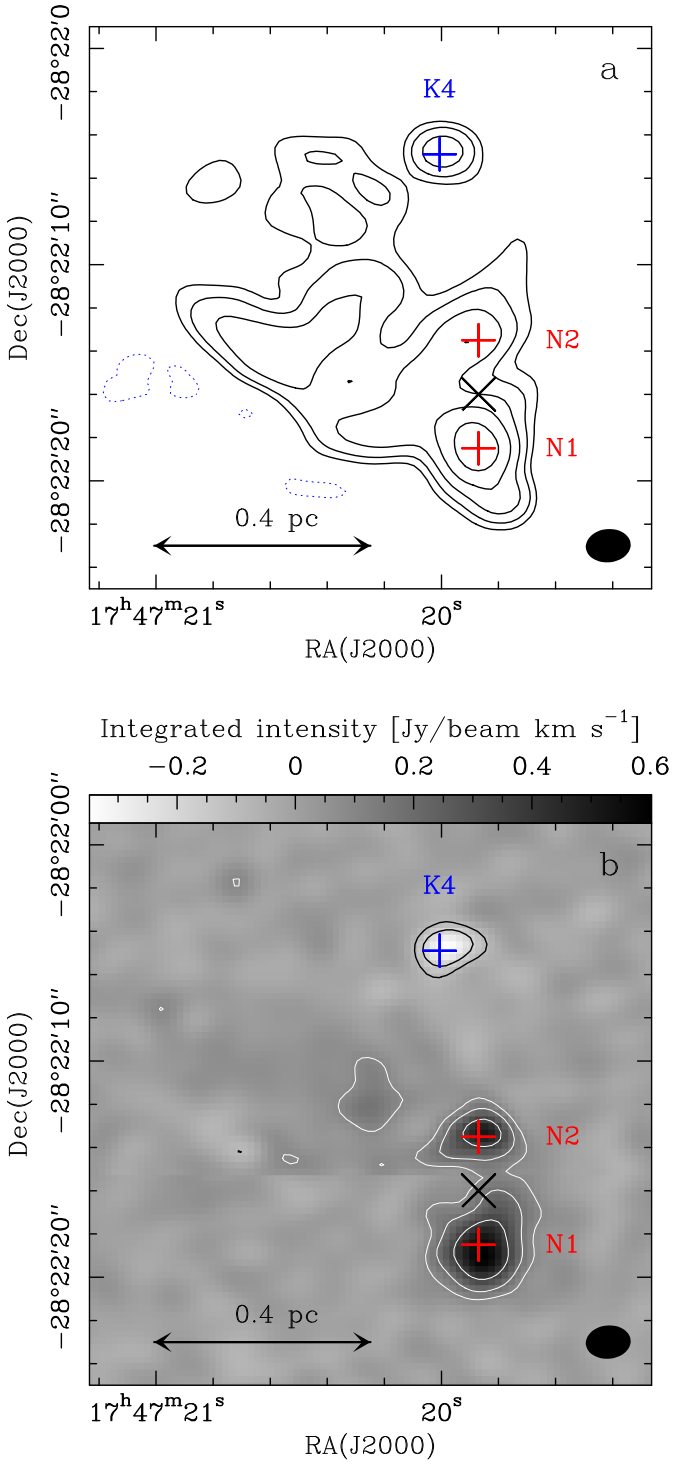

Figure B.1: **a** ALMA continuum map of the Sgr B2(N) region at 85 GHz. The level of the first contour (positive as black solid line and negative as dashed blue line) is 5σ, with σ the rms noise level of 5.4 mJy/beam. The contour step doubles at each contour. **b** Integrated intensity map of the NH_2CHO absorption of the GC diffuse clouds (v_{LSR} = −8.9–6.6 km s^{-1}) at 84.5 GHz. The first contour level (positive in white and negative in black) is 5σ, with σ = 17.7 mJy/beam km s^{-1}. The contour step doubles at each contour. The grey-scale is indicated at the top. The continuum emission was subtracted. In both panels, the filled ellipse shows the synthesised beam (2.1″ × 1.5″), the black cross indicates the phase centre, the red crosses the positions of the hot cores Sgr B2(N1) and Sgr B2(N2), and the blue cross the position of the ultracompact H II region K4.

Appendix C

Small-scale physical and chemical structure of diffuse and translucent molecular clouds along the line of sight to Sgr B2

C.1 Powell's method

Powell's conjugate direction method works in an n-dimensional space, where n is the number of free parameters. The starting point in this n-dimensional space is defined by the initial guesses x_i of the n parameters to fit, with i between 1 and n. The initial guesses define a position in the n-dimensional space: $\vec{p}_0 = (x_1, x_2, ...x_n)$. To converge towards the best-fit parameters, a set of search vectors is needed along which the minimisation is done. The set of n starting vectors $\vec{\xi}_i$ is built by n linearly independent directions. The initial set of search vectors is simply taken parallel to the parameter axes in the n-dimensional space.

The Powell minimisation procedure comprises an inner loop and an outer loop. During the inner loop the minimum in each current direction, that is along each search vector $\vec{\xi}_i$, is determined. The resulting minima along all directions give a new position $\vec{p}_1$ in the n-dimensional space. The vector difference $\Delta\vec{p} = \vec{p}_1 - \vec{p}_0$ between the optimised point $\vec{p}_1$ and the starting point $\vec{p}_0$ is added to the set of search vectors and the vector $\vec{\xi}_i$ which is contributing the most to the new position is removed. The most contributing vector is the one with the smallest angle to the new search vector $\Delta\vec{p}$. The outer loop repeats the process until a given tolerance criterion is met, which can be a maximum number of iterations or a given noise level.

C.2 Automatisation programme

This appendix describes the algorithm of our python programme that fits the absorption spectra automatically (Sect. 5.3.5). The process is done in several iterations. The parameters of the synthetic spectrum resulting from the previous iteration are taken as initial guesses for the next iteration. The following parameters are fitted: the decimal logarithm of the column density $\log_{10}(N_{\rm tot})$, the width $FWHM$, and the centroid velocity v_0 of each velocity component. Different probability distributions around the initial guesses are chosen for these three parameters. The probability distribution for the velocity is uniform over the chosen interval (± 3 km s^{-1}); the probability distribution for the $FWHM$ is a truncated normal distribution with a width of 3 km s^{-1} peaked at the initial guess over the range defined by the channel width as a minimum value and a maximum value of 30 km s^{-1}; the probability distribution for the logarithm of the column density is a normal distribution peaked around the initial guess with a width of 2 (that is two orders of magnitude for the density). The starting points are not the exact initial guesses but randomly selected points around the values following the probability distributions. The procedure follows this sequence:

1. Baseline subtraction for each position using the command base in the GILDAS package CLASS. This yields the continuum level and the spectral line noise level of each spectrum.

2. Search in the continuum-subtracted spectrum for absorption dips with a peak signal-to-noise ratio higher than 4 ($-I_\mathrm{l} \geq 4\sigma$). The programme searches for all channels fulfilling this condition and keeps only those that have $|I_\mathrm{l}|$ higher than their surrounding channels (two channels in each direction). The velocities v_i of these selected channels are then used to fit the spectrum and obtain initial guesses for the column densities $N_\mathrm{tot,i}$ and linewidths $FWHM_i$.

3. Fit of the spectrum performed step by step in four partially overlapping velocity ranges ([-121, -58] km s^{-1}, [-66, -8] km s^{-1}, [-16, 48] km s^{-1}, [40, 100] km s^{-1}). Only the parameters of the components whose initial guess for the centroid velocity is in the currently fitted interval are fitted. The parameters of the other components are kept fixed to their initial guesses for the components in the next velocity range or to their fitted values for the components in the previous velocity range.

   The step-by-step fitting in four velocity ranges is a useful procedure to reduce the computing time. If the maximum number of iterations is executed without reaching the tolerance limit of 2σ, the fit is repeated up to five times (with randomly chosen initial guesses), but in the fourth iteration the noise-tolerance limit is increased to a higher value of 10σ. This step is needed in the cases where the absorption caused by the envelope of Sgr B2 contains channels with $|I_\mathrm{l}| > I_\mathrm{c} + 2\sigma$.

4. Validation of the fit. The aim is to look for missing components which were not identified as peaks at step 2. The programme looks for peaks above a threshold of 5σ in the residuals. The peak velocities of these new components are then used and kept fixed to fit the residuals and estimate their column densities and linewidths. These estimates are used as initial guesses for these new components at step 5.

5. Repeat step 3 once more and then go to step 6.

6. Final check for missing components. The programme repeats step 4 (and step 3), but with a lower threshold of 4σ, then goes to step 7.

7. To get the final synthetic spectrum, the n velocity components are fitted step by step in $n-2$ iterations. Only three components are fitted at once at each iteration, starting with the first three velocity components and then shifting by one component at each subsequent iteration. The best-fit values of the first velocity component of each processed set of three components are kept fixed at the next iterations and the best-fit values of the second and third velocity components are used as initial guesses for the next iteration. This step-by-step fitting procedure decreases the computing time.

   In the case where the fit was not successful for one of the $n-2$ iterations, 11 more repetitions of this fitting procedure are possible. During the repetitions several changes are made in the fitting conditions. The changes are necessary in some cases in order to get a good result. These changes were included after analysing the problems resulting in an unsuccessful fit using a randomly chosen small subsample of the data. The first problem is caused by the optical thickness of absorption lines from the envelope of Sgr B2. The estimated column densities sometimes exhibit very high values up to 10^{17} cm^{-2} which results sometimes in computing problems. Hence, after the third repetition high initial guesses for the column densities in the envelope of Sgr B2 are reduced to 10^{13} cm^{-2} to avoid starting values higher than 10^{15} cm^{-2} for these components. If this still does not result in a successful fit, the reason may be the limited velocity interval in which each peak velocity can be varied to find the best solution. After the sixth repetition the range for the velocity is increased from 6 km s^{-1} to 10 km s^{-1}. If this still does not help the tolerance limit is increased after the ninth iteration.

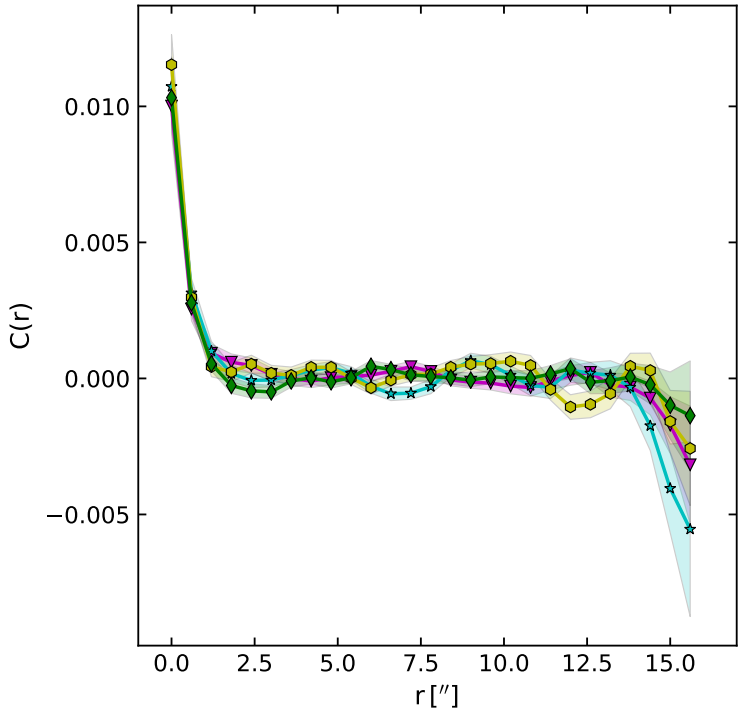

Figure C.1: Two-point auto-correlation function $C(r)$ of four different noise channels next to the transition of c-C_3H_2 as a function of pixel separation r. The coloured regions around the curves represent the standard deviation of the 1000 realisations of the opacity cube.

We check the centroid velocities of the components before each fitting because the presence of two components lying too close to each other leads to calculation problems due to the ambiguity of these components. Therefore, when the velocity difference between two components is smaller than two channels (~3.5 km s^{-1}) we remove the second component. In the case of three components following each other over a velocity range smaller than three channels (~5.3 km s^{-1}), we remove the middle component. Due to this selection of the centroid velocities, the programme seldom fits only one velocity component to the peak at a velocity of about 3 km s^{-1} (see Fig. 5.3).

C.3 Influence of noise

C.3.1 Two-point auto-correlation functions

To evaluate the influence of noise on the two-point auto-correlation functions $C(r)$, we calculated C for several noise channels. In Fig. C.1 the two-point auto-correlation functions of four noise channels next to the transition of c-C_3H_2 are depicted. $C(r)$ shows a correlation at pixel separations smaller than about 2″ which corresponds to the size of the major axis of the beam. At larger pixel separations, $C(r)$ is overall consistent with zero within 3σ.

The signal-to-noise ratios ($C(r)/\sigma_C$) of 48 noise channels (four per molecule) are shown in Fig. C.2. Beyond the separation of 2″ mentioned above, most SNRs are below 3. For separations between 2″ and 6″, some outliers have SNRs between 3 and 5, and only a handful have SNRs between 5 and 6. Beyond 6″, all outliers have SNRs below 4. Therefore, we conclude that the correlation function of a channel containing signal will show a significant correlation beyond 2″ only when $C(r)/\sigma_C$ is higher than 5 for $r < 6''$ and

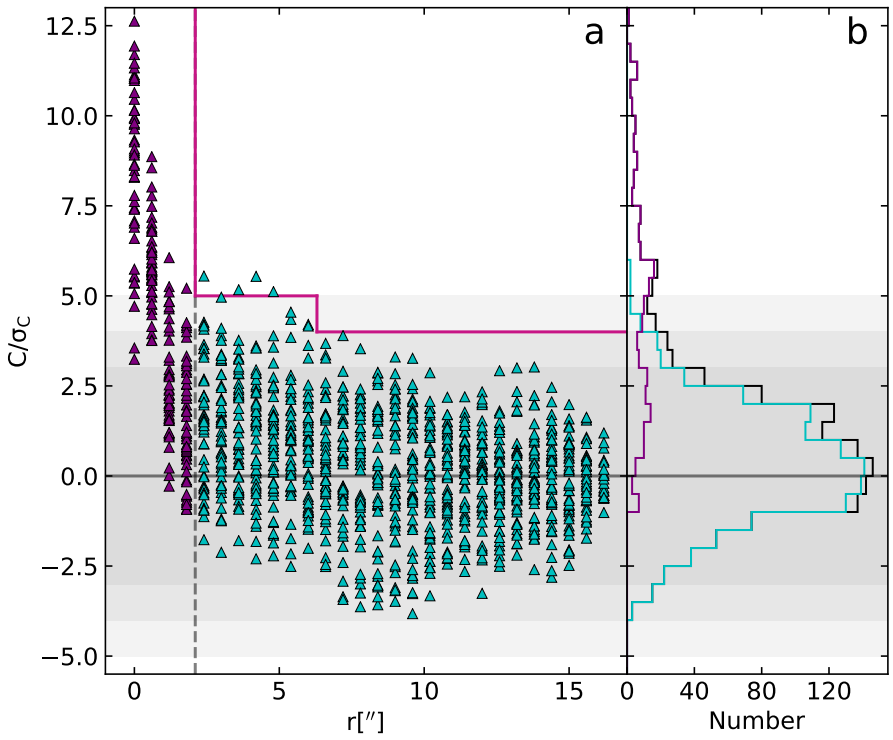

Figure C.2: **a** Signal-to-noise ratio (SNR) of the two-point auto-correlation functions ($C(r)/\sigma_C$) of 48 noise channels, four per molecule, as a function of pixel separation r. All points at pixel separations smaller than the beam are coloured in purple, the other ones in cyan. The vertical dashed line at 2″ corresponds to the major axis of the beam. The area above and to the right of the magenta line is the area where the correlation function of a channel containing signal indicates a significant correlation. **b** Distribution of C/σ_C. The regions of SNR smaller than 3, 4, and 5 are highlighted in shades of grey.

higher than 4 beyond 6″. This condition corresponds to the area located to the right and above the magenta line shown in Fig. C.2.

C.3.2 Probability distribution functions

We investigate here the influence of the noise on the PDFs of the opacity maps. The PDF of c-C_3H_2 at a velocity of $-39.7\,\mathrm{km\,s^{-1}}$ is plotted in Fig. C.3a using all pixels and in panel b after masking the pixels below $3\sigma_{\mathrm{noise}}$. The tail that is visible on the left side of the PDF in panel a is much attenuated in panel b. This tail is therefore dominated by the noise. The noise affects the main properties of the PDF as well. The parameters derived from the Gaussian fit change slightly after masking the noisy pixels, in particular the width is reduced by 10%.

C.3.3 PCA

We investigate here the influence of the noise on the PCA. We perform the PCA for six molecules, using channels that contain only noise. The first two correlation wheels are displayed in Fig. C.4. The power of the first PC is only 30% and the second and third have similar powers of 20.4% and 20.1%. No clear correlation is visible in the wheels. The molecules are randomly distributed in the wheels as expected for noise.

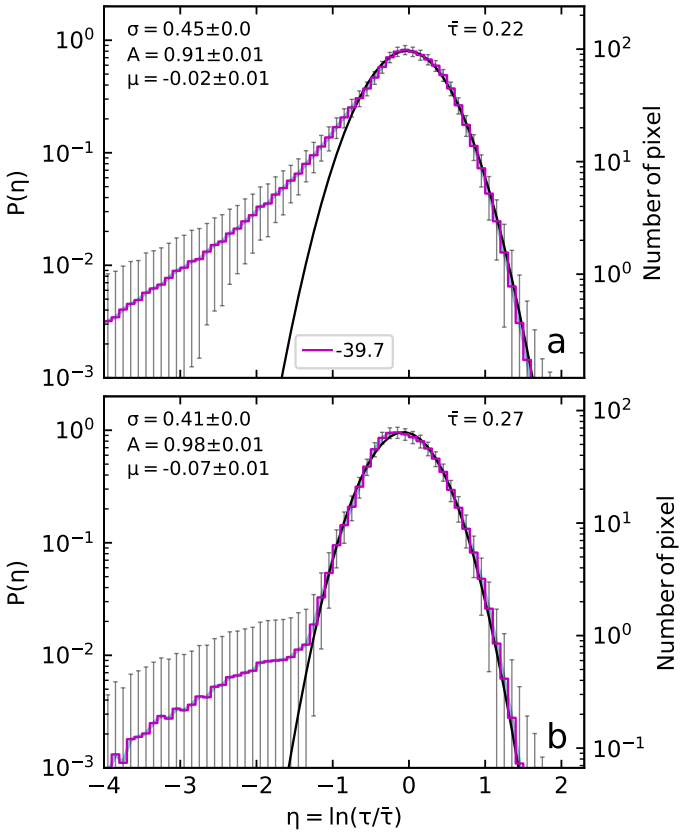

Figure C.3: **a** PDF of c-C_3H_2 using all pixels at a velocity of $-39.7\,\mathrm{km\,s^{-1}}$. **b** PDF of the same velocity component but using only the pixels $\tau/\sigma_\tau > 3$. The results of the Gaussian fit, integral A, dispersion σ, and centre μ, are indicated in the top left corner of each panel. The mean opacity $\bar{\tau}$ is indicated in the top right corner.

C.4 Robustness of PCA

We perform several tests to check the robustness of the principal component analysis applied to our data. First, we test different grid sizes. In the following, a grid size of 1, 2, or 3 means that we use every pixel of the original map, every second pixel, or every third pixel, respectively. With a grid size of 3, some information is lost, because the Nyquist-sampling theorem is not fulfilled. The correlation wheels of the velocity component at $v_{\mathrm{LSR}} = 24.7\,\mathrm{km\,s^{-1}}$ are shown in Fig. C.5. The top, middle, and bottom panels correspond to a grid size of 1, 2, and 3, respectively. The percentages in parentheses give the powers of the PCs (their contributions to the total variance of the data). The ellipses around the arrow heads in the middle and bottom panels represent the uncertainties. They were estimated by shifting the grids by one or several pixels. To allow comparison of the PCs resulting from the different starting points of the grid, we realigned them. We chose the first PCA made in the grid sample to fix the signs of the PCs. We changed the signs of the PCs of the other grids to match these signs. We adopted this procedure following Babamoradi et al. (2013). The correlation wheels shown in the top and middle panels are very similar. We conclude that the PCA results do not depend much on the size of the gris and its starting position, provided the Nyquist-sampling condition is met. However, with a grid size of 3 (bottom panels), the uncertainties become larger and the PCA results start to depend significantly on the starting position of the grid.

We investigate in Fig. C.6 the impact of removing one molecule on the PCA results. We show the first

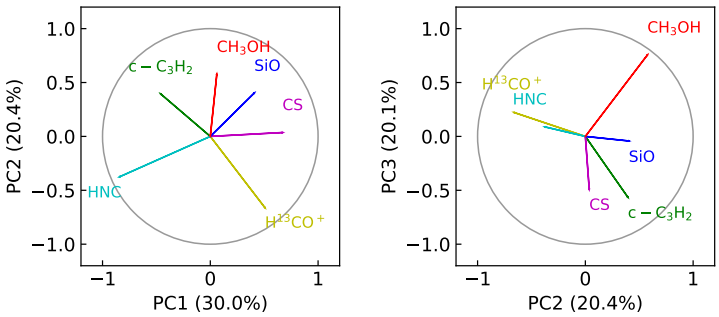

Figure C.4: Correlation wheels for a PCA performed for six molecules using channels that contain only noise. The percentages in parentheses give the contributions of the PCs to the total variance of the data.

correlation wheels at $v_{\rm LSR}$ =24.7 km s^{-1} for grid size 2 in four cases, each one corresponding to one of the four molecules being removed. As long as methanol is used, the PC coefficients are similar to those in Fig. C.5. When methanol is excluded, the PC coefficients change significantly and the power of the first PC is reduced. This means that methanol has a dominant structure for this velocity component.

We investigate in Fig. C.7 the impact of excluding some pixels on the PCA results. We show the first and second correlation wheels for the velocity component at $v_{\rm LSR}$ =24.7 km s^{-1} after excluding 40 pixels (top panels) and 80 pixels (bottom panels). These pixels were chosen randomly and we computed the PCA for 1000 realisations. The ellipses in Fig. C.7 correspond to the dispersion of these 1000 realisations. The results are similar to those in Fig. C.5, except for the molecules with small (< 0.5) PC coefficients.

All together the PCA seems to be robust to all these tests for the velocity component at 24.7 km s^{-1}, for which the first principal component contains most of the variance of the data.

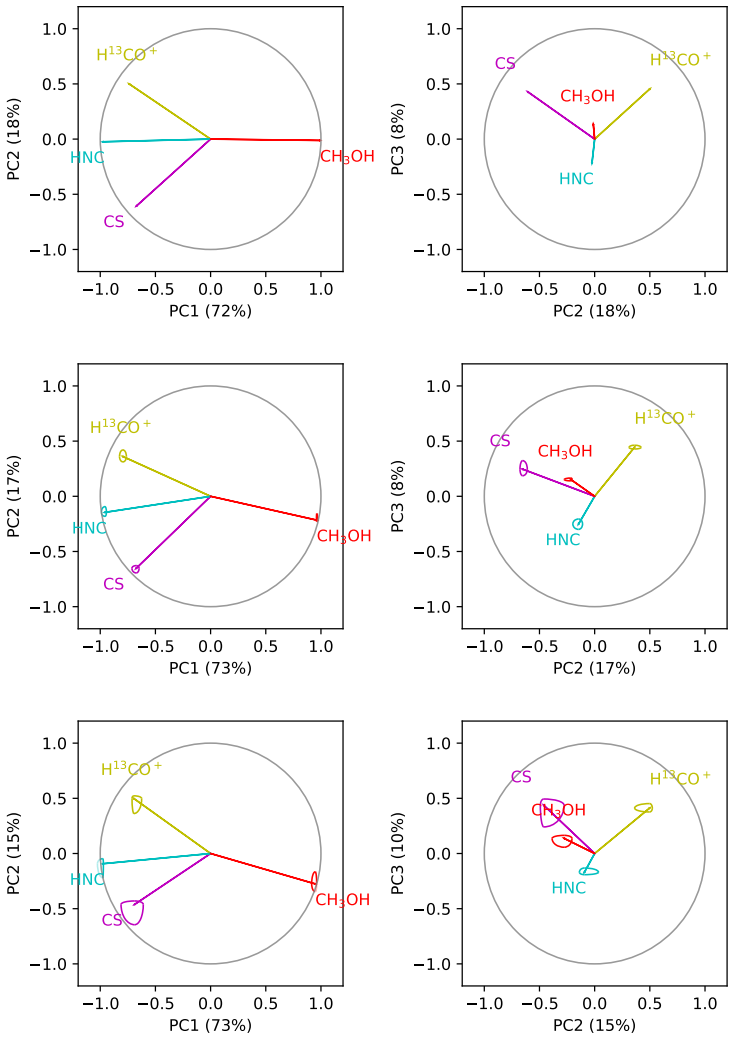

Figure C.5: Correlation wheels for the velocity component at $v_{\mathrm{LSR}} = 24.7\,\mathrm{km\,s^{-1}}$. The percentages in parentheses give the contributions of the PCs to the total variance of the data. The top, middle, and bottom panels represent a grid size of 1, 2, and 3, respectively. The ellipses around the arrow heads in the middle and bottom panels show the uncertainties estimated by shifting the grids.

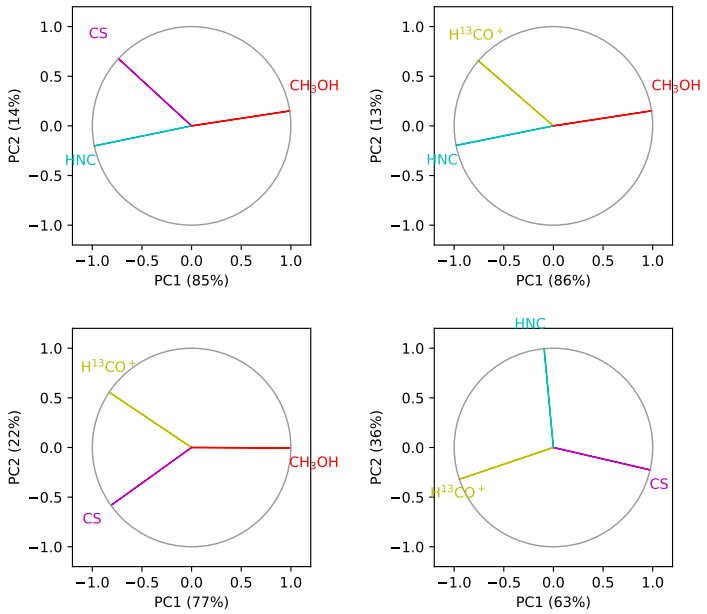

Figure C.6: First correlation wheels for the velocity component at $v_{\rm LSR}$ = 24.7 km s^{-1} for grid size 2. Each panel shows the results of the PCA after removing one of the four molecules used in the middle left panel of Fig. C.5.

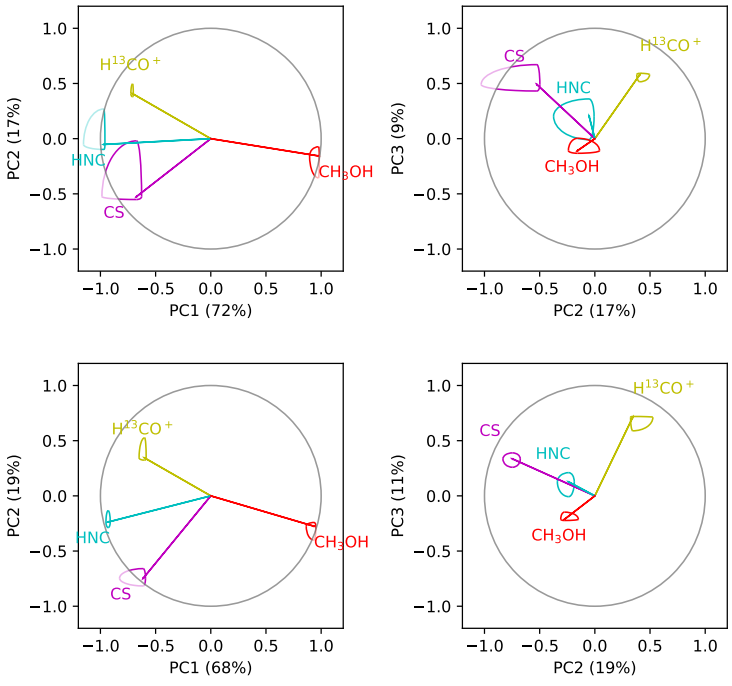

Figure C.7: Correlation wheels for PCs at $v_{\rm LSR}$ =24.7 km s^{-1} for grid size 1 as in Fig. C.5. The first two wheels displayed in the upper panels show the results from the PCA excluding 40 pixels. The wheels in the lower panels the results from excluding 80 pixels. The ellipses around the arrow heads show the uncertainties.

C.5 Spectra

The EMoCA spectra of the 12 investigated molecules towards K4 and the peak of the shell of K6 are shown in Fig. C.8.

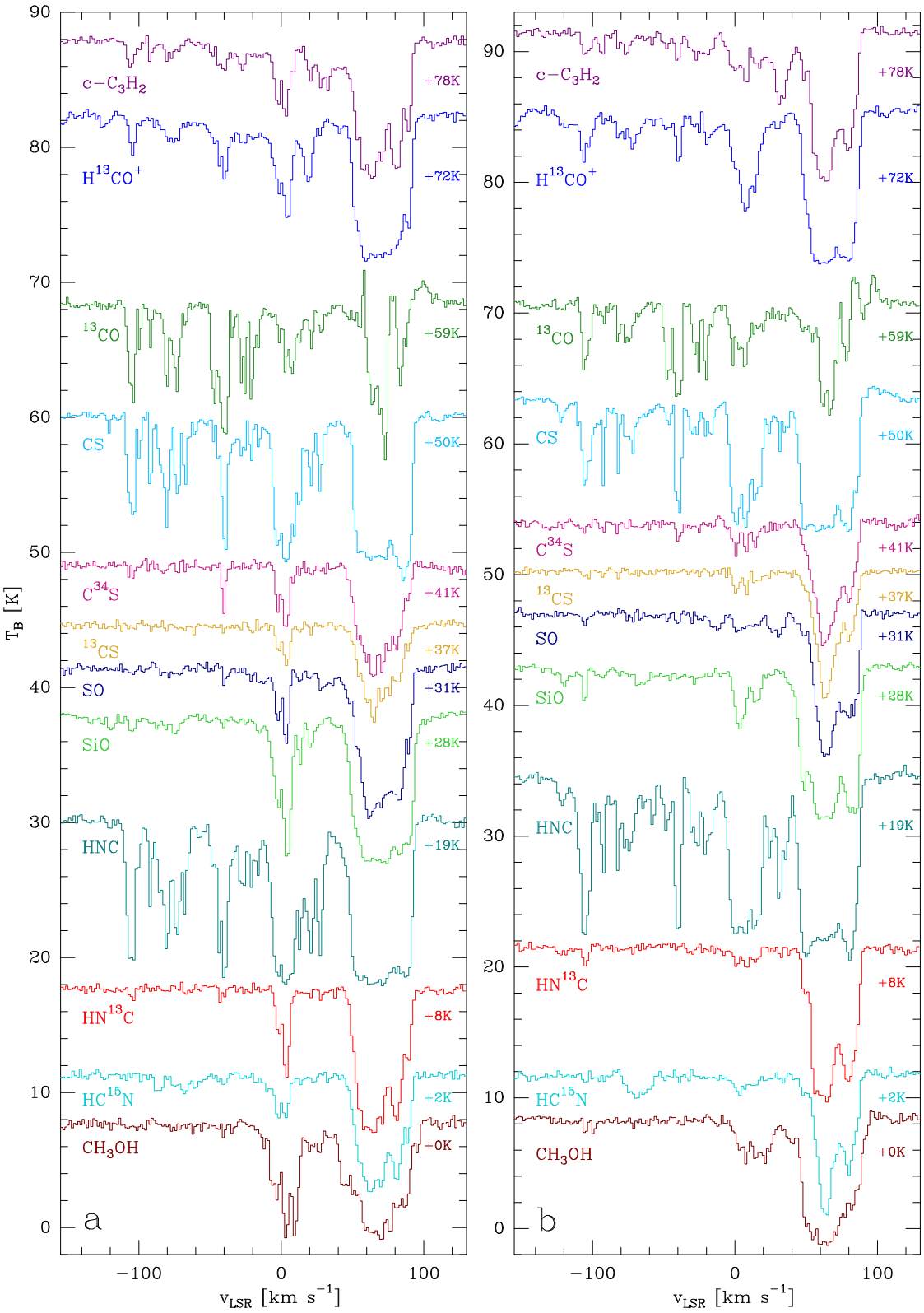

Figure C.8: Spectra of the 12 investigated molecules towards K4 (a) and the peak of the shell of K6 (b). The spectra are shifted vertically by the amount indicated on the right.

C.6 Opacity maps

The opacity and signal-to-noise ratio maps of all molecules except c-C_3H_2 are shown in Figs. C.9–C.30.

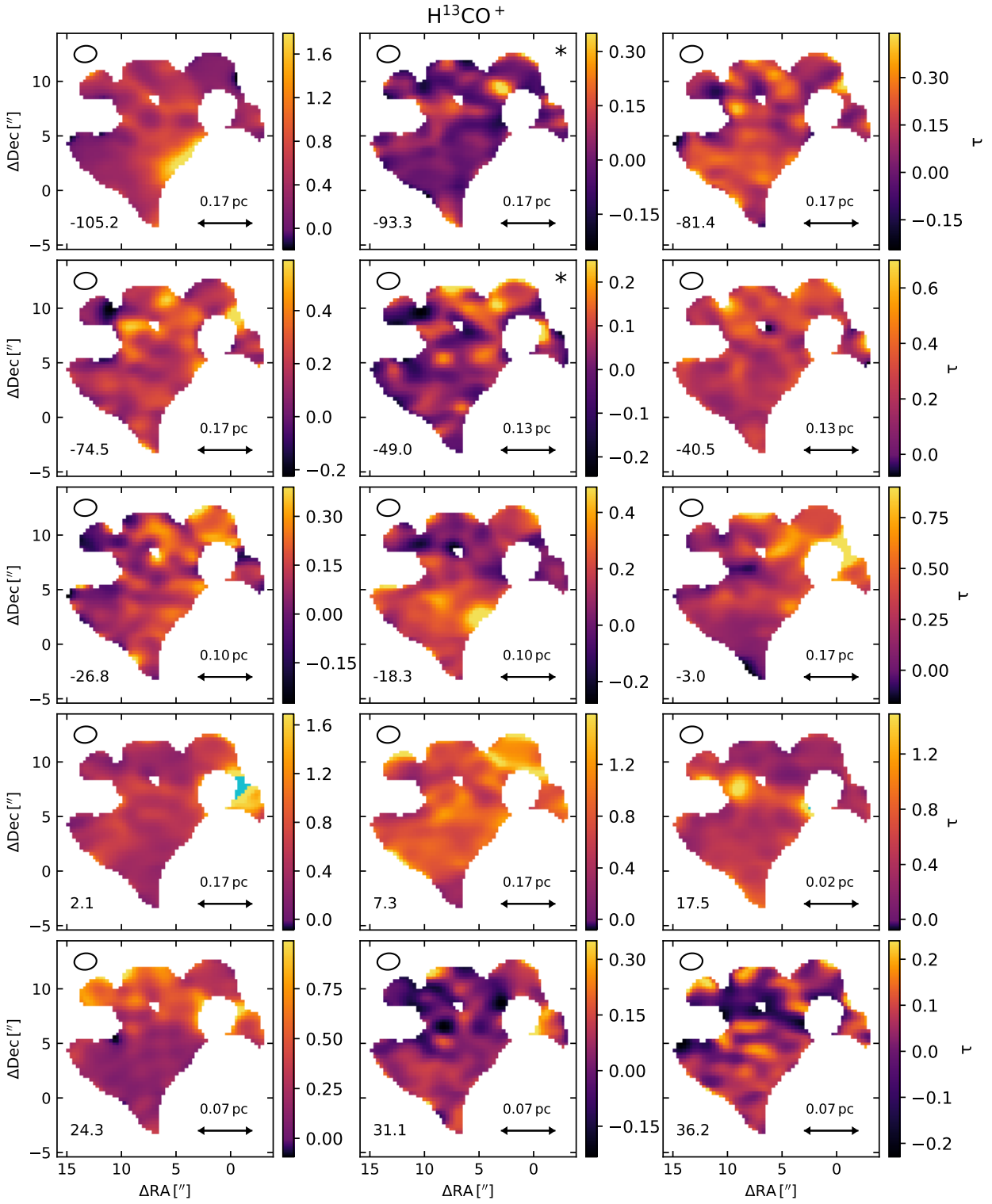

Figure C.9: Same as Fig. 5.6, but for $H^{13}CO^+$. In this figure and the following ones, blue pixels represent pixels that were masked because the absorption is too optically thick.

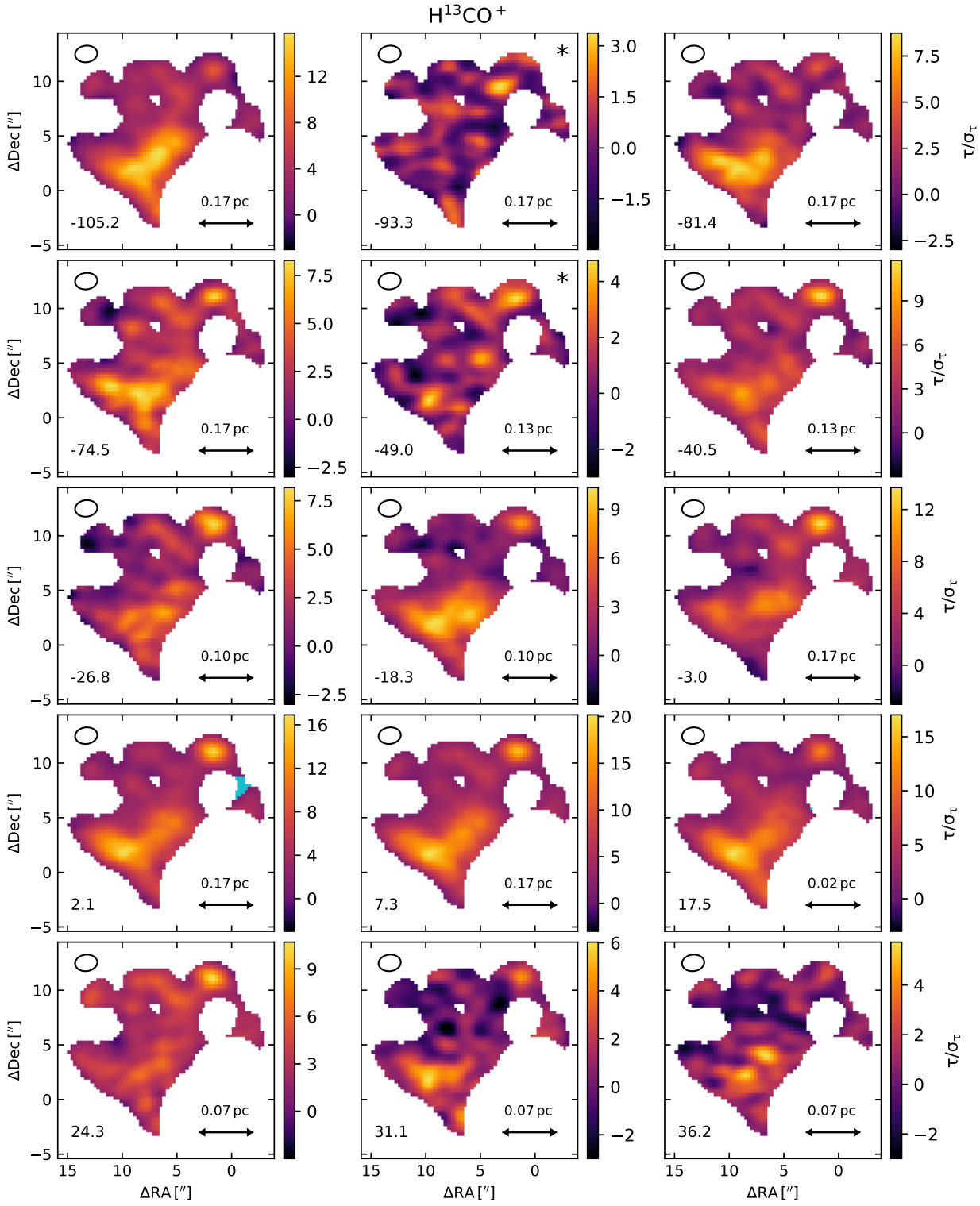

Figure C.10: Same as Fig. 5.7, but for $H^{13}CO^{+}$.

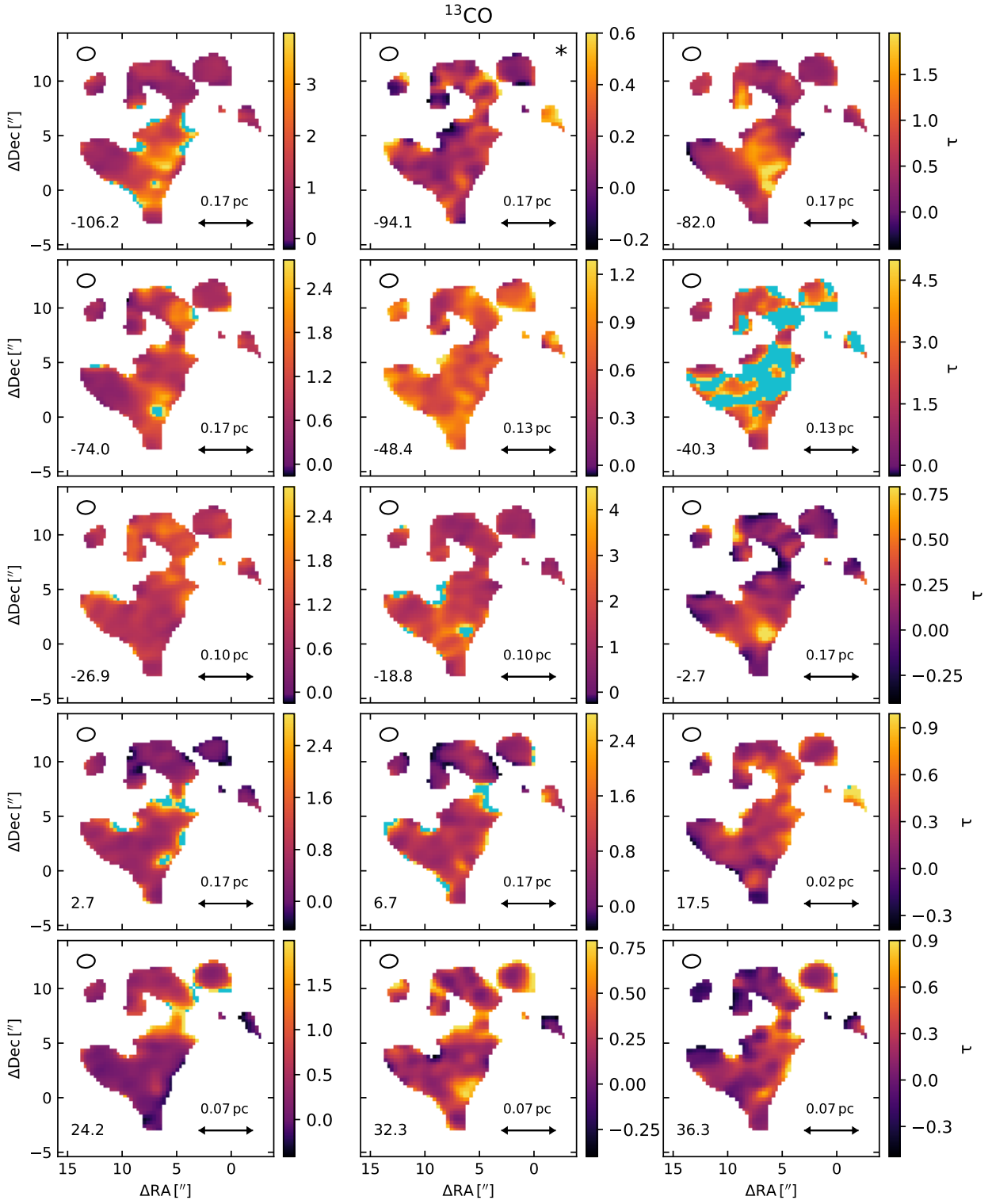

Figure C.11: Same as Fig. 5.6, but for ^{13}CO.

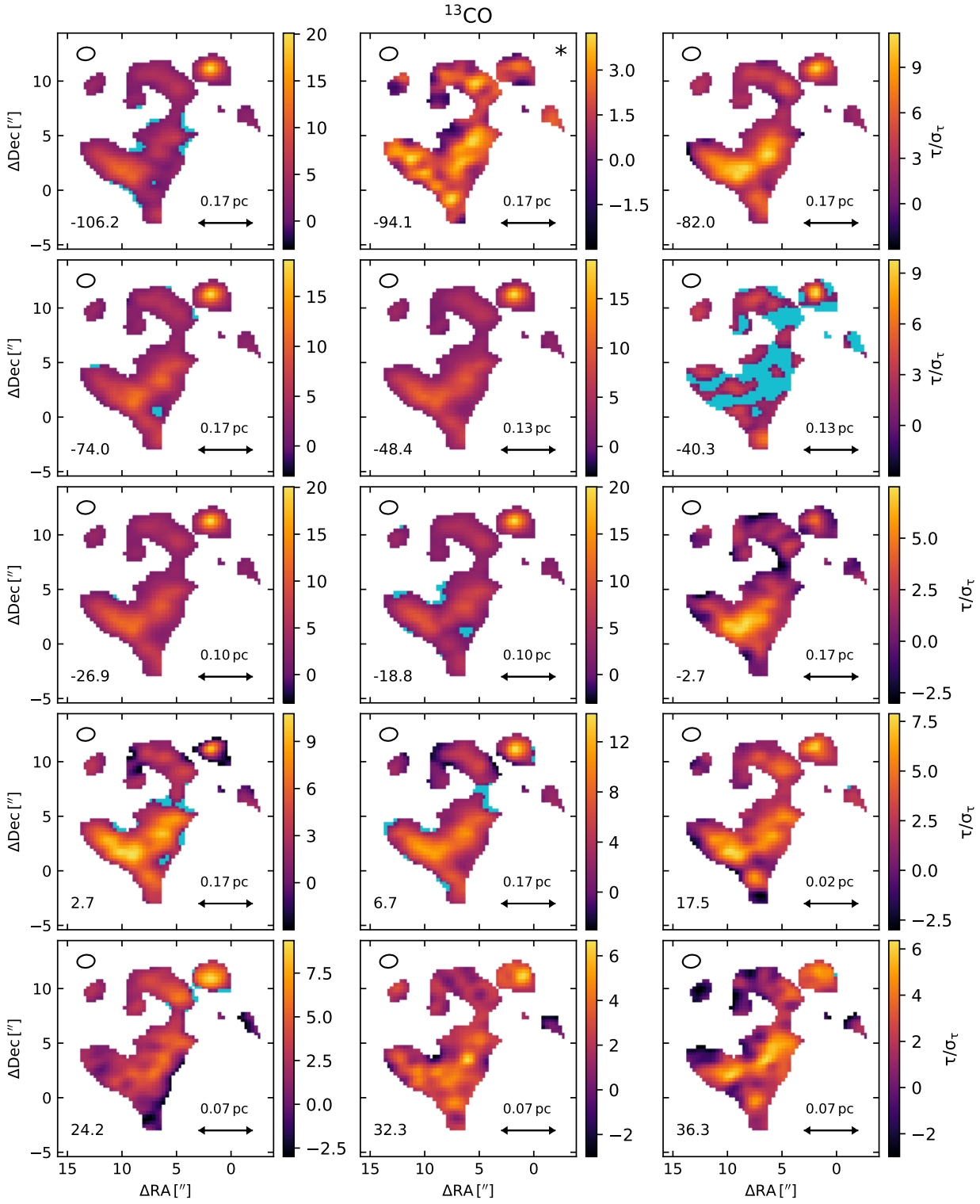

Figure C.12: Same as Fig. 5.7, but for ^{13}CO.

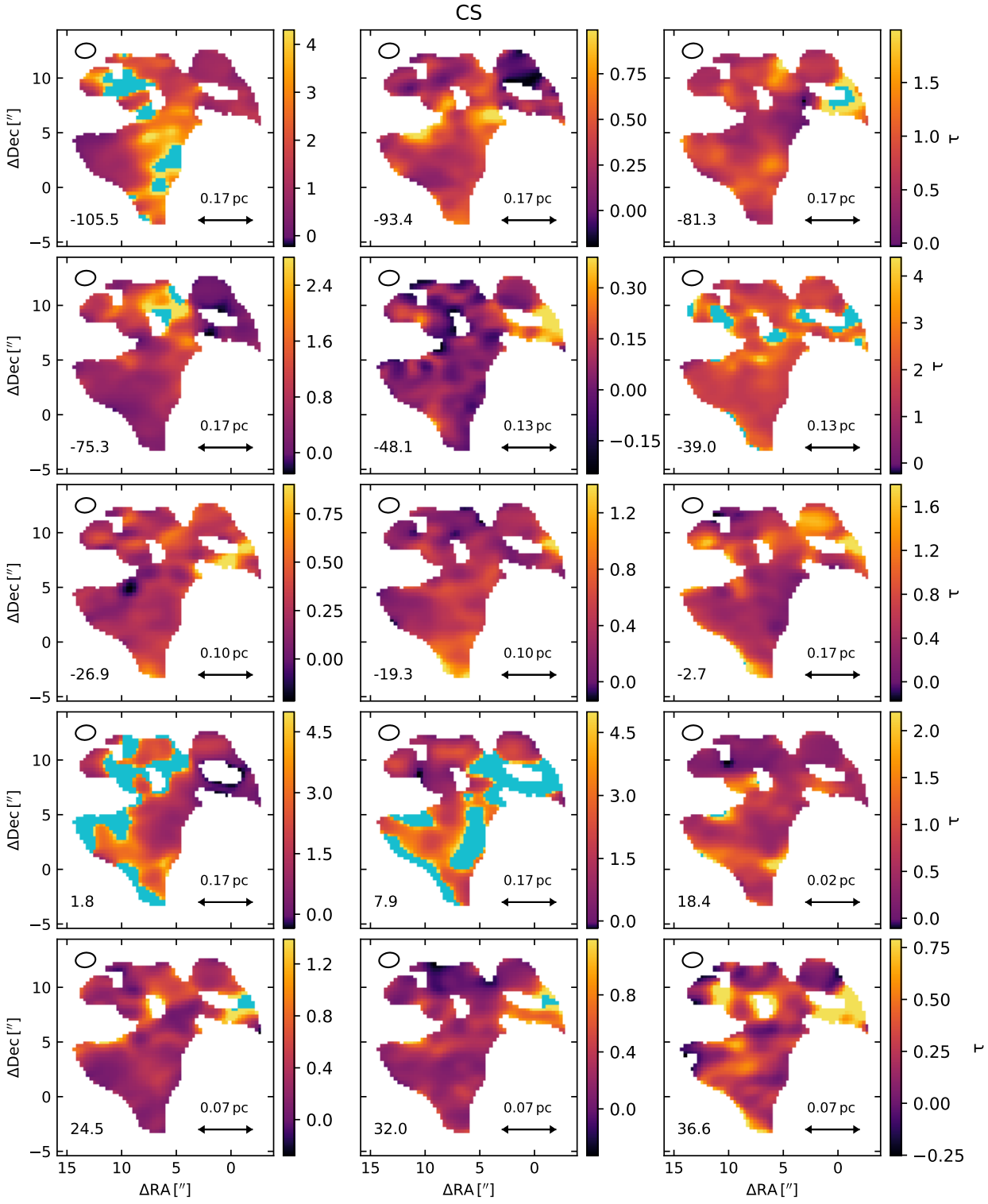

Figure C.13: Same as Fig. 5.6, but for CS.

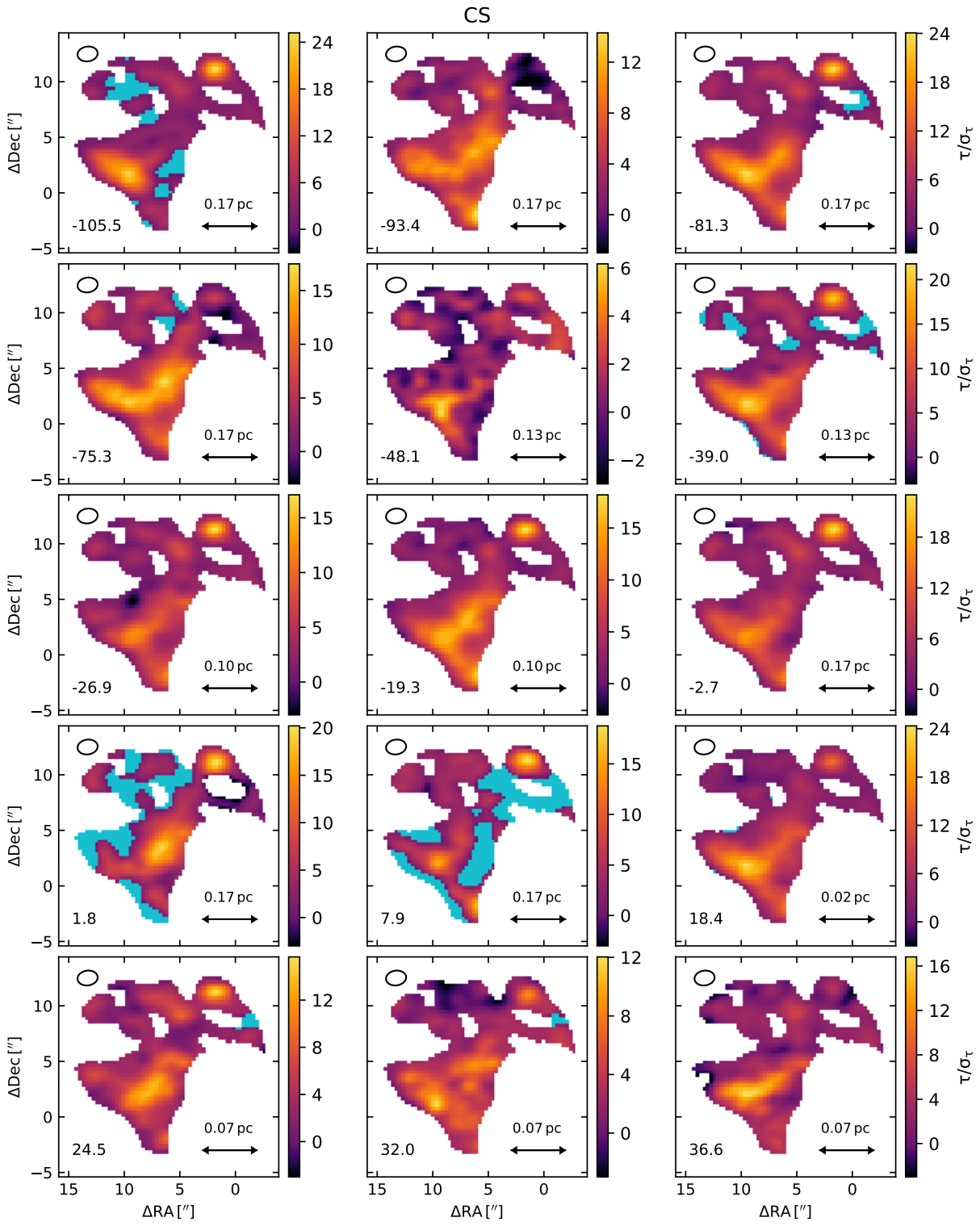

Figure C.14: Same as Fig. 5.7, but for CS.

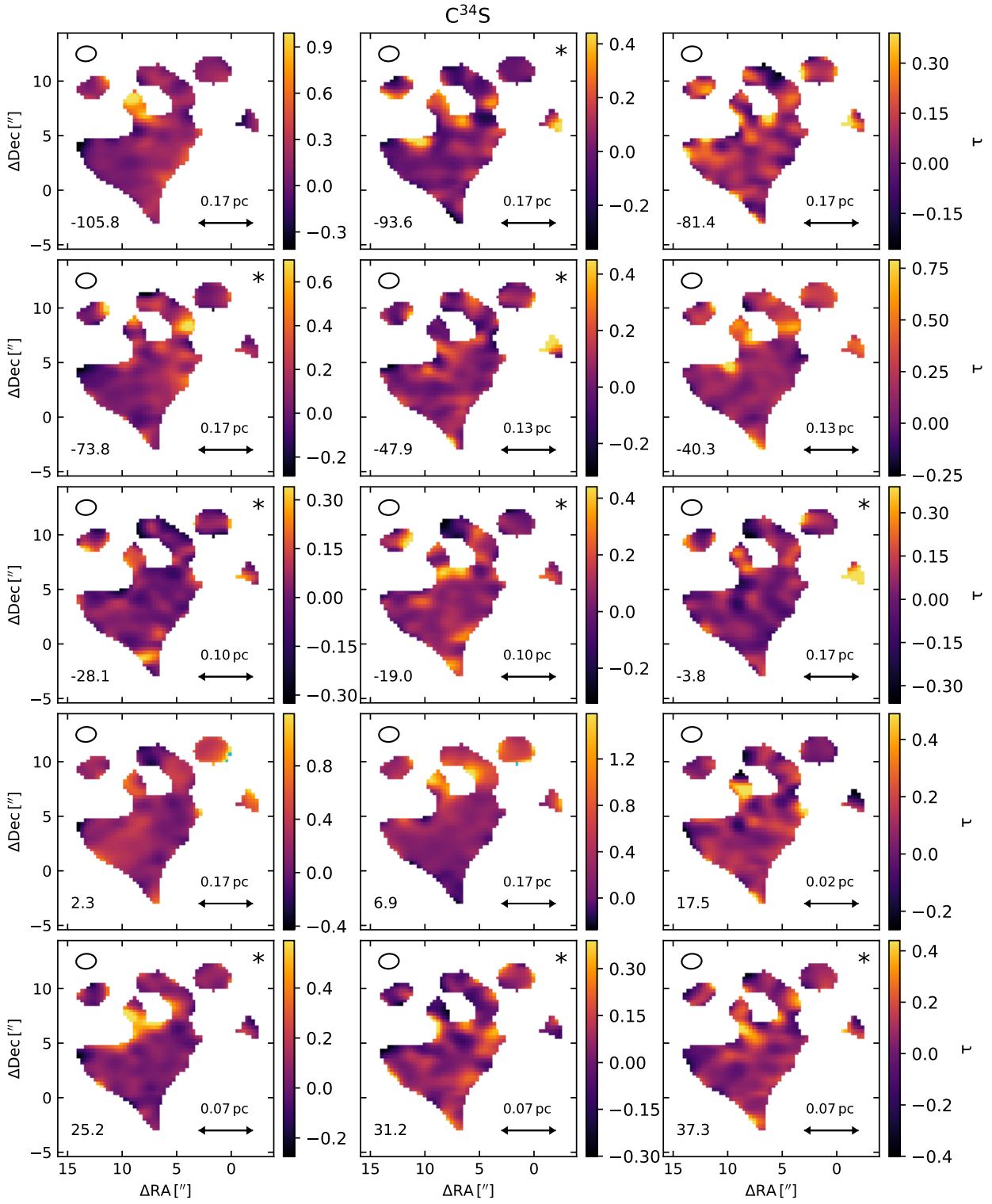

Figure C.15: Same as Fig. 5.6, but for $C^{34}S$.

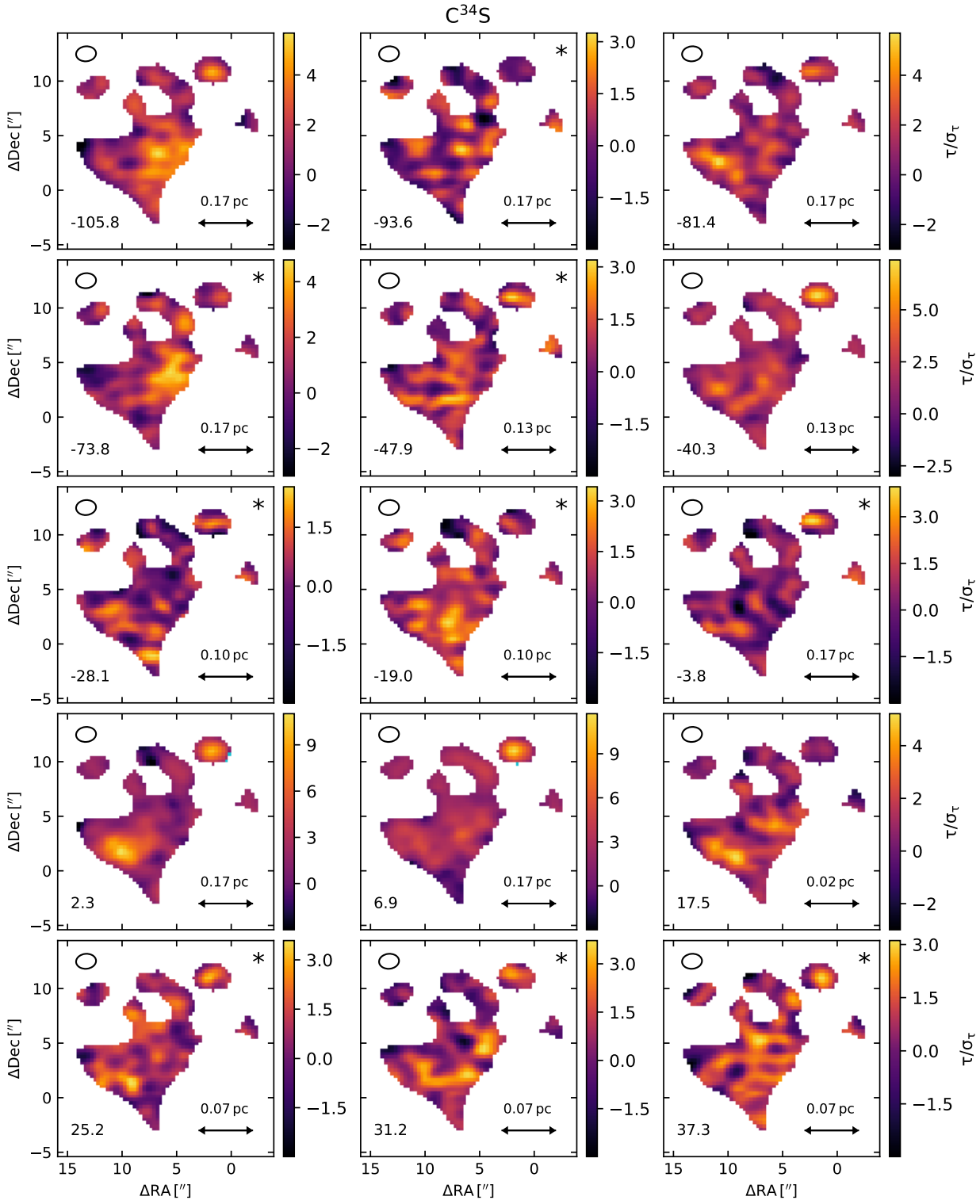

Figure C.16: Same as Fig. 5.7, but for $C^{34}S$.

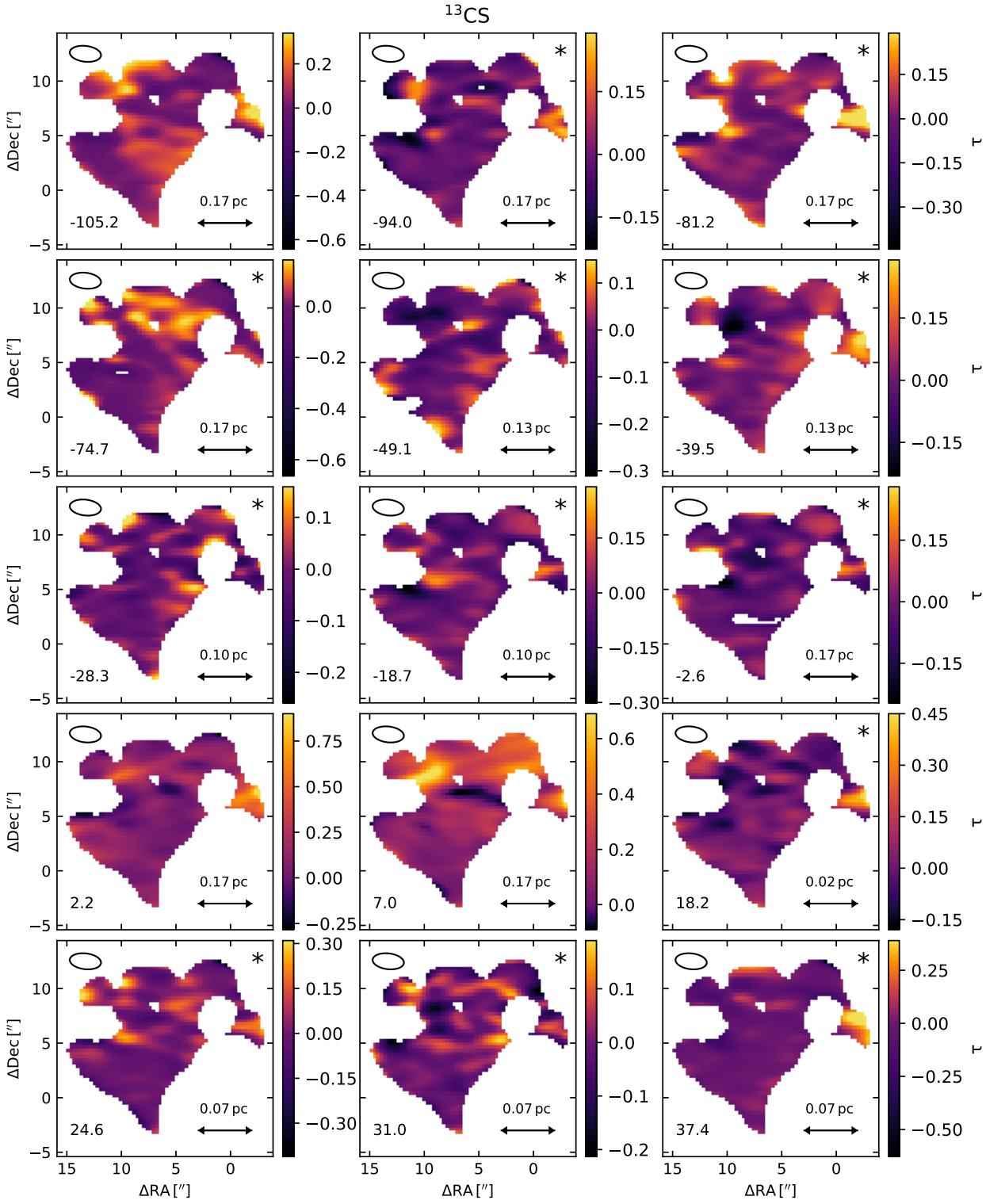

Figure C.17: Same as Fig. 5.6, but for ^{13}CS.

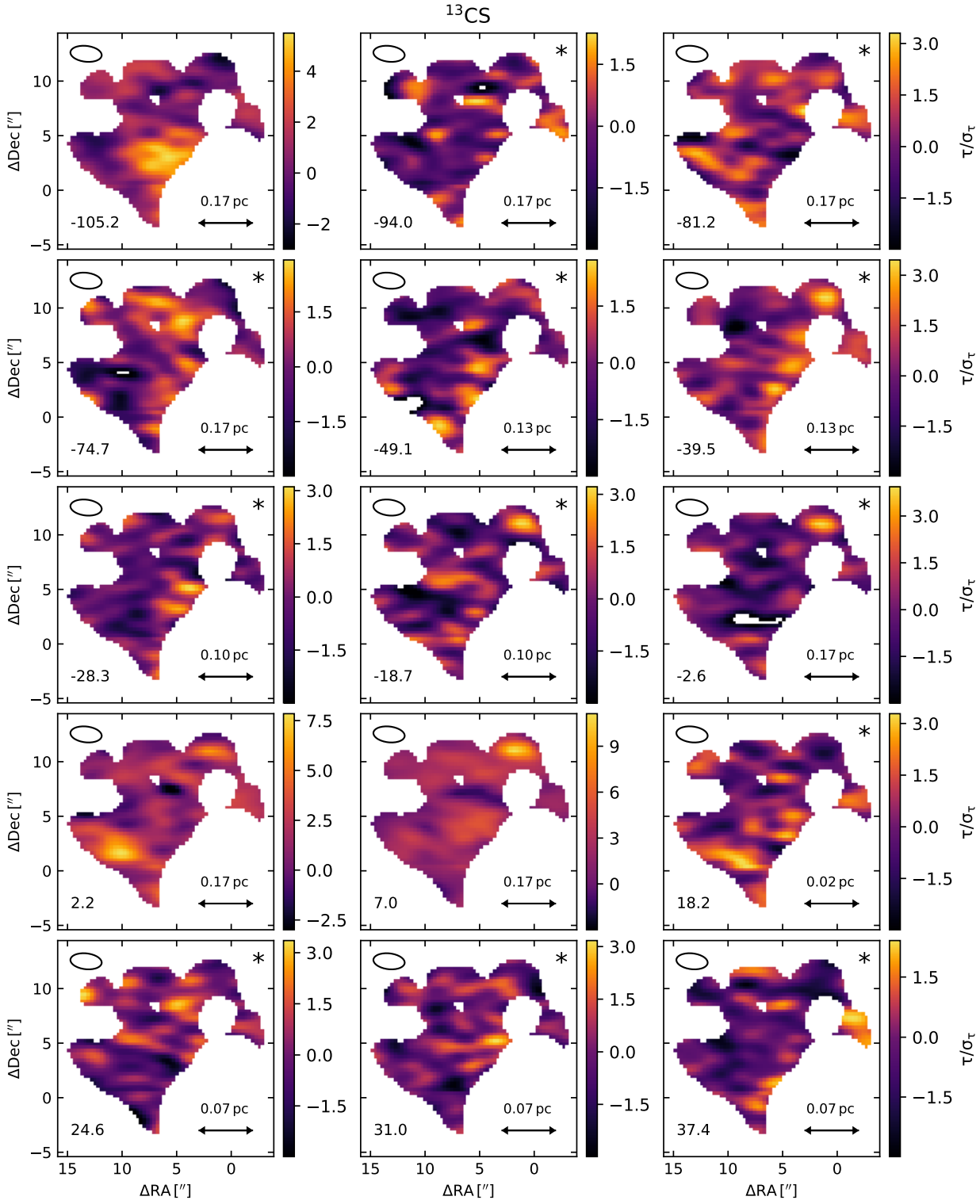

Figure C.18: Same as Fig. 5.7, but for ^{13}CS.

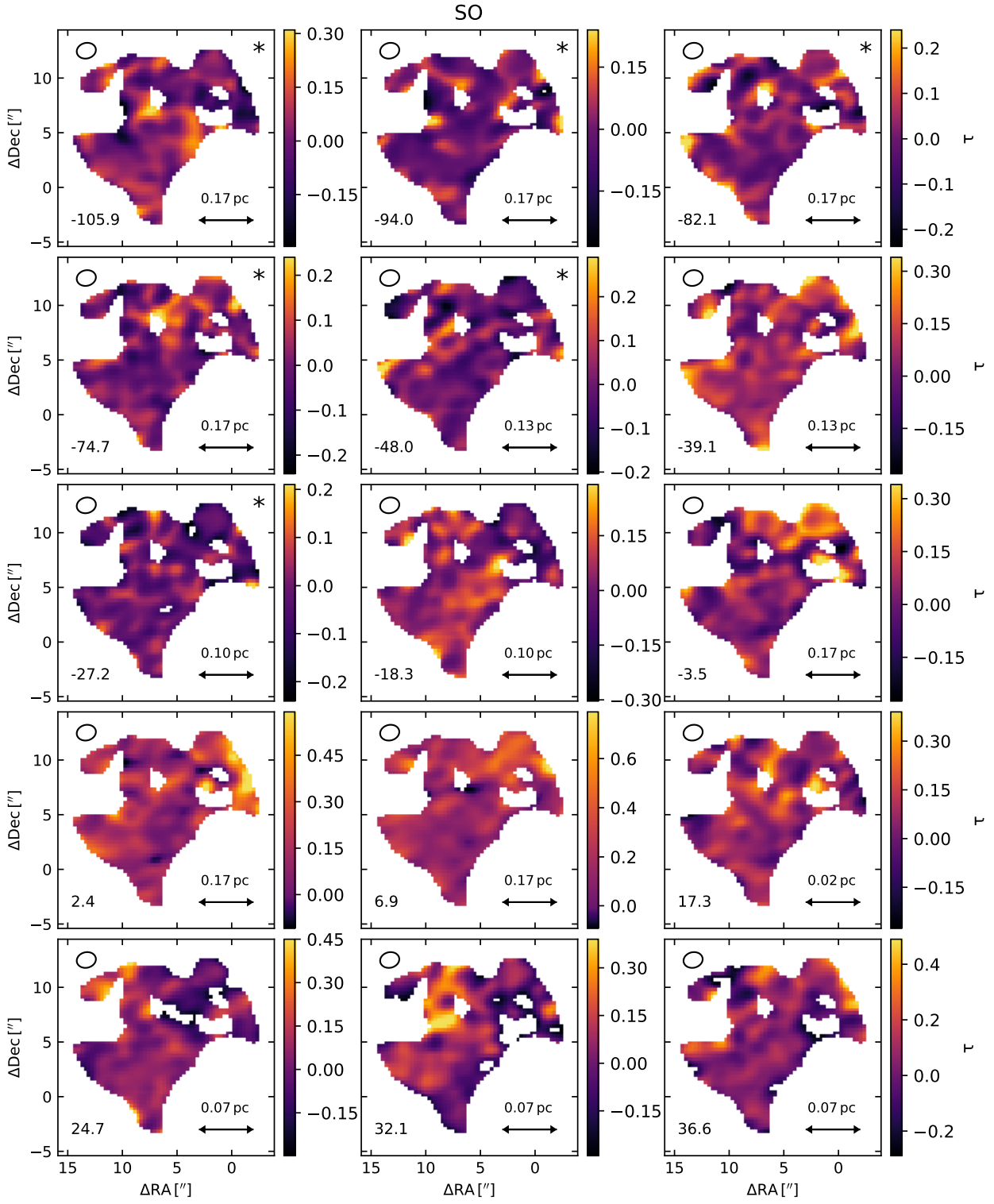

Figure C.19: Same as Fig. 5.6, but for SO.

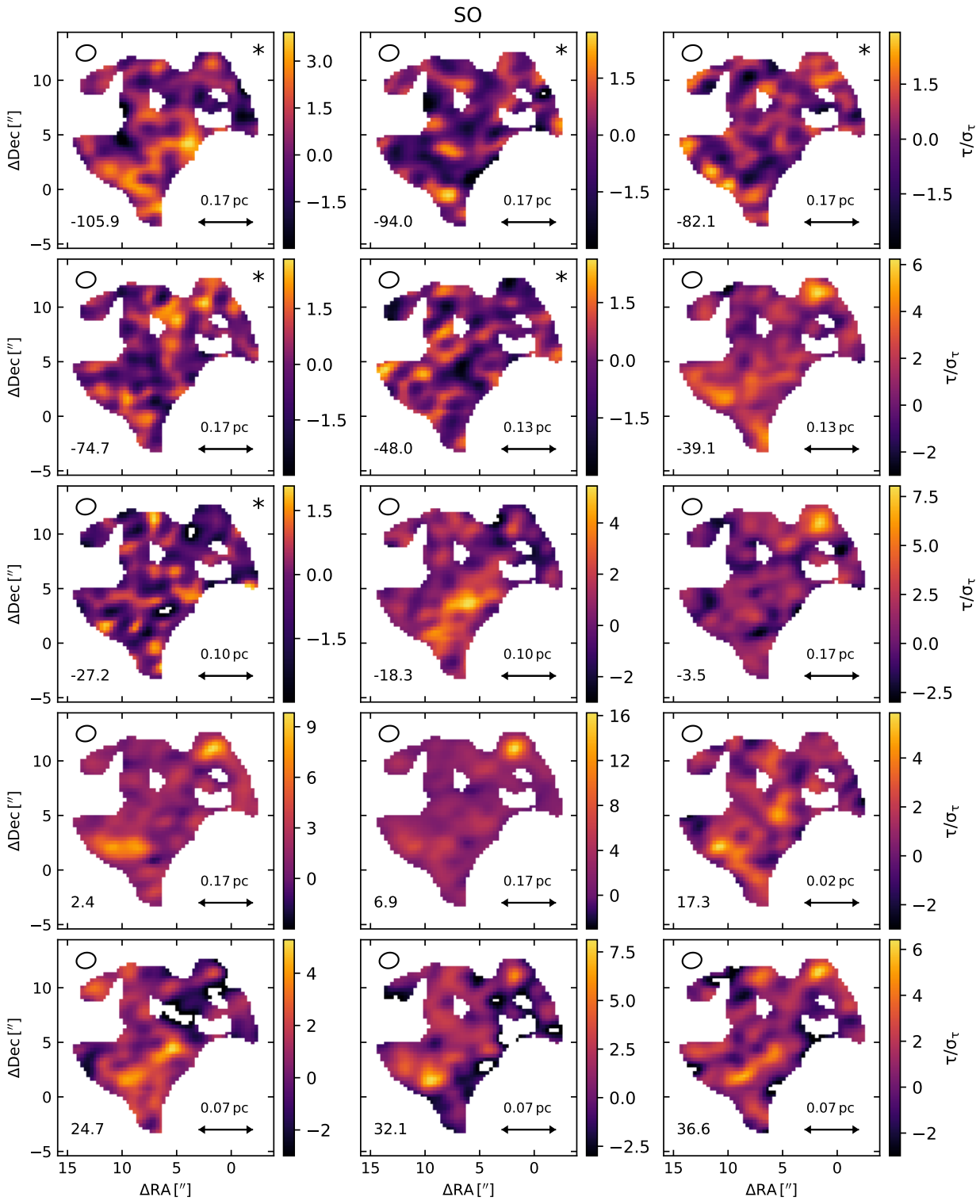

Figure C.20: Same as Fig. 5.7, but for SO.

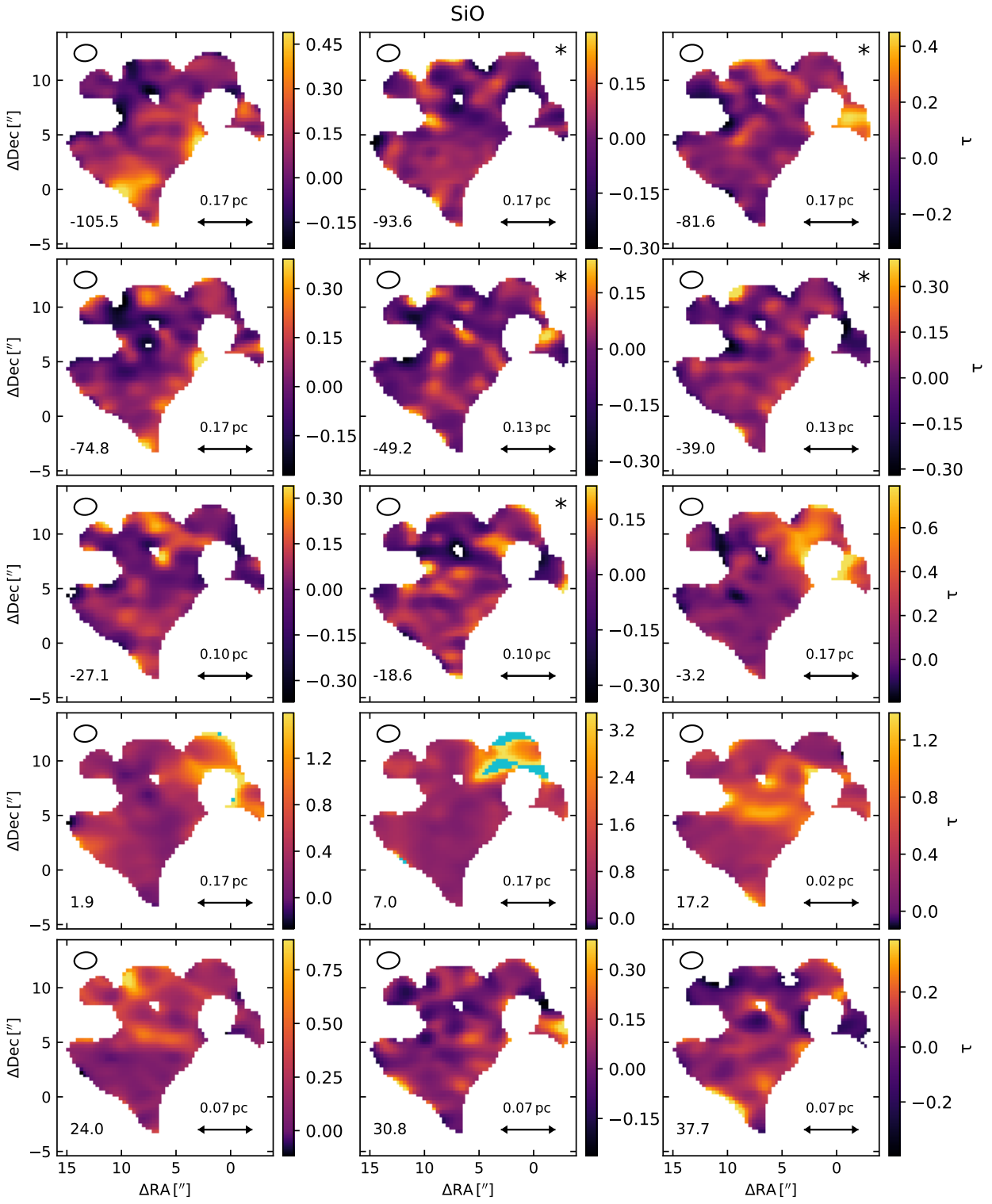

Figure C.21: Same as Fig. 5.6, but for SiO.

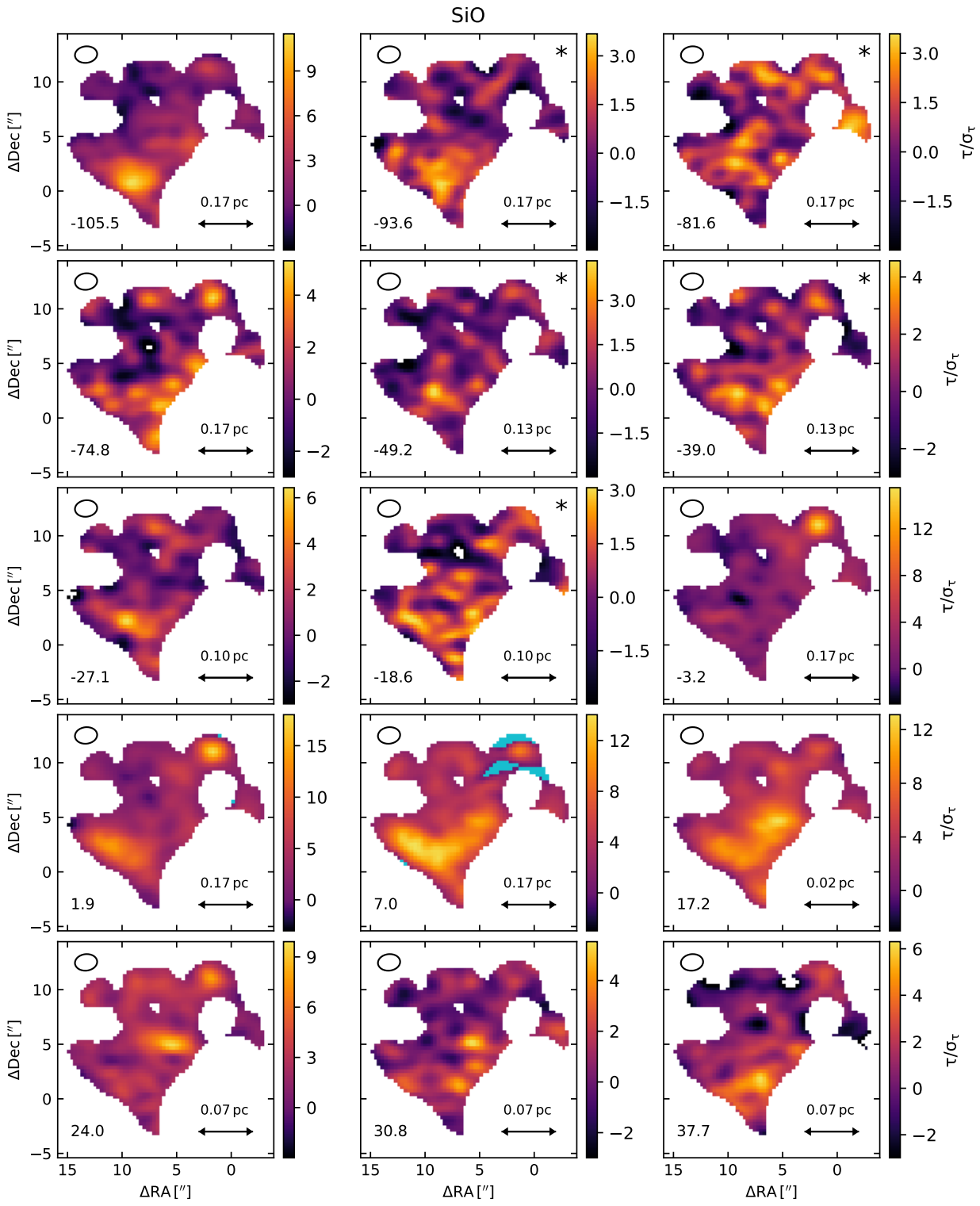

Figure C.22: Same as Fig. 5.7, but for SiO.

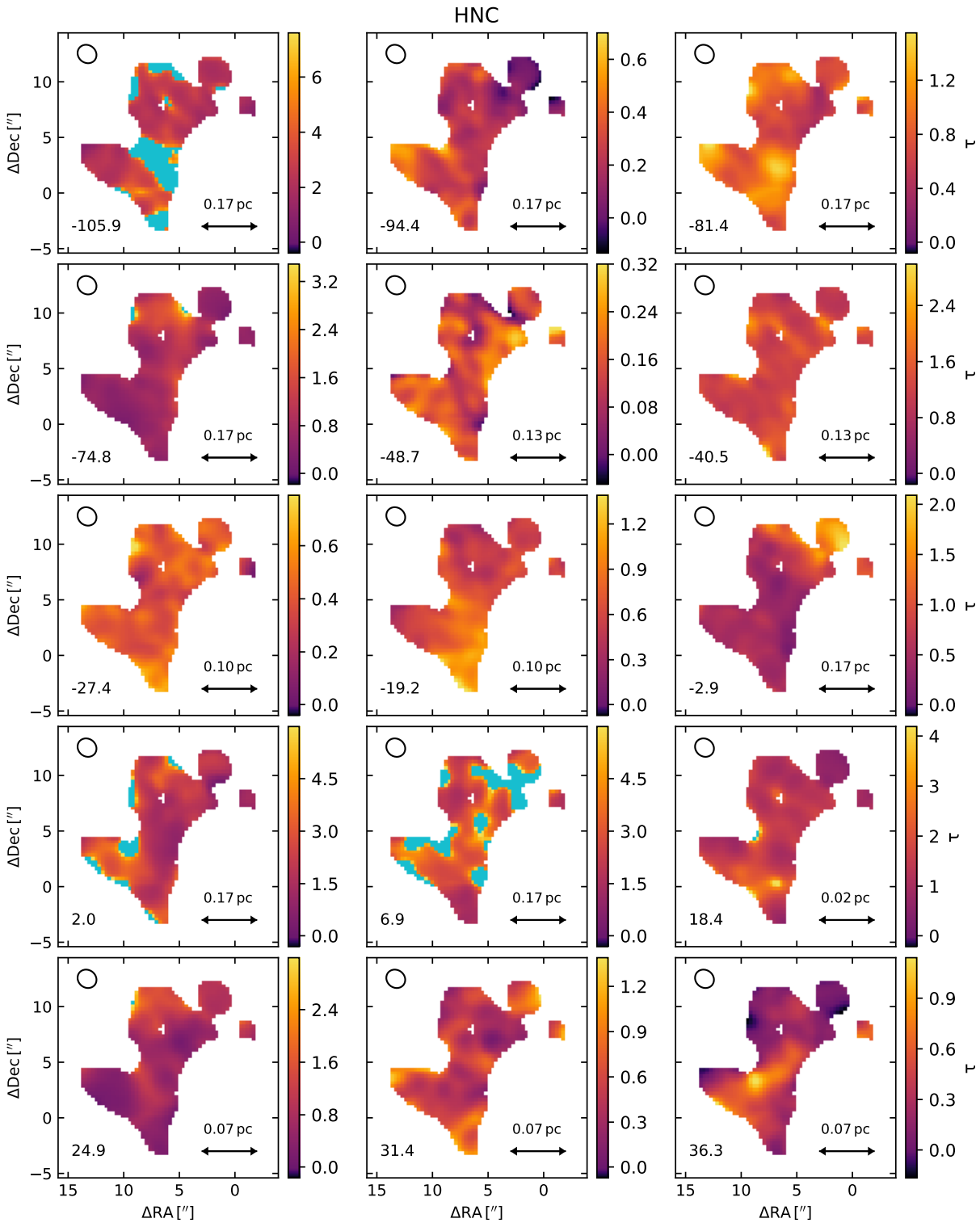

Figure C.23: Same as Fig. 5.6, but for HNC.

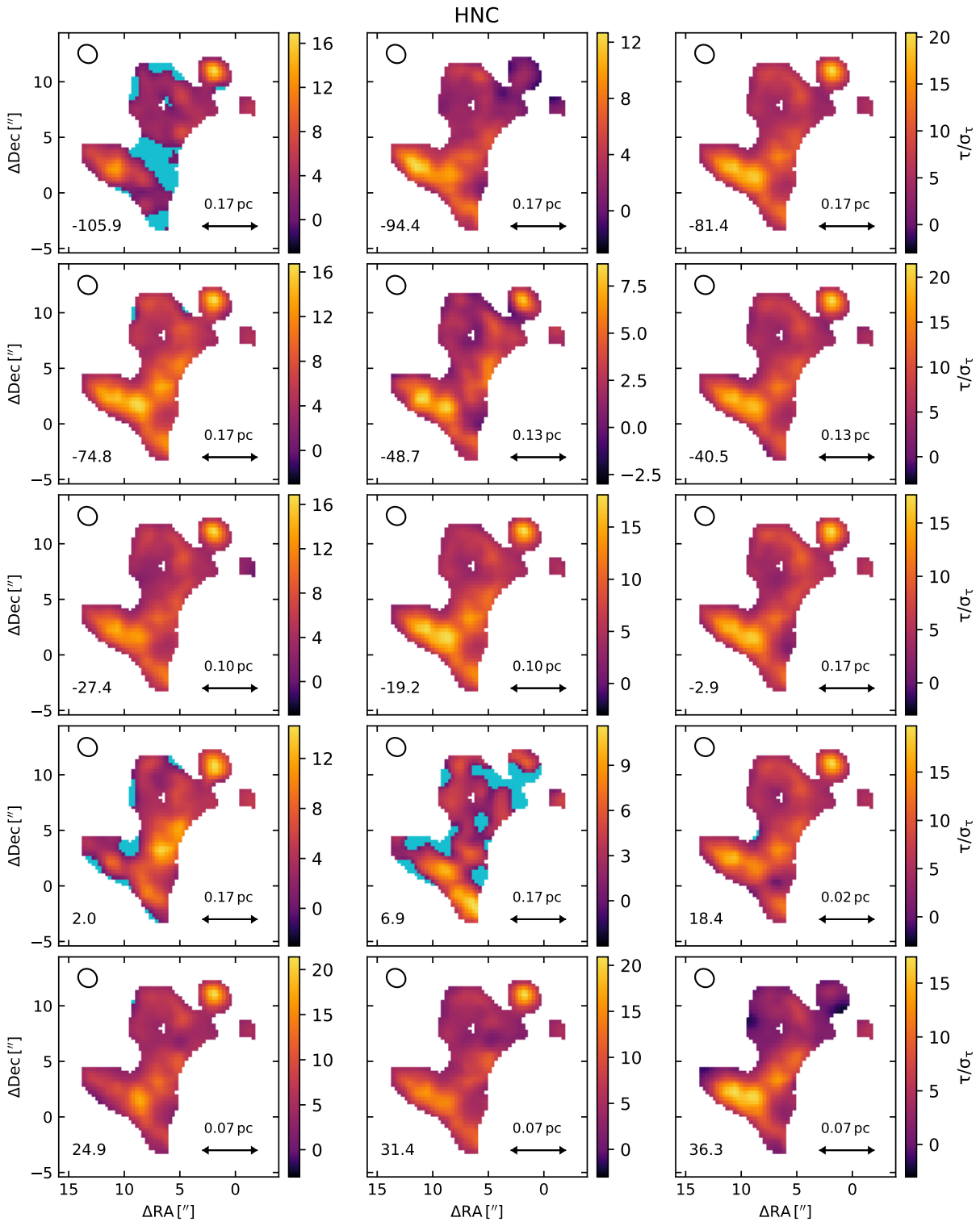

Figure C.24: Same as Fig. 5.7, but for HNC.

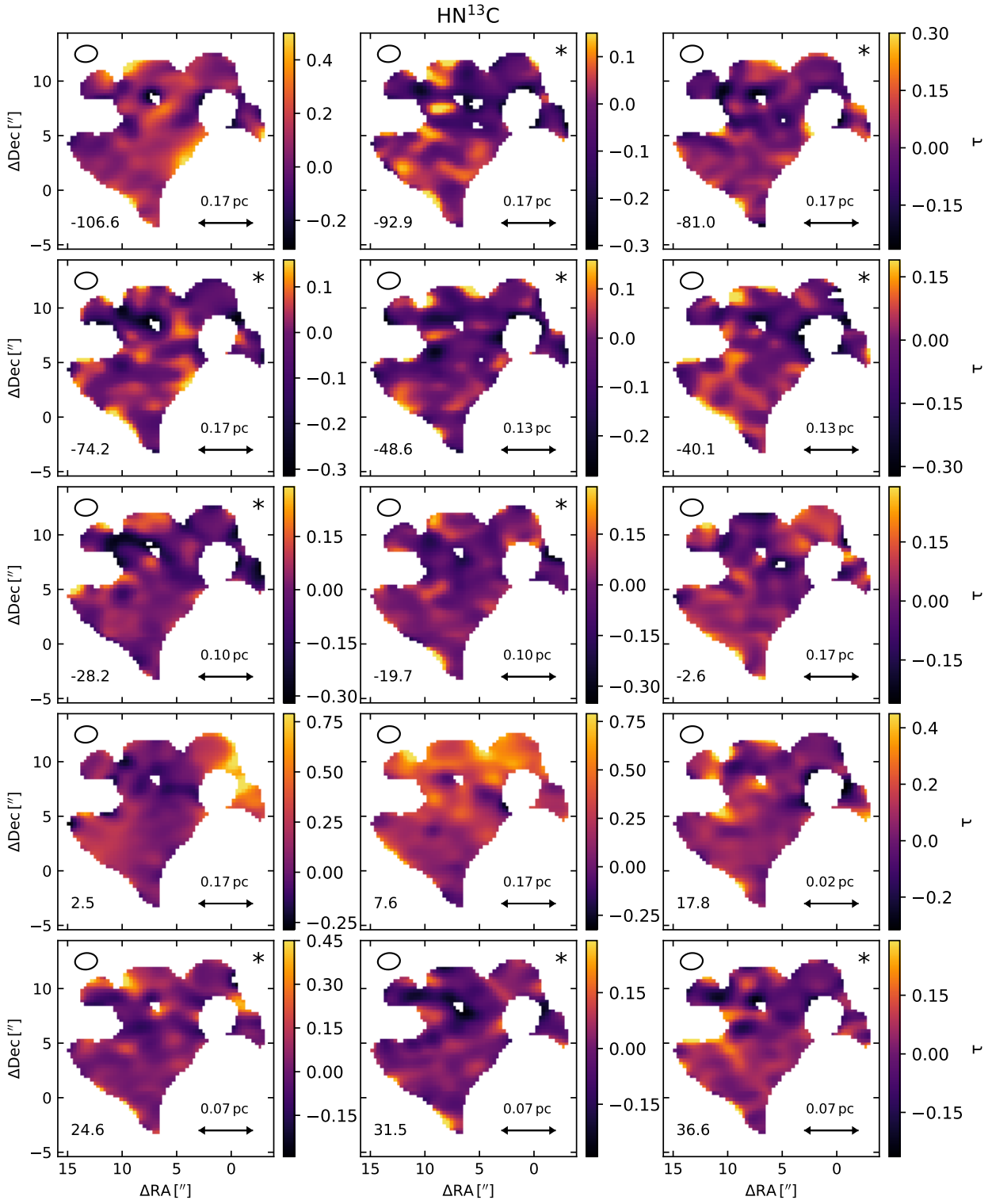

Figure C.25: Same as Fig. 5.6, but for $HN^{13}C$.

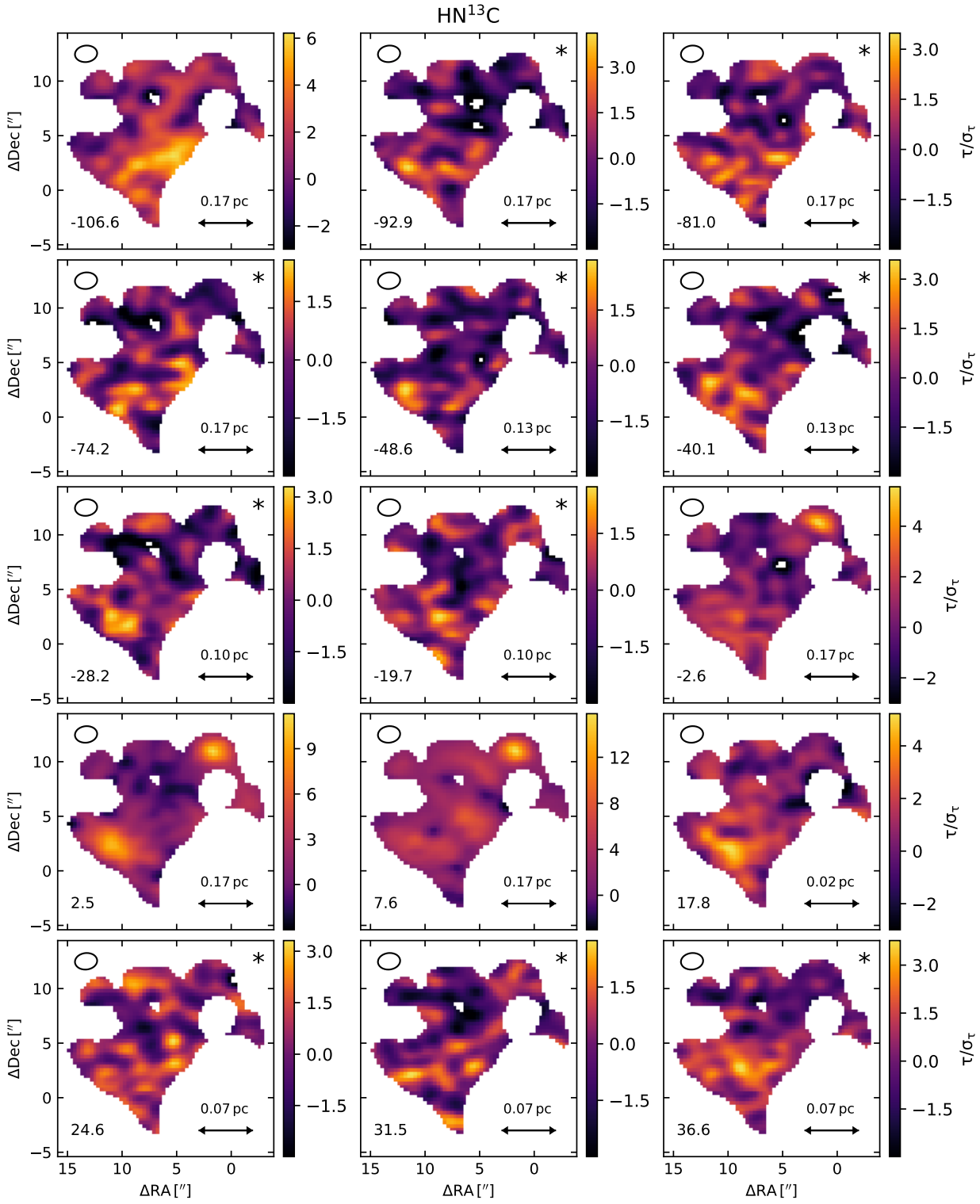

Figure C.26: Same as Fig. 5.7, but for $HN^{13}C$.

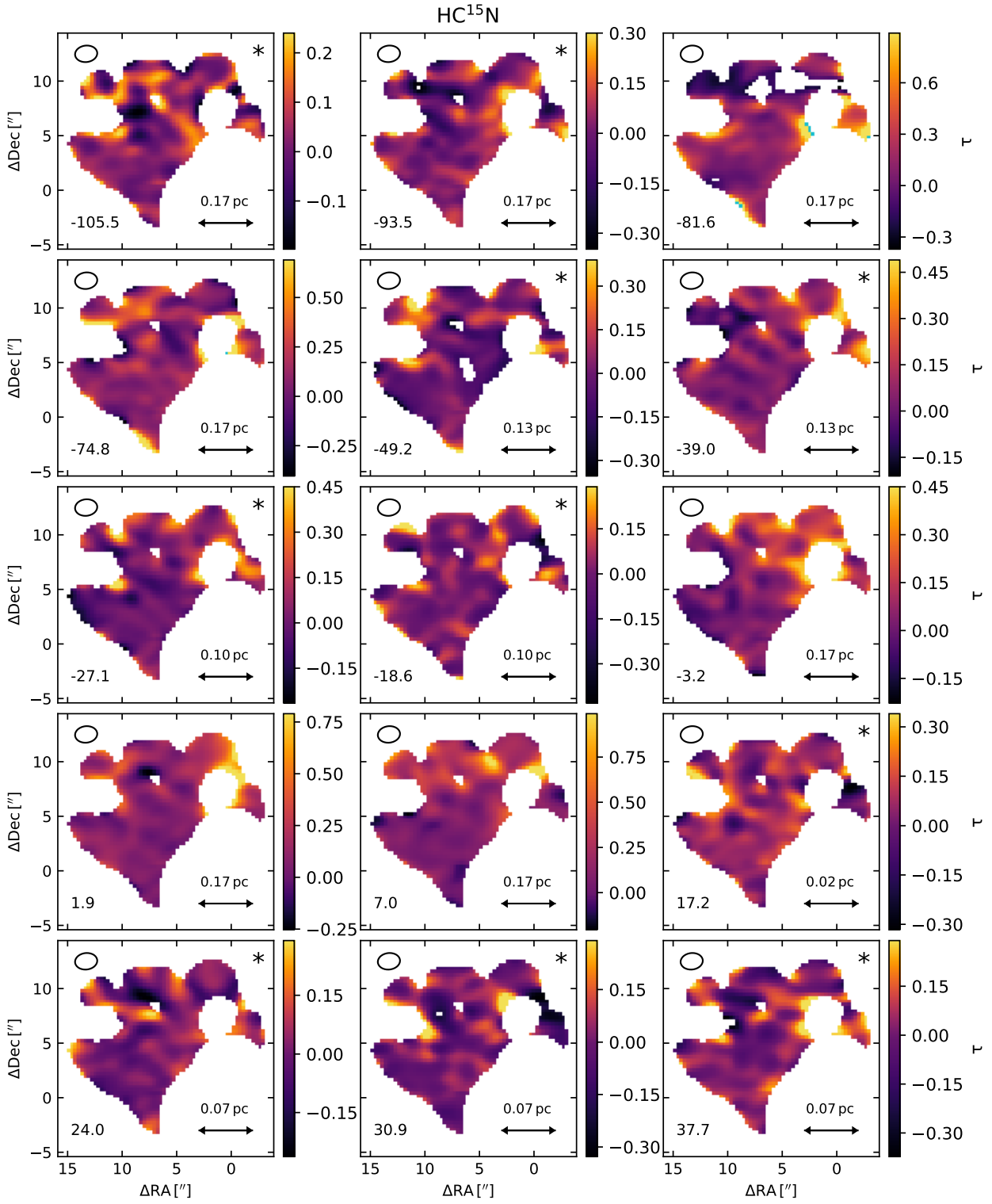

Figure C.27: Same as Fig. 5.6, but for $HC^{15}N$.

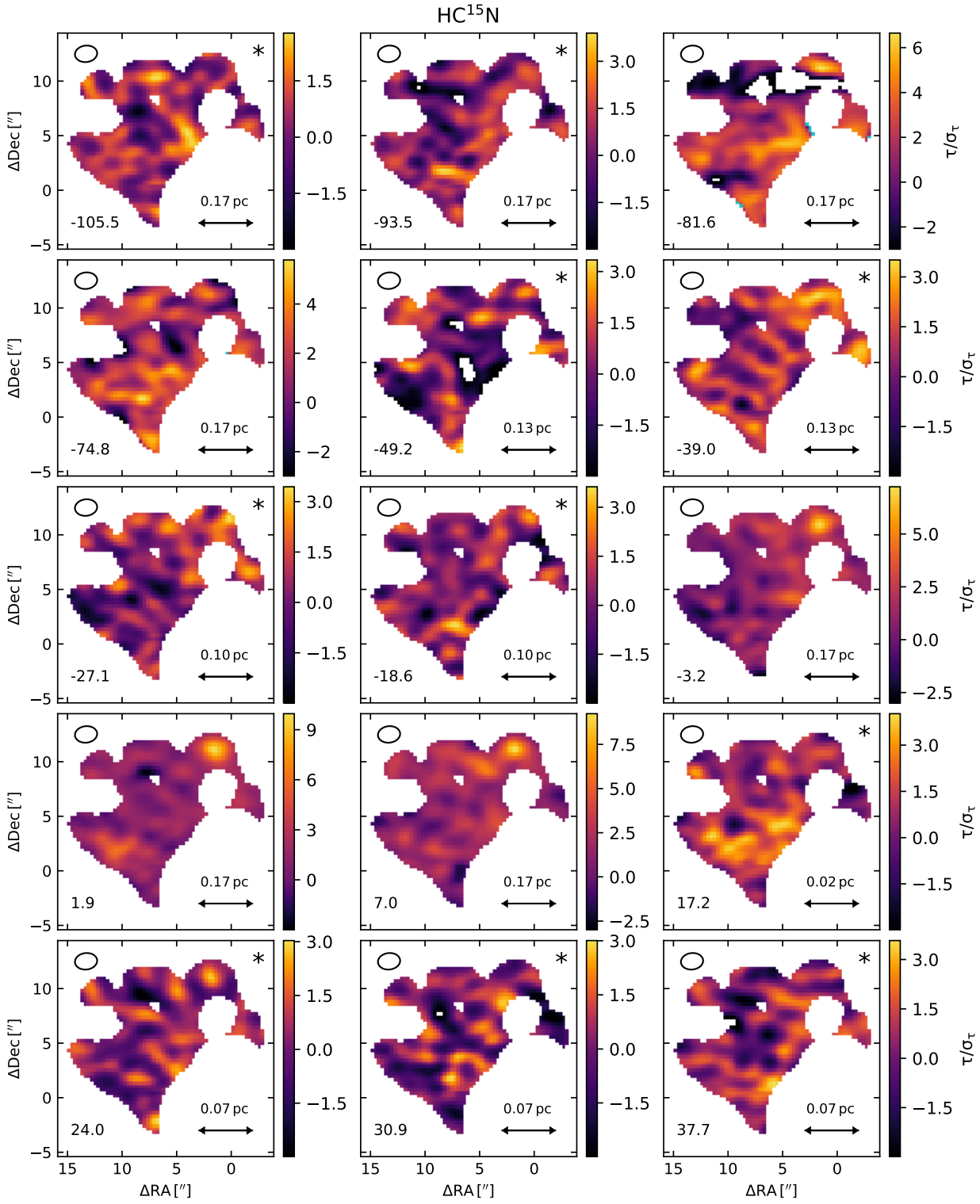

Figure C.28: Same as Fig. 5.7, but for $HC^{15}N$.

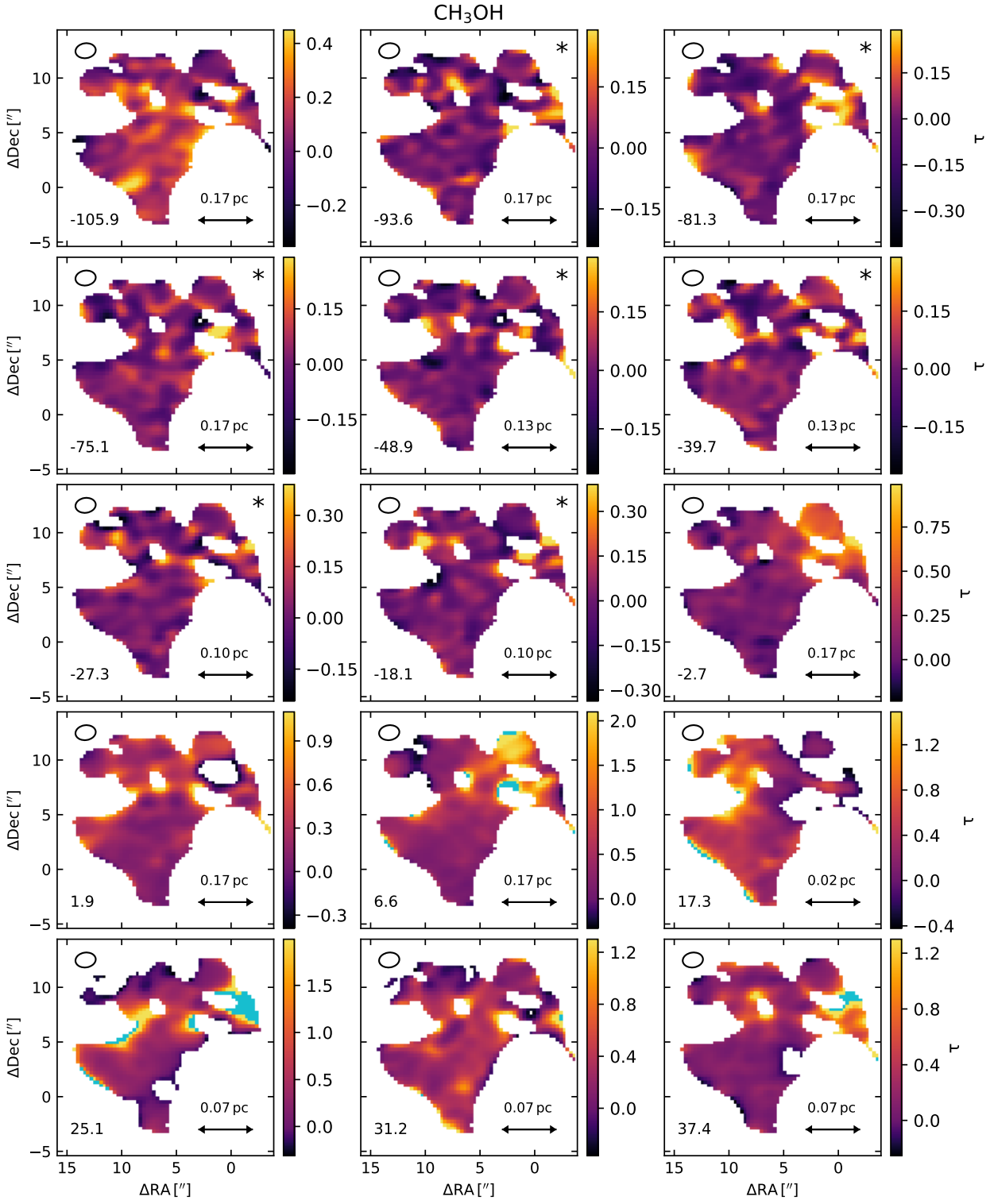

Figure C.29: Same as Fig. 5.6, but for CH_3OH.

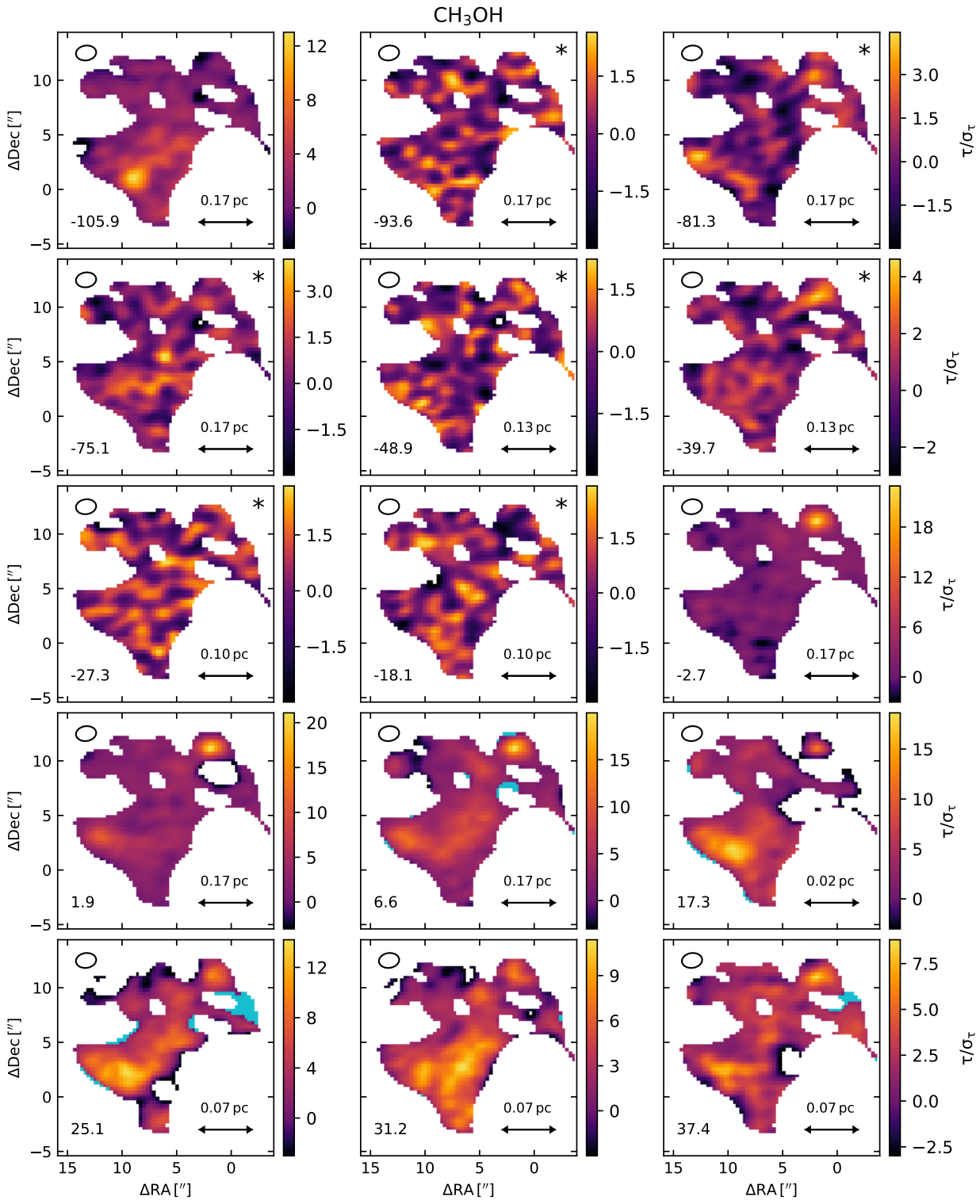

Figure C.30: Same as Fig. 5.7, but for CH_3OH.

C.7 Two-point auto-correlation functions

The two-point auto-correlation functions as a function of angular distance are shown in Figs. C.31–C.40 for all molecules except for c-C_3H_2 and $H^{13}CO^+$. The two-point auto-correlation functions as a function of physical distance are shown in Figs. C.41–C.48 for the eight strongest molecules (c-C_3H_2, $H^{13}CO^+$, ^{13}CO, CS, SO, SiO, HNC, and CH_3OH).

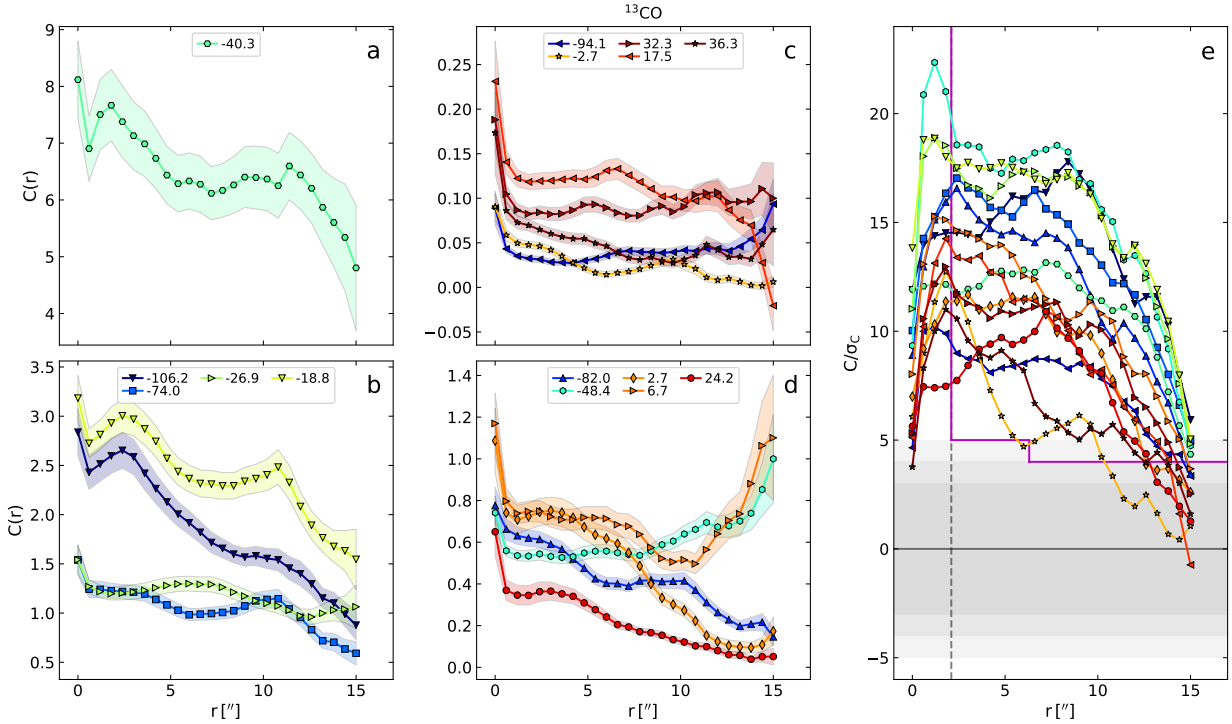

Figure C.31: Same as Fig. 5.8, but for ^{13}CO.

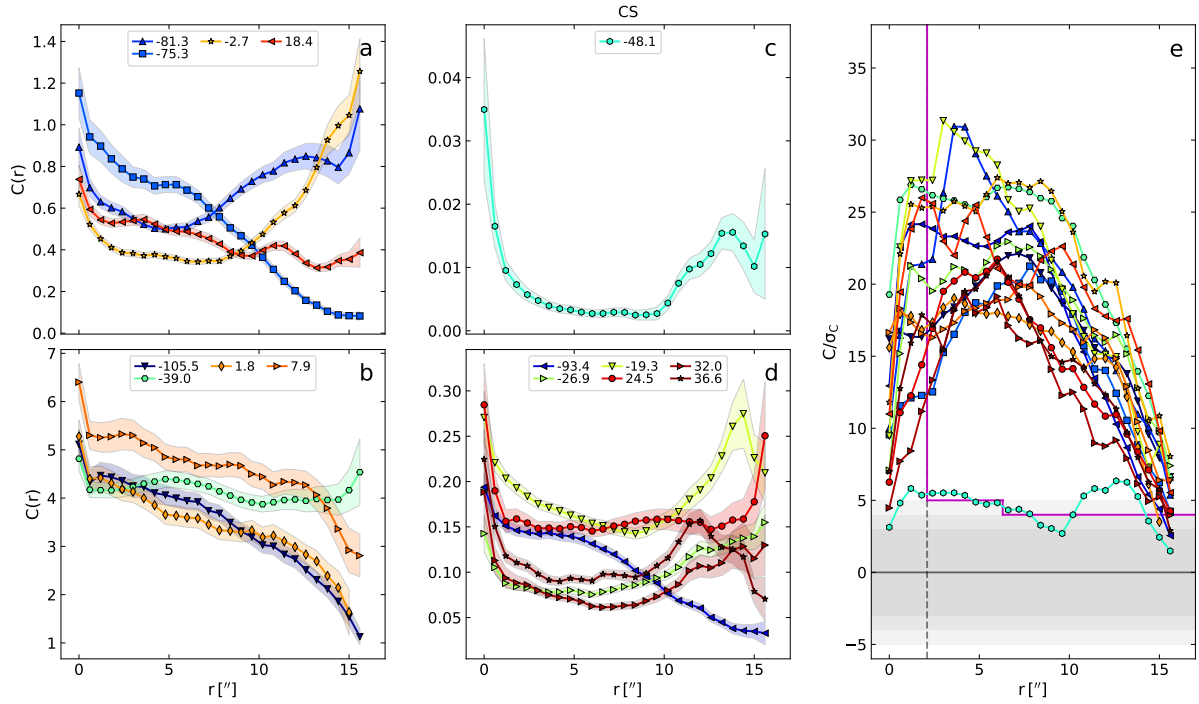

Figure C.32: Same as Fig. 5.8, but for CS.

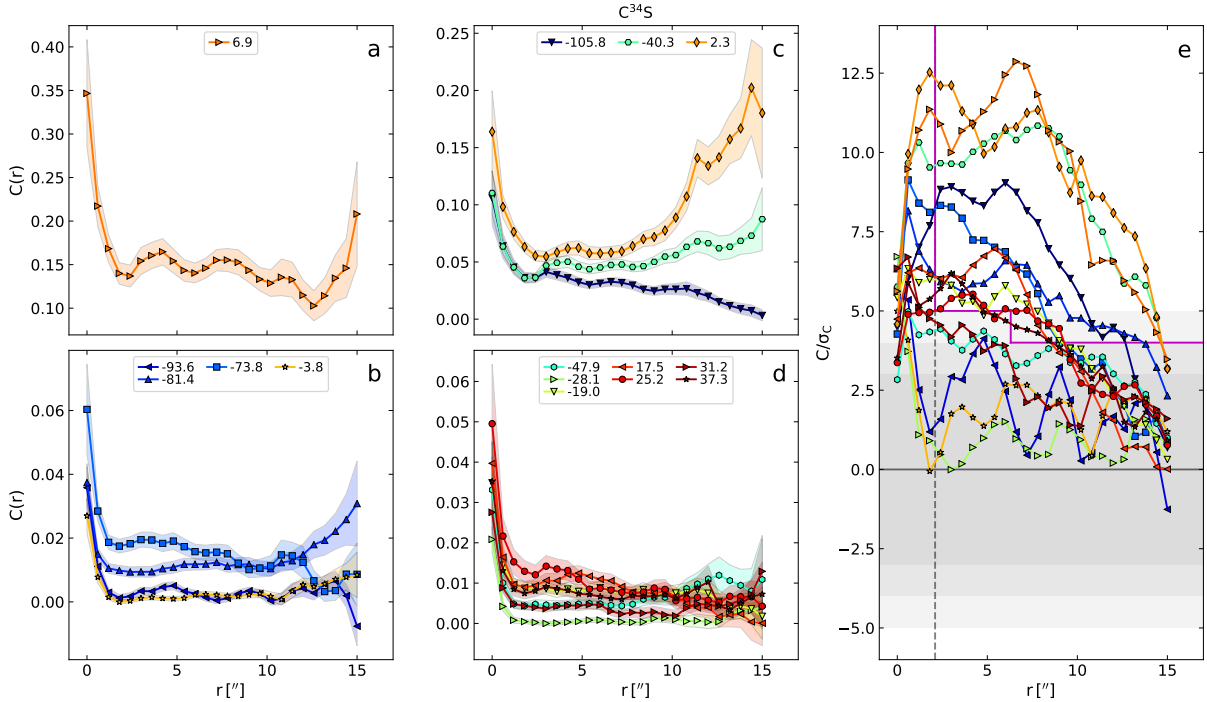

Figure C.33: Same as Fig. 5.8, but for $C^{34}S$.

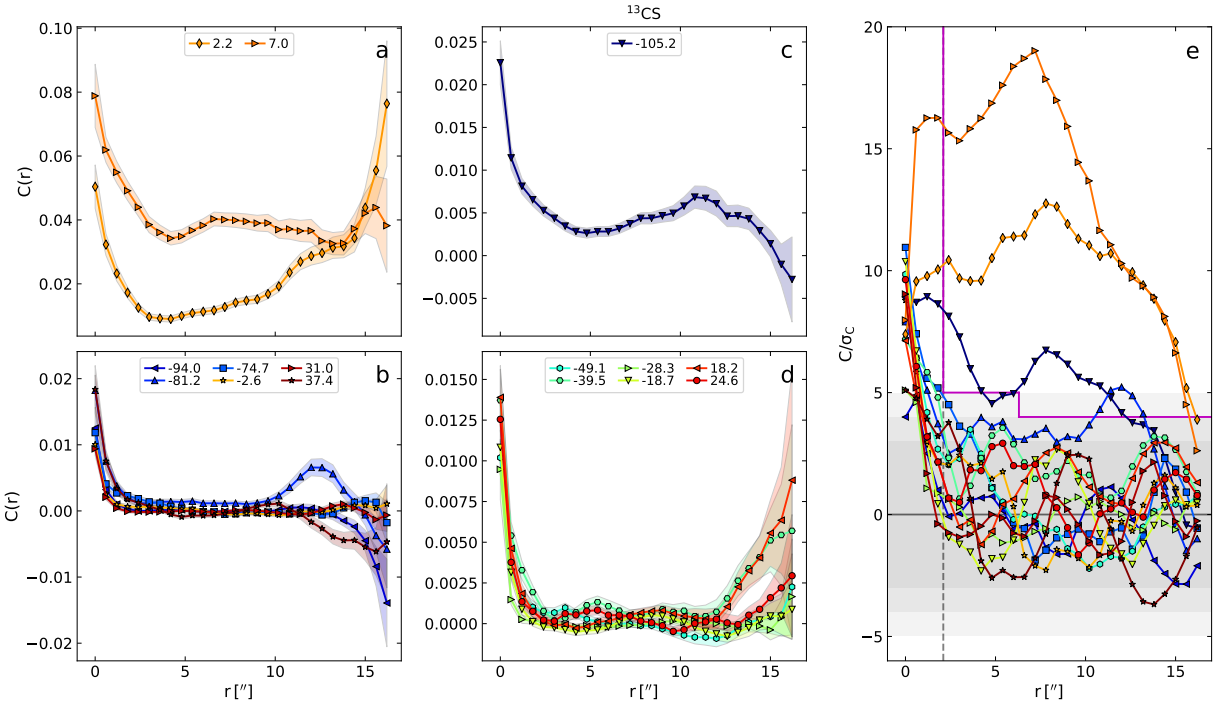

Figure C.34: Same as Fig. 5.8, but for ^{13}CS.

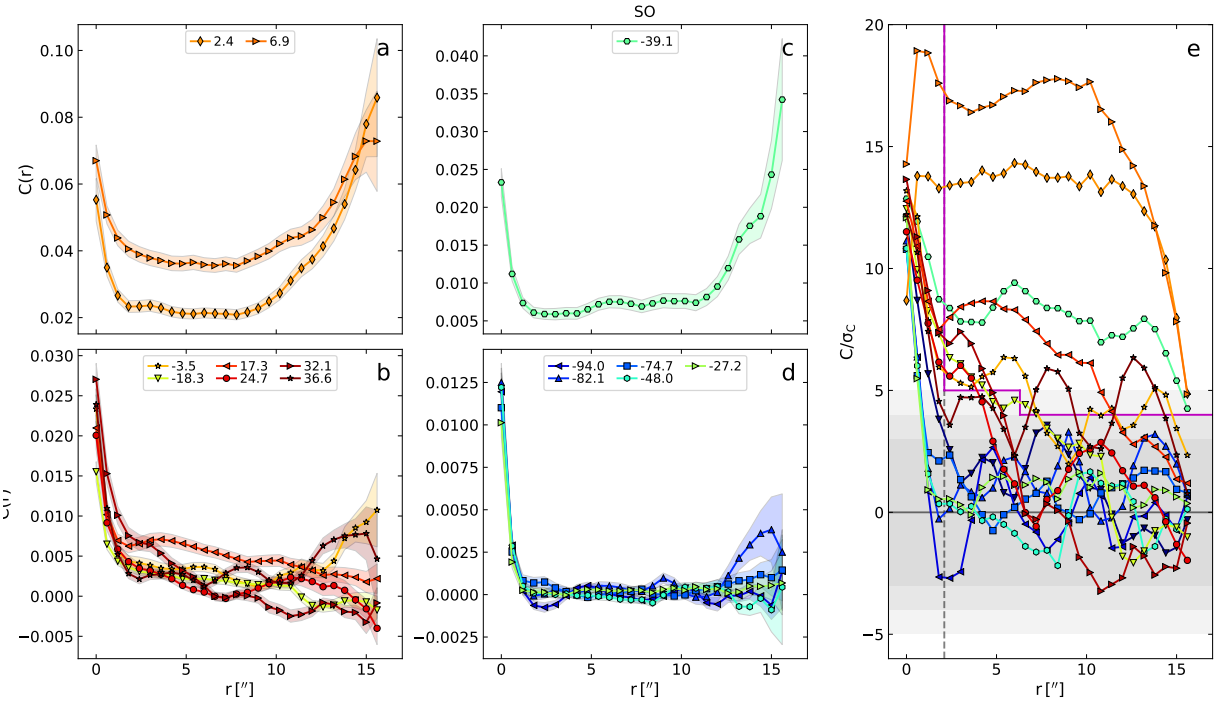

Figure C.35: Same as Fig. 5.8, but for SO.

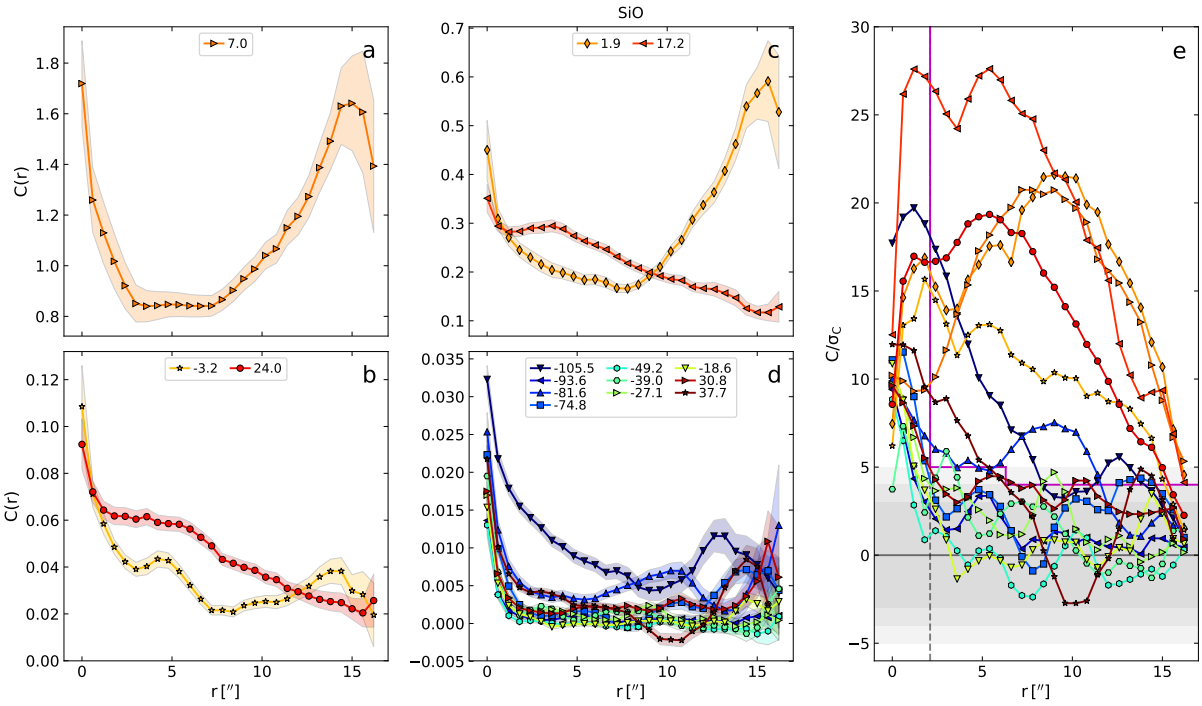

Figure C.36: Same as Fig. 5.8, but for SiO.

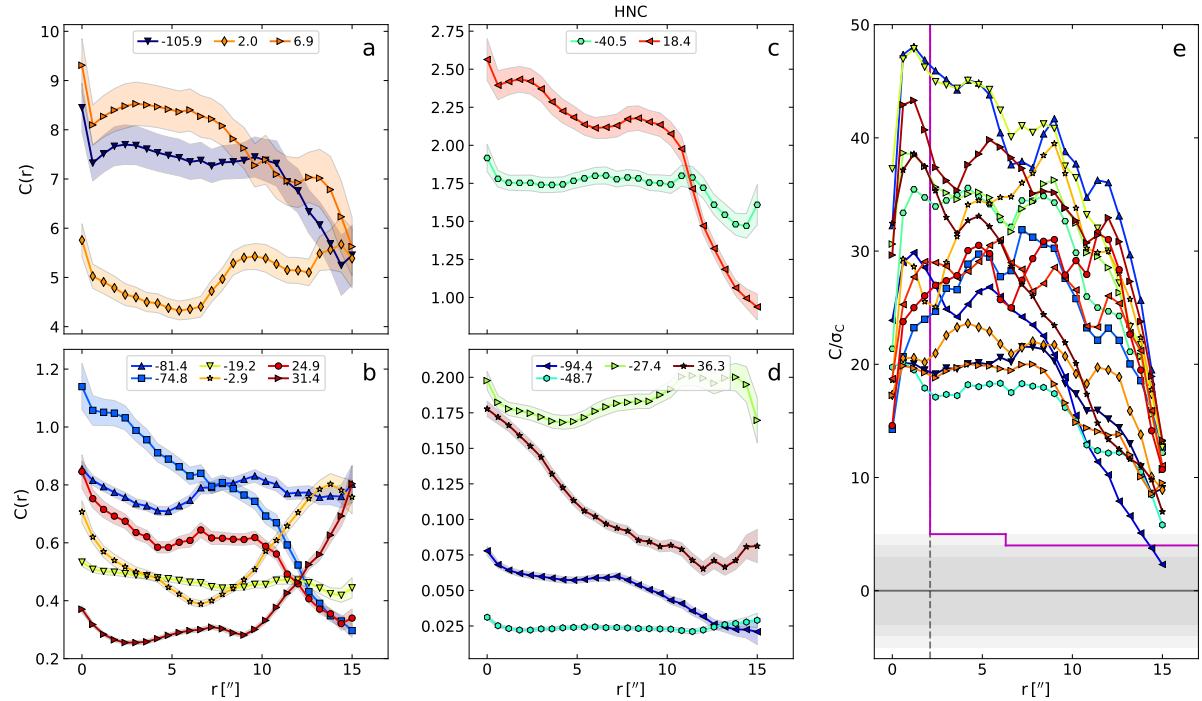

Figure C.37: Same as Fig. 5.8, but for HNC.

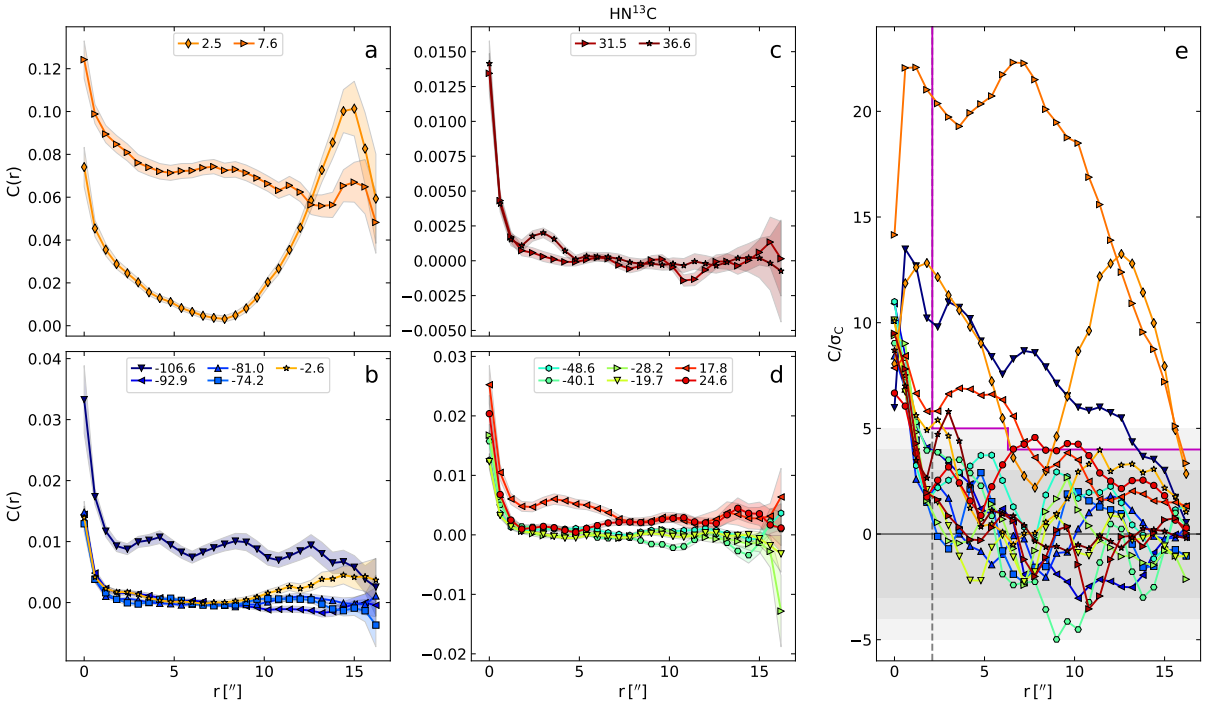

Figure C.38: Same as Fig. 5.8, but for $HN^{13}C$.

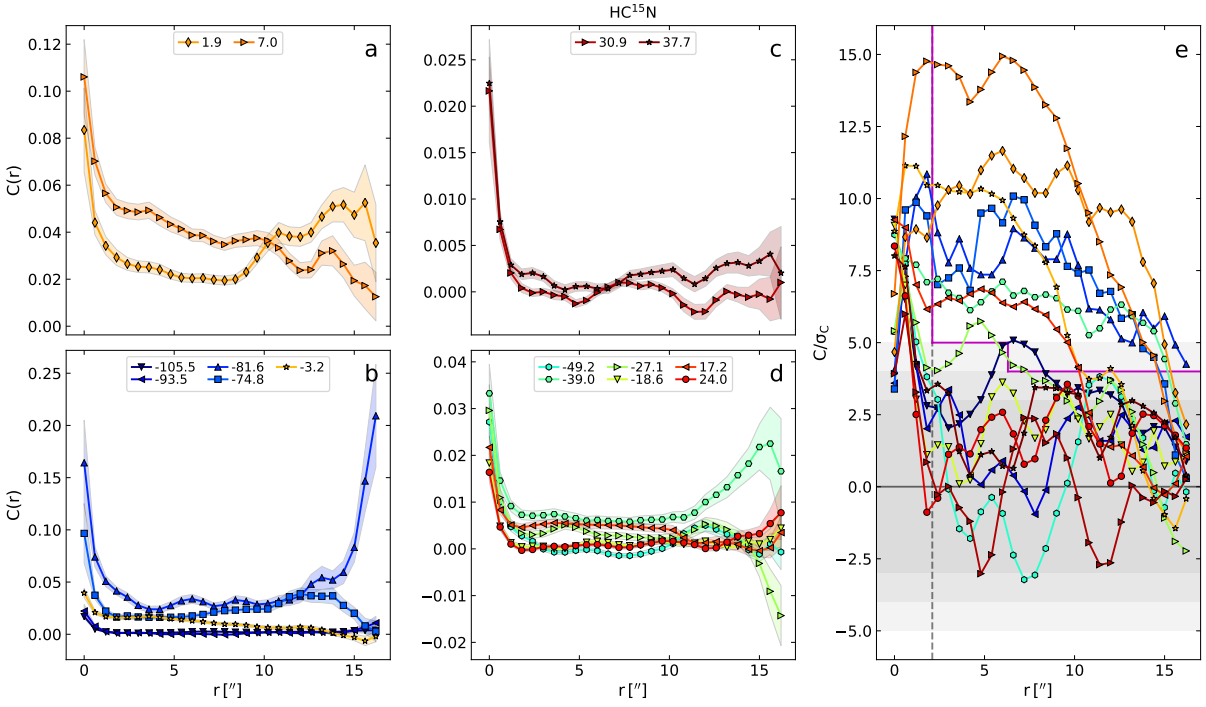

Figure C.39: Same as Fig. 5.8, but for $HC^{15}N$.

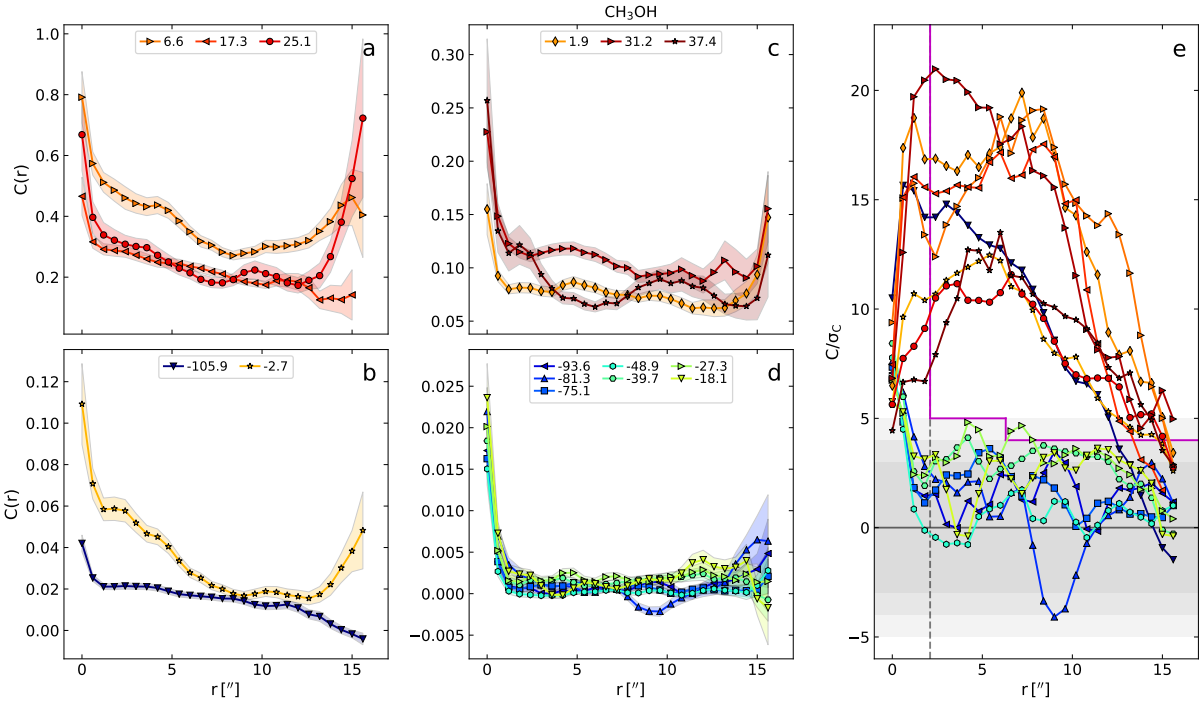

Figure C.40: Same as Fig. 5.8, but for CH_3OH.

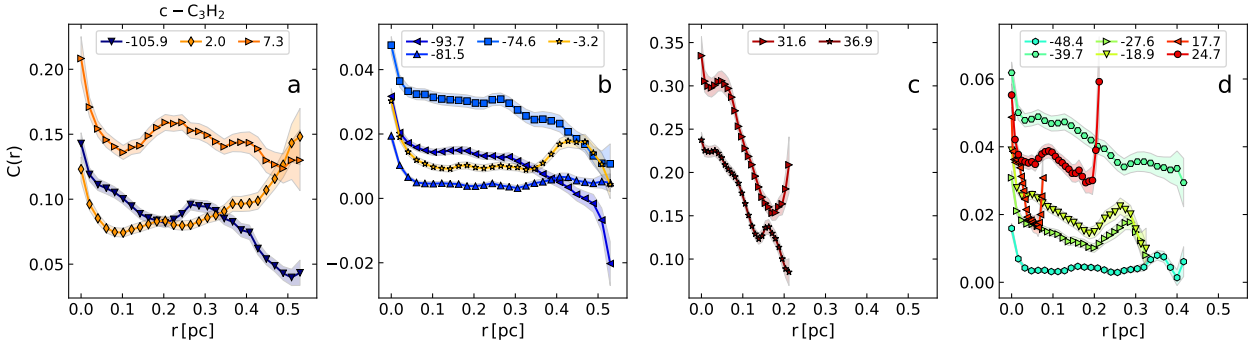

Figure C.41: **a–d** Two-point auto-correlation functions $C(r)$ as a function of physical distance r for the velocity components traced with c-C_3H_2. The points give the mean values of the 1000 realisations and the colour-shaded regions represent the standard deviations (1σ). The centroid LSR velocities of the clouds are indicated in km s^{-1} at the top of each panel.

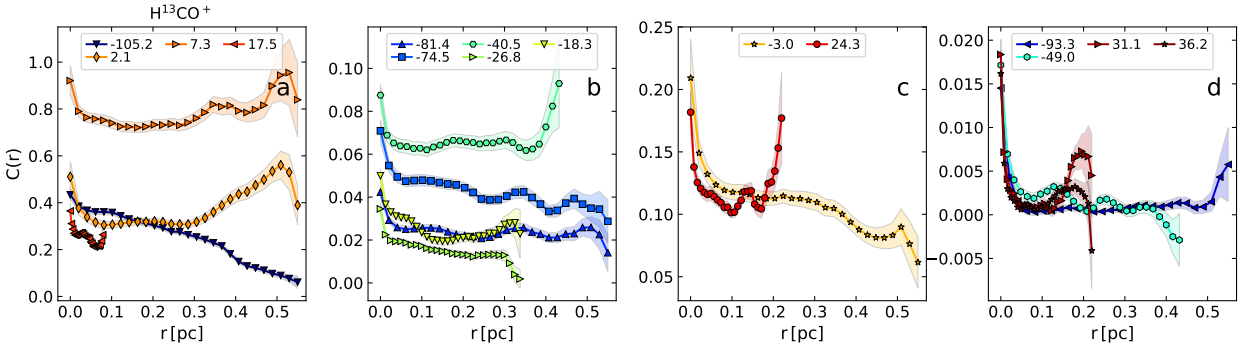

Figure C.42: Same as Fig. C.41, but for $H^{13}CO^{+}$.

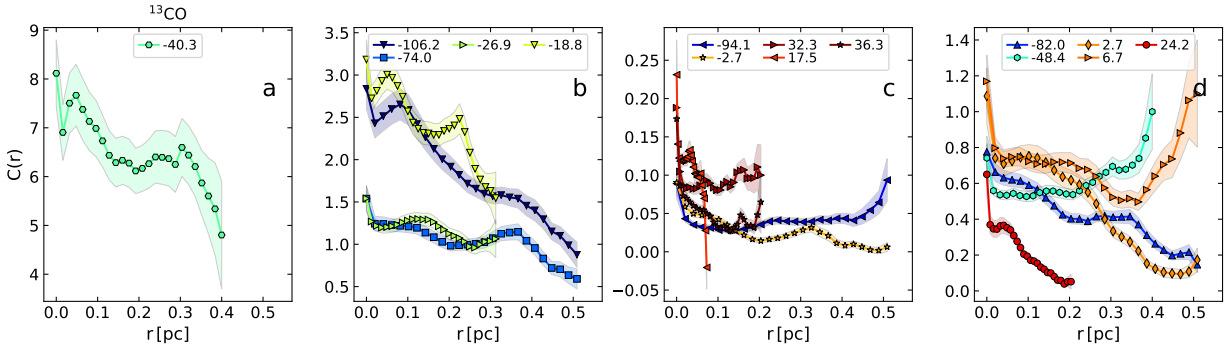

Figure C.43: Same as Fig. C.41, but for ^{13}CO.

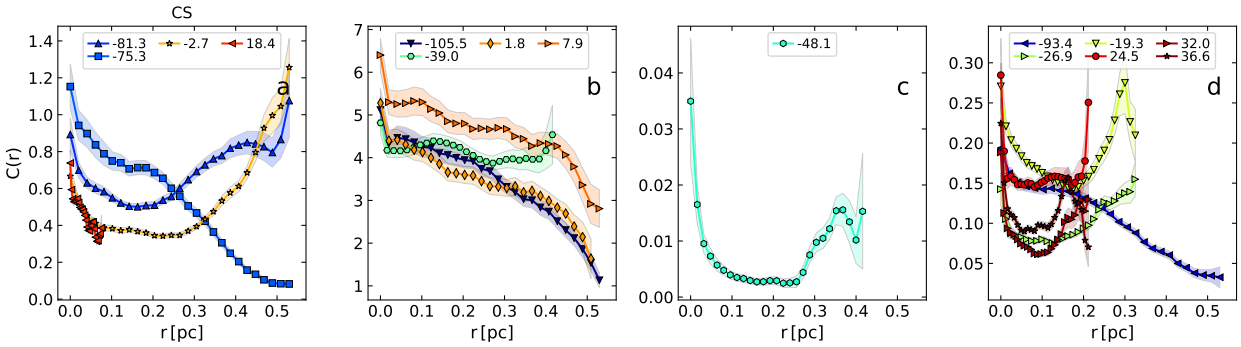

Figure C.44: Same as Fig. C.41, but for CS.

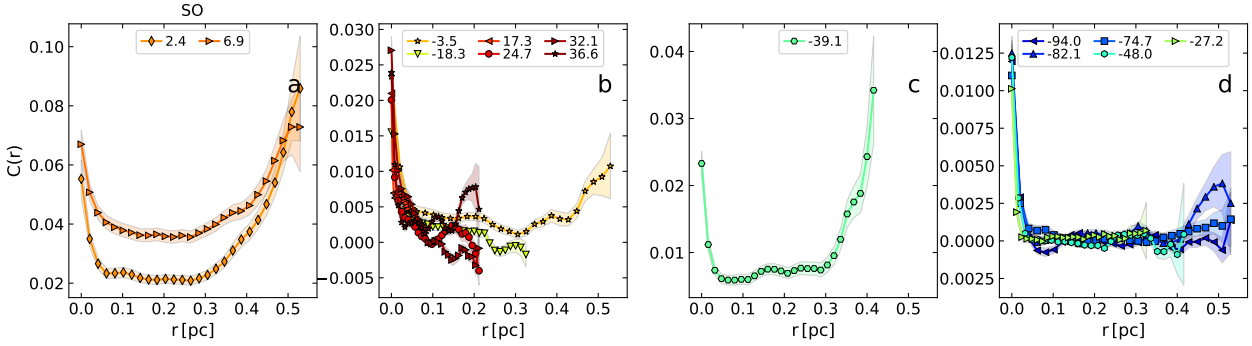

Figure C.45: Same as Fig. C.41, but for SO.

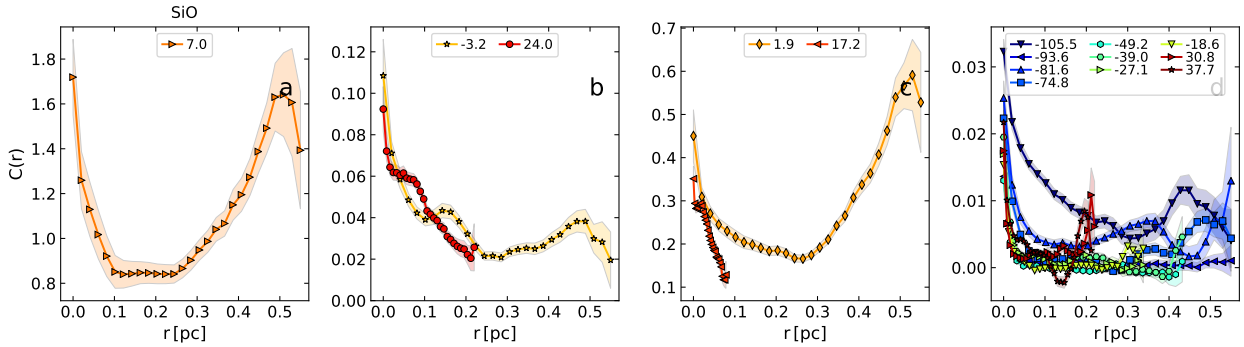

Figure C.46: Same as Fig. C.41, but for SiO.

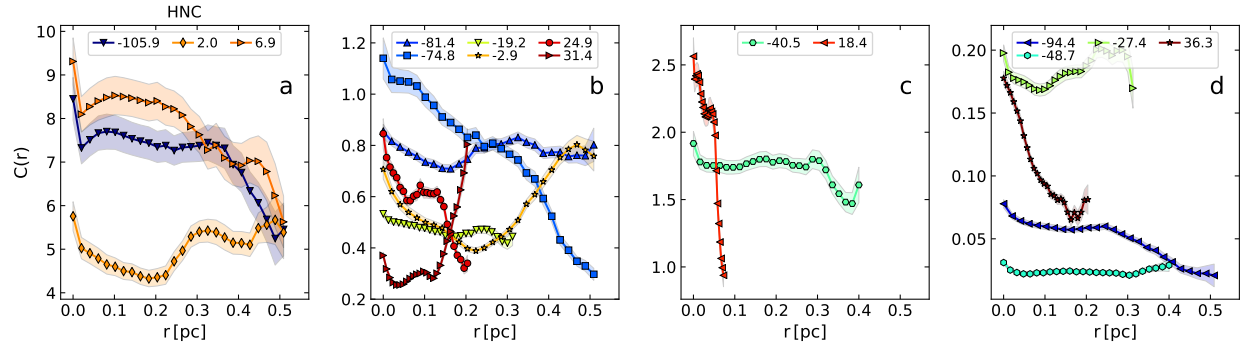

Figure C.47: Same as Fig. C.41, but for HNC.

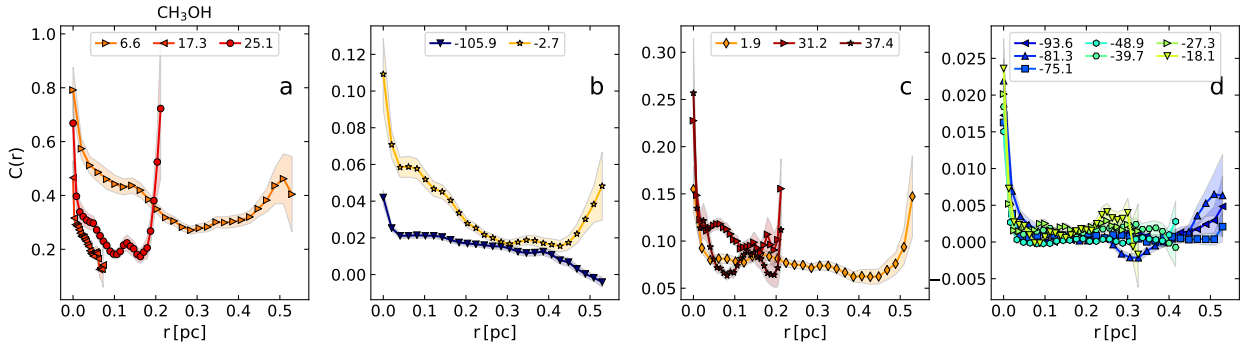

Figure C.48: Same as Fig. C.41, but for CH_3OH.

C.8 Analysis of two-point auto-correlation functions

We analyse here the two-point auto-correlation functions of all molecules except the ones of SiO and SO which are analysed in Sect. 5.4.4. c-C_3H_2 and HNC are detected in all investigated velocity components and trace structures that are more extended than the investigated area ($\gtrsim 15''$) for all components but one, at -93.7 km s^{-1}, for which the size derived from c-C_3H_2 is $\sim 11''$. This component is one of the noisiest for this molecule (with peak SNR below 7) so it is unclear whether this smaller size is significant compared to the other components, especially because the size traced with HNC ($14.4''$) is very close to the size of the

investigated area. We conclude that c-C_3H_2 and HNC trace structures that are more extended than $\sim$ 15″ for all clouds, which corresponds to physical sizes between 0.08 pc in the nearby Sagittarius arm and 0.5 pc in the GC.

^{13}CO and CS also show structures that have sizes larger than ($\gtrsim$ 15″) or similar to ($\sim$ 13–15″) the size of the field of view. The only exceptions are the component at $-2.7\,\mathrm{km\,s^{-1}}$ for ^{13}CO and the one at $-48.1\,\mathrm{km\,s^{-1}}$ for CS. In the former case, the two-point auto-correlation function drops just below the significance threshold at 6″, but increases above this threshold at larger separations and drops below it again for sizes larger than 10.″8 (see Fig. C.31). The corresponding opacity map (see Fig. C.11) shows two compact clumps at (6.″5,0.5″) and (9.″5,10″), hence with a separation of 10″, but one has a SNR below 3 so it may be a noise artefact and the correlation at larger pixel separation may not be real. In the case of CS, the exception concerns the noisiest component, with a peak SNR below 6. The correlation function drops below the significance threshold at 4.″8, but increases above it again at $\sim$ 10″ (see Fig. C.32). However, it remains close to the significance threshold so its shape is not well constrained. Therefore, overall, ^{13}CO and CS trace structures that are more extended than or nearly as extended as the field of view, like c-C_3H_2 and HNC.

H^{13}CO$^+$ traces structures with similar extent as the previous tracers. Four exceptions occur, with very small sizes of 2–3″ or unresolved. All have low SNR in their opacity maps, with a peak SNR below 6 for the component at 31.1 km s^{-1} and below 5 for the other three components. The sensitivity of our data is therefore not sufficient to characterise the structures traced by H^{13}CO$^+$ for these four components.

CH_3OH and HC^{15}N behave in the same way: all components with a peak SNR higher than 5 in their opacity maps, reveal structures that are more extended than the field of view, or at least have sizes larger than 13″ and 11″, respectively.

Only six and three components traced by C^{34}S and ^{13}CS, respectively, have a peak SNR in their opacity map higher than 5 (Figs. C.16 and C.18). Most of them trace extended structures of size similar to the field of view (Figs. C.15 and C.17). The 17.7 km s^{-1} component of C^{34}S and the -105.9 km s^{-1} component of ^{13}CS have smaller Δr_{max} but their peak SNR is barely above 5. The sensitivity of our data is not high enough to characterise the structures of the other velocity components on the basis of these tracers. Because C^{34}S and ^{13}CS are expected to be present in the same regions as CS, that traces extended structures, they clearly show that tracers with a limited sensitivity are not appropriate to constrain the underlying cloud structure. This should be kept in mind when analysing the two-point auto-correlation functions of the other molecules that have low SNR. The case of HN^{13}C is very similar to C^{34}S and ^{13}CS. Only five components have a peak SNR in their opacity map higher than 5 (Fig. C.26). Two of them trace extended structures and two of them have small or unresolved Δr_{max} but with a peak SNR barely above 5. The only exception is the component at 2.5 km s^{-1}, with a correlation length of 7″ and a peak SNR of $\sim$11 in its opacity map. For this velocity component, the main isotopologue, HNC, traces an extended structure with a correlation length larger than the field of view so the shorter correlation length derived from HN^{13}C results from a lack of sensitivity of our data.

C.9 Probability distribution functions

The PDFs of all molecules but c-C_3H_2 are shown in Figs.C.49 to C.59. The results of the Gaussian fits to the PDFs are shown in Fig. C.60 and C.61, and listed in Tables C.2 and C.3.

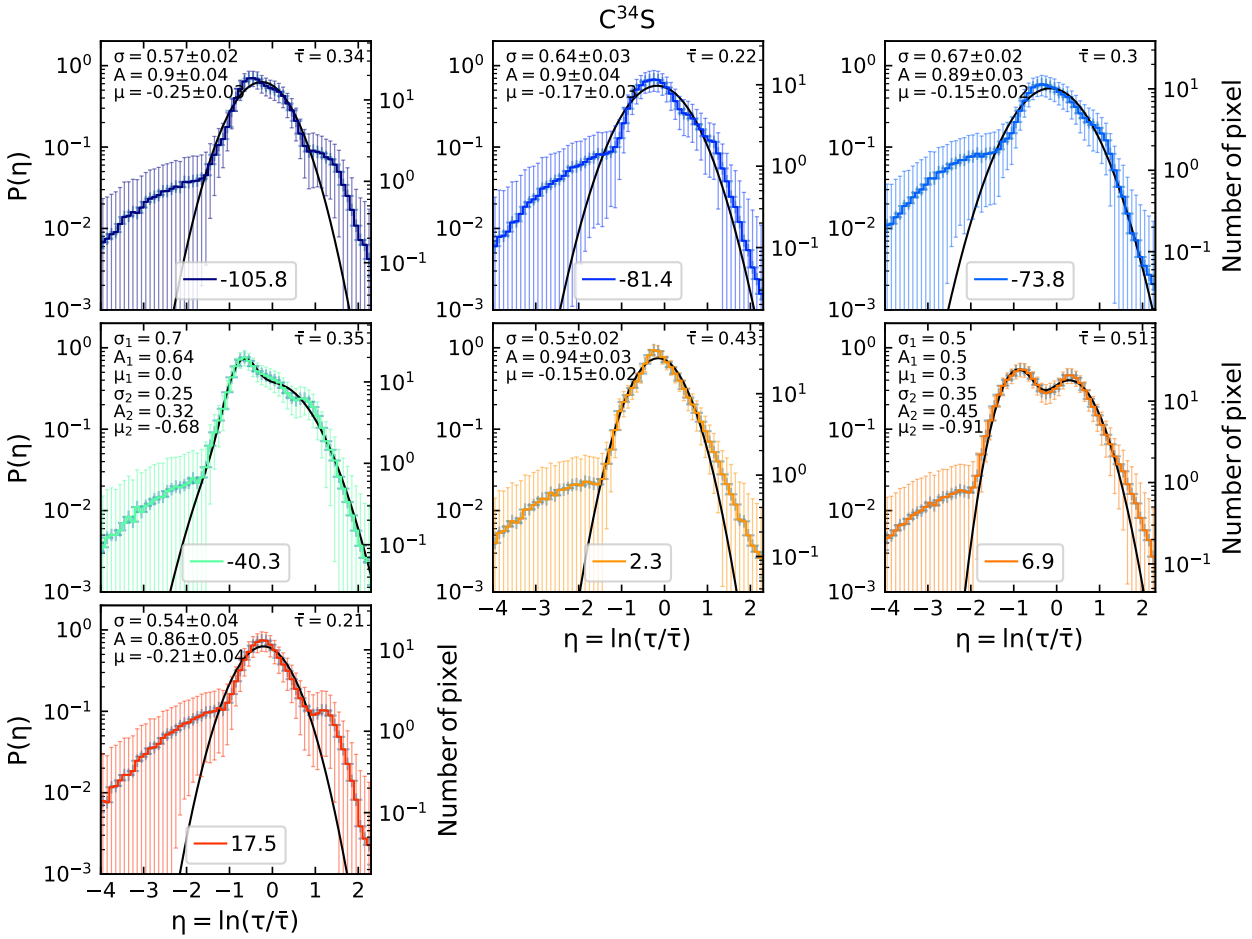

Figure C.49: Same as Fig. 5.10, but for $C^{34}S$.

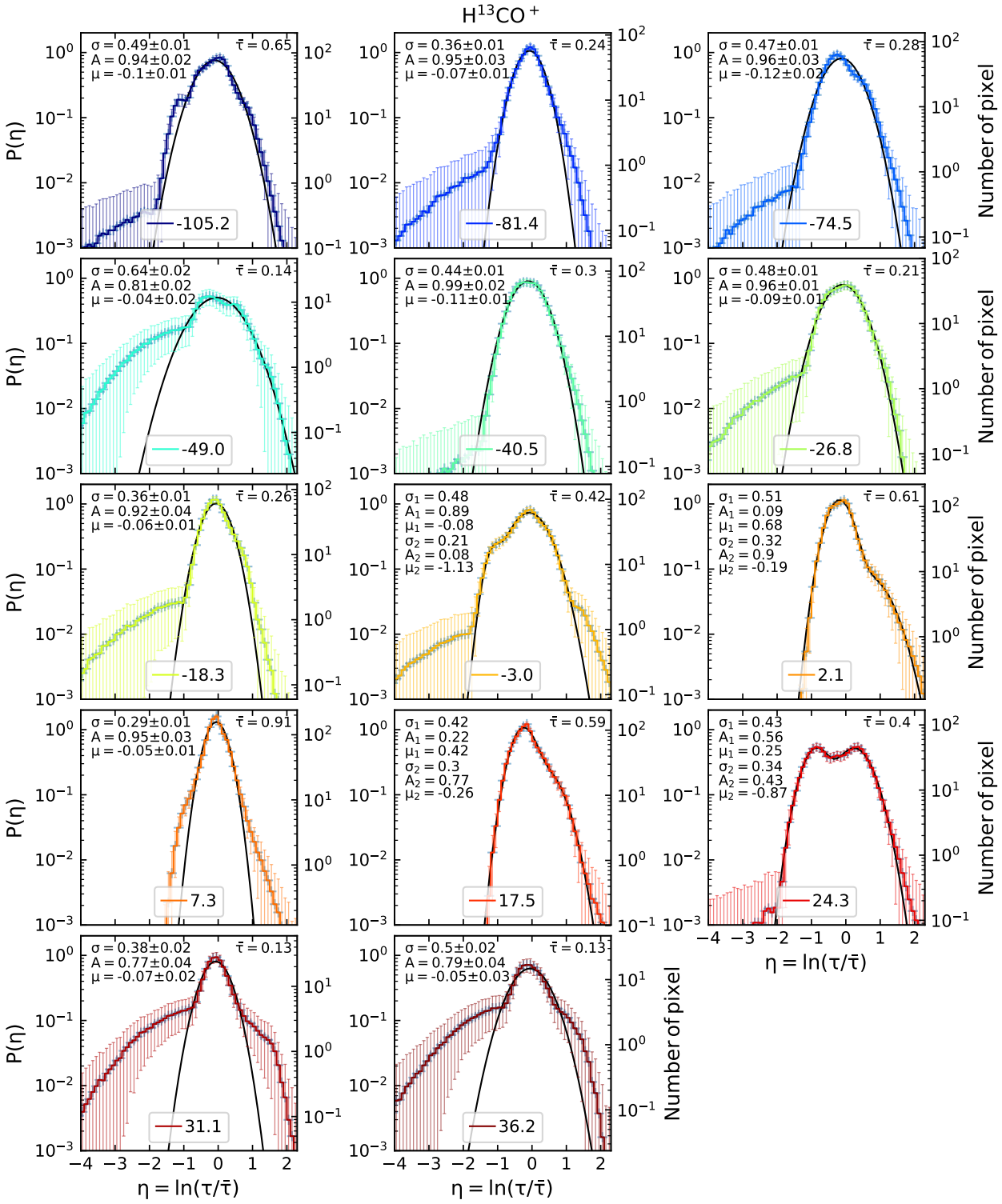

Figure C.50: Same as Fig. 5.10, but for $H^{13}CO^{+}$.

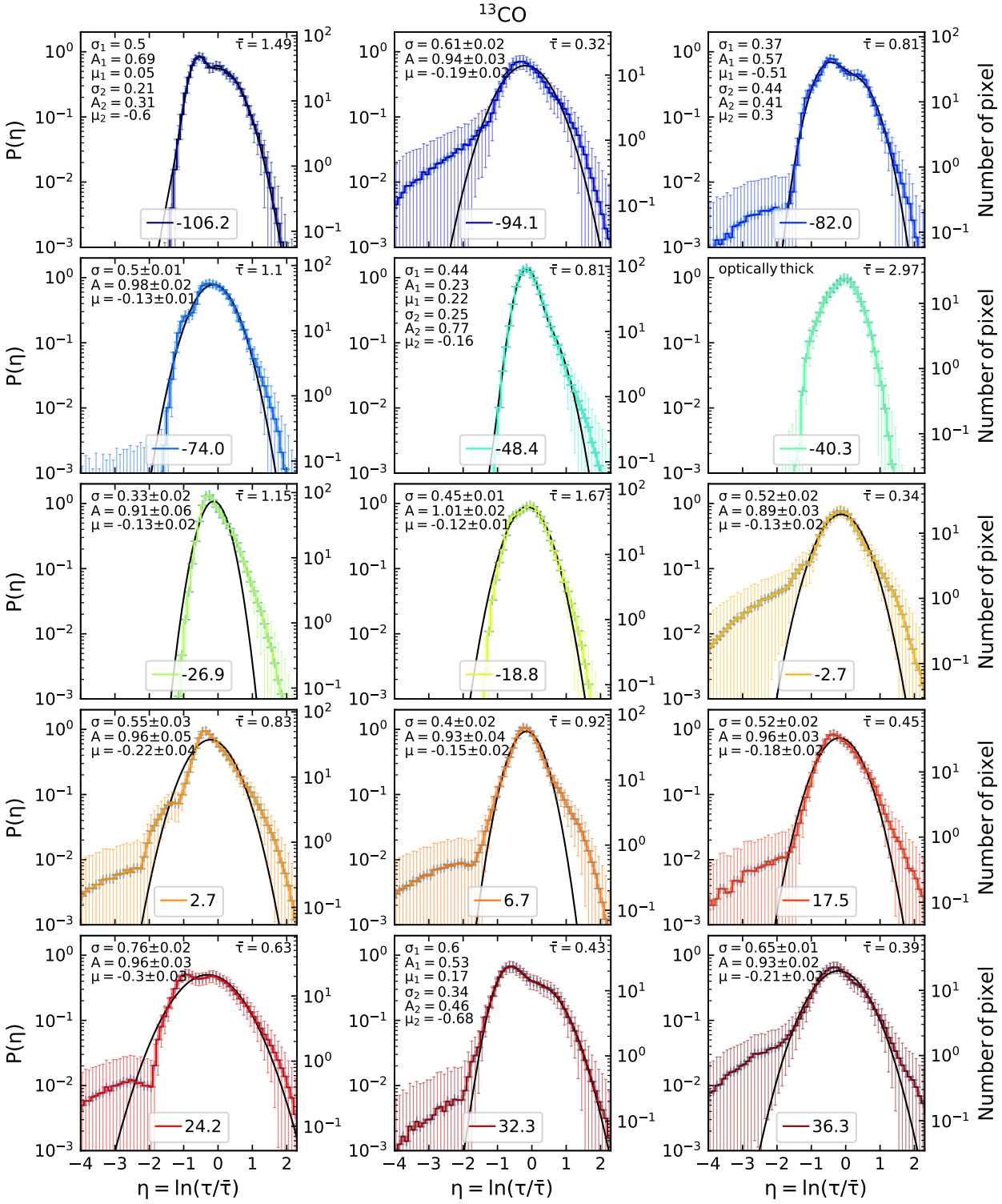

Figure C.51: Same as Fig. 5.10, but for ^{13}CO.

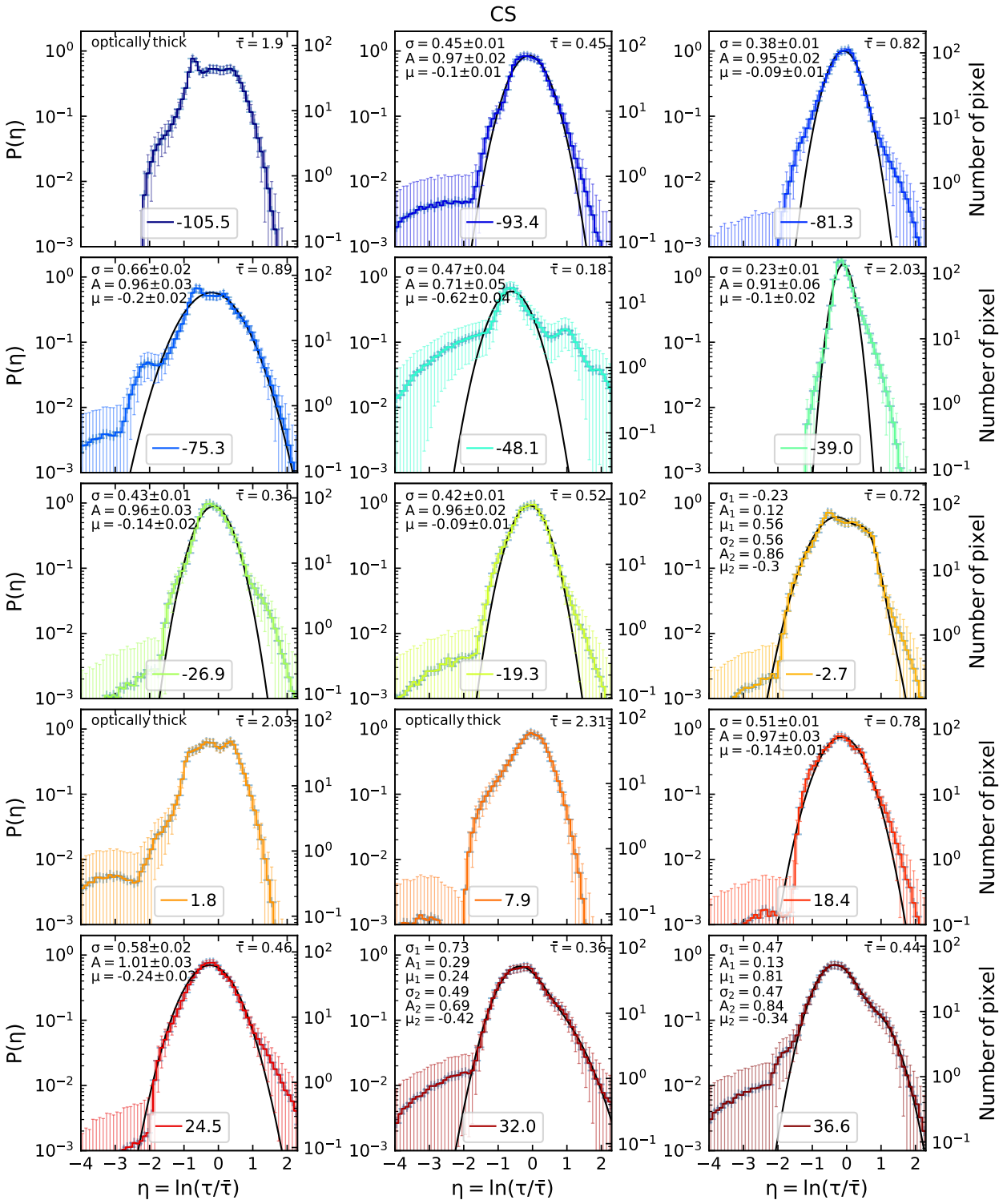

Figure C.52: Same as Fig. 5.10, but for CS.

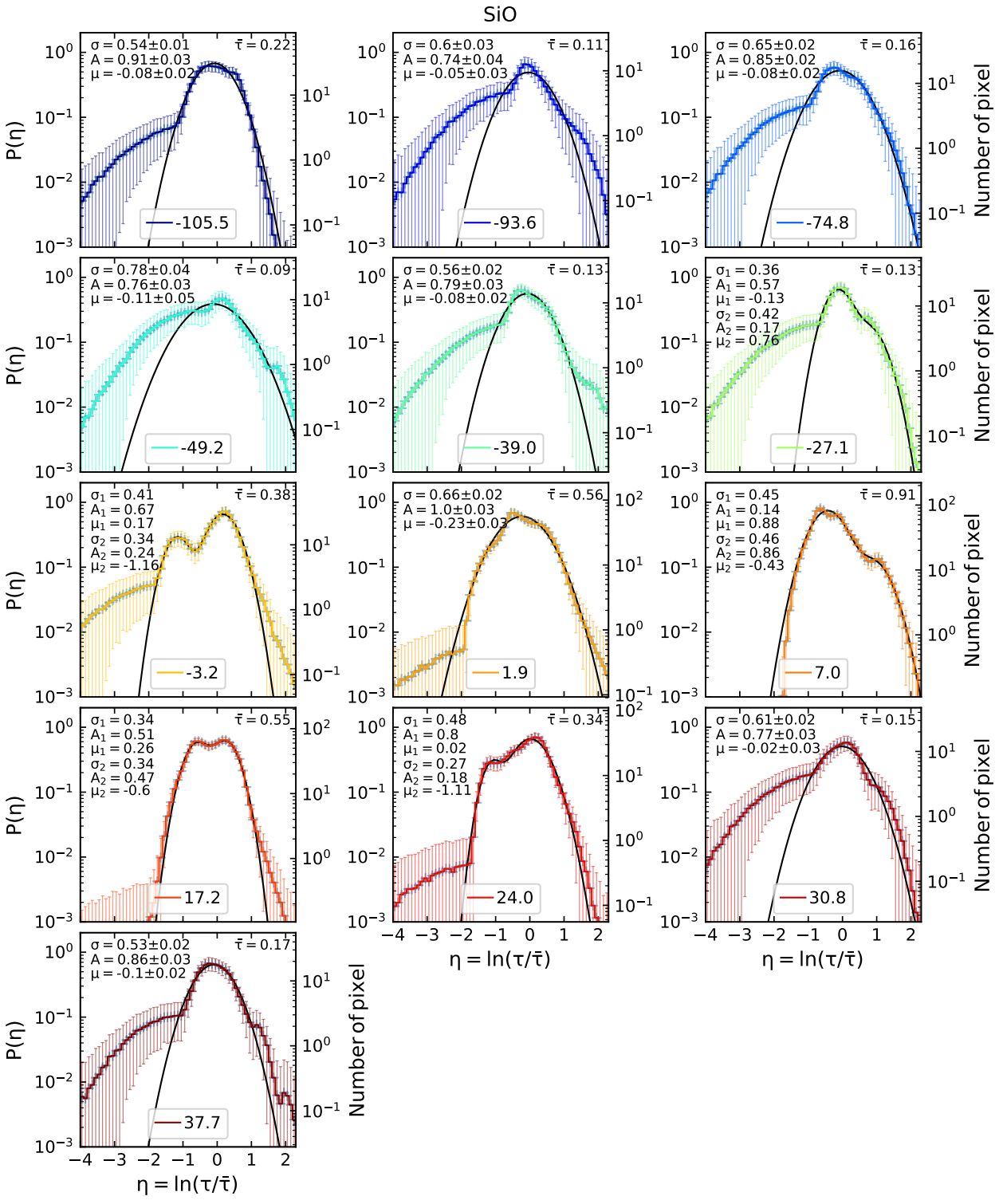

Figure C.53: Same as Fig. 5.10, but for SiO.

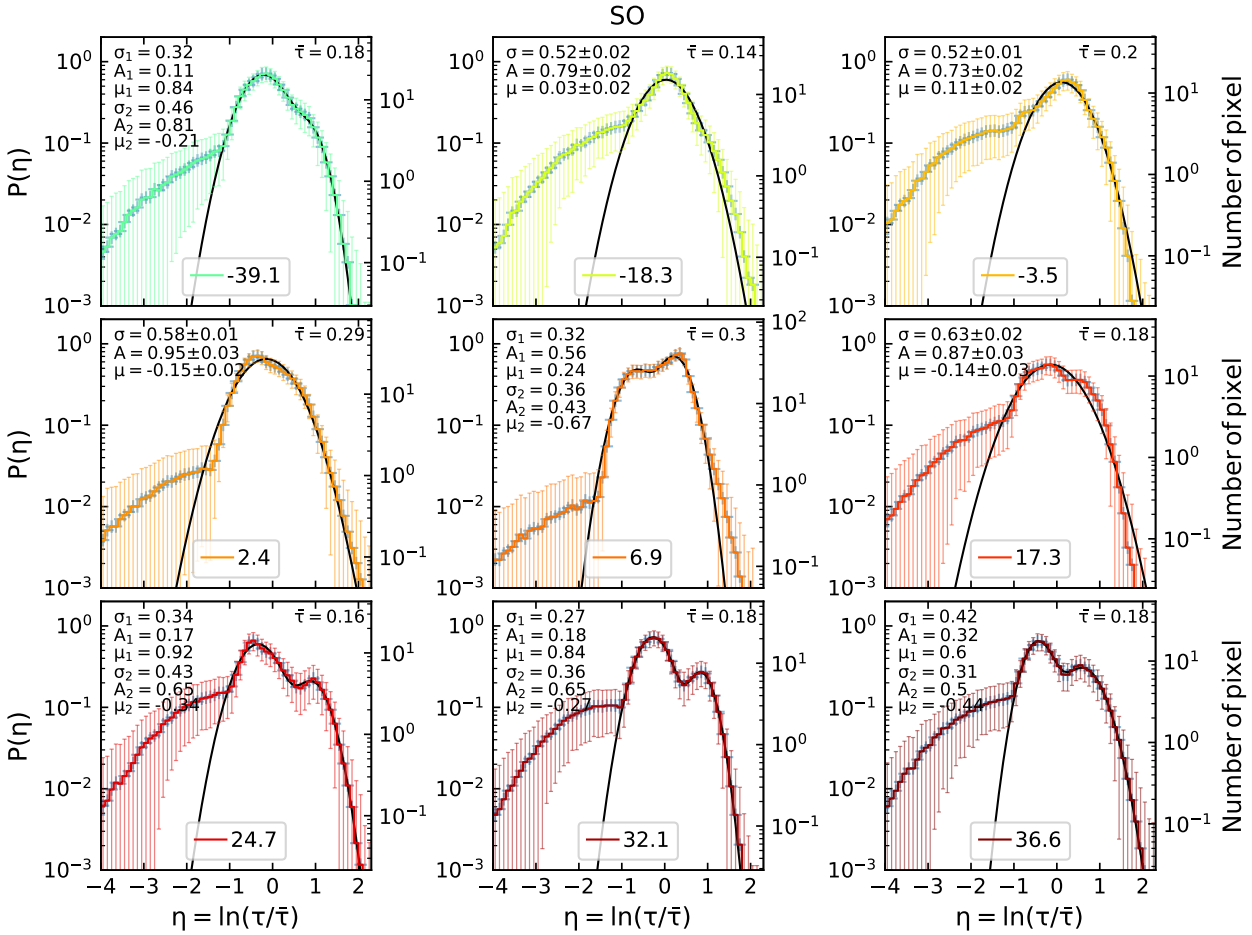

Figure C.54: Same as Fig. 5.10, but for SO.

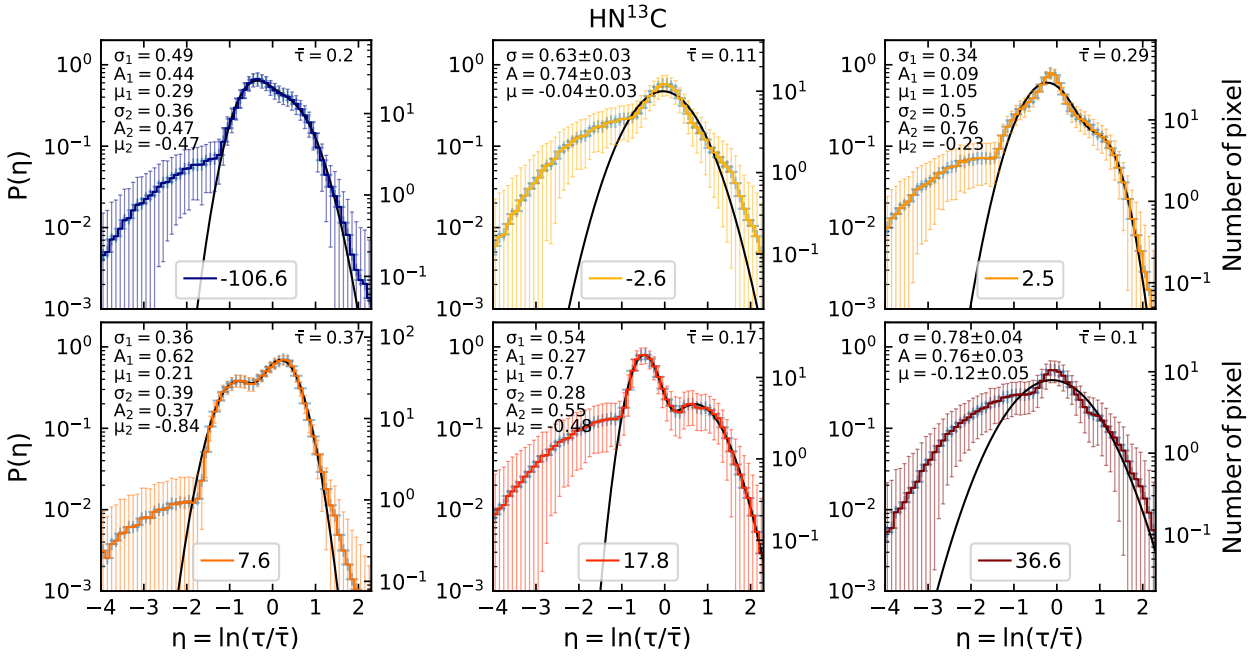

Figure C.55: Same as in Fig. 5.10, but for $HN^{13}C$.

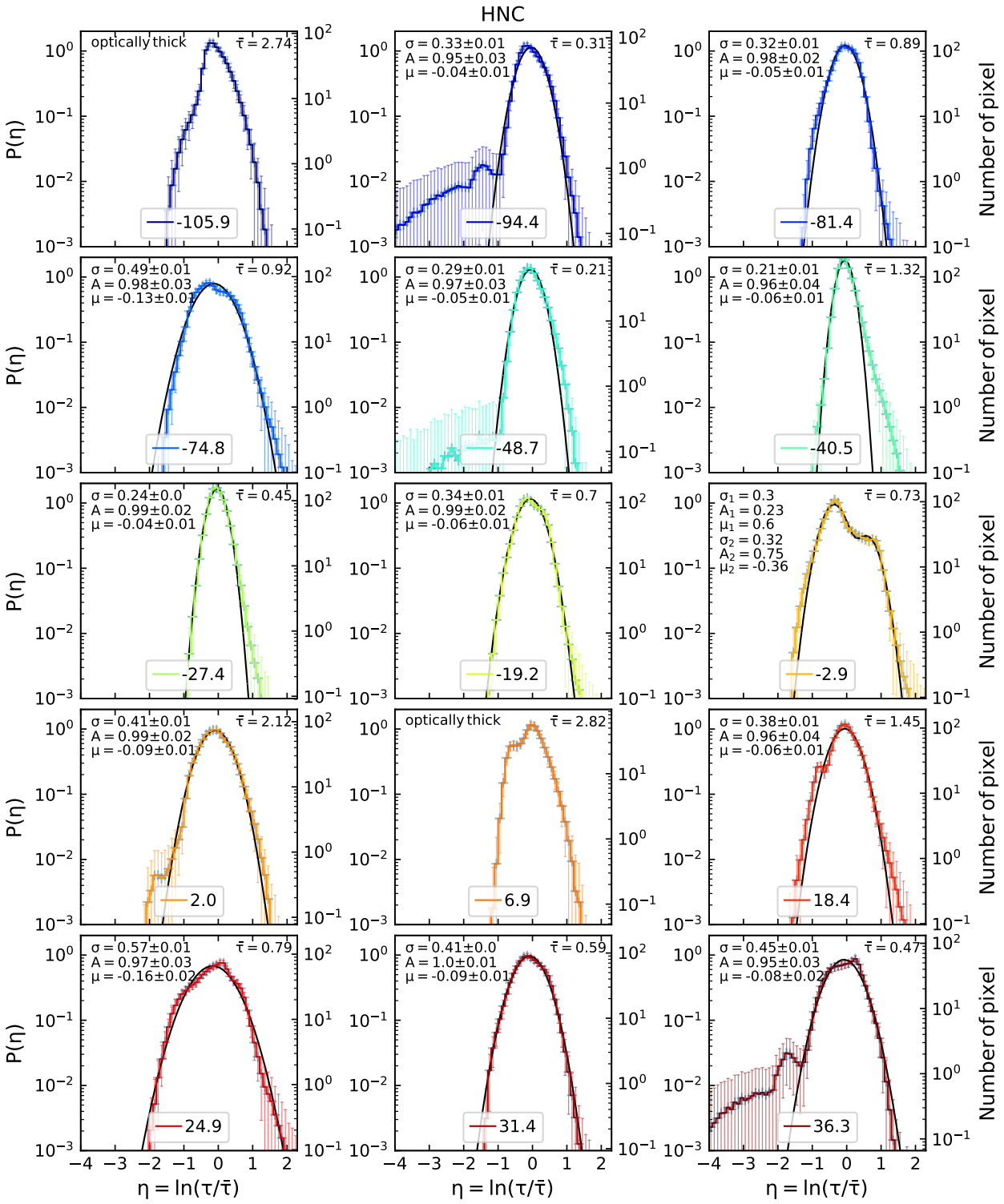

Figure C.56: Same as Fig. 5.10, but for HNC.

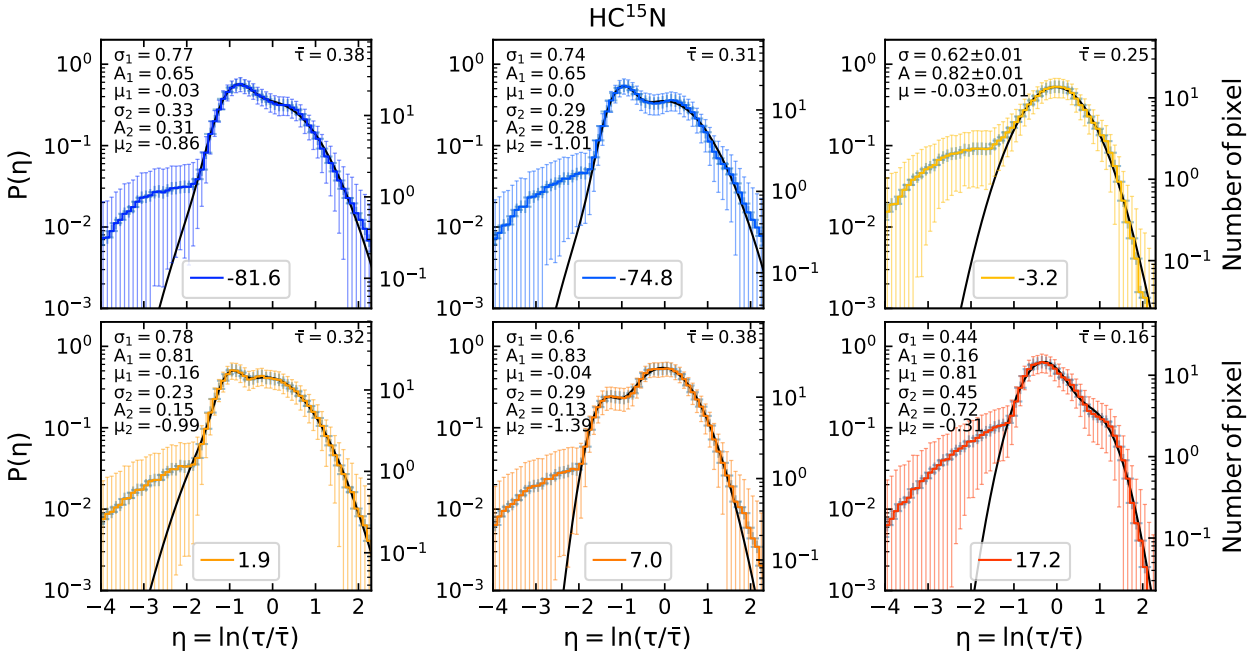

Figure C.57: Same as Fig. 5.10, but for $HC^{15}N$.

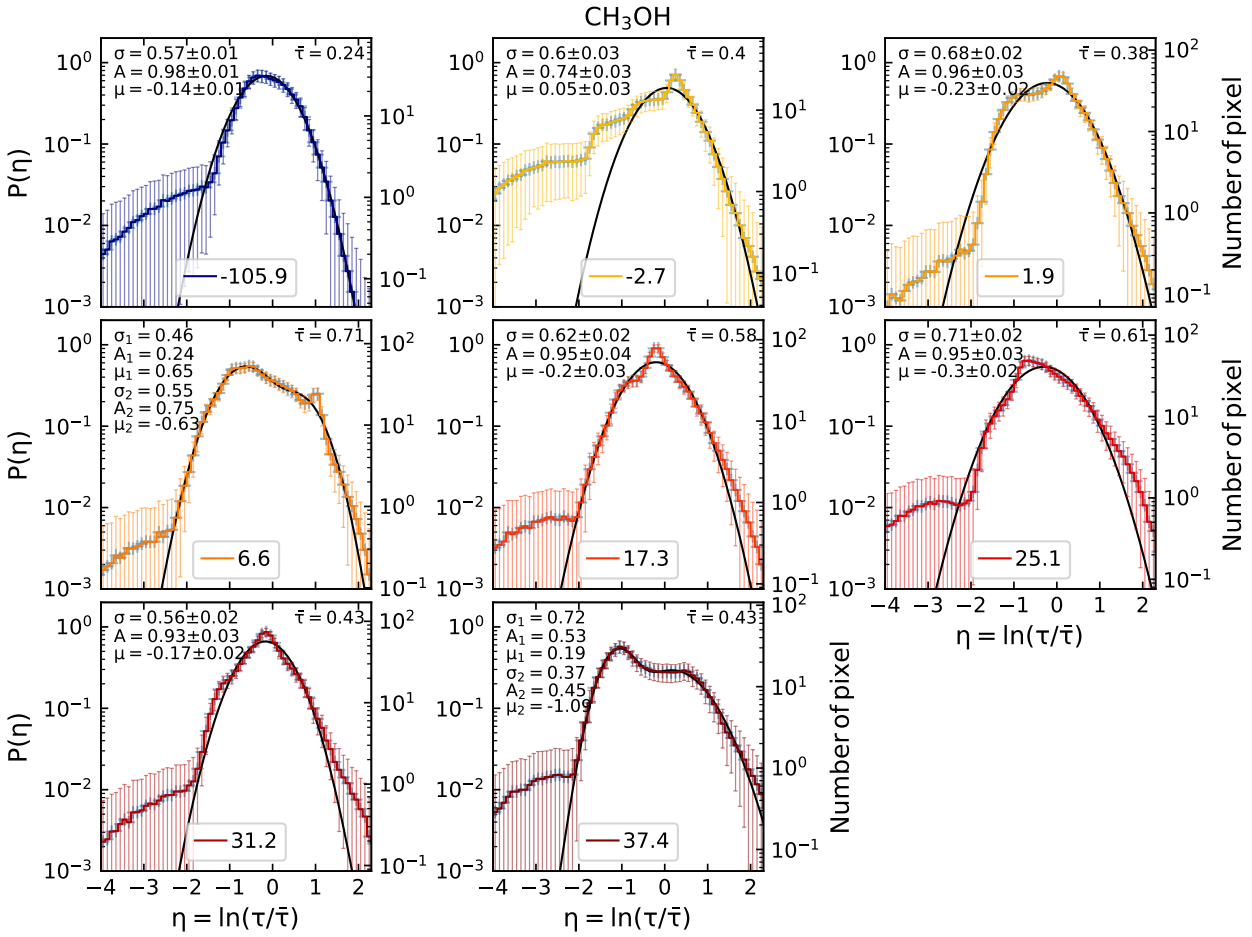

Figure C.58: Same as Fig. 5.10, but for CH_3OH.

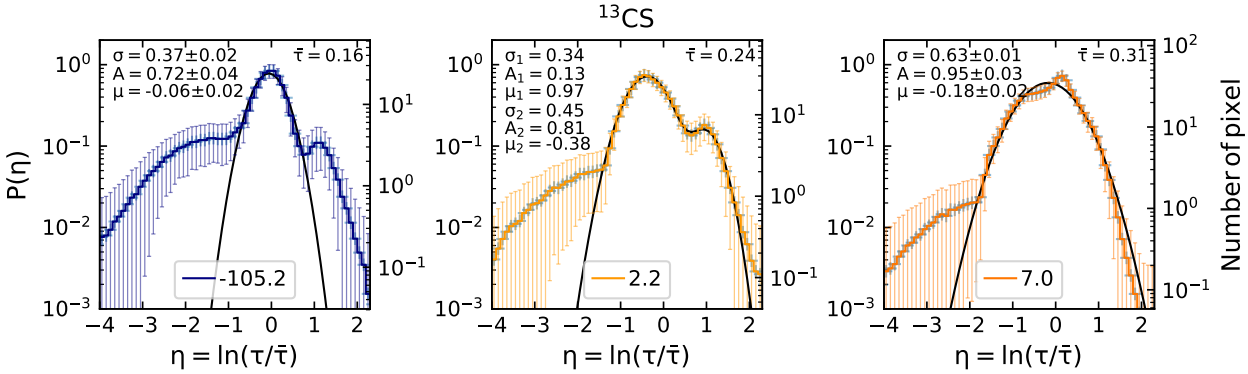

Figure C.59: Same as Fig. 5.10, but for ^{13}CS.

Table C.1: Number of Gaussians fitted to the PDF.

velocity [km s^{-1}]	c-C_3H_2-o	$H^{13}CO^+$	^{13}CO	CS	$C^{34}S$	^{13}CS	SO	SiO	HNC	$HN^{13}C$	$HC^{15}N$	CH_3OH
					Galactic Center							
−105.9	1	1	2	o.t.	1	1	n	1	o.t.	2	n	1
−93.7	1	n	1	1	n	n	n	1	1	n	n	n
−81.5	1	1	2	1	1	n	n	n	1	n	2	n
−74.6	1	1	1	1	1	n	n	1	1	n	2	n
−3.2	2	2	1	2	n	n	1	2	2	1	1	1
2.0	1	2	1	o.t.	1	2	1	1	1	2	2	1
7.3	1	1	1	o.t.	2	1	2	2	o.t.	2	2	2
					3 kpc arm							
−48.4	1	1	2	1	n	n	n	1	1	n	n	n
−39.7	1	1	o	1	2	n	1	1	1	n	n	n
					4 kpc arm							
−27.6	1	1	1	1	n	n	n	2	1	n	n	n
−18.9	1	1	1	1	n	n	1	n	1	n	n	n
					Scutum arm							
24.7	1	2	1	1	n	n	2	2	1	n	n	2
31.6	1	1	2	2	n	n	2	1	1	n	n	1
36.9	1	1	1	2	n	n	2	1	1	1	n	2
					Sagittarius arm							
17.7	2	2	1	1	1	n	1	2	1	2	2	1

Notes. The components for which the SNR is too low are marked with n and the ones for which more than 10% are optically thick are labeled with o.t..

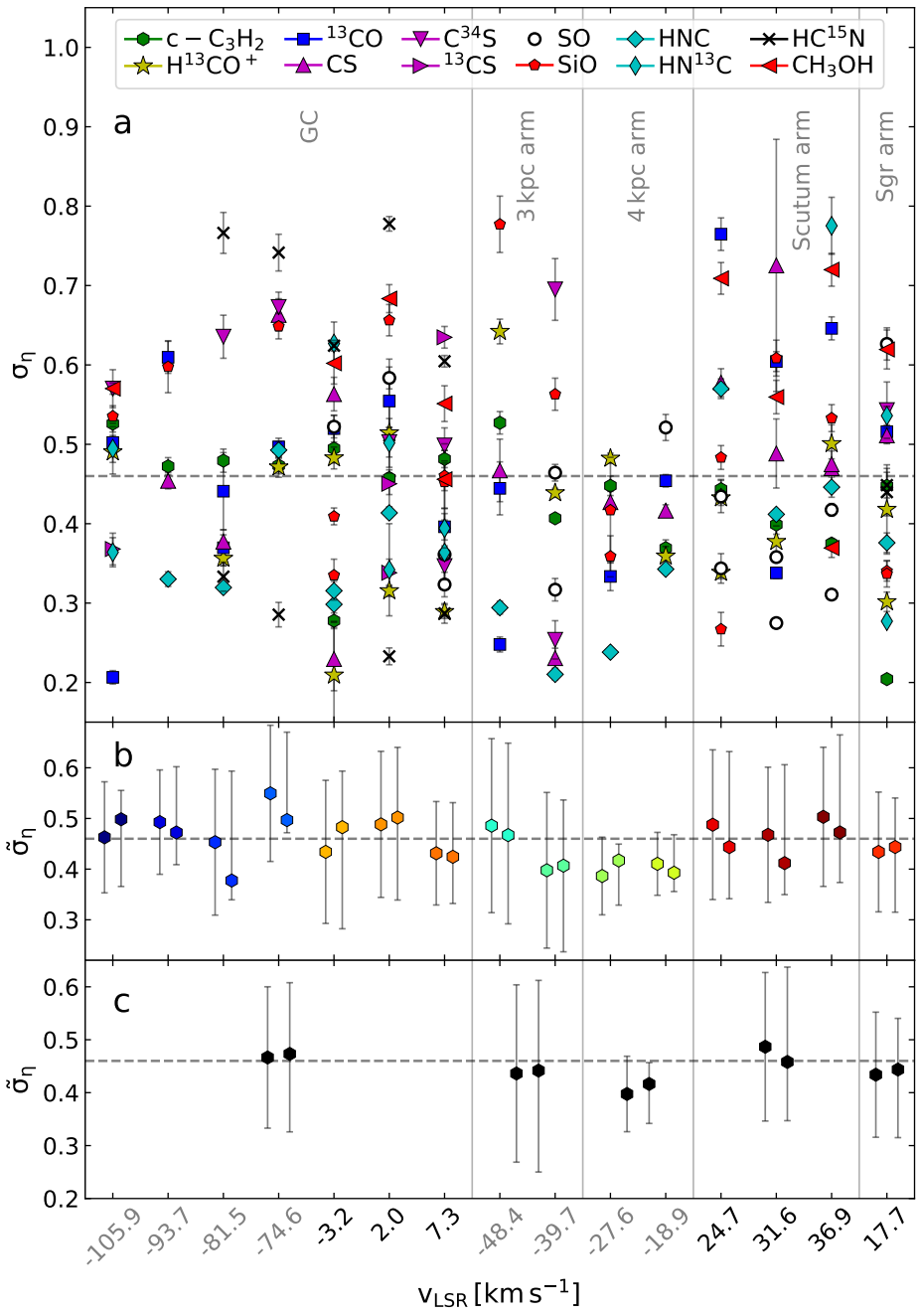

Figure C.60: **a** Widths of the Gaussians fitted to the PDFs of all molecules for 15 velocity components, roughly sorted by their distance to the Galactic Center. **b** Mean (left) and median (right) values for each velocity component. **c** Mean (left) and median (right) values for each subsample of clouds, from left to right: Galactic Center, 3 kpc arm, 4 kpc arm, Scutum arm, Sagittarius arm. The uncertainties represent the standard deviation for the mean and the corresponding percentiles for the median. The dashed line in panels b and c marks the mean value of all data points shown in panel a. Velocity components belonging to Category I and II are coloured in grey and black, respectively.

Table C.2: Mean ($\bar{\sigma}$) and median ($\tilde{\sigma}$) widths of the Gaussians fitted to PDFs for each velocity component.

$v_{\rm LSR}{}^a$ [km s^{-1}]	$\bar{\sigma}$	$\tilde{\sigma}$	$\bar{\sigma}^b$	$\tilde{\sigma}^b$
Galactic Center				
−105.9	0.46 ± 0.11	$0.50^{+0.06}_{-0.13}$		
−93.7	0.49 ± 0.10	$0.47^{+0.13}_{-0.06}$		
−81.5	0.45 ± 0.14	$0.38^{+0.22}_{-0.04}$		
−74.6	0.55 ± 0.13	$0.50^{+0.17}_{-0.02}$	0.47 ± 0.13	$0.47^{+0.13}_{-0.15}$
−3.2	0.43 ± 0.14	$0.48^{+0.11}_{-0.20}$		
2.0	0.49 ± 0.14	$0.50^{+0.14}_{-0.16}$		
7.3	0.43 ± 0.10	$0.42^{+0.11}_{-0.09}$		
3 kpc arm				
−48.4	0.49 ± 0.17	$0.47^{+0.18}_{-0.18}$	0.44 ± 0.17	$0.44^{+0.17}_{-0.19}$
−39.7	0.40 ± 0.15	$0.41^{+0.13}_{-0.17}$		
4 kpc arm				
−27.6	0.39 ± 0.08	$0.42^{+0.03}_{-0.09}$	0.40 ± 0.07	$0.42^{+0.04}_{-0.07}$
−18.9	0.41 ± 0.06	$0.39^{+0.08}_{-0.04}$		
Scutum arm				
24.7	0.49 ± 0.15	$0.44^{+0.19}_{-0.10}$		
31.6	0.47 ± 0.13	$0.41^{+0.19}_{-0.06}$	0.49 ± 0.14	$0.46^{+0.18}_{-0.11}$
36.9	0.50 ± 0.14	$0.47^{+0.19}_{-0.10}$		
Sagittarius arm				
17.7	0.43 ± 0.12	$0.44^{+0.10}_{-0.13}$	0.43 ± 0.12	$0.44^{+0.10}_{-0.13}$

Notes. $^{(a)}$ Channel velocities of c-C_3H_2. $^{(b)}$ Mean and median values for each subsample of clouds.

Table C.3: Mean ($\bar{\sigma}$) and median ($\tilde{\sigma}$) dispersion of the PDFs of the molecules.

molecule	$\bar{\sigma}$	$\tilde{\sigma}$
c-C_3H_2-o	0.43 ± 0.08	$0.45^{+0.04}_{-0.08}$
$H^{13}CO^+$	0.41 ± 0.10	$0.43^{+0.07}_{-0.11}$
^{13}CO	0.47 ± 0.14	$0.48^{+0.13}_{-0.14}$
CS	0.47 ± 0.13	$0.47^{+0.10}_{-0.08}$
$C^{34}S$	0.52 ± 0.14	$0.54^{+0.12}_{-0.16}$
^{13}CS	0.45 ± 0.12	$0.41^{+0.14}_{-0.06}$
SO	0.42 ± 0.11	$0.39^{+0.13}_{-0.07}$
SiO	0.49 ± 0.13	$0.47^{+0.15}_{-0.13}$
HNC	0.36 ± 0.09	$0.34^{+0.11}_{-0.04}$
$HN^{13}C$	0.47 ± 0.14	$0.44^{+0.14}_{-0.09}$
$HC^{15}N$	0.50 ± 0.20	$0.45^{+0.30}_{-0.16}$
CH_3OH	0.58 ± 0.10	$0.59^{+0.11}_{-0.09}$

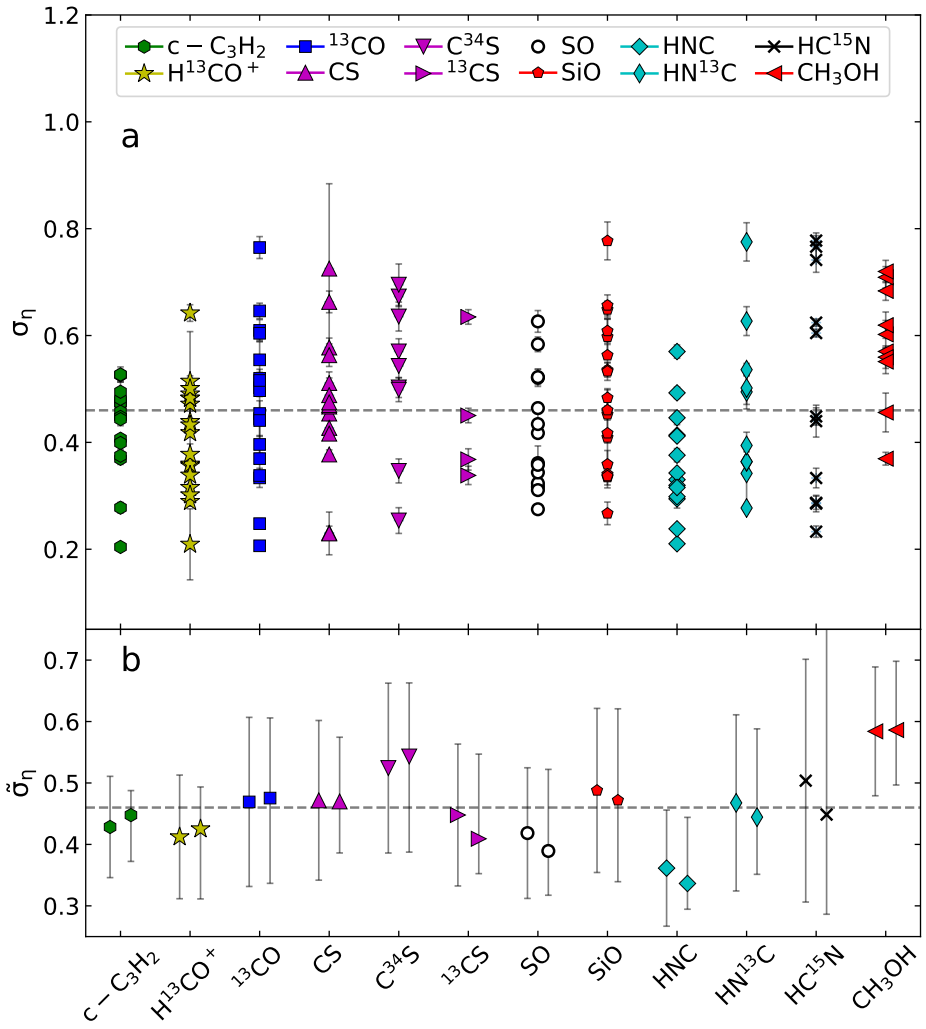

Figure C.61: **a** Widths of the Gaussians fitted to the PDFs of 15 velocity components sorted by molecule. **b** Mean (left) and median (right) values for each molecule. The uncertainties represent the standard deviation for the mean and the corresponding percentiles for the median. The dashed line marks the mean value for all components (see Fig. C.60).

C.10 Maps and coefficients of PCA

The principal components and principal component coefficients for the investigated velocities except for $v_{\rm LSR}$ = 24.7 km s^{-1} are shown in Figs. C.62–C.71.

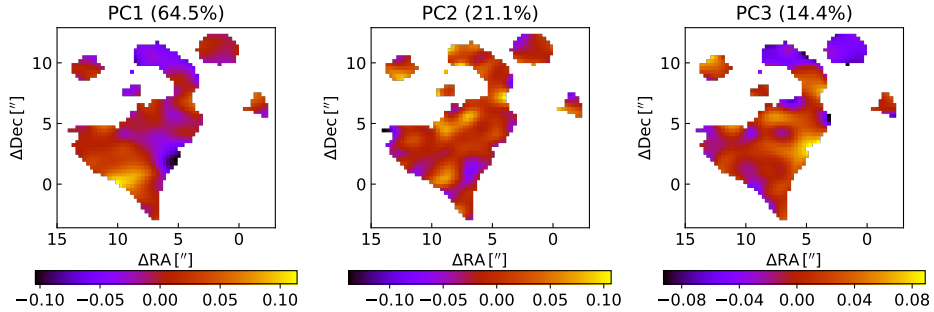

Figure C.62: Same as Fig. 5.18 $v_{\rm LSR}$ =-105.9 km s^{-1}.

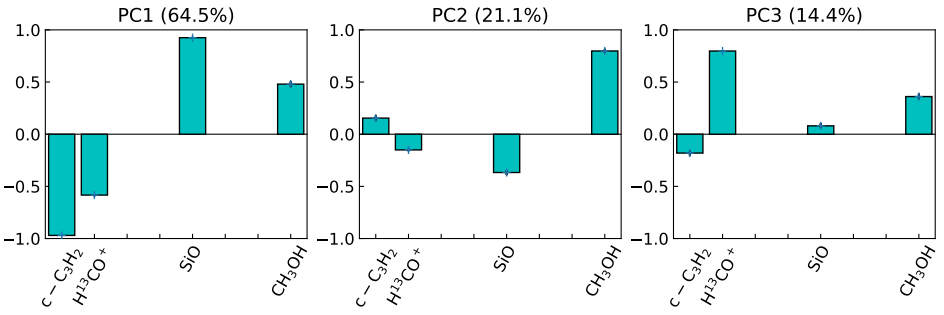

Figure C.63: Same as Fig. 5.19 but for $v_{\rm LSR}$ =-105.9 km s^{-1}.

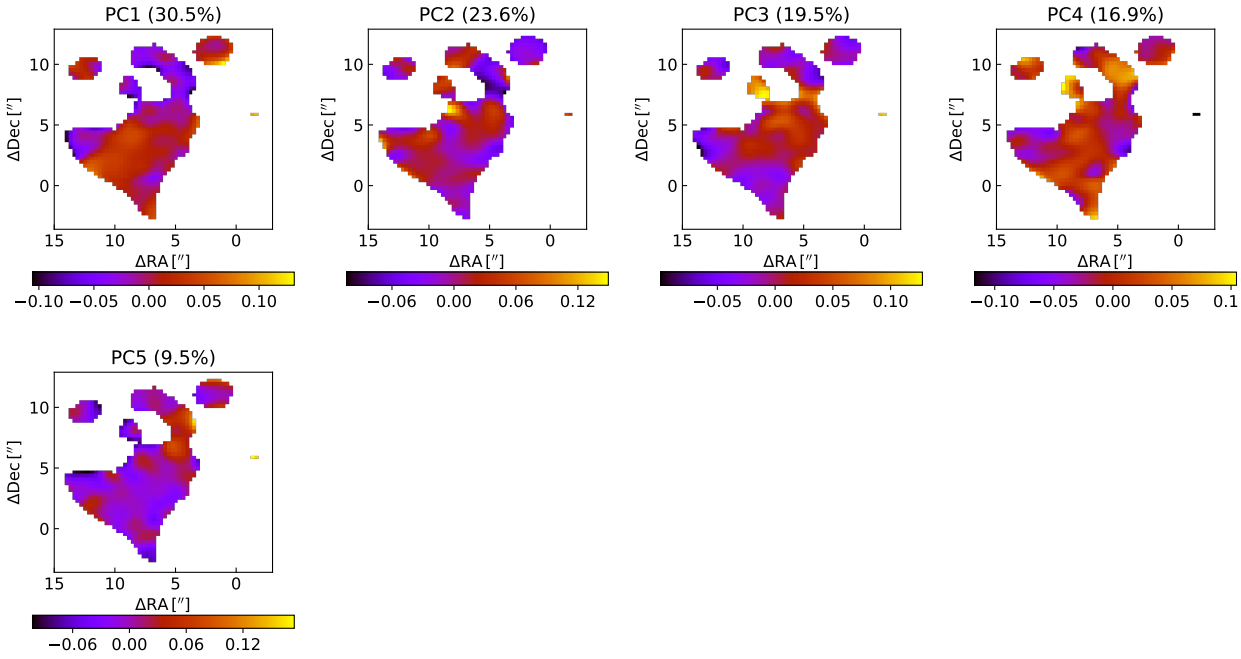

Figure C.64: Same as Fig. 5.18 $v_{\rm LSR}$ =2.0 km s^{-1}.

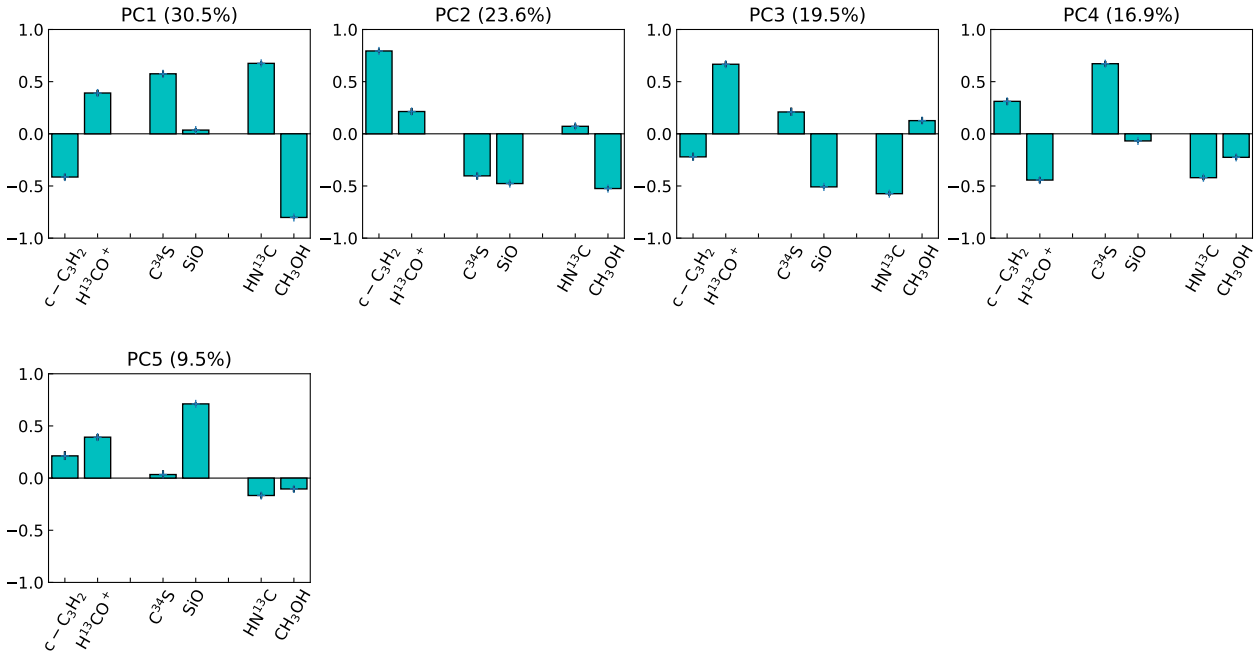

Figure C.65: Same as Fig. 5.19 but for $v_{\rm LSR}$ =2.0 km s^{-1}.

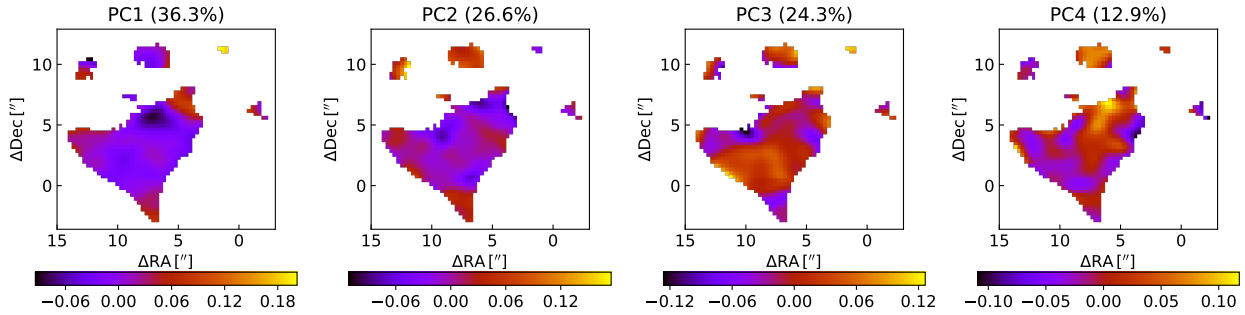

Figure C.66: Same as Fig. 5.18 $v_{\rm LSR}$ =7.3 km s^{-1}.

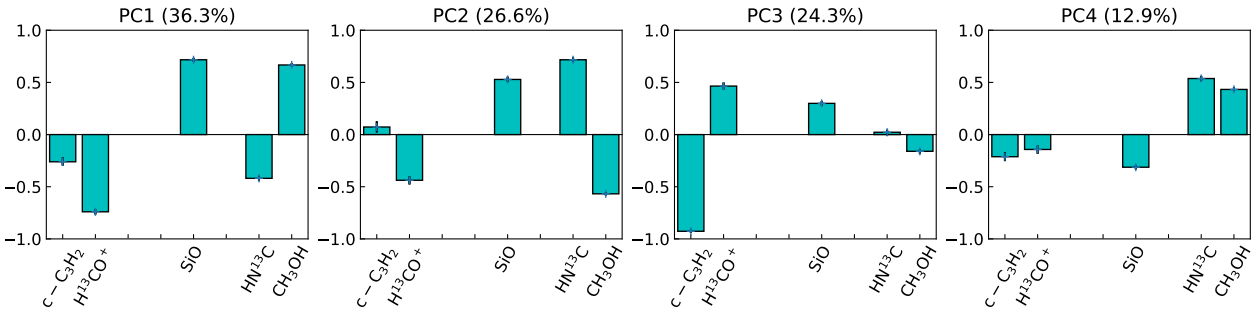

Figure C.67: Same as Fig. 5.19 but for $v_{\rm LSR}$ =7.3 km s^{-1}.

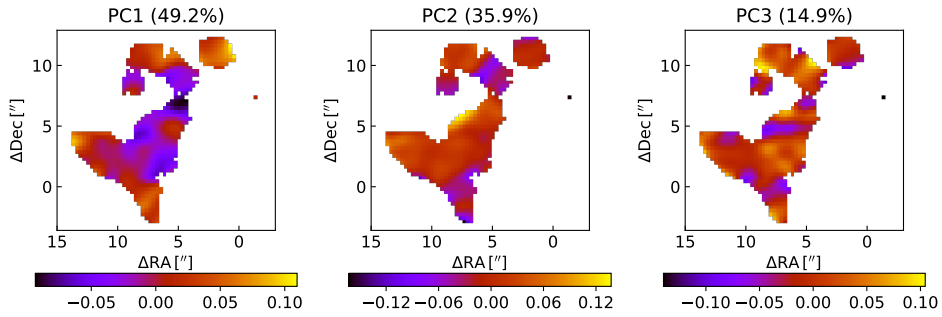

Figure C.68: Same as Fig. 5.18 $v_{\rm LSR}$ =31.6 km s^{-1}.

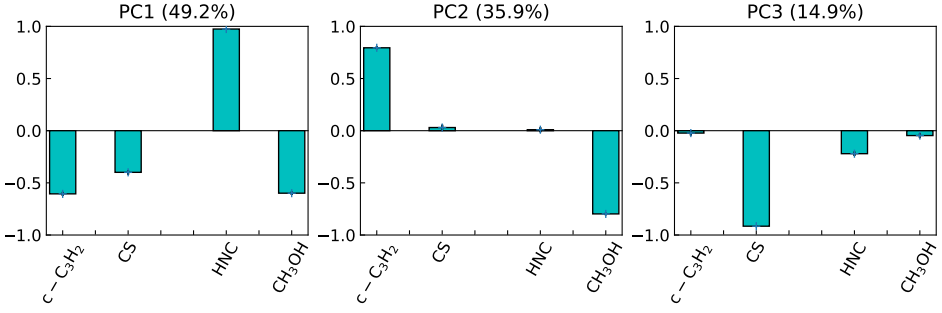

Figure C.69: Same as Fig. 5.19 but for $v_{\rm LSR}$ =31.6 km s^{-1}.

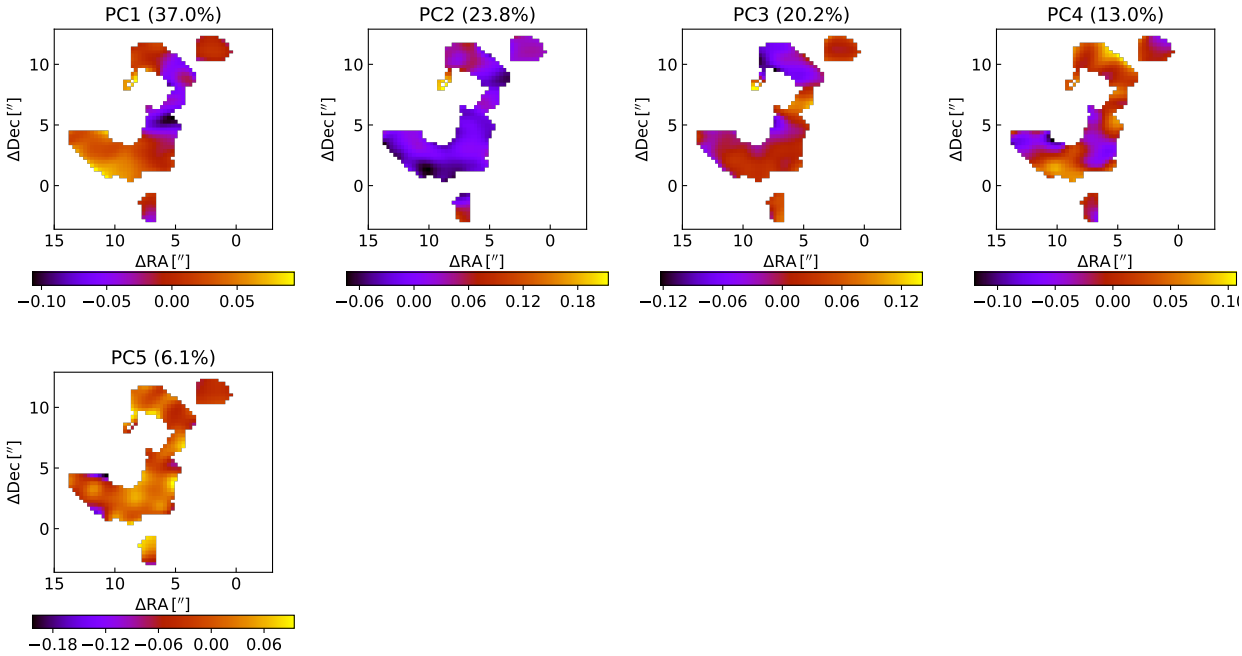

Figure C.70: Same as Fig. 5.18 but for $v_{\rm LSR}$ =17.7 km s^{-1}.

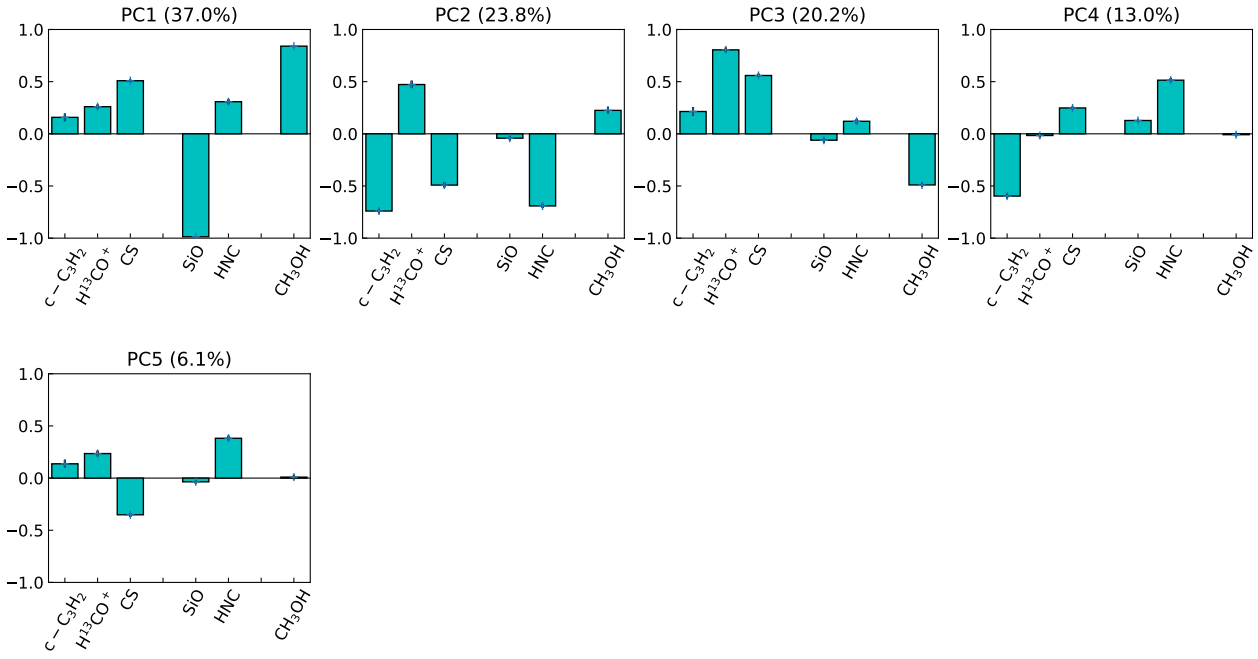

Figure C.71: Same as Fig. 5.19 but for $v_{\rm LSR}$ =17.7 km s^{-1}.

C.11 Mopra maps and spectra

We show here channel maps of four velocity components seen in ^{13}CO 1–0 emission with Mopra, and the averaged Mopra emission spectra of HNC 1–0 and CS 2–1 towards Sgr B2.

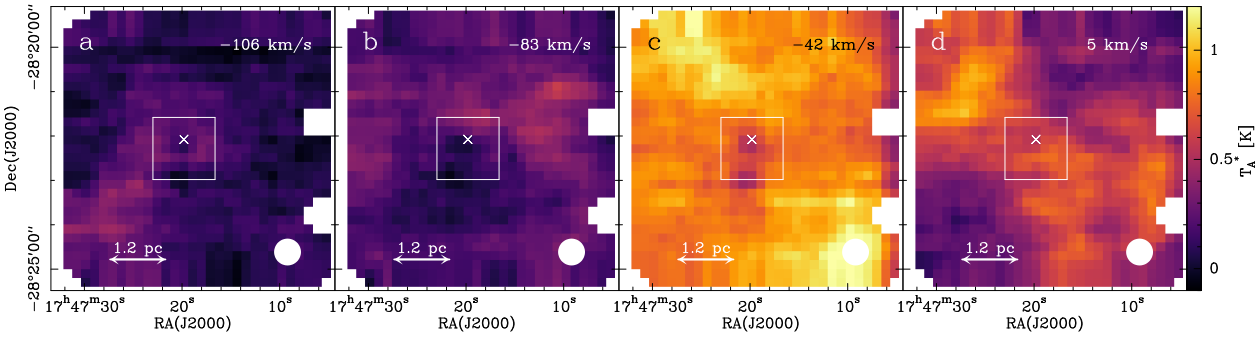

Figure C.72: Same as Fig. 5.22, but for ^{13}CO 1–0 at 11 km s^{-1} (panel **a**), −41 km s^{-1} (**b**), −83 km s^{-1} (**c**), and −106 km s^{-1} (**d**).

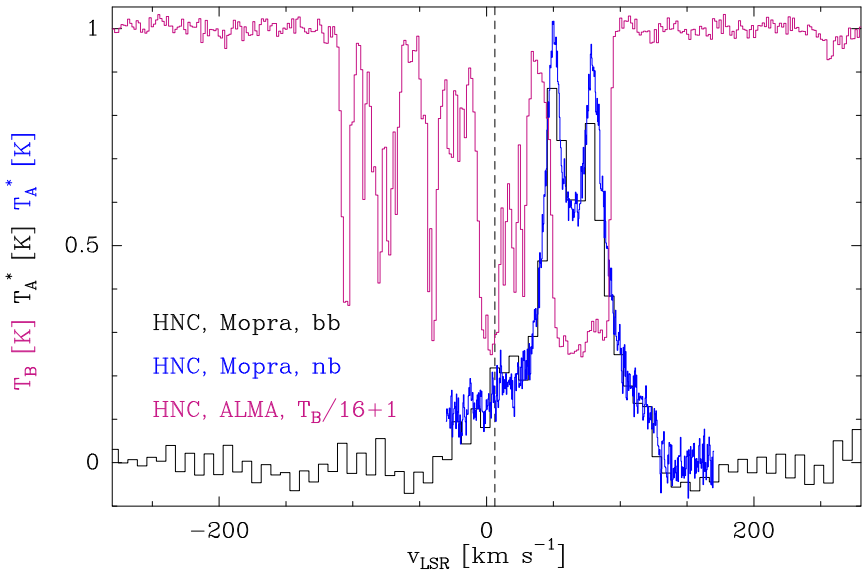

Figure C.73: Same as Fig. 5.23, but for HNC 1–0.

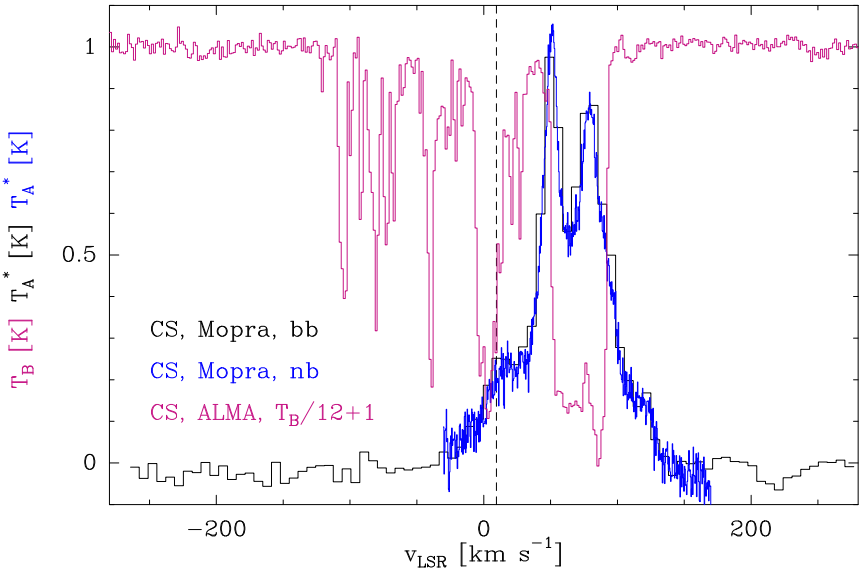

Figure C.74: Same as Fig. 5.23, but for CS 2–1.

C.12 RADEX models

Results of our RADEX calculations for HNC 1–0, CS 2–1, and ^{13}CO 1–0 are shown in Figs C.75–C.77.

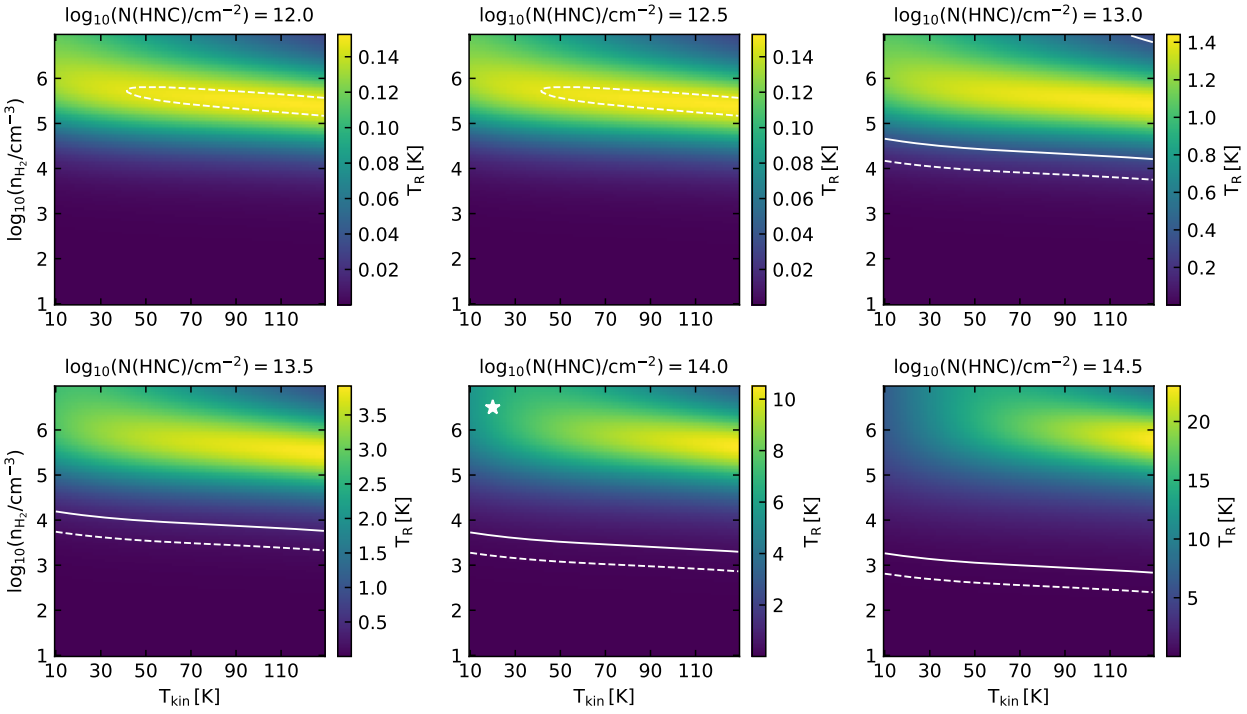

Figure C.75: Same as Fig. 5.25, but for HNC 1–0.

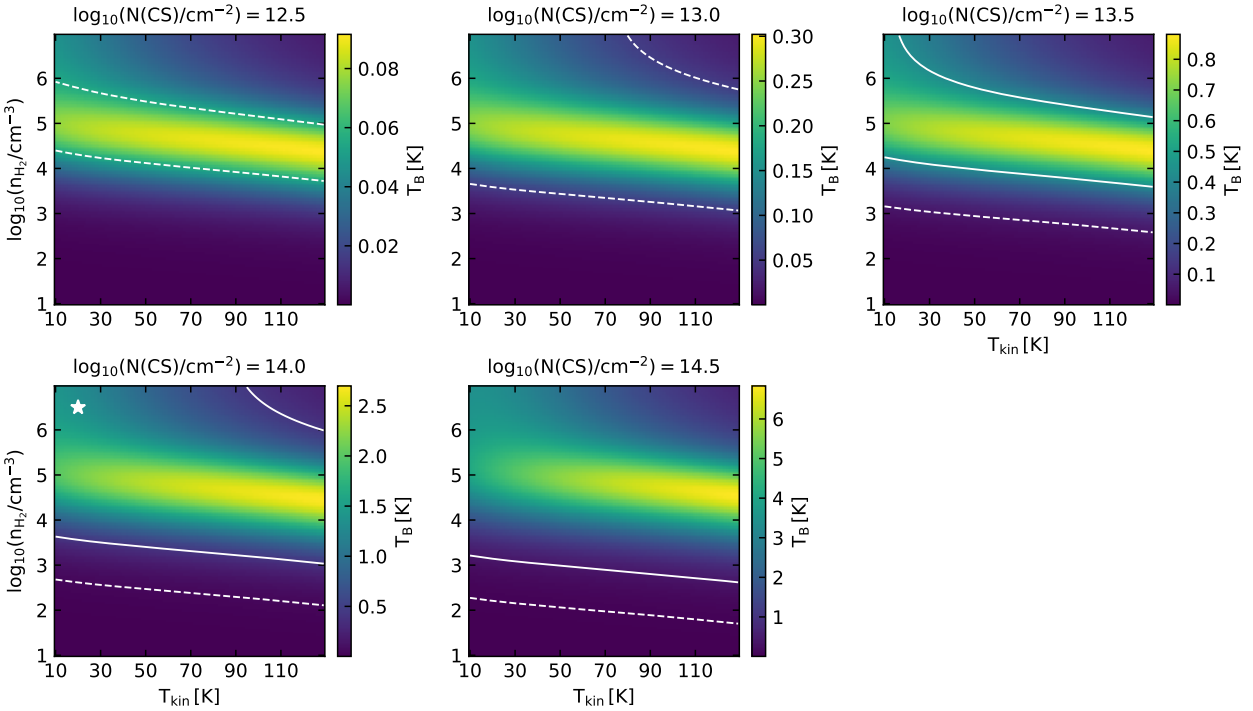

Figure C.76: Same as Fig. 5.25, but for CS 2–1.

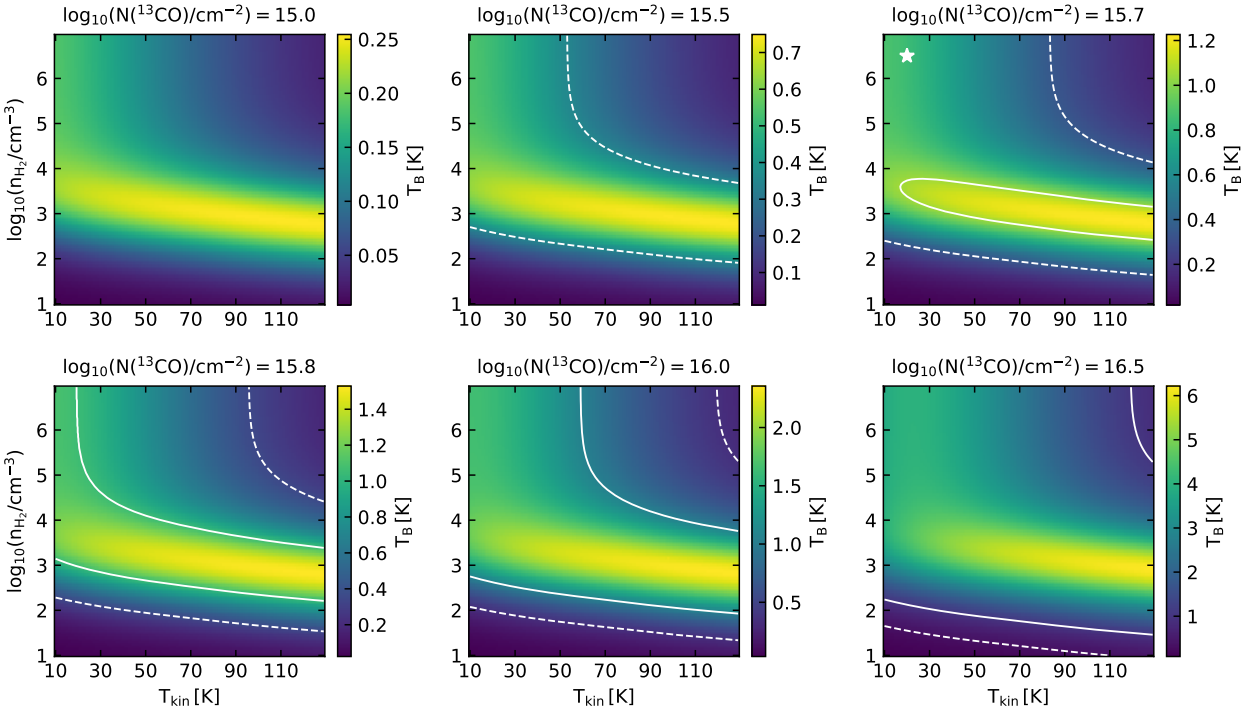

Figure C.77: Same as Fig. 5.25, but for ^{13}CO 1–0. The dashed lines indicate the main beam temperature measured for $v_{\rm LSR} = -83\,{\rm km\,s^{-1}}$.

C.13 Nature of l.o.s. clouds

A modified version of Fig. 2 of Qin et al. (2010) is plotted in Fig. C.78 after correcting the H_2 column densities for the non-uniform abundance profile of HCO^+ discussed in Sect. 5.5.1. The column densities of c-C_3H_2 and H_2 calculated from HCO^+ are plotted against each other in Fig. C.79. The column densities of CCH and c-C_3H_2 are plotted against each other in Fig. C.80.

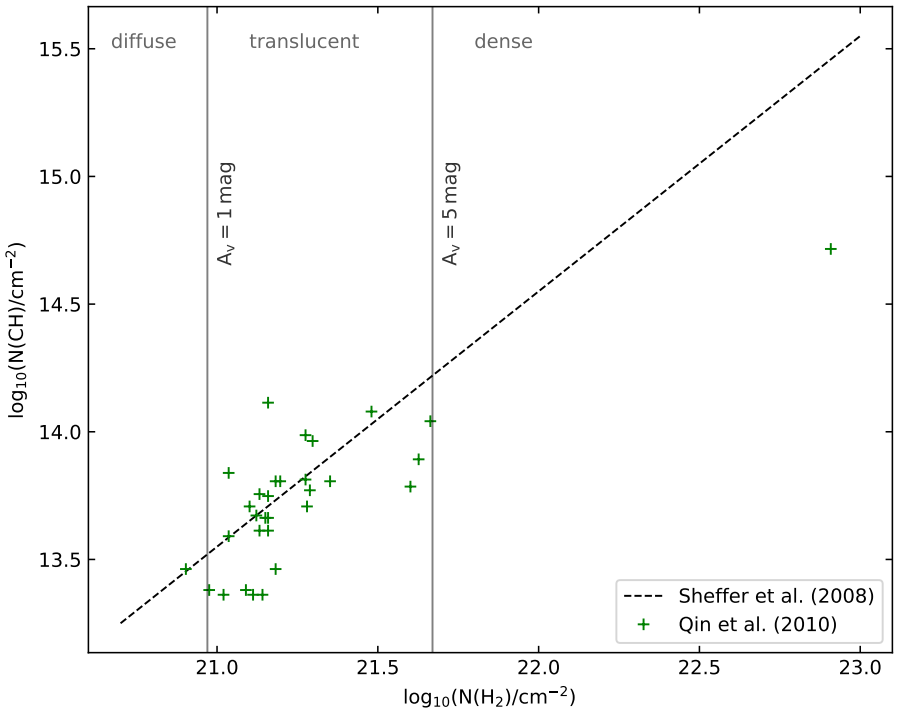

Figure C.78: Based on Fig. 2 of Qin et al. (2010). We rescaled the H_2 values, which they derived from HCO^+ assuming a uniform abundance, using the HCO^+ abundance profile discussed in Sect. 5.5.1. The CH column densities in the translucent regime now follow the same correlation with H_2 as derived for diffuse clouds by Sheffer et al. (2008).

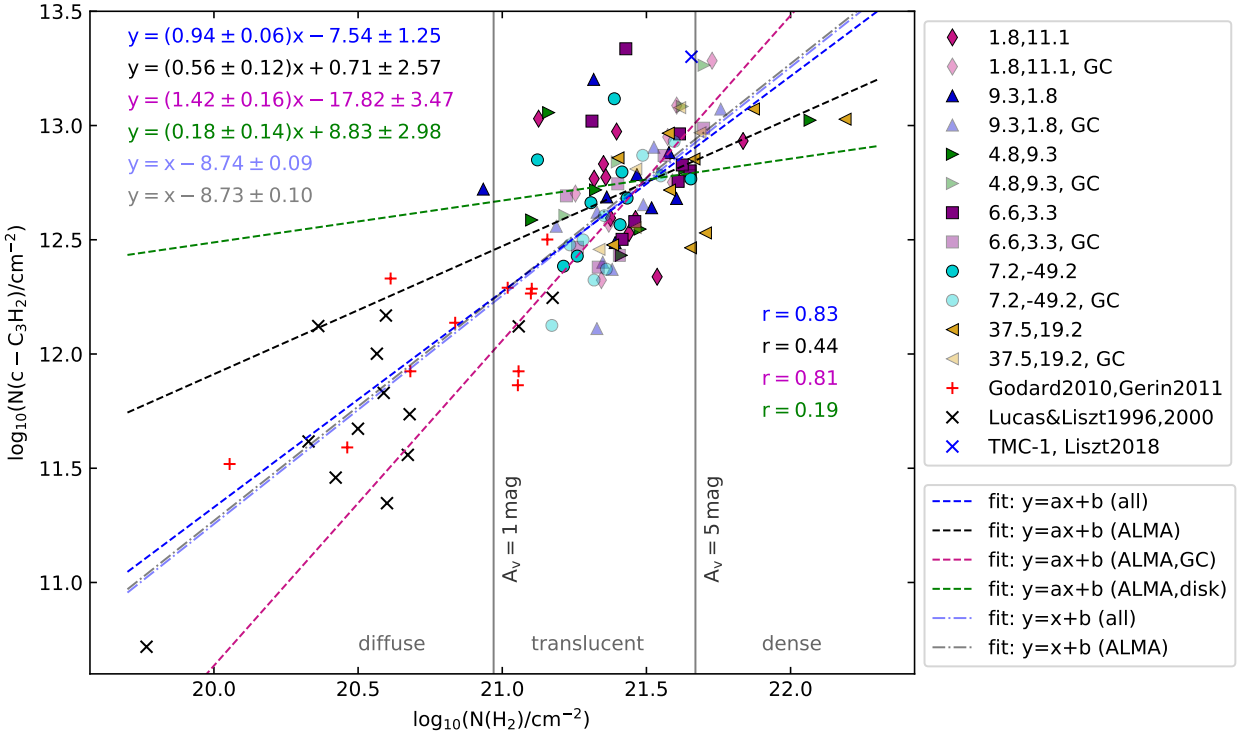

Figure C.79: Same as Fig. 5.26, but for c-C_3H_2. The blue cross represents the translucent cloud TMC-1 (Liszt et al. 2018).

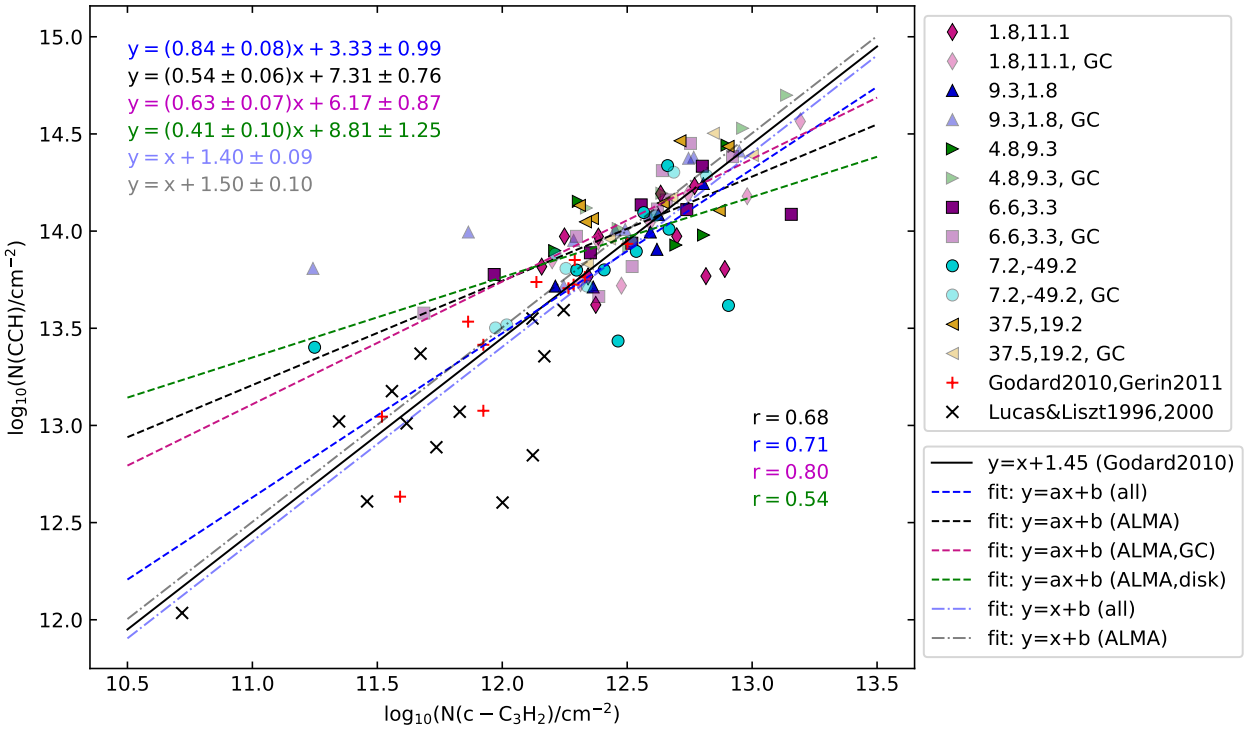

Figure C.80: Same as Fig. 5.26, but CCH plotted against c-C_3H_2. The black line represents a linear fit using only data of diffuse molecular clouds (Godard et al. 2010).

List of Figures

List of Tables